DOE/NASA/0065-83-1
NASA CR 168053

Improved Transistor - Controlled and Commutated Brushless DC Motors For Electric Vehicle Propulsion

(NASA-CR-168053) IMPROVED TRANSISTOR-CONTROLLED AND COMMUTATED BRUSHLESS DC MOTORS FOR ELECTRIC VEHICLE PROPULSION Final Report (Virginia Polytechnic Inst. and State Univ.) 402 p N84-10450 Unclas G3/33 42260

N. A. Demerdash, R. H. Miller, T. W. Nehl, and T. A. Nyamusa
Virginia Polytechnic Institute and State University

January 1, 1983

Prepared for
National Aeronautics and Space Administration
Lewis Research Center
Under Contract DEN 3-65

for

U.S. DEPARTMENT OF ENERGY
Conservation and Renewable Energy
Office of Vehicle and Engine R&D

DOE/NASA/0065-83-1
NASA CR 1658053

Improved Transistor-Controlled and Commutated Brushless DC Motors for Electric Vehicle Propulsion

N. A. Demerdash, R. H. Miller, T. W. Nehl, and T. A. Nyamusa
Virginia Polytechnic Institute and State University
Blacksburg, Virginia 24061
Key Personnel: B. P. Overton, C. J. Ford, and F. A. Fouad

January 1, 1983

Prepared for
National Aeronautics and Space Administration
Lewis Research Center
Cleveland, Ohio 44135
Under Contract DEN 3-65

for
U.S. DEPARTMENT OF ENERGY
Conservation and Renewable Energy
Office of Vehicle and Engine R&D
Washington, D.C. 20585
Under Interagency Agreement DE-A101-77CS51044

TABLE OF CONTENTS

SUMMARY

The development, design, construction, and testing processes of two electronically (transistor) controlled and commutated permanent magnet brushless dc machine systems, for propulsion of electric vehicles are detailed in this report. One machine system was designed and constructed using samarium cobalt for permanent magnets, which supply the rotor (field) excitation. Meanwhile, the other machine system was designed and constructed with strontium ferrite permanent magnets as the source of rotor (field) excitation.

These machine systems were designed for continuous rated power output of 15 hp (11.2 kw), and a peak one minute rated power output of 35 hp (26.1 kw). Both power ratings are for a rated voltage of 115 volts dc, assuming a voltage drop in the source (battery) of about 15 volts. That is, an internal source voltage of 120 volts dc.

Each machine consisted of permanent magnets mounted on the rotor shaft, in addition to a three phase wound armature mounted on the stator. Each machine is controlled by an electronic power conditioner. The power conditioner consists of a two quadrant transistor-based chopper for dc line current and machine torque control purposes, in addition to an inverter/converter arrangement. This inverter/converter portion of the power conditioner consists of a six transistor/antiparallel diode bridge, for inverting dc to ac during motoring, and converting ac to dc during regeneration. One conditioner was designed to operate both the samarium cobalt and strontium ferrite based machines.

Machine-power conditioner system computer-aided simulations were used extensively in the design process. These simulations relied heavily on the magnetic field analysis in these machines using the method of finite elements, as well as methods of modeling of the machine-power conditioner system dynamic interaction. These simulation processes are detailed in this report.

Testing revealed that typical machine system efficiencies at 15 hp (11.2 kw) were about 88% and 84% for the samarium cobalt and strontium ferrite based machine systems, respectively. Both systems met the peak one minute rating of 35 hp. Under a standard SAE drive cycle J227a Schedule D, the cycle efficiencies were found to be 84% and 75%, for the samarium cobalt and strontium ferrite based systems, respectively.

Design Concepts, methods and hardware developed for this system are equally applicable to many other systems such as in electromechanical actuation, industrial and machine tool drives, and robotics.

LIST OF FIGURES

ORIGINAL PAGE IS
OF POOR QUALITY

ORIGINAL PAGE IS
OF POOR QUALITY

LIST OF TABLES

ORIGINAL PAGE IS
OF POOR QUALITY

1.0 INTRODUCTION

1.1 BACKGROUND

Public and U. S. Government attention to the undesirable consequences cf national dependence on foreign sources for supplying the nation's needs of petroleum and its various products has been brought into sharp focus by events which took place in the early 1970's, and continued on throughout the decade of the seventies. A large portion of the nation's petroleum needs is consumed in the form of gasoline used for transportation purposes, particularly in private vehicular use.

A substantial portion of this private vehicular utilization is for purposes of urban and suburban commuting, and other relatively short local trips, for which storage battery powered electric vehicles may be quite suitable. Such electrically powered vehicles appear to represent an attractive alternative, particularly in view of the ease with which one can convert various forms of energy from sources other than petroleum into electric energy. Examples of such alternative "petroleumless" energy sources include:

1. fission type nuclear power plants in which the energy released from the nuclear fuel fission process, in the form of heat, is converted to electric energy by means of conventional steam generator-turbine-generator systems,

2. coal fueled power plants, where heat is again converted to electric energy by means of conventional boiler-turbine generator systems,

3. solar and fuel cells in which solar and chemical energy are converted directly into electricity, and

4. prospective future nuclear fusion based power plants in which generation of electric energy may be accomplished either through a direct energy conversion process, or through conversion to heat, which is then converted to the electric form by means of steam generator-turbine-generator systems, whcih perhaps would be similar in nature to existing conventional systems found in central power stations.

This background of facts and events led the U.S. Department of Energy (DOE) to the initiation of research programs in the areas of electromechanical propulsion and electrical energy storage (battery) research and development. This research included utilization of state of the art technology in the development of improved and new components of electromechanical drive trains for propulsion of electric vehicles. This research effort was managed through an interagency agreement by the National Aeronautics and Space Administration (NASA).

A major component in such a drive train is the prime mover. In this case, the prime mover is a dc electric motor. Usually such a motor is of the conventional brush type traction motor class (series would or heavily compounded shunt motor). Hence, the focus of this investigation was directed toward the development of alternative brushless dc prime mover systems with better potential for further improvements in performance, and perhaps more adaptability to electric passenger vehicle applications.

The recent development of high energy product permanent magnets (rare earth samarium-cobalt alloys), and the development of high power solid state switching devices (power transistors and SCR's) have made it practical to construct electronically commutated brushless dc motor systems, see Reference [1-4].[1] These systems usually consist of an electrical machine connected to a solid state power conditioner (PC). The electrical machine consists of a three phase wound armature mounted on the stator, and a rotor which consists of a steel shaft on which permanent magnets (made from samarium-cobalt or strotium-ferrite for example), are mounted, in order to provide the magnetomotive force necessary for rotor excitation. The three phase armature terminals of the machine are in turn connected to the power conditioner (PC) which consists of a three phase full wave inverter/converter bridge in series with a two-quadrant chopper circuit with its two terminal energy source side connected to the dc source. The dc source is naturally a storage battery in case of installation of such a system in an electric vehicle. A schematic block diagram of such a system is shown in Figure (1.1-1).

Power flows from the dc source to the machine-power conditioner (MPC) system, with the inverter/converter bridge functioning as an inverter during the motoring mode. Also, during motoring the two quadrant chopper may be used for dc line current magnitude limiting and control. Thus, in turn, the chopper controls the motor torque and speed.

Power flows from the mechanical load (stored energy associated with the vehicle inertia and speed), when the machine is functioning as a generator in the regenerative braking mode, while the inverter/converter bridge is functioning as a converter (full wave rectifier bridge). In this regenerative braking mode of operation, the two quadrant chopper

[1] See a separate list of references provided at the end of each chapter in this report.

ORIGINAL PAGE IS
OF POOR QUALITY

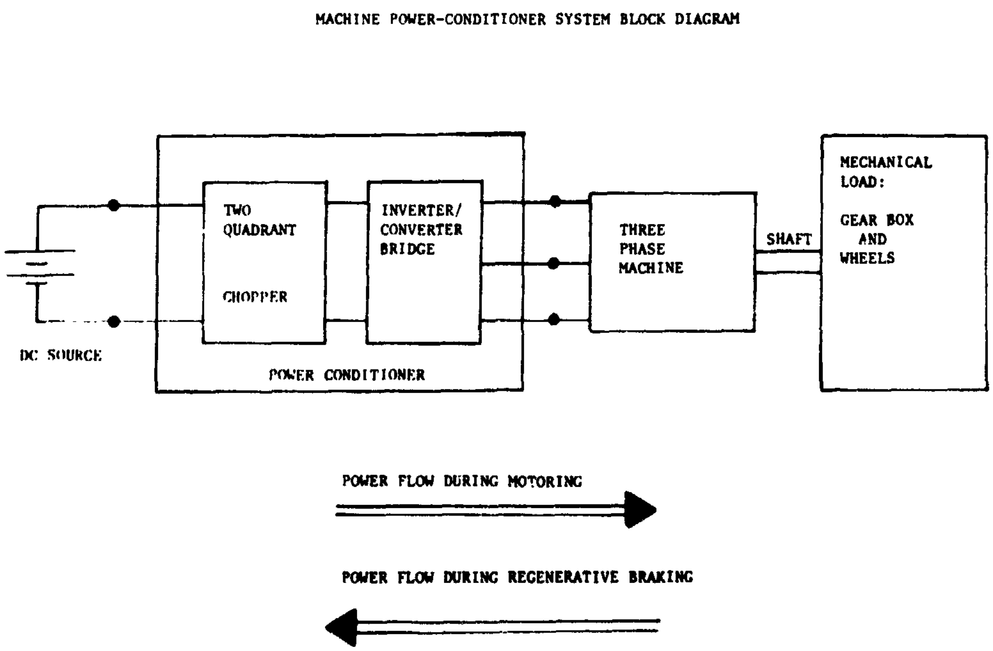

Figure (1.1-1) Functional Block Diagram of a Brushless DC Prime Mover System in an Electric Vehicle from DC Source to Wheels

ORIGINAL PAGE IS
OF POOR QUALITY

is used for dc line current magnitude limiting and control. It also functions as a voltage booster to enable one to feed current into the battery, against the internal dc source (battery) emf. The motoring and regenerative braking modes of operation of the MPC system are required since the system subject of this work must be designed to meet the rigors of the SAE standard J227a - Schedule D, driving cycle, see Reference [5].

A brushless dc MPC system has a number of advantages over a conventional brush type dc traction system. Some of these advantages can be summarized as follows:

1. The elimination of the classical brush type commutator allows one to design such machines for operation at much higher speeds than conventional brush type dc machines. Such high rated speeds lead to considerable reduction in weight and volume of these electronically commutated brushless machines in comparison with brush type machines of the same rated horsepower.

2. The use of permanent magnets leads to the elimination of rotating armatures. Accordingly, with the resulting stationary armature, considerable improvement in the thermal characteristics of such motors can be achieved for a given horsepower rating.

3. The elimination of a rotating armature leads to a number of additional armature winding design simplifications, as well as electromechanical modeling simplifications that render analysis and improvements easier to perform.

4. The brushless MPC systems lend themselves much more readily to further improvements in efficiency and ease of construction resulting from fast developing technologies in solid state power switching, magnet materials, and bearing technology than conventional equivalent systems.

The emergence on the scene of sophisticated computer aided design techniques, has led to the development of very powerful tools for the design of such brushless dc MPC systems. These powerful tools center on

1. the ability to numerically analyze the magnetic fields within machines such as those used in the dc brushless systems at hand, using methods such as the finite element (FE) technique, and hence one can determine with relatively good certainty the values of parameters associated with such machines, as winding inductances, emf waveforms, losses, etc., see References [6] through [9].

2. the ability to use these parameters in models which numerically simulate the dynamic performance of such dc brushless MPC systems, including the effects that such parameters have on the electronic commutation process, etc., see References [4] and [10] through [12].

Accordingly, by means of employing these computer aided design techniques one is able to predict, with a high degree of certainty, peak and rated power capabilities and other critical performance characteristics of such MPC systems during the preliminary design stages. These are the stages during which design modifications, which would be necessary to meet critical performance requirements, can be made easily and without costly modifications to constructed hardware that may otherwise would have been built and found inadequate. This design process will be clearly highlighted and detailed in later chapters of this report.

In light of the above background, the goals set by NASA/DOE were envisaged in two phases for this project, Phase (I) and Phase (II). These goals and the accomplishments achieved throughout this investigation are discussed in Section (1.2) of this report.

1.2 THE PROJECT GOALS AND ACCOMPLISHMENTS

This project was conceived by NASA/DOE to be carried out in two stages or phases, Phase (I) and Phase (II). Phase (I) was envisaged as that during which a functional MPC system (breadboard PC and a preliminary motor) would be built and tested. The experience gained in Phase (I) would serve as the starting point from which Phase (II) of this project would be launched. Phase (II) was envisaged as that portion of the project during which the data base accumulated in Phase (I), in addition to the sophisticated computer aided design methods of References [6-12], would be used to obtain and execute an engineering design of an MPC system (or systems), and test such a system to ensure that it meets all the power and other performance requirements. The Phase (II) design of the MPC system is supposed to bring closer to fruition the goal of practical (or even mass) production of such a system for installation in electric vehicles.

The intended MPC systems to be constructed under Phases (I) and (II) were supposed to provide the capability of propulsion of a 1363 Kg (3000 Lb.) passenger vehicle over a standard SAE J227-a Schedule D drive cycle, of repeated application for two continuous hours, see Reference [5]. This cycle is of a total duration of 122 seconds. According to the specifications of this cycle, Figure (1.2-1), an MPC system must be capable of accelerating such a 1363 Kg vehicle from a speed of zero km/H to a speed of 72.5 km/H (45 mph) in 28 seconds. According to the above drive cycle, this is followed by a 50 seconds period of cruising at 72.5 km/H (45 mph), followed by a period of coasting of 10 seconds, during which a vehicle is brought to stand still (zero speed). To complete the 122 seconds drive cycle, a period of idling 25 seconds long follows the braking period. Also, the intended MPC systems were required to have the capability of propelling such a vehicle at a cruising speed of 88.5 km/H (55 mph) for two hours, as well as propelling the same vehicle at a speed of about 48 km/H (30 mph) over a hill of 10% gradient for a period of one minute.

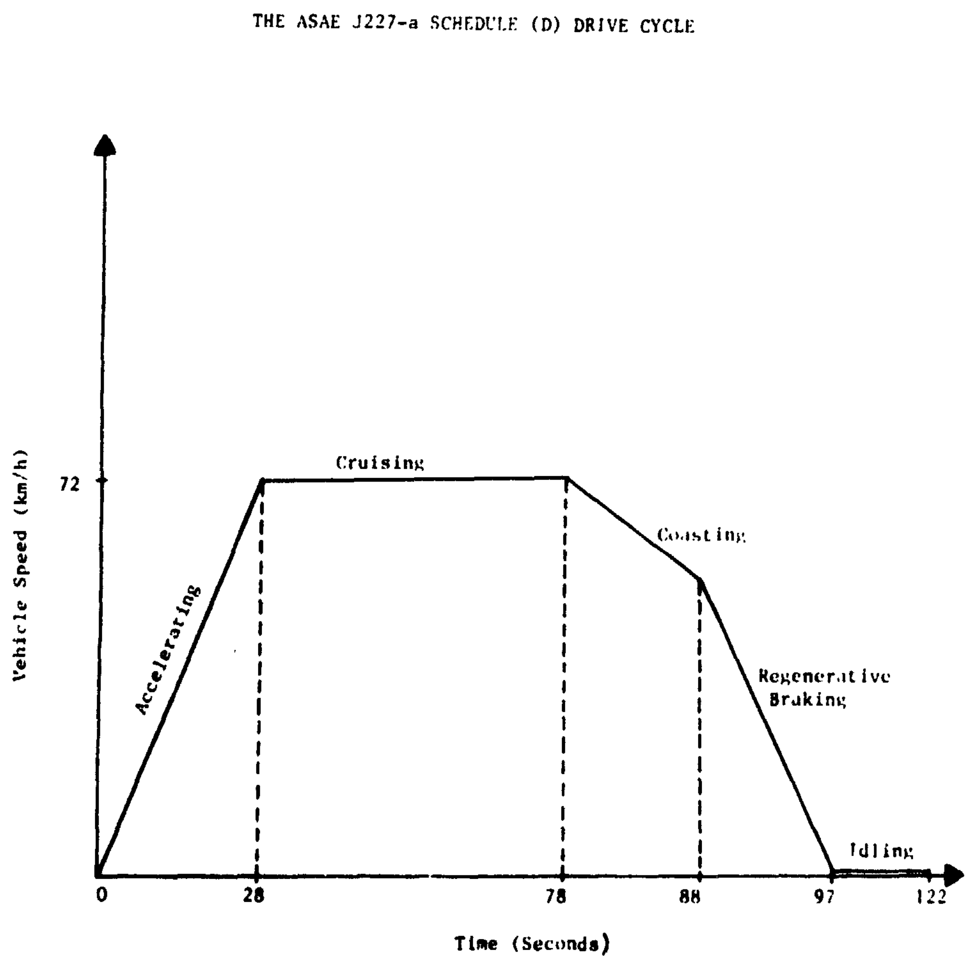

FIGURE (1.2-1) The SAE J227-a Schedule D Drive Cycle

The above design constraints led NASA/DOE to specify that the MPC systems which were to be developed during the course of this investigation, that is Phases (I) and (II), must meet the capability of a continuous two hours rating of 15 hp (11.2 kw) and peak one minute rating of 35 hp (26.1 kw). It was further specified that the tests for peak power rating of 35 hp must immediately follow the two hours 15 hp continuous rating tests, with the machine and power conditioner temperatures at their highest rated values.

It was further stipulated that these MPC systems must be capable of regeneration at rated (15 hp) and peak power (35 hp) conditions. All the above power ratings were to be accomplished using an external dc source of 120 volts.

At this stage, a summary of the salient goals accomplished during Phases (I) and (II) is desirable. It must be emphasized that the main thrust of this report is intended to report the details of the work accomplished in Phase (II) since much of its accomplishments have rendered the work of Phase (I) absolute. Hence, Phase (I) is reported on to the extent necessary to provide the proper background to design decisions taken in the course of performance of Phase (II).

In Phase (I) the following is a summary of the main accomplishments:

1. A 4-pole, samarium-cobalt based permanent magnet, 15 slot three phase armature, brushless dc machine was designed, constructed and tested.

2. A solid state transistor based power conditioner, which consists of a two quadrant chopper in series with a six legged inverter/converter bridge was designed and built in "breadboard" form to operate the 4-pole machine mentioned above.

3. The above MPC system, see the block diagram schematic of Figure (1.1-1), was tested for continuous and peak power rating capabilities, as well as losses and efficiency. The MPC system was found to be capable of developing a 15 hp output for a period of two continuous hours, at an overall MPC system efficiency of about 78.6%.

The MPC failed during testing to meet the requirement of a peak one minute rating of 35 hp output. The peak one minute rating was found to be about 22 hp. This limitation was not due to the motor, which could have met that output requirement of 35 hp easily on the basis of both its tested thermal, electromagnetic, and mechanical characteristics. However, the power conditioner was found to be the weak link in that Phase (I) MPC system. Voltage transients across the power transistors led to failure of switching elements in the inverter/converter bridge, as well as in the chopper at ratings higher than 22 hp output. Major design changes in the power conditioner would have been required. These changes were beyond the scope of Phase (I), and were left for the Phase (II) effort of designing, constructing and testing an improved power conditioner. Further details on the Phase (I) system are to be found in Appendices (5) and (12).

The experience with the motor of Phase (I) highlighted the high cost of rare earth samarium cobalt materials, and the difficulties which may be encountered wtih cobalt with regard to availablity and security of supply. This would be an important factor if such a motor design gained widespread use in vehicular propulsion. These aspects prompted these investigators in concurrence with NASA/DOE to obtain two different designs for the machine associated with this MPC system. The first design was an improvement on the Phase (I) motor, with samarium-cobalt still used as a permanent magnet material, for supplying rotor excitation. The second design was developed assuming the use of the cheaper and more readily available strontium ferrite as the permanent magnet material used for rotor excitation. Both designs were implemented in such a manner that both machines can be operated from the same power conditioner. Accordingly, the following is a summary of the main accomplishements achieved during the course of Phase (II):

1. A 6-pole, samarium cobalt based permanent magnet, 18 slot three phase armature, brushless dc machine was designed, constructed and tested.

2. A 6-pole, strontium ferrite based permanent magnet, 18 slot three phase armature, brushless dc machine was designed, constructed and tested

3. A solid state transistor based power conditioner, was designed and built to operate both of the samarium-cobalt based and strontium-ferrite based machines of Phase (II). The power conditioner consists of a two quadrant chopper in sines with a six legged inverter/converter bridge.

4. The above power conditioner, see the block diagram schematic of Figure (1.1-1), was tested for operating the samarium cobalt based and strontium ferrite based machines mentioned above.

(4.a) In case of operation of the Phase (II) power conditioner (PC) in conjunction with the samarium cobalt based machine of Phase (II), the MPC system was found to be capable of developing a 15 hp output for a period of two continuous hours, at an overall MPC system efficiency of about 87%. Furthermore, the MPC system achieved the requirement of a a peak one minute rating of 35 hp output at an overall MPC system efficiency of 77%.

(4.b) In the case of operation of the Phase (II) power conditioner (PC) in conjunction with the strontium ferrite based machine of Phase (II), the MPC system was found to be capable of developing a 15 hp output for a period of two continuous hours, at an overall MPC system efficiency of about 84%. Furthermore, the MPC system achieved the requirement of a peak one minute rating of 35 hp output at an overall MPC system efficiency of 71%.

The following chapters will detail the steps of development of preliminary designs, final designs, construction, testing and performance characteristics of both systems of Phase (II). Specifically, Chapter (2.0) is dedicated to the MPC system component description, motor-power conditioner interaction, and discussion of the key design paramters. In Chapter (3.0) the preliminary designs fo the samarium cobalt based, an strontium ferrite based machines are arrived at, then analyzed by state of the art computer aided design methods, using finite elements for motor parameter determination, and dynamic simulation methods for motor-power conditioner performance analysis. On the basis of these analysis results, both machine designs are finalized in Chapter (3.0). In Chapter (4.0) the PC design steps are detailed. Meanwhile, in Chapter (5.0) the test procedure, test results and resulting analysis of performance of both motor systems of Phase (II) are given. Based on the results of Chapter (5.0) and the work detailed in the previous chapters an improvement assessment is made in Chapter (6.0) for both machines of Phase (II) and their power conditioner.

REFERENCES

1. Delco Electronics, "Final Report on the Electromechanical Flight Control Actuator," Final Report NASA-JSC Contract No NAS9-14952, General Motors Corporation, Delco Electronics Div., Santa Barbara Operations, Goleta, CA, 1978.

2. Sawyer, B. and Edge, J. T., "Design of a Samarium-Cobalt Brushless DC Motor for Electromechanical Actuator Applications," Proceedings of the IEEE-National Aerospace and Electronics Conference, Dayton, Ohio, 1977.

3. Edge, J. T., "An Electromechanical Actuator Technology Development Program," Paper No. 780581, Society of Automotive Engineers, Proceedings of the Aerospace Fluid Power and Control Technologies Symposium

   1978.

4. Demerdash, N. A., and Nehl, T. W., "Dynamic Modeling of Brushless DC Motors for Aerospace Actuation," IEEE Transactions on Aerospace and Electronic Systems, Vol. 16, No. 6, 1980, pp. 811-821. [See Appendix (7).]

5. "Electric Vehicle Test Procedure-SAE J227a," Society of Automative Engineers, Inc., 1976.

6. Fouad, F. A. , Nehl, T. W., and Demerdash, N. A., "Magnetic Field Modeling of Permanent Magnet Type Electronically Operated Synchoronous Machines Using Fintie Elements," IEEE Transactions on Power Apparatus and Systems, PAS-Vol. 100, 1981, pp. 4125-4135. [See Appendix (1).]

7. Fouad, F. A., Nehl, T. W., and Demerdash, N. A., "Permanent Magnet modeling for Use in Vector Potential Finite Element Analysis in Electrical Machinery," IEEE Transations on Magnetics, Vol. MAG-17, 1981, pp. 3002-3004. [See Appendix (2).]

8. Nehl, T. W., Fouad, F. A. and Demerdash, N. A., "Determination of Saturated Values of Rotating Machinery Incremental and Apparant Inductance by a Perturbation Method." IEEE Transactions on Power Apparatus and Systems, PAS-Vol. 101, 1982, pp. 4441-4451. [See Appendix (3).]

9. Demerdash, N. A., Fouad, F. A., and Nehl T. W., "Determination of Winding Inductances in Ferrite Type Permanent Magnet Electric Machinery by Finite Elements," IEEE Transactions

on Magnetics, Vol. MAG-18, 1982, pp. 1052-1054. [See Appendix (4).]

10. Nehl, T. W., Fouad, F. A., Demerdash, N. A., "Digital Simulation of Power Conditioner-Machine Interaction for Electronically Commutated DC Permanent Magnet Machines," IEEE Transactions on Magnetics, Vol. MAG-17, No. 6, 1981, pp 3284-3286. [See Appendix (6).]

11. Nehl, T. W., Fouad, F. A., Demerdash, N. A., and Maslowski, E., "Dynamic Simulation of Radially Oriented Permanent Magnet Type Electronically Operated Synchronous Machines With Parameters Obtained from Finite Element Field Solutioins," IEEE Transactions on Industry Applications, Vol. IA-18, No. 2, pp. 172-182, 1982. [See Appendix (5).]

12. Nehl, T. W., Demerdash, N. A., Fouad, F. A., "Impact of Winding Inductances and Other Parameters on the Design and Performance of Brushless DC Motors," Paper accepted for publication in the IEEE Transactions on Power Apparatus and Systems, and Presentation at the 1984 IEEE-PES Winter Meeting, Dallas, Texas. [See Appendix (8).]

2.0 GENERAL DESCRIPTION OF MOTOR-CONDITIONER SYSTEM

2.1 MOTOR-CONDITIONER SYSTEM COMPONENTS

The major components of the motor-conditioner system are the motor, which converts the energy from electrical to mechanical form, the power electronics, which convert the electrical energy from dc to ac of the proper frequency and phase (and vice-versa during regenerative braking), and the low-level electronics, which receive information concerning the state of the system and the desired operation and furnish the appropriate control signals to the power electronics. This arrangement is shown schematically in Figure (2.1-1). Each of these major components can be divided into smaller component groupings. These more detailed component groupings are described below.

The motor itself can be divided into several components. The rotor consists of a shaft on which are milled six flat surfaces for mounting the magnets. These magnets (either samarium-cobalt or strontium ferrite) furnish the magnetic excitation for the field of the machine. The region of the shaft on which the magnets are mounted serves as a yoke for conducting the flux between poles. Surrounding these magnets is a non-magnetic steel sleeve which serves to hold the magnets securely in place. After this sleeve has been shrunk into place, the entire rotor assembly is plotted to insure dimensional stability of the magnet positions. This rotor is mounted to the stator by means of sealed ball bearings.

The stator consists of the housing, the lamination stack, and the windings. The totally enclosed, non-ventilated housing, which protects the motor from dust and other adverse environmental factors, is made of black anodized aluminum for good heat transfer. The silicon steel laminations have eighteen slots, as shown in Figure (2 1-2) for the samarium-cobalt and strontium ferrite machines. These eighteen slots provide for one slot per phase per pole. In each slot are four coil sides, each coil consisting of four turns, each turn consisting of 12 strands of No. 16 AWG magnet wire. The coils are connected in series into two windings per phase. These windings can be connected in series for low speed, high torque operation or in parallel for high speed, low torque operation.

Attached to the motor at the end opposite the output shaft end is a position sensor. The fuction of this sensor is to measure the rotor position at 30° (electrical) intervals and to transmit this information to

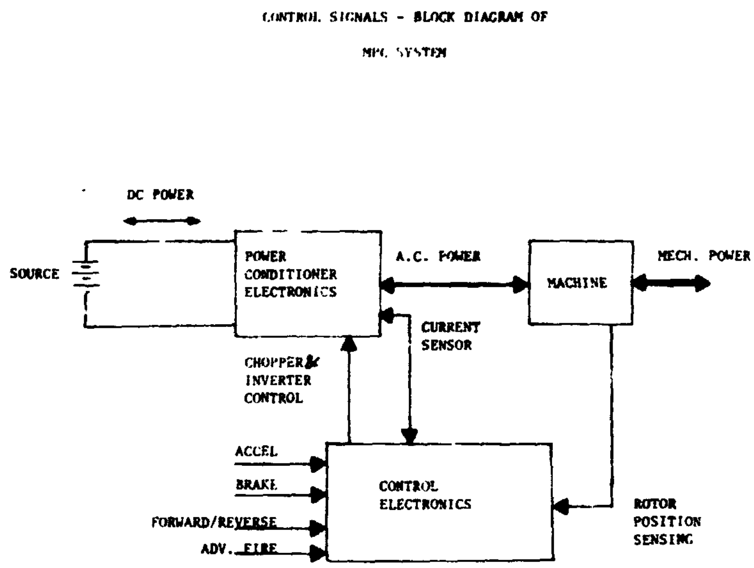

FIGURE (2.1-1) Block Diagram of Motor-Conditioner System

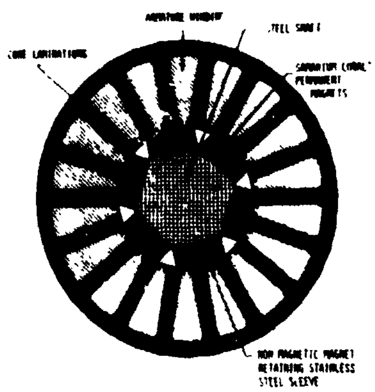

Cross-Section of the Samarium-Cobalt Motor-Outer Lamination Diameter = 6.518 Inches (16.556 cm)

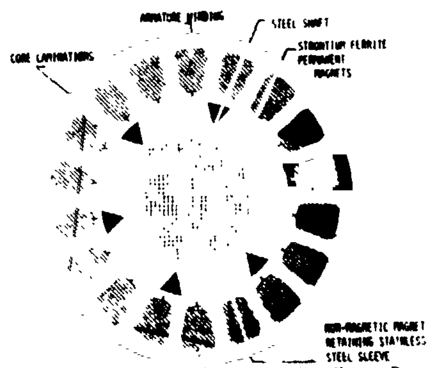

Cross-Section of the Ferrite Motor-Outer Lamination Diameter = 6.518 Inches (16.556 cm)

FIGURE (2.1-2) Stator Laminations for Samarium Cobalt and Strontium Ferrite Based Machines the low-level control electronics for processing. This sensor consists of a set of six magnets attached to the rotor which set up a radial field pattern similar to the main field. On the stator, just outside of these magnets are mounted two sets of three Hall sensors each. Within each set, these sensors are mounted 120 electrical degrees apart. When acted upon by the magnets, which have a flux pattern which changes every 180 electrical degrees, an appropriate change occurs in the electrical output every 60 electrical degrees. The second set of Hall-Effect sensors is identical to the first, but is mounted at a position equivalent to 30 electrical degrees away from the first set. This provides a second set of switching signals in the proper phase to provide for advanced firing of the inverter transistors when this is necessary.

The signals from the rotor position sensor, processed by the low-level electronics, control the power electronics so as to apply to the motor the phase current pattern shown in Figure (2.1.3). In this figure, the commutation of the phase currents is accomplished by the three phase inverter/converter (motoring/regenerative braking) bridge comprising the six transistors, Q_1 through Q_6, and the six diodes, D_1 through D_6. The current control is accomplished by the two quadrant chopper comprising transistors Q_M and Q_B diodes D_M and D_B.

In the motoring mode the chopper regulates the current to the motor by turning on Q_M if the inductor current is too low. When the inductor current has increased by a predetermined increment beyond the set value, Q_M turns off, and the inductor current flows through diode D_M until it has decreased to the value which causes Q_M to turn on. During regenerative braking, the transistor Q_B is turned on until the inductor current has risen by an increment above the set value. Q_B is then turned off, and the inductor current flows through D_B and into the battery.

In the motoring mode, proper switching of Q_1 through Q_6 leads to phase a, b and c waveforms such as are idealized in Figure (2.1-3). In this figure one can see the existence of six distinct armature states. This establishes in the motor a stator (armature) mmf which travels in discrete jumps of 60 electrical degrees. The rotor mmf (magnets) is continually forced to follow that motion. The result is equivalent to a synchronous machine in which the torque angle (between the two mmf's) varies during each switching cycle between an initial 120° and a final 60° electrical angle. For advanced firing of the transistors, this angle varies between 150° and 90° electrical as shown in Figure (2.1-4).

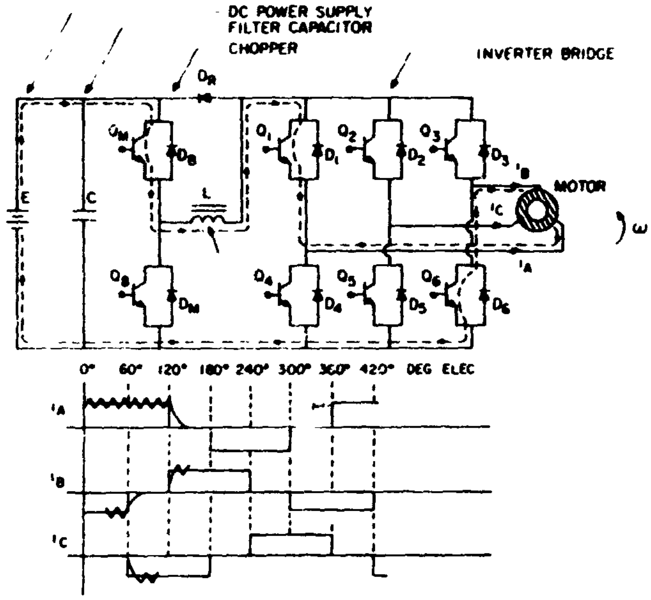

MOTOR POWER CONDITIONER SCHEMATIC AND IDEALIZED MOTOR CURRENTS

FIGURE (2.1-3) Motor-Power Conditioner Network Schematic

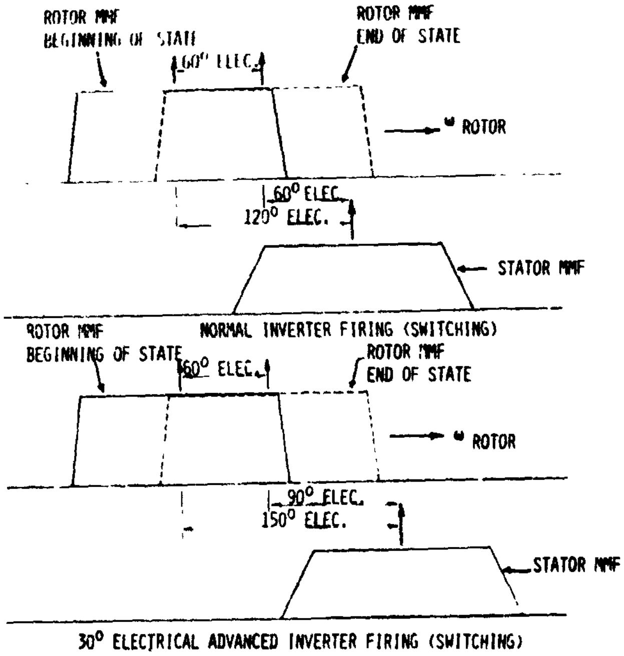

FIGURE (2.1-4) Advanaced Firing Concept

The diodes, D_1 through D_6, provide current paths during the switching operation when the inverter transistors are momentarily off. They also function as a three-phase full wave rectifier bridge in the regenerative braking mode. Diode D_R provides a path for the inductor current during the switching instances when the path through the inverter is momentarily blocked.

In order to minimize the power devices used, which reduces cost, and to prevent any accidental firing of Q_M and Q_B simultaneously, a single transistor was used for both functions. This transistor was switched between the two positions by means of a DPDT relay.

The inductor, L, served to reduce the frequency of the chopper operation, thereby reducing the switching losses. This inductor, consisting of 25 turns of 10 strands of No. 8 AWG magnet wire on a triple thick L-10 core, had an inductance of 425μH at 200A. In order to maintain the hysteresis between turn on and turn off of Q_M within 15A, the maximum chopping frequency is about 4.5KHz.

Each power transistor is driven by a base drive circuit. This circuit receives a signal from the low-level electronics through an optical coupler for voltage isolation and furnishes a current of sufficient amplitude to saturate the power transistors. It is also capable of driving the power transistor base negative with respect to the emitter so as to remove rapidly the stored charge during turn-off. Each base drive circuit is powered by a separate output module of a multiple output d.c. power supply.

In order to prevent excessive voltage spikes during turn-off of the power transistors, each inverter transistor was furnished with a snubber circuit consisting of a diode shunted resistor and a capacitor as shown without detail in Figure (2.1-5). These snubbers were not adequate for the chopper transistor. Therefore, the collector and emitter terminals of this transistor were clamped to the positive and negative busses to further reduce voltage spikes. This method, which is shown in Figure (2.1-6), although very effective in reducing the amplitude of the spikes, caused some increase in switching loss.

The commutation control function of the low-level electronics was accomplished by a pair of 256 x 4 programmable read-only memories (PROMS) type N825126. The configuration of the low-level control electronics is shown schematically in Figure (2.1-7), the eight inputs to these PROMS consisted of the six rotor position sensor outputs together with signals representing the selection of forward/reverse operation and normal/advanced firing of the inverter transistors. Six of the PROM outputs (three from each PROM) were used to control the six inverter transistors. The other output of each PROM was used as an alarm signal to indicate an illegal combination of input signals from the rotor position sensor. Each PROM was equipped with two "inhibit" inputs. One of these inputs was used to shut down the inverter in case of certain alarm signals. The other was used to inhibit the inverter operation in the braking mode.

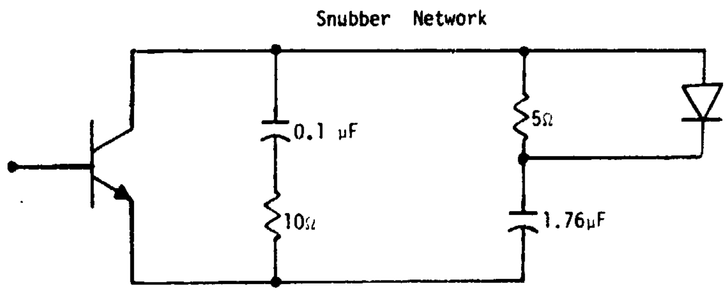

FIGURE (2.1-5) Snubber Network

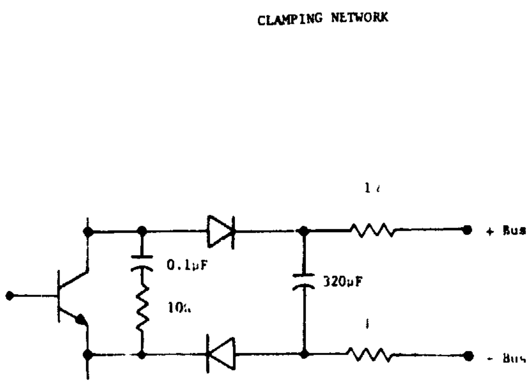

FIGURE (2.1-6) Clamping Network

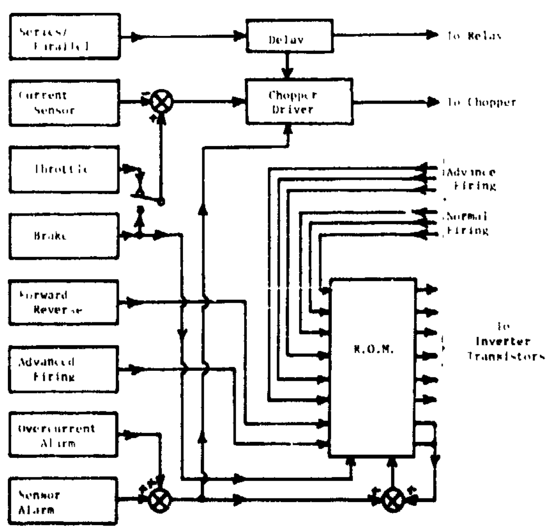

FIGURE (2.1-7) Logic Diagram

ORIGINAL PAGE IS
OF POOR QUALITY

The other major component of the low-level electronics package was the accelerator/brake torque control. This control provided the signal to the chopper transistor to maintain the proper current through the system. Two Hall effect current sensors were placed in series with the filter inductor. One of these was used to measure current in the motoring mode, the other in the regenerative braking mode. Each of these sensors was buffered by an operational amplifier which also served to balance the output to zero when the inductor current was zero. The output of these buffer amplifiers was compared to the buffered output of the accelerator and brake potentiometers. The difference was fed to a pair of op-amps which contained a small amount of positive feedback so as to saturate either positive or negative with enough hysteresis to establish the desired hysteresis in the inductor current. Details with the necessary schematics are given later in Chapter (4.0).

A signal, taken directly from the brake potentiometer, was amplified and used to control the relay which switches the chopper transistor from the motoring to the braking position. A 500 m second pulse generator was used to turn off the chopper transistor during the switching process from motoring to braking or vice-versa. This insured that all switching was done "dry", and permitted the use of a much smaller relay contact than would otherwise have been possible.

A circuit was also provided to control a relay for switching from parallel to series operation of the motor at low-speed, high-torque operation. Since the drive cycle specifications can be met without series operation, this relay has not been included. However, the inclusion of the control electronics would make the addition of such a relay a simple matter. The same pulse generator which turns off the chopper transistor during motoring/braking switching is connected to turn the transistor off during series/parallel switching also, so as to insure "dry" switching.

Three protective circuits have been provided, any one of which, when activated, will inhibit the ROMs and turn off the inverter. The first, which has been mentioned above, is activated by the ROMs themselves in case of an illegal rotor position sensor command. The second responds to a measurement of excessive inductor current. The third detects and responds to an excessive difference between the two current sensors. If any of these alarm signals is activated, an alarm toggle circuit is energized and furnishes the inhibit signal to the ROMs. The low-level electronics package is powered by three separate output modules in the same dc supply package which powers the base drives.

2.2 MOTOR-CONDITIONER INTERACTION

The electromagnetic interactions between the PCU (power conditioner

SIX SWITCH THREE PHASE INVERTER

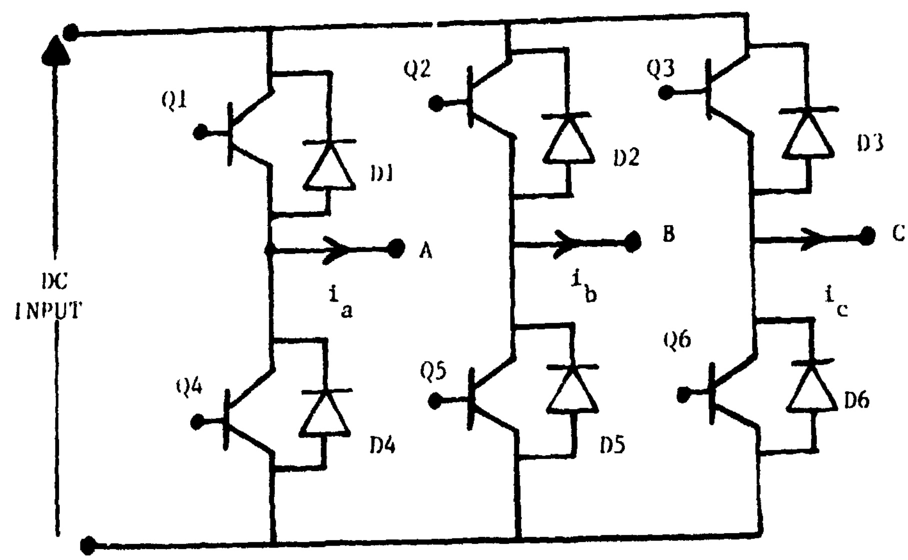

FIGURE (2.2-1) Six Switch, Three Phase Inverter.

unit) and the machine during motoring are explained by examining the relationship between the stator mmf, produced by the injected phase currents, and the mmf distribution produced by the permanent magnet rotor. The stator mmf is produced by the injected three phase currents. The injection of these currents is accomplished by the three phase inverter bridge shown in Figure (2.2-1). The injected phase currents are shown as rectangular blocks of current of 120 electrical degrees duration. The phase relationship between these currents and the open circuit phase to neutral emfs during the motoring mode of operation are given in Figures (2.2-2) and (2.2-3) for 0° and 30° commutation advance, respectively. The status of the six inverter transistors during a complete ac cycle are also given in these figures. Inspection of these figures reveals that each ac cycle can be divided into six discrete current states of 60° electrical duration.

In machines with one slot per pole per phase, as is the case here, the stator winding, when carrying such currents, produces a spatial mmf distribution in the air-gap, such as shown in Figure (2.2-4). This mmf interacts with the spatial air-gap mmf distribution produced by the permanent magnet rotor. These mmfs produce torque on both the rotor and stator assemblies that is proportional in magnitude to the product of the positive mmf peaks times the sine of the angle between them. The magnitude of the stator mmf is proportional to the magnitude of the current flowing in the stator winding, while the rotor mmf is constant because it is supplied by permanent magnets (poles). Therefore, the machine torque is a function of only the stator current and the displacement between the rotor and stator mmfs, as shown in Figure (2.2-5). Examination of the torque equation given in this figure reveals that the average machine torque is maximized by centering the stator phase current conduction period around the point where the rotor and stator mmfs are displaced by 90 electrical degrees, that is zero commutation advance. The conduction period during each current state is for 60 electrical degrees, therefore for maximum average torque, the phase current is switched "on" when the mmfs are 120 degrees apart, and switched "off" when this angle closes to 60 degrees. During one complete period of the stator phase currents (360 electrical degrees) this pattern is repeated six times, resulting in a stator mmf which takes discrete jumps (or hops) of 60 electrical degrees at a time as shown in Figure (2.2-4). The six jumps per cycle result in the idealized torque profile shown in Figure (2.2-5). Machines with mmfs of high harmonic content, on the other hand, produce torque profiles which are more triangular in nature with sharper peaks depicted by the dashed line.

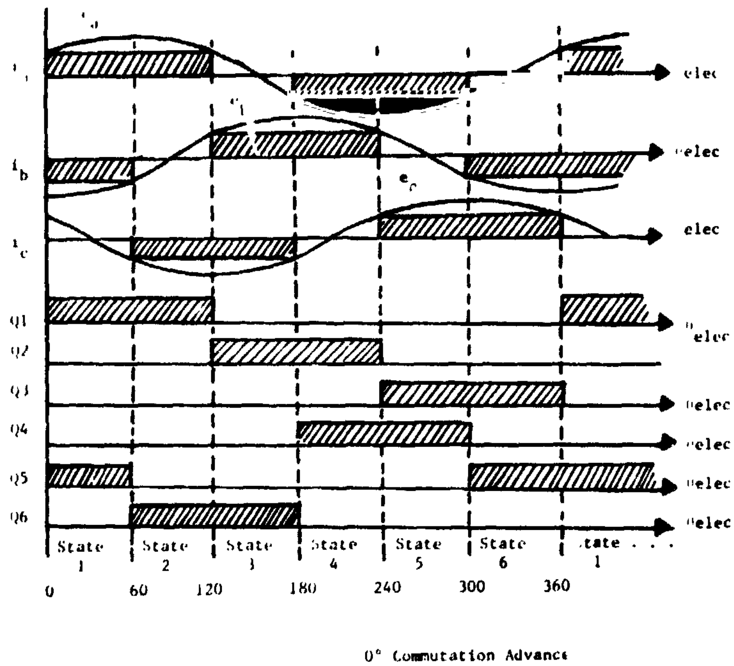

FIGURE (2.2-2) Inverter Switching Sequence During Motoring, 0° Commutation Advance.

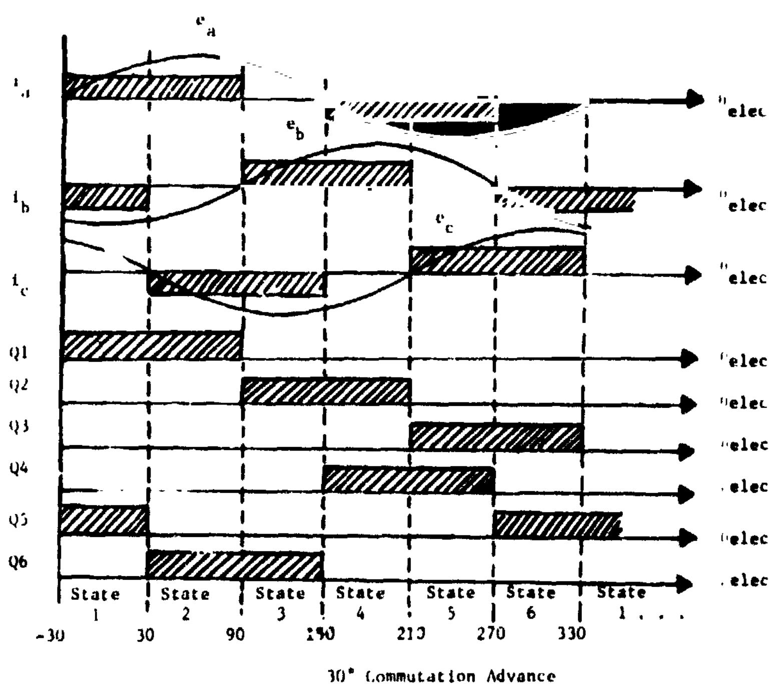

FIGURE (2.2-3) Inverter Switching Sequence During Motoring, 30° Commutation Advance

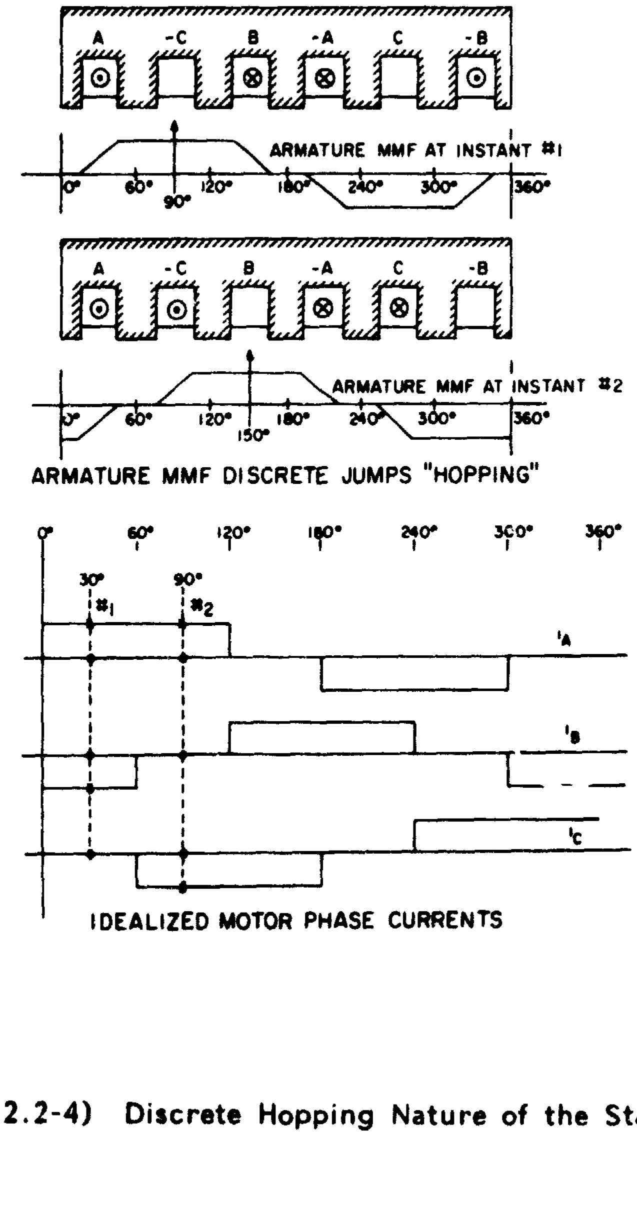

FIGURE (2.2-4) Discrete Hopping Nature of the Stator MMF.

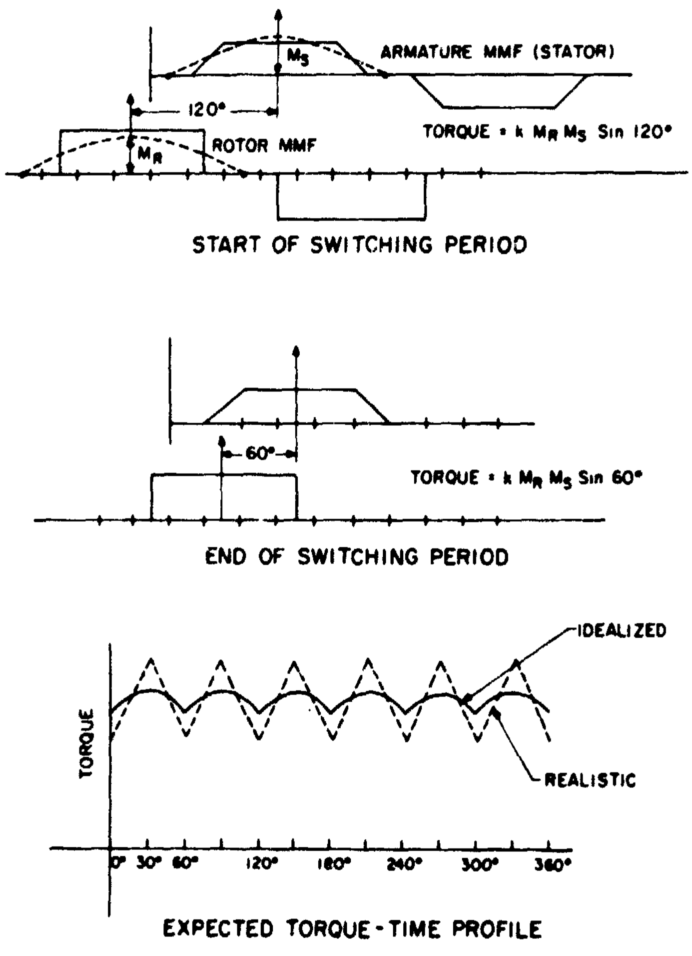

FIGURE (2.2-5) Machine Torque Production

The above description is valid for most loads encountered during the motoring mode of operation including the rated 15 hp point. Under heavy loads, however, such as the peak 35 hp point, the phase currents are injected 30 electrical degrees earlier than in the previous case in order to reduce the magnitude of the phase back emfs opposing the current buildup. This advance in the injection of the phase currents with respect to the phase back emfs is referred to as advanced firing or 30 degree commutation advance. The effects of advanced firing on the overall system performance are discussed in greater detail in the Section (2.3).

In terms of machine torque production, however, the effect of advancing the firing angle is a dramatic increase in machine torque at a given speed due to a higher current buildup, but with a much larger torque ripple. The higher machine torque is due to the increased rate of current buildup in this case.

In terms of the relationship between the stator and rotor mmfs, the advanced firing means that at the beginning of a state these mmfs are separated by 150 degrees electrical. Since the period of a given current state lasts for 60 electrical degrees, the angle between the two MMF's shrinks to 90 degrees electrical at the end of that state. Therefore at the beginning of a state, the electromagnetic torque, T_{em}, is given by

$$T_{em} = kM_RM_S \sin 150°$$

while at the end of a state T_{em} becomes

$$T_{em} = kM_RM_S \sin 90°$$

This pattern is repeated six times per electrical cycle, resulting in the idealized torque profile given by the solid line in Figure (2.2-6). The dashed line represents the corresponding torque profile. For zero commutation advance with the stator and rotor magnitudes of the mmfs M_S and M_R held constant. Notice that the commutation advance of 30 degrees results in a much larger torque ripple (50%) versus (13.4%) for zero advance. There is also a decrease in the average value of the torque constant (sensitivity). In the case of zero advance, the average torque is given by

$$\text{Average } [T_{em_{0°}}] = (6kM_SM_R/2\pi) \int_{60°}^{120°} \sin\theta d\theta = 0.955 \text{ p.u.} \qquad (2.2\text{-}1)$$

For the case of advanced firing we have

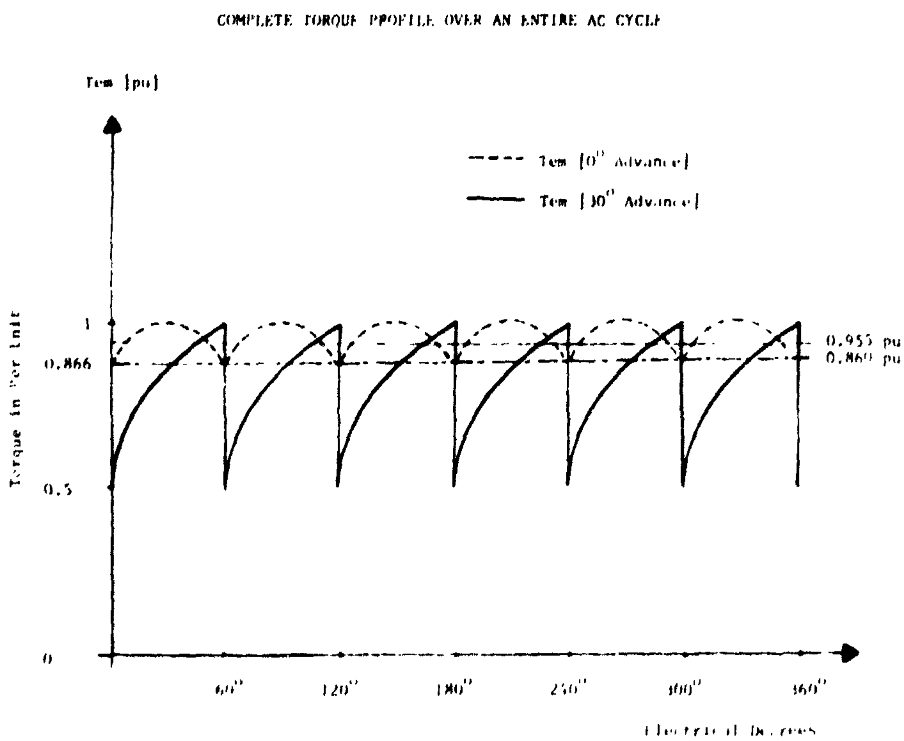

FIGURE (2.2-6) Idealized Machine Torque Profiles with 0° and 30° Commutation Advance

$$\text{Average } [T_{em_{30°}}] = (6kM_S M_R/2\pi) \int_{30°}^{90°} \sin\theta d\theta = 0.827 \text{ p.u.} \quad (2.2\text{-}2)$$

Therefore the percent reduction in the average torque (horsepower) at a given operating point is

$$\text{Torque Reduction} = [(0.955\text{-}0.827)/0.955] \times 100 = 13.4\% \quad (2.2\text{-}3)$$

It will be shown later in this report that this small reduction in the average value of the electromagnetic torque constant is more than compensated for by the much larger values of phase currents, and hence M_S, that can be achieved by advancing the firing by 30 degrees at a given machine speed. In fact it will be demonstrated later by means of both test and simulation results that both the samarium cobalt and strontium ferrite machines could not have reached the peak one minute rating of 35 hp without this shift in the firing angle.

It must be emphasized that the torque profiles given in Figures (2.2-5) and (2.2-6) are only approximate. This is due mainly to the following three factors:

1. The phase currents cannot be switched instantaneously due to winding inductances. Consequently the mmfs do not jump instantaneously during the transition from one current state to another. This point is illustrated in Figure (2.2-7) by means of the idealized and the more realistic torque profiles during advanced firing. The realistic torque profile reflects the fact that in an actual machine the mmf's do not change instantaneously and hence the length of the commutation period, δ_c, is greater than zero.

2. The phase voltages and currents contain harmonics which influence the machine torque. The phase voltages were assumed sinusoidal and the currents rectangular as shown in Figures (2.2-2) and (2.2-3), for purposes of this initial analysis.

3. The effects of magnetic saturation in the machine are neglected for purposes of this initial analysis. These effects are all included later in Chapters (3.0) and (4.0) on the dynamic simulation model of the system.

TORQUE PROFILE WITH 30°e ADVANCED COMMUTATION

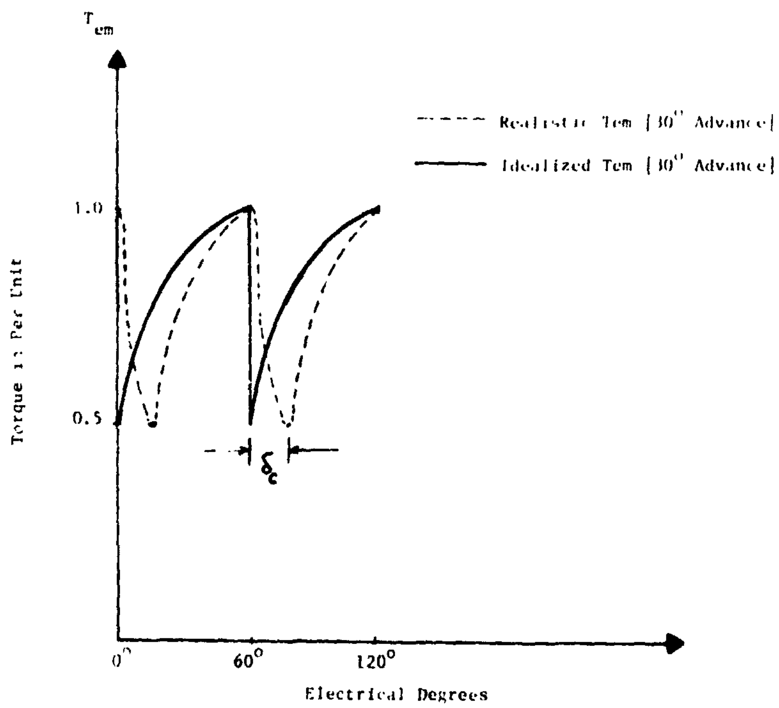

FIGURE (2.2-7) Comparison between Idealistic and Realistic Torque Profile with 30° Commutation Advance

2.3 DISCUSSION OF IMPACT OF KEY DESIGN PARAMETERS ON SYSTEM RATING

The question of whether or not a given machine-power conditioner design can meet its specified ratings depends largely on the behavior of the phase currents during the commutation period. Four factors which strongly influence this behavior are: 1) the maximum dc supply voltage 2) the winding inductances, 3) the induced winding emf waveforms, and 4) the instant in time at which commutation is initiated. In this work, the dc supply voltage was constrained to a maximum value of 120 volts. Therefore, this section will concentrate on the impact of the remaining three factors on the system performance and rating, subject to this dc voltage constraint. The analysis presented in this section is for illustrative purposes only. Details on the computer aided design and analysis performed in support of this project are given in Chapters (3.0) and (4.0).

The key factor affecting the maximum power rating of a given machine-power conditioner system is whether or not a current of a specified magnitude can be successfully commutated from one phase to another at the rated speed. If for example, the winding inductances are too large, then the period required to perform this commutation may exceed the maximum time allowed for this process at the given speed. In such cases, the phase currents would not build up to the specified values, and hence the machine output power would be reduced. The emfs and commutation angle can have similar impact on the machine output.

2.3.1 DESCRIPTION OF COMMUTATION

The rectangular block (wave) nature of the three phase machine currents produces a stator mmf which ideally takes instantaneous jumps of sixty electrical degrees at the onset of each current state. In other words, the phase currents are commutated instantaneously. In reality, the stored magnetic energy associated with the machine windings, due to the winding currents, precludes the possibility of such instantaneous jumps of the stator mmf. The magnitude of the stored energy is proportional to the values of the winding inductances and proportional to the square of the winding currents. Therefore, the winding inductances play a key role in how close to the ideal case would a given machine-power conditioner system behave especially at peak ratings where the winding currents reach their maximum.

Another factor which affects the overall machine-power conditioner rating and performance is the shape and magnitude of the induced winding emf waveforms. In order for the machine to operate in the motoring mode, the line to line induced winding emfs must be lower than the battery voltage minus all the ohmic (iR) drops. The rate of current buildup during this mode of operation is a linear function of the difference between the battery voltage (minus all iR drops), and the opposing winding emf. Since the magnitudes of the winding emfs are linearly proportional to the machine speed, the rate of current buildup is therefore inversely proportional to the machine speed. Consequently, both the shape and magnitude of the emf waveform at a given speed and load are important factors that need to be examined in such systems.

In addition to varying the machine inductances and emfs, one can control the maximum-power rating of the machine-power conditioner system by varying the instant of firing of the inverter transistors with respect to the induced phase winding emfs. The instant of this firing is referred to here as the commutation angle, and was discussed in the previous section.

The impact of these three factors on the system ratings and performance will be illustrated here by means of a typical example. In particular, the process of commutating the current from Phase a to Phase b will be examined in detail.

The current pattern in the machine-power conditioner unit during the transition from positive current in Phase a to positive current in Phase b is shown in Figure (2.3-1). During this commutation period, the current in Phase a decays from its initial average value of 1 pu to zero, while the current in Phase b builds up from a value of zero to 1 pu. The relationship between the phase currents and emfs during this period is displayed in Figure (2.3-2) for the case where there is no commutation advance. The commutation period, τ_C, in this case, is defined as the time interval between the points in time at which transistor Q_1 is switched off (start of commutation) and the point in time at which D_4 ceases conduction (end of commutation).

There are three possible commutation patterns depending upon speed, load, etc. These three patterns are shown in Figure (2.3-3). The first of these, Case 1, occurs when the decaying current, i_a, decreases at a faster rate than the rising current, i_b. This occurs when the machine is operating near maximum speed. The change in the slope of the rising current at the point in time, $t = t_2$, is due to the turn off of diode D_4 when i_a reaches zero. Notice that this causes the chacteristic notch in the current waveform, see Figure (2.3-4). In the second case, the magnitudes of the slopes of i_a and i_b are equal. This is due to equal time constants associated with the transients of the decaying and rising currents. In this case there is no reflected transient in i_c. The third case occurs at low machine speeds when the rising current, i_b, increases at a more rapid rate than the rate at which the current, i_a, decreases. Notice that in this case the current transient is a spike rather than a notch.

The Machine Power-Conditioner (MPC) System

During a Commutation Period

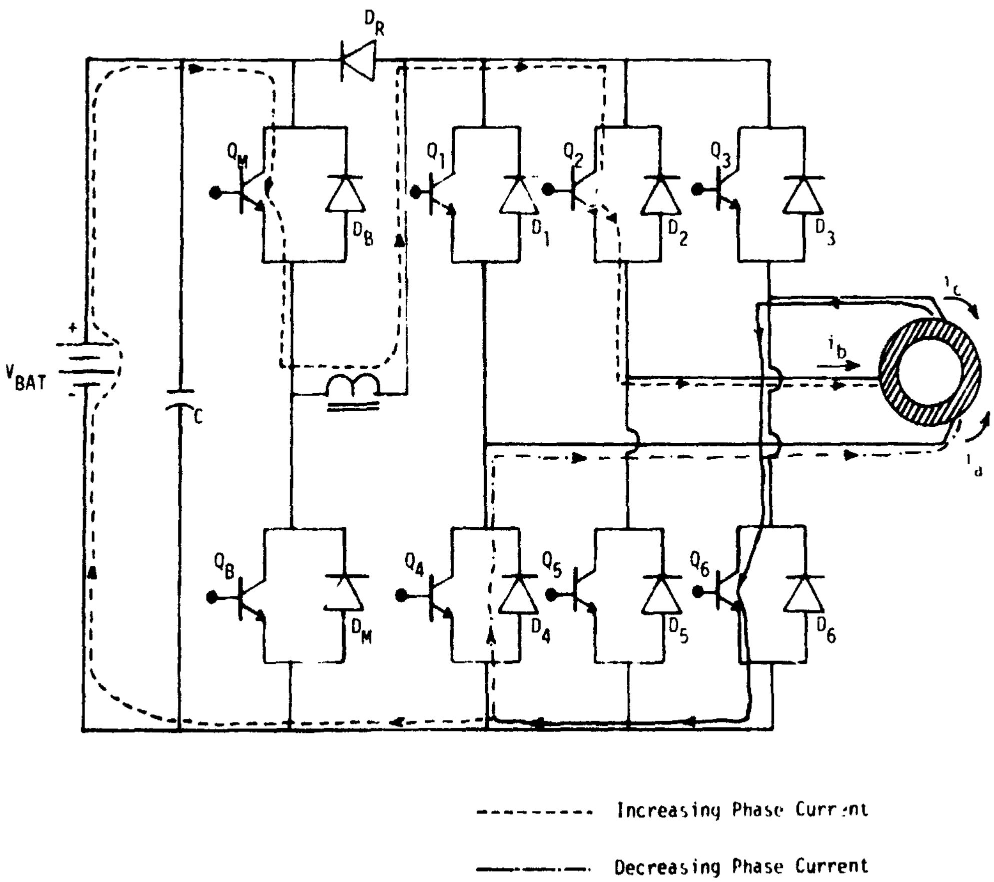

FIGURE (2.3-1) Current Patterns During the Commutation of Current from Phase (a) to Phase (b)

Commutation of Phase Currents with o° Advance

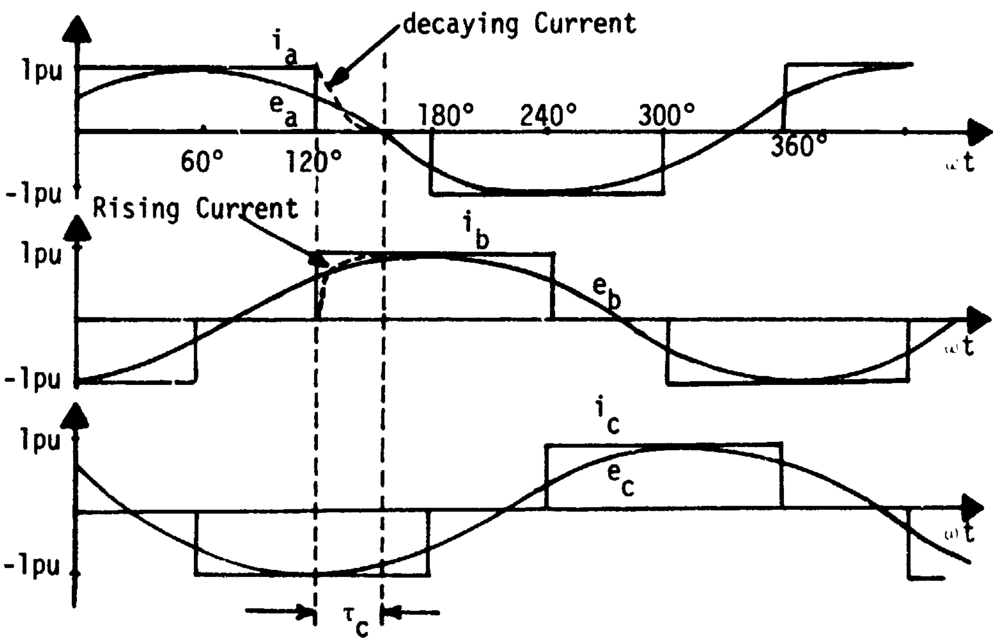

$$e_a = E\,sin(\omega t + 30 - \delta c)$$

$$e_b = E\,sin(\omega t - 90 - \delta c)$$

$$e_c = E\,sin(\omega t - 210 - \delta c)$$

FIGURE (2.3-2) Status of Phase Currents and EMFs During Commutation of Phase Current From Phase (a) to Phase (b), With a Commutation Advance Angle, δ_c = 0°.

Phase Current Spikes During Commutation

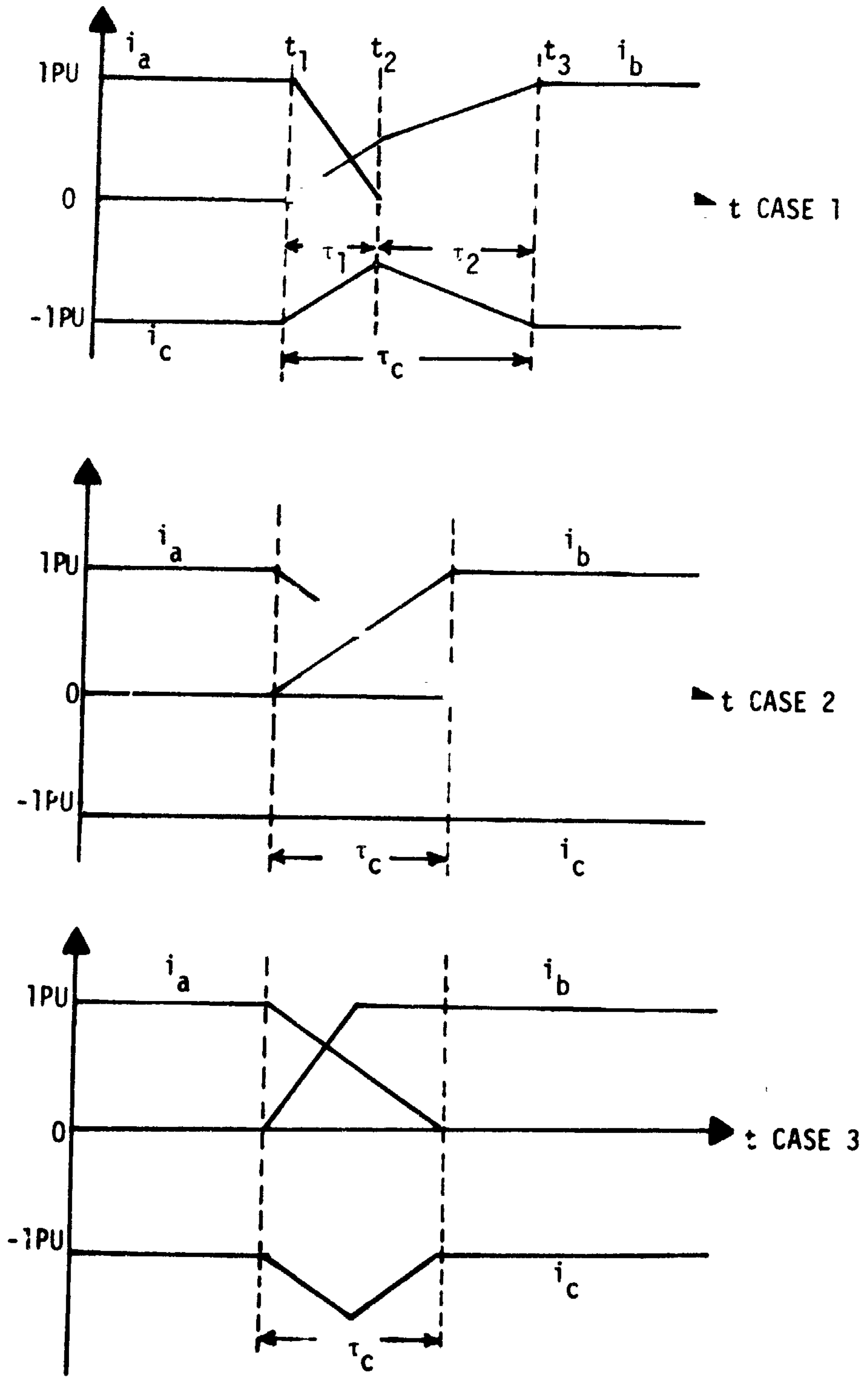

FIGURE (2.3-3) Behaviour of Phase Currents During Commutation

COMMUTATION TIME CONSTANTS DEPICTED BY OSCILLOGRAM OF PHASE CURRENT

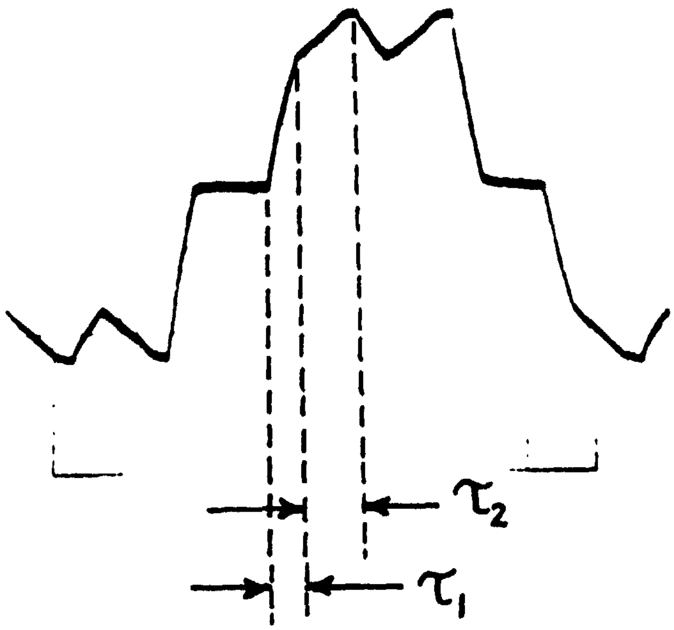

FIGURE (2.3-4) Actual Shape of the Phase Current at Rated Load Showing Commutation Periods, τ_1 and τ_2.

Attention here will be focused on the first case, since it is applicable at the maximum power points, and therefore is important in determining the maximum rating of a given MPC system. The commutation period will be divided into two regions. The first, τ_1, corresponds to a period in which i_a decays to zero through diode, D_4, while the second covers the period after D_4 turns off. This is the time during which i_b is still increasing, and occurs before diode, D_R, turns off, see Figure (2.3-3). The actual shape of the Phase current under these conditions is shown in Figure (2.3-4).

Simplified network models of the machine-power conditioner during these two periods are given in Figures (2.3-5) and (2.3-6), respectively. Notice that during both τ_1 and τ_2 the chopper inductor, L_{CH}, is effectively shorted by the diode, D_R. This is due to the fact that there is no path for the entire chopper inductor current through the inverter during the commutation period. Immediately after the completion of commutation, diode, D_R, turns off and the circuit of Figure (2.3-7) can be used to approximate the MPC system performance. The machine model per Phase, in all three cases consists of a series connected resistance, inductance, and induced emf.

THE FIRST COMMUTATION INTERVAL, τ_1

The first commutation interval, τ_1, lasts from time, $t = t_1$, to $t = t_2$, see Figure (2.3-3). This is the period during which both diodes, D_4 and D_R, are conducting. During this period, the Phase a current decays through diode, D_4 while the Phase b current increases through transistor Q_2. The diode, D_R, provides a path for the chopper inductor current which is larger than the current through Phase b. The current passing through D_R is equal to the difference between the choke current and the Phase b current. To simplify the analysis, and to avoid obscuring the discussion on the effects of the various factors on the system rating, the voltage drops in the switching elements will be neglected in this discussion. However, these voltage drops were not neglected in the design calculations. It also must be pointed out that these voltage drops are included in the detailed computer aided analysis of the system performance which is given in Chapter (4.0).

EQUIVALENT NETWORK MODEL OF MPC SYSTEM - DURING COMMUTATION

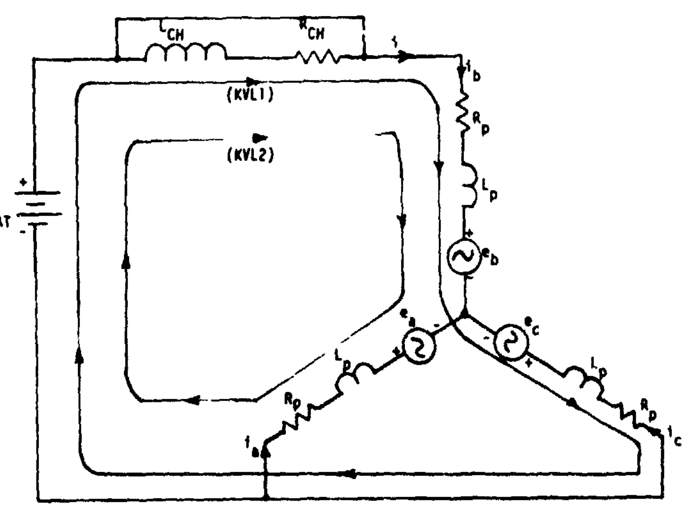

FIGURE (2.3-5) Equivalent Circuit Model of MPC System During Commutation of Current from Phase a to Phase b Before the Recovery of Diode, D_R and D_4.

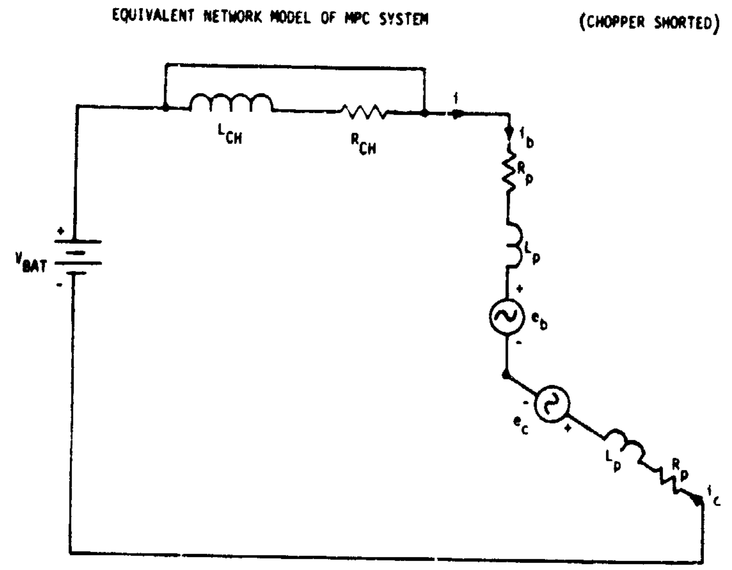

FIGURE (2.3-6) Equivalent Circuit Model of MPC System During Commutation of Current from Phase a to Phase b Before the Recovery of Diode, D_R and, After Recovery of Diode, D_4.

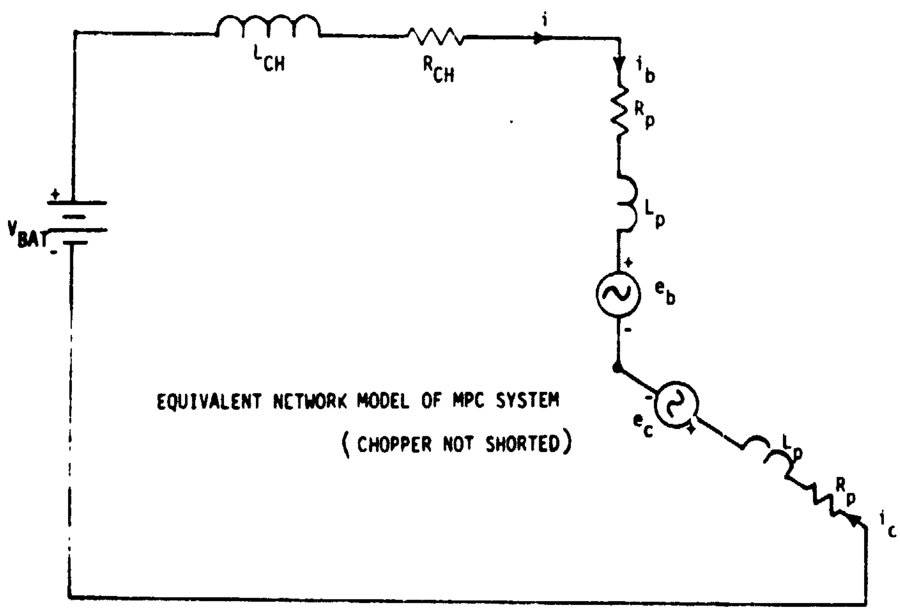

FIGURE (2.3-7) Equivalent Circuit Model of MPC System at Completion of Commutation, Diodes, D_R and D_4 Recovered.

Based upon the above mentioned assumptions, one can obtain the time derivative of i_b by writing two Kirchoff voltage loop equations for the loops shown in Figure (2.3-5), in addition to one Kirchoff current equation at the neutral. After some simplifications this yields the following:

$$(di_b/dt) = [(2/3)V_{BAT} - R_p i_b - e_b]/L_p \tag{2.3-1}$$

The Phase to neutral voltages, e_a, e_b, and e_c, are defined in Figure (2.3-2), and below as follows:

$$e_a = E\sin(\omega t + 30° - \delta_c) \tag{2.3-2}$$
$$e_b = E\sin(\omega t - 90° - \delta_c) \tag{2.3-3}$$
$$e_c = E\sin(\omega t - 210° - \delta_c) \tag{2.3-4}$$

where, δ_c is the commutation advance in electrical degrees. The amplitude of these emfs, E, is linearly proportional to the machine speed, N(RPM). The measured emf constants E_{sc} and E_{sF} for the samarium cobalt and strontrium ferrite machines respectively are

$$E_{SC} = 0.00689N \quad \text{Volts} \tag{2.3-5}$$

$$E_{SF} = 0.00600N \quad \text{Volts} \tag{2.3-6}$$

The measured values of effective winding inductances (phase-to-neutral = half-line-to-line) for the two machines are designated as $L_{P_{SC}}$ and $L_{P_{SF}}$ for the samarium cobalt an strontium ferrite machines, respectively, and have values as follows:

$$L_{P_{SC}} = 44.95 \quad \mu H \tag{2.3-7}$$
$$L_{P_{SF}} = 46.00 \quad \mu H \tag{2.3-8}$$

The phase to netural winding resistances were also measured and were found to be equal to

$$R_{P_{SC}} = 0.00235 \quad \text{Ohms} \tag{2.3-9}$$
$$R_{P_{SF}} = 0.00245 \quad \text{Ohms} \tag{2.3-10}$$

Substitution of these machine parameters, in conjunction with an assumed battery voltage of 115 volts yields two expressions for the time derivative of i_b, namely

$$di_b/dt|_{SC} = [76.67-0.00235i_b-0.00689N\sin(\omega t-90°-\delta_c)]/44.95 \times 10^{-6}$$
$$= 1.706 \times 10^6-52.28i_b - 153.3N\sin(\omega t - 90° - \delta_c) \tag{2.3-11}$$

and

$$di_b/dt|_{SF} = [76.67-0.00245i_b-0.006N\sin(\omega t-90°-\delta_c)]/46.00 \times 10^{-6}$$
$$= 1.667 \times 10^6-53.26i_b-130.4N\sin(\omega t-90°-\delta_c) \qquad (2.3\text{-}12)$$

Inspection of Figures (2.3-2) and (2.3-3) reveals that at the beginning of the commutation period under consideration $t = t_1$, ωt equals 120 electrical degrees. Substitution of ωt = 120 electrical degrees into Equations (2.3-11) and (2.3-12) gives the initial rate of current buildup at the start of the commutation period. The value of this initial di/dt is a key factor in determining the peak rating of the MPC system. This is the case because the rate of current rise is maximum at this point due to the fact that the induced emf opposing current buildup as well as the voltage drop from the winding resistance are both at their minimums. Because of the finite amount of time available to commutate the Phase currents, the peak rating of such MPC systems at a given speed is directly related to the values of the initial rates of current buildup.

In order to illustrate these points, Equation (2.3-11) should be used to approximate the behavior of i_b during the first commutation interval, τ_1, for the samarium, cobalt machine. Let it be assumed that the maximum period available during this interval is thirty electrical degrees, which is a reasonable assumption based upon experience with oscillograms of the Phase currents of such MPC systems at rated condition. Based upon this assumption, the maximum time available to complete τ_1 is a function of machine speed and can be written as follows:

$$\tau_{1max} = 1.6667/N \quad \text{Seconds} \qquad (2.3\text{-}13)$$

where N is the speed in RPM.

Because of the time varying nature of the induced Phase emfs, the time derivative of i_b given in Equation (2.3-11) is also time varying. Therefore, in order for one to obtain an average value of this derivative neglecting R_p, the average value of e_b during τ_1 is obtained as follows:

a. <u>For Zero Commutation Advance $\delta_c = 0°$</u>

$$e_{b_{AVG}} = 6/\pi \int_{120°}^{150°} [153.3N\sin(\theta - 90°)]d\theta$$
$$= 107.31N \quad \text{Volts} \qquad (2.3\text{-}13)$$

Therefore, the average value of di_b/dt as a function of machine speed, neglecting R_p, becomes

$$di_b/dt|_{AVG} = (1.706 \times 10^6 - 107.31N) \text{ Amperes/Second} \quad (2.3\text{-}14)$$

b. For Thirty Degree Commutation Advance $\delta_c = 30°$

$$e_{b_{AVG}} = 6/\pi \int_{120°}^{150°} [153.3N\sin(\theta - 120°)]d\theta$$

$$= 39.23N \quad \text{Volts} \quad (2.3\text{-}15)$$

and therefore one obtains the following:

$$di_b/dt|_{AVG} = (1.706 \times 10^6 - 39.23N) \text{ Amperes/Second} \quad (2.3\text{-}16)$$

The values of i_b at the end of τ_{1max} can be now approximated as follows: a) for $\delta_c = 0°$

$$i_b(t_2)|_{\delta_c=0°} = \tau_{1max}[di_b/dt|_{AVG,\delta_c=0°}]$$

$$= (2.84 \times 10^6/N - 178.8) \text{ Amperes} \quad (2.3\text{-}17)$$

b) for $\delta_c = 30°$

$$i_b(t_2)|_{\delta_c=30°} = \tau_{1max}[di_b/dt|_{AVG,\delta_c=30°}]$$

$$= (2.84 \times 10^6/N - 65.38) \text{ Amperes} \quad (2.3\text{-}18)$$

Notice that advancing the firing of the inverter transistors by 30 electrical degrees increases the final value of the rising Phase current during the first commutation period, τ_1.

A better understanding of the interactions between N, τ_{1max}, δ_c, di_b/dt, and i_b is possible by plotting the quantities defined in Equations (2.3-13), (2.3-14), (2.3-16), (2.3-17), and (2.3-18) versus machine speed, N, as shown in Figure (2.3-8). Notice that the maximum available time to complete the first commutation period, τ_{1max}, is inversely proportional to the machine speed, N. Notice, using the same assumptions as above, one can see that the average value of the time derivative of the increasing Phase current also decreases with machine speed, but at a linear rate. Since the amount of current buildup during τ_{1max} is a function of the product of τ_{1max} times the average value of the derivative of the Phase current with respect to time, it is easy to see that the magnitude of this current buildup decreases very rapidly with increasing N. This behavior is clearly shown in Figure (2.3-8).

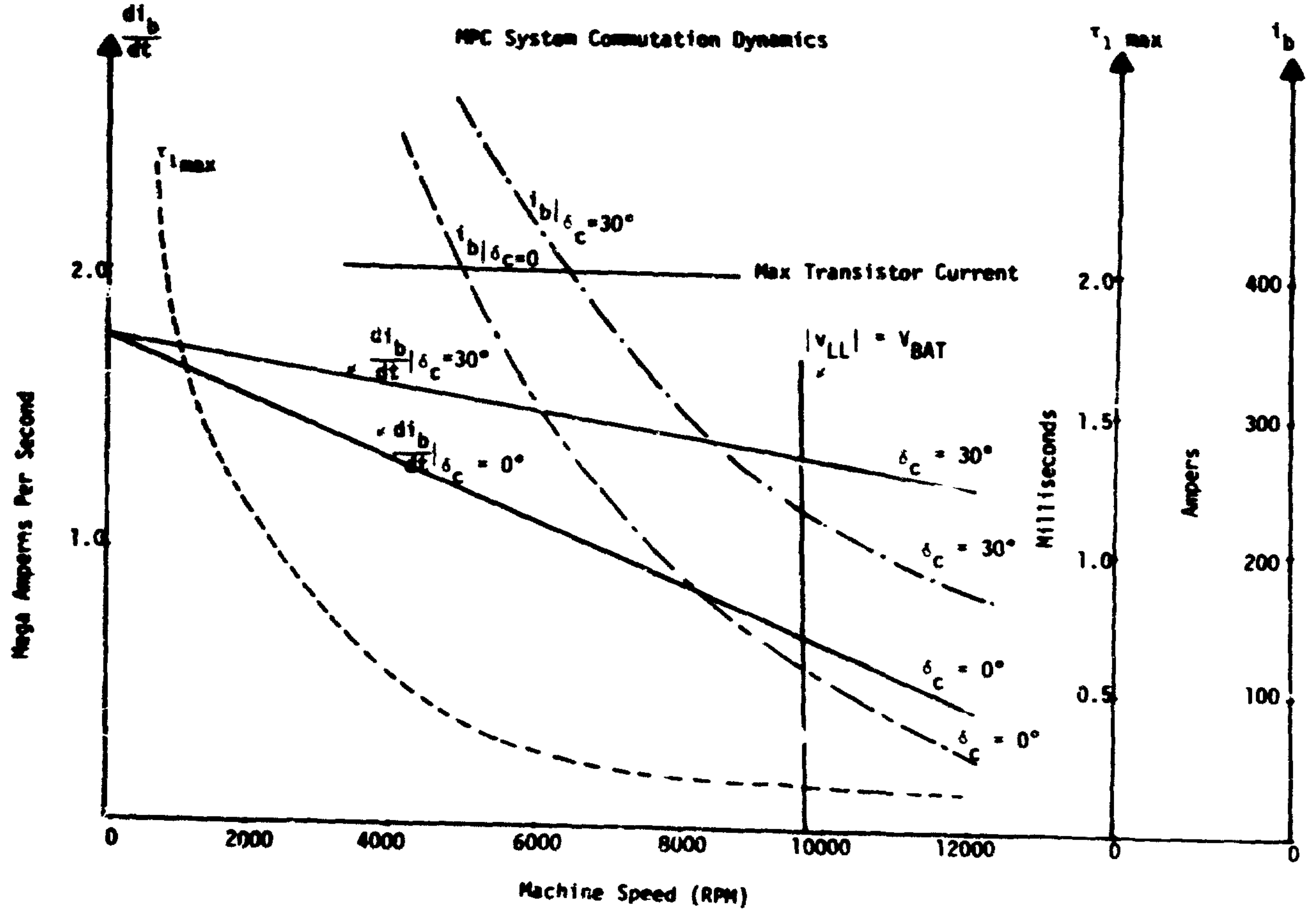

FIGURE (2.3-8) Approximate Values of τ_{1max}, i_b, and di_b/dt During the First Commutation Period, τ_1, for Zero and Thirty Electrical Degrees of Commutation Advance ($\delta_c = 0°$ and $\delta_c = 30°$)

EFFECT OF COMMUTATION ADVANCE ON MACHINE RATING

The effect of the commutation advance angle, δ_c, on the magnitude of current buildup is also clearly shown in Figure (2.3-8). Notice that for $\delta_c = 30°$, the value of the current buildup is consistantly higher than that for $\delta_c = 0°$. Since the power rating of the MPC system is proportional to the sum of the products of the phase currents and emfs, the advanced firing case, that is when $\delta_c = 30°$, increases the MPC system power rating over the entire speed range.

EFFECT OF WINDING INDUCTANCE ON MACHINE RATING

The effects of machine winding inductances on the system rating can be deduced from Equation (2.3-1) and Figure (2.3-8). Notice that the rate of current buildup in a phase is inversely proportional to the value of effective phase to neutral winding inductance. Therefore, both the slopes and initial values of (di_b/dt) for $\delta_c = 0°$ see $\delta_c = 30°$, see Figure (2.3-8), are inversely proportional to the value of the inductance. Consequently, high values of effective phase to neutral machine inductance will result in smaller current buildups, at a given frequency, than would be the case with lower inductances. Therefore, it results in a lower MPC system power rating at that speed (frequency). Winding inductances can be reduced by decreasing the total number of turns since the inductance is proportional to the square of the number of series turns. Inductances can also be reduced through redesigning slot dimensions and other geometries of the magnetic ciruit. The reduction of machine winding inductances and the impact of these reductions on the overall MPC system performance and ratings are analyzed in detail in Chapters (3.0) and (4.0) of this report, by means of sophisticated magnetic field analysis and machine-power conditioner dynamic simulation techniques.

IMPACT OF MACHINE PHASE TO NEUTRAL EMF WAVESHAPES ON SYSTEM RATINGS

The discussion up to this point has only been centered on sinusoidal phase-to-neutral emf waveforms as shown in Figure (2.3-2). However, in machines with fewer number of slots per pole per phase, such as the case here, the phase-to-neutral voltage will contain a strong influence of some of the low order odd harmonics. This is especially the case if no means for harmonic reduction is employed. The third harmonic can be eliminated by a coil pitch of 120 electrical degrees (2 slots). Also, this harmonic is absent at the line to line terminals of a Y-connected armature. On the other hand, the harmonics (5,7,11,13,...) in the gap flux density distribution cannot be reduced by short chording for such armatures with one slot per pole per phase of the type at hand. In this case, skewing or fractional slot windings are required. These points concerning the emf waveform are elaborated on further in Chapter (3.0).

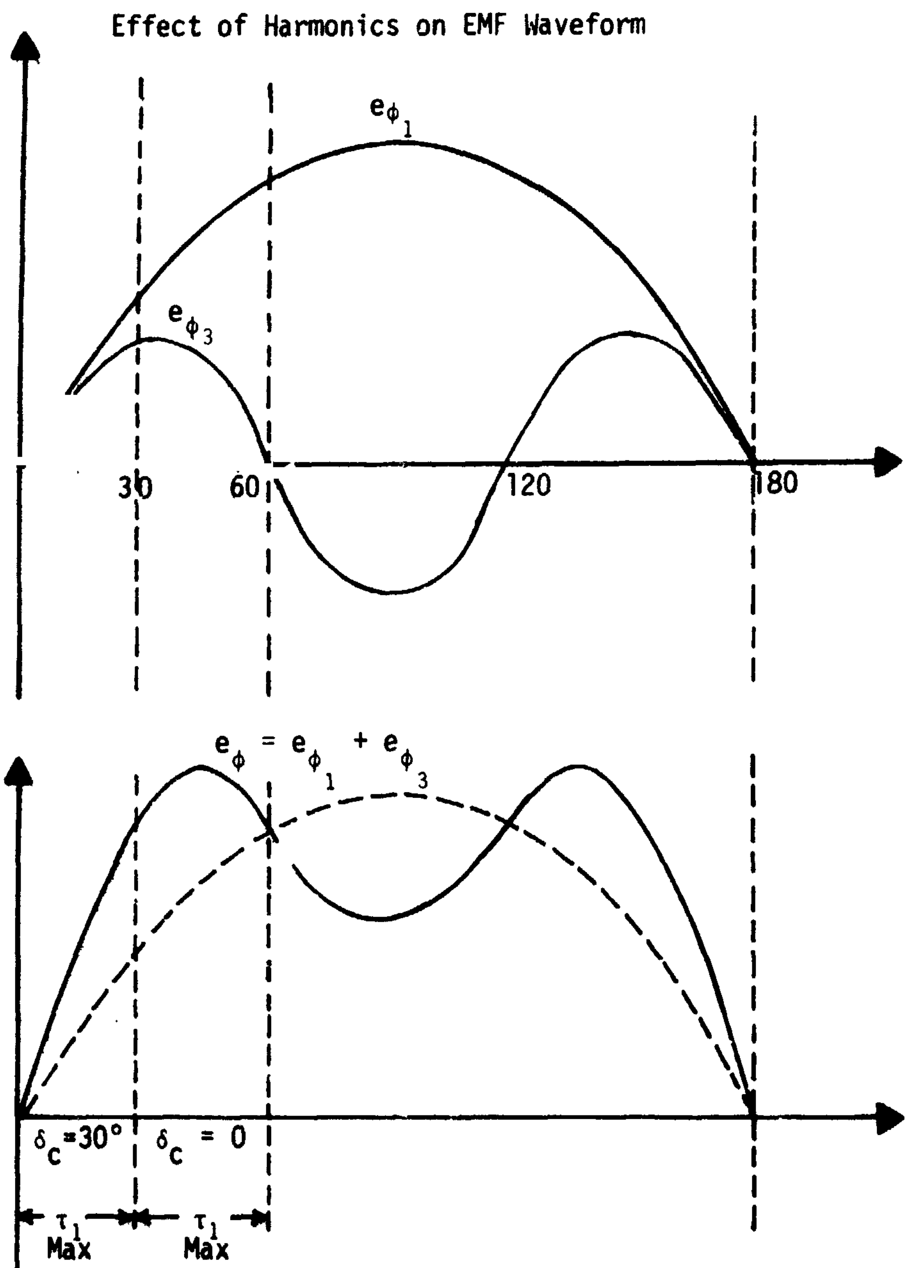

FIGURE (2.3-9) Effect of the Third Harmonic Component on the Induced Phase EMF During the First Commutation Period - Commutation Advance δ_c = 0° and 30°.

The impact of the emf harmonics can be deduced by examining Figure (2.3-9) which gives an example of a phase emf with a fundamental and a third harmonic component. The sum of these two components is also plotted in this figure. Inspection of this figure reveals that the third harmonic increases the phase emf during commutation, and therefore decreases the rate of current buildup for both cases of zero and thirty degree commutation advance. Therefore, the total current buildup and maximum power rating at a given speed is reduced by this harmonic. The impact of other harmonics on the rate of current buildup can be determined in a similar manner. The harmonics in the emf waveforms of the samarium cobalt and strontium ferrite machines were reduced by skewing the stator core as will be detailed in Chapter (3.0). The proper degree of skewing was determined by means of finite element analysis of the magnetic field in these machines in conjunction with a dynamic model of the machine - power conditioner (MPC) system which is given in Chapters (3.0) and (4.0).

THE SECOND COMMUTATION INTERVAL τ_2

The second commutation interval begins when the decaying Phase current reaches zero, (diode D_4 turns off). The simplified circuit model for this case is given in Figure (2.3-6). The rate of current rise in this case becomes:

$$di_b/dt = [V_{BAT} - 2R_p i_b + e_c - e_b]/(2L_p) \qquad (2.3\text{-}19)$$

This rate of current rise is considerably less than that during the first commutation interval. For this reason, and because the majority of the current buildup occurs during the first commutation period, the second commutation interval, τ_2, will not be considered further.

COMPLETION OF COMMUTATION

Commutation is completed as soon as the diode, D_R, recovers (turns off). This occurs when the increasing (rising) phase current reaches the value of the chopper inductor currrent. After D_R turns off, the chopper inductor is no longer shorted, but is now in series with two legs of the three-phase machine armature winding and the battery as shown in Figure (2.3-7). In this case, the time derivative of i_b beomes:

$$di_b/dt = [V_{BAT} - i_b(R_{CH} + 2R_p) + e_c - e_b]/(L_{CH} + 2L_p) \qquad (2.3\text{-}20)$$

In the two systems under consideration here, the chopper inductance, L_{CH}, was chosen roughly ten times the value of L_p in order to keep the switching losses within reasonable bounds. For this reason, the rate of current rise during this period is relatively low in comparison with the previous two periods, and therefore has little impact on the MPC system rating.

The above discussions have highlighted the impact of various parameters on the MPC system performance and ratings. It was shown that the machine inductances and emfs are critical factors in determining whether or not a given power and speed rating could be met by a given MPC system design. It was also demonstrated that the peak power rating at a given speed could be significantly increased by advancing the firing of the inverter switches by thirty electrical degrees.

The analysis presented in this section required a number of aproximations and simplifications as described earlier. Hence, this analysis was intended only for qualitative and illustrative purposes. The actual analysis of the two machine systems was performed using two computer aided design tools. The first of these is a finite element magnetic field analysis set of programs (package) developed for use in this investigation. This package was used in the determination of machine flux densities, winding inductances and induced emf waveforms. This analysis included the effects of magnetic saturation on these parameters. The calculated machine parameters were used in a detailed dynamic simulation model of the MPC system which included the voltage drops in the power switches, as well as the harmonics in the induced armature emfs. These computer aided analysis techniques and their applications to the design and analysis of the two systems at hand are discussed in detail in Chapter (3.0).

3.0 MOTOR DESIGN

In this chapter, preliminary designs for samarium cobalt based, and strontium ferrite based machines are arrived at. These designs are analyzed with the help of computer aided design tools to ascertain their suitability for meeting the rated (15 hp) and peak power (35 hp) requirements, when operating in conjunction with an electronic power conditioner. Based on the computer aided analysis both machine designs are finalized for implementation, and the subsequent final machine parameters and hardware are described.

3.1 PRELIMINARY DETERMINATION OF MAGNETIC CIRCUIT GEOMETRY AND WINDING PARAMETERS

An outline of the basic approach used in designing a magnetic circuit geometry and winding parameters [1,2] shall be considered in this section.

The main objective of producing a motor with a commercially feasible combination of cost, efficiency, power rating, size, and weight for use in electric passenger vehicles was borne in mind. In particular, the specifications of the customer were:

1. an electronically commutated permanent magnet dc machine for operation in motoring and generating modes,
2. a nominal voltage rating of 120 volts,
3. a design adaptable to voltages ranging from 96v to 240v,
4. a design allowing for proper motor operation at voltage down to 60% of nominal to allow for battery voltage variations,
5. batteries used as the power (voltage) source,
6. an output power of 15 hp (11.2 kw) for 2 hours at a vehicle speed of 55 mph (86 km/hr),
7. operation as both motor and generator for 1 minute at 35 hp (26.1 kw) at a vehicle speed of 30 mph (48 km/hr), and
8. shaft speed and torque left to the discretion of the designer.

With the above specifications, the following steps were applied to come up with a suitable magnetic circuit geometry and winding design:

ORIGINAL PAGE IS
OF POOR QUALITY

STEP 1 :

Consider the main dimensions of the machine; that is, D, the stator bore diameter, and L, the stator core length. The total flux (or magnetic loading) around the stator periphery at the airgap is given by

$$M_L = p\phi \tag{3.1-1}$$

where p = number of poles, and ϕ = flux per pole.

The total current (or electric loading) flowing around the stator periphery is given by

$$E_L = CI_C \tag{3.1-2}$$

where C is the total number of active conductors (in this type of machines, two thirds of the total conductors are active at any time, that is, current carrying conductors around the periphery), and I_C is the current in each active conductor.

The average flux density, B_{av}, at the airgap is thus given by

$$B_{av} = p\phi/\pi DL = \phi/\tau L \tag{3.1-3}$$

where $\tau = \pi D/p$, is the pole pitch. The current density at the stator periphery, J_S, is given by

$$J_S = CI_C/\pi D \tag{3.1-4}$$

Now, the power developed in the armature, P_a, is given by

$$P_a = EI_a = \phi C\omega pI_a/a \tag{3.1-5}$$

where ω is the speed of the rotating periphery of the rotor in mechanical rad/sec, a is the number of parallel paths in the armature winding, I_a is the armature current, and E is the machine induced voltage. Rewriting P_a as a function of the magnetic and electric loadings, we have

$$P_a = (p\phi)(CI_a/a)\omega = (p\phi)(CI_C)\omega$$

where $I_C = I_a/a$. Therefore, it follows that

$$P_a = M_L E_L \omega \tag{3.1-6}$$

Expressing this power in terms of the machines main dimensions, one can write

$$P_a = (\pi D L B_{av})(\pi D J_S) = K_0 D^2 L\omega \quad (3.1\text{-}7)$$

where $K_0 = \pi^2 B_{av} J_S$.

Hence, the power developed in the armature is proportional to the shaft speed, ω, stator core length, L, and square of the stator bore diameter, D. However, the volume of the active portion of the machine is $(\pi D^2 L/4)$. Therefore, from Equation (3.1-7), this volume, Vol., becomes

$$Vol = K_1 P_a/\omega \quad (3.1\text{-}8)$$

where $K_1 = \pi/4K_0$.

Equation (3.1-8) demonstrates that the volume of the active portion of the machine is inversely proportional to the speed. Thus, by maintaining a constant output, a machine designed to operate at a greater speed will have a smaller size and hence entail lesser cost as opposed to a machine designed to operate at a lesser speed. Therefore, in reducing the size, a designer selects the highest practical speed taking into account the limitations of mechanical stresses, and rotational loss considerations (bearings, windage, etc.).

In addition, given that the volume varies inversely with K_0, the size (and consequently the cost) of the machine is reduced by making K_0 as large as possible. Recall that K_0 is proportional to the product of the magnetic and electric loadings for a given machine.

Of course, the magnetic loading is dependent on the maximum flux density in the iron parts, iron losses, and magnetizing current. The heat dissipated per unit area of stator surface is proportional to the electric loading. Hence, in order to minimize heat dissipation, the electric loading must be reduced. Otherwise, forced ventilation would be required. For our electronically commutated motor, the option of using forced air cooling is permitted if the need arises. The electric loading is dependent on the number of conductors per slot, and the current per conductor in such slots. The number of conductors per slot is dependent on a factor known as the fill factor, and a useful rule of thumb is that the fill factor should not exceed 65% for classes of machines such as this one. It should be brought to the reader's attention that the fill factor for round conductors is lower than that factor for rectangular conductors.

With the above rules in mind, the following basic parameters concerning the samarium cobalt machine of Phase (II) were chosen. This choice is based on experience with such designs:

1. number of poles, $p = 6$,

2. number of teeth, $N_t = 18$,

3. pole span, P_S = 0.666, notice that the pole span here is the ratio of the pole width to pole pitch,

4. lamination axial length (stack height), S_h = 10.16 cm (4.0 in),

5. Stator outer diameter, D_{os} = 16.556 cm (6.518 in), and

6. Stator inner diameter, D_{is} = 7.777 cm (3.062 in).

Consider the permanent magnet (pole) as shown in Figure (3.1-1). The magnet (pole) width, M_w, is given by the sum of the number of magnet pieces bonded together times the axial depth (width) per magnet. That is, for a pole consisting of 4 pieces, of 0.9 in depth for each, M_w = (0.9)(4) = 3.6 in (9.14 cm). The minimum height of the pole, based on the geometry of Figure (3.1-1), is H_{min} = 0.393 in (0.99 cm). The maximum height of the pole, based on the same figure, is H_{max} = 0.49 in (1.24 cm). The radial distance from the bottom of the magnet (pole) to the rotor center, based on Figure (3.1-1), is R = 0.975 in (2.48 cm). The rotor outer diameter, see Figure (3.1-1) is

$$D_{or} = 2(H_{max} + R) = 2.93 \text{ in } (7.44 \text{ cm}).$$

A nonmagnetic stainless steel sleeve was used to secure the poles firmly on the rotor. An outer sleeve diameter, $D_{s\ell v}$ of 3.0 in (7.62 cm) implies a sleeve thickness, $T_{s\ell v}$, as follows

$$T_{s\ell v} = (D_{s\ell v} - D_{or})/2 = 0.035 \text{ in. } (0.0889 \text{ cm})$$

Thus the clearance between the rotor and stator, C_ℓ, becomes

$$C_\ell = (D_{is} - D_{s\ell v})/2 = 0.031 \text{ in. } (0.0787 \text{ cm})$$

and the nonmagnetic gap (air + sleeve), which is equivalent to air magnetically, is

$$G_{ap} = T_{s\ell v} + C_\ell = 0.066 \text{ in. } (0.1676 \text{ cm})$$

pole pitch, $\tau_p = \pi D_{is}/p$ = 1.6032 in. (4.072 cm)

Having determined the magnet, rotor, and stator bore dimensions, the operating point of the permanent magnet can now be found as described next in Step 2.

TYPICAL RADIAL MAGNET-ROTOR POLE GEOMETRY

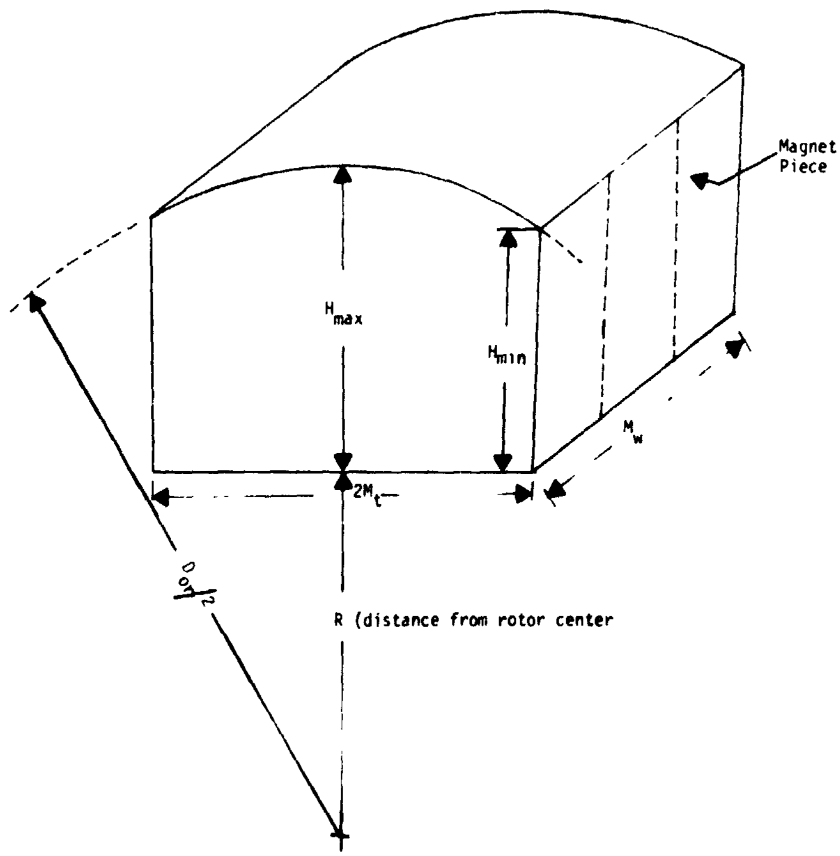

FIGURE (3.1-1) Schematic of Permanent Magnet

ORIGINAL PAGE IS
OF POOR QUALITY

STEP 2:

Now one proceeds to calculate the magnet operating point as follows: Based on Figure (3.1-1), the magnet radial thickness, $M_t = 1.046/2 = 0.523$ in (1.328 cm).

Hence, the magnet area is given by

$$M_a = M_t \bullet \min(S_h, M_w) = (0.523)(3\bullet6) = 1.8828 \text{ in}^2 \ (12.147 \text{ cm}^2).$$

The pole arc calculated at the stator bore is hence given by

$$\text{pole arc} = D_{is}\pi P_s/p = 1.0678 \text{ in } (2.712 \text{ cm}).$$

Now, the slot span, S_s, can be obtained as

$$S_s = \pi D_{is}/N_t = 0.5344 \text{ in } (1.357 \text{ cm}).$$

and a reasonable slot opening is chosen to be $w_s = 0.085$ in (0.216 cm). Thus, Carter's coefficient becomes

$$K_s = (5\ \text{Gap} + w_s)S_s/((5\text{Gap} + w_s)s_s - W^2) = 1.034.$$

Also, the permeance (reciprocal of reluctance or the ratio of flux to mmf) per pole in the air gap becomes

$$P_p = (\text{pole arc})(\min(S_h, M_w)/K_s\text{Gap}$$
$$= 56.33 \text{ Gauss-inch/Oersted } (1.798 \times 10^{-6} \text{ wb/AT}).$$

The permeability of the magnet material is given by

$$\mu_\ell = B/H = (\phi/M_a)/(F/L)$$

where ϕ is the flux per pole, F is the mmf, and L is the length of the magnetic path. Hence,

$$\mu_\ell = P_pL/M_a = (56.33)(2)H_{min}/4M_a$$
$$= 5.88 \text{ Gauss/Oersteds} (7.389\ \mu\text{H/m}).$$

This gives the slope of the no-load line of the magnetization curve so that the point of instersection of this line with the B-H characteristic supplied by the magnet manufacturer is the operating point (OP) as shown in Figure (3.1-2). The B-H characteristic selected was that of HICOREX 90B Samarium Cobalt; an 18 million Gauss-Oersted Hitachi product, see Figure (3.1-2). The operating point corresponding to an operating flux density, B_{OP}, was found to be

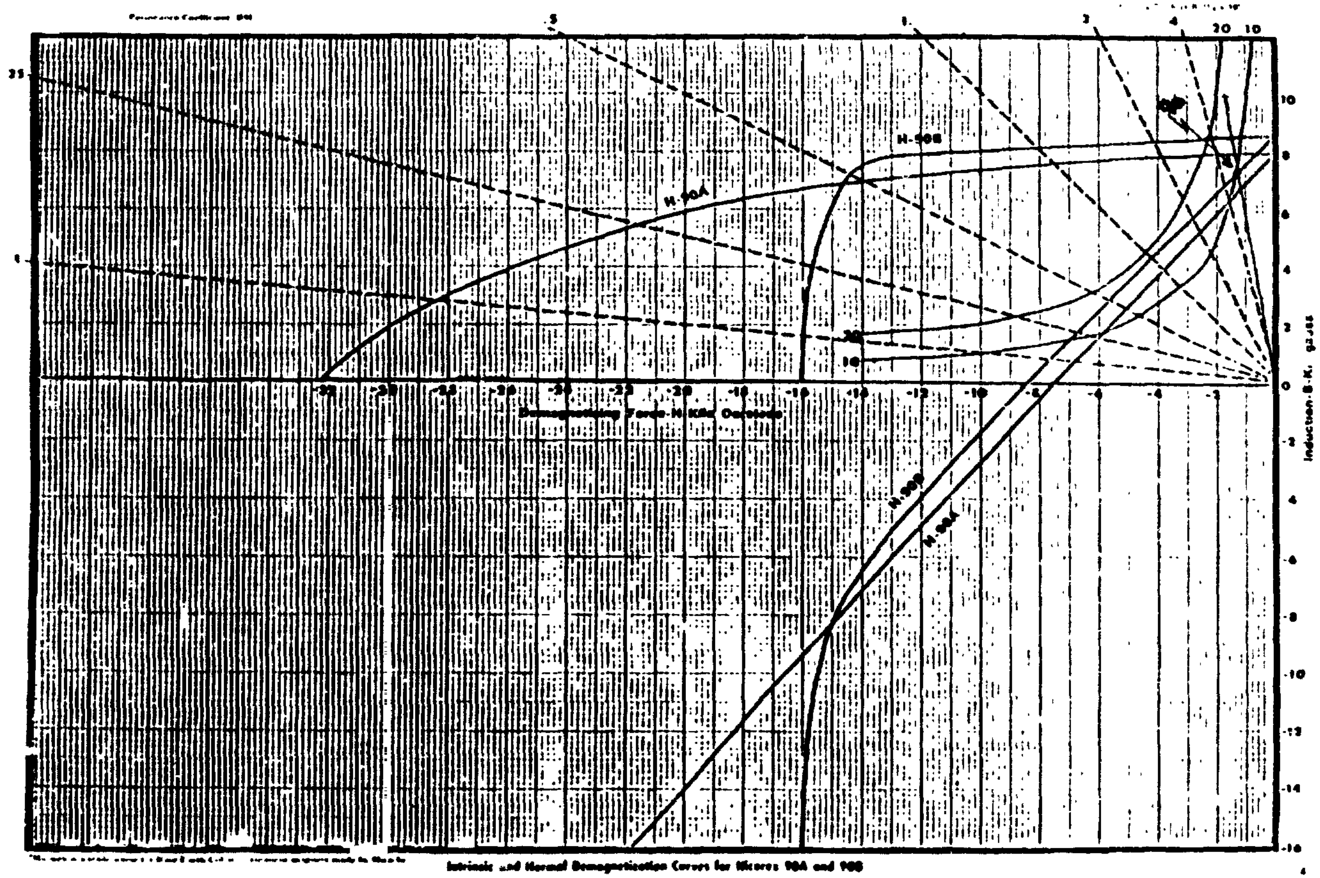

FIGURE (3.1-2) Operating Point of the Magnet
in the Samarium Cobalt Machine

ORIGINAL PAGE IS
OF POOR QUALITY

$$B_{OP} = 7.20 \text{ KGauss} = 7.20 \times 1000 \times 6.45$$
$$= 46440 \text{ lines/in}^2 \ (0.72 \text{ wb/m}^2).$$

Therefore, the magnet flux per pole is

$$\phi_m = B_{OP} \times 2M_a = 174874 \text{ lines } (1.749 \times 10^{-3} \text{ wb}).$$

Assuming in this preliminary design process a 5% leakage factor, unique to a radially oriented permanent magnet on a rotor of this type, it follows that the leakage correction factor is 1.05. Therefore, the airgap flux per pole, ϕ_a, becomes

$$\phi_a = 174874/1.05 = 166540 \text{ lines/pole } (1.665 \times 10^{-3} \text{ Wb/pole})$$

Since the airgap area, Ag is

$$A_g = (\text{pole arc})(M_w) = 3.84 \text{ in}^2 \ (24.77 \text{ cm}^2)$$

it follows that the airgap flux density, B_g, is

$$B_g = 166540/3.84 = 43.32 \text{ K lines/in}^2 \ (0.668 \text{ Wb/m}^2)$$

Having obtained the operating point of the permanent magnet, and found the airgap flux density, one proceeds now to find the flux densities throughout the magnetic circuit, and calculate the slot dimensions.

STEP 3:

Now one proceeds to the calculation of the slot dimensions as follows: A schematic of a stator slot is shown in Figure (3.1-3). From practical considerations, the wedge used for firmly securing the winding in the slot has a thickness, W_e, of about 0.062 in (0.157 cm). Let the thickness of the insulating slot liner be, S_ℓ = 0.012 in (0.030 cm) It follows that the slot winding area, S_{wa}, is given by

$$S_{wa} = [(x+z)/2 - 2s_\ell][(D_{A2}-D_{A1})/2-W_\ell-2S_\ell]$$

where the distance, x, Figure (3.1-3), is given as

$$x = D_{A1}\pi/N_t - T_w.$$

TYPICAL ARMATURE (STATOR) SLOT GEOMETRY

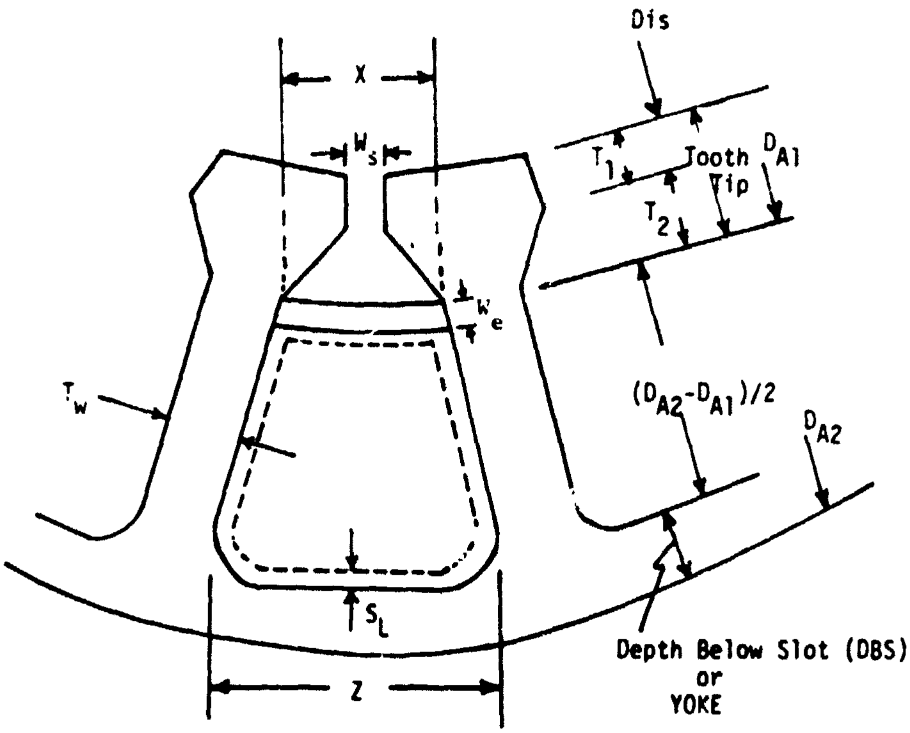

FIGURE (3.1-3) Schematic of a Stator Slot

In Figure (3.1-3), assuming that $T_1 = 0.04$ in (0.102 cm) and $T_2 = 0.02$ in (0.051 cm), it follows that the TOOTH TIP = $T_1 + T_2 = 0.06$ in (0.152 cm), and $D_{A1} = D_{is} + 2X$ (TOOTH TIP) = 3.182 in (8.08 cm). Also, assuming that the average width of a tooth, Figure (3.1-3), T_w = 0.302 in (0.767 cm) and the yoke thickness, YOKE = 0.302 in (0.767 cm) one can write, using Figure (3.1-3), x = 0.253 in. (0.643 cm), $D_{A2} = D_{OS}$ - 2YOKE = 5.914 in (15.02 cm). Therefore, one can calculate $S_{wa} = 0.5984$ in² (3.86 cm²).

For a double layer winding (2 coil-sides per slot) with 5 conductors per coil-side, 12 Number 16AWG strands of wire (diameter = 0.054 in = 0.137 cm) were used to form a conductor. The total number of wires per slot is therefore given by

$$N_{WS} = (2)(5)(12) = 120 \ .$$

A good check for the slot parameters is to calculate the slot fill factor which is the ratio of the square of the wire diameter times the number of wires (a quantity proportional to the area of the slot occupied by the conductors) to the slot winding area. As was mentioned earlier, the fill factor should not exceed 65%. That is,

$$\text{fill factor}(D^2N) = [120 \times (0.054)^2]/0.5984) \times 100 = 58.5\%$$

The above result implies that the slot parameters obtained are acceptable.

Now, one proceeds next to Step 4, in which one calculates the torque associated with this design, at rated current conditions in Step 4.

STEP 4:

Considering the fundamental components of the stator mmf and the equivalent magnet (rotor) mmf, the relationship between the torque produced and the angle between the peaks of the two mmfs is sinusoidal. Assuming instantaneous commutation (no significant delay in current switching due to winding inductance), the maximum average torque will be obtained when commutation starts at a relative angle between the above mentioned two mmf peaks of 120 electrical degrees. The next commutation step occurs when that angle drops to 60 electrical degrees. Ideally, maintaining throughout the commutation process, an angle between the two mmfs of 90 electrical degrees would yield maximum torque. However, the nature of the electronic commutation process associated with the current source inverter at hand would not permit such an angle to remain constant. This process of angle variation is displayed graphically with the useful portion of the torque angle characteristic indicated by the shaded area in Figure (3.1-4). Further elaboration on torque production and profile in this type of machine was given earlier in Chapter (2.0). At the peak of this sinusoid, the torque is given by:

IDEAL TORQUE PRPOFILE DURING A STATE OF 60°e- NORMAL COMMUTATION

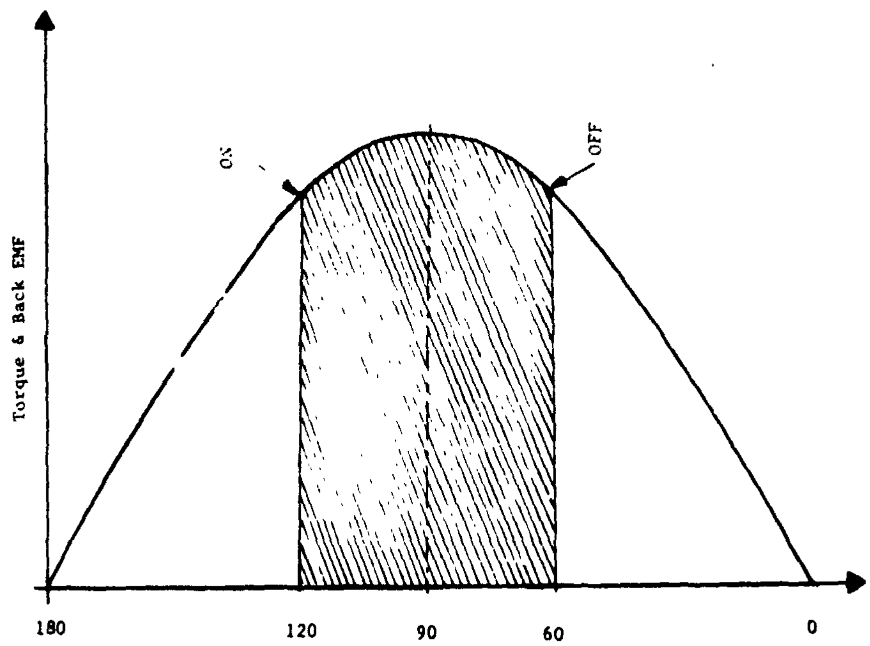

FIGURE (3.1-4) Torque - Angle Characteristic

$$\text{Torque} = Kp^2\pi(cK_\ell\, K_w I/2p)10^{-8} \qquad (3.1\text{-}9)$$

where p is the number of poles,

ϕ is the flux per pole (in lines),

c is the total number of active conductors,

K_w is the winding factor,

I is the current per conductor (Amperes),

K is a constant of proportionality, in case of using torque units in ounce-inch, k = 71 oz•in/Ampere•lines,

K_ℓ is the factor which relates the phase voltage to the effective line to line voltage (derived below),

and $cK_w I/2p$ is the winding Ampere-turns per pole. The torque sensitivity, S_t is the torque per Ampere, and is given by

$$S_t = \text{Torque}/I = Kp^2\phi(cK_\ell K_w/2p)10^{-8} \qquad (3.1\text{-}10)$$

Assuming 5 conductors per layer per slot, the total number of active conductors is given by

$$c = (10 \text{ conductors/slot})(2 \text{ slots/pole})(6 \text{ poles}) = 120 \text{ conductors}$$

Notice that for a 6 pole, 18 slot machine, there are 3 slots per pole. However, it must be emphasized that for this type of machine, only two phases carry current at any given time (neglecting commutation).

Accordingly, in this design, at any given time, two out of three slots per pole carry current (active slots). The calculated number of active conductors (c = 120) implies that the series connection is assumed. That is, there is one conducting path per phase. Hence, there are 30 turns (or 60 conductors) in series per phase.

Here, the pitch factor is given by

$$K_p = \sin 180/2 = 1$$

For 3 slots per pole, the electrical angle between slots (or slot pitch) is

$$\text{slot pitch} = 180/3 = 60 \text{ electrical degrees}$$

and for a 3 phase winding, the number of slots per pole per phase (or slots per phase belt) is 1. Therefore, the distribution factor is one, and the winding factor, k_w, is given by

$$K_w = K_d K_p = 1$$

Since the conditioner sees the line to line voltage, $v_{\ell\ell}$, instead of the line to neutral voltage, $v_{\ell n}$, then the power supplied to the conditioner is approximated as

$$P_c = \sqrt{3} v_{\ell n} I_\ell = 2(\sqrt{3} v_{\ell n}/2) I_\ell \ .$$

The power contributed per active phase is $\sqrt{3} v_{\ell n} I_\ell/2$. From this, one concludes that the factor K_ℓ is given by $K_\ell = \sqrt{3}/2 = 0.866$.

For this class of machines, substituting K = 71 oz-in/Ampere-lines as mentioned earlier, the torque sensitivity for the series connection is given by Equation (3.1-10), and is

$$S_t = (71)(6)^2(166540)(120)(0.866)(1)(10^{-8})/2(6)$$

= 36.86 oz.in/Ampere = 0.192 ft.lb./Ampere(0.260 Newton•m/Amp)

For the parallel connection (2 conducting paths per phase) of the machine winding, the torque sensitivity becomes half that for the series connection. That is,

$$S_t = 0.192/2 = 0.096 \text{ ft.lb./Ampere } (0.130 \text{ Newton}\bullet\text{m/Amp}).$$

A procedure identical to Steps 1 through 4 was followed in arriving at a magnetic circuit and winding design for the strontium ferrite No. 8 based machine. The resulting machine parameters for this strontium ferrite based machine are given below in Table (3.1-1). For comparison purposes, the corresponding machine parameters of the samarium cobalt based design of Phase (II) is also given in the Table. Furthermore, in the interest of completeness of this comparison, the corresponding parameters obtained for a 4-pole samarium cobalt machine, arrived at using a similar design process during Phase (I), is also given in the third column of the table.

The above calculated preliminary machine volume and geometry are used in Section (3.2), described next, to obtain the machine open-circuit emf waveforms, inductances, and flux distributions, on the basis of which simulation of the MPC system characteristics is carried out in Section (3.3), where the design of both machines is finalized.

TABLE (3.1-1) SUMMARY OF PARAMETERS CORRESPONDING TO PRELIMINARY DESIGNS OF THE PHASE (II) SAMARIUM COBALT AND STRONTIUM FERRITE BASED MACHINES

Machine Parameter (Figure 3.1-1 to 3.1-5)	Samarium Cobalt Machine Phase (II)	Strontium Ferrite Machine Phase (II)	Samarium Cobalt Machine Phase (I)
p	6	6	4
N_t	18	18	15
P_s	0.666	0.666	0.650
S_h	4.0in(10.16cm)	8.50in(21.59cm)	6.00in(15.24cm)
D_{OS}	6.518in(16.55cm)	6.518(16.55cm)	6.50in(16.51cm)
D_{is}	3.062in(7.78cm)	4.071in(10.34cm)	3.062in(7.78cm)
M_w	3.60in(9.14cm)	8.75in(22.22cm)	6.30in(16.00cm)
H_{min}	0.393in(0.998cm)	0.613in(1.56cm)	0.34in(0.864cm)
H_{max}	0.49in(1.24cm)	0.740in(1.88cm)	0.50in(1.27cm)
R	0.975in(2.48cm)	1.225in(3.11cm)	0.97in(2.46cm)
D_{or}	2.93in(7.44cm)	3.93in(9.98cm)	2.94in(7[illegible]m)
$T_{s\ell v}$	0.035in(0.0889cm)	0.035in(0.0889cm)	0.035in(0.0889cm)
C_ℓ	0.031in(0.079cm)	0.035in(0.089cm)	0.026in(0.066cm)
G_{ap}	0.066in(0.168cm)	0.070in(0.178cm)	0.061in(0.155cm)
τ_p	1.6032in(4.07cm)	2.13in(5.41cm)	2.405in(6.11cm)

ORIGINAL PAGE IS OF POOR QUALITY

CON'T. TABLE (3.1-1)

Machine Parameter (Figure 3.1-1 to 3.1-5)	Samarium Cobalt Machine Phase (II)	Strontium Ferrite Machine Phase (II)	Samarium Cobalt Machine Phase (I)
M_t	0.523in(1.33cm)	0.695in(1.76cm)	0.72in(1.83cm)
M_a	$1.8828in^2$ ($12.15cm^2$)	$5.907in^2$ ($38.11cm^2$)	$4.32in^2$ ($27.87cm^2$)
S_s	0.523in(1.36cm)	0.71in (1.80cm)	0.6413in(1.63cm)
K_s	1.034	1.024	1.06
P_p	56.33 Gauss-in/Oersted (1.798×10^{-6}wb/AT)	168.34 Gauss-in/Oersted (5.37×10^{-6}wb/AT)	145 Gauss-in/Oersted 4.63×10^{-6}wb/AT)
μ_ℓ	5.88 Gauss/Oersted (7.39μH/m)	8.74 Gauss/Oersted (10.98μH/m)	5.7 Gauss/Oersted (7.16μH/m)
B_{op}	46440 lines/in^2 (0.72 wb/m^2)	22575 lines/in^2 (0.35wb/m^2)	45472 lines/in^2 (0.705wb/m^2)
ϕ_a	166540 lines/pole (1.665×10^{-3}wb/pole)	25400 lines/pole (2.54×10^{-3}wb/pole)	374170 lines/pole (3.74×10^{-3}wb/pole)
A_g	$3.84in^2$($24.77cm^2$)	$12.06in^2$($77.8cm^2$)	$9.847in^2$($63.53cm^2$)

ORIGINAL PAGE IS
OF POOR QUALITY

CON'T. TABLE (3.1-1)

Machine Parameter (Figure 3.1-1 to 3.1-5)	Samarium Cobalt Machine Phase (II)	Strontium Ferrite Machine Phase (II)	Samarium Cobalt Machine Phase (I)
B_g	43.32 K lines/in2 (0.668wb/m²)	21.06 K lines/in² (0.325wb/m²)	38.0 K lines/in² (0.586wb/m²)
W_e	0.062in(0.157cm)	0.062in(0.157cm)	0.125in(0.317cm)
S_ℓ	0.012in(0.030cm)	0.012in(0.030cm)	0.015in(0.038cm)
Tooth Tip	0.06in(0.15cm)	0.075in(0.19cm)	0.05in(0.13cm)
Yoke	0.302in(0.77cm)	0.25in(0.63cm)	0.55in(1.40cm)
T_w	0.302in(0.77cm)	0.217in(0.55cm)	0.36in(0.91cm)
X	0.253in(0.64cm)	0.520in(1.32cm)	0.302in(0.77cm)
Z	0.730in(1.85cm)	0.833in(2.11cm)	0.772in(1.96cm)
S_{wa}	0.5984in²(3.86cm²)	0.530in²(3.42cm2	0.488in²(3.[illegible]5cm²)
N_{ws}	120	104	48
fill factor	58.5%	57.2%	56.07%
C	120	96	40
K_w	1	1	0.783
K_ℓ	0.866	0.866	1
S_t (series)	0.192ft-lb/Amp (0.26Nm/Amp)	0.234ft-lb/Amp (0.32Nm/Amp)	0.0867ft-lb/Amp (0.12Nm/Amp)
S_t (parallel)	0.096ft-lb/Amp (0.13Nm/Amp)	0.117ft-lb/Amp (0.16 Nm/Amp)	--------

3.2 FINITE ELEMENT ANALYSIS AN RESULTING MAGNETIC CIRCUIT AND WINDING DESIGN

In order to analyze the performance characteristics of a machine, it is necessary to know the flux distribution (or the flux densities throughout the cross section of such a machine) under its normal rated operating conditions. In the case of the two machines, namely the samarium cobalt and strontium ferrite based permanent magnet machines of interest in this project, which are being designed for use in electric passenger vehicle propulsion, the finite element (FE) method [3-7] was used to obtain the flux distributions, and subsequent machine parameters such as midgap flux density waveforms, induced emf waveforms in the armature, armature winding inductances, etc.

3.2.1 FINITE ELEMENT METHOD AND MIDGAP FLUX DENSITY

This method is one of several numerical methods such as the finite difference (FD) method which have previously been used in the analysis of magnetic fields in electrical machines [8-18]. Although the finite difference (FD) method appears to be simpler to understand, it possesses some disadvantages [17,28] in comparision with the FE method which render the approach less suitable for application in this project. The FE method is essentially a numerical technique of solving the magnetic vector potential (m.v.p.) partial differential equation governing the field distribution in two dimensional magnetostatic problems of the type at hand. The FE method is based on the concept of the magnetic vector potential (m.v.p.), A, where

$$\nabla \times \bar{A} = \bar{B} \tag{3.2-1}$$

and B is the sought-after magnetic flux density.

The magnetostatic fields in electrical machines are govered by the following Maxwell's equations:

$$\nabla \bullet \bar{B} = 0 \tag{3.2-2}$$

and

$$\nabla \times \bar{H} = \bar{J} \tag{3.2-3}$$

where H is the magnetic field intensity and J is the current density. Using the constitutive relationship given by

$$\bar{H} = \nu\bar{B} \tag{3.2-4}$$

ORIGINAL PAGE IS
OF POOR QUALITY

where ν is the reluctivity assumed to be a function of both position and magnetic flux density, in combination with Equations (3.2-1) through (3.2-3), the partial differential Equation [12-17] to be solved becomes

$$\nabla \times (\nu(\nabla \times A)) = J \tag{3.2-5}$$

A solution to (3.2-5) arises from a consideration of the total energy stored in the magnetic fields throughout the machine. A functional expression [15,19] for this energy is given by

$$F(A) = \iint_s [\tfrac{1}{2}(B \bullet H) - J \bullet A] dxdy \tag{3.2-6}$$

The minimization of this functional with the aid of the theory of variational calculus, in the two dimensional form, satisfies the partial differential Equation (3.2-5) governing the two dimensional field, in addition to the associated natural (Neummann) and Dirichlet boundary conditions [15,19]. In the two dimensional magnetic field case, involving machines of the type treated here, the following additional simplifications are valid [8-23]:

$$J = J_z\, a_z \tag{3.2-7}$$

where a_z is a unit vector in the z direction, and the flux density, B, is two dimensional in the x-y directions, that is:

$$B = B_x\, a_x + B_y\, a_y \tag{3.2-8}$$

$$A = A_z\, a_z. \tag{3.2-9}$$

The z direction is assumed to be the axial direction in any of the machines at hand, while the x and y directions are in the plane of the cross section of such devices.

With the help of first order triangular elements, the minimization of the functional in Equation (3.2-6) can be carried out numerically by means of a finite element discretization grid, which spans the entire field region being considered.

The resulting m.v.p.s at the FE grid nodes represent a numerical solution to Equation (3.2-5) which satisfies the necessary boundary conditions [15-21]

Since a closed form solution to Equation (3.2-5) cannot be obtained here, a numerical technique such as the FE method is used. This FE technique consists, as alluded to above, of dividing the machine cross section into subregions called elements in which the m.v.p. is a polynomial function of the nodal values of m.v.p. as well as the x and y coordinates of a position in a given element. The most commonly used element is the triangular element which yields a first order polynomial function for the m.v.p.s [9-18].

Focusing our attention on permanent magnet machines (and the electronically controlled class of these machines in particular), an adaption is made in order to implement the FE method. This involves the modeling of the magnetization effect of a permanent magnet by an equivalent winding consisting of a coil in series with a magnetic core whose B-H characteristic in the first quadrant is that of the demagnetization part of the permanent magnet shifted from the second quadrant of the normal four quadrant B-H curve, as described in References (18) and (19) with more detail. These References (18) and (19) are included in Appendices (1) and (2). The magnetomotive force of the equivalent coil becomes the product of the magnet height times its coercivity, H_C, for rectangular shaped magnets. In this approach, non-rectangular shaped magnets are divided up into magnet sections with rectangular shapes which approximate the original nonrectangular shape of a given magnet. Thus the process yields surface currents which are assigned to nodes (or elements) in the finite element grids. Figure (3.2-l) shows an example of such surface currents for the magnet shapes encountered in this work.

With the aid of an automatic grid generating scheme described in Reference [29], and summerized in Reference [20], the magnet model, and the finite element method, a system of nonlinear simultaneous algebraic equations is arrived at. These simultaneous algebraic equations are then solved using a nonlinear equation solver (Newton-Raphson), see References [29] and [30].

The solution of the nonlinear equations yields a periodic flux density distribution throughout the machine cross section (as a function of space angle). Since this flux distribution is periodic, the theory of Fourier Series implies that the flux can be expressed as a linear combination of sine and cosine terms [20,29]. Hence, one can write the following:

$$B(\theta) = \sum_{h=1}^{\infty} [a_h \cos(h\theta) + b_h \sin(h\theta)] \tag{3.2-10}$$

where

$B(\theta)$ is the flux density as a function of the space angle, θ, in electrical degrees (or radians),

h is the order of the harmonic
a_h and b_h are the fourier coefficients.

However, the flux density is found to contain only odd harmonics. Thus, Equation (3.2-10) becomes

$$B(\theta) = \sum_{h=1}^{\infty} b_{2h-1} \sin(2h-1)\theta. \qquad (3.2\text{-}11)$$

These flux densities are useful in determining flux linkages, emfs, core losses, etc.

3.2-2 EMFS:

Equation (3.2-11) assumes an infinite number of harmonics. For practical purposes, harmonic terms beyond the N^{th} term, ($N \approx 11$ in this case), the fourier coefficient, b_{2h-1}, is insignificant. The above equation can thus be rewritten as follows:

$$B(\theta) = \sum_{h=1}^{N} b_{2h-1} \sin[(2h-1)\theta + \delta_{2h-1}]. \qquad (3.2\text{-}12)$$

Defining the machine effective core length as ℓ, and the pole pitch as τ_p, the harmonic flux per pole, Φ_{2h-1}, is given by

$$\Phi_{2h-1} = (2/\pi)(\tau_p/2h-1)\ell b_{2h-1}. \qquad (3.2\text{-}13)$$

Consequently, the electromotive force induced in the armature phase is calculated from the flux linkages based on midgap flux density distribution, and can be expressed in Fourier series form as follows:

$$e(t) = \sum_{h=1}^{N} 2\pi f(2h-1)\Phi_{2h-1} T_{ph} K_{w_{2h-1}} \cos[2\pi f(2h-1)t + \delta_{2h-1})\qquad (3.2\text{-}14)$$

or as a function of the space angle

$$e(\theta) = \sum_{h=1}^{N} 2\pi f(2h-1)\Phi_{2h-1} T_{ph} K_{w_{2h-1}} \cos[(2h-1)\theta + \delta_{2h-1}] \qquad (3.2\text{-}15)$$

where f is the fundamental frequency (equal to 120 × rotor rpm/number of poles), T_{ph} is the number of series turns per phase and $K_{w_{2h-1}}$ is the winding factor for the harmonic of order (2h-1). This expression yields the emf waveforms induced in the armature phase windings, which serve as forcing functions in the simulation model used to predict the dynamic characteristics and other performance quantities resulting from the interaction between the machine and its power conditioner as detailed in Section (3.3).

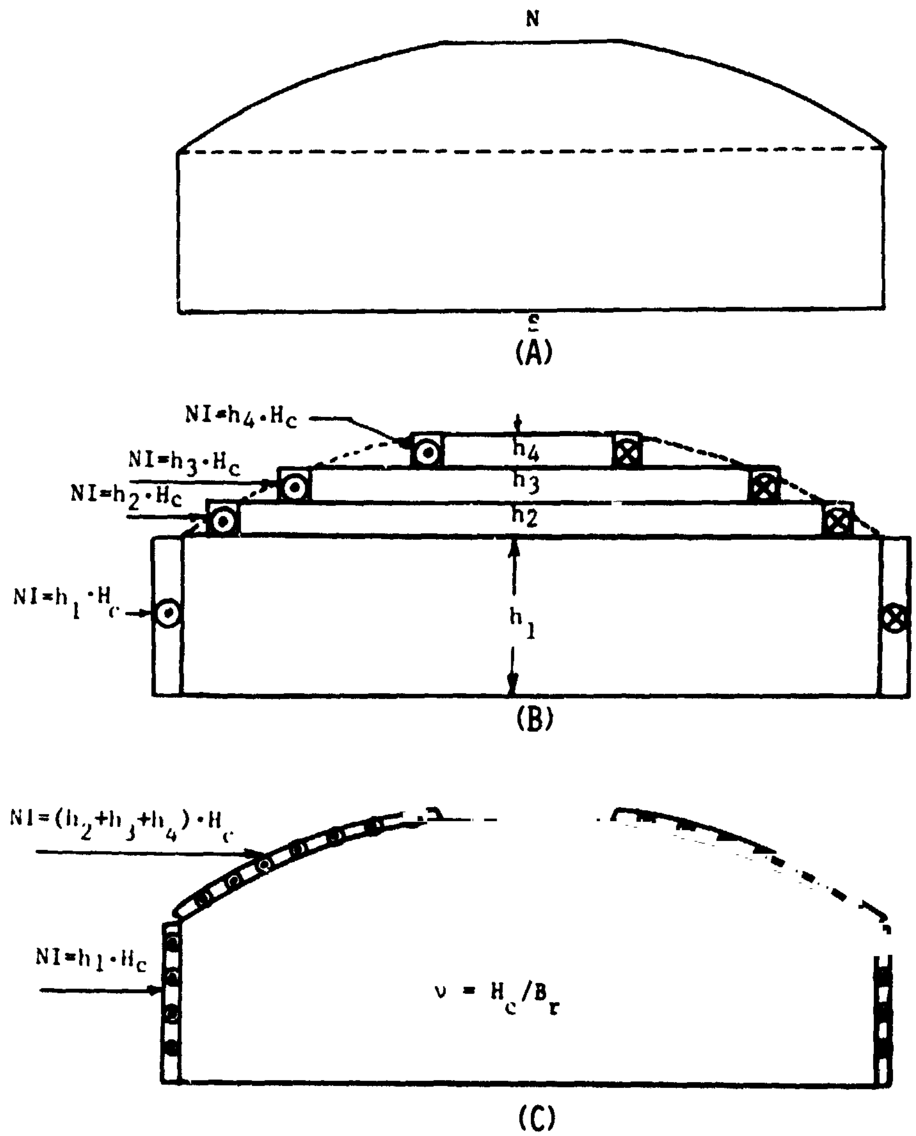

FIGURE (3.2-1) Representation of Equivalent Magnetic Effect for the Magnet Shapes of the Brushless Machines for Purposes of Finite Element Field Analysis

3.2.3 WINDING INDUCTANCES:

In calculating the machine winding inductances, an energy and current pertubations technique [22,23], coupled with the FE method, is applied. For this type of electronically commutated brushless dc machine, its armature consists of three phase windings, which can equivalently be represented as three magnetically coupled coils. Only two of these three coils are excited at any given time other than short commutation periods. Let the current through its coils 1 and 2 be i_1 and i_2, and let v_1 and v_2 be the terminal voltages of coils 1 and 2, and λ_1 and λ_2 be the flux linkages of coils 1 and 2, respectively. Then, one can write the following:

$$v_1 = R_1 i_1 + \partial\lambda_1/\partial t \tag{3.2-17}$$

$$v_2 = R_2 i_2 + \partial\lambda_2/\partial t \tag{3.2-18}$$

but $\lambda_1 = \lambda_1(i_1, i_2, \theta)$ and $\lambda_2 = \lambda_2(i_1, i_2, \theta)$.

These flux linkages are naturally dependent on the rotor position angle θ. Hence, one can write

$$v_1 = R_1 i_1 + \partial\lambda_1/\partial i_1 \bullet di_1/dt + \partial\lambda_1/\partial i_2 \bullet di_2/dt + \partial\lambda_1/\partial\theta \bullet d\theta/dt \tag{3.2-19}$$

$$v_2 = R_2 i_2 + \partial\lambda_2/\partial i_1 \bullet di_1/dt + \partial\lambda_2/\partial i_2 \bullet di_2/dt + \partial\lambda_2/\partial\theta \bullet d\theta/dt \tag{3.2-20}$$

If the rotor is held at a fixed position, the term $(d\theta/dt)$ becomes zero. In Equations (3.2-19) an (3.2-20) the $(\partial\lambda/\partial i)$ terms are the incremental inductances (see Reference [29]), L_{jk}. Hence, one can write

$$L_{jk} = \partial\lambda_j/\partial i_k, \; j \text{ (and } k) = 1,2. \tag{3.2.21}$$

In addition to the incremental inductances, other accepted definitions of saturated inductances [35,36,37] are as follows:

$$\text{apparent inductance } L_{jk}^{apt} = \lambda_{jk}/i_k \tag{3.2-22}$$

$$\text{effective inductance } L_{jk}^{eff} = 2w_{jk}/i_k^2 \tag{3.2-23}$$

where w_{jk} is the energy associated with the mutual magnetic effect stored in the magnetic field of the machine. A plot of the mutual flux linkage, λ_{jk}, linking coil j due to current i_k in coil k is given in Figure (3.2-2). This figure shows the geometrical interpretation of the incremental, apparent, and effective mutual inductances. In this figure point b represents the operating point of a given magnetic circuit, which will be referred to here as the quiescent point of the magnetic circuit, and it is the point around which one calculates the above mentioned inductances to define the parameters of such a nonlinear device. Here, one has the following:

$$\text{effective inductance} = ac/oa \tag{3.2-25}$$

$$\text{incremental inductance} = ad/oa. \tag{3.2-26}$$

Notice that the area ocf equals the shaded area obe, and od is parallel to the tangent through the quiescent point b. Also, notice that ac = $2w_j/i_k$. Hence ac/oa = $2w_{jk}/i^2{}_k$. A similar interpretation can be applied for incremental, apparent and effective self inductance terms, L_{jj}^{inc}, L_{jj}^{apt}, and L_{jj}^{eff}, respectively. Notice, always these values must be reevaluated at each different operating (quiescent) point when nonlinearities in the magnetic circuit are expected.

Since all the inductance terms which are encountered in the development which is to follow are of the incremental type, the superscript, inc, is dropped from our formulation. Hence, for a fixed rotor position Equation (3.2-19) and (3.2-20) become

$$v_1 = R_1 i_1 + L_{11}\, di_1/dt + L_{12}\, di_2/dt \tag{3.2-27}$$

$$v_2 = R_2 i_2 + L_{21}\, di_1/dt + L_{22}\, di_2/dt \tag{3.2-28}$$

The instantaneous power input into coil j is

$$\begin{aligned} P_j &= v_j i_j \\ P_j &= R_j i_j^2 + i_j L_{j1}\, di_1/dt + i_j L_{j2}\, di_2/dt \\ P_j &= P_{Rj} + P_{\phi j} \end{aligned} \tag{3.2-29}$$

Here in this case, j = 1,2. Here also, $P_{Rj} = R_j i_j^2$ is the Ohmic power dissipated in the jth coil. $P_{\phi j}$ is the power stored in the magnetic field of the device. The magnetic energy input into the j^{th} coil over a time period of t is given by

$$w_{\phi j} = \int_0^t P_{\phi j} \cdot dt. \tag{3.2-30}$$

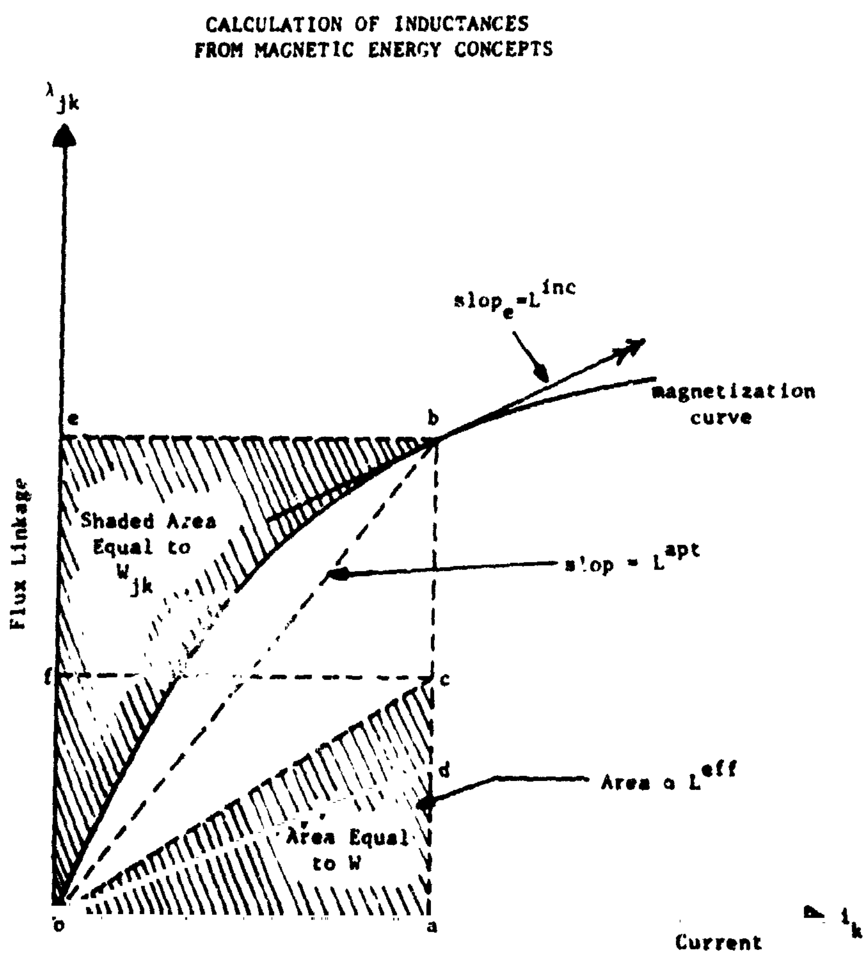

FIGURE (3.2-2) Geometrical Interpretaion of Apparent, Effective, and Incremental Inductance

ORIGINAL PAGE IS
OF POOR QUALITY

Hence, the total energy stored in the field of both coils over the time, t, can be written as:

$$w_\phi = \sum_{j=1}^{2} \sum_{k=1}^{2} \int_{i_k(0)}^{i_k(t)} L_{jk} d\, i_K . \qquad (3.2\text{-}31)$$

Suppose that both currents i_1 and i_2 are perturbed by incremental amounts Δi_1 and Δi_2 so that the magnetic saturation conditions throughout the machine are almost undisturbed, and hence, the incremental inductances remain practically the same. Under such circumstances the change in stored energy becomes

$$\Delta w_\phi = \sum_{j=1}^{2} L_{jj}(i_j \Delta i_j + \Delta i_j^2)$$

$$+ \sum_{j=1}^{2} \sum_{\substack{k=1 \\ k \neq j}}^{2} (i_j + \Delta i_j/2) L_{jk} \Delta i_k \qquad (3.2\text{-}32)$$

so that the new stored energy is now

$$\bar{w}_\phi = w_\phi + \Delta w_\phi . \qquad (3.2\text{-}33)$$

From the assumption that the incremental inductances are not changed in value due to small perturbations, Δi_j, it is easily seen that $\partial L_{jk}/\partial(\Delta i_j) = 0$ and $\partial w_\phi/\partial(\Delta i_j) = 0$. Taking the derivative of Equation (3.2-33) with respect to Δi_j and substituting in Equation (3.2-32), yields the following:

$$\partial \bar{w}_\phi/\partial(\Delta i_j) = L_{jj}(i_j + \Delta i_j)$$

$$+ \sum_{\substack{k=1 \\ k \neq j}}^{2} [i_k L_{kj} + (1/2)\, \Delta i_k (L_{jk} + L_{kj})] \qquad (3.2\text{-}34)$$

Differentiating Equation (3.2-34) with respect to Δi_j and Δi_k, yields the self and mutual inductances, which are accordingly expressed in terms of $\overline{w}_\phi$ as follows:

$$L_{jj} = \partial^2 \overline{w}_\phi / \partial(\Delta i_j)^2 \tag{3.2-35}$$

and

$$\tfrac{1}{2}(L_{jk}+L_{jk})_{j \neq k} = [\partial^2 \overline{w}_\phi / \partial(\Delta i_j)\partial(\Delta i_k]$$

However, for this type of machine, the mutual inductances are between two identical windings located on the same armature, hence the two coils are experiencing the same saturation conditions. One can therefore write

$$L_{jk} = L_{kj}. \tag{3.2-37}$$

Therefore,

$$L_{jk} = \partial^2 \overline{w}_\phi / \partial(\Delta i_j)\partial(\Delta i_k), j \neq k. \tag{3.2-38}$$

Through perturbing i_j and i_k by $\pm\, \Delta i_j$ and $\pm\, \Delta i_k$, the stored energies become $\overline{w}_\phi(i_i+\Delta i_j, i_k+\Delta i_k)$, $\overline{w}_\phi(i_j-\Delta i_j, i_k + \Delta i_k)$, $\overline{w}_\phi(i_j + \Delta i_j, i_k - \Delta i_k)$, and $\overline{w}_\phi(i_j - \Delta i_j, i_k - \Delta i_k)$. Expanding these energies in Taylor series form about the energy $\overline{w}_\phi(i_j, i_k)$ of the operating (quiescent)point, truncating terms beyond the second order terms, and combining these equations, one can write the following:

$$\begin{aligned}\partial^2 \overline{w}_\phi / \partial(\Delta i_j)\partial(\Delta i_k) \approx {} & [w_\phi(i_j+\Delta i_j, i_k+\Delta i_k) \\ & - \overline{w}_\phi(i_j-\Delta i_j, i_k+\Delta i_k) - \overline{w}_\phi(i_j+\Delta i_j, i_k-\Delta i_k) \\ & + \overline{w}_\phi(i_j-\Delta i_j, i_k-\Delta i_k)]/4\Delta i_j \Delta i_k\end{aligned} \tag{3.2-39}$$

$$\begin{aligned}= {} & [w_\phi(i_j+\Delta i_j, i_k+\Delta i_k) - w_\phi(i_j-\Delta i_j, i_k+\Delta i_k) \\ & - w_\phi(i_j+\Delta i_j, i_k-\Delta i_k) + w_\phi(i_j-\Delta i_j, i_k-\Delta i_k)]/4\Delta i_j \Delta i_k \\ & + [\Delta w_\phi(i_j+\Delta i_j, i_k+\Delta i_k) - \Delta w_\phi(i_j-\Delta i_j, i_k+\Delta i_k) \\ & - \Delta w_\phi(i_j+\Delta i_j, i_k-\Delta i_k) + \Delta w_\phi(i_j-\Delta i_j, i_k-\Delta i_k)]/4\Delta i_j \Delta i_k.\end{aligned} \tag{3.2-40}$$

The second term of the right hand side of Equation (3.2-40) is zero if Equation (3.2-32) is substituted into (3.2-40). Thus,

$$\partial^2\overline{w}_\phi/\partial(\Delta i_j)\partial(\Delta i_k) = [w_\phi(i_j+\Delta i_j, i_k+\Delta i_k) - w_\phi(i_j-\Delta i_j, i_k+\Delta i_k)$$
$$- w_\phi(i_j+\Delta i_j, i_k-\Delta i_k) + w_\phi(i_j-\Delta i_j, i_k-\Delta i_k)]/4\Delta i_j\Delta i_k \qquad (3.2\text{-}41)$$

Similarly, expanding $\overline{w}_\phi(i_j+\Delta i_j)$ and $\overline{w}_\phi(i_j-\Delta i_j)$ about $\overline{w}_\phi(i_j)$ and combining both equations,

$$[w_\phi(i_j-\Delta i_j)-2w_\phi(i_j)+w\phi(i_j+\Delta i_j)]/(\Delta i_j)^2$$
$$[w_\phi(i_j-\Delta i_j)-2w_{f.}(i_j)+w_\phi(i_j+\Delta i_j)]/(\Delta i_j)^2. \qquad (3.2\text{-}42)$$
$$[\Delta w_\phi(i_j-\Delta i_j)-2\Delta_\phi(i_j)+\Delta w_\phi(i_j+\Delta i_j)]/(\Delta i_j)^2$$

It is also easily found that the second term on the right hand side of this equation is zero. Thus,

$$[w_\phi(i_j-\Delta i_j)-2w_\phi(i_j)+2w_\phi(i_j+\Delta i_j)](\Delta i_j)^2. \qquad (3.2\text{-}43)$$

Accordingly, on the basis of Equations (3.2-35), (3.2-38), (3.2-41), and (3.2-43), the incremental self and mutual inductance terms L_{jj} and L_{jk} can be approximated in terms of the perturbed stored energy as follows:

$$L_{jj} \quad [w_\phi(i_j-\Delta i_j)-2w_\phi(i_j)+w_\phi(i_j+\Delta_j)]/(\Delta i_j)^2 \qquad (3.2\text{-}44)$$

and

$$L_{jk} \quad [w_{f.}(i_j+\Delta i_j, i_k+D.i_k)-w_\phi(i_j-\Delta i_j, i_k+\Delta i_k)$$
$$-w_\phi(i_j+\Delta i_j, i_k-\Delta i_k)+w_\phi(i_j-\Delta i_j, i_k-\Delta i_k)]/4\Delta i_j\Delta i_k \qquad (3.2\text{-}45)$$

One examines next the method of calculation of the various energy terms of Equations (3.2-44) and (3.2-45). The energy stored in the material of the machine is given by

$$W = \int_{B_1}^{B_2} H dB \qquad (3.2\text{-}46)$$

where the magnetic field intensity, H, is a function of the reluctivity, ν, and the flux density, B, [22]. The flux density is given by a solution of the algebraic equations obtained from a finite element discretization of the material cross section of the machine. Magnetic field solutions are obtained at the quiescent and perturbed points. Equation (3.2-46) is applied to each element for each of these field solutions to obtain the various energy terms in the right hand side of Equations (3.2-44) and (3.2-45). The inductances are then given by substituting these various energy terms into these equations. The reluctivity mentioned above is defined in terms of two values, namely the incremental reluctivity, ν_e^{inc}, and apparent reluctivity, ν_e^{app}, for each discretized element, e, evaluated at the quiescent point along the magnetization curve as follows·

$$\nu_e^{inc} = (\partial H/\partial B)_{quiescent} \tag{3.2-47}$$

$$\nu_e^{app} = (H/B)_{quiescent}. \tag{3.2-48}$$

In general,

$$\nu_e^{inc} \leq \nu_e^{app}$$

where the equal sign applies for linear magnetic materials or the linear part of the B-H characteristic of a nonlinear material. The above definitions of incremental and apparent reluctivities associated with a given element in an FE grid, as well as the energy perturbations per unit elemental volume associated with the two reluctivities are geometrically depicted in Figures (3.2-3) and (3.2-4). The energy perturbations per element are shown in shaded areas for equal field intensity perturbations. Notice the energy perturbation associated with the apparent reluctivity is larger than that associated with the incremental reluctivity. The energy perturbations for each element are calculated on the basis of Figures (3.2-3) and (3.2-4) which depend in turn on the quiescent point associated with each element. Since the current perturbations in Equations (3.2-44) and (3.2-45) are small, the reluctivity of each element in the FE grid can be assumed constant for these current increments and equal to either the incremental or apparent reluctivity value defined by Equation (3.2-47) or Equation (3.2-48) for the quiescent point under consideration. Thus, the solution for the field associated with the perturbed excitations is obtained from the quiescent point field solution by solving the global system of m.v.p. equations once, with the excitation perturbation as the forcing function using, either the incremental or apparent elemental reluctivities. A detailed explanation of calculating the L_{jj} and L_{jk} is given in Reference [22] which is included in Appendix (3) of this report for convenience.

The methods described above in Sections (3.2.1) through (3.2.3) were used in the determination of the various parameters (flux distributions, armature emf waveforms, armature winding inductances, etc.) associated with the samarium cobalt and strontium ferrite based machines, using the preliminary design data given earlier in Section (3.1) of this report. These are the parameters which are crucial to the simulation of the dynamic characteristics of the machine power conditioner interaction. Details are given next in Section (3.2.4) on parameter determination, and in Section (3.3) on the use of these parameters in the dynamic simulation.

ORIGINAL PAGE IS
OF POOR QUALITY

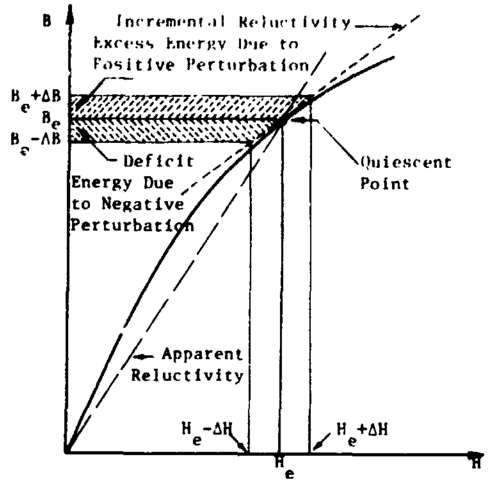

Change in Energy Stored Due to Perturbation
of Excitation in an Element.

$$\tilde{W} = \sum_{e=1}^{ne} w_e \pm \sum_{e=1}^{ne} \nu_e^{inc} \cdot (\Delta B_e) \cdot B_e \cdot d_m$$

Perturbation Along Incremental Reluctivity Line

FIGURE (3.2-3) Change in Energy Per Unit Elemental Volume Due to Perturbed Excitation, Using Incremental Reluctivity

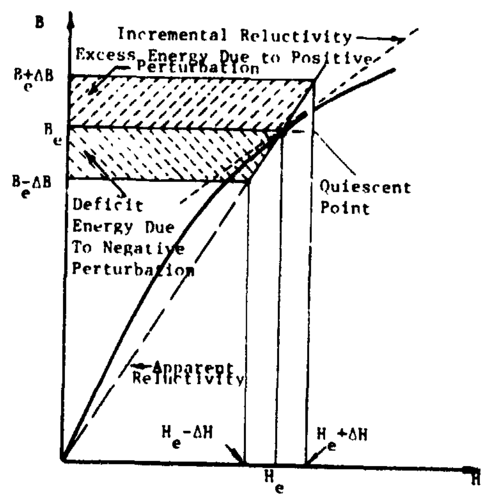

Change in Energy Stored Due to Perturbation
of Excitation in an Element.

$$\tilde{W} = \sum_{e=1}^{ne} w_e \pm \sum_{e=1}^{ne} \nu_e^{apt} \cdot (\Delta B_e) \cdot B_e \cdot d_m$$

Perturbation Along Apparent Reluctivity Line

FIGURE (3.2-4) Change in Energy Per Unit Elemental Volume Due to Perturbed Excitation, Using Apparent Reluctivity

ORIGINAL PAGE IS
OF POOR QUALITY

3.2.4 RESULTS OF SAMARIUM COBALT AND STRONTIUM FERRITE BASED MACHINES

In this work, two machines were designed, based on the use of two different permanent magnet materials. The preliminary designs of both were given earlier in Section (3.1). One machine uses high energy product samarium cobalt permanent magnets as a source of excitation on the rotor and the other machine uses less costly and more readily available strontium ferrite No. 8 permanent magnets for rotor excitation. The design steps described in Section (3.1) were also used in that section to arrive at a suitable preliminary machine volume, magnetic circuit geometry, and winding design subject to the required machine performance given earlier in Section (1.2). It is important to point out that in Section (3.1), skewing was not considered. However, it will be shown later in this section that skewing is necessary to improve the machine characteristics, and to enable the MPC systems to reach some of the required power ratings.

The calculated preliminary machine geometry was used in conjunction with the automatic FE grid generating scheme mentioned in Section (3.2-1) to arrive at a discretized machine cross section shown in Figures (3.2-5) and (3.2-6) for the samarium cobalt and ferrite machines, respectively. Both machines were then analyzed by calculating their midgap flux density waveforms, and armature winding inductances at no load. It was found from previous work that the emf waveforms [20,27,29] in such permanent magnet machines are hardly affected by the load current (armature mmf). Further work [23] demonstrated that normal armature load current hardly affects the values of the armature winding inductances. This is largely because of the low level of magnetic saturation prevalent in the magnetic circuits of these machines, and the relatively small ampere turns of the armature mmf in comparison with that of the permanent magnets under normal operating conditions (operating power range for these machines). Hence, the magnetic field analysis presented here is largely carried out at no load.

Figures (3.2-7) and (3.2-8) show the no load flux distributions resulting from the finite element analysis for a given rotor position for the samarium cobalt and strontium ferrite machines, respectively. Figures (3.2-9) and (3.2-10) are the waveforms for the rotor positions shown in the flux plots of Figures (3.2-7) and (3.2-8) of the samarium cobalt and strontium ferrite machines, respectively. Notice that the peak midgap flux density for the samarium cobalt machine is about 49,000 lines/in^2 (0.760 Tesla) compared with 19,000 lines/in^2 (0.294 Tesla) for the strontium ferrite machine. In addition, Figure (3.2-11) depicts the midgap flux densities at no load for the strontium ferrite machine at two rotor positions, the first of which is a position different from that given earlier in Figure (3.2-10), while the second is a repeat of Figure (3.2-10) for ease of comparision between the effects two rotor positions. The first flux density wave form (top) in Figure (3.2-11) shows a dip around the peak value of the flux density for a slot opening opposite the center of the magnet. The second figure (bottom) shows two dips centered around the peak value of the flux density for

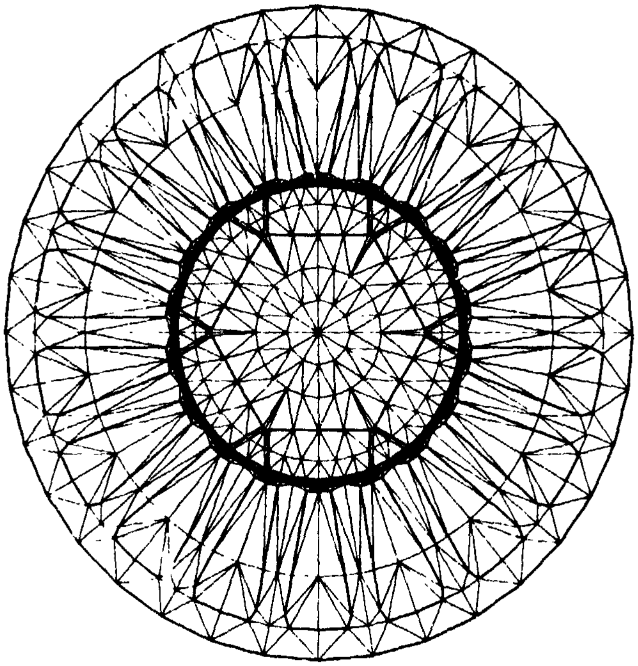

FIGURE (3.2-5) Finite Element Grid of Samarium Cobalt Machine at a Given Rotor Position

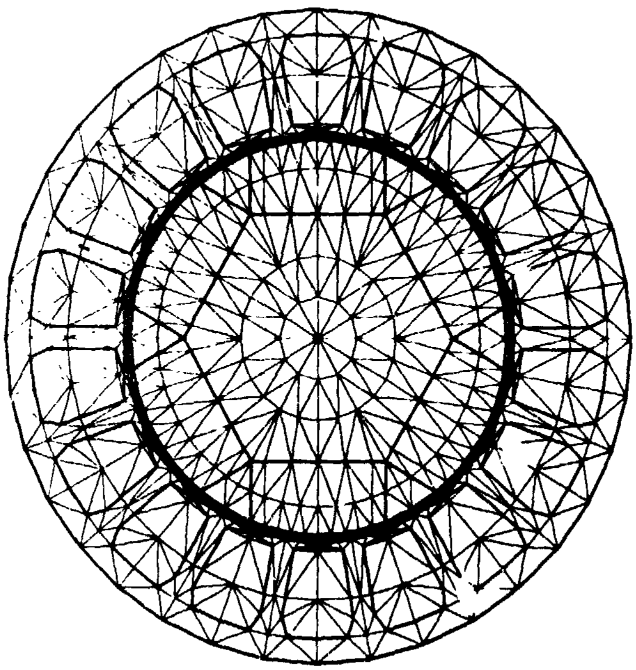

FIGURE (3.2-6) Finite Element Grid of Strontium Ferrite Machine at a Given Rotor Position

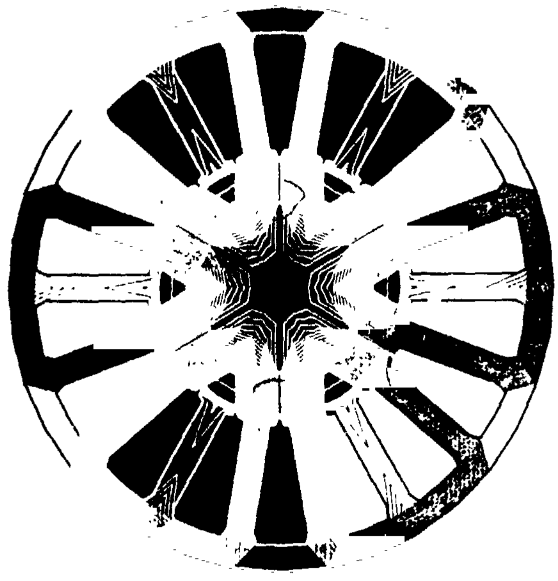

FIGURE (3.2-7) No-Load Equal MVP Conturs (Flux Plot) of the Samarium Cobalt Machine for a Given Rotor Position

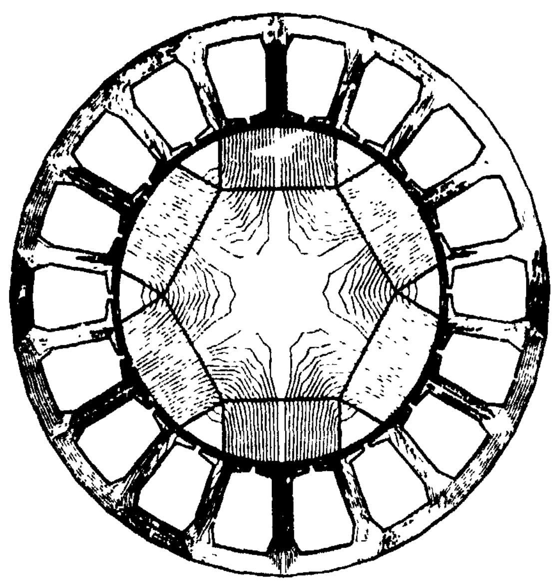

FIGURE (3.2-8) No-Load Equal MVP Conturs (Flux Plot) of the Strontium Ferrite Machine for a Given Rotor Position

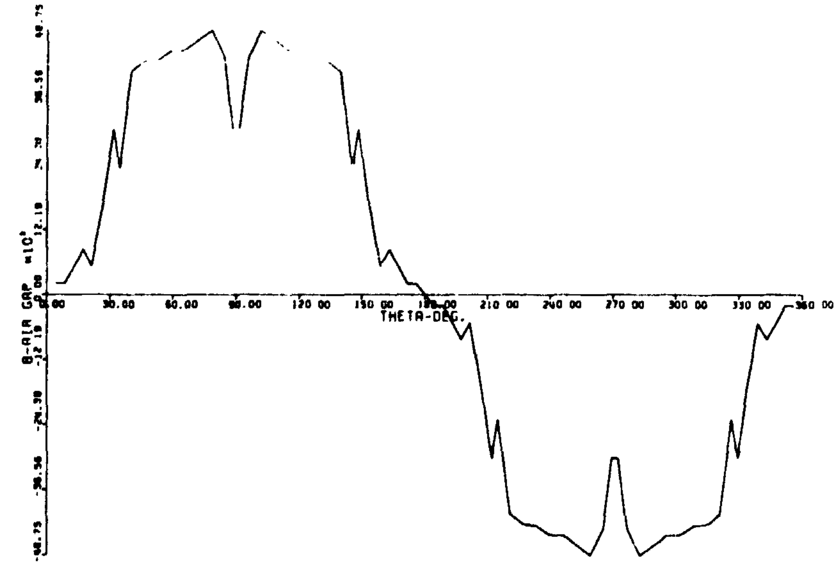

IROTAT= 1
NO LOAD

FIGURE (3.2-9) Midgap Flux Density Waveform at No Load in the Samarium Cobalt Machine - Peak Value 48,750 lines/in²

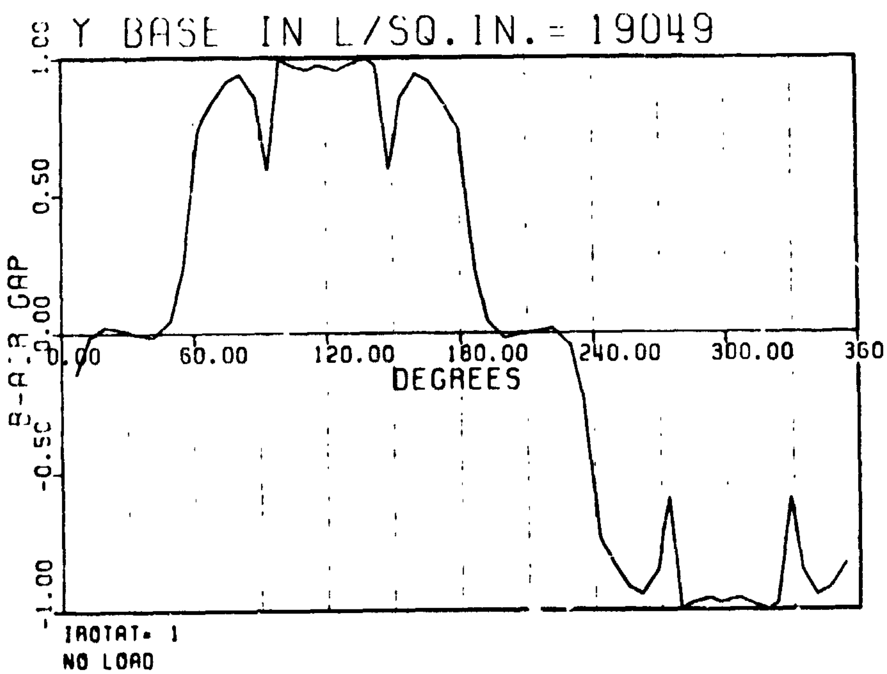

IROTAT= 1
NO LOAD

FIGURE (3.2-10) Midgap Flux Density Waveform at No Load in the Strontium Ferrite Machine - Peak Value 19,050 lines/in²

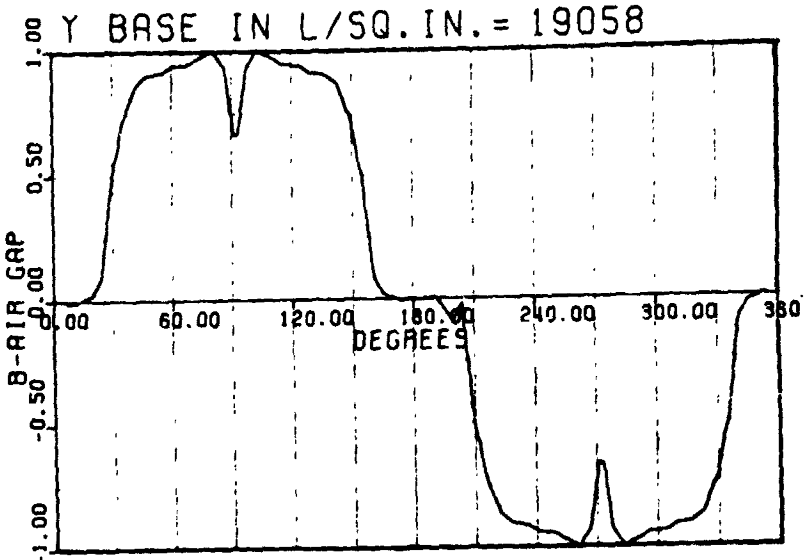

(A)

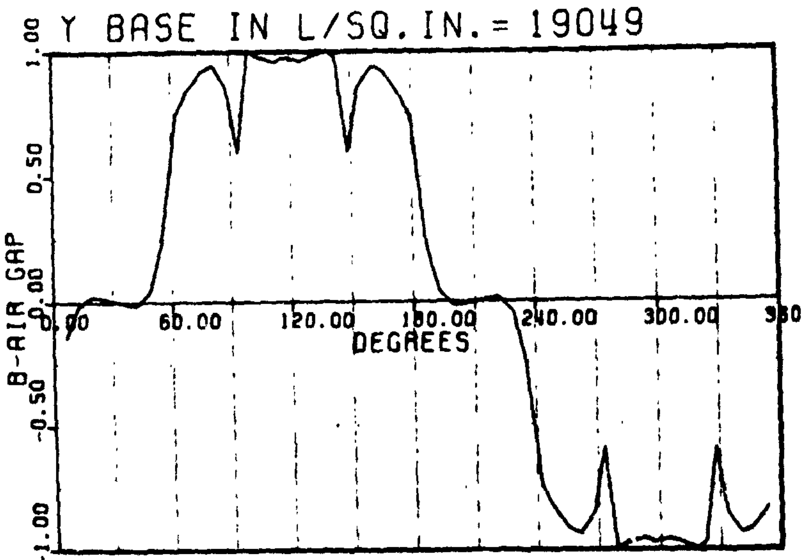

(B)

FIGURE (3.2-11) Midgap Flux Density Waveforms at No Load in the Strontium Ferrite Machine - Peak Values are 19,058 lines/in² and 19,049 lines/in² Respectively

ORIGINAL PAGE IS
OF POOR QUALITY

two slot openings which are located opposite to the center of the magnet. For these two different rotor positions, the peak flux densities show little or no difference between one another in magnitude, 19,058 lines/in² (0.303 Tesla), and 19,049 lines/in² (0.302 Tesla), respectively. This demonstrates that flux levels are almost not affected by changes in the rotor position.

Under rated load, armature phase currents (A, -A, B, -B, C, -C) were injected in the proper conductor locations in the finite element grids, at stator slot locations according to the actual phase belt distribution for a full pitched integral slot winding machine (1 slot per pole per phase arrangement for both machines). Recall that for these electronically commutated dc machines, only two of the three windings are excited throughout the duration of a state. Here, the ac cycle consists of six states as explained earlier. The exceptions are the very short commutation periods which are neglected here. The phase belt distribution of the above phase currents in the machine cross section can be easily obtained from the fact that the three phase armature winding is a double layer full pitched integral slot winding with one slot per pole per phase. Corresponding finite element analysis of the magnetic fields in the samarium cobalt and strontium ferrite machines under rated load were performed. Figure (3.2-12) shows the flux distribution by means of equal m.v.p. contours under rated load in the samarium cobalt machine. The corresponding midgap flux density waveform under load is given in Figure (3.2-13). Notice that the peak flux density of about 50,000 lines/in² (0.775 Tesla) is only due to the slight magnetization by the armature mmf on one end of the magnet. The slight increase in flux density on one end of the magnet is almost totally cancelled out by an opposite demagnetization effect of the armature reaction (mmf) on the other end of the magnet. The net result is that load has little or no effect on the magnitude of the total flux per magnet in comparison to the no load values, for rated current values.

Figure (3.2-14) shows the flux distribution by means of equal m.v.p. contours under rated load in the strontium ferrite machine for the same rotor position given earlier in the no load flux plot of Figure (3.2-8). The corresponding midgap flux density waveform under load is given in Figure (3.2-15). Again, it must be noticed that the peak flux density of about 18,680 lines/in² (0.290 Tesla) is only slightly lower than that at no load namely about 19,050 lines/in²) (0.295 Tesla) due to the slight overall demagnetization caused by the armature mmf.

To illustrate possible effects that a change in the rotor position would have on the level of magnetization throughout the magnetic circuit of the strontium ferrite machine, a second equal m.v.p. plot corresponding to a second rotor position is given in Figure (3.2-16) for a rated load case. The corresponding midgap flux density waveform under load is given in the top frame of Figure (3.2-17), where the peak value of the flux density is about 18,470 lines/in² (0.286 Tesla). For convenience of comparison the flux density waveform corresponding to the earlier rotor position of Figures (3.2-14) and (3.2-15) is repeated in the bottom frame of Figure (3.2-17), where the peak density is about

FIGURE (3.2-12) Equal MVP Contours of the Samarium Cobalt Machine at Rated Load for a Given Rotor Position

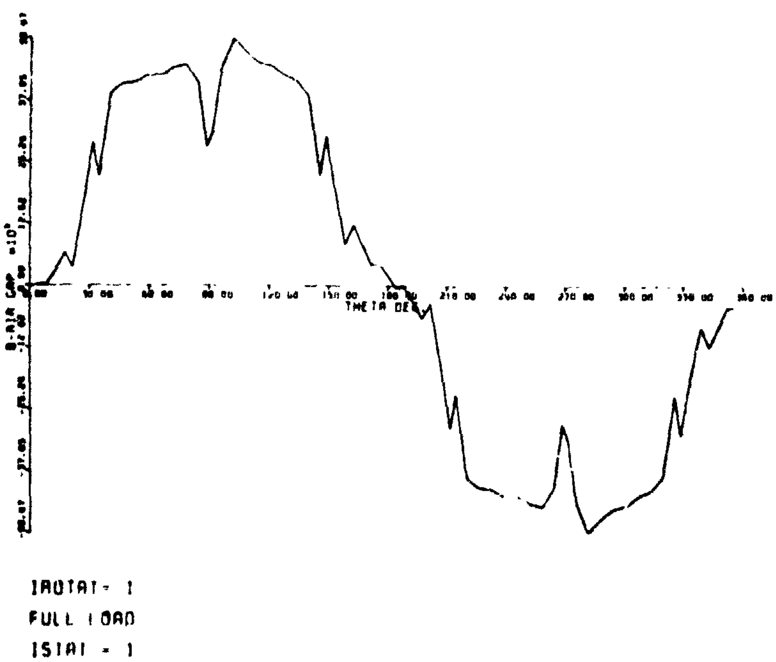

FIGURE (3.2-13) Midgap Flux Denisty Waveform at Rated Load in the Samarium Cobalt Machine - Peak Value 50,470 lines/in²

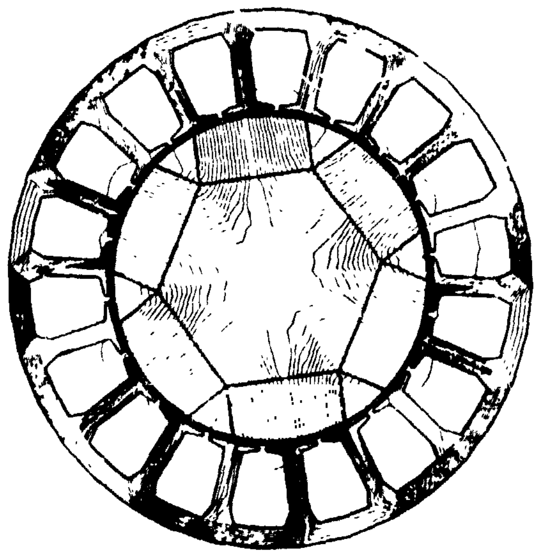

FIGURE (3.2-14) Equal MVP Contours of the Strontium Ferrite Machine at Rated Load for Rotor Postion No. 1

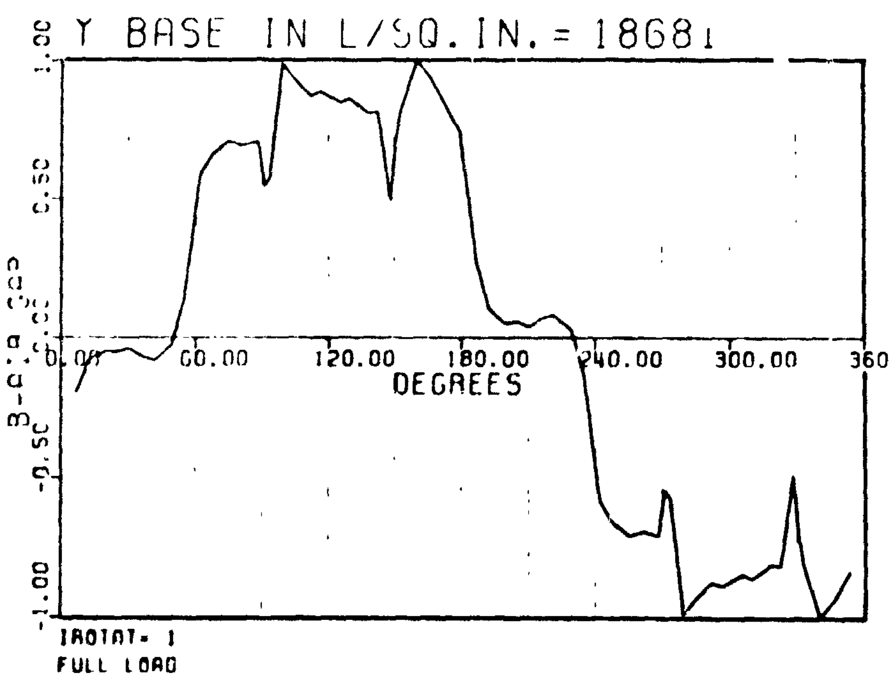

FIGURE (3.2-15) Midgap Flux Density Waveform at Rated Load in the Strontium Ferrite Machine for Roter Position No. 1 - Peak Value 18,680 lines/in²

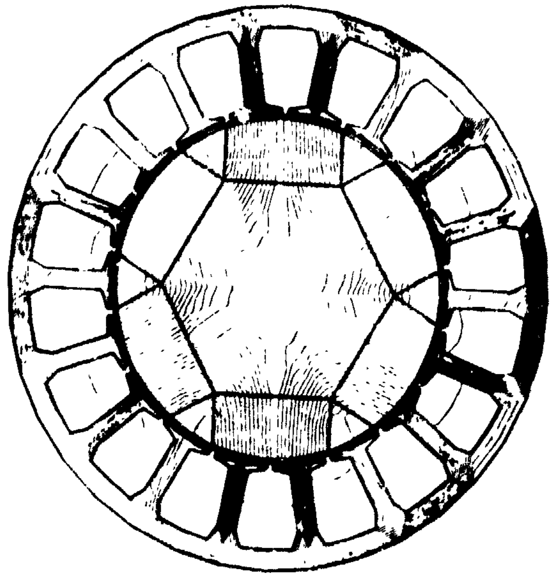

FIGURE (3.2-16) Equal MVP Contours of the Strontium Ferrite Machine at Rated Load for Rotor Position No. 2

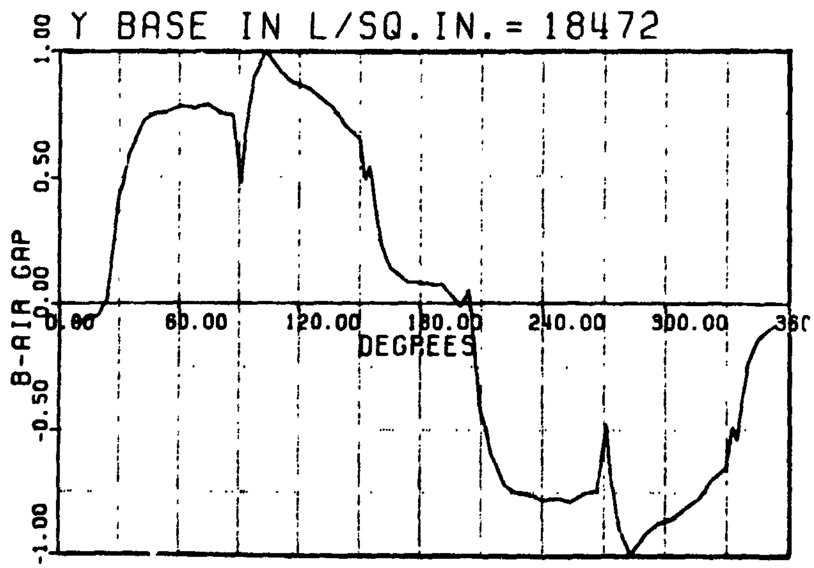

(A)

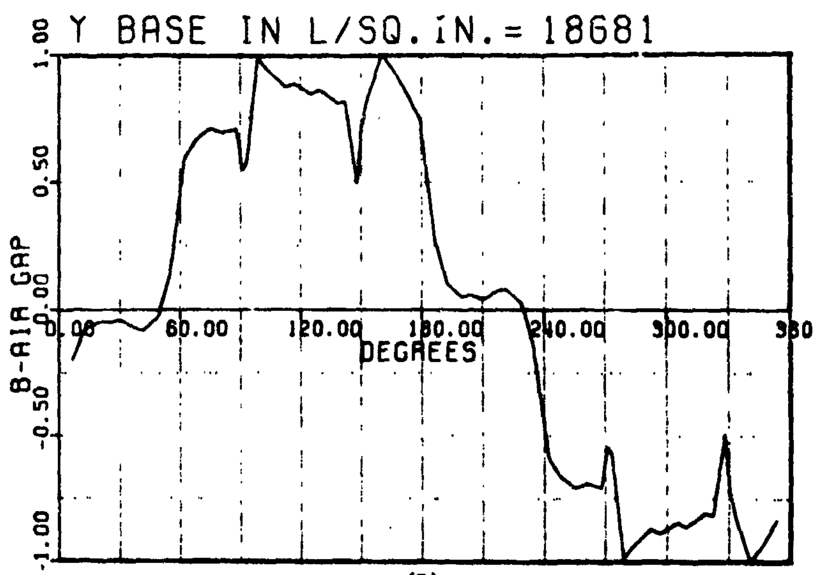

(B)

FIGURE (3.2-17) Midgap Flux Density Waveforms at Rated Load in the Strontium Ferrite Machine for two Rotor Positions No.'s 2 and 1 - Peak Values are 18,470 lines/in² and 18,680 lines/in²

C-Q

ORIGINAL PAGE IS
OF POOR QUALITY

18,680 lines/in^2 (0.290 Tesla). Again this also indicates that the effect of the rotor position on the total flux picture is rather insignificant in this case. This justifies the neglect of any saliency effects in the machine-power conditioner dynamic simulation models which are to follow. The lack of any significant saliency effect is further demonstrated in the results of the armature self and mutual inductances, which are given later in this section. Finally, it should be observed from the above results of the two machines that the armature mmf at rated loads has an insignificant influence on the overall magnetization picture in these machines, hence this justifies relying on the no load emf waveforms as sources of excitation in the machine-power conditioner dynamic simulation results which will be given in Section (3.3).

The emf waveforms were obtained as described in Section (3.2.2). Since the profiles of the no load (or rated load) midgap flux density were similar for both machines under investigation, one would expect that the emfs of both machines would have very similar profiles. Hence, emf waveforms will be shown only for the strontium ferrite machine. This choice is largely based on the fact that the (BH) energy product of the ferrite magnet material was considerably lower than that product for the samarium cobalt material. Hence, this leads to a considerably larger core for the strontium ferrite machine, with all indications of possible higher armature winding inductances. Hence, it was believed that if electric commutation difficulties are to be encountered, which may inhibit peak power capabilities (35 HP or 26 KW) of the MPC system, the strontium ferrite machine would be the likely "candidate" to lead to such difficulties. Hence, it was believed that if the analysis showed the strontium ferrite design to be capable of the peak 35 HP output, it would follow that no difficulties should be encountered in satisfying the same peak power requirement for the samarium cobalt design.

It should be reemphasized that due to the lower energy product strontium ferrite magnets in comparison to the samarium cobalt magnets, the ferrite machine had to be designed with a larger axial core length to meet the power rating of the samarium cobalt machine. Since the winding inductance is proportional to the axial machine length, the longer the armature core the higher the winding inductance. The higher the inductance, the lower the rates of phase current buildup during commutation. Therefore more of the studies (including MPC dynamic simulations) were performed on the ferrite machine case. In the absence of a built prototype (from which experimental results can be obtained), the calculated machine parameter values are sufficient enough to judge the accuracy of the design. The validity of such emf calculations was demonstrated earlier in Reference [20], inluded in Appendix [1] for convenience.

With the above points in mind, the top frame of Figure (3.2-18) shows the no load armature emf waveform of the strontium ferrite machine assuming no armature slot skewing. Notice the high harmonic content in this emf waveform.

Phase (I) of this project encompassed the design, construction and testing of a 4-pole samarium cobalt machine with a 5 slot armature, entailing a fractional slot winding to reduce harmonics. However, fractional sloting represents difficulties in manufacturing, and hence extra labor and construction costs. Accordingly, it was decided in Phase (II) to resort to a lower cost method for armature emf harmonic reduction, namely by skewing the armature slots. Furthermore, in the machines of Phase (II), the number of poles was increased to six and the number of slots was increased to 18 (entailing a simpler integral slot winding). This change also reduced the complexity of the machine winding and corresponding cost of construction. However, abandoning the fractional slot winding for the integral slot winding, causes the slot harmonics to increase in the absence of other means of harmonic reduction, as was seen in the waveform in the top frame of Figure (3.2-18). Examining the effects of stator slot skewing, see References [24] and [25] of Appendices [5] and [6] and Reference [29], on the back emf, an improvement in the emf profile was noticed as shown by comparing the middle and bottom frames of Figure (3.2-18) for half armature slot and full armature slot skewing, respectively with the top frame of the same figure, where no skewing was assumed. Notice the closeness to a sinusoid of the profile with a skewing by a full slot pitch. Skewing is accounted for analytically by including a skewing factor k_s in the winding factor calculated in Section (3.1). For the Phase (II) samarium cobalt and strontium ferrite based motors, k_s is given by:

$$k_s = \sin \tfrac{1}{2} (\pi/3)/ \tfrac{1}{2} (\pi/3)$$

Implying that the winding factor, k_w, is

$$k_w = k_s k_d k_p = 0.955$$

and the low speed (series connection) torque sensitivity becomes

$$S_t = 0.183 \text{ ft.lb./ampere } (0.248 \text{ Nm/A}).$$

At high speed (parallel connection), the corresponding torque sensitivity is

$$S_t = 0.091 \text{ ft.lb./ampere } (0.124 \text{ Nm/A}).$$

Table (3.2-1) summarizes the peak armature emf constants for the 4 and 5 turns per coil per phase for the samarium cobalt armature and the 3 and 4 turns per coil per phase for the strontium ferrite armature, when both are onnected for normal rated operation. That is, two parallel paths per phase. Notice that these are 3 coils per phase in both machines. Hence, a 4 turns per coil per phase winding is the same as a 12 turns per phase winding, and so on. These values are given assuming full slot skewing.

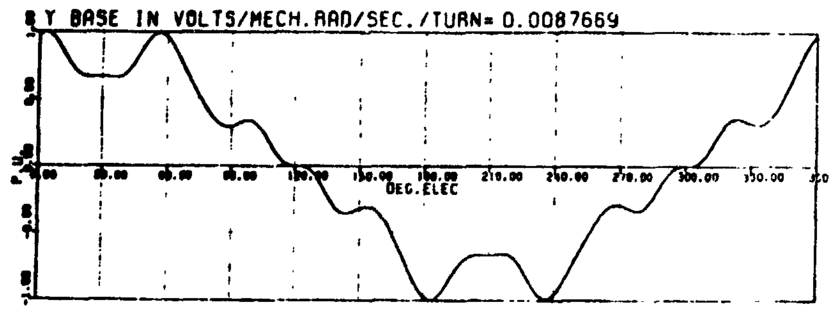

A. Unskewed Stator.

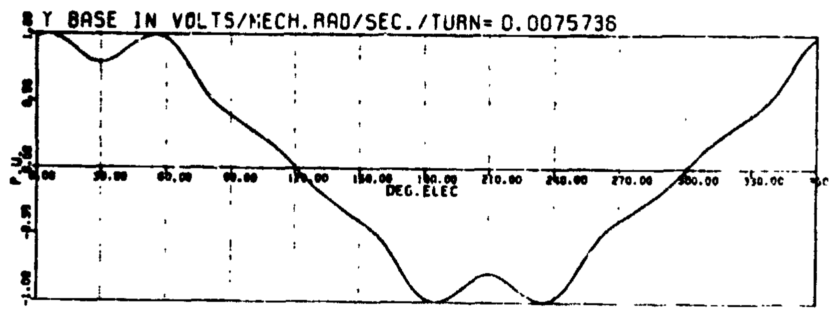

B. One Half Slot Skewing.

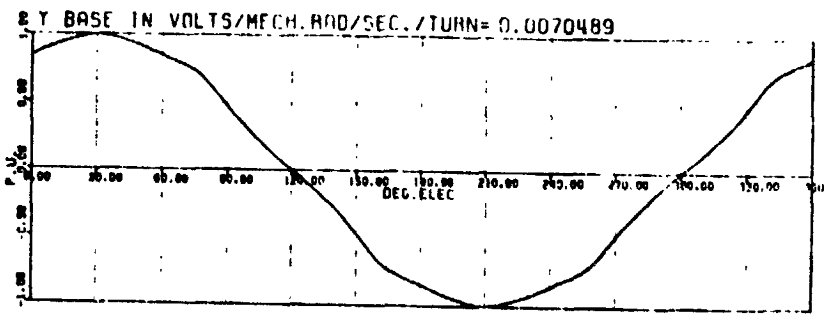

C. One Slot Skewing.

FIGURE (3.2-18) No Load Armature EMF Waveforms Calculated by the FE Analysis for the Strontium Ferrite Machine, Assuming no Armature Slot Skewing, Half Slot Skewing, and Full Slot Skewing

ORIGINAL PAGE IS
OF POOR QUALITY

3.2.5 RESULTS OF SAMARIUM COBALT AND STRONTIUM FERRITE BASED MACHINE DESIGN APPLICATIONS - ARMATURE WINDING INDUCTANCE CALCULATIONS

The various armature winding inductances in an electroncially commutated brushless dc machine of th: type at hand are depicted in a machine winding schematic of Figure (3.2-19). These inductances are phase self inductances, L_{aa}, L_{bb}, and L_{cc}, as well as the mutual inductances between the phases, $L_{ab} = L_{ba}$, $L_{bc} = L_{cb}$, and $L_{ca} = L_{ca}$. The line to line inductance terms are consequently $(L_{aa} + L_{bb} \pm 2L_{bc})$, $(L_{bb} + L_{cc} \pm 2\ L_{bc})$ and $(L_{cc} + L_{aa} \pm 2\ L_{ca})$. Upon determining the magnetic field in such a machine using the FE method one can utilize the current and energy perturbation technique of Section (3.2.3) to calculate the incremental and apparent values of these inductance terms at any desired load (or no load) condition at any given rotor position, θ.

For example, in order to calculate the self inductance terms at no load at a given rotor position, θ, one requires the calculation of the quiescent energy term, w(0), and the perturbed energy terms $w(-\Delta i_j)$ and $w(\Delta i_j)$ the subscript j here can be a, b or c. Because of the three phase armature winding symmetries, and the fact that only two windings are excited at any given instant, j = 1, 2, which refers to a and b, or b and c, or c and a. In order to calculate the above quiescent and perturbed energy terms, the magnetic field inside the machine must be calculated for these three conditions. These field distributions are shown in Figures (3.2-20) through (3.2-22) for the quiescent point at no load, the perturbed point due to a current perturbation of (Δi_j) in one of the windings, and the perturbed point due to a current perturbation of $(-\Delta i_j)$ in the same phase winding, respectively, for the samarium cobalt machine. Similar field solutions were obtained for the strontium ferrite machine in order to calculate the corresponding inductance terms. These are not shown here in the interest of brevity. It should be pointed out that close inspection of Figures (3.2-20) through (3.2-22) reveals that the current perturbations are so small that these flux distributions are almost the same with or without current perturbations. In order to calculate the self inductances of the armature phases at rated load, the energy term $w(i_j,i_k)$ is calculated from a magnetic field solution obtained with two phase currents, i_j and i_k, present in the armature coils, where j can be a or b or c and k can be a or b or c, $j \neq k$. Next, the excitation is disturbed in the winding for which the self inductance is to be calculated, that is a current $(i_j + \Delta i_j)$ is assumed and a corresponding magnetic field solution and energy term, $w(i_j + \Delta i_j,\ i_k)$, are calculated. Finally, the excitation is disturbed in the same winding, that is a current $(i_j - \Delta i_j)$ is assumed and a corresponding magnetic field and energy term, $w(i_j - \Delta i_j,\ i_k)$ are calculated.

TABLE (3.2-1) FE DETERMINED AND MEASURED BACK EMF CONSTANTS (Volts/Mech. Radian/Sec)

	SAMARIUM COBALT	
	15 turns/phase	12 turns/phase
FE MEASURED	0.0866 Not Available	0.0693 0.0658
	FERRITE	
	12 turns/phase	9 turns/phase
FE MEASURED	0.0792 Not Available	0.0594 0.0573

ORIGINAL PAGE IS
OF POOR QUALITY

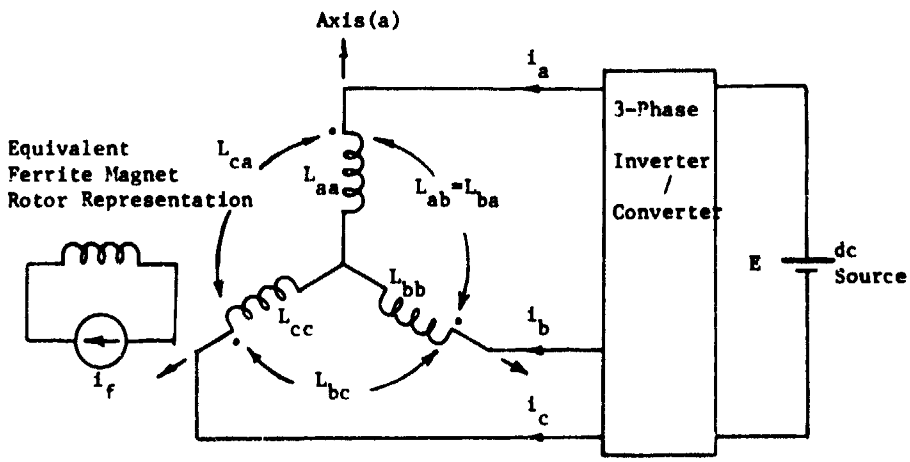

Schematic Representation of Machine-Power Conditioner System

FIGURE (3.2-19) Schematic of Machine Phase Windings and Inductances

The field solutions in the samarium cobalt machine case are shown for $(i_j + \Delta i_j, i_k)$ and $(i_j - \Delta i_j, i_k)$ in Figures (3.2-23) and (3.2-24), re spectively. Upon substitution of the energy terms $w(i_j, i_k)$, $w(i_j + \Delta i_j, i_k)$ and $w(i_j - \Delta i_j, i_k)$ in Equation (3.2-44) one obtains the self inductance for the j winding, j can be a, or b or c. In the field perturbation process, if one uses the incremental elemental reluctivities, or the apparent elemental reluctivities, Figures (3.2-3) and (3.2-4), respectively, one obtains the incremental or apparent winding self inductance, respectively.

It must be emphasized that the process of magnetic field solution under perturbed current conditions is a noniterative one, since linearization around the quiescent solution point is assumed. However, the solution for the magnetic field corresponding to each quiescent operating point is of the nonlinear iterative type, and is obtained using the Newton-Raplson method.

In order to determine the effect of the rotor position on the winding self inductances, quiescent field solution points are obtained at various rotor positions. These quiescent field solutions are then perturbed to obtain the various inductances at various rotor positions. Three examples of such quiescent field solutions calculated at the beginning, middle and end of one of the six states in an ac cycle. These solutions are depicted by equal m.v.p. contour plots in Figures (3.2-25) through (3.2-27) for the rotor position at the beginning, middle and end of a state, respectively. Similar solutions were obtained in the case of the ferrite machine. However, in the interest of brevity they will not be shown here.

The same process was repeated in calculating the mutual inductances at no load and at rated load for both the samarium cobalt and the strontium ferrite machines, respectively. In the no load case, the current perturbations are $(\Delta i_j, \Delta i_k)$, $(-\Delta i_j, \Delta i_k)$, $(\Delta i_j, -\Delta i_k)$, and $(-\Delta i_j, -\Delta i_k)$ where j and k (=1 and 2) but $j \neq k$, and the corresponding energy terms $w(\Delta i_j, \Delta i_k)$, $w(-\Delta i_j, \Delta i_k)$, $w(\Delta i_j, -\Delta i_k)$, and $w(-\Delta i_j, -\Delta i_k)$ were obtained from the perturbed field solutions. Upon substituting these energy terms in Equation (3.2-45) one obtains the mutual inductance term, L_{jk}, where j can be a, b, or c and k can be a, b, or c, $j \neq k$. The incremental or apparent inductances would result upon using the incremental or apparent elemental reluctivities in the solution for the field perturbation, respectively.

At rated load, the perturbed field solutions are obtained for perturbed excitations such as $(i_j + \Delta i_j, i_k + \Delta i_k)$, $(i_j - \Delta i_j, i_k + \Delta i_k)$, $(i_j + \Delta i_j, i_k - \Delta i_k)$, and $(i_j - \Delta i_j, i_k - \Delta i_k)$. The corresponding energy terms are $w(i_j + \Delta i_j, i_k + \Delta i_k)$, $w(i_j - \Delta i_j, i_k + \Delta i_k)$, $w(i_j + \Delta i_j, i_k - \Delta i_k)$, and $w(i_j - \Delta i_j, i_k - \Delta i_k)$. Here again, j can be a, b or c, and k can be a, b or c, $j \neq k$. Upon substitutuion of these energy terms into Equation (3.2-45) one obtains the mutual inductances under load condi-

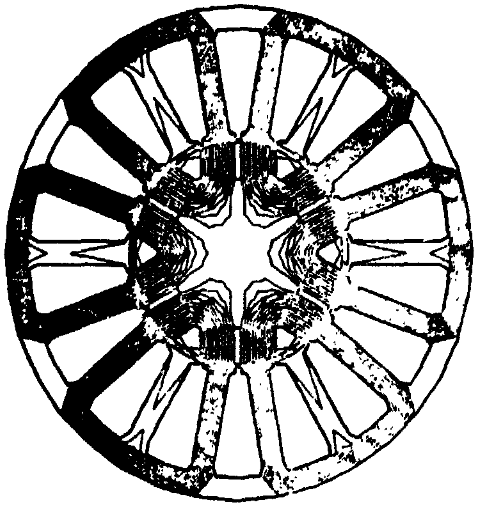

FIGURE (3.2-20) The Field Distribution for a Quiescent Point at No Load for A Given Rotor Position - The Samarium Cobalt Machine

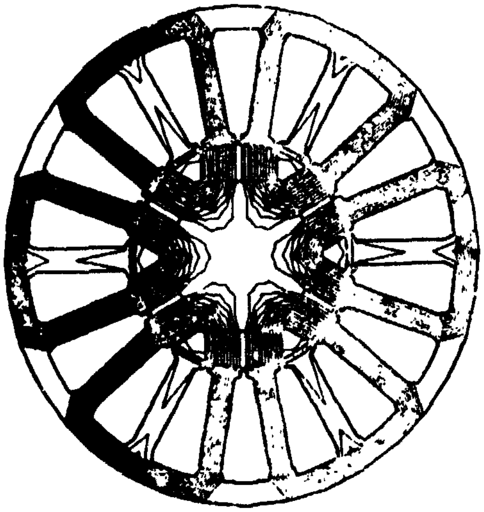

FIGURE (3.2-21) The Perturbed Field at No Load Due to $(+\Delta i_j)$ For the Rotor Position in FIGURE (3.2-20)

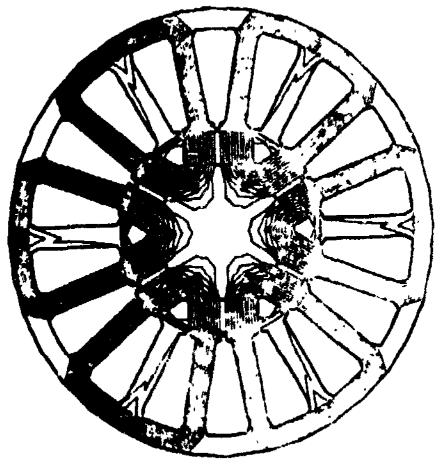

FIGURE (3.2-22) The Perturbed Field at No Load Due to $(-\Delta i_j)$ For the Rotor Position in FIGURE (3.2-20)

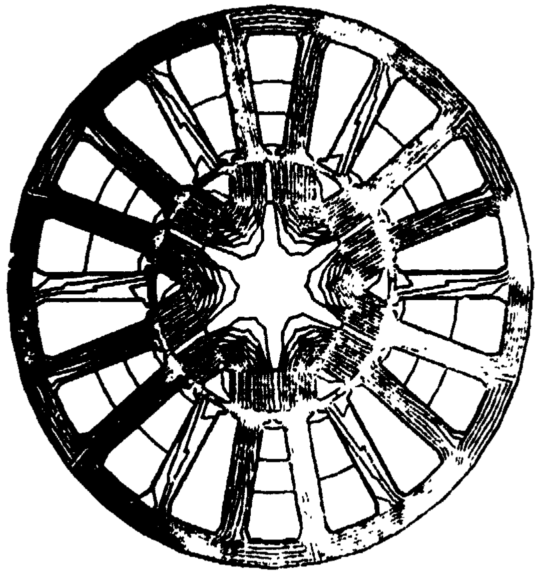

FIGURE (3.2-23) Perturbed Field Solution Due to a Perturbed Current ($i_a + \Delta i_a$, i_b)

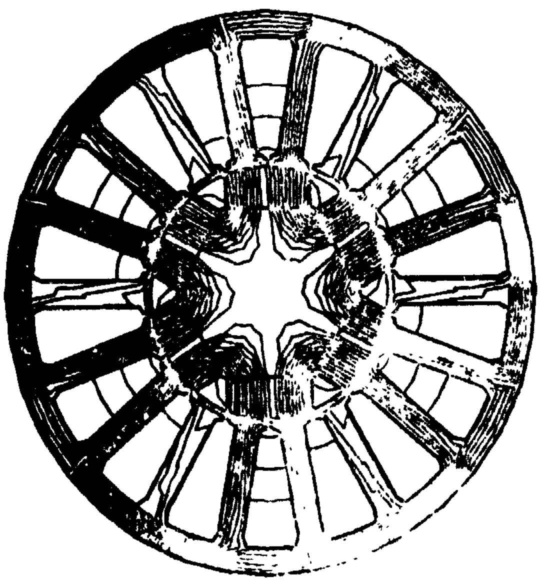

FIGURE (3.2-24) Perturbed Field Solution Due to a Perturbed Current ($i_a - \Delta i_a$, i_b)

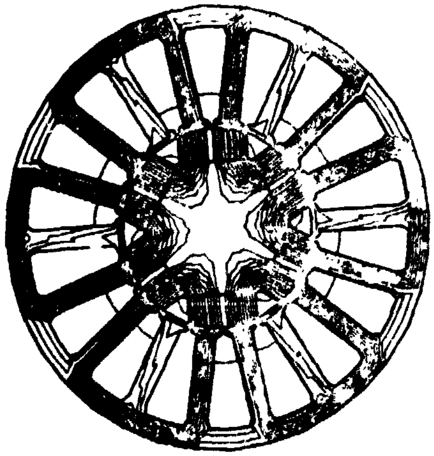

FIGURE (3.2-25) Quiescent Field Soltuion at Rated Load, Rotor Position at Beginning of State No. 1

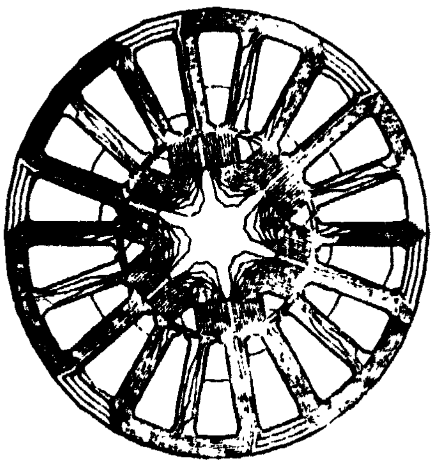

FIGURE (3.2-26) Quiescent Field Solution at Rated Load, Rotor Position at Middle of State No. 1

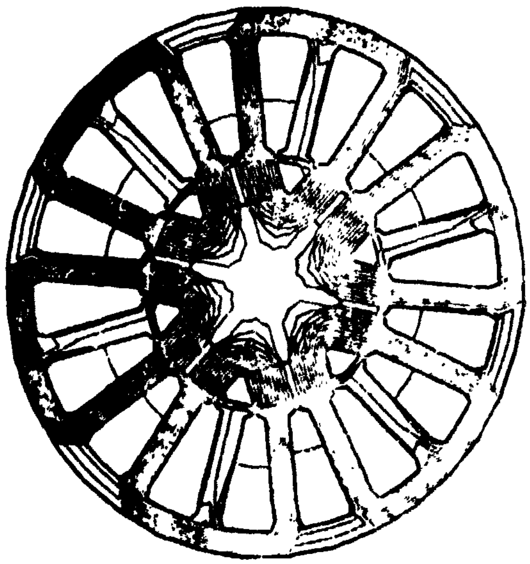

FIGURE (3.2-27) Quiescent Solution at Rated Load, Position at End of State No. 1

tion for any specified rotor position. This process was carried out for both the samarium cobalt and strontium ferrite machines. Again, the effect of rotor position on the mutual inductances can be studied by varying the rotor position and repeating the solution for the perturbed fields and associated energy terms as described above. In the above figures, notice that the flux plots differ very little due to the very small perturbation currents.

The series and parallel arrangements of each phase winding, see Figures (3.2-28) and (3.2-29), were implemented to obtain a different torque sensitivity for the low speed (series connection) and high speed (parallel connection) operations. However, it should be pointed out that parallel operation was later found to be sufficient to cover the entire required operating range of the MPC system for this application.

Calculation of the self and mutual inductances for both machines revealed that load and rotor position had small effects on the values of these inductances in comparison to their respective no load values. This will be shown in detail in data which will be given shortly. Furthermore, subsequent calculation of the inductances of the samarium cobalt machine assuming a winding with 5 and 4 turns per coil (that is 15 and 12 turns per path per phase in the parallel connection) and calculation of the inductances of the strontium ferrite machine assuming a winding with 4 and 3 turns per coil (that is 12 and 9 turns per path per phase in the parallel connection) gave values which were shown by the dynamic MPC system simulation to require choosing the lower number of turns for each machine. This will be detailed in Section (3.3). Accordingly, the machines were built with the 12 turns per path per phase and 9 turns per path per phase for the samarium cobalt and strontium ferrite cases, respectively. Subsequently, the phase-to-neutral (self) inductances, and line-to-line inductances were measured at no load with the aid of an RLC Digibridge. These inductances were also calculated using the perturbation method outlined above. A comparison between the calculated and measured inductances at no load, as well as the effect of change in rotor position at no load will be given next. Furthermore, calculations are used to predict the effect of load on these inductances, where measurement was not possible under such conditions. These results are also given next. Again, the line-to-line and phase-to-neutral inductances for the series and parallel connections were measured at no load for both machines with the aid of an ac RLC Digibridge, at different rotor positions (or angles), see References [22] and [23], which are included in Appendices [3] and [4] for convenience. The measured line-to-line inductance $L(\theta)_{line(a)-line(b)}$ from terminal (a) to terminal (b) is given in terms of the self inductances, $L_{aa}(\theta)$ and $L_{bb}(\theta)$, and the mutual inductance, $L_{ab}(\theta)$, for a given rotor positions (θ), as follows:

$$L(\theta)_{line(a)-line(b)} = L_{aa}(\theta) + L_{bb}(\theta) + 2L_{ab}(\theta) \qquad (3.2\text{-}49)$$

Figure (3.2-30) shows the incremental and apparent values of the inductance, $L_{aa}(\theta)$, for the series arrangement of the phase winding, while Figure (3.2-31) shows the incremental and apparent values of the

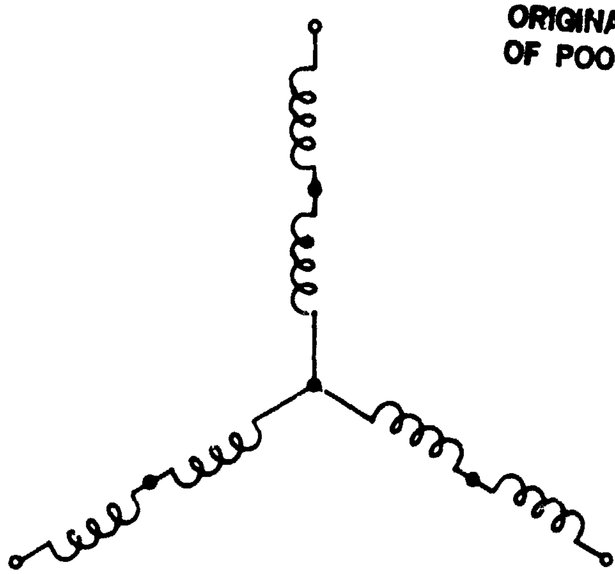

LOW SPEED

FIGURE (3.2-28) Series Winding Connection

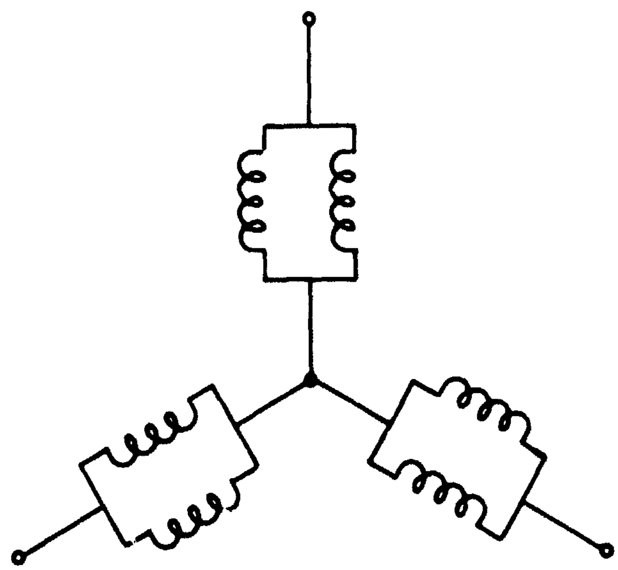

HIGH SPEED

FIGURE (3.2-29) Parallel Winding Connection

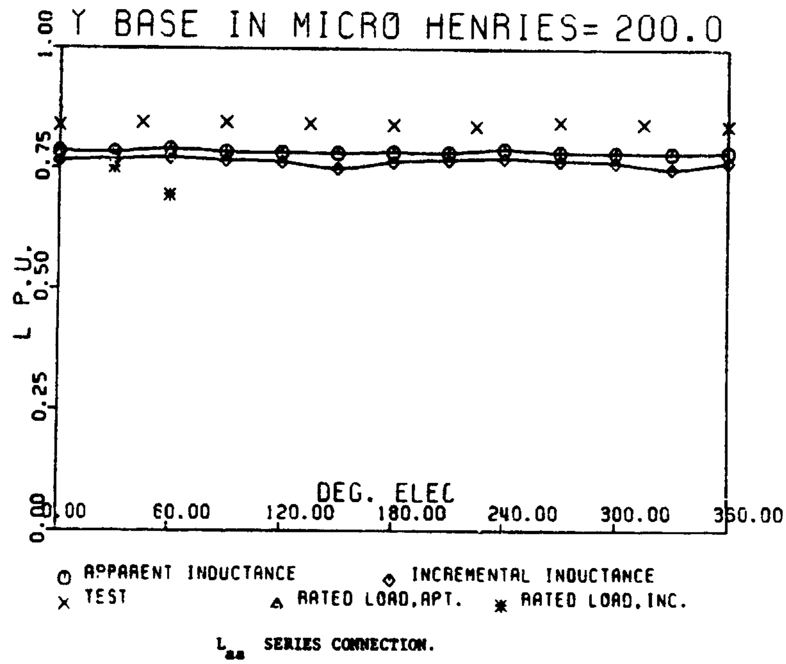

FIGURE (3.2-30) Armature Winding Self Inductance Per Phase, $L_{aa}(\theta)$, for Series Connection, Function of Rotor Postion - Samarium Cobalt Machine

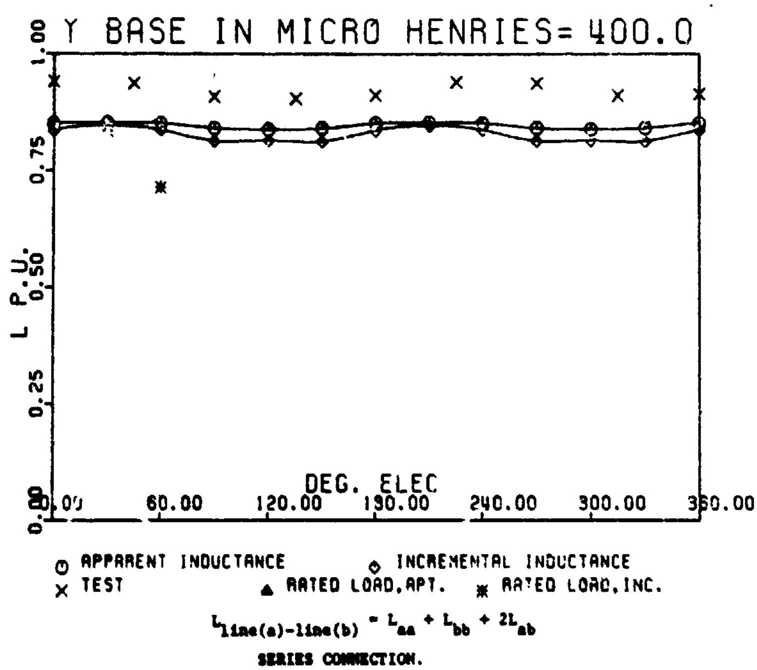

FIGURE (3.2-31) Line to Line Armature Winding Inductance, For Series Connection, Function of Rotor Postion - Samarium Cobalt Machine

TABLE (3.2-2) MEASURED INDUCTANCES OF THE Y-CONNECTED SAMARIUM COBALT MACHINE.

Test	Phase Winding Connection	Inductance (μH) versus Rotor Angle Rotor Angle - Electrical Degrees				
		0°	45°	90°	135°	180°
Phase to Neutral	Series	168.1	169.3	169.5	168.9	168.5
Phase to Neutral	Parallel	42.1	42.5	42.4	42.4	42.0
Line to Line	Series	376.7	375	363.6	361.5	364.7
Line to Line	Parallel	93.8	93.3	90.9	89.9	90.8
Test	Phase Winding Connection	Inductance (μH) versus Rotor Angle Rotcr Angle - Electical Degrees				
		225°	270°	315°	360°	
Phase to Neutral	Series	168.1	169.8	169.0	168.3	
Phase to Neutral	Parallel	42.2	42.4	42.4	42.2	
Line to Line	Series	376.2	375	364.3	365.7	
Line to Line	Parallel	93.9	93.5	91.0	91.0	

ORIGINAL PAGE IS OF POOR QUALITY

ORIGINAL PAGE IS
OF POOR QUALITY

inductance, $L_{line(a)-line(b)}$, for the series arrangement of the phase winding, for the samarium cobalt machine as function of the rotor position, (θ), over a complete ac cycle cycle (360°e). These calculated values were obtained assuming twelve (12) turns per parallel path per phase. Notice, the "x" points represent corresponding measured values.

Figure (3.2-32) shows the incremental and apparent values of the phase winding, while Figure (3.2-33) shows the incremental and apparent values of the inductance, $L_{line(a)-line(b)}$, for the parallel arrangement of the phase winding, for the samarium cobalt machine as a function of the rotor position angle, (θ). Again, 12 turns per parallel path per phase were assumed, and here also, the "x" points represent the corresponding measured values. There exists little difference between the incremental and the apparent inductance values because the magnetic material is lightly saturated (almost unsaturated).

A summary of the measured values of inductances as a function of rotor position for the samarium cobalt machine is given in Table (3.2-2). There is very little effect of the rotor position on the calculated and measured inductances due to the large effective airgap which includes the very high reluctivity region of the permanent magnet material. However, the calculated values of inductances under load condition are affectd by the load current as indicated over a period of 60°e corresponding to one of the six states in an ac cycle. This is shown in the samarium cobalt machine case by the astrisk (*) points in Figures (3.2-30) through (3.2-33). The effect of the load on the inductance values is still marginal, and can be neglected with no significant influence on evaluation of the overall MPC system performance at rated load.

Calculations were performed to determine the inductances of the strontium ferrite machine in a similar fashion to that described above for the samarium cobalt machine. An example quiescent no load field solution for a given rotor position is shown in equal m.v.p. contours in Figure (3.2-34), and an example quiescent rated load field solution for a given rotor position of the same machine is given in Figure (3.2-35). The corresponding calculated and measured values of the incremental phase to neutral self inductance and line to line incremental inductance at no load are plotted versus rotor angle in Figures (3.2-36) and (3.2-37), respectively. Notice, the values of these inductances were also calculated at typical rated load over two states and are shown by the asterisks (*) in both figures. In this case, load had almost no effect on the values of machine inductances. This is largely due to the lower flux densities prevalent in the case of this machine in comparison to the samarium cobalt case. All calulations and measurements were for a winding with 9 turns per path per phase.

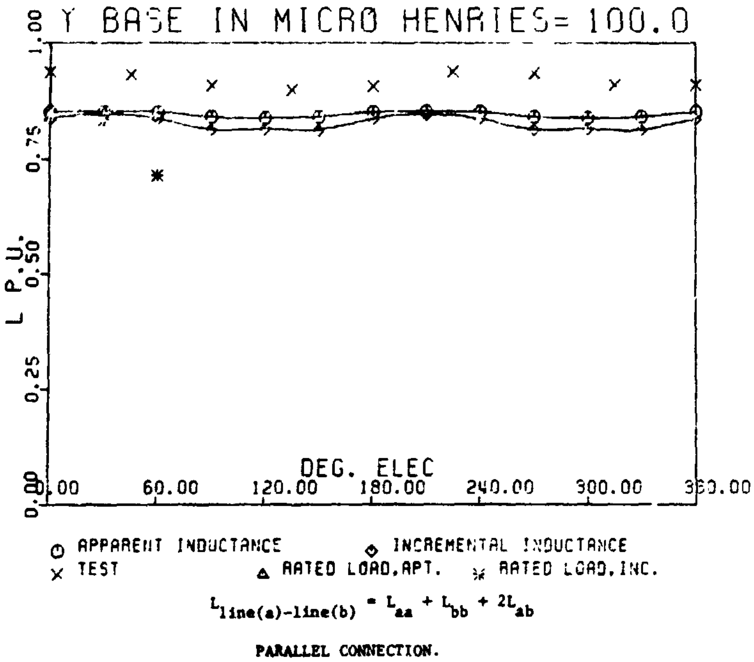

FIGURE (3.2-32) Line to Line Armature Winding Inductance, For Parallel Connection, Function of Rotor Postion - Samarium Cobalt Machine

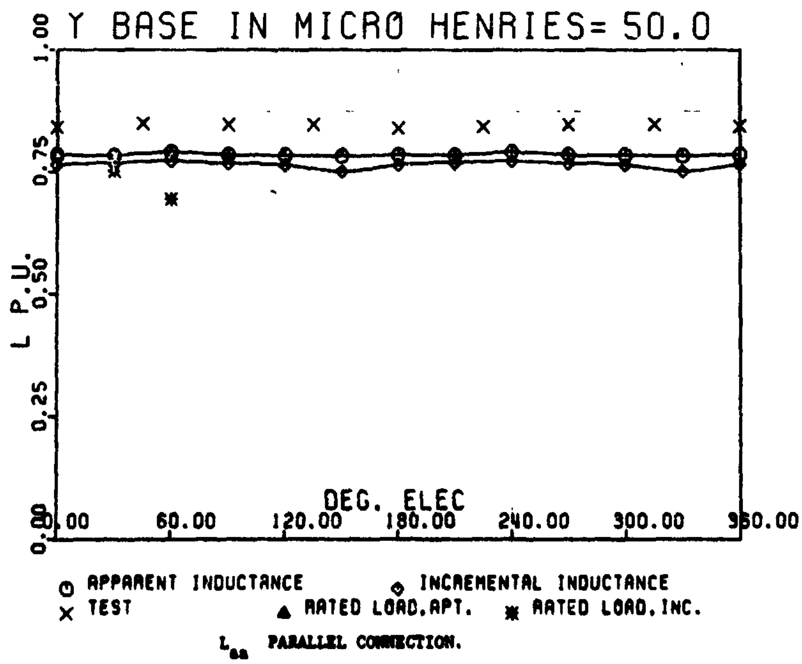

FIGURE (3.2-33) Armature Winding Self Inductance Per Phase, $L_{aa}(\theta)$, for Parallel Connection, Function of Rotor Postion - Samarium Cobalt Machine

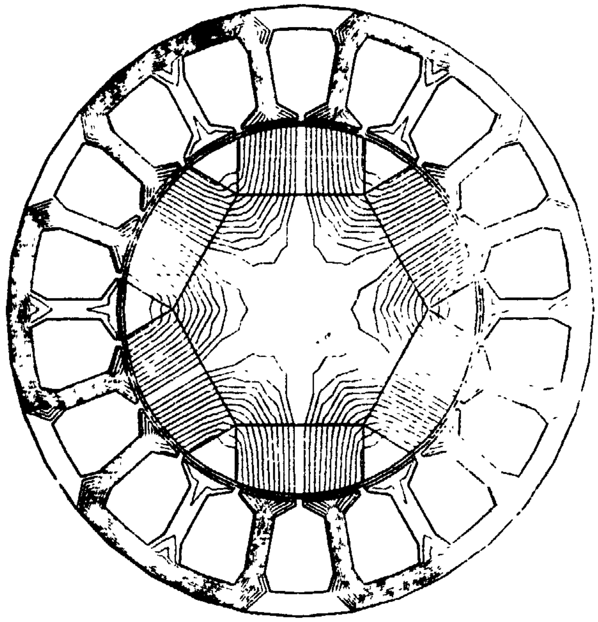

FIGURE (3.2-34) Example No Load Quiescent Field Solution Point for Calculation of Strontium Ferrite Machine Inductances

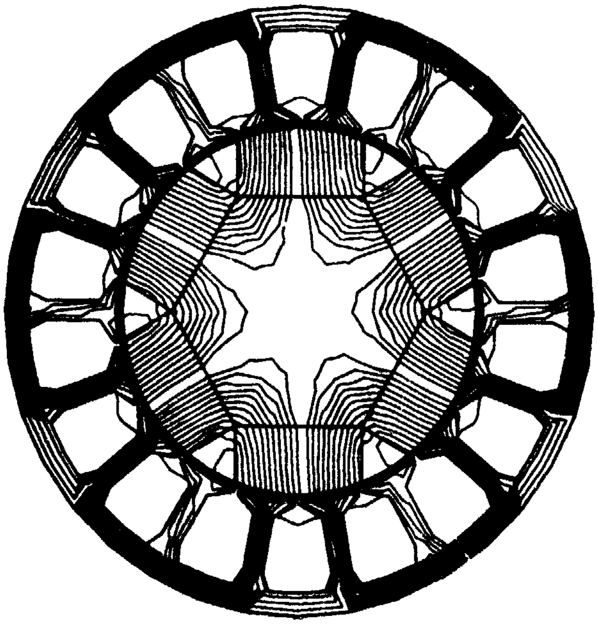

FIGURE (3.2-35) Example Rated Load Quiescent Field Solution Point for Calculations of Strontium Ferrite Machine Inductances

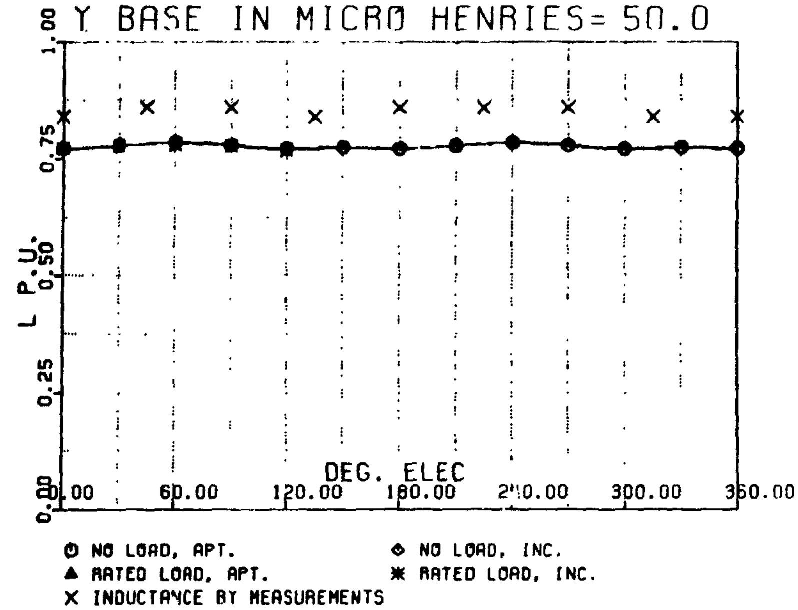

Measured and Calculated Phase to Neutral Inductance

FIGURE (3.2-36) Armature Winding Self Inducatance per Phase, $L_{aa}(\theta)$, for Parallel Connection, Function of Rotor Position - Strontium Ferrite Machine

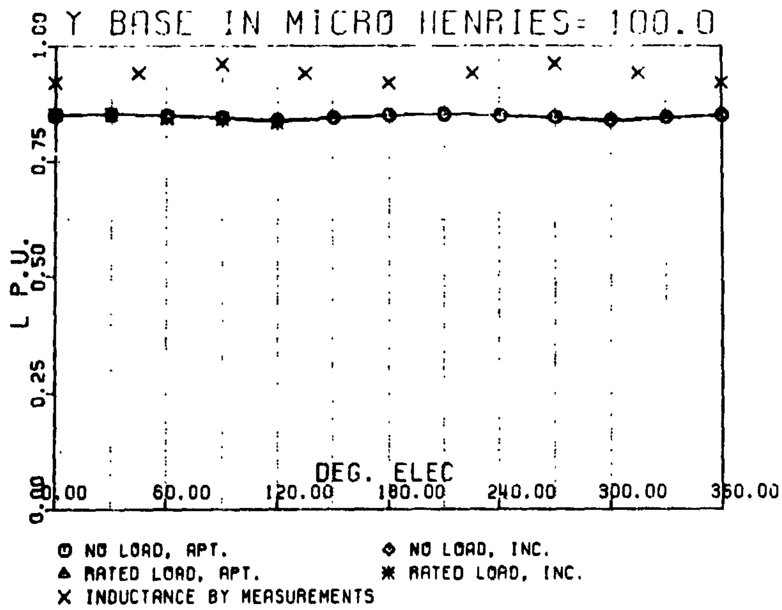

Measured and Calculated Line to Line Inductance

FIGURE (3.2-37) Line to Line Armature Winding Inducatances, for Parallel Connection, Function of Rotor Position - Strontium Ferrite Machine

ORIGINAL PAGE IS OF POOR QUALITY

TABLE (3.2-3) FE DETERMINED AND MEASURED
(LINE TO LINE) INDUCTANCES.
SAMARIUM COBALT

	12 turns/phase	15 turns/phase
FE	41.85μH	63.35μH
MEASURED	44.95μH	Not available
	STRONTIUM FERRITE	
	9 turns/phase	12 turns/phase
FE	42.5μH	75.5μH
MEASURED	46.0μH	Not available

The average line-to-line inductances were calculatd for the cases of windings with 12 and 15 turns per path per phase for the samarium cobalt case, and 12 turns per path per phase for the strontium ferrite case for subsequent use in the dynamic simultions. These values are given, with the corresponding test values when available, in Table (3.2-3).

As shown in Table (3.2-3), the measured values of the inductances are higher than the calculated ones. This difference is due to end-leakage inductance which is naturally included in the measured values whereas end-leakage inductances are not accounted for in the calculated values because of the two dimensional nature of the numerical field solutions obtained. It is essential to point out that where not indicated, calculations were made using the winding with 12 turns/path/phase for the samarium cobalt and 9 turns/path/phase for the strontium ferrite machine. The 15 turns/path/phase for the samarium cobalt and 12 turns/path/phase for the strontium ferrite were used in the preliminary design of the machines. These were abandoned subsequent to analysis and results which will be revealed in Section (3.3).

Also, as mentioned earlier, measurements were used essentially to satisfy the calculated results. However, in the absence of the measured values, the calculated ones are accurate enough to predict the behavior of the MPC systems. These calculated inductances as well as other design options and consequent parameters are used in the next section to determine the final design particulars of both machines.

3.3 ASSESSMENT OF DESIGN OPTIONS THROUGH DYNAMIC SIMULATION OF MACHINE SYSTEM

A model for simulating the dynamic and transient behavior (including the all important commutation transients associated with transistor switching operations) of the electronically controlled machine systems being considered here, will now be utilized in the process of designing such systems. The machine associated with this system consists of a rotor on which radially oriented permanent magnets are mounted, and a stationary three phase armature which is conrolled by a transistorized current source power conditioner described earlier in Chapters (1.0) and (2.0). This analysis technique and the resulting simulation model were described earlier in the literature in References [24] and [26]. These references are included, for convenience, in Appendices (5) and (7) respectively. However, for the sake of continuity and completeness of this document, a brief recapitulation of the details of this method is deemed appropriate at this stage.

As mentioned in Section (3.2), key parameters used in this dynamic simulation model such as midgap flux density, emf, and winding inductances were obtained by application of the method of two dimensional finite element solution of nonlinear magnetostatic fields to the two machines subject of this report. These key parameters were used in the dynamic simulation model to analyze the commutation transients and determine the extent, if necessary, of armature slot skewing, the sufficient number of turns per coil, and whether or not advanced firing is useful, and if so, by what angle must one advance the transistor switching instant?

Given that the power conditioner utilized here is (ideally) of the rectangular-wave currrent-source type, the armature magnetomotive force (mmf) is of a discretely and rotationally stepping nature in space, as was detailed earlier in Chapter (2.0). This is quite different from the usual smoothly rotating mmf of a conventional balanced three phase armature which is supplied with balanced three phase sinusoidally time varying armature currents. As such, the classical phasor diagram (frequency domain) type of analysis is not applicable here, since the machine is continuously in a dynamic state due to the continuous switching of phase currents. A substitute method of analysis of the performance of such a machine, and its associate conditioner, is that in which one uses digital simulation techniques to represent the continuous switching and commutation transients. This simulation technique results in a discrete time nonlinear equivalent network model of the combined system of power conditioner and machine. The topology of such a network is continuously changing due to the electronic switching process taking place throughout an ac cycle on the armature side. Hence, one resorts to network graph methods and techniques [27,28] to obtain the necessary state models representing the six states which necessarily occur in the ac cycle associated with MPC systems of the type at hand.

ORIGINAL PAGE IS
OF POOR QUALITY

3.3-1 MODEL DESCRIPTION - MACHINE EQUIVALENT CIRCUIT

Consider a network model for the radially oriented permanent magnet machine part of this MPC system. This machine, a schematic diagram of which was given earlier in Figure (3.2-19), comprises three windings which are the a, b, and c armature phases, in addition to the electromagnetic effect of the permanent magnets on the rotor. This effect can be duplicated by the presence of an equivalent fourth rotating winding, in a very similar manner to a field winding in a synchronous machine. However, in this case the field current is constant, and hence the equivalent field winding appears as if it is supplied by current from a constant current source. This fourth winding is designated as an equivalent winding (f) for the permanent magnet system, whose mmf is proportional to the coercivity of the magnet material times the magnet height (geometries), as described in References [20] and [21], which are included in Appendices (1) and (2) for convenience.

Since the magnet materials used here were samarium cobalt and strontium ferrite, and given that the conductivities of these materials are low, including relatively small induced eddy currents in the thin high resistivity stainless steel sleeves, used for securing (retaining) the magnets on the rotors, see Reference [34] included in Appendix (9) for convenience, rotor damping effects were neglected, with no adverse effects on the accuracy of the simulation. The phase to neutral voltages, v_a, v_b, and v_c, and the voltage of the equivalent field winding, v_f. can be expressed in terms of the various winding resistances, inductances and currents as follows:

$$\begin{bmatrix} v_a \\ v_b \\ v_c \\ v_f \end{bmatrix} = \begin{bmatrix} R_a & 0 & 0 & 0 \\ 0 & R_b & 0 & 0 \\ 0 & 0 & R_c & 0 \\ 0 & 0 & 0 & R_f \end{bmatrix} \begin{bmatrix} i_a \\ i_b \\ i_c \\ i_f \end{bmatrix}$$

$$+ \, d/dt \left\{ \begin{bmatrix} L_{aa} & L_{ab} & L_{ac} & L_{af} \\ L_{ba} & L_{bb} & L_{bc} & L_{bf} \\ L_{ca} & L_{cb} & L_{cc} & L_{cf} \\ L_{fa} & L_{fb} & L_{fc} & L_{ff} \end{bmatrix} \begin{bmatrix} i_a \\ i_b \\ i_c \\ i_f \end{bmatrix} \right\} \qquad (3.3\text{-}1)$$

where R_a, R_b, and R_c are the armature line-to-neutral phase winding resistances, R_f is the equivalent field winding resistance, L_{aa}, L_{bb}, and L_{cc} are the armature line-to-neutral incremental self inductances, L_{ff} is the equivalent field winding incremental self inductance, and $L_{ab}, \ldots L_{fc}$ are the incremental mutual inductances. In this case, consider the voltage v_a, which can be also expressed as

$$v_a = R_a i_a + d\lambda_a/dt \tag{3.3-2}$$

where $\lambda a = \lambda a(i_a, i_b, i_c, i_f, \theta)$ is the flux linkage. The angle θ is the armature coil position with request to a given rotating reference, or the rotor position with respect to a stator reference. Hence one can write the following:

$$\begin{aligned} d\lambda_a/dt = {} & \partial\lambda_a/\partial i_a \bullet di_a/dt \\ & + \partial\lambda a/\partial i_b \bullet di_b/dt \\ & + \bullet\bullet\bullet + \partial\lambda a/\partial\theta \bullet d\theta/dt \end{aligned} \tag{3.3-3}$$

Notice that the terms $(\partial\lambda a/\partial i_a)$, $(|M||g|_a/|M|i_b)$,..... are the incremental inductances $L_{aa} = \partial\lambda a/\partial i_a$, $L_{ab} = \partial\lambda a/\partial i_b$,..., and $d\theta/dt = \omega$, the angular rotation of the field with respect to the armature winding, that is the rotor speed. Given that no significant demagnetizations were experienced at armature currents of values near the magnitude of the rated design currents, as evidenced earlier in Section (3.2) and in the work of References [20] through [23], the incremental mutual inductance terms L_{fa}, L_{fb}, and L_{fc} representing the effect of armature reaction on the equivalent field winding can safely be neglected. Since the equivalent field winding is supplied from a constant current source, the derivative $di_f/dt = 0$. Hence Equation (3.3-1) can be rewritten as follows:

$$\begin{aligned} \begin{bmatrix} v_a \\ v_b \\ v_c \end{bmatrix} = {} & \begin{bmatrix} R_a & 0 & 0 \\ 0 & R_b & 0 \\ 0 & 0 & R_c \end{bmatrix} \begin{bmatrix} i_a \\ i_b \\ i_c \end{bmatrix} \\ & + d/dt \left\{ \begin{bmatrix} L_{aa} & L_{ab} & L_{ac} \\ L_{ba} & L_{bb} & L_{bc} \\ L_{ca} & L_{cb} & L_{cc} \end{bmatrix} \begin{bmatrix} i_a \\ i_b \\ i_c \end{bmatrix} \right\} \\ & + [i_f]\ d/dt \begin{bmatrix} L_{af} \\ L_{bf} \\ L_{cf} \end{bmatrix} \end{aligned} \tag{3.3-4}$$

ORIGINAL PAGE IS
OF POOR QUALITY

For these machines (samaraium cobalt and strontium ferrite), it was found that the variation of the armature windings' self and mutual incremental inductances, as well as line-to-line incremental inductance with respect to rotor position was negligible. This can be clearly ascertained from the results of Section (3.2) and References [22] and [23] included in Appendices (3) and (4). Thus, little error is introduced by assumming that the phase self and mutual incremental inductances are constant and independent of rotor position, θ. That is,

$$L_{aa} = L_{bb} = L_{cc} = L \qquad (3.3\text{-}5)$$

$$L_{ab} = L_{ba} = L_{ac} = L_{bc} = L_{cb} = M \qquad (3.3\text{-}6)$$

$$R_a = R_b = R_c = R \qquad (3.3\text{-}7)$$

$$\begin{bmatrix} v_a \\ v_b \\ v_c \end{bmatrix} = \begin{bmatrix} R & 0 & 0 \\ 0 & R & 0 \\ 0 & 0 & R \end{bmatrix} \begin{bmatrix} i_a \\ i_b \\ i_c \end{bmatrix} + \begin{bmatrix} L & M & M \\ M & L & M \\ M & M & L \end{bmatrix} \bullet d/dt \begin{bmatrix} i_a \\ i_b \\ i_c \end{bmatrix} + [i_f]\ d/dt \begin{bmatrix} L_{cf} \\ L_{bf} \\ L_{cf} \end{bmatrix} \qquad (3.3\text{-}8)$$

since L_{af}, L_{bf}, L_{cf} are functions of the rotor posiion, θ(t), one can write

$$\left[i_f\right] d/dt \begin{bmatrix} L_{af}(\theta) \\ L_{bf}(\theta) \\ L_{bf}(\theta) \end{bmatrix} = \left[i_f\right] \begin{bmatrix} \partial L_{af}/\partial\theta \\ \partial L_{bf}/\partial\theta \\ \partial L_{cf}/\partial\theta \end{bmatrix} \bullet d\theta/dt \qquad (3.3\text{-}8)$$

The induced emf in phase 'a' due to the permanent magnet rotor flux is given by

$$e_a = d(i_f L_{af})/dt = i_f\ (dL_{af}/dt) + L_{af}\ (di_f/dt) \qquad (3.3\text{-}9)$$

But i_f is independent of time, therefore

ORIGINAL PAGE IS
OF POOR QUALITY

$$e_a = i_f(dL_{af}/dt) = i_f(\partial L_{af}/\partial\theta)\bullet(d\theta/dt)$$
$$= i_f(\partial L_{af}/\partial\theta) \bullet \omega \qquad (3.3\text{-}10)$$

where ω is the anglar speed of the rotor. Hence, the vector in Equation (3.3-3) is nothing other than the induced emfs in the a, b, and c phases of the armature, e_a, e_b, and e_c respectively. Accordingly, one can write the following:

$$\begin{bmatrix} e_a \\ e_b \\ e_c \end{bmatrix} = \omega i_f \begin{bmatrix} \partial L_{af}/\partial\theta \\ \partial L_{bf}/\partial\theta \\ \partial L_{cf}/\partial\theta \end{bmatrix} \qquad (3.3\text{-}11)$$

Equation (3.3-11) gives an expression for the no-load phase-to-neutral back emf of the motor as a function of:

1. rotor angular speed, ω,
2. the permanent magnet equivalent field excitation current, i_f, and
3. the rate of change of the magnetic coupling between stator and rotor with respect to the rotor position, θ.

These no-load emfs, e_a, e_b, and e_c, are readily obtained from the finite element field solutions as detailed in Section (3.2).

Because the three phases of the machines at hand are , Y-connected with a floating neutral point (i.e. not grounded), one can write

$$i_a + i_b + i_c = 0 \qquad (3.3\text{-}12)$$

and

$$di_a/dt + di_b/dt + di_c/dt = 0. \qquad (3.3\text{-}13)$$

From Equation (3.3-8), it follows that

$$v_a = Ri_a + L(di_a/dt) + M(di_b/dt + di_c/dt) + i_f(dL_{af}/dt) \qquad (3.3\text{-}14)$$

Substituting Equation (3.3-13) into Equation (3.3-14) one obtains

$$v_a = Ri_a + (L\text{-}M)\, di_a/dt + e_a \qquad (3.3\text{-}15)$$

Writing similar expressions for v_b and v_c as for v_a in Equation (3.3-15), Equation (3.3-8) can be rewritten as follows:

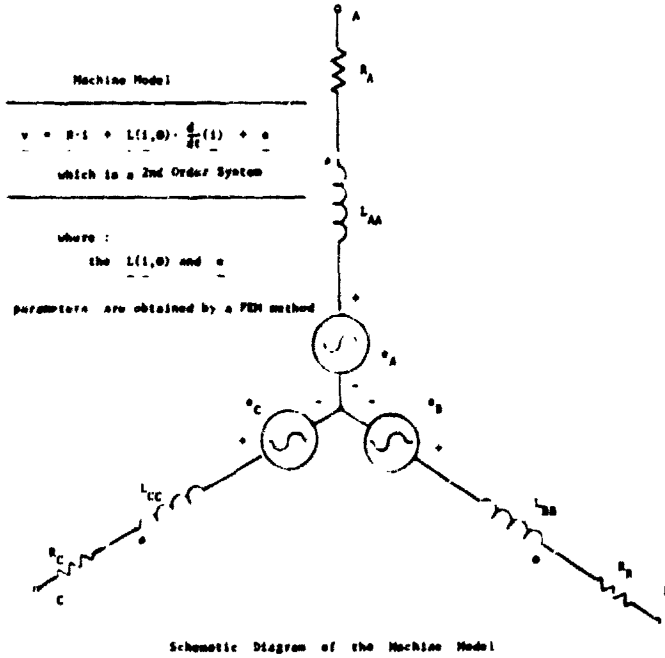

FIGURE (3.3-1) Machine Model.

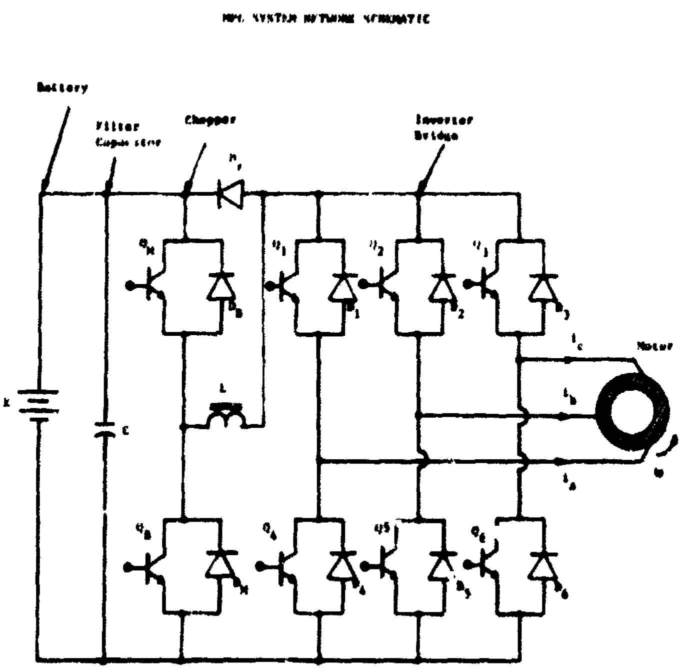

FIGURE (3.3-2) Power Conditioner Schematic

ORIGINAL PAGE IS
OF POOR QUALITY

$$\begin{bmatrix} v_a \\ v_b \\ v_c \end{bmatrix} = \begin{bmatrix} R & 0 & 0 \\ 0 & R & 0 \\ 0 & 0 & R \end{bmatrix} \begin{bmatrix} i_a \\ i_b \\ i_c \end{bmatrix} +$$

$$\begin{bmatrix} (L-M) & 0 & 0 \\ 0 & (L-M) & 0 \\ 0 & 0 & (L-M) \end{bmatrix} \bullet d/dt \begin{bmatrix} i_a \\ i_b \\ i_c \end{bmatrix} + \begin{bmatrix} e_a \\ e_b \\ e_c \end{bmatrix}. \qquad (3.3\text{-}16)$$

Equation (3.3-16) is a decoupled system of equations which can be easily solved. The schematic representation of Equation (3.3-16) is shown in Figure (3.3-1). In this schematic the inductances $L_{AA} = L_{BB} = L_{CC} = (L-M)$ of Equation (3.3-16), and $R_a = R_b = R_c = R$. It should be pointed out that (L-M) is equal to half the line-to-line armature winding inductance of Figures (3.2-31), (3.2-33), and (3.2-37).

3.3.2 MODEL DESCRIPTION - POWER CONDITIONER EQUIVALENT CIRCUIT

Now, one considers the development of an equivalent network model to the power conditioner which is shown schematically in Figure (3.3-2). In such a PC equivalent circuit model, transistors are represented as nonlinear resistors having very low values during the "on" state and having extremely highvalues during the "off" state of a particular transistor. This is to simulate numerically the process of switching "on" and switching "off" of the inverter as well as the chopper transistor of the PC. This is the switching "on" and "off" mandated by the electronic communtation process in the inverter, as well as the line current and torque control process accomplished by the chopper. Both functions were explained in detail in Chapter (2.0). In a similar manner, diodes are represented as resistors with extremely low resistance values when they are in the "forward biased" mode, and represented as resistors with extremely high values when operating in the "reverse biased" mode. The input filter capacitor is represented as a time-invariant capacitance. The dc source (battery) is represented as an ideal source of emf in series with a resistor equal to the anticipated internal resistance of typical batteries. Here, the chopper inductor is represented as a constant inductance independent of the saturation status in the inductor core. This is justified by the low level of saturation in such an inductor in the normal operating range of the MPC system.

3.3.3 MODEL DESCRIPTION - COMBINED MPC SYSTEM MODEL

Combining the equivalent circuit models of the machine and the power conditioner described above, one obtains the network graph shown in Figure (3.3-3). In this graph the dark lines represent the twigs (T) of the chosen tree and the lighter lines represent the links (L) of the

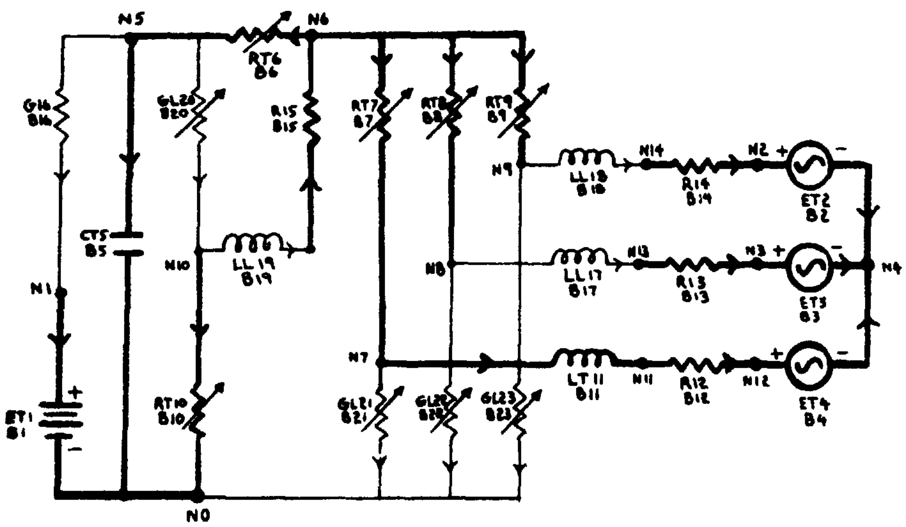

FIGURE (3.3-3) Machine - Power Conditioner System Network Graph cotree. To distinguish between different branches and their components, of the graph, two different labels are given per branch. For example, B1 denotes branch No. 1. The second letter attached to the components C, E, L, and R (for capacitor, emf, inductor, and resistor) identifies the component in a link or twig and its number in the nework graph. Node NO is assumed to be grounded, and therefore is taken as the reference for the other node voltages. Branch currents are denoted by IB followed by the appropriate branch number while the branch voltages are denoted by VB and followed by the corresponding branch number.

Having identified the tree, cotree, twigs and their components, and the links and their components, standard graph theory techniques are applied as described in Reference [28] and described for this type of system in References [26] and [27], see Reference [26] in Appendix (7). The result of applying these techniques is a set of first-order differential equations (also called state-space equations) of the form

$$\dot{\underline{X}} = \underline{A}\underline{X} + \underline{B}\underline{U} \tag{3.3-17}$$

In Equation (3.3-17) $\underline{X}$ is a vector of the cotree inductor currents comprising the current through the chopper inductor and the currents through two of the machine inductances (since only two of the three phase windings are excited at a time, and the three phase currents must always add up to zero, $i_a + i_b + i_c = 0$, hence only two of the three phase currents are independant variables), and the tree capacitor voltages.

The vector $\underline{U}$ is the forcing function vector consisting of the battery voltage and the three back emfs e_a, e_b, and e_c obtained from the finite element field analysis of the machines, as given in Section (3.2). The matices $\underline{A}$ and $\underline{B}$ are the nonlinear coefficient matrices formed by the inductance (chopper inductor, and motor inductances, where motor inductances are determined by finite elements as described earlier), capacitance, and resistance values of the network components. For explicit expressions of the state space equations, see Reference [26] which is included in Appendix (7) for convenience. While most of the network components are given, it must be restated that the back emfs and machine inductances were obtained from finite element field analysis during the design stage and were subsequently confirmed by test after construction of the machines. Figure (3.3-4) shows a simplified flow chart of the algorithm used to implement the above MPC system model.

This dynamic simulation model which is suited for the type of electronically commutated, brushless dc machine systems, with radially oriented permanent magnets, has been used to simulate the dynamics of two systems of this type. These systems were independently designed and tested. A comparison between the results of the testing of these two systems and the corresponding results of the dynamic simlations verified the validity and excellent accuracy of results of the numerical simulation. These test and numerical simulation results are displayed in current and voltage oscillogram and computer simulated waveform comparisons included in References [2] and [24] given here in Appendices (7) and (5), respectively.

COMPUTER AIDED FINALIZATION OF CHOICE OF DESIGN OPTIONS

Having developed the dynamic network model of the power conditioner-permanent magnet machine system for the samarium cobalt and strontium ferrite based machines, and developed a finite element based model for determination of machine parameters, these two models are used in the development and choice of practical options of design modifications to be applied to the preliminary design, in order to insure that the final design of the MPC systems when implemented, will meet the various rated and peak power equirements. These options of design modifications center on:

1. the number of turns per coil in the armature phase windings, and

2. whether armature slot skewing is a necessity and if so, what is the necessary skewing angle,

3. the question of whether the concept of advanced commutation (advanced firing of the inverter transistors which was discussed in Chapter (2.0)) enhances the ability of the MPC system to achieve higher horsepower outputs, and if so, what is a suitable commutation advance angle?

The determination of these various options for design modifications was accomplished by utilizing the combined power conditioner-permanent magnet machine dynamic performance model at various current commands and speeds, using the back-emf profiles and winding inductances obtained from the finite element solution of the magnetic field in these machines, as described in Section (3.2.2). The models are used to predict the performance of the MPC systems, that is, maximum output horsepower capabilities, currents and voltages througout the MPC system, etc. when two different sets of numbers of turns per coil are used in the windings of the samarium cobalt and strontium ferrite based machine, respectively. In the samarium cobalt machine case, the effects of the use of 5 and 4 turns per coil (15 and 12 turns/path/phase) were simulated. The number of turns influences heavily the machine winding inductance, which in turn influences the MPC system performance, such as magnitudes and widths of voltage spikes across the inverter transistors, as well as rates of buildup of commutated phase currents. In the strontium ferrite machine case, the effects of the use of 4 and 3 turns per coil (12 and 9 turns/path/phase) were simulated. Notice that there are three coils per phase in both machines. Hence, for the

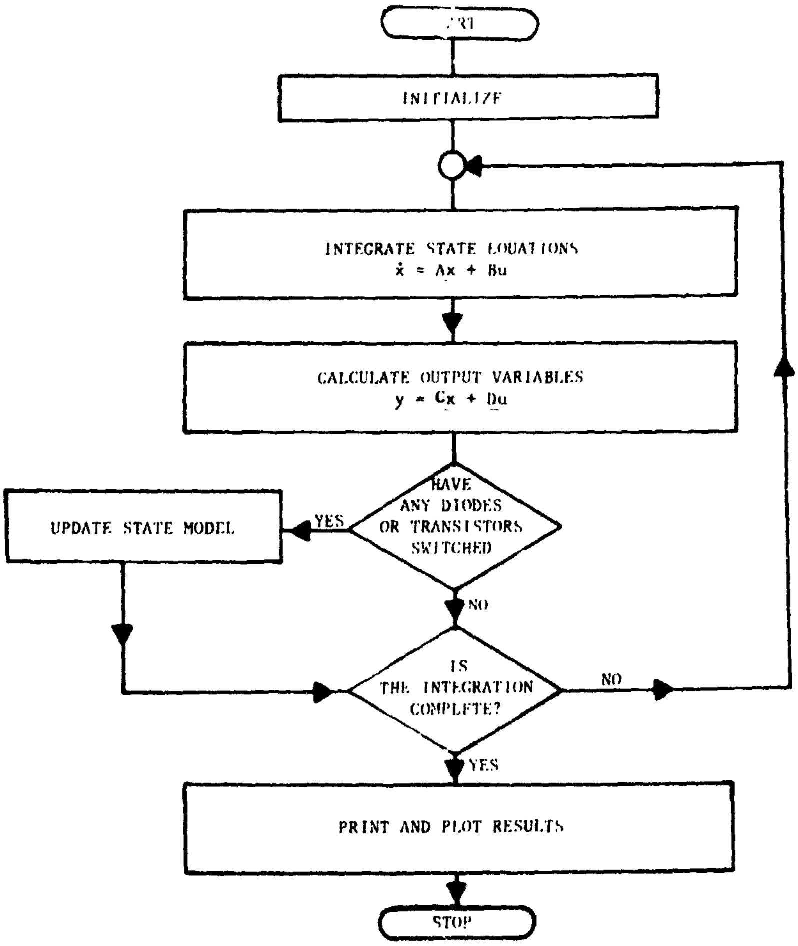

FIGURE (3.3-4) Flow Chart of Machine - Power Conditioner Dynamic Model samarium cobalt case, winding designs of 15 and 12 turns per path per phase were simulated, while in the strontium ferrite case, winding designs of 12 and 9 turns per phase were simulated. The effects of stator slot skewing and commutation advance angle on the output characteristics of both machines were also investigated. Recall that by commutation advance (or advanced firing) angle, one means the relative displacement between the peak of the fundamental of the phase current and the fundamental of the induced armature phase emf. That is, the firing angle corresponds to the time at which one of the transistors of the power conditioner inverter is turned "on" to allow the buildup of current in a given phase. Hence, zero commutation advance means that the two phase current and emf peaks have zero displacement between them, and a 30° electrical (30°E) advanced firing is the angle by which the peak of the fundamental of the phase current leads the peak of the fundamental of the phase emf. In this MPC system for zero degrees of commutation advance, a phase current is "switched on" 30°E after the zero crossing in the phase emf waveform, and "switched off" 150°E after that very zero crossing in the emf waveform. When the inverter transistors' firing is advanced by an angle, δ, the above angles become $(30-\delta)$°E and $(150-\delta)$°E, respectively.

As mentioned earlier, because the energy product of the strontium ferrite material is considerably less than that of the samarium cobalt material, there is more likelihood for the strontium ferrite machine not to meet the output power requirements than the samarium cobalt machine. This is the main reason why most of the simulation runs which will be shown next were made on the stontium ferrite machine. So that if the strontium ferrite machine meets the power requirements, so most likely will the samarium cobalt machine.

The samarium cobalt and strontium ferrite machines are required to produce at least 15hp (11 kw) continuous and 35hp (26.1 kw) peak ratings. These power ratings have to be developed under a maximum supply voltage of 120V stipulated by the contractor, maximum transistor currents of 400 A which was dictated by the maximum available current capacity of transistors in the market at the time of construction, and machine speed range of 6000 to 9000 rpm dictated by mechanical consideration for the type of rotors and bearings being considered. Using the emf and inductance values obtained from the finite element analysis discussed earlier, simulation studies were done that yielded performance results which are discussed next.

The maximum powers and peak currents developed by the 15 turn/path/phase and 12 turns/path/phase winding designs of the samarium cobalt machine between 6000 and 9000 rpm were determined using the MPC dynamic simulation model describe earlier in this section, and are shown in Figures (3.3-5) and (3.3-6) respectively. From Figure (3.3-5), the 15 turn/path/phase winding machine is unable to attain the

35hp (26.1 kw) peak within the prescribed speed range. On the other hand, not only does the 12 turn/path/phase winding version meet the peak power specifications, but Figure (3.3-6) shows that the phase currents are less than the 400A. Similar studies were performed on the 12 turns/path/phase and 9 turns/path/phase winding design versions of the strotium ferrite machine as indicated by Figures (3.3-7) and (3.3-8). Again, notice that the version with the lower number of turns meets both the peak power and phase current requirements. The reason why the peak electromagnetic power developed was much less in magnitude than the required 35hp (26.1 kw)peak for the 12 turns/path/phase winding as opposed to the lower 9 turns/path/phase winding for the strontium ferrite machine is explained [24] next.

The MPC dynamic simulation model at hand was used to obtain the starting current profiles on the armature side of the strontium ferrite machine in the motoring mode. This was done for the case with 12 turns/path/phase and 9 turns/path/phase, assuming the same initial value of phase current, with no commutation advance. The resulting starting current profiles were plotted until the phase current reached a steady state value. These two cases for 12 turns and 9 turns are shown in Figures (3.3-9) and (3.3-10), where the steady state ac phase current maximum value of about 28 Amperes and 250 Amperes were reached, respectively. Obviously the lower the number of turns the lower the inductances of the machine armature winding, the higher the current build up rates during commutation, and the higher the steady state values of current and developed power. Advancing the firing angle by 30°E leads to the starting and steady state current profile given in Figure (3.3-11), with a maximum steady state ac phase current of about 340 Amperes. Further evidence of the benefits of advanced firing will be discussed later in this section.

The above results indicate that a lower number of turns in both machines enhance the MPC system power and current capabilities, and facilitate the all important electronic commutation process of the phase currents. Therefore, the 12 turns/path/phase winding design for the samarium cobalt and the 9 turns/path/phase winding for the strontium ferrite machines were selected for the final design.

Earlier in Section (3.2.4), it was stated that integral slot windings for both machines (that is, 18 slots and 6 poles which means one slot/pole/phase) will be used instead of fractional slot windings in order to reduce complexities in th construction process. In so doing, the emf harmonics were increased as was shown in Section (3.2). In order to reduce these harmonics, it was decided to explore the possibility of skewing the stator core by a total amount of half a slot and a full slot pitch as described in Reference [25], which is included in Appendix (6) for convenience. The effect of skewing was analytically accounted for by means of a skewing factor included in the winding factor. Figure (3.3-12) shows a typical effect of skewing of the stator slots on the induced armature waveforms. This emf was obtained from the finite element determined mid gap flux density distribution as discussed in

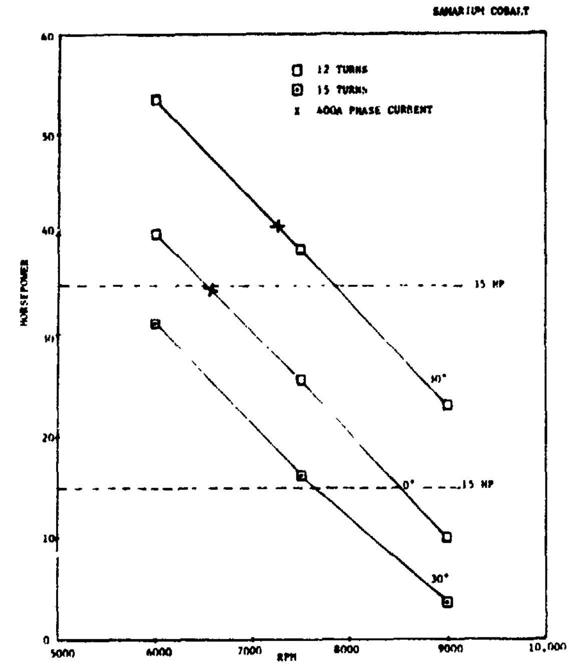

FIGURE (3.3-5) Maximum Power Curves for the Samarium Cobalt Machine

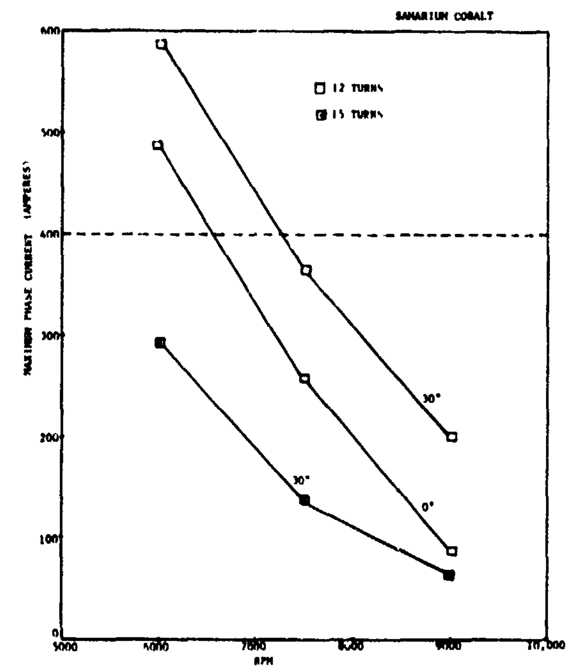

FIGURE (3.3-6) Peak Current Curves for the Samarium Cobalt Machine

ORIGINAL PAGE IS
OF POOR QUALITY

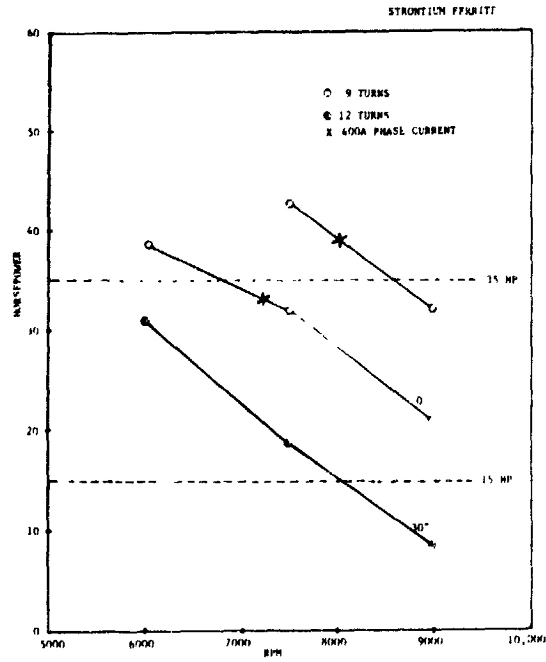

FIGURE (3.3-7) Maximum Power Curves for the Strontium Ferrite Machine

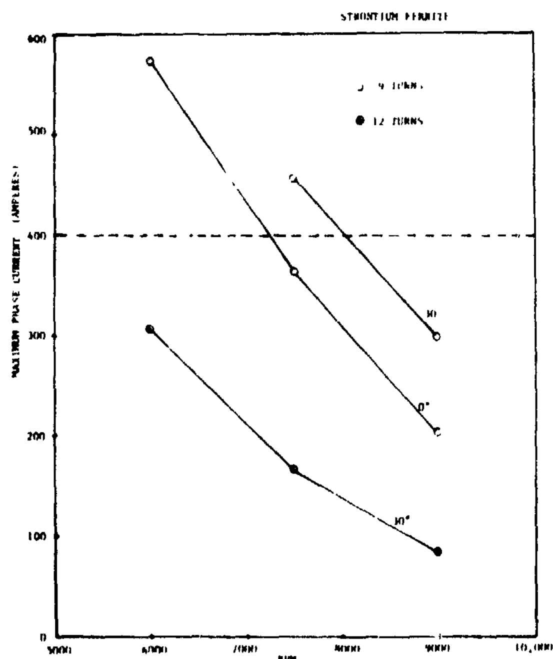

FIGURE (3.3-8) Peak Current Curves for the Strontium Ferrite Machine

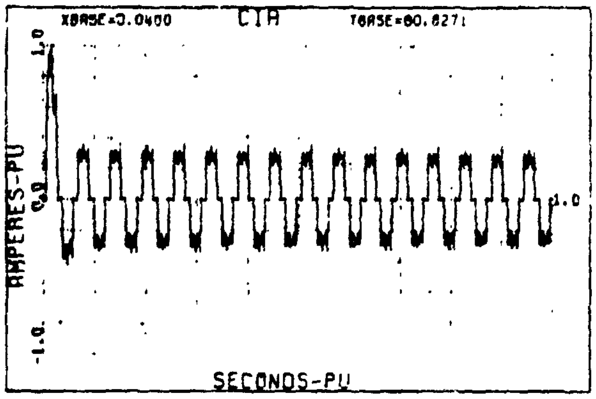

FIGURE (3.3-9) Simulated Current Buildup in the Strontium Ferrite Machine for 12 Turns and Zero Degrees E Commutation Advance

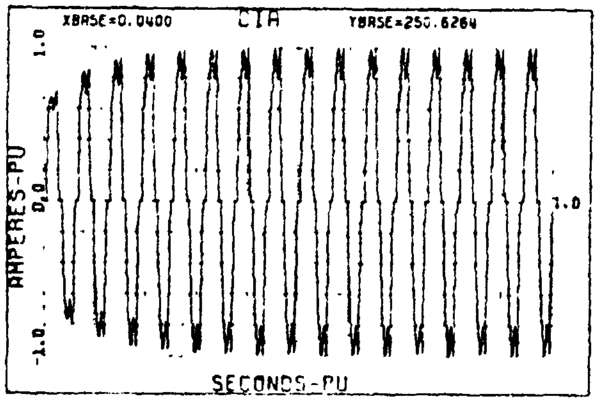

FIGURE (3.3-10) Simulated Current Buildup in the Strontium Ferrite Machine for 9 Turns and Zero Degrees E Commutation Advance

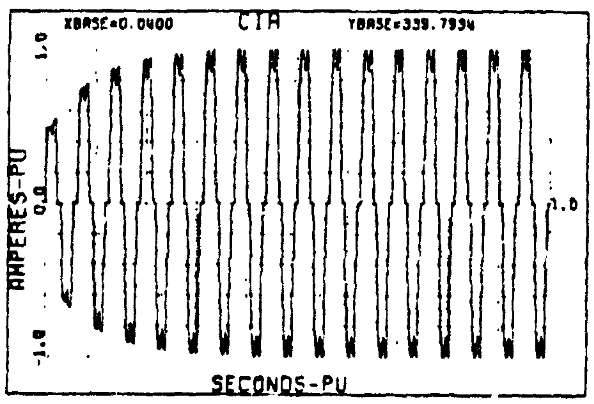

FIGURE (3.3-11) Simuıated Current Buildup in the Strontium Ferrite Machine for 9 Turns and 30°E Commutation Advance

Section (3.2). This figure shows the emf in the case of the strontium ferrite machine, with no skewing, half stator slot skewing and a full stator slot skewing. Notice that the armature skewed by a stator slot pitch produces a waveform approaching a sinusoid, which is better than in the case of either no armature skewing or armatue skewing by a half stator slot pitch.

The resulting emf waveforms with a full slot skewing, for the samarium cobalt and strontium ferrite machines, with the chosen final number of turns/path/phase are shown in Figures (3.3-13) and (3.3-14), respectively. The corresponding emf sensitivity constants in Volts/Mechanical Radian/Second were given earlier in Table (3.2.1). The effect of skewing was also investigated using computer simulated waveforms determined by the dynamic simulation model applied to the strontium ferrite machine case. The phase currents and elctromagnetic torque for the case of no skewing, half slot pitch skewing, and full slot pitch skewing were obtained by simulation. This is shown in Figures (3.3-15) through (3.3-17). As shown by the values indicated at the top of the waveform, steady state phase currents, indicative of MPC system capability increase from 200 Amperes to 227 Amperes when one skews the aramature winding by one stator slot pitch. Thus, it was decided to skew the armatures of both machines by a full stator slot pitch.

Another factor which affects the machine output is the commutation angle. This aspect is detailed in Reference [33], which is included in Appendix (8) for convenience. Recall that a commutation advance of 0°E means that the phase current is injected 30°E after the zero crossing of the phase emf. Normal firing is a commutation advance of 0°E. Consider Figure (3.3-18) showing a sketch of the emf and phase current waveforms during normal firing, and at a commutation advance of 30 degrees electrical. The period of conduction (when a phase current flows) is 120°E. It can be seen that at normal firing, both waveforms are centered with respect to one another, thus maximizing the volt-ampere product for a given current and speed. However, under heavy loads, this normal firing angle limits the maxiumum value of current buildup. This is because higher values of emf oppose this current buildup at the instant of switching-on a phase under normal firing. Therefore, by advancing the commutation to a point where the emf is reduced (to zero), one allows a larger rate of current buildup, thus permitting capabilities for heavier loads.

The above results and discussion lead one to look favorably upon the idea of advanced commutation, which was analyzed by simulation of "advanced firing" using the model at hand. The effect of advanced firing on machine performance is clearly illustrated by the computer simulated waveforms of Figures (3.3-19)* and (3.3-20)* for the strontium ferrite machine. These figures are plots of the simulated machine phase current and elecromagnetic torque for the cases of zero°E and 30°E of advanced firing of the strontium ferrite machine system. Figures (3.3-21)* and (3.3-22)* are plots of the simulated phase current for the cases of 0°E and 30 degrees electrical commutation advance for the 12

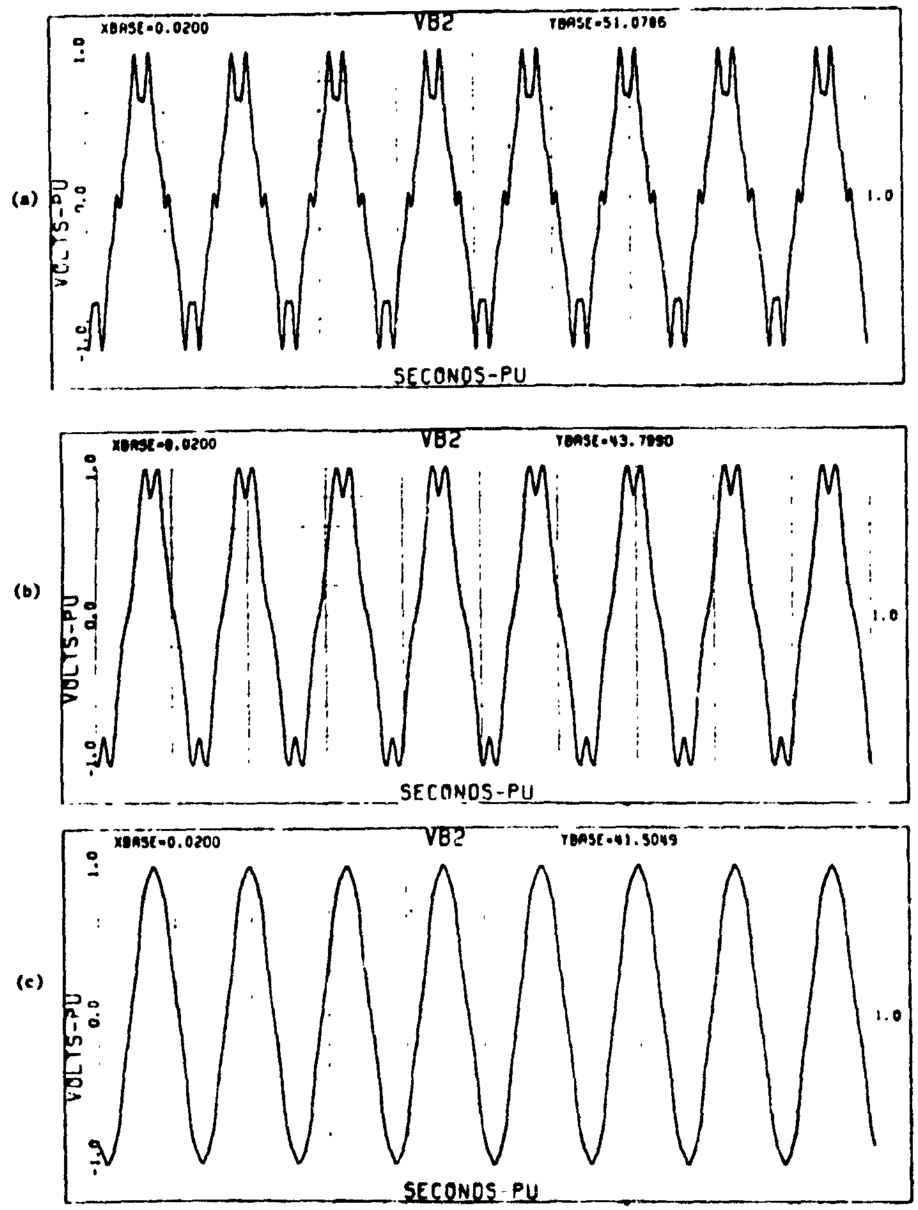

Phase to Neutral Open Circuit Voltage Waveform for a) No Skewing, b) Half Slot Pitch Skewing, c) Full Slot Pitch Skewing.

FIGURE (3.3-12) Typical Effect of Skewing on Armature Induced EMF in the Strontium Ferrite Machine for No Skewing, Half Slot Skewing, and Full Slot Skewing at 8000 rpm.

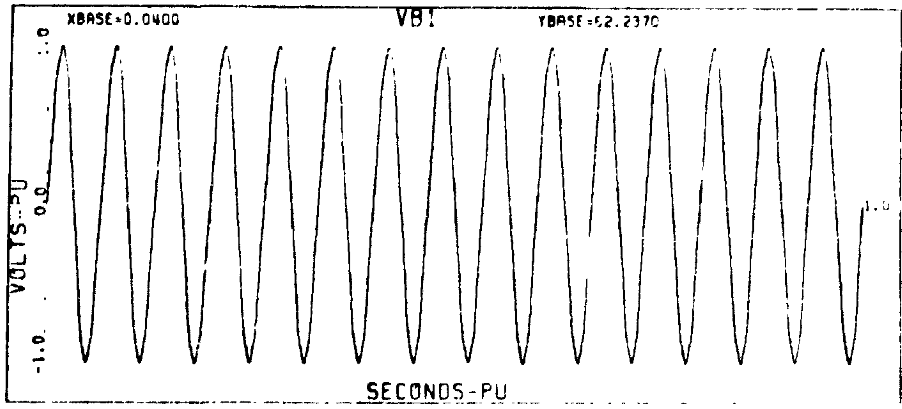

FIGURE (3.3-13) Armature Induced EMF Waveform of the Samarium Cobalt Determined by Finite Elements, 9000 r.p.m.

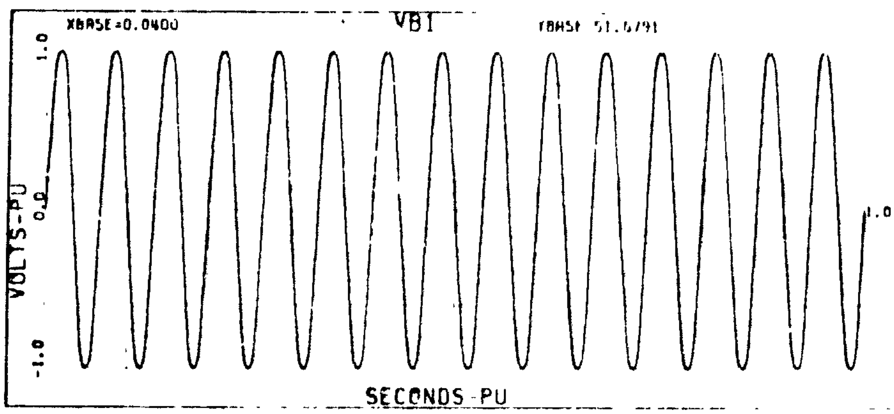

FIGURE (3.3-14) Armature Induced EMF Waveform of the Strontium Ferrite Determined by Finite Elements, 9(XX) r.p.m.

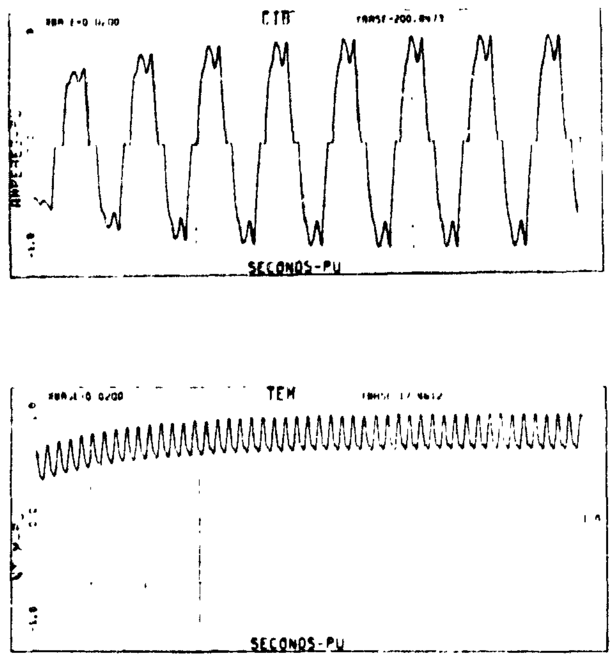

FIGURE (3.3-15) Strontium Ferrite Machine Phase Current and Electromagnetic Torque in Amperes and Newton Meter, No Skewing, Zero Commutation Advance, at 8000 r.p.m., 9 Turns/Path/Phase.

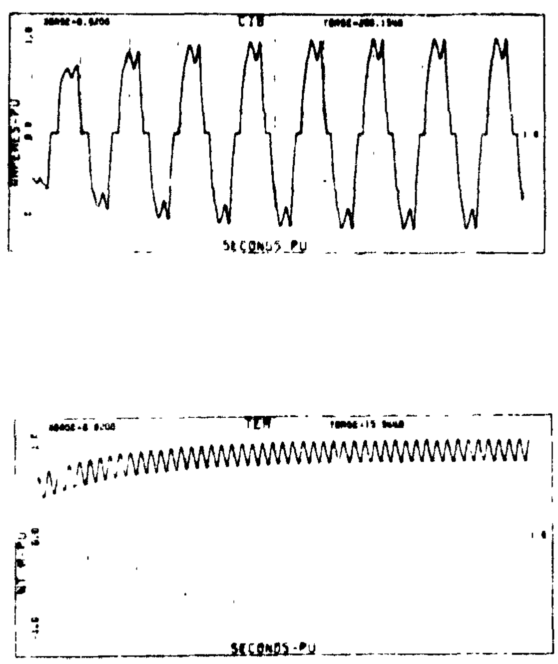

FIGURE (3.3-16) Strontium Ferrite Machine Phase Current and Electromagnetic Torque in Amperes and Newton Meter. Half Slot Skewing, Zero Commutation Advance, at 8000 r.p.m., 9 Turns/Path/Phase.

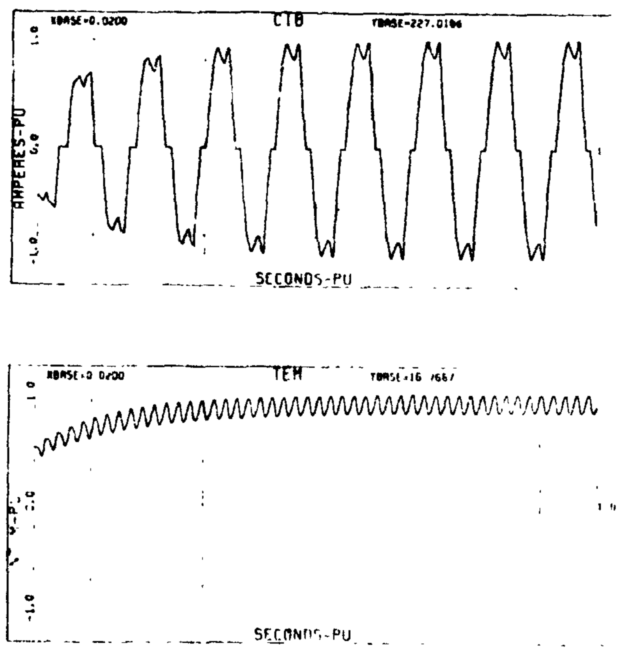

FIGURE (3.3-17) Strontium Ferrite Machine Phase Current and Electromagnetic Torque in Amperes and Newton Meter, One Slot Skewing, Zero Commutation Advance, at 8000 r.p.m., 9 Turns/Path/Phase

ADVANCED AND NORMAL COMMUTATION OF

PHASE CURRENTS IN MPC SYSTEM

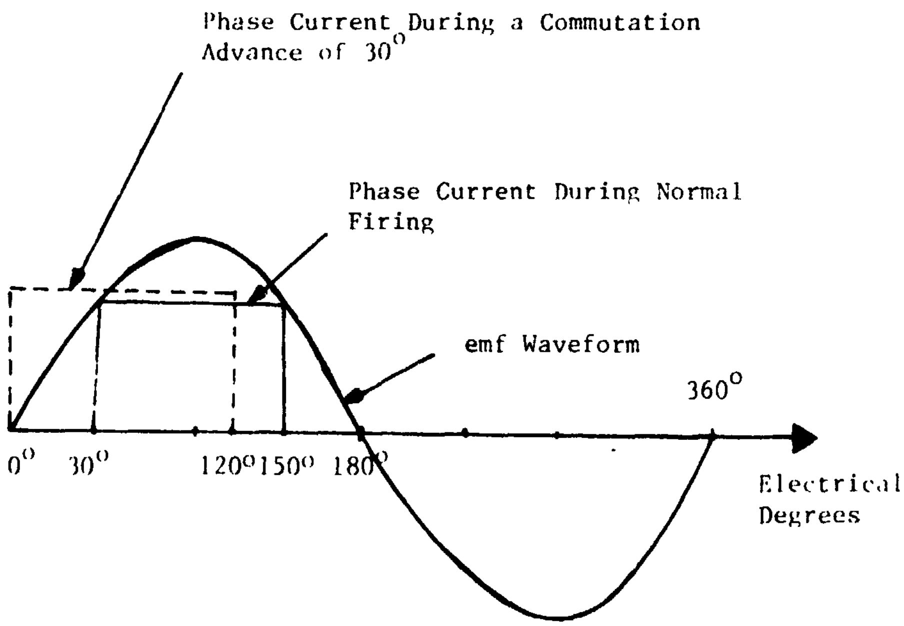

FIGURE (3.3-18) Armature Induced Phase EMF and Phase Current for Normal and Advanced Commutation by 30° Electrical,

ORIGINAL PAGE IS
OF POOR QUALITY

turns/phase winding at 9000 rpm of the samarium cobalt machine system. As these figures indicate, the values of the phase current and electromagnetic torque increased remarkably as the commutation advance changed from 0 degrees to 30 degrees electrical. The effect of advancing commutation on the developed electromagnetic power is further illustrated for the case of the samarium cobalt machine in Figures (3.3-23)* and (3.3-24)*, where advanced commutation by 30 degrees electrical lead to an increase in maximum electromagnetic power from 17.4kw to 23.2kw. Hence, a commutation advance of 30° electrical was selected to be used in the final design, thus requiring a rotor position sensor which permitted this capability of 0°E and 30°E of advanced commutation for both machines.

The above effective use of computer simulation tools in assessing various design options led to the choice of reduced numbers of turns/path/phase of 12 and 9 for the samarium cobalt and strontiumm ferrite machines, respectively. It also led to the decision to skew both armatures by one stator slot pitch, an led to the choice of providing advanced commutation capabilities in the rotor position sensor and power conditioner, in order to insure meeting all the rated and peak power requirements. Thus, final machine designs were arrived at as described in the next Section (3.4).

3.4 FINALIZATION OF MOTOR DESIGN

In the previous two sections, it was shown that it is highly desirable to introduce three motor design modifications on the original preliminary designs of the samarium cobalt and strontium ferrite based machines given in Section (3.1). These three motor design modifications can be summerized as follows:

1. It was found from finite element magnetic field analysis, Section (3.2), that skewing the armature (stator) slots by one slot pitch leads to considerable reduction in the harmonic content of the induced armature emf waveforms. The reduction in the harmonic content of the induced armature emf had an additional beneficial effect on the peak power capability of the machine at hand, which was demonstrated by the results of the dynamic analysis of the MPC systems' interaction, Section (3.3). Accordingly, it was decided to skew the armature slots by one slot pitch.

2. It was found from finite element magnetic field analysis, Section (3.2), that a reduction in the number of turns per path per phase from 15 turns/path/phase to 12 turns/path/phase (from 5 turns/coil to 4 turns/coil) in the case of the samarium cobalt based machine, and a corresponding reduction in the number of turns per phase from 12 turns/path/phase to 9 turns/path/phase (from 4 turns/coil to 3 turns/coil) in the case of the strontium ferrte based machine, led to a considerable reduction in the armature inductances. This was shown, on the basis of

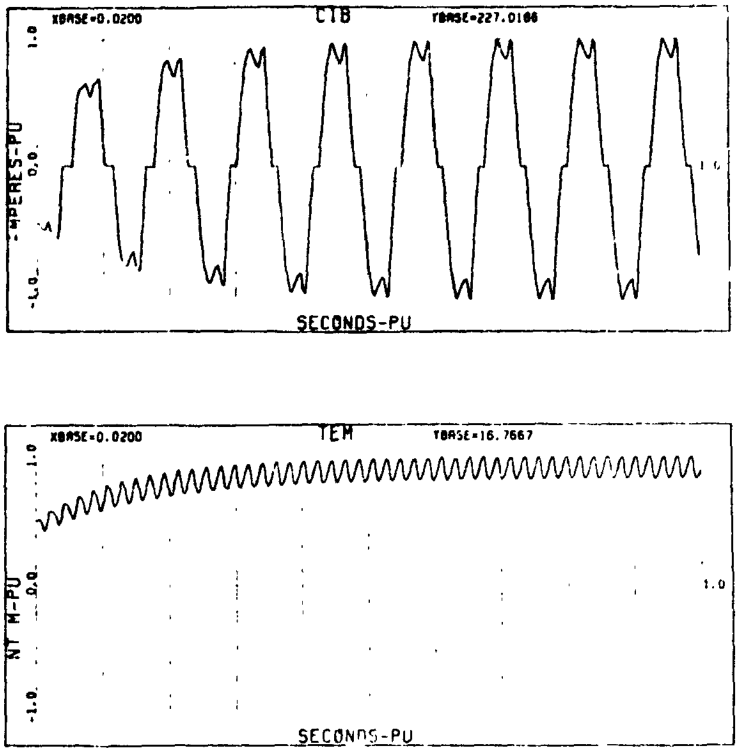

FIGURE (3.3-19) Phase Current and Electromagnetic Torque for the Case of 0° Advanced Commutation of the Strontium Ferrite Machine, at 8000 r.p.m., 9/Turns/path/phase

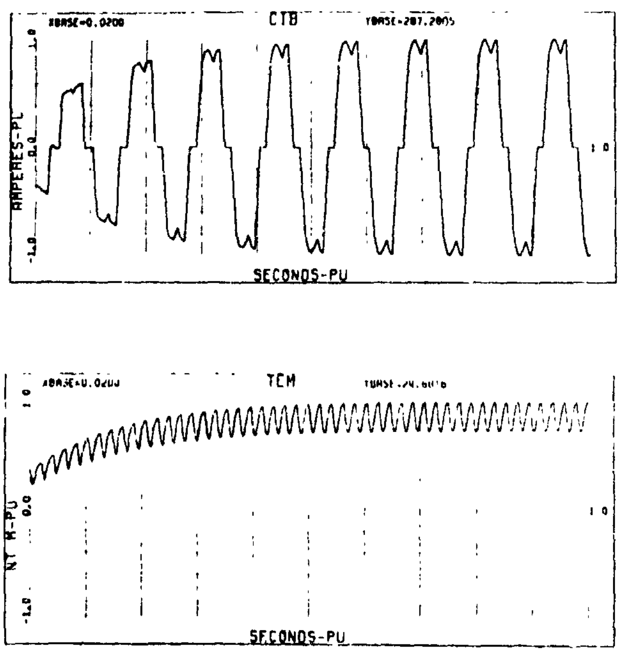

FIGURE (3.3-20) Phase Current and Electromagnetic Torque for the Case of 30° Advanced Commutation of the Strontium Ferrite Machine, at 8000 r.p.m., 9/Turns/path/phase.

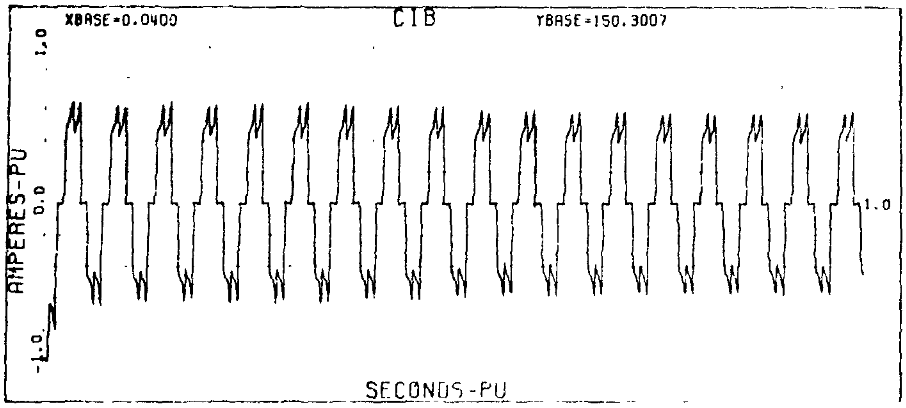

FIGURE (3.3-21) Phase Current of the Samarium Cobalt Machine with the 12 Turn Winding at 9000 rpm and 0° Advanced Commutation

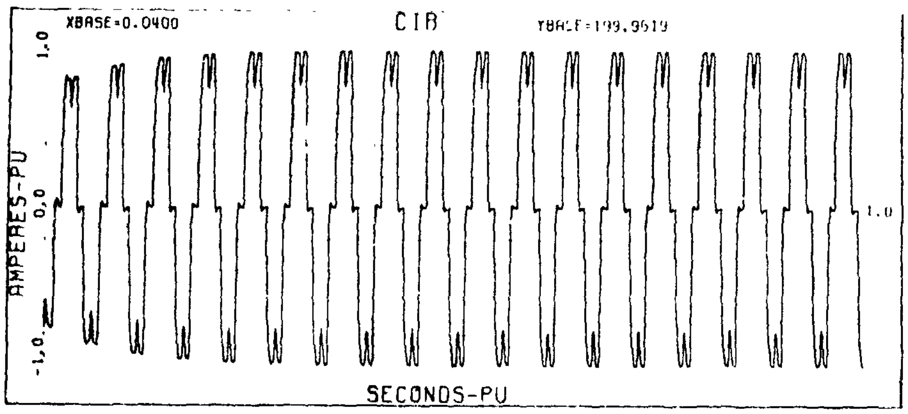

FIGURE (3.3-22) Phase Current of the Samarium Cobalt Machine with the 12 Turn Winding at 9000 rpm and 30° Advanced Commutation.

ORIGINAL PAGE IS OF POOR QUALITY

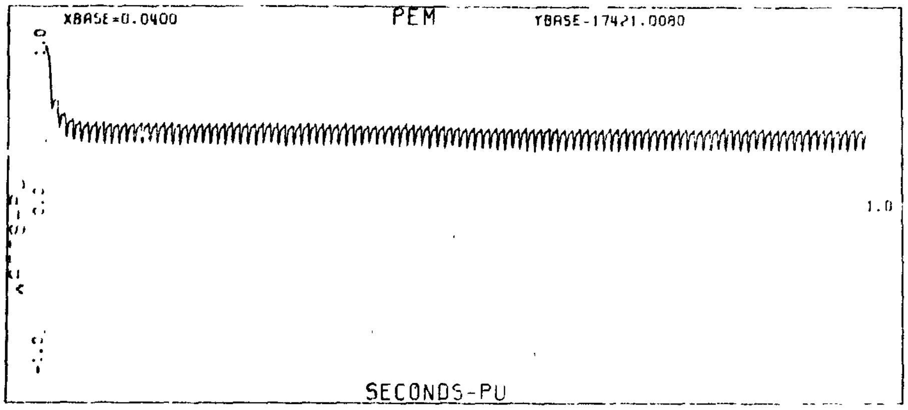

FIGURE (3.3-23) Electromagnetic Power of the Samarium Cobalt Machine with the 12 Turn Winding at 9000 rpm and 0° Commutation Advance

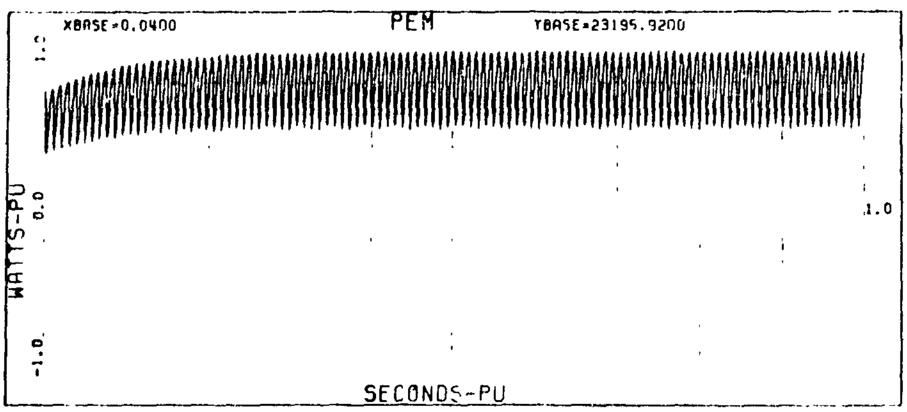

FIGURE (3.3-24) Electromagnetic Power of the Samarium Cobalt Machine with the 12 Turn Winding at 9000 rpm and 30° Commutation Advance.

ORIGINAL PAGE IS
OF POOR QUALITY

the dynamic analysis of the MPC systems' performance of Section (3.3), to lead to a considerable increase in the peak power capability of both motor systems (with the machine armatures connected in the parallel mode). Therefore, it was decided to build both machine armature windings with the lesser number of turns per phase, namely 12 turns/path/phase and 9 turns/path/phase in the samarium cobalt and strontium ferrite based designs, respectively.

3. It was demonstrated on the basis of the analysis of the dynamic performance of the MPC systems in Section (3.3) that advancing the switching "on" and "off" of the inverter transistors by 30 degrees electrical (advanced firing by 30°E) leads to dramatic increases in the peak power capabilities of both machines, and facilitates considerably the process of phase current commutation that must take place every 60°E in the ac cycle on the armature side of the inverter/converter bridge. Therefore, it was decided to design and build the rotor position sensors of both machines with a capability of normal switching "on" and "off" of the inverter transistors (zero advanced firing), as well as a capability of advanced firing by 30°E in the ac cycle on the armature side.

With the three above design modifications decided upon on the basis of the results of the aforementioned computer aided design methods (finite element determination of machine parameters, Section (3.2), and simulation of the MPC system dynamic interaction using the FE determined parameters, Section (3.3), the two preliminary machine designs given earlier in Section (3.1) were finalized. Accordingly, the final designs of both samarium cobalt based, and strontium ferrite based machines led to the two armature core designs shown schematically in Figures (3.4-1) and (3.4-2). The main design dimensions, and machine parameters are given below in Table (3.4-1).

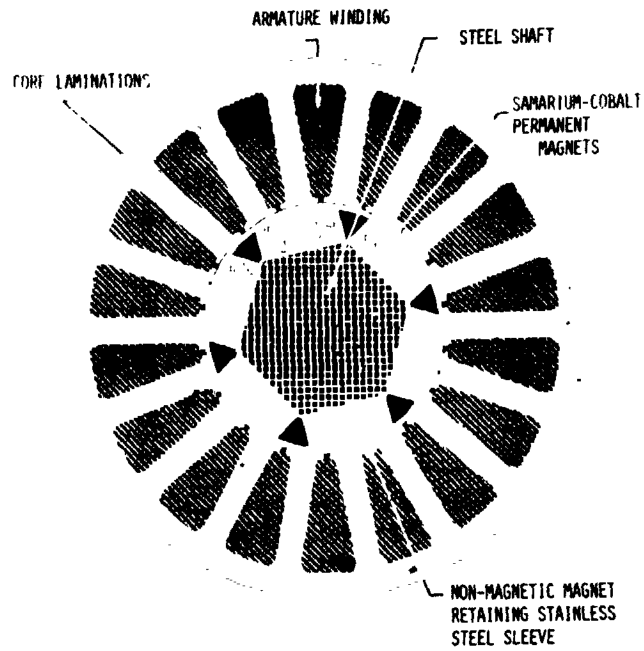

FIGURE (3.4-1) Cross Section of the Samarium Cobalt Machine

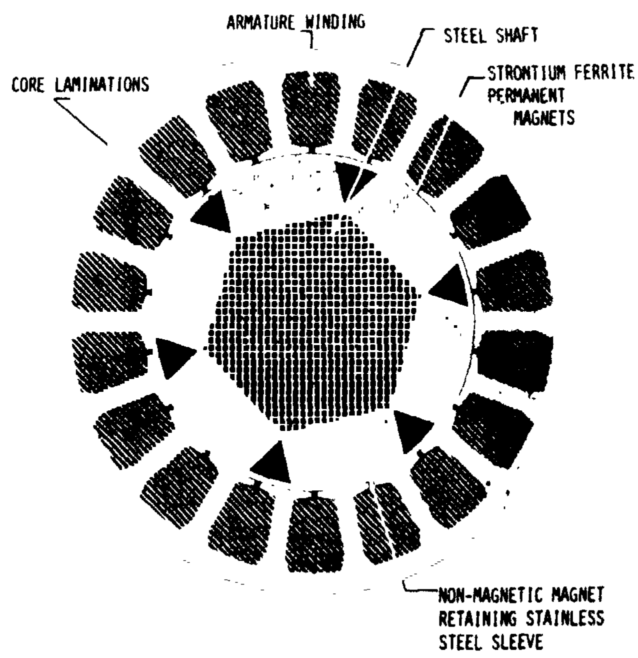

FIGURE (3.4-2) Cross Section of the Strontium Ferrite Machine

TABLE (3.4-1) PARAMETERS AND CHARACTERISTICS OF THE SAMARIUM-COBALT BASED AND STRONTIUM FERRITE BASED MOTORS FROM DESIGN CALCULATIONS AND TEST

Parameter and Units	Samarium Cobalt Co_5 Design	Strontium Ferrite Number 8 Design
motor outside diameter, in. (cm)	7.88(20.02)	7.88(20.02)
motor length, in. (cm)	13.35(33.91)	18.85(47.88)
weight, lbs. (kg)	60.0(27.2)	127.0(57.16)
stator lamination outside diameter, in. (cm)	6.518(16.56)	6.518(15.56)
stator lamination stack length, in. (cm)	4.00(10.16)	8.50(21.59)
stator lamination inside diameter, in. (cm)	3.062(7.78)	4.071(10.34)
number of stator slots	18	18
number of poles	6	6
rotor (magnet str.) outside diameter, excluding sleeve, in. (cm)	2.930(7.44)	3.930(9.98)
rotor outside diameter including sleeve, in. (cm)	3.000(7.62)	4.000(10.16)
rotor (magnet structure) axial length, in. (cm)	3.60(9.14)	8.75(22.23)

TABLE (3.4-1) CON'T.

Parameter and Units	Samarium Cobalt Co_5 Design	Strontium Ferrite Number 8 Design
magnet (radial) length (in direction of magnetization), in. (cm)	0.490(1.24)	0.740(1.88)
magnet cross-sectional area per pole (perpendicular to flux), $in.^2(cm^2)$	3.766(24.30)	12.163(78.47)
total magnet volume (all poles), $in^3(cm^3)$	11.072(181.4)	54.004(885.0)
total magnet weight (all poles), lbs. (kg)	3.23(1.47)	9.56(4.34)
rotor inertia constant, lb. ft. $sec.^2(kg.m^2)$	0.00234(0.0317)	0.01200(0.0163)
Y-connected armature winding	yes	yes
armature winding configuration. (connection)	series/parallel	series/parallel
method of harmonic reduction	skewing by one stator slot	skewing by one stator slot
maximum allowable winding temp. °C	170.0	170.0

TABLE (3.4-1) CON'T.

Parameter and Units	Samarium Cobalt Co_5 Design	Strontium Ferrite Number 8 Design
rated input voltage (on dc side), volts	120.0	120.0
rated armature current (on dc side), amperes	125.0	125.0
rated horsepower, hp.	15.0	15.0
*speed at rated horsepower, r.p.m.	*8680	*8840
*torque sensitivity, at high speed armature winding connection, lb. ft./ampere (Newton Meter/Ampere)	*0.0885(0.22999)	*(0.0992)
back emf sensitivity (constant) at peak of sine wave for high speed armature winding connection, volts/mech. radian/sec.	0.1200	0.0993
armature winding resistance (line to line) for high speed armature connection 25°C, ohms	0.0047	0.049
*torque sensitivity at low speed armature connection, lb. ft/ampere (Newton Meter/ampere)	*0.1770(0.23998)	*0.1464(0.19849)

TABLE (3.4-1) CON'T.

Parameter and Units	Samarium Cobalt Co_5 Design	Strontium Ferrite Number 8 Design
back emf sensitivity at peak of sine wave for low speed armature connection volts/mech. radian/sec.	0.2400	0.1986
armature winding resistance resistance (line to line) for high speed armature connection 25°C,ohms	0.0047	0.0049
*torque sensitivity at low speed armature connection, ib.ft./ampere (Newton Meter/ampere)	*0.1770(0.23998)	0.1464(0.19849)
back emf sensitivity at peak of sine wave for low speed armature connection, volts/mech. radian/sec.	0.2400	0.1986
armature winding resistance (line to line) for low speed armature connection 25°C, ohms	0.0188	0.0196
maximum r.p.m. for low speed armature connection, r.p.m.	4300	4500

TABLE (3.4-1) CON'T.

Parameter and Units	Samarium Cobalt Co_5 Design	Strontium Ferrite Number 8 Design
maximum horsepower hp	35.0 (26.1 kw)	35.0 (26.1 kw)
*motor speed at maximum horsepower r.p.m.	*6900	*6750
armature current at maximum horsepower amperes	291.6	291.6
Thermal Time Constant (minutes)	35 min.	15 min.
Steady State Top Rise Above Amb. 25°C	128°C	113°C
*Obtained from test Measurements		

On the basis of the final designs summarized above, the samarium cobalt based and strontium ferrite based machines were constructed. A pictorial review of the construction steps may be useful here.

Figures (3.4-3) and (3.4-4) show the stator core of the samarium cobalt based machine after assembly, before and after installation of the slot lining material. Notice the six inch long scale included in the picture for proper perspective. Figures (3.4-5) through (3.4-8) show the armature of the samarium cobalt based machine installed in its aluminum housing, viewed from different angles. Again, notice the six inch long scale included for proper perspective. Figure (3.4-9) depicts the samarium cobalt magnet based rotor in its finished form after installation of the nonmagnetic stinless steel magnet retainment sleeve. The major components of the samarium cobalt based motor: the armature in its casing, the end bells, the rotor, the rotor position sensor, and through-bolts are all shown in Figure (3.4-10), with a six inch long scale again for proper perspective. Finally, Figures (3.4-11) through (3.4-13) depict the assembled samarium cobalt based machine including its rotor position sensor at one end of the shaft.

FIGURE (3.4-3) Stator Core View No. 1
Samarium Cobalt Machine

FIGURE (3.4-4) Stator Core View No. 2
Samarium Cobalt Machine

ORIGINAL PAGE
BLACK AND WHITE PHOTOGRAPH

FIGURE (3.4-5) Armature View Number 1 Samarium Cobalt Machine

FIGURE (3.4-6) Armature View Number 2 Samarium Cobalt Machine

FIGURE (3.4-7) Armature View Number 3 Samarium Cobalt Machine

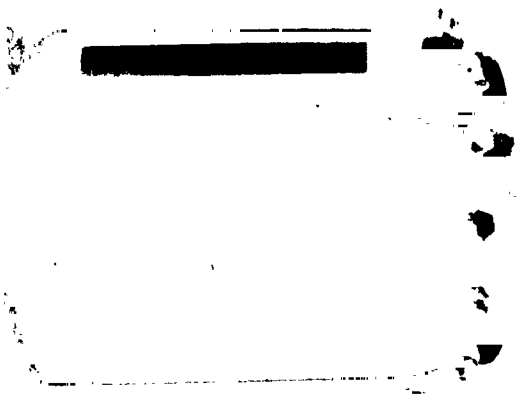

FIGURE (3.4-8) Armature View Number 4 Samarium Cobalt Machine

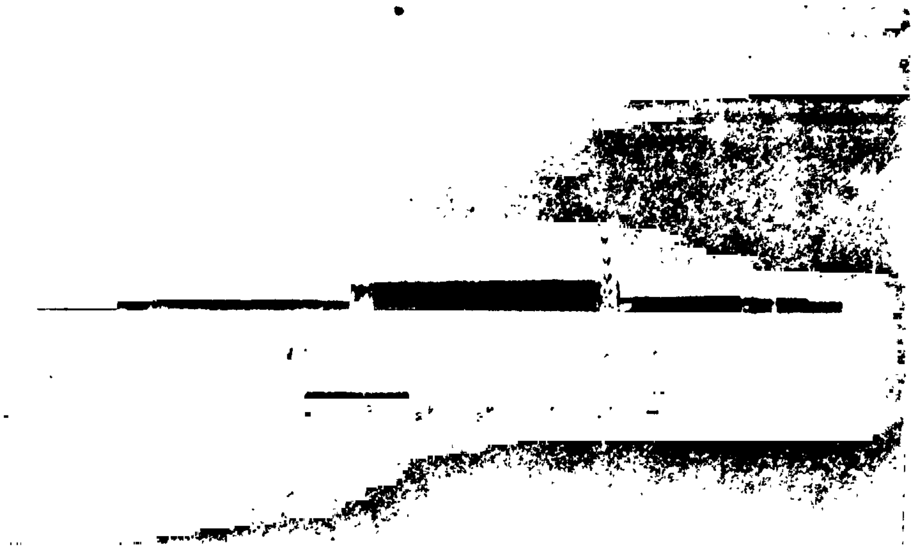

FIGURE (3.4-9) Assembled Rotor
Samarium Cobalt Machine

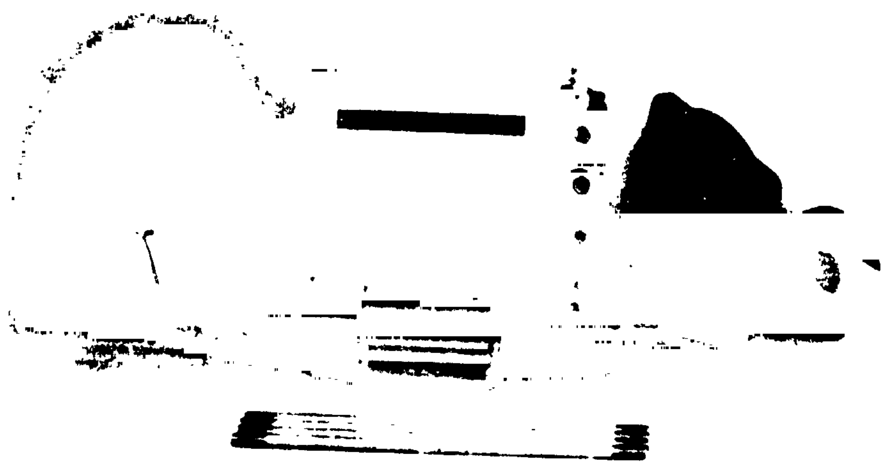

FIGURE (3.4-10) Components of Samarium
Cobalt Machine

ORIGINAL PAGE
BLACK AND WHITE PHOTOGRAPH

Figures (3.4-14) and(3.4-15) show the stator core of the strontium ferrite based machine after assemoly, while Figures (3.4-16) and (3.4-17) depict that core during the process of installing the armature winding. Notice the six inch long scale included in the pictures for proper perspective. Figures (3.4-18) through (3.4-21) show the completed armature after it was installed in its aluminum housing, again notice the six inch long scale included in these pictures. Figures (3.4-22) and (3.4-23) show the rotor shaft and magnet assembly, while Figure (3.4-24) depicts the complete rotor assembly after installing the nonmagnetic stainless steel magnet retainment sleeve. Figure (3.4-25) illustrates the completed armature in its housing, as well as the rotor, in the presence of the six inch long scale for proper perspective. Finally, Figures (3.4-26) through (3.4-28) depict the assembled strontium ferrite based machine including its rotor position sensor at one end of the shaft. Notice the presence of a twelve inch long scale included in these pictures for proper perspective.

For comparison purposes, Figures (3.4-29) and (3.4-30) illustrate the completely assembled samarium cobalt and srontium ferrite based machines side by side. For proper perspective notice the presence of a twelve inch long scale in both of these pictures. Both of these machines are designed for operation by the same power conditioner whose design is detailed in the next Chapter (4.0).

FIGURE (3.4-11) Assembled Samarium Cobalt Machine View Number 1

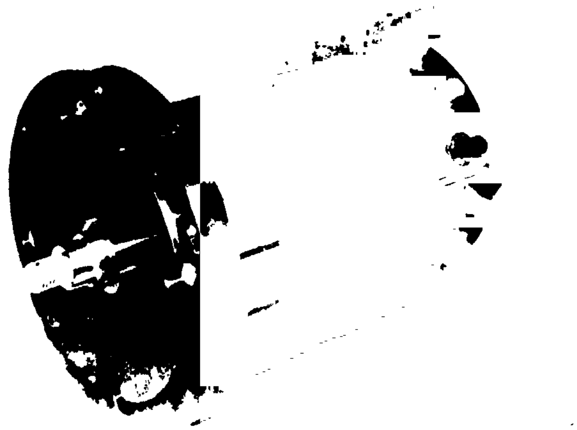

FIGURE (3.4-12) Assembled Samarium Cobalt Machine View Number 2

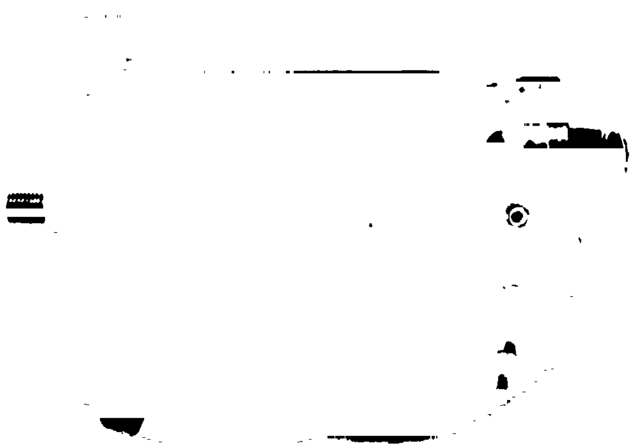

FIGURE (3.4-13) Assembled Samarium Cobalt Machine View Number 3

ORIGINAL PAGE
BLACK AND WHITE PHOTOGRAPH

FIGURE (3.4-14) Sator Core View Number 1
Strontium Ferrite Machine

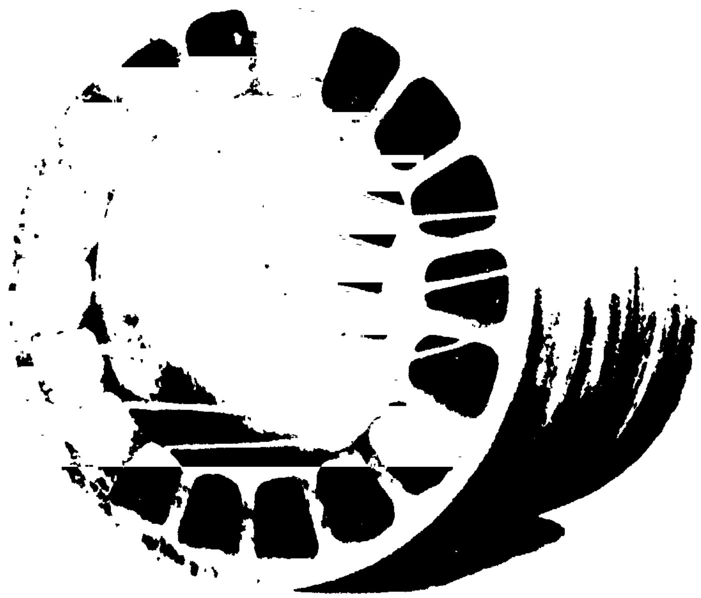

FIGURE (3.4-15) Sator Core View Number 2
Strontium Ferrite Machine

FIGURE (3.4-16) Partially Wound Armature
View Number 1 - Strontium Ferrite Machine

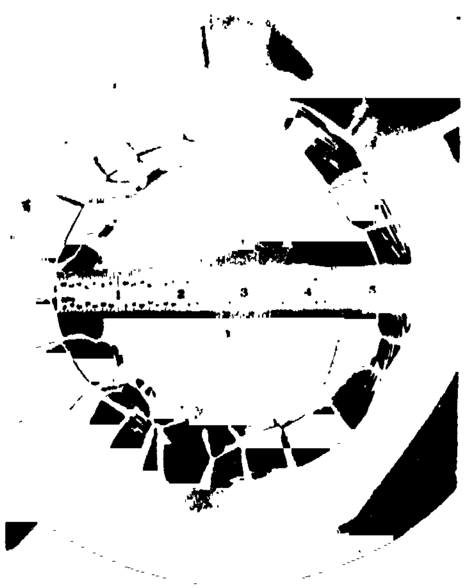

FIGURE (3.4-17) Partially Wound Armature
View Number 2 - Strontium Ferrite Machine

ORIGINAL PAGE
BLACK AND WHITE PHOTOGRAPH

FIGURE (3.4-18) Armature View Number 1 Strontium Ferrite Machine

FIGURE (3.4-19) Armature View Number 2 Strontium Ferrite Machine

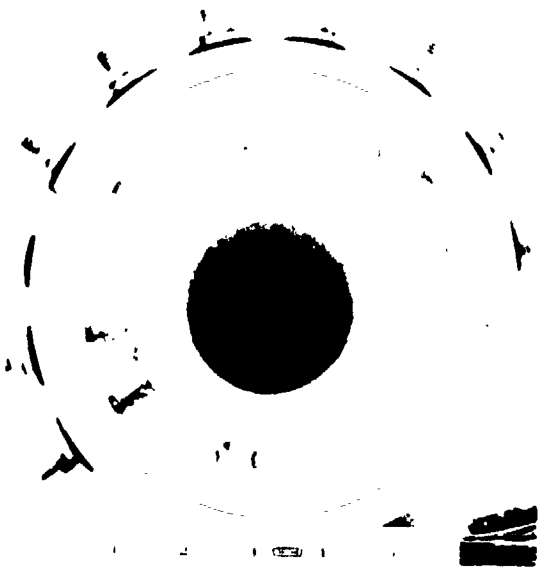

FIGURE (3.4-20) Armature Number 3 Strontium Ferrite Machine

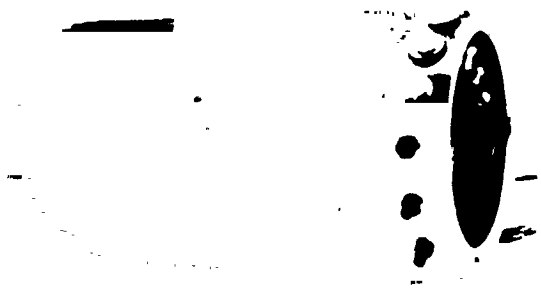

FIGURE (3.4-21) Armature View View Number 4 Strontium Ferrite Machine

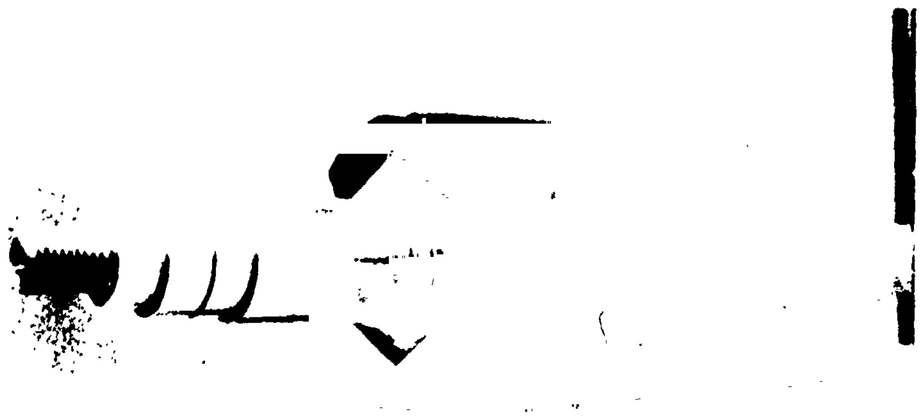

FIGURE (3.4-22) Shaft and Magnet View Number 1 - Strontium Ferrite Machine

FIGURE (3.4-23) Shaft and Magnet View Number 2 - Strontium Ferrite Machine

FIGURE (3.4-24) Shaft and Magnet View Number 3 - Strontium Ferrite Machine

ORIGINAL PAGE
BLACK AND WHITE PHOTOGRAPH

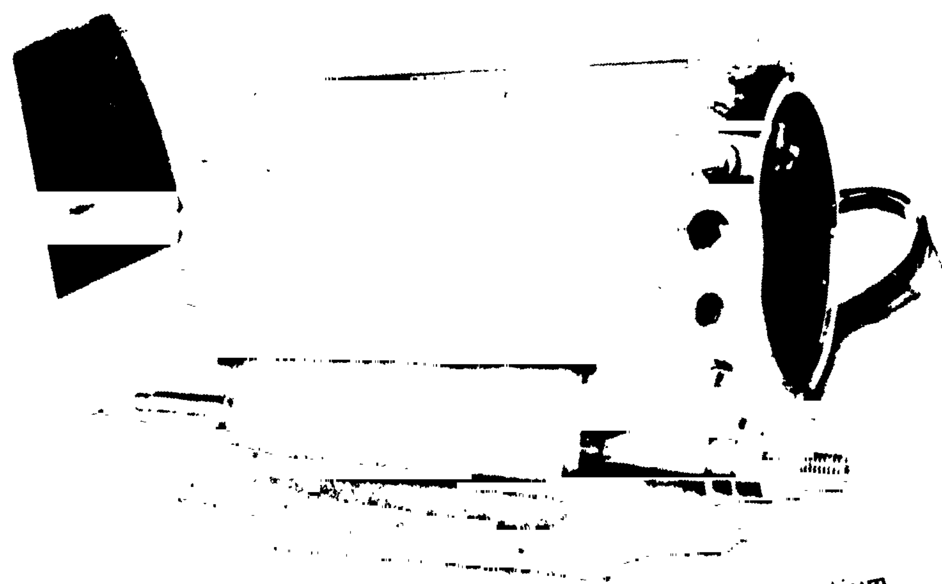

FIGURE (3.4-25) Components of Strontium Ferrite Machine

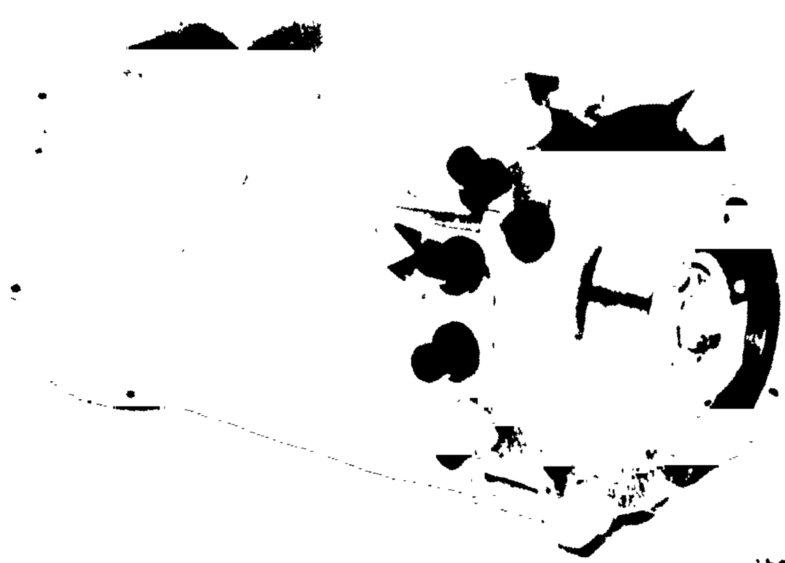

FIGURE (3.4-26) Assembled Strontium Ferrite View Number 1

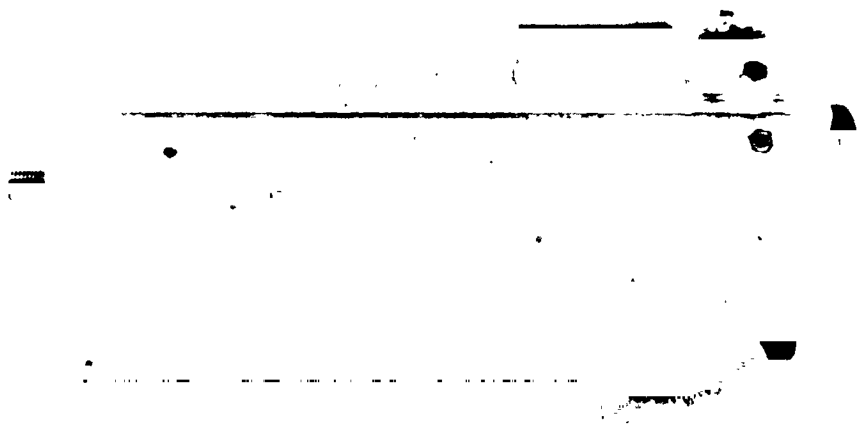

FIGURE (3.4-27) Assembled Strontium Ferrite
View Number 2

FIGURE (3.4-28) Assembled Strontium Ferrite
View Number 3

ORIGINAL PAGE
BLACK AND WHITE PHOTOGRAPH

ORIGINAL PAGE
BLACK AND WHITE PHOTOGRAPH

FIGURE (3.4-29) Samarium Cobalt and Strontium Ferrite Machines View Number 1

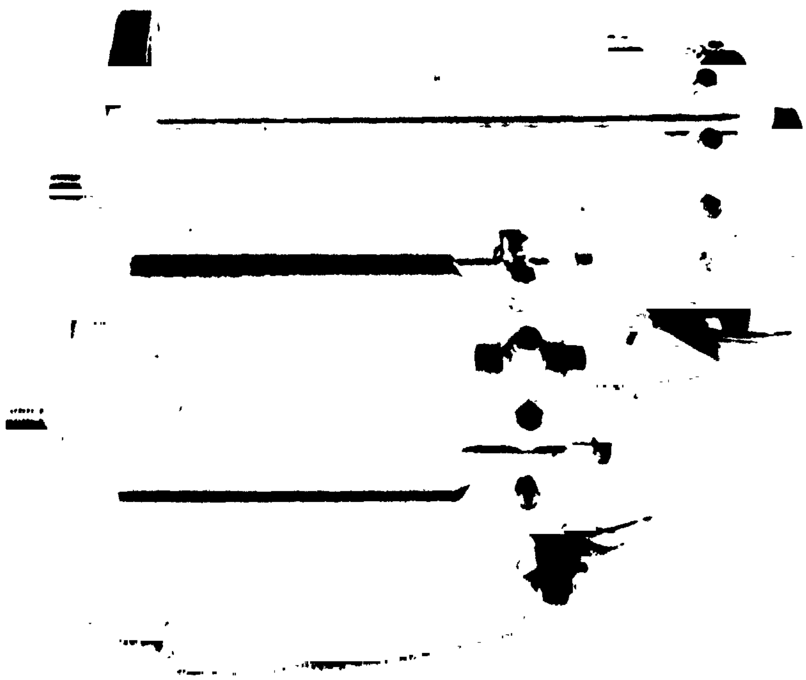

FIGURE (3.4-30) Samarium Cobalt and Strontium Ferrite Machines View Number 2

REFERENCES CITED IN CHAPTER (3.0)

1. Overton, B. P., "Notes on Machine Design," Industrial Drives Division, Kollmorgen Corporation, Radford, VA.

2. Sawhney, A. K., A Course in Electrical Machine Design, Dhanpat Rai & Sons, Delhi-110006, 1977.

3. Zienkiewicz, O. C., The Finite Element in Engineering Science, McGraw-Hill Book Company, London, 1971.

4. Alan, J. D., The Finite Element Method, Clarendon Press, Oxford, 1980.

5. Huebner, Kenneth H., The Finite Element Method for Engineers, New York: John Wiley & Sons, 1975.

6. Desai, C. S. and Abel, J. F., Introduction to the Finite Element Method, New York: Van Nostrand Reinhold Co., 1972.

7. Strag, G. andFix, G. J., An Analysis of the Finite Element Method, Englewood Cliffs, NJ, Prenice-Hall, Inc., 1973.

8. Ahmed, S. V. and Erdelyi, E. A., "Nonlinear Vectcr Ptential Equations for Highly Saturated Heteroplar Electrical Machines," IEEE Transactions on Aero-Space, Vol. 2, pp. 896-903, 1964.

9. Erdelyi, E. A., Ahmed, S. V., and Hopkins, R. E., "Nonlinear Theory of Synchronous Machines On-Load," Transactions IEEE, Power Apparatus and Systems, Vol. PAS-85, pp. 792-801, 1966.

10. Erdelyi, E. A. and Fuchs, E. F., "Nonlinear Magnetic Field Analysis of D.C. Machines - Part I: Theoretical Fundamentals, and Part II: Application of the Improved Treatment," Transactions IEEE Power Apparatus and Systems, Vol. PAS-89, pp. 1546-1564, 1970.

11. Demerdash, N. A., Hamilton, H. B. and Brown, G. W., "Simulation for Design Purposes of Magnetic Fields in Turbogenerators with Symmetrical and Asymmetrical Rotors - Part I Model Development and Solution Tehnique," IEEE Transactions On Power Apparatus and Systems, PAS, Vol. 91, 1972, pp. 1985-1992.

12. Demerdash, N. A. and Hamilton, H. B., "Simulation for Design Purposes of Magnetic Fields in Turbogenerators with Symetrical

and Asymmetrical Rotors - Part II - Model Calibration and Applications," IEEE Transactions on Power Apparatus and Systems, PAS, Vol. 91, 1972, pp. 1992-1999.

13. Demerdash, N. A. and Hamilton, H. B., "Use of Computerized Magnetic Field Solutions in Design Optimization of Turbogenerators," IEEE Transactions on Magnetics, Vol. MAG-11, pp. 1532-1534, 1975.

14. Silvester, P. and Chari, M. V. K., "Finite Element Solution of Saturable Magnetic Field Problems," IEEE Transactions on Power Apparatus and Systems, Vol. PAS-89, pp. 1642-1652, 1970.

15. Chari, M. V. K. and Silvester, P., "Analysis of Turbo Alternative Magnetic Field by Finite Elements," IEEE Transactions on Power Apparatus and Systems, Vol. PAS-90, pp. 454-464, 1971.

16. Demerdash, N. A. and Nehl, T. W., "An Evaluation of the Methods of Finite Elements and Finite Differences in the Solution of Nonlinear Electromagnetic Fields in Electical Machines," IEEE Transactions on Power Apparatus an Systems, PAS, Vol. 98, pp. 74-87, 1979.

17. Anderson, O. W., "Transformer Leakage Flux Program Based on the Finite Element Method," IEEE Transactions on Power Apparatus and Systems, Vol. PAS-92, pp. 682-689, 1973.

18. Brauer, John R., "Saturated Magnetic Energy Functional for Finite Element Analysis of Electric Machines," Conference Paper C-75-151-6, IEEE-PES Winter Meeting, New York, January 26-31, 1975.

19. Fouad, F. A., Nehl, T. W., and Demerdash, N. A., "Magnetic Field Modeling of Permanent Magnet Type Electronically Operated Synchronous Machines Using Finite Elements," IEEE Transactions on Power Apparatus and Systems, Vol. PAS-100, 1981, pp. 4125-4135.

20. Fouad, F. A., Nehl, T. W., Demerdash, N. A., "Permanent Magnet Modeling for Use in Vector Potential Finito Element Analysis in Electrical Machinery," IEEE Transactions on Magnetics, Vol. MAG-17, 1981, pp. 3002-3004.

21. Nehl, T. W., Fouad, F. A., and Demerdash, N. A., "Determination of Saturated Values of Rotating Machinery Incremental and Apparent Inductances by a Perturbation Method." IEEE Transactions on Power Apparatus and Systems Vol. PAS-101, 1982, pp. 4441-4451.

22. Demerdash, N. A., Fouad, F. A., and Nehl, T. W., "Determination of Winding Inductances in Ferrite Type Permanent Magnet Electric Machinery by Finite Elements," IEEE Transactions on Magnetics, Vol. MAG-18, 1982, pp. 1052-1054.

23. Nehl, T. W., Fouad, F. A., Demerdash, N. A., and Maslowski, E., "Dynamic Simulation of Radially Oriented Permanent Magnet Type Electronically Operated Synchronous Machines With Parameters Obtained From Finite Element Field Solutions," IEEE Tranactions on Industry Applications, Vol. IA-18, pp. 172-182, 1982.

24. Nehl, T. W., Fouad, F. A., and Demerdash, N. A. "Digital Simulation of Power Conditioner - Machine Interaction for Electronically Commutated DC Permanent Magnet Machines." IEEE Transactions on Magnetics, Vol. MAG-17, 1981, pp. 3284-3286.

25. Demerdash, N. A., and Nehl, T. W., "Dynamic Modeling of Brushless DC Motors for Aerospace Actuation," IEEE Transactions on Aerospace and Electronic Systems, Vol. AES-16, No. 6, 1980, pp. 811-821.

26. Nehl, T. W., "A discrete time model of a power conditioner-fed permanent magnet brushless dc motor system for aerospace and electric vehicle applications for design purposes using finite elements for machine parameter determination," Ph.D. Dissertation, EE Dept., Virginia Polytehnic Institute and State University, Blacksburg, VA, May 1980.

27. Balabanian, N. and Bickart, T. A., Electrical Network Theory, New York: Wiley, 1969.

28. Fouad, F. A. "Finite Element Analysis for Design and Optimization Purposes for Electronically Operated Electric Machines in Propulsion and Actuation Applications," Ph.D. Dissertation, Electrical Engineering Department, Virginia Polyechnic Institute and State University, 1981.

29. Nehl, T. W., "Comparison Between the Finite Difference Methods Applied to Nonlinear Magnetic Fields in Power Apparatus," M. S. Thesis, Virginia Polytechnic Institute and State University, Blacksburg, Virginia, October 1976.

30. Fano, R. M., Chu, L. J., and Adler, R. B., "Electromagnetic Fields, Energy and Forces," The MIT Press, 1968.

31. Demerdash, N. A., "Finite Element Analysis of Electromagnetic Fields in Electrical Devices," Class Notes for EE 5321 and EE 5322, Virginia Polytechnic Institute and State University, Blacksburg, VA 24061, 1979.

32. Nehl, T. W., Demerdash, N. A., Fouad, F. A., "Impact of Winding Inductances and Other Parameters on the Design and Performance of Brushless DC Motors," Paper Accepted for Publication in the IEEE Transactions on Power Apparatus and Systems. (Will be Presented at the 1984 IEEE-PES Winter Meeting, Dallas, TX.)

33. Nagarkatti, A. K., Mohammed, O. A., and Demerdash, N. A., "Special Losses in Rotors of Electronically COmmutated Brushless dc Motors Induced by Non-Uniformity Rotating Armature MMFS," IEEE Transactions on Power Apparatus and Systems, Vol. PAS-101, 1982, pp. 4502-4507.

34. Rader, L. T. and Litscher, E. C., "Some Aspects of Inductance When Iron is Present," Trans. AIEE, Vol. 63 (1944), March, pp. 133-139.

35. Matsch, L. W., "Electromagnetic and Elecromechanical Machines," Intext Educational Publishers, 1972.

36. Fano, R. M., Chu, L. J., and Adler, R. B., "Electromagnetic Fields, Energy, and Forces," The MIT Press, 1968.

4.0 POWER CONDITIONER

The power conditioner, the design of which is detailed in this chapter, is depicted in the photographs of Figures (4.0-1) through (4.0-3). The power components are described next.

4.1 POWER COMPONENTS

The power components of the power conditioner at hand are the transistor switches, the chopper inductor, the filter capacitor and all the associated diodes, and other support equipment. All these are detailed below.

4.1.1 POWER TRANSISTORS

The choice of transistors for the inverter and chopper functions was very straightforward. At the time (early 1980), there was only one transistor available at reasonable cost of sufficiently high ratings to perform these functions without resorting to paralleling techniques. This was the Toshiba Giant Transistor 2SD648. This transistor was rated at 300V (V_{CEO}) and 400A (I_C). This voltage rating was barely adequate to handle the sum of the supply voltage plus the back e.m.f. plus an allowance for switching transients. No other transistor was available with a collector current rating over 300A. while having an adequate voltage rating except a Power Tech transistor at about three times the cost. Since peak power conditioners required an inductor current of slightly over 300A, this eliminated other transistors. The use of this transistor had several deleterious effects on the final design:

1. the mechanical mounting provision required excessive space, causing the total electronics package to be unnecessarily large (even though it was within the specifications), and

2. the lack of external access to the base of the output transistor of the Darlington pair caused the turnoff time to be long, which led to higher switching losses than necessary.

Transistors more suitable are now available, and their use is discussed in Section 6.2.

FIGURE (4.0-1) The Power Conditioner Viewed From the Chopper Choke and Filter Capacitor Side

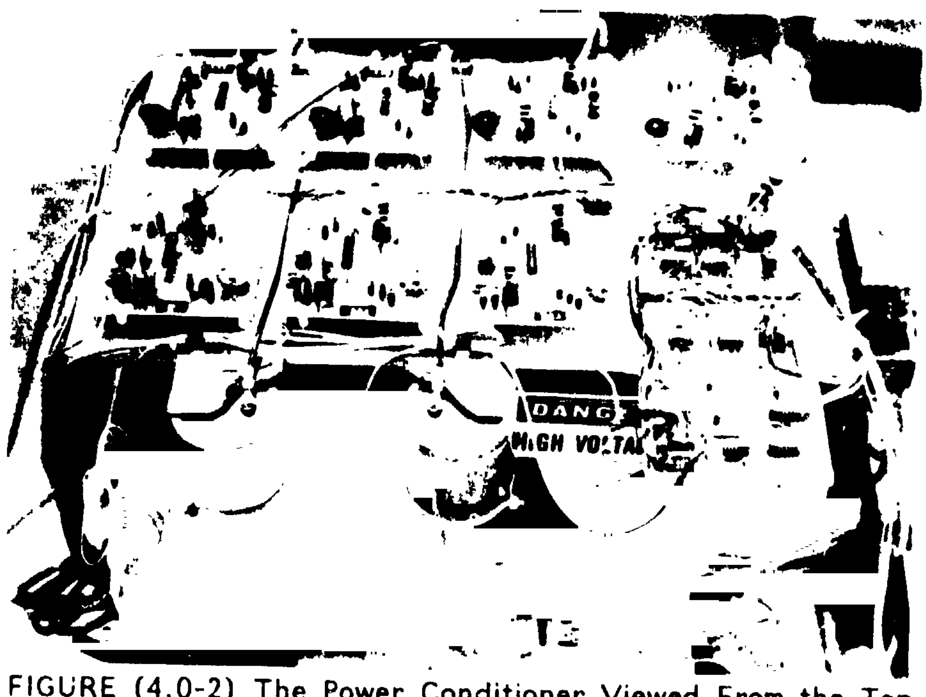

FIGURE (4.0-2) The Power Conditioner Viewed From the Top With the Base Drive Circuits in Full View

ORIGINAL PAGE
BLACK AND WHITE PHOTOGRAPH

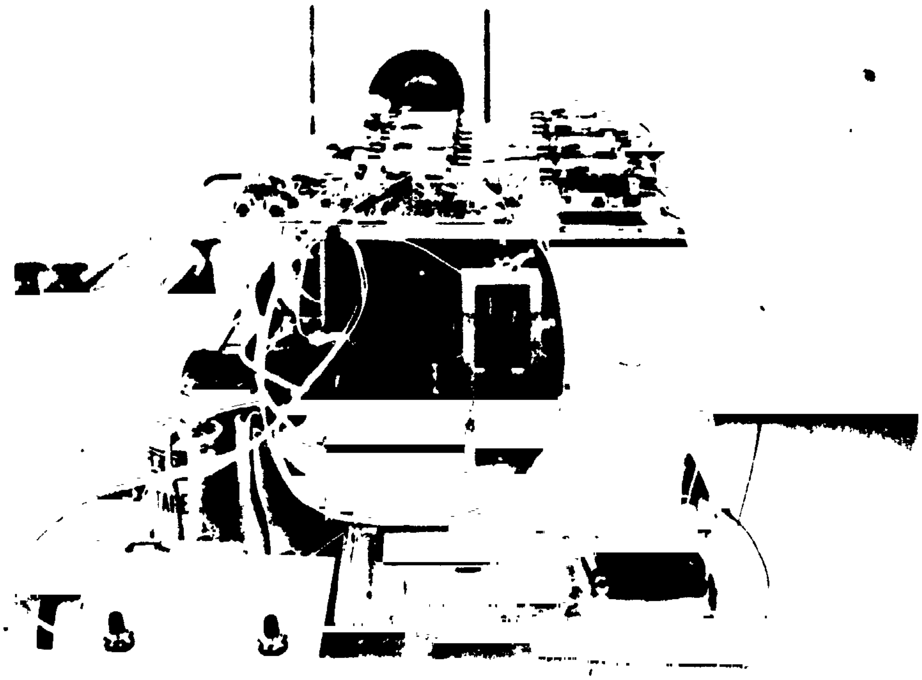

FIGURE (4.0-3) The Power Conditioner - A Side View

ORIGINAL PAGE
BLACK AND WHITE PHOTOGRAPH

In order to prevent any possiblity of transistors Q_M and Q_B of Figure (2.1-3) turning on simultaneously due to any noise or malfunction in the control electronics, one transistor was used for both functions, the collector and base being switched to the appropriate circuit points by a DPDT relay. A relay to perform this function which would take advantage of the "dry" (no-load) switching characteristics was designed and built in-house. The control of this relay is discussed in Section 4.4.2.

4.1.2 SNUBBER DESIGN

The snubbers (shown in Figure (4.1-1)) were designed to absorb the energy stored in the distributed inductance of the leads of the power transistors. This distributed inductance was estimated to be less than .25μH. Using this value, the energy stored at a transistor current of 300A is

$$w = \tfrac{1}{2}LI^2 = \tfrac{1}{2} \times .25\times 10^{-6} \times 300^2 = .0113\ J.$$

It was necessary that the snubber capacitor absorb this energy without allowing the transistor voltage to exceed about 275V, when the steady state open circuit voltage across the transistor may be as high as 230V. Since the energy stored in the capacitor is $CE^2/2$, the capacitance may be found from the relation:

$$\tfrac{1}{2} \times C \times (E^2_{max} - E^2_{o.c.}) = w$$

or

$$C = 2w/[E^2_{max} - E^2_{o.c}] = 2\times.0113/275^2 - 230^2] = 1\mu F.$$

To provide a safety factor, a value of 1.76μF was used.

To insure that this capacitor was completely discharged during the time that the power transistor was conducting, the time constant of the RC circuit was taken to be a maximum of 10μs. Thus, if RC = 10μs,

$$R = 10 \times 10^{-6}/1.76 \times 10^{-6} = 5.7\Omega.$$

A value of 5Ω was used. Since, at each discharge of the snubber capacitor, an energy of $CE^2/2$ is dissipated in the resistor, the power rating of this resistor must be

$$P = \tfrac{1}{2}CE^2f_m = \tfrac{1}{2} \times 1.76 \times 10^{-6} \times 275^2 \times 450 = 30W$$

for the inverter transistors and

$$P = \tfrac{1}{2} \times 1.76 \times 10^{-6} \times 275^2 \times 5000 = 333W$$

for the chopper transistor.

Not only would the power dissipated in the snubber resistor of the chopper be excessive, but the distributed inductance of this portion of the circuit was too high for the 1.76μF capacitor. Therefore, the switching transient for this transistor was suppressed by clamping to the positive and negative busses. The clamping network is shown in Figure (4.1-2). This proved to be a very effective means of transient suppression, restricting the peak voltage across the transistor to about 150V. However, it did not improve the operation of the transistor within the safe operating area.

4.1.3 BASE DRIVE DESIGN

The base drives for the power transistors were designed to provide a base current of 4A at a base-emitter voltage of 2V. In order to remove the stored charge and to turn off the transistor as rapidly as possible, the base drive was designed to apply a negative voltage to the base- emitter junction when the transistor is to be turned off. This was accomplished by using a bridge circuit made up of complementary npn-pnp transistors. The transistors chosen for this purpose were ZN6486 npn transistors and ZN6489 pnp transistors. The circuit is shown in Figure (4.1.3).

Shown in this figure is the 6N135 optical coupler which provides electrical isolation between the low-level electronics and the base drive. When current flows through the input diode of this device, the light sensitive transistor is turned on. This causes a low voltage to be applied to the gates of the VN46AF field effect transistors, turning them off. This, in turn, allows the drains to rise to their high level. Point X is driven high and point Y is driven low by the inverter transistor VN46AF. Thus, a positive V_{BE} is established. When the input is deenergized, the process is reversed to establish a negative voltage V_{BE}.

The .25Ω resistor serves to limit the base current in the power transistor. With a base-emitter voltage of about 2V on the power transistor in saturation and a collector-emitter voltage of about 1V on each drive transistor, a total voltage drop of about 4V is expected across the transistors at saturation. Since the supply voltage is 5V, a drop of 1V is expected on this resistor at a base current of 4A. Thus the value of .25Ω was chosen.

4.1.4 CHOPPER INDUCTOR DESIGN

The function of the chopper inductor is to reduce the switching frequency of the chopper. A maximum chopper frequency no greater than 5kHz was desired. This frequency would be attained when the

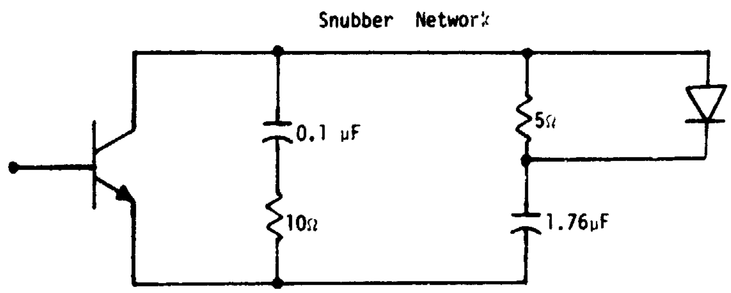

FIGURE (4.1-1) Snubber Network

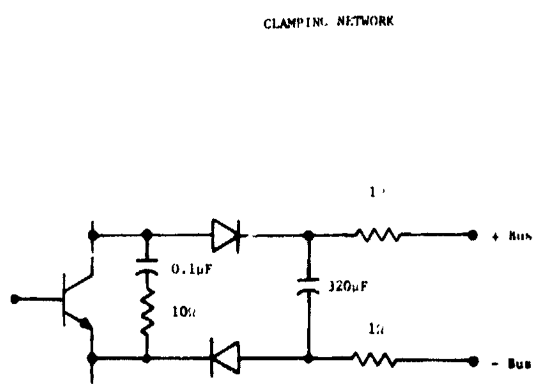

FIGURE (4.1-2) Clamping Network

back emf was one half of the applied voltage. Under these consditions, the on and off times of the chopper would be equal. It was decided to use a current differential of 15A. That is, the chopper was turned off at a current level 15A higher than the current at which it was turned on. On the basis of these values, the necessary inductance was calculated as

$$L = [v\Delta T/\Delta I] = [57.5 \times .0001/15] = .383\text{mH}.$$

This inductance was to be obtained at 200A inductor current.

The core of the inductor was chosen as Allegheny-Ludlum Steel Corporation lamination L-10, in .014 inch (.036 cm) thick AISI alloy number M-15. A triple thick lamaination stack was used, so that the cross-sectional area of the core, A_c was 1.25 inch (3.175 cm) by 3.75 inch (9.525 cm). The window area was 1.5 inch (3.81 cm) by 3.5 inch (8.89 cm). An air gap length, L_a of .125 inch (.3175 cm) was used. The effective air gap area was found by adding the gap length to each of the cross-sectional dimensions as 1.375 inch (3.493 cm) by 3.875 inch (9.843 cm). Thus the effective air gap area, A_g, was

$$A_g = 3.493 \times 9.843 = 34.4 \text{ cm}^2$$

and the permeance of the gap was

$$P = A_g\mu_0/2L_a = 34.4 \times 10^{-4} \times 4\pi \times 10^{-7}/2\times.31.75 \times 10^{-2}$$
$$= 6.8 \times 10^{-7} \text{ MKS units.}$$

If the flux density in the core, B_C, at 200A is taken to be 1.2 Tesla, with a stacking factor of .94, then the flux density in the air gap is

$$B_g = B_C k_s[A_C/A_g]$$
$$= 1.2 \times .94 \times [1.25 \times 3.75/1.375 \times 3.875] = .992 \text{ Tesla.}$$

Then the mmf of the air gap is

$$F_g = B_g \; [l_a/\mu_0] = .992 \times .3175 \times 10^{-2} \times 2/[4\pi \times 10^{-7}]$$
$$= 5013 \text{ AT.}$$

At a flux density of 1.2 Tesla, the field intensity in the core is given by the manufacturer's data as 4 Oersted or 318 AT per meter. The length of the core is given as .38m, so that the mmf in the core is

$$F_C = L_C \times H_C = .38 \times 318 = 121 \text{ AT.}$$

Thus, the total mmf is 5134AT. If the current is 200A, then the number of turns,

$$N = F/I = 5134/200 = 25 \text{ turns.}$$

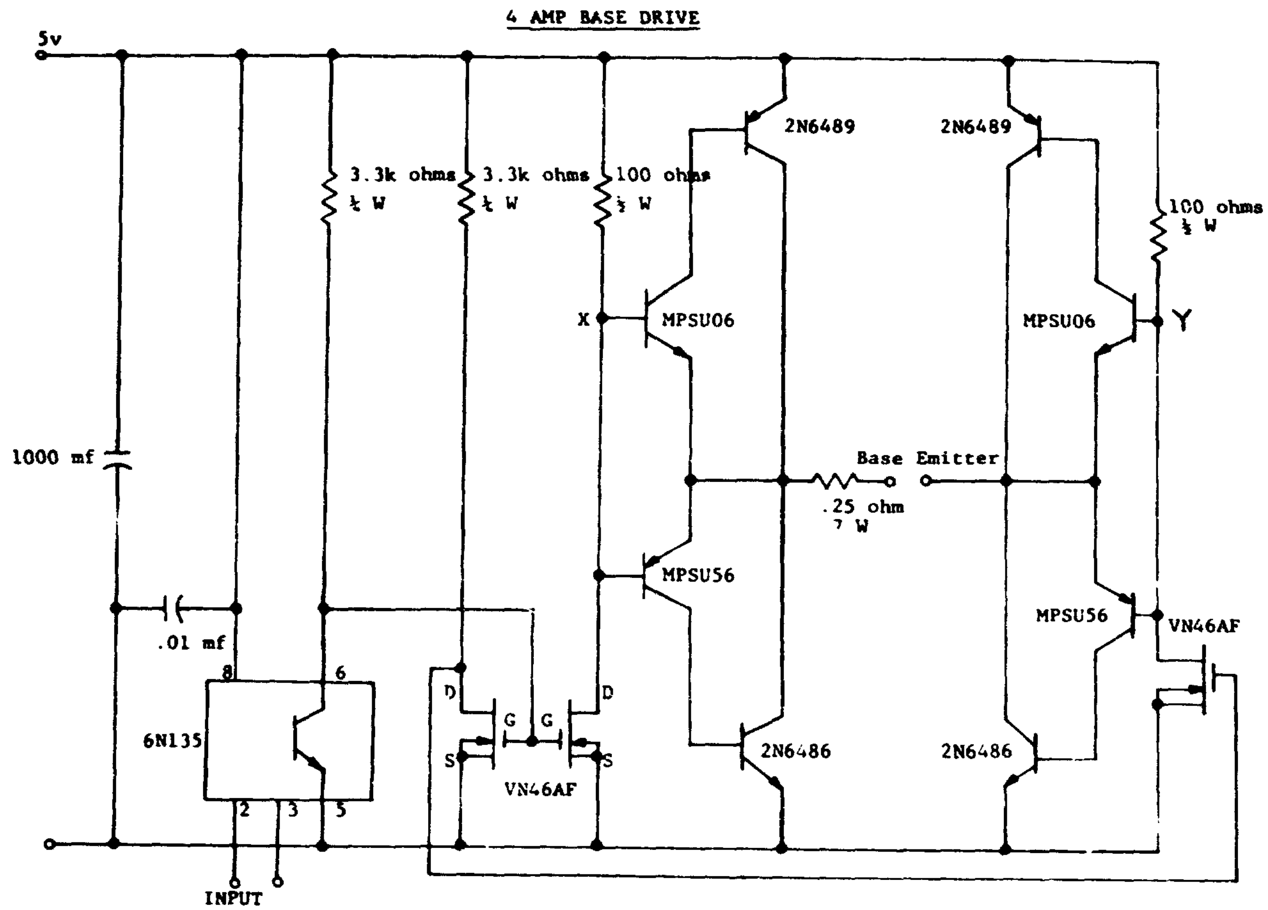

FIGURE (4.1-3) Base Drive

ORIGINAL PAGE IS OF POOR QUALITY

ORIGINAL PAGE IS
OF POOR QUALITY

Since the reluctance of the core is almost negligible, the inductance can be calculated as

$$L = N^2P = 25^2 \times 6.8 \times 10^{-7} = 425\mu H.$$

The windings were made of Number 8 AWG magnet wire, 25 turns/layer, 5 layers/coil, 2 coils, giving a total of 10 strands in parallel.

The length of the average turn is 13 inches. Thus, the length of 25 turn coil is 27.1 ft. The resistance of Number 8 AWG wire is .794Ω/1000 ft. The winding resistance is

$R = 27.1 \times .794/10 = 2.15m\Omega$. This gives a calculated copper loss at rated current of 120A of 31W. Since Number 8AWG copper wire weighs 50 lb./1000 ft. the weight of the winding is

$$W = 27 \times 10 \times 50/1000 = 13.5 \text{ lb}.$$

The core weight is given as 17.7 lb., so that the total weight of the inductor is 31.2 lb.

4.2 COOLING OF POWER CONDITIONER COMPONENTS

The power conditioner unit consists of seven Toshiba Giant G-TR2SD648-1 transistors, [1], as well as eight International Rectifier 400 Ampere fast recovery rectifiers, [2]. Both of these devices use a "hockey-puck" type package which allows double side cooling. The maximum operating junction temperatures are 125°C and 175°C for the transistor and diode respectively. To prevent failure of these devices due to excessive junction temperatures during the normal and peak operating conditions, temperature limits on the transitors and diodes of 115°C an 165°C were imposed in order to provide a 10°C minimum safety margin.

Thermal data on these two devices can be found in References [1] and [2]. Based upon this data, a simplified steady state thermal model of these elements can be expressed in terms of three thermal resistances R_{JC}, R_{CS}, and R_{SA} as shown in Figure (4.2-1). Here R_{JC} represents the thermal resistance between the junction and the case while R_{CS} an R_{SA} represent the thermal resistances between the case and the sink and between the sink and ambient respectively.

The power dissipated in these devices is assumed to flow from the junction to the case, from the case to the heat sink, and finally from the heat sink into ambient as shown in Figure (4.2-1). Consequently the dissipated power P_D can be expressed in terms of the thermal resistances (R_{JC}, R_{CS} R_{SA}) and the junction, case, sink, and ambient temperatures (T_J, T_C, T_S, T_A) as follows:

$$P_D = [T_J - T_C]/R_{JC} \text{ [Watts]} \quad (4.2\text{-}1)$$

$$P_D = [T_C - T_S]/R_{CS} \text{ [Watts]} \quad (4.2\text{-}2)$$

$$P_D = [T_S - T_A]/R_{SA} \text{ [Watts]} \quad (4.2\text{-}3)$$

Since both R_{JC} and R_{CS} are known from the data sheets, [1] and [2], there is only one unknown parameter remaining and that is the thermal resistance of the heat sinks.

The maximum allowable value of R_{SA} such that the thermal limits of the transistors and diodes are not exceeded can be determined by examining the operating points at which the losses are maximum. For the two systems, subject of this report, this corresponds to the 35hp peak operating point. Even though the 35hp peak rating is for one minute only, which is less than the time required to reach steady state temperatures, the heat sinks were sized to handle this load continuously as a safety precaution.

It will be assumed that at the 35hp operating point the inverter-motor system has an overall efficiency of 75% with an input battery voltage of 115V and the maximum ambient temperature of 50°C. The average dc current flowing into the inverter in this case would be

$$I_{DC} = [(35 \times 746/0.75)/115] = 302.7\text{A} \quad (4.2\text{-}4)$$

At the peak rating point, the chopper transistor Q_M would be on continuously and would therefore have to handle I_{DC} continuously. The inverter transistors on the other hand, see this current only one third of the time. Therefore Q_M bears the heaviest thermal load at this operating point.

To calculate the chopper losses under these conditions requires the value of $V_{CE_{sat}}$ for the value of I_{DC} given in Equation (4.2-4). The transistor data sheets, [1], indicate that with a nominal base current of 4 Amperes, the collector to emitter voltage drop of this transistor at a current of 302.7 [A] is 1.40 [V]. Therefore the forward conduction losses are

$$P_D = V_{CE_{sat}} I_{DC} = 302.7 \times 1.40 = 423.8\text{[Watts]} \quad (4.2\text{-}5)$$

Assuming that the junction temperature of the transistor is limited to T_J = 115°C, then the temperature differential between the sink and the maximum ambient temperature of 50°C is

$$T_S - T_A = (115 - 423.8 \times 0.04) - 50 = 48.048°\text{C} \quad (4.2\text{-}6)$$

Consequently the maximum thermal resistance of the chopper transistor heat sink, such that T_J is below 115°C, is given by:

THERMAL MODEL OF TRANSISTORS AND DIODES

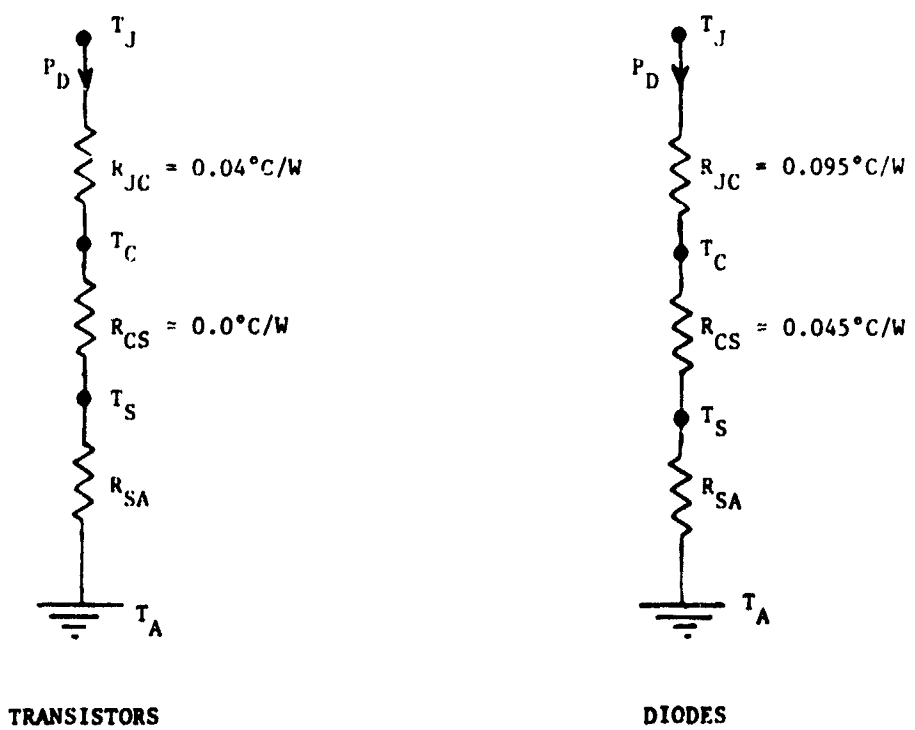

FIGURE (4.2-1) Steady State Thermal Model of Power Conditioner Transistors and Diodes

$$R_{SA} = 48.048/423.8 = 0.113[°C/W] \qquad (4.2\text{-}7)$$

To reduce the overall system complexity and cost, it was decided not to use liquid cooling. Therefore only forced or natural ventilation using air as the heat transfer medium was examined. Also since both the transistors and diodes use a hockey puck package, it was decided to utilize double sided cooling to maximize the heat transfer.

Based upon the size of the transistors and the mounting clamps, a heat sink with a width of five inches and a length of about six inches (.152 m) was determined as the minimum size required to adequately mount these transistors. These specifications were met by two six inch long heat sinks, Thermalloy Number 6740 heat sink extrusions, Reference [3].

The maximum allowable power dissipation vs CFM of air flow for this heat sink are plotted in Figure (4.2-2) assuming a maximum junction temperature of 115°C at ambient temperatures of 25 and 50°. These curves were plotted using thermal data of this heat sink from data obtained in Reference [3]. Notice that even at the maximum ambient temperature of 50°C, this heat sink can handle the full 423.8 Watt load with 96 CFM of forced ventilation. Consequently this sink was chosen since it is close to the minimum size heat sink necessary for the given transistor cooling configuration.

In the case of the diodes, the length of the heat sinks was reduced from 6 inches (.452 m) to 4.5 inches (.114 m) due to a smaller diode package and because of the higher allowable junction temperatures of 175°C (limited to 165°C). Since the maximum junction temperature of the diodes was limited to 165°C, the maximum power dissipations versus CFM at ambient temperatues of 25 and 50°C was obtained using data given in (3], and is plotted in Figure (4.2-3). The diode power loss, with a constant dc current of 300[A] corresponding to 35hp is only 332[W]. This amount of heat can easily be dissipated by the heat sink without exceeding the T_J limit of 165°C.

The above mentioned diode and transistor heat sinks were mounted in a tunnel with the heat sink fins aligned with the axis of the tunnel. Two ventilation fans were mounted at the end closest to the chopper transistors in order to provide the coolest air for this switch. Temperature measurements of the transistor and diode temperatures verified that all switching devices remained within safe temperature limits under all operating conditons with the ventilation fans on.

4.3 POSITION SENSOR

In order to control the firing of the inverter transistors during commutation, it is necessary to know which state of the commutation sequence is appropriate. It is thus necessary to sense the rotor position

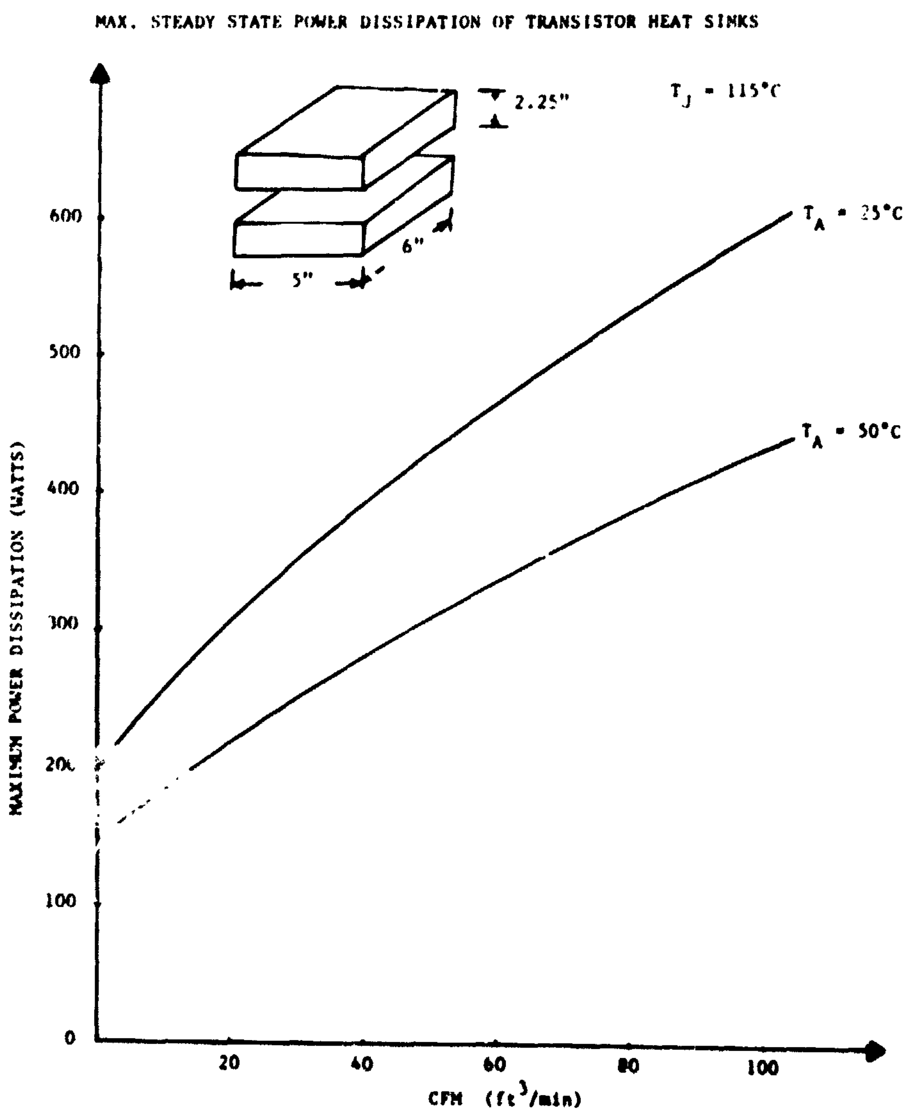

FIGURE (4.2-2) Maximum Steady State Power Dissipation Versus ft³/minutes of Air Flow for the Transistor Heat Sinks

ORIGINAL PAGE IS OF POOR QUALITY

MAX. STEADY STATE POWER DISSIPATION OF DIODE HEAT SINKS

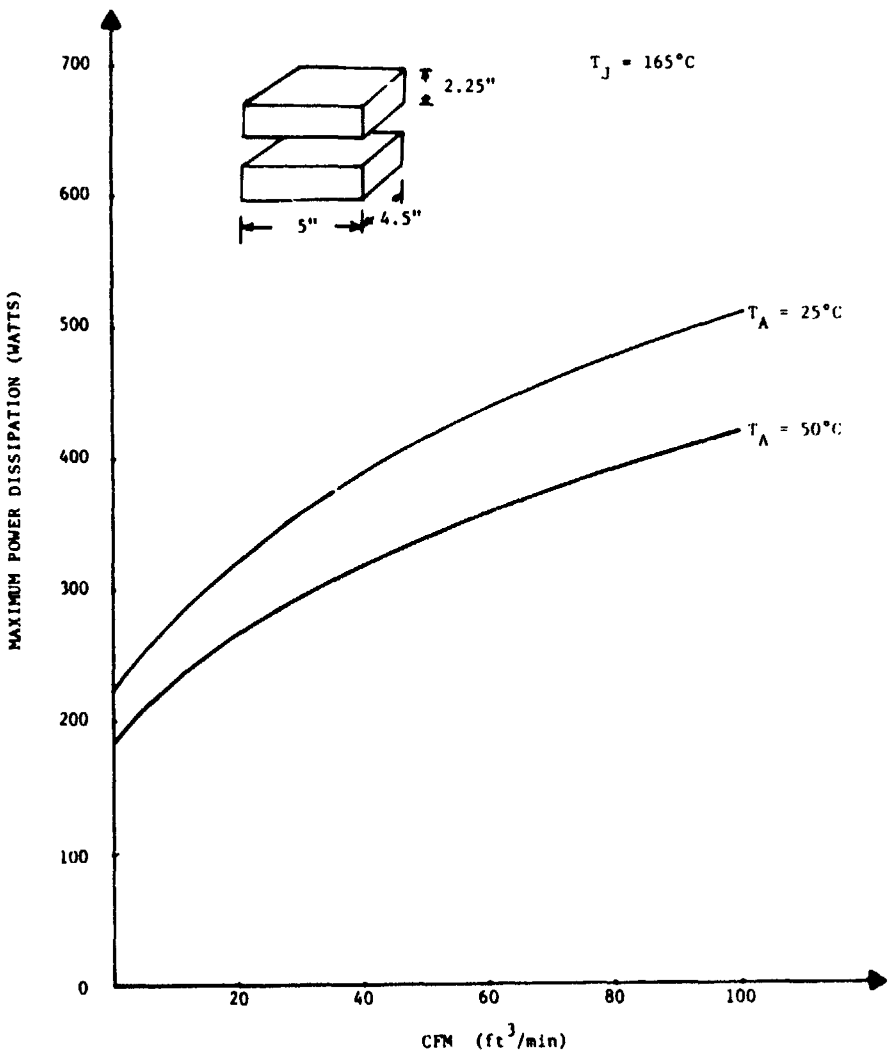

FIGURE (4.2-3) Maximum Steady State Power Dissipation Versus ft³/minutes of Air Flow for the Diode Heat Sinks and to find in which 60°E arc the rotor is positioned. This sensing is accomplished by two sets of three Hall sensors mounted on the stator. These Hall sensors are excited by a six pole permanent magnet field mounted on the rotor.

4.3.1 SENSOR ROTOR

The assembly of the rotor of the position sensor is shown in Figure (4.3-1). Each of the six magnets shown is made of samarium-cobalt and has cross-sectional dimensions of .008m (.3in.) by .012m (.462 in.). These magnets are mounted on a hexagonal hub .021m (.812in.) across the flats. After mounting, potting and grinding the magnets, a retaining sleeve is cemented in place on the outer diameter. This sleeve, made of soft magnetic steel, increases the pole span and provides structural integrity for the rotor at high speed to avoid depending on the cement holding the magnets to the hub.

The flux density in the air gap is calculated to be .315 Tesla (20.3KL/in^2).

4.3.2 SENSOR STATOR

The stator assembly of the rotor position sensor (exclusive of the housing and mounting hardware) is shown in Figure (4.3-2). The laminations are made of 29 guage AISI type M-15 steel. These are cemented together and machined to receive the Hall effect sensors These sensors are spaced 20° apart mechanically, which provides a spacing of 60°E. The second set of sensors is mounted 130° from the first. Thus, for advanced firing, the second set of sensors is located 390°E (or 30°E) from the first set. As a result of this geometry, the output of the sensors is as shown in Figure 4.4-2 of the next section.

4.4 LOW LEVEL CONTROL ELECTRONICS

The function of the low level control electronics is to control the firing of the power transistors of the inverter and chopper in accordance with the rotor position, the commanded motoring or braking torque, the desired direction of rotation, and the need for advanced firing. In addition, there are several protective functions which are incorporated into this system. The circuit diagram of the low level control electronics is shown in Figure (4.4-1). The dc power supply for the low level control electronics, as well as the base drives, was a commercially available multiple output supply.

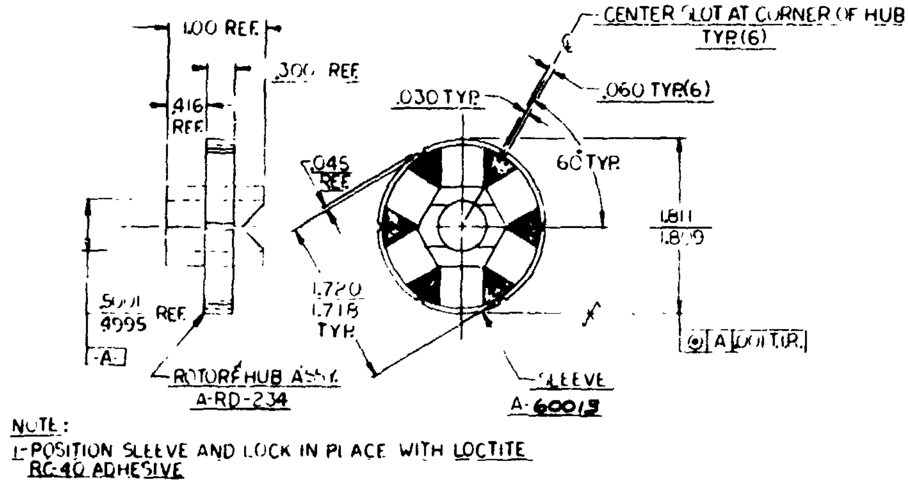

FIGURE (4.3-1) RPS Rotor Assembly

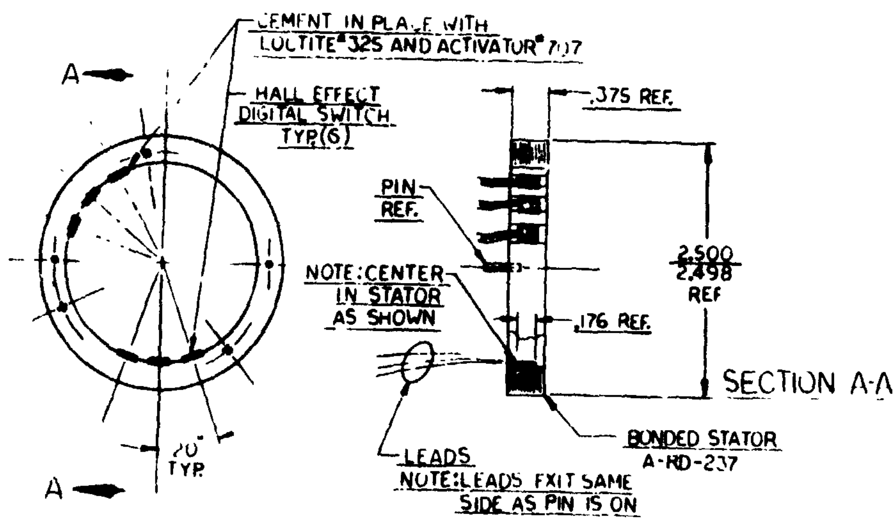

FIGURE (4.3-2) RPS Stator Assembly

ORIGINAL PAGE IS
OF POOR QUALITY

4.4.1 THE PROM

The heart of the control electronics network is a 256 × 8 bit PROM which is composed of two N82S126 PROMs operating in parallel. The eight input signals to this PROM are the six rotor position outputs (normal and advanced firing), the forward/reverse signal, and the normal/advanced firing signal. Six of the eight outputs (three on each PROM) are used for controlling the inverter transistors. The other two outputs (one on each PROM) are used to control an alarm circuit to shut down the inverter in the case of an illegal set of inputs from the rotor position sensor.

Figure (4.4-2) is a timing diagram showing the state of the six outputs of the rotor position sensor for any shaft position, together with the necessary state of the inverter transistors for proper torque production. On the basis of this diagram, the contents of the PROM are chosen as in Table 4.4.1. In setting up this table, the input number is the hexadecimal equivalent of the binary number $a_7a_6a_5a_4a_3a_2a_1a_0$ where a_7 = normal/advanced firing signal (l = advanced).

a_6 = forward/reverse signal (l = reverse)

a_5 = rotor position sensor output C'

a_4 = rotor position sensor output B'

a_3 = rotor position sensor output A'

a_2 = rotor position sensor output C

a_1 = rotor position sensor output B

a_0 = rotor position sensor output A.

Thus, for a command of forward, advanced firing when A, A' and B' are high and B,C and C' are low, the input number would be 10110100 binary or B4 hexadecimal.

The output number is the hexadecimal equivalent of the binary number $b_7b_6b_5b_4b_3b_2b_1b_0$ where

b_7 = output 4 of PROM U4 (0 = alarm)

b_6 = output 3 of PROM U4 (0 = Q6 on)

b_5 = output 2 of PROM U4 (0 = Q5 on)

b_4 = output 1 of PROM U4 (0 = Q4 on)

b_3 = output 4 of PROM U3 (0 = alarm)

b_2 = output 3 of PROMU3 (0 = Q3 on)

b_1 = output 2 of PROM U3 (0 = Q2 on)

b_0 = output 1 of PROM U3 (0 = Q1 on)

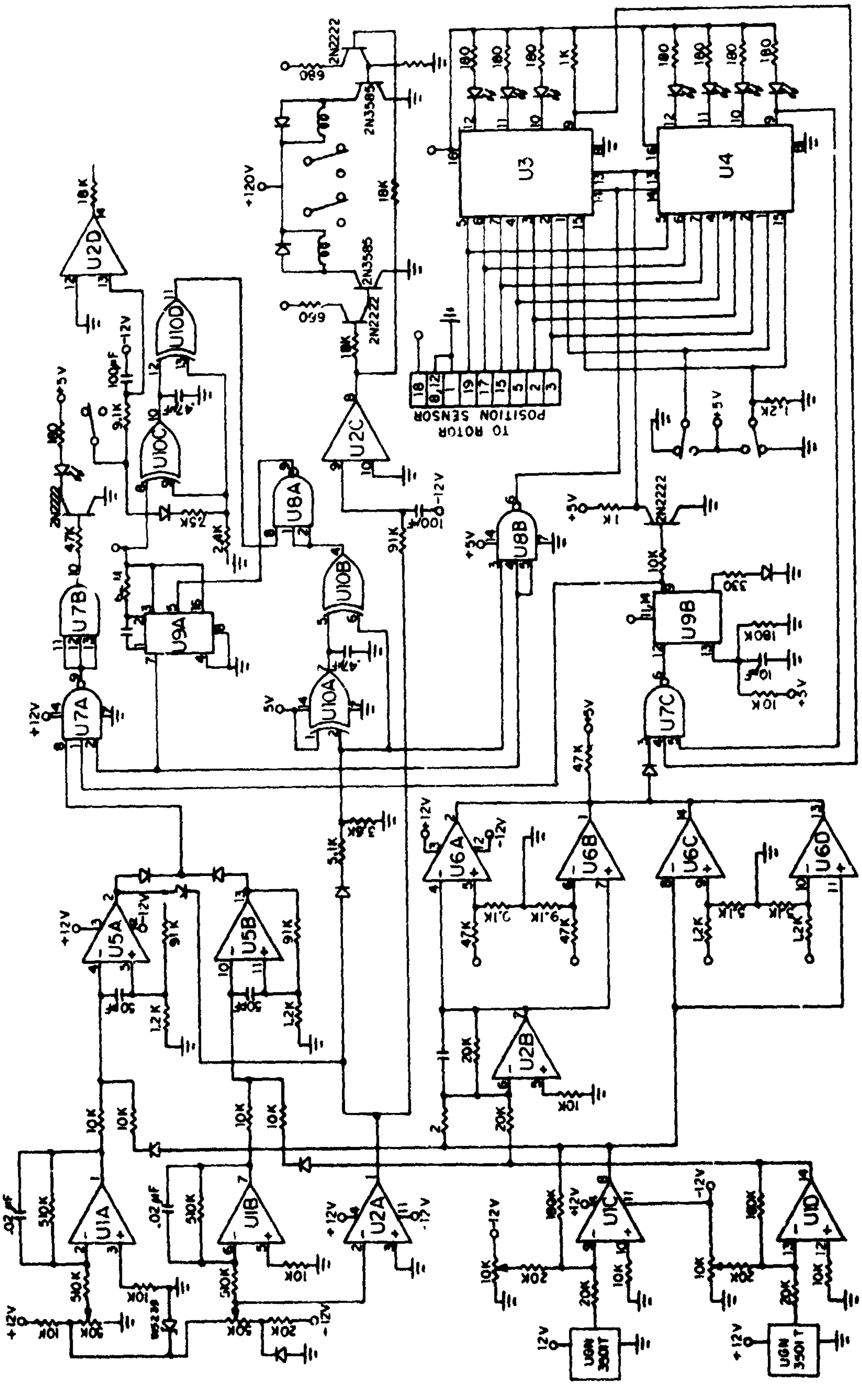

FIGURE (4.4-1) Low Level Control Electronics

Reverse

Position	A B C	Normal Q_1 2 3 4 5 6	A' B' C'	Advanced Q_1 2 3 4 5 6
0				
30	0 0 0	0 1 0 1 0 0	0 0 0	0 1 0 0 0 1
60	0 0 0	0 1 0 1 0 0	1 0 0	0 1 0 1 0 0
90	1 0 0	0 0 1 1 0 0	1 0 0	0 1 0 1 0 0
120	1 0 0	0 0 1 1 0 0	1 1 0	0 0 1 1 0 0
150	1 1 0	0 0 1 0 1 0	1 1 0	0 0 1 1 0 0
180	1 1 0	0 0 1 0 1 0	1 1 1	0 0 1 0 1 0
210	1 1 1	1 0 0 0 1 0	1 1 1	0 0 1 0 1 0
240	1 1 1	1 0 0 0 1 0	0 1 1	1 0 0 0 1 0
270	0 1 1	1 0 0 0 0 1	0 1 1	1 0 0 0 1 0
300	0 1 1	1 0 0 0 0 1	0 0 1	1 0 0 0 0 1
330	0 0 1	0 1 0 0 0 1	0 0 1	1 0 0 0 0 1
360	0 0 1	0 1 0 0 0 1	0 0 0	0 1 0 0 0 1

Forward

Position	A B C	Normal Q_1 2 3 4 5 6	A' B' C'	Advanced Q_1 2 3 4 5 6
0				
30	0 0 0	1 0 0 0 1 0	0 0 0	1 0 0 0 1 0
60	0 0 0	1 0 0 0 1 0	1 0 0	1 0 0 0 0 1
90	1 0 0	1 0 0 0 0 1	1 0 0	1 0 0 0 0 1
120	1 0 0	1 0 0 0 0 1	1 1 0	0 1 0 0 0 1
150	1 1 0	0 1 0 0 0 1	1 1 0	0 1 0 0 0 1
180	1 1 0	0 1 0 0 0 1	1 1 1	0 1 0 1 0 0
210	1 1 1	0 1 0 1 0 0	1 1 1	0 1 0 1 0 0
240	1 1 1	0 1 0 1 0 0	0 1 1	0 0 1 1 0 0
270	0 1 1	0 0 1 1 0 0	0 1 1	0 0 1 1 0 0
300	0 1 1	0 0 1 1 0 0	0 0 1	0 0 1 0 1 0
330	0 0 1	0 0 1 0 1 0	0 0 1	0 0 1 0 1 0
360	0 0 1	0 0 1 0 1 0	0 0 0	1 0 0 0 1 0

FIGURE (4.4-2) Timing Diagram (RPS - Inverter)

Thus, for the previous example with an input of B4, the output from Table (4.4.1) would be 11101011 binary or EB hexadecimal. It should be noted that this PROM configuration permits advanced firing for either direction of rotation.

In addition to the data inputs, each PROM chip has two inhibit gates, CE_1 and CE_2. The presence of a positive voltage on either gate will prevent any output from going negative and thus turns off the inverter transistors. One of these inhibit gates is used to turn off the inverter during regeneration. The signal to accomplish this is taken from the brake potentiometer through U2A and U8B to inhibit gate CE_1. . second signal which can operate this inhibit gate through U8B is the current inhibit signal from pulse generator U9A. The second inhibit gate, CE_2, is controlled by the flip-flop U9B, which is actuated by any alarm signal received from NAND gate U7C.

4.4.2 TORQUE CONTROL AND BRAKING

The control of the torque of the machine in both motoring and regenerative braking modes is accomplished by controlling the current flowing to or from the machine. This is done by measuring the current in the chopper inductor, comparing it to a reference signal coming from the accelerator or brake potentiometer, and turning the chopper transistor on or off according to whether the difference is positive or negative by a sufficient amount.

The inductor current is sensed by measuring the mmf around the inductor lead with a pair of Hall sensors which will be described in the next section. The outputs of these sensors are amplified by operational amplifiers U1C and U1D. These op-amps also remove the bias from the sensor signals. At the same time, the output of the accelerator or brake potentiometers is being filtered and buffered by op-amps U1A and U1B.

For motoring control, the output of U1A, which becomes more negative as the accelerator setting is increased, is added to the output of U1C, which becomes more positive as the inductor current increases. The input to pin 4 of U5A will be positive f the inductor current exceeds the commanded value and negative if it is smaller than the commanded value. A small amount of positive feedback is provided to pin 5 of U5A to generate a hysteresis of about 15A in the inductor current. If the inductor current is high enough to overcome the hysteresis of U5A, the output of this comparator will be low, causing the output of NAND gate U7A to be high, the output of NAND gate U7B to be low, turning off the 2N2222 transistor and, therefore, turning off the chopper transistor. If the inductor current is low enough to overcome the hysteresis of U5A, an opposite switching effect occurs, turning on the chopper transistor, providing the inhibit inputs 1 and 2 of NAND gate U7A are positive.

TABLE (4.4-1) PROM CONTENTS

PROM CONTENTS

I	O	I	O	I	O	I	O	I	O	I	O	I	O	I	O
00	DE	20	DE	40	ED	60	ED	80	DE	A0	DB	C0	BD	E0	BE
01	BE	21	BE	41	EB	61	EB	81	DE	A1	DB	C1	BD	E1	BE
02	77	22	77	42	77	62	77	82	DE	A2	DB	C2	BD	E2	BE
03	BD	23	BD	43	DB	63	DB	83	DE	A3	DB	C3	BD	E3	BE
04	DB	24	DB	44	BD	64	BD	84	DE	A4	DB	C4	BD	E4	BE
05	77	25	77	45	77	65	77	85	DE	A5	DB	C5	BD	E5	BE
06	EB	26	EB	46	BE	66	BE	86	DE	A6	DB	C6	BD	E6	BE
07	ED	27	ED	47	DE	67	DE	87	DE	A7	DB	C7	BD	E7	BE
08	DE	28	DE	48	ED	68	ED	88	BE	A8	77	C8	ED	E8	77
09	BE	29	BE	49	EB	69	EB	89	BE	A9	77	C9	ED	E9	77
0A	77	2A	77	4A	77	6A	77	8A	BE	AA	77	CA	ED	EA	77
0B	BD	2B	BD	4B	DB	6B	DB	8B	BE	AB	77	CB	ED	EB	77
0C	DB	2C	DB	4C	BD	6C	BD	8C	BE	AC	77	CC	ED	EC	77
0D	77	2D	77	4D	77	6D	77	8D	BE	AD	77	CD	ED	ED	77
0E	EB	2E	EB	4E	BE	6E	BE	8E	BE	AE	77	CE	ED	EE	77
0F	ED	2F	ED	4F	ED	6F	DE	8F	BE	AF	77	CF	ED	EF	77
10	DE	30	DE	50	ED	70	ED	90	77	B0	EB	D0	77	F0	DE
11	BE	31	BE	51	EB	71	EB	91	77	B1	EB	D1	77	F1	DE
12	77	32	77	52	77	72	77	92	77	B2	EB	D2	77	F2	DE
13	BD	33	BD	53	DB	73	DB	93	77	B3	EB	D3	77	F3	DE
14	DB	34	DB	54	DB	74	DB	94	77	B4	EB	D4	77	F4	DE
15	77	35	77	55	77	75	77	95	77	B5	EB	D5	77	F5	DE
16	EB	36	EB	56	BE	76	BE	96	77	B6	EB	D6	77	F6	DE
17	ED	37	ED	57	DE	77	DE	97	77	B7	EB	D7	77	F7	DE
18	DE	38	DE	58	ED	78	ED	98	BD	B8	ED	D8	EB	F8	DB
19	BE	39	BE	59	EB	79	EB	99	BD	B9	ED	D9	EB	F9	DB
1A	77	3A	77	5A	77	7A	77	9A	BD	BA	ED	DA	EB	FA	DB
1B	BD	3B	BD	5B	DB	7B	DB	9B	BD	BB	ED	DB	EB	FB	DB
1C	DB	3C	DB	5C	BD	7C	BD	9C	BD	BC	ED	DC	EB	FC	DB
1D	77	3D	77	5D	77	7D	77	9D	BD	BD	ED	DD	EB	FD	DB
1E	EB	3E	EB	5E	BE	7E	BE	9E	BD	BE	ED	DE	EB	FE	DB
1F	ED	3F	ED	5F	DE	7F	DE	9F	BD	BF	ED	DF	EB	FF	DB

Regenerative braking is controlled by an identical process. Additionally, when a braking command is generated by the brake potentiometer, the output of U2A is switched negative. The negative output of U2A performs three functions:

1. the output of the accelerator comparator U5A is clamped low;

2. the relay which switches the chopper transistor from the motoring to the braking configuration is driven to the braking position through the time delay circuit of U2C; and

3. a negative pulse is generated by the exclusive OR gates U10A and U10B, which is transmitted through AND gate U8A to pulse generator U9A. This triggers a 500ms negative pulse, which inhibits the firing of the chopper transistor and the inverter transistors during the time of the relay switching. Thus, the relay is never carrying appreciable current during the switching operation.

4.4.3 THE CURRENT SENSOR

It became evident early in the design process that the use of a shunt for current sensing would introduce a large power loss. In order to avoid this loss, an electronic sensor using Hall effect devices was designed and built. This sensor detected the magnetic field surrounding the wire carrying the current and generated a voltage proportional to the field intensity.

The Hall effect sensors used were Sprague Electric Company type UGN-3501T Linear Output "Hall Effect" Sensors. These sensors have a nominal output voltage of 3.6 Volts with no magnetic field. This output voltage varies by about 6.67 Volts per Tesla of magnetic flux. The maximum linear range of the device is about ±0.2 Tesla. In order to obtain the maximum sensitivity appropriate to this application, the flux density of 0.2 Tesla should correspond to 300A. Such a flux density required the use of a magnetic core.

A ferrite core (Magnetics Incorporated type 41605-TC material G) was placed around the wire in order to increase the magnetic field due to the current. It was desired to obtain a flux density of 0.2 Tesla with only one turn of wire. This would permit the sensor to be slipped over the wire. To achieve such a flux density would require an air gap of .074 inches. This would be too small to insert the Hall effect devices. Thus, an air gap of .093 inches (.236 cm) was used. This air gap, at a magnetomotive force of 300 Ampere-turns, has a field intensity of 1.27×10^{5} Ampere-turns per meter which corresponds to a flux density of .16 Tesla. Given the sensitivity of the Hall effect devices, the output of the device changes by about 1 Volt at an inductor current of 300 Ampere.

4.4.4 PROVISION FOR SERIES-PARALLEL OPERATION

At the outset of the project, it was not clear whether the drive cycle requirements for acceleration could be met with a limiting current of about 300 Amperes. For this reason, provision was made to double the number of turns per phase, and so to double the torque constant, by using two sets of coils which could be connected either in a series or parallel configuration. A relay was to be used to accomplish this switching. Provision for driving this relay has been provided in the control electronics.

A switch has been provided which furnishes a signal to the inputs of U2D, U10C, and U10D. The output of U2D can be used to control a pair of power transistors to drive a relay which would accomplish the series-parallel switching operation. The exclusive OR gates U10C and U10D generate a negative pulse any time the selector switch is operated in either direction which triggers the current inhibit pulse generator U9A to turn off the chopper and inverter transistors during the switching operation.

A commercially available relay capable of performing this switching operation would have been prohibitively expensive. An attempt was made to fabricate a relay which would take advantage of the "dry switching" characteristic of the application. This relay did not perform satisfactorily. Since it was found that the system permitted performance within the specified drive cycle without this series-parallel switching provision, the relay an its associated power transistors were removed. This does restrict the accelerating capability at low speed, even though the sytem performance is within specifications. For this reason, the low-level electronics still retains this switching capability to permit the addition of the relay, if desired.

4.4.5 PROTECTIVE CIRCUITS

In Section 4.4.1, the provision for alarm signals to deactivate the PROM and turn off the inverter transistors was mentioned. There are three such alarm signals incorporated into the system:

1. The fourth output of either PROM will go negative if that PROM receives an illegal input from the rotor position sensor.

2. Failure of a current sensor will cause the alarm buss to go negative.

3. Excessive inductor current will cause the alarm buss to go negative.

The first of these alarm functions was discussed in Section 4.4.1. The last two functions are accomplished primarily in comparator chip U6.

Elements U6A and U6B are used to detect the failure of a current sensor. Since the two sensors are used in opposite senses (that is, one goes more positive and one more negative for increasing current), the sum of the two outputs should remain near zero. This sum is formed in U2B and applied to comparators U6A and U6B in opposite senses. Thus, an excessive discrepancy of either polarity between the two sensor outputs will generate an alarm signal.

Comparator elements U6C an U6D are used to detect an excessive current of either polarity through the inductor and to generate an alarm signal by drawing down the output buss.

It should be noted that when the output of flip-flop U9B is in the alarm state (pin 9 low), this signal is fed to the NAND gate U7A as well as to the PROM. In this way, the chopper transistor, as well as the inverter transistors, is turned off during any alarm condition.

Any time an alarm triggers U9B, there is a visual indication of this in the LED connected to the output of the flip-flop.

REFERENCES CITED IN CHAPTER (4)

1. Toshiba Giant Transstor Catalog and Technical Data, Toshiba Corporation, Tokyo Japan, March 1, 1979.

2. 401 PDL Series, Power Silicon Rectifiers, Data Sheet Number PD-2.02, International Rectifier, Semiconductor Division, El Segundo, California, April 1973.

5.0 PERFORMANCE OF MACHINE-POWER CONDITIONER SYSTEMS

In this chapter, the results of testing of the samarium cobalt and strontium ferrite based machines, whose designs were described in Chapter (3.0), when both machines are operated by the power conditioner detailed earlier in Chapter (4.0), are detailed for both the motoring and regeneration modes.

First the test setups used in obtaining all the experimental data are detailed in Section (5.1). The raw data resulting from the testing process is given in Section (5.2), while the methods of power loss and efficiency calculations are given in Section (5.3). In Section (5.4), some resulting data corrections are introduced, in addition to MPC system loss interpolation formulas. Finally, in Section (5.6) the MPC systems' losses and efficiencies under the standard SAE J227-a Schedule D drive cycle are obtained.

5.1 TEST SETUPS OF MPC SYSTEMS

Setup (1)

The bulk of the performance test data were obtained during MPC system tests which were conducted using a test setup (1) depicted schemtically in Figure (5.1-1). In this test setup, the MPC system undergoing testing is connectd to (energized from) a dc supply which consists of a motor-generator (MG) set filtered with a shunt capacitance of about 0.1 Farad to simulate a battery. Proper current, voltage, and power instrumentation at the conditioner dc input side, and at the machine (armature) ac input terminals is indicated in Figure (5.1-1).

The machine is connected through a torque transducer and a pulley-belt system to the dynamometer. Proper torque and speed instrumentation are shown in the schematic of Figure (5.1-1). Proper instrumentation for machine and conditioner temperatures was achieved by thermocouples. The instrumentation for a number of these variables was connected to a data acquisition (DA) system as indicated schematically in Figure (5.1-1), and detailed for the 16 channels of the DA system in Table (5.1-1).

It must be emphasized that this setup (1) permits the flow of power from the dc supply, through the MPC system, to the dynamometer and vice versa, as indicated by the arrows of power flow in Figure (5.1-1).

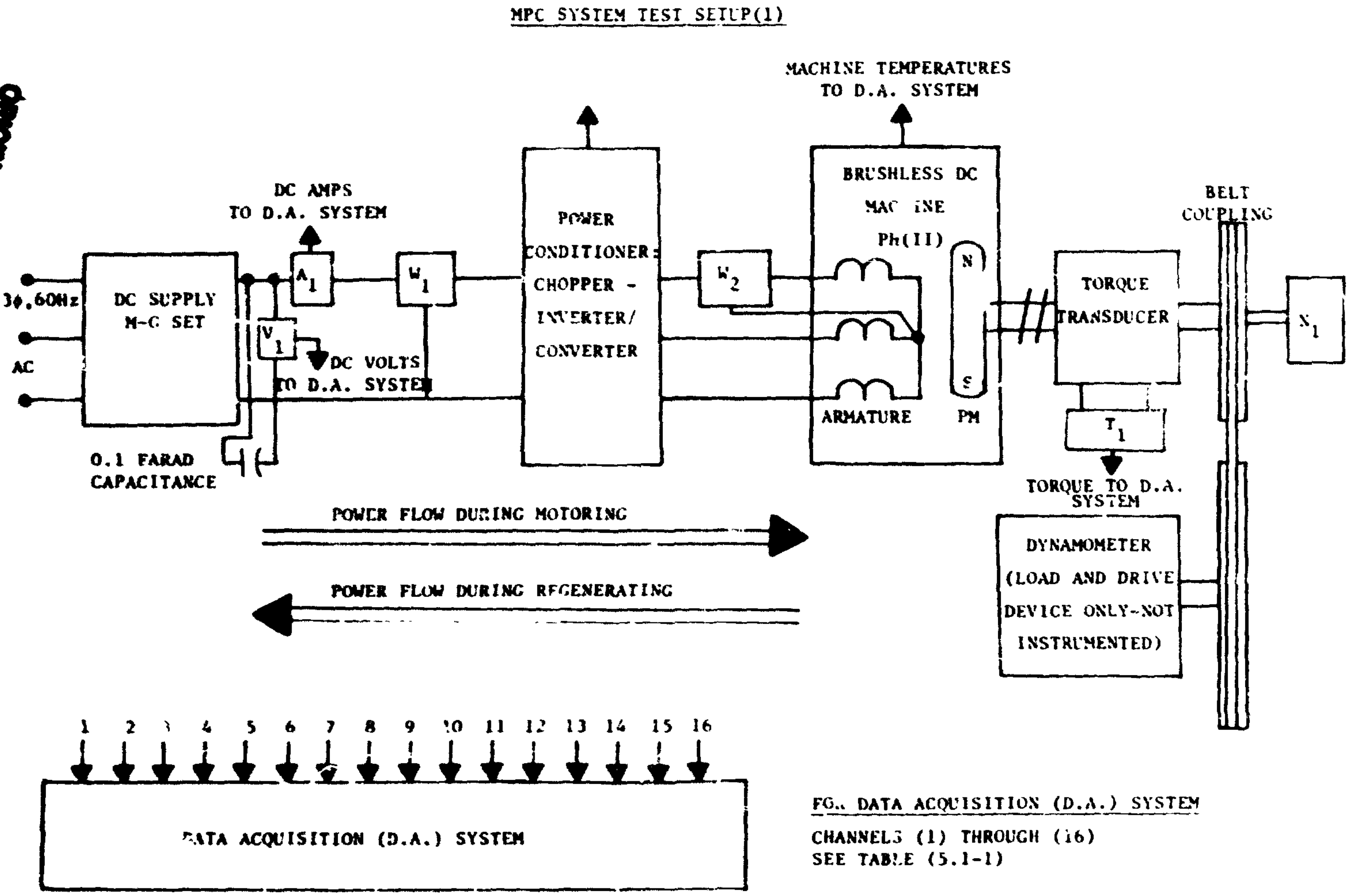

FIGURE (5.1-1) Motor-Power Conditioner Test Setup (1)

TABLE (5.1-1). IDENTIFICATION OF FUNCTIONS OF DATA LOGGER CHANNELS.

CHANNEL	FUNCTION
1	(Ambient) Room Temperature °C, θ_1
2	End bell (front) °C, θ_2
3	End bell (rear) (RPS Housing) °C, θ_3
4	Motor housing (center) °C, θ_4
5	Motor core (center of stack) °C, θ_5
6	Motor core (end of sack) °C, θ_6
7	Motor end turns °C, θ_7
8	Inverter Transistor Case °C, θ_8
9	Chopper Transistor Case °C, θ_9
10	Inverter diode sink °C, θ_{10}
11	Chopper diode case °C, θ_{11}
12	Air intake to PCU °C, θ_{12}
13	Air exhaust from PCU °C, θ_{13}
14	Average input dc current (before capactor-bank) amperes, I
15	Average input dc voltage (parallel to capacitor-bank) volts, V
16	Motor torque ft. lb (Feet-pound), T

C-3

TABLE (5.1-2) IDENTIFICATION OF INSTRUMENTATION IN TEST SETUP (1) - SEE FIGURE (5.1-1).

INSTRUMENT	FUNCTION	IDENTIFICATION AND TYPE
V_1	Voltmeter	Monitor Labs, Inc., Data Logger, Model 9300, S/N 96 (Voltmeter for Comparison: Fluke, Digital Multimeter, Model 8012A, S/N 2190862)
A_1	Ammeter	Monitor Labs, Inc., Data Logger, Model 9300, S/N 96 with a 200A/100mV Shunt, G.E. Number 50-140034RLAA
W_1	Wattmeter	Clarke Hess, Digital V-A-W meter, Model 255, S/N 440, with T and M Research Products, Inc., Coaxial Shunt, Model K 20,000-40, S/N 7914
W_2	Wattmeter	Clarke Hess, Digital V-A-W meter, Model 255, S/N 240, with T and M Research Products, Inc., Coaxial Shunt, Model K 20,000-40, S/N 6011
T_1	Torque Transducer	Torque Sensor-Lebow Associates, Inc.-Model 1604-2k, S/N 406, with Transducer Indicator-Lebow Associates, Inc.-Model 7535, S/N 428 (Also recorded by Data Logger identified above)
N_1	Tachometer	General Radio Strobotac, Model 1531-AB, Inland Instrument Number E13
--	Temperatures	Type J Thermocouple Wire With Data Logger identified above - Thirteen Temperatures Throughout MPC system, See Table (5.1-1)

FIGURE (5.1-2) Setup (1) When Testing the Samarium Cobalt Machine

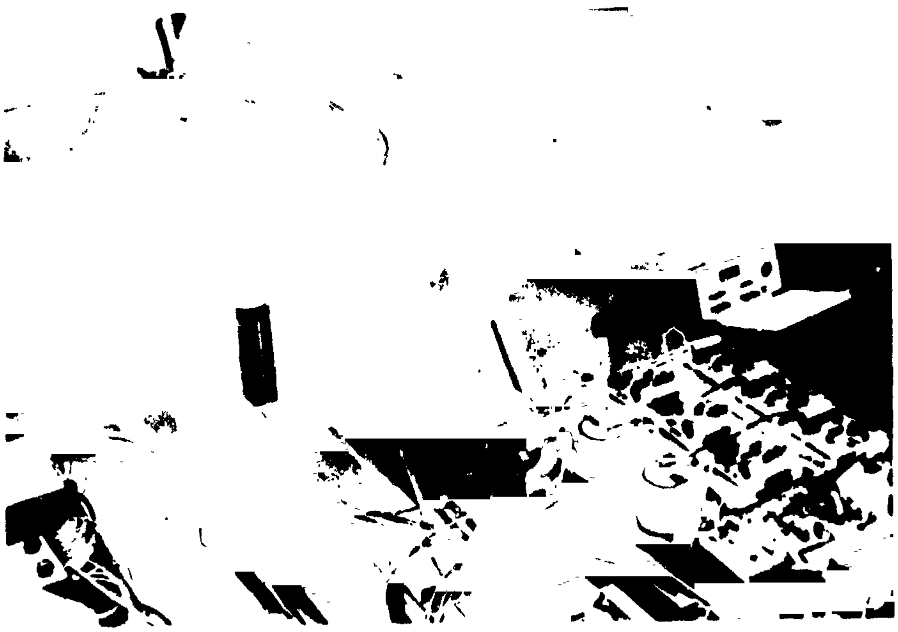

FIGURE (5.1-3) Setup (1) When Testing the Strontium Ferrite Machine

Thus, setup (1) provides the capabilities necessary for testing the MPC systems in the motoring as well as the regenerating modes of operation. Proper identification of the various instruments used in Setup (1) is given in Table (5.1-2). Photographs of the Setup (1) while conducting tests on the MPC systems are shown in Figures (5.1-2) and (5.1-3).

Setup (2)

Due to production scheduling constraints at the manufacturers' premises, a limited number of motoring test runs on both MPC systems had to be carried out using setup (2), which is shown schematically in Figure (5.1-4). In this test setup, the MPC system undergoing testing is connected to (energized from) a static converter dc supply. Proper current, voltage, and power instrumentation at the conditioner dc input side, and at the machine (armature) ac input terminals is indicated in this figure. The machine undergoing testing is solidly coupled to the Phase (I) machine, which in turn functions as an alternator (generator) the ouput of which is dissipated in adjustable load racks (adjustable resistance load), with proper output instrumentation. Proper instrumentation for machine and conditioner temperatures was through thermocouples.

It must be emphasized that this Setup (2) permits the flow of power from the dc supply, through the MPC sytem, to the Phase (I) machine which is acting as an alternator, in one direction as indicated by the arrow of power flow in Figure (5.1-4). Thus Setup (2) provides for testing the MPC systems in the motoring mode of operation only. Proper identification of the various instruments used in Setup (2) is given in Table (5.1-3). Photographs of this test setup are shown in Figure (5.1-5) and (5.1-6).

The results of testing the samarium cobalt and strontium ferrite based machines to determine their various performance characteristics, when operating in conjunction with the power conditioner detailed in Chapter (4.0), are given in the next secion. The bulk of the testing runs for both machines were performed using the testing Setup (1), Figure (5.1-1), while the remaining runs were performed using the testing Setup (1), Figure (5.1-4).

TABLE (5.1-3) IDENTIFICATION OF INSTRUMENTATION IN TEST SETUP (2) - SEE FIGURE (5.1-2)

INSTRUMENT	FUNCTION	IDENTIFICATION AND TYPE
V_1	Voltmeter	Fluke, Digital Multimeter, Model 8021A, S/N 2190765
A_1	Ammeter	Fluke, Digital Multimeter, Model 8050A, S/N 2856340, with T and M Research Products, Inc., Coaxial Shunt, Model K20,000-40, S/N 6011
W_2	Wattmeter	Clarke Hess, Digital V-A-W meter, Model 255, S/N 440, with T and M Research Products, Inc., Coaxial Shunt, Model K20,000-40, S/N 7914
N_1	Tachometer	Shimpo Ind. Co., Ltd., Digitacho DT-103B, S/N 770430
A_2 & A_3	Ammeters	Weston, AC Ammetrs, Model 433, S/N 182976 and S/N 183051, with Electrical Instrument Service Inc., Current Transformers, Model TR-2A S/N ES9089 and S/N ES9090, respectively.
W_3	Wattmeter	Sensitive Research, Polyphase Wattmeter, Model PDLW, S/N ES10728, With the above mentioned Current Transformers.

MPC SYSTEM TEST SETUP(2)

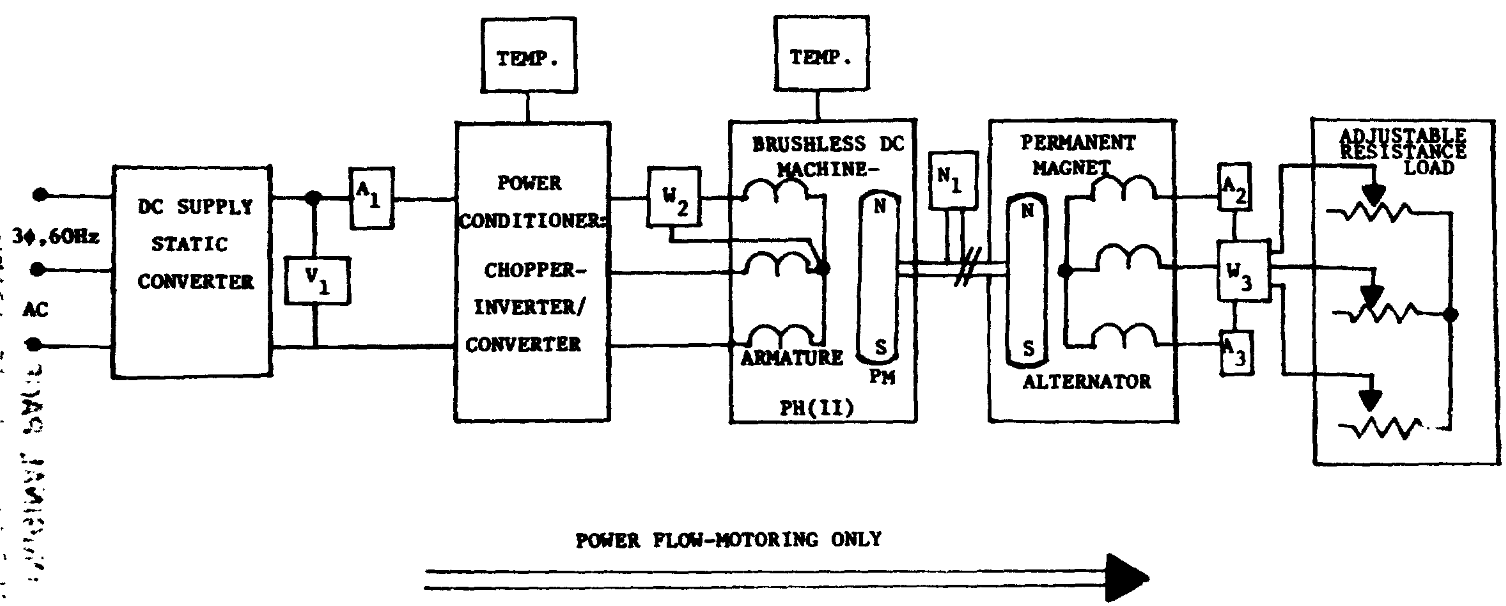

FIGURE (5.2-4) Motor-Power Conditioner Test Setup (2)

ORIGINAL PAGE IS
OF POOR QUALITY

FIGURE (5.1-5) Setup (2) When Testing
Samarium Cobalt Machine

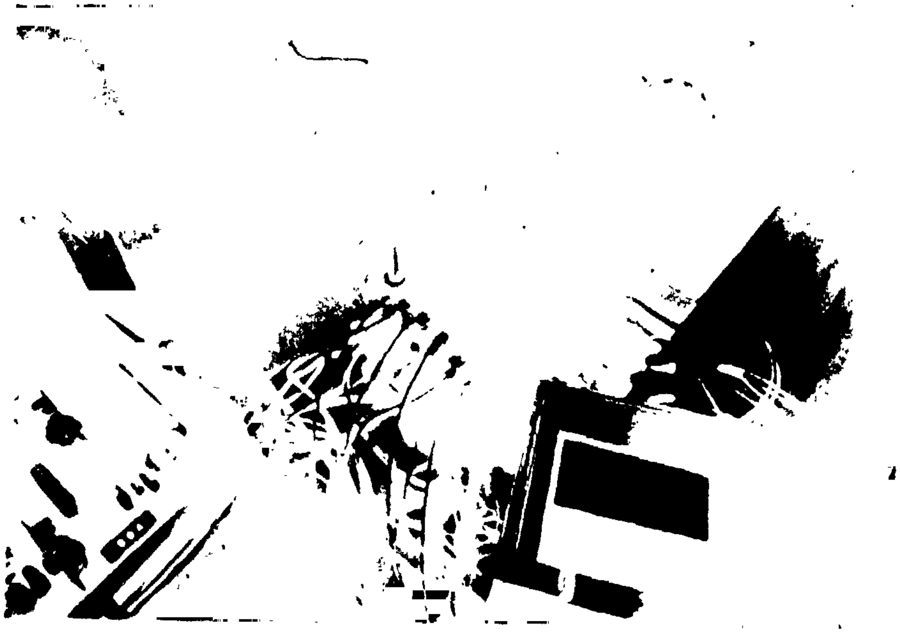

FIGURE (5.1-6) Setup (2) When Testing
Strontium Ferrite Machine

ORIGINAL PAGE
BLACK AND WHITE PHOTOGRAPH

5.2 TEST RESULTS OF MPC SYSTEMS

THE SAMARIUM COBALT BASED MACHINE

The samarium cobalt based machine, the design of which is detailed in Chapter (3.0), was built and tested while in operation in conjuction with the power conditioner, whose design was detailed in Chapter (4.0), under various load conditions. This included a two hour run at a rated load of 15 hp (11.2 kw) motor output, followed immediately by a one minute run at a peak load of 35 hp (26.1 kw) motor output. For the purpose of identification of the various load runs, the run numbers are plotted in Figure (5.2-1), with coordinates designated by the inductor current (which is approximately proportional to the developed torque) versus the machine speed, that is, the points are plotted in the Ampere-RPM plane. This data was recorded when the machine was operated with parallel connected armature paths.

The dc inductor current is not to be confused with the dc line current which is delivered from the source to the MPC system during motoring, and delivered from the MPC system to the source during regeneration. Notice that without chopping, the dc inductor current is approximately equal to the dc line current, whereas during chopping the inductor current is considerably greater than the dc line current.

Each run is identified in this current - speed plane of Figure (5.2-1) by a run identification number. These identification numbers do not follow any pattern in this diagram, but are rather based on the sequence in which these runs were performed. These numbers have been preserved in their original form in order to make it easier to relate to the raw data in these investigators' files. Thus, as far as the reader is concerned, the run identification numbers are of no consequence, except for book keeping purposes. Notice, in the current-speed plane, Figure (5.2-1), only one run, namely run 98, required advanced commutation by 30° in the inverter bridge. This run, which is the peak load run of 35 hp (26.1 kw) motor output is designated by a cross (+) rather than the usual dots for normal runs with no advanced commutation (firing). It should be pointed out that run 64 is that in which the MPC system was loaded for two continuous hours at its rated output of 15 hp (11.2 kw).

The results of the various runs (for the motoring mode) in the inductor current-speed plane of Figure (5.2-1) are given in Table (5.2-1), except for the two hour rated hp run number 64, which is given separately in Tables (5.2-2) and (5.2-3). Table (5.2-2) contains the various MPC system current, voltage, input and output power, torque, as well as speed values taken at increments of 5 minutes throughout the test period of 125 minutes, while Table (5.2-3) contains the

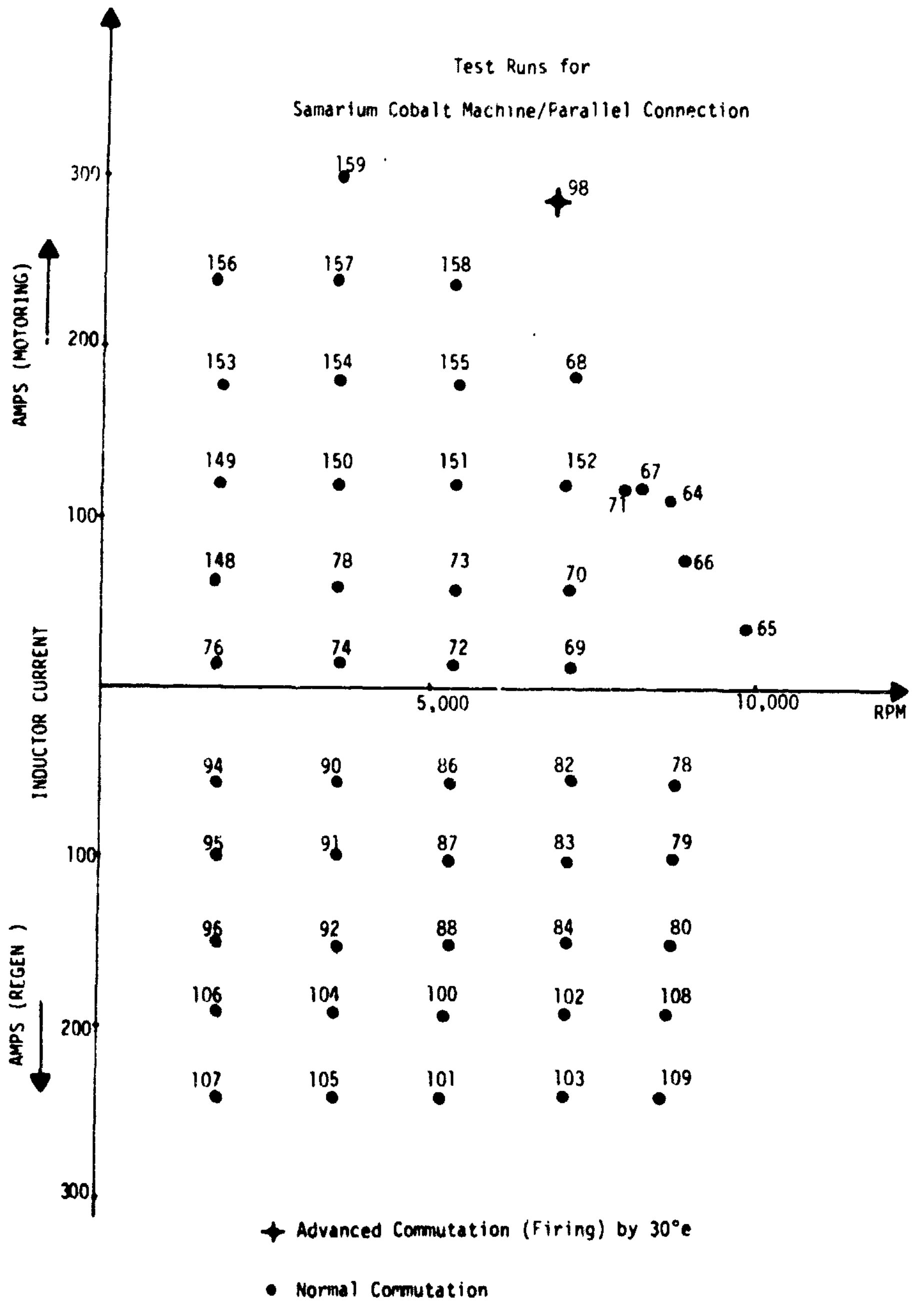

FIGURE (5.2-1) Inductor Current (Torque) - Speed Plane for the Samarium Cobalt Machine With Parallel Connected Armature Paths.

thirteen temperatures previously defined in Table (5.1-1), recorded at increments of 5 minutes, also throughout the 125 minutes run 64.

In Tables (5.2-1) and (5.2-2), the following symbols designated the various currents, voltages, input and output powers, torque, as well as speed in the MPC system under consideration:

> I = dc line current (not to be confused with inductor current) of MPC system in Ampres (A),
>
> V = dc supply voltage into MPC system in Volts (V),
>
> P_{in} = total power input into MPC system including 200 Watts consumed by the low level control electronics, in Watts (W),
>
> T = shaft output torque of motor in Newton Meters (NM),
>
> N = the motor shaft speed in RPM,

and

> P_{out} = total shaft output power from the MPC system in Watts (W).

Notice that in Tables (5.2-1) and (5.2-2) there is an entry for each data set which indicates whether such data was obtained using the test Setup (1) of Figure (5.1-1), or such data was obtained using the test Setup (2) of Figure (5.1-4).

Furthermore, the ambient temperature, θ_1, the motor core (center stack) temperature, θ_5, the motor end turn temperature, θ_7, the inverter transistor case temperature, θ_8, and the chopper transistor case temperature, θ_9, are plotted over the 125 minutes duration of the rated 15 hp run number 64, in Figure (5.2-2), when the power conditioner was tested in conjunction with the samarium cobalt based machine.

The results of the various runs for the regeneration mode in the current-speed plane of Figure (5.2-1) are given for this samarium cobalt based machine in Table (5.2-4). This table contains the various MPC system, current, voltage, input and output power, torque as well as speed values. Also, one must notice that in this table, P_{in} represents a mechanical input which is used to drive the samarium cobalt machine as a generator feeding a six legged converter (full wave rectifier bridge) that is equal to the torque times the speed. Meanwhile, P_{out} represents the gross electric power returned to the battery from the MPC system minus 200 Watts consumed in the low level control electronics. These runs were performed exclusively using test Setup (1), Figure (5.1-1), where power flow reversal was possible.

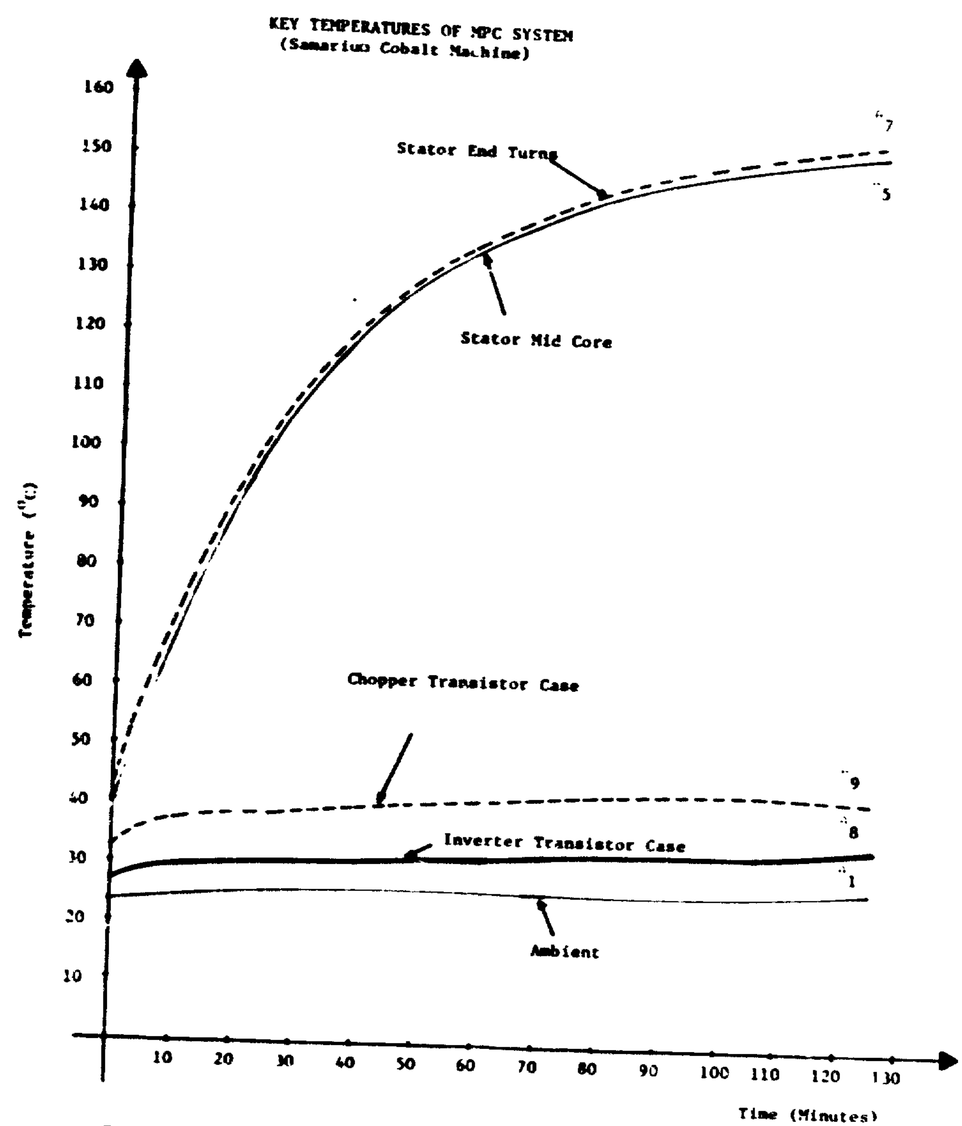

FIGURE (5.2-2) Temperature Rise in the MPC System (Samarium Cobalt Case), Run 64, at 15 hp Output for 125 Minutes Duration

ORIGINAL PAGE IS
OF POOR QUALITY

TABLE (5.2-1) TEST DATA OF MOTORING RUNS FOR THE SAMARIUM COBALT BASED MACHINE WHEN ARMATURE PATHS WERE CONNECTED IN PARALLEL

*When Test Setup (2) Was Used, These Variables Were Obtained Indirectly by Calculations from Measured Quantities

RUN No.	TEST Setup	N, RPM	I, Amps	T, NM	V, Volts	P_{in}, Watts	P_{out}, Watts
65	1	9830	38.14	4.07	115.86	5618.9	4189.6
66	1	8960	83.98	6.75	116.23	9961.0	6333.4
67	1	8230	127.74	15.25	115.78	14989.7	13143.1
68	1	7200	197.10	25.08	115.90	13043.9	18909.9
69	1	7140	9.72	1.69	115.97	1327.2	1263.6
70	1	7180	43.00	5.76	115.85	5181.5	4330.9
71	1	8000	119.04	14.57	116.01	14009.8	12206.1
72	1	5400	7.46	1.35	115.28	1060.0	763.4
73	1	5400	33.36	5.76	114.57	4022.0	3258.5
74	1	3600	5.24	2.03	115.98	807.7	765.3
75	1	3600	22.84	6.10	116.13	2852.4	2299.6
76	1	1790	3.24	2.03	115.90	575.5	380.5
98	1	6900	290.08	36.27	116.93	34119.0	26207.5
148	2	1865	14.10	6.42*	116.20	1838.4	1254.5*
149	2	1814	29.6	13.37*	115.70	3624.7	2539.8*
150	2	3600	63.1	15.34*	115.70	750.7	5784.6*
151	2	5400	85.6	15.26*	117.00	10215.2	8631.1*
152	2	7165	98.4	13.15*	115.4	11555.4	9864.8*
153	2	1812	58.9	23.90*	115.3	6991.2	4536.1*
154	2	3758	106.50	25.13*	117.70	12735.0	9962.9*
155	2	5620	148.90	24.80	118.90	17804.2	1453.9*
156	2	1935	86.80	31.10	115.20	10199.4	6301.9*
157	2	3700	152.00	32.39*	117.00	17984.0	12548.4*
158	2	5428	222.90	32.60	117.60	26413.0	18530.0*
159	2	3720	221.30	38.05*	117.00	26092.1	14824.1*

ORIGINAL PAGE IS
OF POOR QUALITY

TABLE (5.2-2) TEST DATA OF THE 15 hp RATED OUTPUT 125 MINUTES RUN NO. 64 FOR THE SAMARIUM COBALT BASED MACHINE WHEN ARMATURE PATHS WERE CONNECTED IN PARALLEL-TEST SETUP (1) WAS USED, DATA TAKEN EVERY 5 MINUTES

TIME Min.	N, RPM	I, AMPS	T, NM	V, Volts	P_{in} Watts	P_{out} Watts
0	8560	110.86	12.88	115.32	12984.4	11545.9
5	8510	110.14	12.54	115.50	12921.2	11176.4
10	8550	109.60	12.54	115.43	12851.1	11228.9
15	8580	109.82	12.54	115.39	12872.1	11267.1
20	8600	109.38	12.54	115.66	12850.9	11293.4
25	8570	110.46	12.54	115.46	12953.7	11254.0
30	8660	110.00	12.20	115.84	12932.3	11066.0
35	8620	109.72	12.54	115.48	12870.5	11219.7
40	8680	109.38	12.54	115.89	12876.0	11398.4
45	8700	109.46	12.20	116.05	12902.8	11114.9
50	8680	110.16	12.20	115.99	12977.4	11089.4
55	8660	110.12	12.20	115.89	12961.8	11063.8
60	8640	110.64	12.54	115.81	13013.2	11345.9
65	8660	109.98	12.20	115.88	12944.5	11063.8
70	8660	110.28	12.20	115.87	12978.1	11063.8
75	8660	110.64	12.20	115.87	13019.9	11063.8
80	8660	110.56	12.20	115.83	13017.2	11063.8
85	8630	111.42	12.54	115.88	13111.3	11332.8
90	8650	111.64	12.20	116.03	13153.6	11051.1
95	8650	111.88	12.54	116.18	13198.2	11359.0
100	8660	111.80	12.54	115.94	13162.1	11372.2
105	8660	110.74	12.20	115.99	13135.2	11063.8
110	8660	111.40	12.54	116.03	13049.2	11063.8
115	8660	111.40	12.20	116.00	13085.6	11063.8
120	8660	111.14	12.20	115.94	13985.5	11063.8
125	8660	111.14	12.20	116.10	13135.9	11063.8

TABLE (5.2-3) TEMPERATURE TEST DATA OF THE MPC SYSTEM (SAMARIUM COBALT BASED MACHINE) FOR THE 15 hp RATED OUTPUT 125 MINUTES RUN NO. 64 AS INDICATED BY THEROMOCOUPLES DEFINED IN TABLE (5.1-1)-TEST SETUP (1) WAS USED, DATA TAKEN EVERY 5 MINUTES

Time, Min.	θ_1, °C	θ_2, °C	θ_3 °C	θ_4 °C	θ_5 °C	θ_6 °C
0	24.2	29.2	29.1	37.7	40.4	41.6
5	24.5	36.2	33.2	49.8	57.3	58.7
10	24.6	42.7	38.0	60.2	71.7	72.8
15	24.6	48.6	42.8	68.7	83.6	84.4
20	24.7	53.9	46.5	75.9	93.5	94.1
25	25.2	58.6	50.8	82.2	102.0	102.6
30	25.1	62.7	54.3	87.7	109.3	109.8
35	25.4	66.2	57.4	92.3	115.4	115.7
40	25.4	69.2	59.5	96.0	120.6	120.8
45	25.6	72.0	62.5	99.7	125.0	125.2
50	25.9	74.1	64.2	102.3	129.0	129.0
55	25.9	76.1	66.1	104.8	132.4	132.3
60	26.1	78.0	67.6	106.7	135.3	135.2
65	26.0	79.5	68.7	108.8	137.9	137.7
70	26.2	80.7	69.8	111.0	140.1	139.8
75	26.2	82.0	71.2	112.3	141.9	141.7
80	26.2	83.1	72.1	113.6	143.6	143.3
85	26.4	84.0	73.0	114.8	145.2	144.8
90	26.6	85.0	73.1	115.6	146.7	146.3
95	26.6	85.8	73.8	116.6	147.9	147.6
100	26.8	86.5	74.5	117.3	149.2	148.8
105	26.6	87.1	74.7	118.3	150.2	149.8
110	27.0	87.7	74.8	119.3	151.2	150.6
115	26.8	88.4	75.5	119.7	151.7	151.2
120	26.9	88.6	76.1	119.8	152.3	151.8
125	27.2	89.1	76.0	120.3	153.0	152.5

ORIGINAL PAGE IS
OF POOR QUALITY

TABLE (5.2-3) Continued

Time, Min.	θ_7, °C	θ_8, °C	θ_9, °C	θ_{10}, °C	θ_{11}, °C	θ_{12}, °C	θ_{13} °C
0	41.6	28.3	32.8	27.3	27.4	25.6	27.3
5	59.3	29.3	36.2	29.1	29.1	25.8	28.3
10	73.7	29.8	37.5	30.5	30.1	26.0	28.9
15	85.5	30.1	38.2	31.5	31.0	25.7	29.4
20	95.4	30.3	38.7	32.2	31.6	26.2	29.8
25	103.8	30.7	39.1	32.7	31.9	26.5	30.1
30	111.1	31.1	39.3	33.0	32.2	26.8	30.3
35	117.2	31.2	39.5	33.2	32.6	27.0	30.6
40	122.3	31.6	39.8	33.6	32.8	27.1	31.1
45	126.7	32.0	40.3	34.0	33.2	27.6	31.3
50	130.5	32.2	40.4	34.2	33.6	28.0	31.7
55	133.8	32.3	40.7	34.6	33.9	27.8	31.8
60	136.8	32.7	41.0	34.9	34.2	28.1	32.1
65	139.3	32.8	41.3	35.1	34.3	28.2	32.3
70	141.4	32.9	41.4	35.3	34.7	28.8	32.6
75	143.3	33.2	41.6	35.6	34.8	28.0	32.7
80	145.0	33.5	41.6	35.7	35.0	28.3	32.8
85	146.6	33.5	41.9	36.0	35.2	29.0	33.2
90	148.0	33.5	42.0	36.2	35.4	29.0	33.2
95	149.3	33.5	42.2	36.2	35.5	28.7	33.2
100	150.5	33.7	42.3	36.4	35.6	28.9	33.5
105	151.6	33.7	42.3	36.5	35.6	28.8	33.5
110	152.3	33.9	42.5	36.6	36.0	29.4	33.8
115	153.0	33.8	42.5	36.6	36.0	29.0	33.8
120	153.6	33.8	42.5	36.8	36.1	29.0	33.8
125	154.2	34.0	42.7	36.9	36.2	29.1	34.0

5.2.2 THE STRONTIUM FERRITE BASED MACHINE

The strontium ferrite based machine, the design of which is also detailed in Chapter (3.0), was built and tested while in operation in conjunction with the power conditioner developed in the course of this investigation, see Chapter (4.0). Testing was carried out under various load conditions. This included a two hour run at rated load of 15 hp (11.2 kw) motor output, followed immediately by a one minute run at a peak load of 35 hp (26.1 kw) motor output. The dc chopper inductor current, and the speed recorded for each of these test runs, as well as those corresponding inductor currents and speeds for all other pertinent load runs are plotted in the chopper inductor current (Amperes)-speed (RPM) plane of Figure (5.2-3). This data was recorded when the machine was operated with parallel connected armature paths. Again, the dc inductor current is not to be confused with the dc line current which is delivered from the source to the MPC system during motoring, and delivered from the MPC system to the source during regeneration. Again, notice that without chopping the dc inductor current is approximately equal to the dc line current, whereas during chopping the inductor current is considerably greater than the dc line current.

Notice, in the current-speed plane of Figure (5.2-3) runs 138 and 140 required advanced commutation by 30°E in the with inverter bridge. Run 138, which is the peak load run of 35 hp (26.1 kw) motor output is again designated by a cross (+) rather than the usual dots for normal runs with no advanced commutation (firing). It should be pointed out that run 3 is that in which the MPC system was loaded for two continuous hours at its rated output of 15 hp (11.2 kw). The current and speed data for run 3 is almost identical to run 6.

The results of the various runs for the motoring mode in the inductor current-speed plane of Figure (5.2-3) are given in Table (5.2-5), except for the two hour rated power run number 3, which is given separately in Tables (5.2-6) and (5.2-7). Table (5.2-6) contains the various MPC system current, voltage, input and output power, torque as well as speed values taken at increments of 5 minutes throughout the test period of 145 minutes, except for a ten minute interruption between the 65 min. and the 75 min. points. This interruption, which was not due to any MPC system failure but due to reasons external to the MPC system, was compensated for by extending the test duration to 145 min. in lieu of the required 120 min. test duration. Table (5.2-7) contains the thirteen temperatures previously defined in Table (5.1-1), recorded at increments of 5 minutes throughout the 145 minutes run number 3, except for the 10 minute interruption period. The symbolism in the tables is identical to that used and previously explained in the samarium cobalt case given above.

Furthermore, the temperatures, θ_1, θ_5, θ_7, θ_8, and θ_9, which were defined earlier in this section, are plotted over the 145 minutes duration of the rated 15 hp run number 3, in Figure (5.2-4), when the power conditioner was tested in conjunction with the strontium ferrite based machine.

ORIGINAL PAGE IS
OF POOR QUALITY

TABLE (5.2-4) TEST DATA OF REGENERATION RUNS FOR THE SAMARIUM COBALT BASED MACHINE WHEN ARMATURE PATHS WERE CONNECTED IN PARALLEL

** For these runs no net power can be returned to battery, speed and torque are too low.

RUN NO.	TEST SETUP	N, RPM	I, AMPS	T, NM	V, VOLTS	P_{in}, WATTS	P_{out}, WATTS
77	1	8750	8.12	1.08	116.35	989.6	744.8
78	1	8750	37.40	5.15	117.20	4718.9	4183.3
79	1	8720	63.22	8.81	117.78	8044.9	7246.0
80	1	8700	86.04	12.34	118.15	11242.5	9965.6
81	1	7140	6.30	0.95	116.24	710.3	532.3
82	1	7140	29.54	5.15	116.91	3850.6	3253.5
83	1	7120	49.78	8.81	117.54	6568.8	5651.1
84	1	7100	66.98	12.07	117.81	8974.2	7690.9
85	1	5360	4.66	1.08	116.03	606.2	340.7
86	1	5350	21.58	5.15	116.68	2885.3	2318.0
87	1	5350	35.90	8.68	117.13	4863.0	4005.0
88	1	5320	47.66	11.79	117.41	6568.3	5395.8
89	1	3590	2.78	1.08	116.03	406.0	122.6
90	1	3590	14.00	5.15	116.47	1936.1	1430.6
91	1	3580	22.90	8.68	116.69	3254.1	2472.2
92	1	3560	30.20	11.79	109.45	4395.3	3105.4
93	1	1800	1.30	0.95	116.00	179.1	* *
94	1	1800	6.22	5.02	116.19	946.2	522.7
95	1	1790	9.78	8.68	116.28	1627.0	937.2
96	1	1800	12.10	11.52	116.40	2171.5	1208.4
100	1	5330	56.20	14.37	94.84	8020.7	5130.0
101	1	5400	55.00	16.54	95.45	9353.1	5049.8
102	1	7100	77.98	14.51	115.97	10788.3	8843.3
103	1	7100	78.30	15.59	82.97	11491.3	6296.5
104	1	3600	34.10	14.78	106.79	5571.9	3441.5
105	1	3600	32.80	15.32	107.27	5775.5	3318.4
106	1	1800	12.60	14.91	115.94	2810.5	1260.8
107	1	1800	9.70	15.45	115.96	2912.2	924.8
108	1	8600	98.00	14.64	116.00	13184.6	11168.0
109	1	8600	98.68	15.73	115.94	14166.3	11241.0

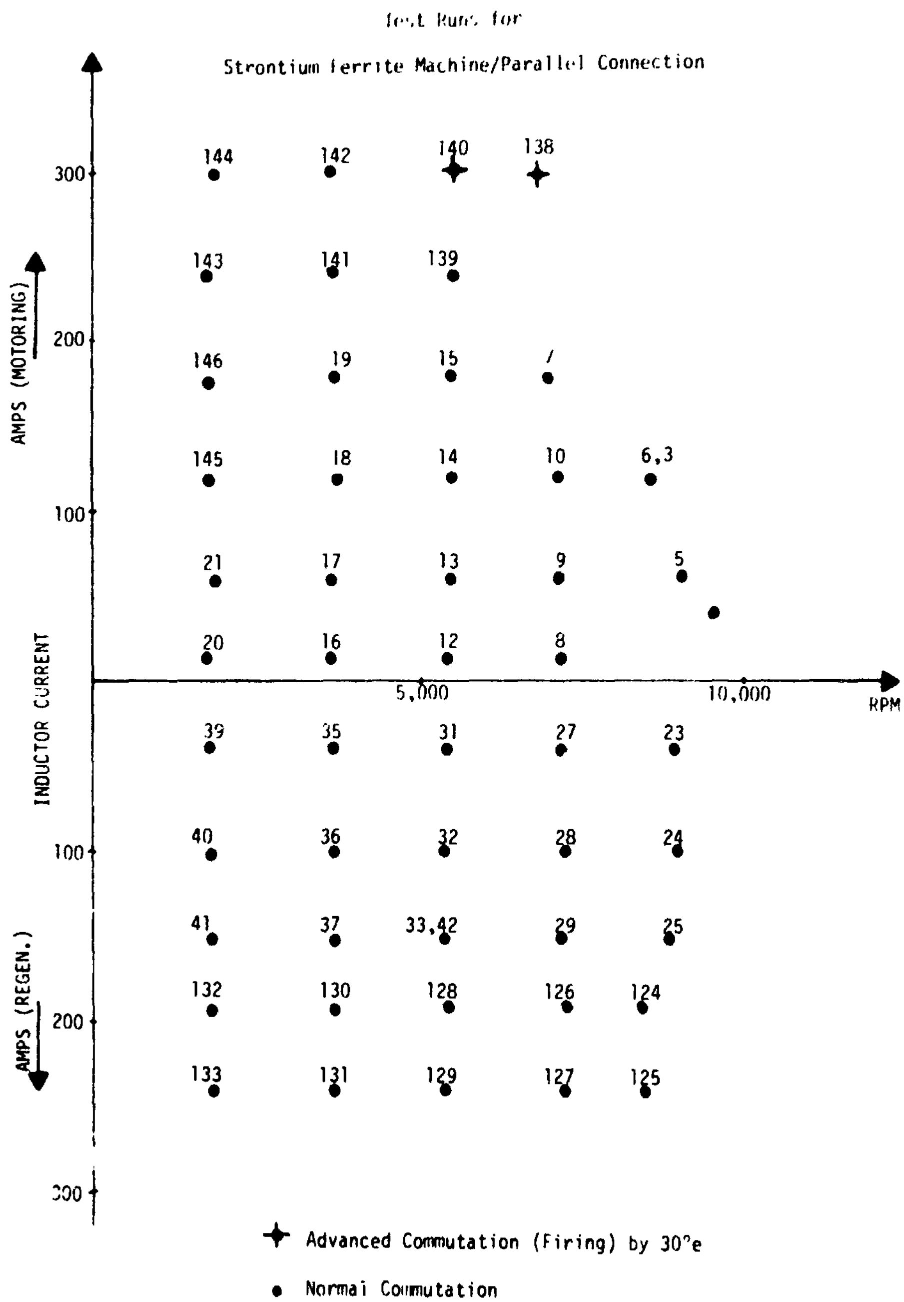

FIGURE (5.2-3) Inductor Current (Torque) - Speed Plane for the Strontium Ferrite Machine with Parallel Connected Armature Paths.

ORIGINAL PAGE IS OF POOR QUALITY

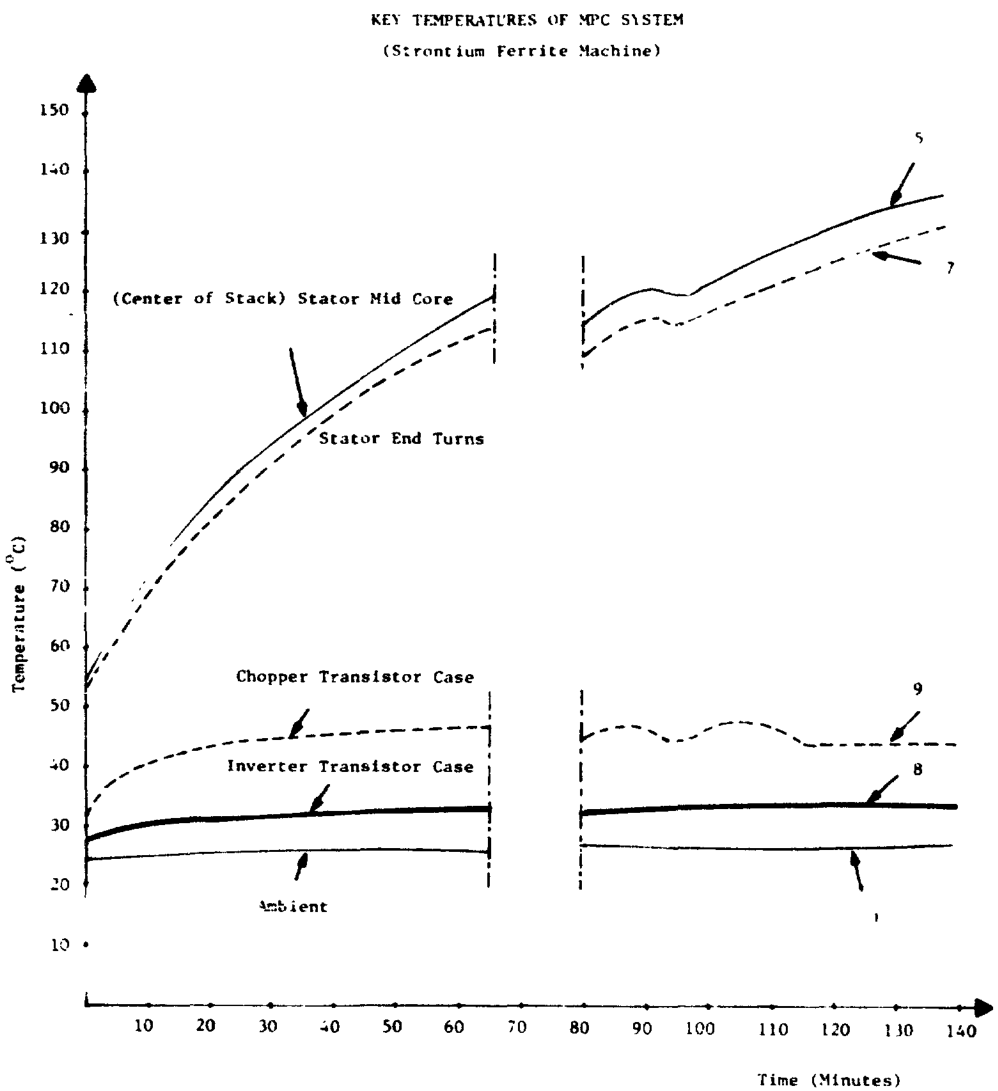

FIGURE (5.2-4) Temperature Rise in the MPC System (Strontium Ferrite Case), Run 3, at 15 hp Output For 145 Minutes Duration.

ORIGINAL PAGE IS
OF POOR QUALITY

TABLE (5.2-5) TEST DATA OF MOTORING RUNS FOR THE STRONTIUM FERRITE BASED MACHINE WHEN ARMATURE PATHS WERE CONNECTED IN PARALLEL

*In this case there appeared to be an error in the torque measurements which are rectified in the last two columns.

RUN NO.	TEST SETUP	N, RPM	I, AMPS	T,* NM	V, Volts
4	1	9440	34.74	4.07	108.65
5	1	8900	61.76	7.12	107.93
6	1	8500	119.90	14.57	115.61
7	1	6950	178.74	23.73	115.85
8	1	7110	7.78	1.69	115.96
9	1	7110	40.48	6.44	115.29
10	1	7160	104.16	14.57	114.15
12	1	5450	6.24	2.03	116.00
13	1	5450	36.96	7.12	114.83
14	1	5470	86.94	15.25	113.44
15	1	5600	168.72	26.44	111.32
16	1	3580	4.12	2.03	115.90
17	1	3590	25.22	7.12	115.93
18	1	3760	62.64	12.54	115.02
19	1	3660	108.14	24.40	116.02
20	1	1700	2.50	2.03	115.88
21	1	1850	15.10	7.12	115.88
138	1	6750	297.58	37.69	120.92
139	1	5400	222.26	31.86	114.30
140	1	5400	260.05	38.37	116.00
141	1	3600	176.04	33.35	116.10
142	1	3600	225.08	37.42	117.00
143	1	1800	87.22	30.78	116.20
144	1	1800	109.32	34.44	115.60
145	1	1800	36.17	15.18	115.70
146	1	1800	58.28	24.00	116.30

ORIGINAL PAGE IS
OF POOR QUALITY

TABLE (5.2-5) Continued

P_{in}, Watts	P_{out}, Watts	Corrected T, Watts	Corrected P_{out}, Watts
3974.5	4023.4	2.67	2639.4
6865.8	6635.9	5.72	5331.1
14061.6	12969.0	13.17	11722.8
20907.0	17270.7	22.33	16251.8
1102.2	1258.3	0.29	215.9
4866.9	4795.0	5.04	3752.6
12089.9	10924.5	13.17	9874.8
923.8	1158.6	0.63	359.6
4444.1	4063.5	5.72	3264.5
10062.5	8735.5	13.85	7933.5
18981.9	15505.2	25.04	14684.2
677.5	761.0	0.63	236.2
3123.7	2676.7	5.72	2150.4
7404.8	4937.6	11.14	4386.3
12746.4	9351.9	23.00	8815.3
489.7	361.4	0.63	112.2
1949.8	1379.4	5.72	1108.1
36183.4	26641.5	36.29	25651.9
25604.3	18016.4	30.46	17224.7
30365.8	21697.7	36.97	20906.0
20638.2	12572.6	31.95	12044.9
26534.4	14107.0	36.02	13579.2
10335.0	5801.9	29.38	5538.0
12837.4	6491.8	33.04	6227.9
4384.9	2861.4	13.78	2597.5
6978.0	4523.9	22.60	4260.0

ORIGINAL PAGE IS
OF POOR QUALITY

TABLE (5.2-6) TEST DATA OF THE 15 hp RATED OUTPUT 145 MINUTE RUN NO. 3 FOR THE STRONTIUM FERRITE BASED MACHINE WHEN ARMATURE PATHS WERE CONNECTED IN PARALLEL - TEST SETUP (1) WAS USED, DATA TAKEN EVERY FIVE MINUTES

*Defective Data Point

TIME, MIN.	N, RPM	I, AMPS	T, NM	V, VOLTS
0	8460	114.56	13.55	114.98
5	8760	107.24	12.88	115.63
10	8840	107.32	12.54	115.62
15	8800	108.08	12.54	114.67
20	8780	108.86	12.20	113.48
25	8750	109.64	12.54	112.56
30	8750	110.16	12.20	111.52
35	8810	110.32	12.20	111.59
40	8750	111.08	12.20	110.64
45	8800	111.60	12.20	110.61
50	8720	113.10	12.20	109.65
55	8800	113.88	12.20	110.28
60	8800	114.40	12.54	109.75
65	8780	114.70	12.20	109.19
TEN MINUTE INTERRUPTION OCCURED DUE TO EMERGENCY EXTERNAL TO MPC SYSTEM				
80	8740	113.24	12.20	108.98
85	8800	114.34	12.20	109.02
90	8740	115.44	12.20	108.34
95*	8800*	82.20*	8.81*	98.12*
100	8800	115.18	12.20	108.75
105	8780	115.74	12.20	108.26
110	8850	116.26	12.20	107.77
115	8870	116.34	12.20	107.94
120	8880	116.60	12.20	107.61
125	8900	117.48	12.20	107.68
130	8900	117.48	12.20	107.74
135	8900	117.60	12.20	107.26
140	8910	118.08	12.20	107.39
145	8910	118.30	12.20	107.14

TABLE (5.2-6) Continued

P_{in}, Watts	P_{out}, Watts	Corrected T, Watts	Corrected P_{out}, Watts
13372.1	12004.3	12.15	10764.0
12600.2	11815.6	11.48	10531.1
12608.3	11609.8	11.14	10312.5
12593.5	11556.0	11.14	10265.9
12553.4	11219.3	10.80	9930.0
12541.1	11490.4	11.14	10207.6
12485.0	11178.8	10.80	9896.0
12510.6	11255.5	10.80	9963.9
12489.9	11178.8	10.80	9896.0
12544.1	11242.7	10.80	9952.6
12601.4	11140.5	10.80	9862.1
12758.7	11242.7	10.80	9952.6
12755.4	11556.0	11.14	10265.9
12714.1	11178.8	10.80	9930.0
TEN MINUTE INTERRUPTION OCCURED DUE TO EMERGENCY EXTERNAL TO MPC SYSTEM			
12540.9	11166.1	10.80	9884.7
12665.3	11242.7	10.80	9952.6
12706.8	11166.1	10.80	9884.7
8265.5*	8121.3*	7.41	6828.6
12715.8	11242.7	10.80	9952.6
12730.0	11217.2	10.80	9930.0
12719.3	11306.6	10.80	10009.1
12757.7	11332.1	10.80	10031.7
12747.3	11344.9	10.80	10043.0
12805.0	11244.9	10.80	10043.0
12857.3	11370.5	10.80	10065.7
12813.8	11370.5	10.80	10065.7
12880.6	11383.2	10.80	10077.0
12874.7	11383.2	10.80	10077.0

TABLE (5.2-7) TEMPERATURE TEST DATA OF THE MPC SYSTEM (STRONTIUM FERRITE BASED MACHINE) FOR THE 15 hp RATED OUTPUT 145 MINUTES RUN NO. 3 AS INDICATED BY THEROMOCOUPLES DEFINED IN TABLE (5.1-1)-TEST SETUP (1) WAS USED, DATA TAKEN EVERY 5 MINUTES

Time, Min.	θ_1, °C	θ_2, °C	θ_3, °C	θ_4, °C	θ_5, °C	θ_6, °C
0	24.2	39.8	40.8	48.2	53.5	54.0
5	24.7	41.8	40.8	56.6	64.5	64.5
10	24.7	44.4	41.7	63.1	72.1	72.0
15	25.0	47.5	43.5	68.2	78.8	78.8
20	25.2	50.2	45.8	73.0	84.7	84.7
25	25.2	52.8	48.2	76.3	90.0	89.9
30	25.3	55.1	50.2	80.0	94.7	94.6
35	25.2	57.1	52.2	83.0	98.8	98.8
40	25.4	49.1	54.2	86.3	102.6	102.7
45	25.7	60.8	56.6	88.5	106.2	106.3
50	25.8	63.5	58.7	91.2	109.5	109.7
55	25.7	64.1	59.9	93.3	112.6	113.0
60	25.7	65.6	61.2	95.6	115.7	116.0
65	26.0	67.0	63.0	97.3	118.5	118.8
TEN MINUTES INTERRUPTION OCCURRED DUE TO EMERGENCY EXTERNAL TO MPC SYSTEM						
80	26.3	67.2	64.4	94.2	113.6	114.2
85	26.2	67.7	63.8	97.0	117.2	117.6
90	26.4	68.8	64.3	98.8	120.2	120.6
95*	26.3*	70.0*	65.3*	98.2*	118.6	118.7*
100	26.5	70.0	65.3	99.4	121.2	121.6
105	26.8	70.7	64.7	101.5	123.9	121.6
110	27.0	72.1	66.1	103.0	126.4	126.7
115	26.7	72.8	67.8	104.7	128.3	128.8
120	26.9	73.8	67.7	106.3	130.2	130.7
125	27.0	74.8	68.3	107.2	132.0	132.4
130	27.1	75.3	69.6	108.5	133.6	134.2
135	27.0	76.3	70.3	109.7	135.2	135.7
140	27.1	76.9	71.3	110.4	136.7	137.1
145	27.2	77.7	71.4	111.3	138.0	138.5

* Problems with thermocouples

TABLE (5.2-7) Continued

θ_7, °C	θ_8, °C	θ_9, °C	θ_{10}, °C	θ_{11}, °C	θ_{12}, °C	θ_{13}, °C
52.3	28.2	31.8	28.5	28.7	34.4	28.0
61.7	31.1	38.2	31.0	30.9	39.2	29.8
69.1	30.8	40.6	33.2	33.0	37.4	30.7
75.8	31.2	42.2	34.8	34.5	36.1	31.1
81.4	31.5	43.2	36.3	36.1	34.5	31.8
86.4	31.9	43.9	37.5	37.2	37.4	32.2
90.9	32.1	44.5	38.3	38.2	38.6	32.5
94.9	32.4	44.9	39.3	39.2	41.8	33.4
98.5	32.5	45.5	40.0	39.8	39.7	33.1
101.8	32.7	45.6	40.5	40.3	38.3	33.0
105.0	32.9	46.0	40.9	40.8	36.0	33.2
108.0	33.2	46.3	41.5	41.5	38.2	33.6
110.8	33.5	46.7	42.2	42.1	39.1	34.0
113.4	33.7	47.2	42.5	42.5	44.1	34.3
TEN MINUTES INTERRUPTION OCCURED DUE TO EMERGENCY EXTERNAL TO MPC SYSTEM						
108.9	33.2	44.7	41.6	41.6	37.0	33.4
112.3	33.7	46.1	42.0	42.1	39.5	34.1
115.2	34.1	47.1	42.5	42.5	42.1	34.5
114.2*	33.2*	44.5*	42.8*	42.8*	42.7*	36.3*
116.1	34.1	46.6	43.0	43.0	40.8	36.7
118.8	34.4	47.6	43.6	43.3	37.8*	37.1
121.1	34.6	46.0	42.8	41.6	----	37.0
123.0	34.5	44.5*	41.0	39.7	----	35.2
124.7	34.6	44.1	39.7	38.6	----	34.7
126.4	34.6	43.9	38.8	37.9	----	34.2
128.0	34.8	43.9	38.4	37.6	----	34.2
129.5	34.7	44.1	38.3	37.5	----	34.2
130.9	34.8	44.1	38.2	37.4	----	34.2
132.2	35.0	44.2	38.3	37.4	----	34.2

* Problems with thermocouples

Similarily, the results of the various regeneration runs, performed using setup (1), which are plotted in the current-speed plane of Figure (5.2-[illegible]) are given for this strontium ferrite based machine in Table (5.2-8)

5.2.3 THE THERMAL CHARACTERISTICS OF THE MPC SYSTEMS

Thermocouples were placed at thirteen key locations throughout the MPC systems to monitor the temperatures, θ_1 through θ_{13}, which were defined in Table (5.1-1). The tabulation of these temperatures during the two hour rated load (15 hp) runs was given for the samarium cobalt and strontium ferrite based system in Tables (5.2-3) and (5.2-7) respectively. Five most important temperatures were selected and plotted versus time in Figures (5.2-2). and (5.2-4) for the above mentioned MPC system, respectively. Those temperatures were; the ambient, the stator mid core (center of stack), the stator end turns, the chopper transistor case, and the inverter transistor case. It must be noticed that the samarium cobalt based machine appeared to reach steady state temperatures quicker than the strontium ferrite machine. This is largely due to the lesser weight and smaller volume of the samarium cobalt unit in comparison with the strontium ferrite unit. The transistor case temperatures (chopper and inverter) appear to stabilize quickly in both cases. Notice that there was a 10 minute shutdown period in the strontium ferrite case, which was compensated for by the larger running time as shown in Figure (5.2-4).

No forced ventilation was used with the machines. However, forced ventilation by appropriately chosen fans, and air ducting was used for the power conditioner, as detailed earlier in Chapter (4.0).

5.2.4 TYPICAL CURRENT AND VOLTAGE OSCILLOGRAMS THROUGHOUT THE MPC SYSTEMS OBTAINED USING TEST SETUP (2) TAKEN AT 7.5, 15, and 35 hp

Various voltage and current wave forms at approximately 7.5 hp, 15 hp, and 35 hp motor output were obained at about rated MPC system voltage, using test setup (2), Figure (5.1-4). A list of these oscillograms is given in Table (5.2-9) for the samarium cobalt based MPC system, with oscillograms shown in Figures (5.2-5) through (5.2-22). Meanwhile, a list of these oscillograms is given in Table (5.2-10) for the strontium ferrite based MPC system, with oscillograms shown in Figures (5.2-23) through (5.2-40).

ORIGINAL PAGE IS
OF POOR QUALITY

TABLE (5.2-8) TEST DATA OF REGENERATION RUNS FOR THE STRONTIUM FERRITE BASED MACHINE WHEN ARMATURE PATHS WERE CONNECTED IN PARALLEL

* For these runs an error in the torque transducer is corrected for in the last two columns.

** For these runs no net power can be returned to battery, torque is too low.

RUN NO.	TEST SETUP	N, RPM	I, AMPS	T,* NM	V, VOLTS
22	1	8820	1.38	0.00	116.17
23	1	8820	37.34	3.73	117.23
24	1	8780	61.04	6.44	117.[illegible]
25	1	8780	81.20	9.49	118.17
26	1	7120	6.54	0.00	116.49
27	1	7120	28.86	3.73	117.07
28	1	7100	47.78	6.44	117.40
29	1	7100	64.92	9.49	117.90
30	1	5400	4.56	0.00	116.30
31	1	5400	19.90	3.05	116.67
32	1	5400	34.78	6.10	117.11
33	1	5360	46.98	9.49	117.45
34	1	3610	3.02	0.00	116.25
35	1	3610	13.24	3.05	116.41
36	1	3608	22.72	6.10	116.76
37	1	3606	30.00	9.49	109.09
38	1	1800	1.36	0.00	116.08
39	1	1800	6.00	3.39	116.25
40	1	1803	9.74	6.44	116.32
41	1	1804	12.10	9.49	116.43
42	1	5410	48.24	9.49	117.31
124	1	8430	66.64	13.56	117.88
125	1	8450	85.42	14.37	115.65
126	1	7180	72.76	12.88	115.60
127	1	7140	69.40	13.83	115.00
128	1	5400	53.00	13.56	115.00
129	1	5400	51.20	14.64	115.00
130	1	3600	32.10	13.83	115.00
131	1	3620	29.50	14.51	115.00
132	1	1810	11.40	13.56	115.60
133	1	1810	8.6	14.91	115.00

ORIGINAL PAGE IS
OF POOR QUALITY

TABLE (5.2-8) Continued

P_{in},* Watts	P_{out}, Watts	Corrected T, NM	Corrected P_{in}, Watts
0.0	**	1.40	1293.2
3445.2	4177.4	5.13	4738.2
5921.2	6978.3	7.84	7208.4
8705.6	9395.4	10.89	9989.9
0.0	561.8	1.40	1043.8
2781.1	3178.6	5.13	3814.9
4788.2	5409.4	7.84	5829.1
7055.9	7454.1	10.89	8096.8
0.0	330.3	1.40	791.7
1724.7	2121.7	4.45	2516.4
3449.5	3873.1	7.50	4241.1
5326.7	5317.8	10.89	6612.5
0.0	151.1	1.40	529.3
1153.0	1341.3	4.45	1682.3
2304.8	2452.8	7.50	2833.7
3583.6	3072.7	10.89	4112.3
0.0	**	1.40	263.9
639.0	497.5	4.79	902.9
1215.9	933.0	7.84	1480.3
1792.8	1208.8	10.89	2057.3
5376.4	5459.0	10.89	6169.6
11970.6	10013.1	14.96	13206.5
8684.3	8211.0	14.28	10737.0
10340.7	7781.0	15.23	11387.4
7668.0	5895.0	14.96	8459.7
8278.7	5688.0	16.04	9070.4
5213.8	3491.5	15.23	5741.6
5500.5	3192.5	15.91	6031.2
2570.2	1117.8	14.96	2835.6
2826.1	789.0	16.31	3091.4

In these tables, the following is an explanation of the symbolism used:

I_{ph} is the motor phase current,

I_{ch} is the chopper inductor (choke) current,

V_{CE}(inv) is the inverter traansistor collector to emiter voltage,

V_{CE}(QM) is the chopper transistor collector to emiter voltage,

V_{LN} is the phase to neutral voltage on the machine side,

and

V_{LL} is the line to line voltage on the machine side.

These oscillograms are self explanatory, and should be examined carefully by the interested reader (referring to the appropriate key in either table (5.2-9) or Table (5.2-10). Notice that Figures (5.2-7), (5.2-13), (5.2-15), (5.2-21), (5.2-25), (5.2-31), and (5.2-39) represent a magnified view of the collector to emiter voltages during the various transistor switching transisents. This is in order to show the voltage spikes which accompanied the switching process, after proper snubbing was applied. Details of the necessary snubber circuits were included earlier in Chapter (4.0).

The reader is invited to observe the effect of advanced firing at 15 and 35 hp motor output on the various current and voltage waveforms. Also, attention is drawn to the effect of chopping on these current and voltage oscillograms at 7.5 hp motor output. All this is shown for both the samarium cobalt based and strontium ferrite based MPC systems.

In the next section, methods of calculation of the various MPC system perfromance characteristics are detailed. Proper examples are given using the test data detailed in this section.

ORIGINAL PAGE IS
OF POOR QUALITY

TABLE (5.2-9) OSCILLOGRAMS OBTAINED FROM THE SAMARIUM COBALT MACHINE SYSTEM

I. Motoring, QM Fully on, 0° Advance, 115 V, 15.1 Hp (11.3 kw) at Load Rack

I_{ph}	20 mV/div (R_{shunt} = .0002488Ω)	.5 ms/div	Figure (5.2-5)
V_{CE}(inv)	20 V/div	.5 ms/div	Figure (5.2-6)
V_{CE}(inv)	50 V/div	5 μs/div	Figure (5.2-7)
V_{LL}	50 V/div	.5 ms/div	Figure (5.2-8)
V_{LN}	50 V/div	.5 ms/div	Figure (5.2-9)

II. Motoring, QM Fully on, 30° Advance, 105V, 15.8 (11.8 kw) Hp at Load Rack

I_{ph}	20 mV/div (R_{shunt} = .0002488Ω)	.5 ms/div	Figure (5.2-10)

III. Motoring, QM Chopping, 0° Advance, 115 V, 7.5 Hp (5.6 kw) at Load Rack

I_{ph}	10 mV/div (R_{shunt} = .0002488Ω)	.5 ms/div	Figure (5.2-11)
V_{CE}(QM)	20 V/div	50 μs/div	Figure (5.2-12)
V_{CE}(QM)	20 V/div	.5 μs/div	Figure (5.2-13)
V_{CE}(inv)	20 V/div	.5 μs/div	Figure (5.2-14)
V_{CE}(inv)	20 V/div	5 μs/div	Figure (5.2-15)
V_{LL}	50 V/div	.5 ms/div	Figure (5.2-16)
V_{LN}	20 V/div	.5 ms/div	Figure (5.2-17)

TABLE (5.2-9) Continued

IV. Motoring, QM Fully on, 30° Advance, 120 V, 35 Hp (26. kw) at Load Rack

V_{LN}	50 V/div	.5 ms/div	Figure (5.2-18)
V_{LL}	50 V/div	.5 ms/div	Figure (5.2-19)
V_{CE}(inv)	20 V/div	.5 ms/div	Figure (5.2-20)
V_{CE}(inv)	50 V/div	5 μs/div	Figure (5.2-21)
I_{ph}	50 mV/div	.5 ms/div	Figure (5.2-22)

(R_{shunt} = .0002488|L|)

ORIGINAL PAGE IS
OF POOR QUALITY

ORIGINAL PAGE IS
OF POOR QUALITY

TABLE (5.2-10) OSCILOGRAMS OBTAINED FROM THE STRONTIUM FERRITE MACHINE SYSTEMS

I. Motoring, QM Fully on, 0° Advance, 115 V, 14.2 Hp (10.6 kw) at Load Rack

I_{ph}	20 mV/div (R_{shunt} = .0002488Ω)	.5 ms/div	Figure (5.2-23)
V_{CE}(inv)	20 V/div	.5 ms/div	Figure (5.2-24)
V_{CE}(inv)	50 V/div	.5 μs/div	Figure (5.2-25)
V_{LL}	50 V/div	.5 ms/div	Figure (5.2-26)
V_{LN}	50 V/div	.5 ms/div	Figure (5.2-27)

II. Motoring, QM Fully on, 30° Advance, 105V, 15.8 (11.8 kw) Hp at Load Rack

I_{ph}	20 mV/div (R_{shunt} = 0.0002488Ω)	.5 ms/div	Figure (5.2-28)

III. Motoring, QM Chopping, 0° Advance, 115 V, 7.6 Hp (5.7 kw) at Load Rack

I_{ph}	10 mV/div (R_{shunt} = .0002488Ω)	.5 ms/div	Figure (5.2-29)
V_{CE}(QM)	20 V/div	50 μs/div	Figure (5.2-30)
V_{CE}(QM)	50 V/div	.5 μs/div	Figure (5.2-31)
V_{CE}(MV)	20 V/div	.5 ms/div	Figure (5.2-32)
V_{LN}	20 V/div	.5 ms/div	Figure (5.2-33)
V_{LL}	50 V/div	.5 ms/div	Figure (5.2-34)
I_{ch}	.5 V/div (37.8 mv/A)	.2 ms/div	Figure (5.2-35)

TABLE (5.2-10) Continued

IV. Motoring, QM Fully on, 30° Advance, 120 V, 33.9 Hp (25.3 kw) at Load Rack

V_{LN}	50 V/div	.5 ms/div	Figure (5.2-36)
V_{LL}	50 V/div	.5 ms/div	Figure (5.2-37)
V_{CE}(inv)	20 V/div	.5 ms/div	Figure (5.2-38)
V_{CE}(inv)	50 V/div	5 μs/div	Figure (5.2-39)
I_{ph}	50 mV/div	.5 ms/div	Figure (5.2-40)

(R_{shunt} = .0002488|L|)

ORIGINAL PAGE IS
OF POOR QUALITY

Fig. (5.2-5)

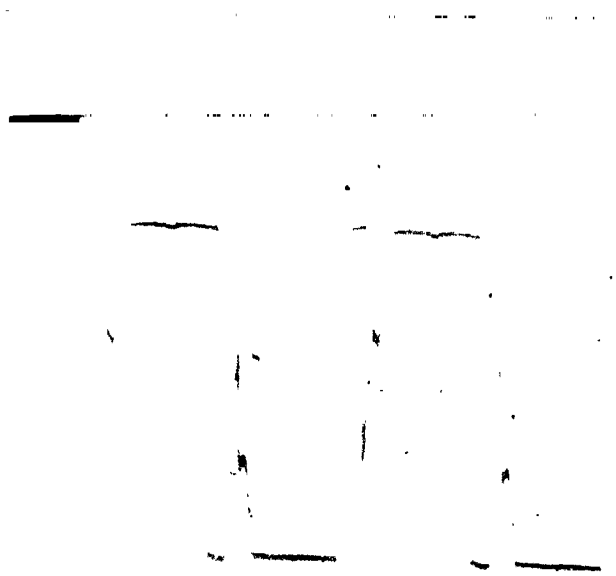

Fig. (5.2-6)

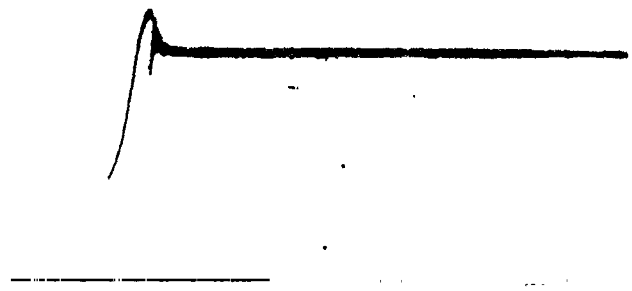

Fig. (5.2-7)

Fig. (5.2-8)

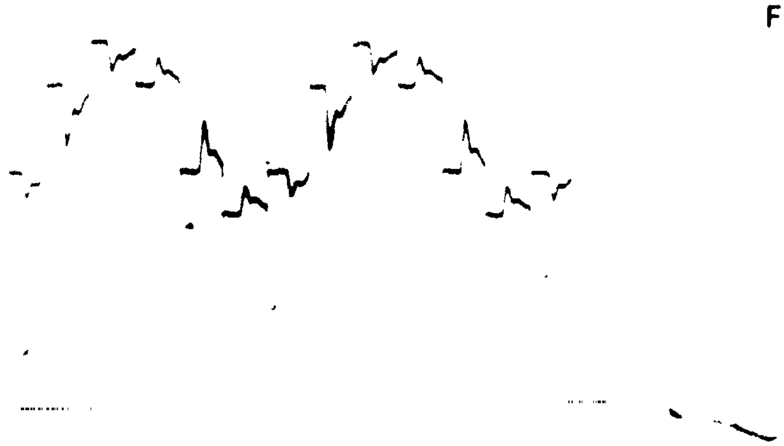

Fig. (5.2-9)

ORIGINAL PAGE
BLACK AND WHITE PHOTOGRAPH

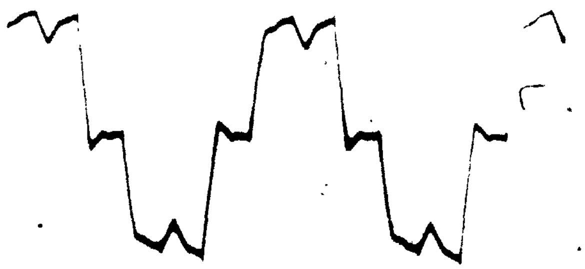

Fig. (5.2-10)

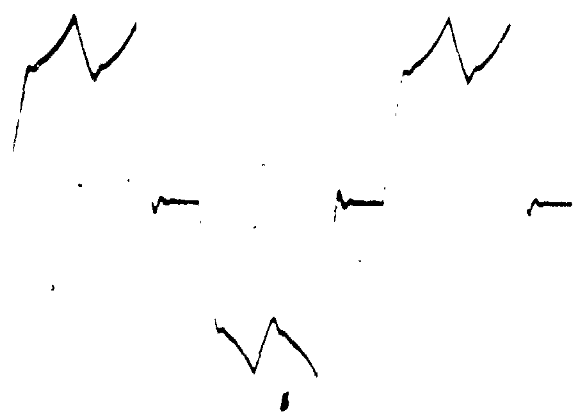

Fig. (5.2-11)

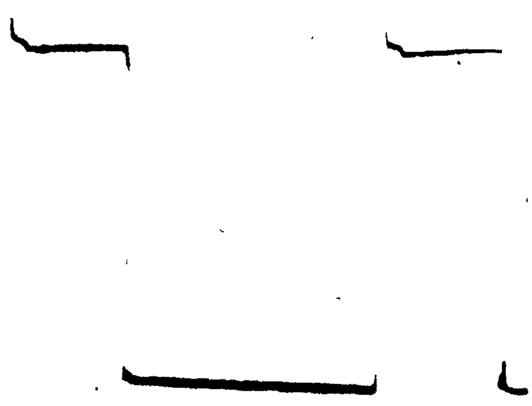

Fig. (5.2-12)

ORIGINAL PAGE
BLACK AND WHITE PHOTOGRAPH

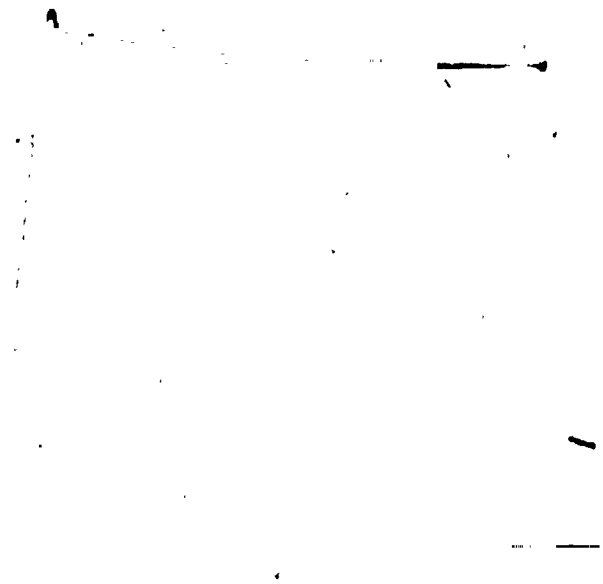

Fig. (5.2-13)

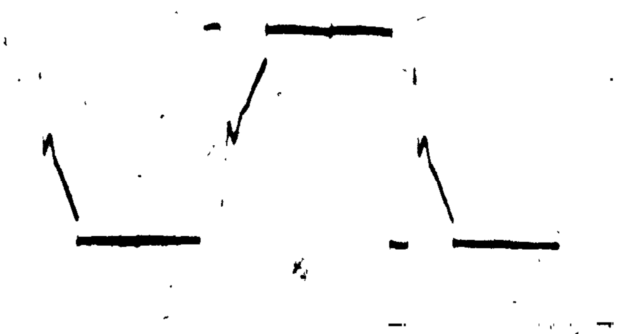

Fig. (5.2-14)

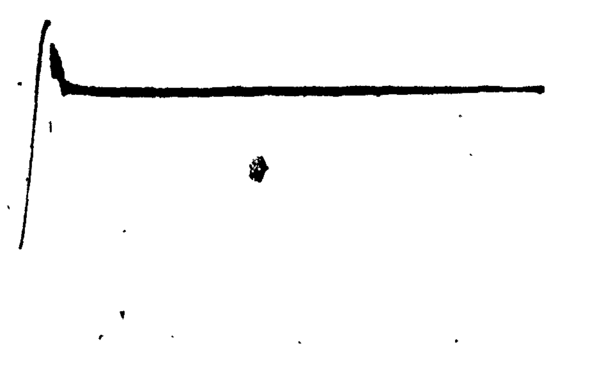

Fig. (5.2-15)

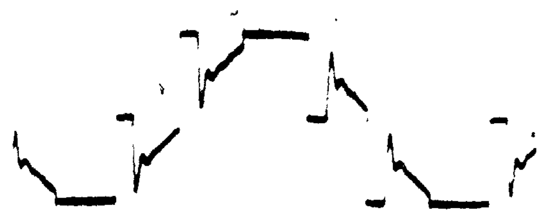

Fig. (5.2-16)

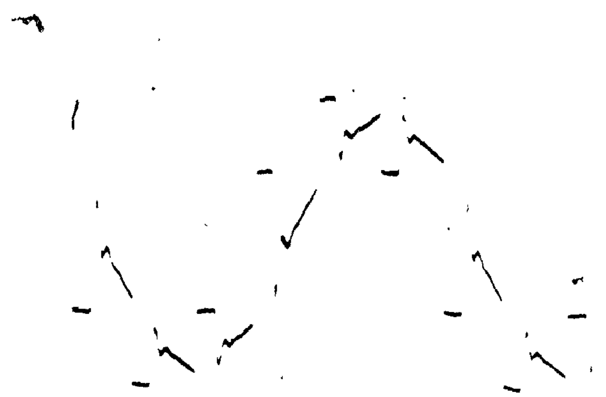

Fig. (5.2-17)

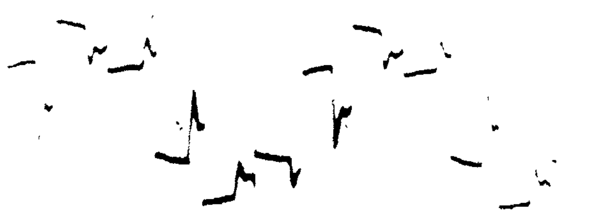

Fig. (5.2-18)

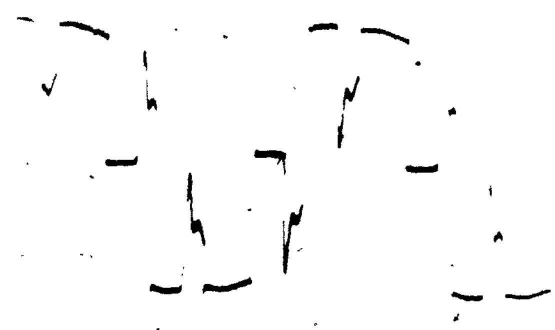

Fig. (5.2-19)

Fig. (5.2-20)

Fig. (5.2-21)

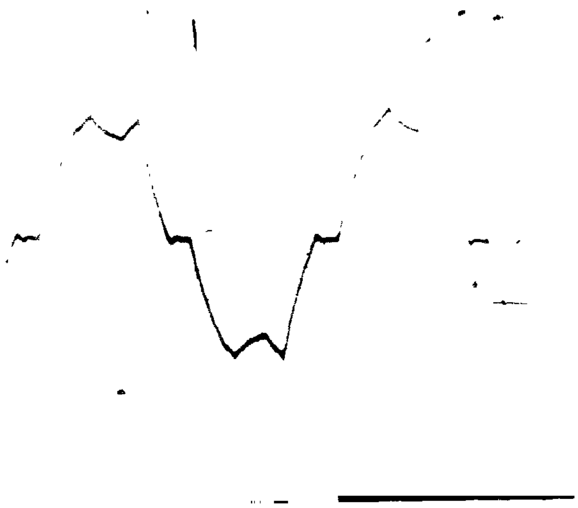

Fig. (5.2-22)

ORIGINAL PAGE
BLACK AND WHITE PHOTOGRAPH

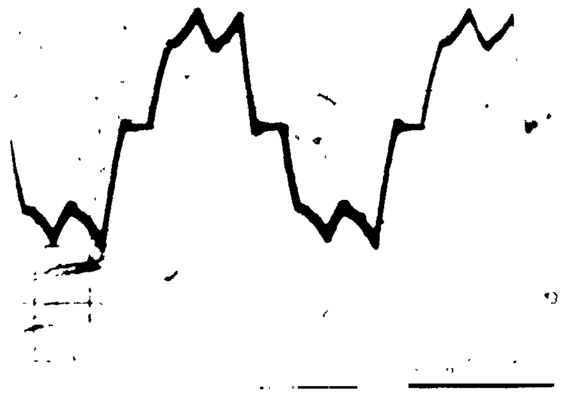

Fig. (5 2-23)

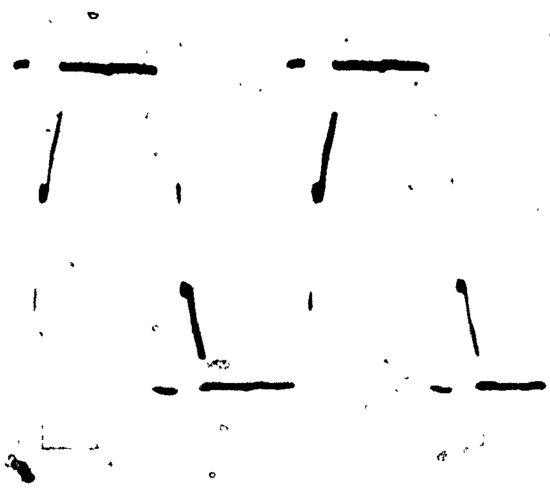

Fig. (5.2-24)

Fig. (5.2-25)

ORIGINAL PAGE
BLACK AND WHITE PHOTOGRAPH

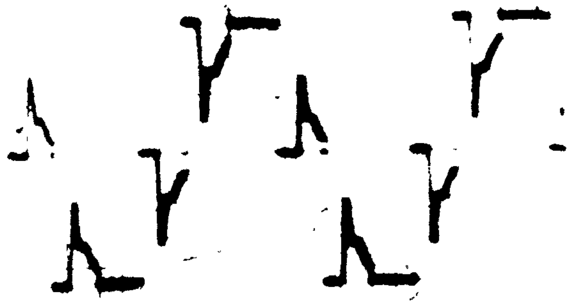

Fig. (5.2-26)

Fig. (5.2-27)

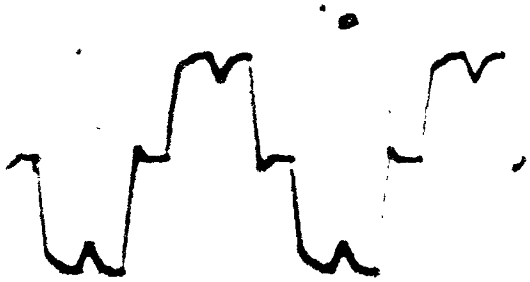

Fig. (5.2-28)

ORIGINAL PAGE
BLACK AND WHITE PHOTOGRAPH

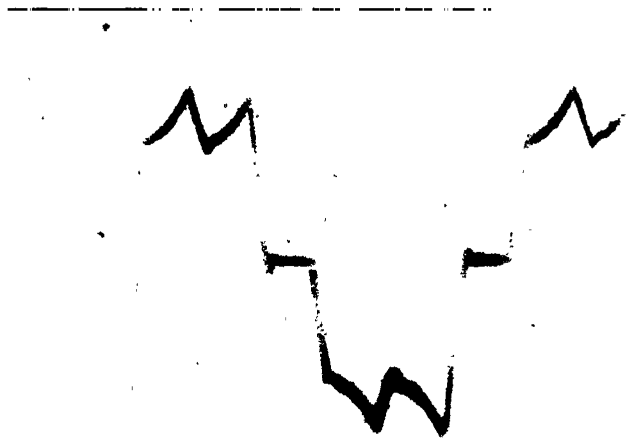

Fig. (5.2-29)

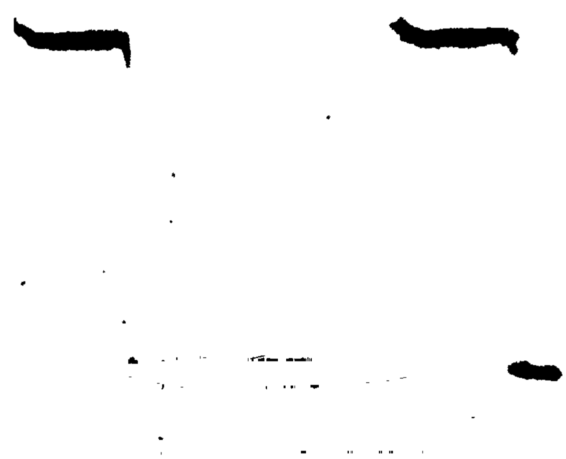

Fig. (5.2-30)

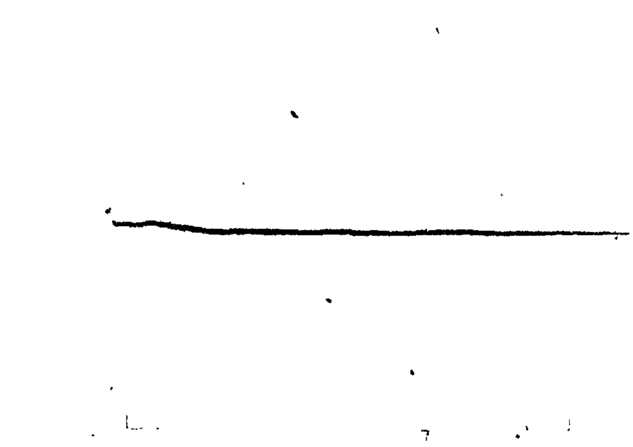

Fig. (5.2-31)

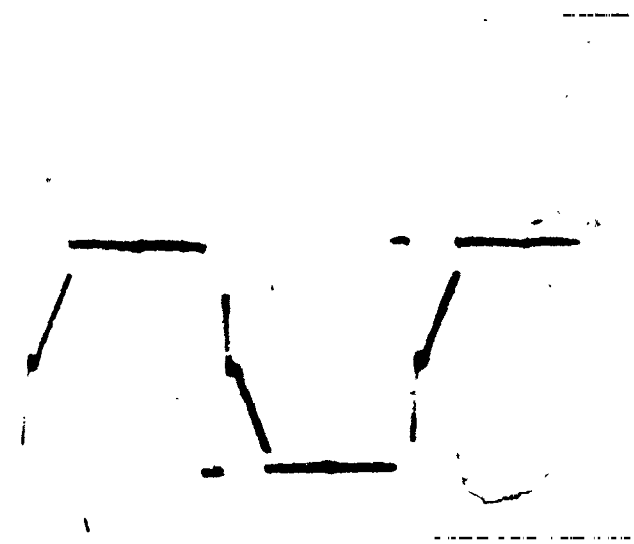

Fig. (5.2-32)

Fig. (5.2-33)

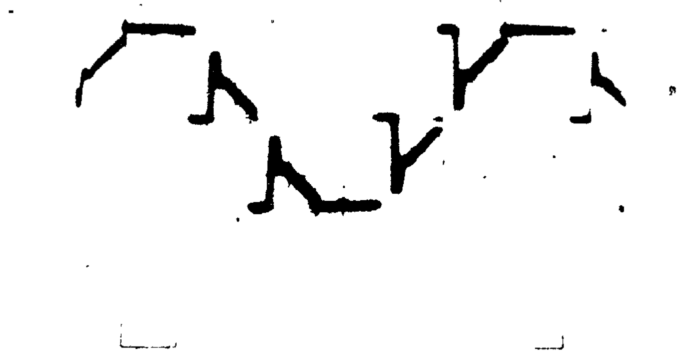

Fig. (5.2-34)

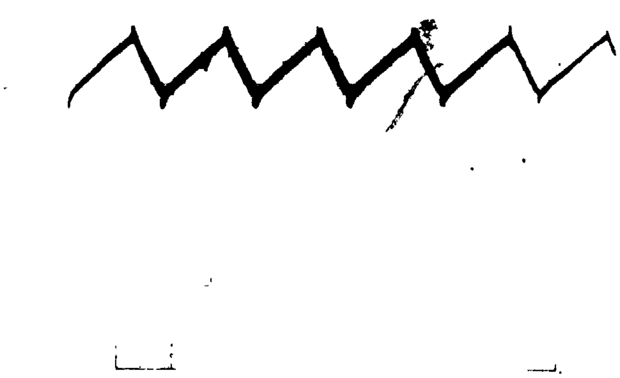

Fig. (5.2-35)

Fig. (5.2-36)

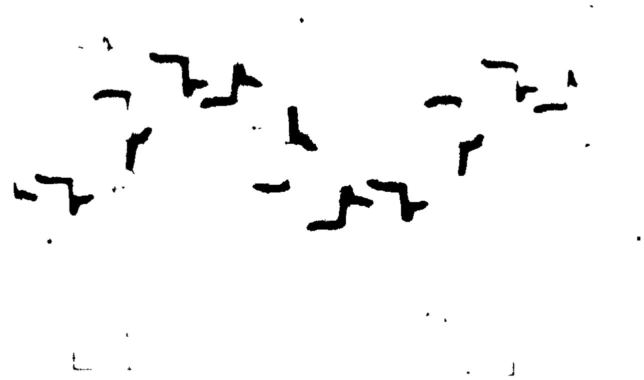

Fig. (5.2-37)

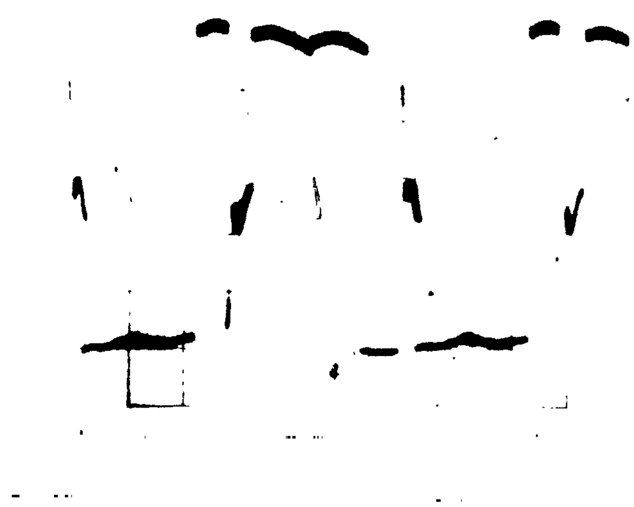

Fig. (5.2-38)

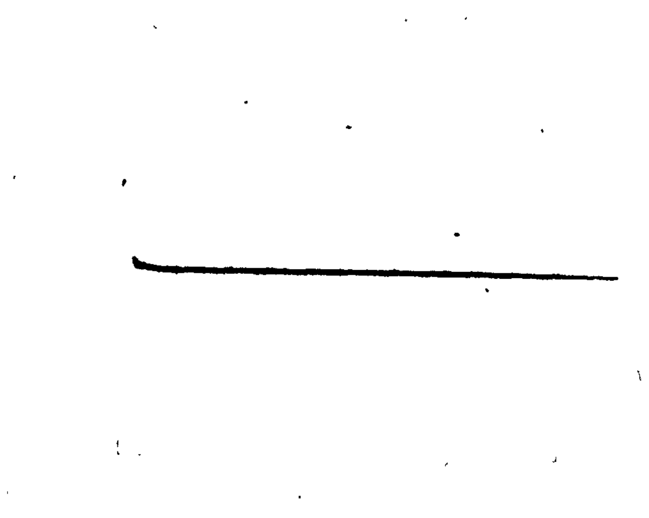

Fig. (5.2-39)

Fig. (5.2-40)

ORIGINAL PAGE
BLACK AND WHITE PHOTOGRAPH

5.3 METHODS OF CALCULATION OF MPC SYSTEMS PERFORMANCE CHARACTERISTICS

One of the most important parameters, which determines how satisfactory the performance and design of a given MPC system are, is the system efficiency. In order to determine this efficiency, one requires knowledge of the total input power into the MPC system and the total output power from the system. The difference between the input power and the output power is the system losses which can be broken down into ohmic, rotational, switching, and stray loss components. However, the switching losses are related to the rotor position, and its speed. Hence, they can be associated with the rotational loss component.

In this section, the method of determining the input and output powers for both test setups (1) and (2), Figures (5.1-1) and (5.1-4), will be outlined. Based on such input and output power data, the efficiencies will be calculated. It will then be shown that, due to an error in the torque measurements taken by means of a torque transducer, for the strontium ferrite based MPC system on a certain date, the corresponding efficiency values were found to be unrealistically high. Upon close examination of those torque readings, in conjunction with all the other data collected with it on that date (input power, speed, etc.), it was found that there exists a constant torque offset in all these readings. The determination of the magnitude of this offset is explained later in this section. It must be pointed out that no correction was required for the test data associated with the samarium cobalt based MPC system, the data of which were taken on other dates.

After making the necessary offset correction in the torque values, the input power, output power, system losses, and efficiencies were recalculated for the strontium ferrite based MPC system. On an inductor current-speed plane, curves of constant efficiency were plotted for both MPC systems, as will be given later on in this section. Finally, on the basis of the loss data obtained from the various test runs, generalized loss formulas for the calculation of losses and efficiencies of both MPC systems, for motoring and regenerating modes of operation, as functions of machine speed and torque, were developed. These equations were obtained using a least squares fit of the system loss data obtained by tests for both the samarium cobalt and strontium ferrite based machines.

5.3.1 METHODS OF CALCULATION OF SYSTEM INPUT AND OUTPUT POWER FOR TEST SETUPS (1) AND (2) WITH EXAMPLES

Setup (1): For test setup (1), in the motoring mode, the input power, P_{in}, was calculated as the product of the dc line voltage, V, read by voltmeter, V_1, Figure (5.1-1), times the dc line current, I, read by ammeter, A_1. That is

$$P_{in} = V \cdot I + 200 \quad \text{Watts.} \tag{5.3-1}$$

The 200 watts term represents the power consumed by the low level control electronics, which were supplied independently in this setup. However, in an actual vehicle situtation this power must be supplied by the battery. Justification of neglect of the effect of the voltage ripples in the dc line voltage on the input power, P_{in}, was based on observation of this ripple magnitude on an oscilloscope screen, where it was found to be in the millivolt range and consequently insignificant.

Upon examination of the test setup (1), Figure (5.1-1), it becomes obvious that the output power, P_{out}, can be calculated as

$$P_{out} = T \cdot N(2\pi/60) \quad \text{Watts} \tag{5.3-2}$$

where, T is the torque reading of the transducer, T_1, in Newton Meters, and N is the machine speed in RPM, measured by the tachometer, N_1. A pictorial display of the above is given in Figure (5.3-1).

Example (1): Consider motoring run number 67 in Table (5.2-1) in which; V = 115.78 Volts, I = 127.74 Amperes, N = 8230 RPM, and T = 15.25 NM. For this run we have,

$$P_{in} = 115.78 \times 127.74 + 200.0 = 14989.7 \text{ Watts}$$

$$P_{out} = 15.25 \times 8230 \times 2\pi/60 = 13143.1 \text{ Watts}$$

Therefore, the overall motoring system efficiency, η_{system}, at this torque and speed is

$$\eta_{system} = (P_{out}/P_{in}) \times 100\%$$
$$= (13143.1/14989.7) \times 100 = 87.7\%.$$

For the regeneration mode the input power, P_{in}, is the mechanical power delivered by the dynamometer, and hence can be calculated as follows

$$P_{in} = T \cdot N(2\pi/60) \quad \text{Watts.} \tag{5.3-3}$$

ORIGINAL PAGE IS OF POOR QUALITY

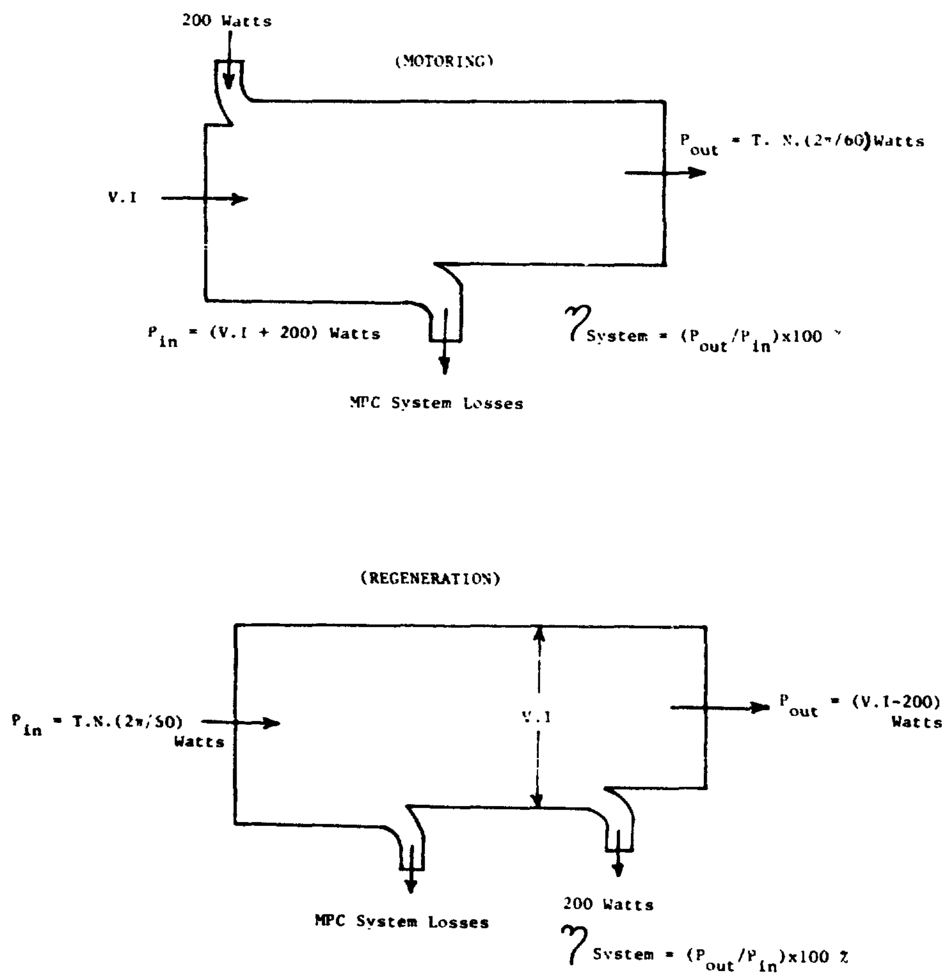

FIGURE (5.3-1) Power Flow - Test Setup (1)

ORIGINAL PAGE IS
OF POOR QUALITY

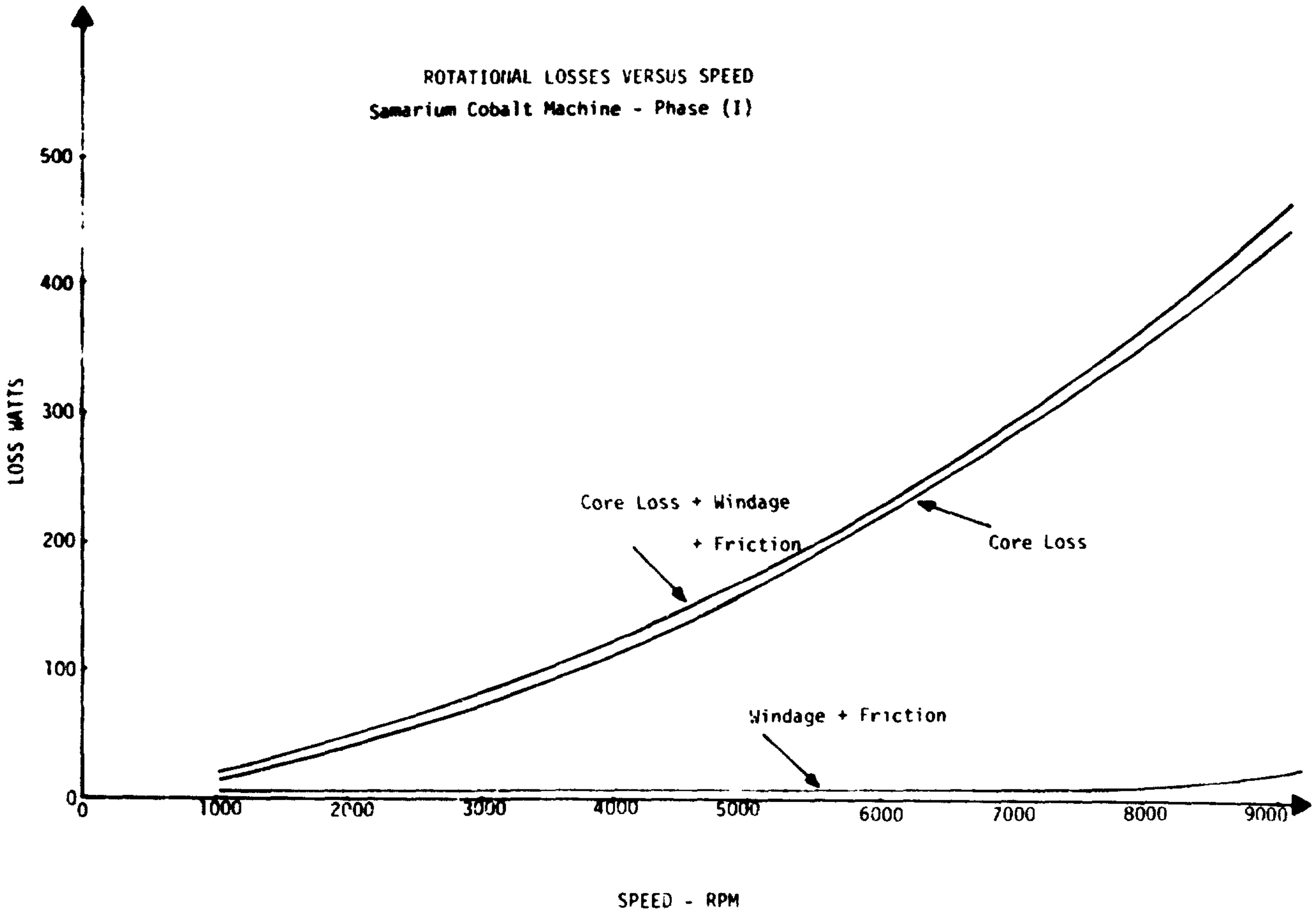

FIGURE (5.3-2) Rotational Losses as Function of Speed for the Permanent Magnet Alternator of Test Setup (1)

All symbols are as previously defined.

The output power, P_{out}, is the net electrical power returned to the battery. That is

$$P_{out} = V \bullet I - 200 \quad \text{Watts} \qquad (5.3\text{-}4)$$

where the 200 Watts represent the power which must be supplied from the battery to the low level control electronics of the MPC system in an actual vehicular propulsion situation.

Example (2): Consider regeneration run number 108 in Table (5.2-4) in which; V = 116.00 Volts, I = 98.00 Amperes, N = 8600 RPM, and T = 14.64 NM. For this run we have,

$$P_{in} = 14.64 \times 8600 \times 2\pi/60 = 13184.6 \text{ Watts}$$

$$P_{out} = 116.00 \times 98.00 - 200 = 11168\ 0 \text{ Watts.}$$

Therefore, the overal regeneration MPC system efficiency, η_{system}, at this torque and speed is

$$\begin{aligned}\eta_{system} &= (P_{out}/P_{in}) \times 100\% \\ &= (11168.0/13184.6) \times 100\% = 84.7\%.\end{aligned}$$

setup (2): For test setup (2), which functions only in the motoring mode, see Figure (5.1-4), the input power, P_{in}, was calculated as the product of the dc line voltage, V, read by voltmeter, V_1, Figure (5.1-4), times the dc line current, I, read by ammeter, A_1. That is

$$P_{in} = V \bullet I + 200 \quad \text{Watts.} \qquad (5.3\text{-}5).$$

Again, the 200 Watts term represents the power consumed by the low level control electronics, which were supplied independently in this set-up. However, in an actual vehicle situation this power must be supplied by the battery. Again, the voltage ripple effect in the dc line was found to be insignificant as mentioned above.

Upon examining test setup (2) of Figure (5.1-4), it becomes obvious that the output power, P_{out}, is the sum of three power components. These power components are:

1. P_{out}^{alt} = the output power of the permanent magnet alternator, given by the reading of wattmeter, W_3, which is the power dissipatated in the resistance load.

2. P^{alt}_{ohmic} = the ohmic losses in the armature of the permanent magnet alternator, which is given by knowledge of the armature current reading, $I^{alt.}$, of ammeter A_2 or A_3, and the armature resistance per phase, r_a, of that alternator. Thus, P^{alt}_{ohmic} is given as, $P^{alt}_{ohmic} = 3 \cdot (I^{alt})^2 \cdot r_a$ Watts(5.3-6).

3. $P^{alt}_{rotational}$ = the rotational losses of the permanent magnet alternator, which are determined once the speed is read by tachometer, N_1, and is read from an experimentally obtained curve of these rotational losses as function of speed. This rotational loss curve is given for convenience in Figure (5.3-2).

Accordingly, the output power, P_{out}, in test setup (2) is given by

$$P_{out} = P^{alt}_{out} + P^{alt}_{ohmic} + P^{alt}_{rotational} \tag{5.3-7}$$

A pictorial display of the above is given in Figure (5.3-3).

Example (3): Consider motoring run number 158 in Table (5.2-1)in which; V = 117.60 Volts, I = 222.90 Amperes, N = 5428 RPM, P_{out} = 17889 Watts, and $I^{alt.}$ = 109.5 Amperes. At a speed of 5428 RPM, the rotational losses of the permanent magnet alternator, $P^{alt}_{rotational}$, is read from Figure (5.3-2) as

$$P^{alt}_{rotational} = 193 \text{ Watts.}$$

For an alternator current, $I^{alt.}$, of 109.5 Amperes, the alternator armature ohmic losses, P^{alt}_{ohmic}, for an armature resistance per phase, r_a = .01246 Ohms at 35°C (r_a = 0.01200 Ohms at 25°C)

$$P^{alt}_{ohmic} = 3 \times 0.01246 \times (109.5)^2 = 448 \text{ Watts.}$$

Hence, P_{out} of the MPC system, Equation (5.3-7), becomes,

$$P_{out} = 17889.0 + 448 + 193 = 18530.0 \text{ Watts.}$$

Here, the input power is

$$P_{in} = 117.60 \times 222.90 = 26413.0 \text{ Watts.}$$

Therefore, the overall motoring MPC system efficency, η_{system}, at this load is

$$\eta_{system} = (P_{out}/P_{in}) \times 100\% = (18530.0/26413.0) \times 100\% = 70.2\%.$$

It may be of interest to some readers to separate the MPC system losses into two components, one loss component would be losses in the machine and the other would be losses in the power conditioner. Although, this will not be done here, because of lack of need for such loss identification, these authors wish to provide the data base on which such loss separation can be accomplished. In order to accomplish this task one needs to know the rotational losses as function of motor speed for both machines, as well as the resistance values per phase of the armature windings of both machines.

Figures (5.3-4) and (5.3-5) contain plots of the rotational losses obtained by test versus machine speed for the samarium cobalt and the strontium ferrite based machines, respectively. It should also be pointed out that the armature resistances per phase for parallel path connection, (line to neutral) at 21.7°C are 0.00238 Ohms and 0.00236 Ohms, obtained from tests performed on the samarium cobalt, and strontium ferrite machines, respectively. These data may be of interest to those who may wish to separate the MPC system losses into motor losses and power conditioner losses.

5.3.2 IDENTIFICATION AND CORRECTION OF ERRORS IN TEST DATA TAKEN AT LOW TORQUE POINTS - DETERMINATION OF TORQUE OFFSET

During the analysis of the test data of the strontium ferrite based MPC system, see Tables (5.2-5), (5.2-6), and (5.2-8), a discrepancy became apparent when unrealistically high efficiencies were calculated at various operating points in both the motoring and regenerating modes. In order to find reasons for this discrepancy, the electrical power, P_e, and the mechanical power, P_m, were ploted versus torque at speeds of 3500, 5400 and 7200 RPM, for both the motoring and regenerating modes, as shown in Figures (5.3-6), (5.3-7), and (5.3-8), respectively. Notice that in the motoring mode, the electrical power, P_e, is the input power, P_{in}, into the MPC system, and the mechanical power, P_m, is the output power, P_{out}, from the MPC system. Meanwhile, in the regenerating mode, the electrical power, P_e, is the output power, P_{out}, returned to the battery from the MPC system, and the mechanical power, P_m, is the input power, P_{in}, into the MPC system.

POWER FLOW-TEST SETUP (2)

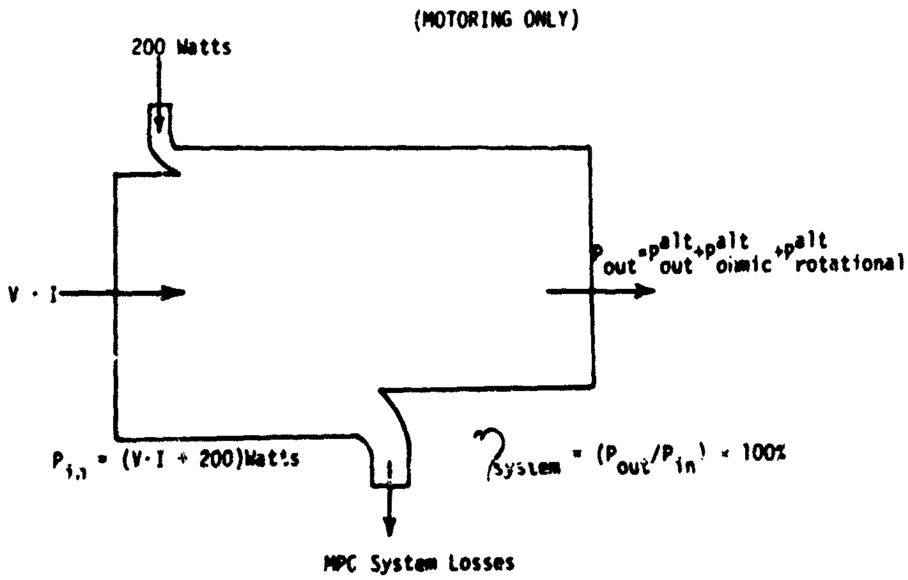

FIGURE (5.3-3) Power Flow - Test Setup (2)

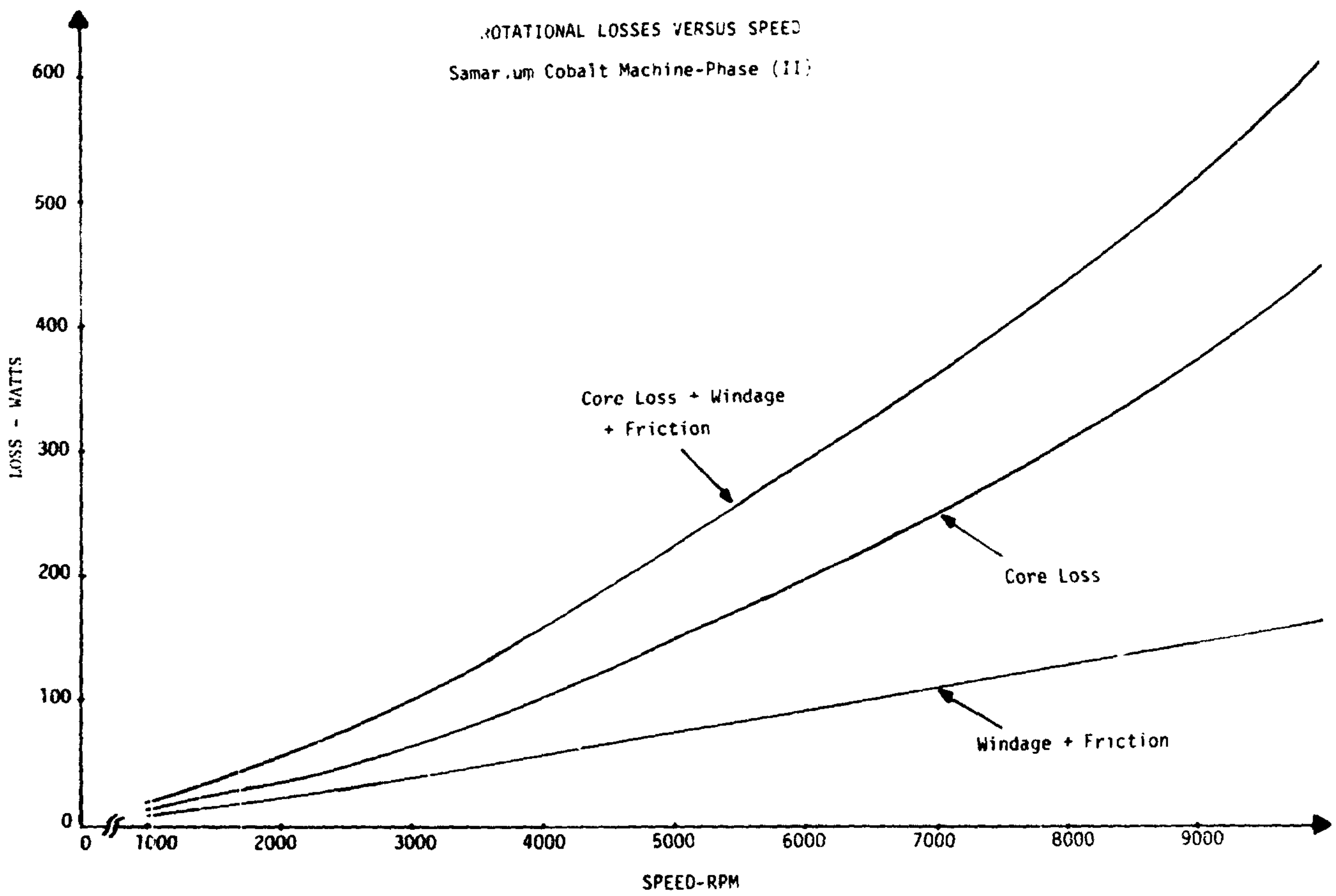

FIGURE (5.3-4) Rotational Losses Versus Speed - Samarium Cobalt Machine

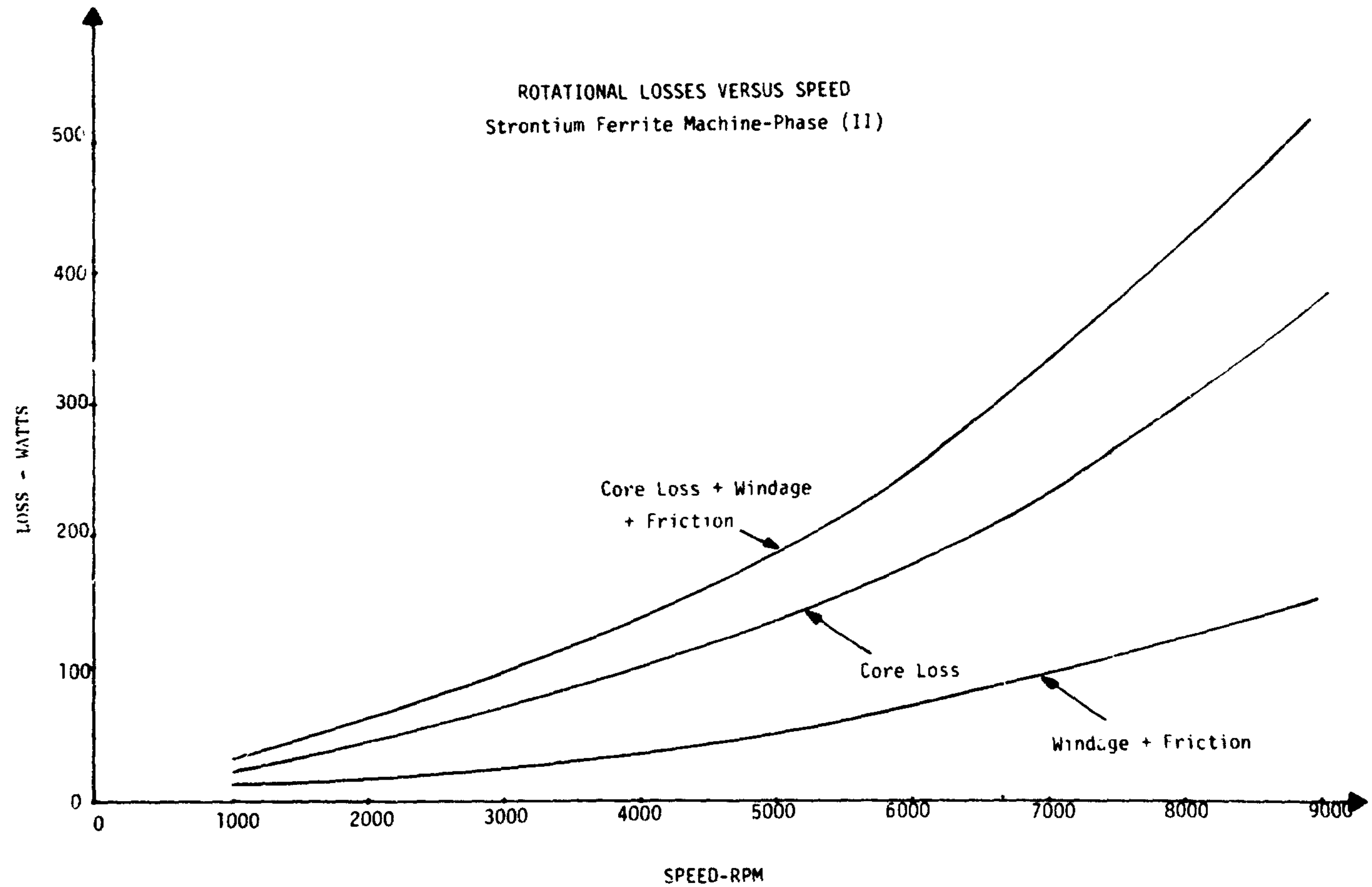

FIGURE (5.3-5) Rotational Losses Versus Speed - Strontium Ferrite Machine

ORIGINAL PAGE IS
OF POOR QUALITY

Upon close examination of Figures (5.3-6) through (5.3-8), it becomes evident that the discrepency in values of MPC system efficiency could be accounted for by a shift of the P_m curves by a certain torque value. This shift compensates for a constant error (offset) in the torque transducer readings. The magnitude of this shift is determined such that at no load (zero torque, that is zero mechanical power, P_m) the electrical power, P_e, is equal to the rotational losses at the given speed, plus the 200 Watts of low level control electronic losses, plus a reasonable no-load loss in the power components of the power conditioner. This torque magnitude was found, on the basis of Figures (5.3-6) through (5.3-8), to be equal to 1.4 Newton Meters error in the torque transducer readings. Accordingly, after the application of this shift, Figures (5.3-6) through (5.3-8) yielded Figures (5.3-9) trough (5.3-11).

The above means that an increase in the torque reading for the regeneration runs and a decrease in the torque readings for the motoring runs by 1.4 Newton Meters of torque at any speed is necessary throughout Tables (5.2-5), (5.2-6) and (5.2-8). This yields the additional corrected torque, and output or input power columns given in these tables for the strontium ferrite based MPC system, for motoring and regeneration, respectively.

5.3.3 DETERMINATION OF INTERPOLATION FORMULAS FOR SYSTEM LOSS.

The performance data for both the samarium cobalt and strontium ferrite based MPC systems were given in Section (5.2) in terms of speed, torque, current, voltage, and input as well as output powers. From the input and output powers, the system loss corresponding to a given speed and torque was easily obtained as shown earlier in this section. However, in order to show the system loss (or system performance) at various speeds and torque, cumbersome tables were given for both MPC systems operating in the motoring and regenerating modes as shown in Section (5.2). Presenting the data in this manner makes it rather difficult to utilize such information, as in the calculation of the system drive cycle efficiency. Furthermore, the tabulated data presents no direct insight as to how parameters such as the speed and torque may affect the system losses.

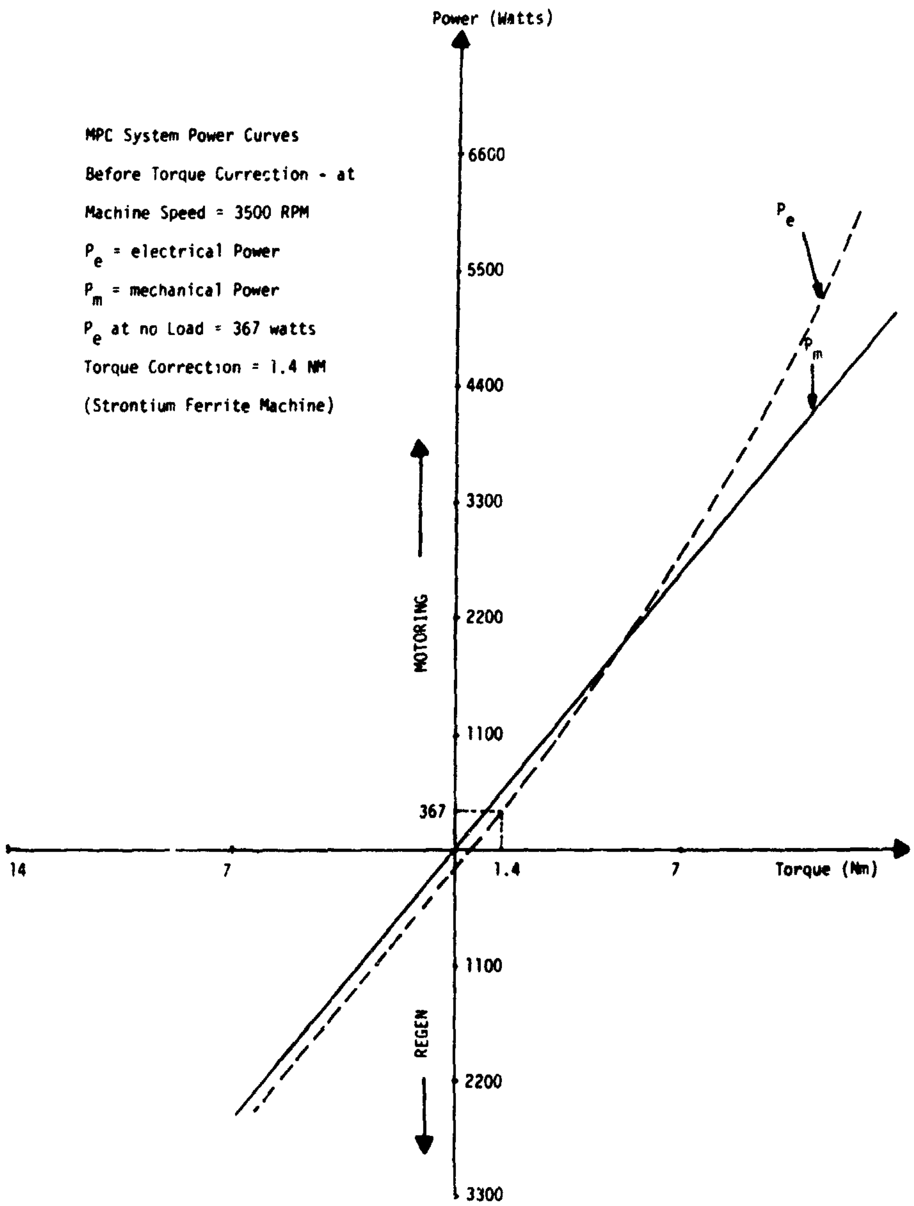

FIGURE (5.3-6) Plot of Electrical and Mechanical Powers Versus Torque at 3500 RPM for the Strontium Ferrite MPC System Before Torque Shift

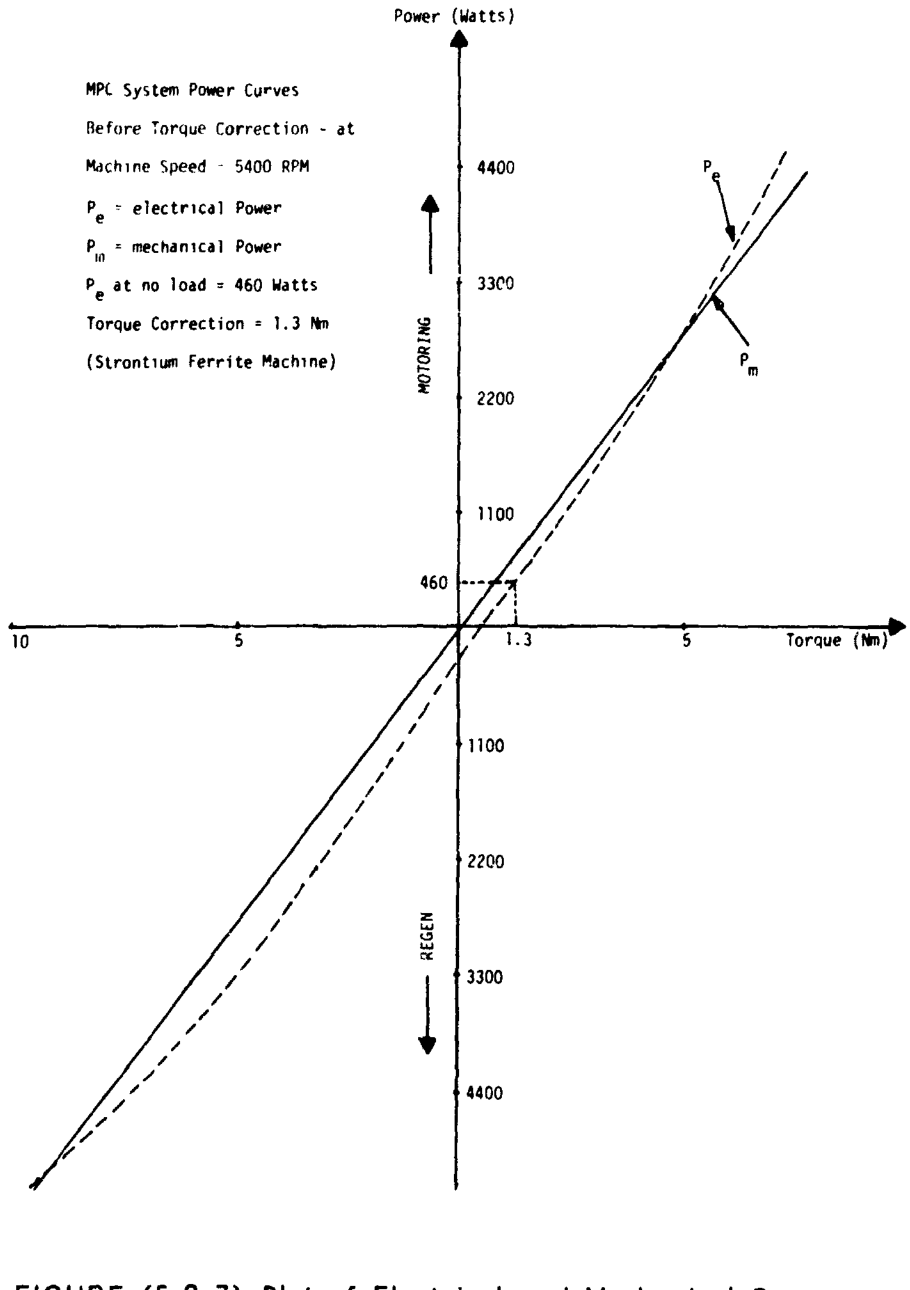

FIGURE (5.3-7) Plot of Electrical and Mechanical Powers Versus Torque at 5400 RPM for the Strontium Ferrite MPC System Before Torque Shift

ORIGINAL PAGE IS
OF POOR QUALITY

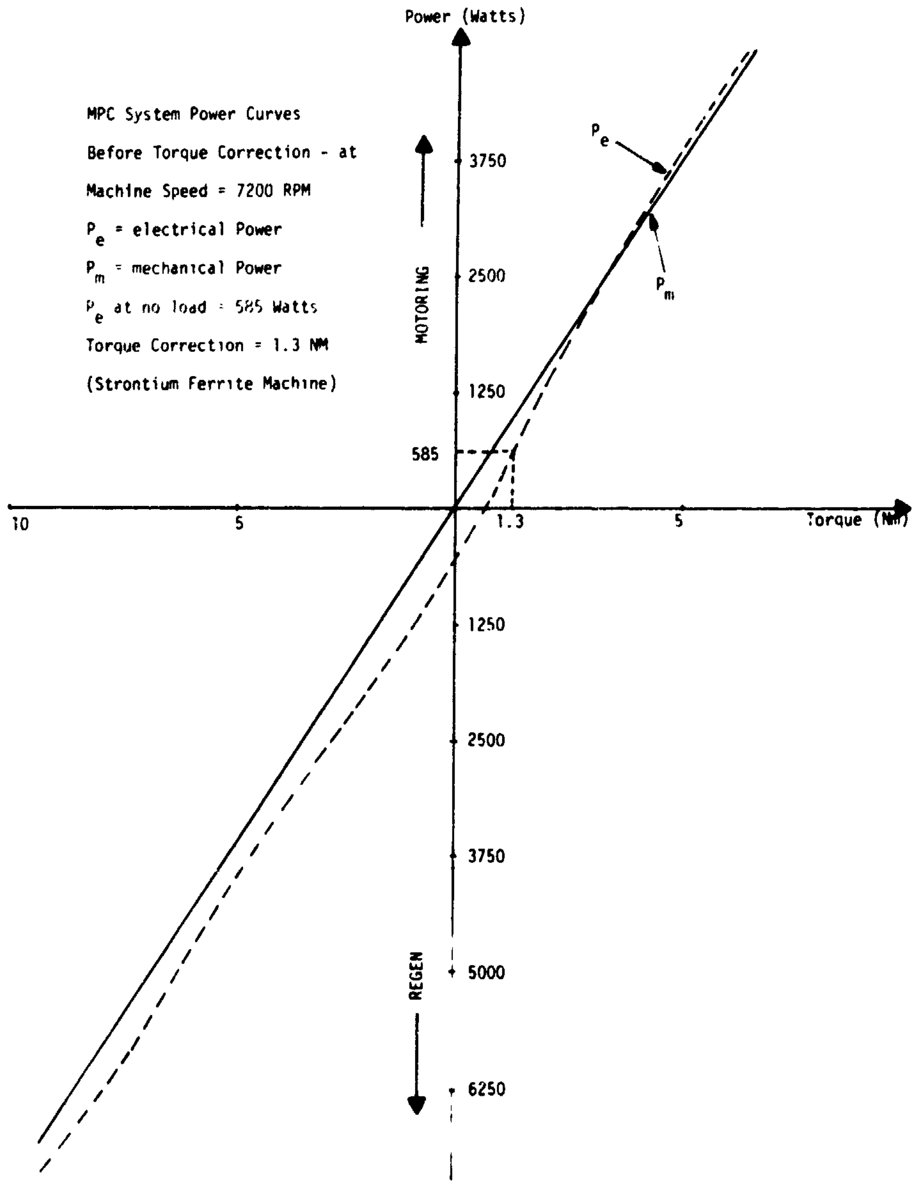

FIGURE (5.3-8) Plot of Electrical and Mechanical Powers Versus Torque at 7200 RPM for the Strontium Ferrite MPC System Before Torque Shift

ORIGINAL PAGE IS OF POOR QUALITY

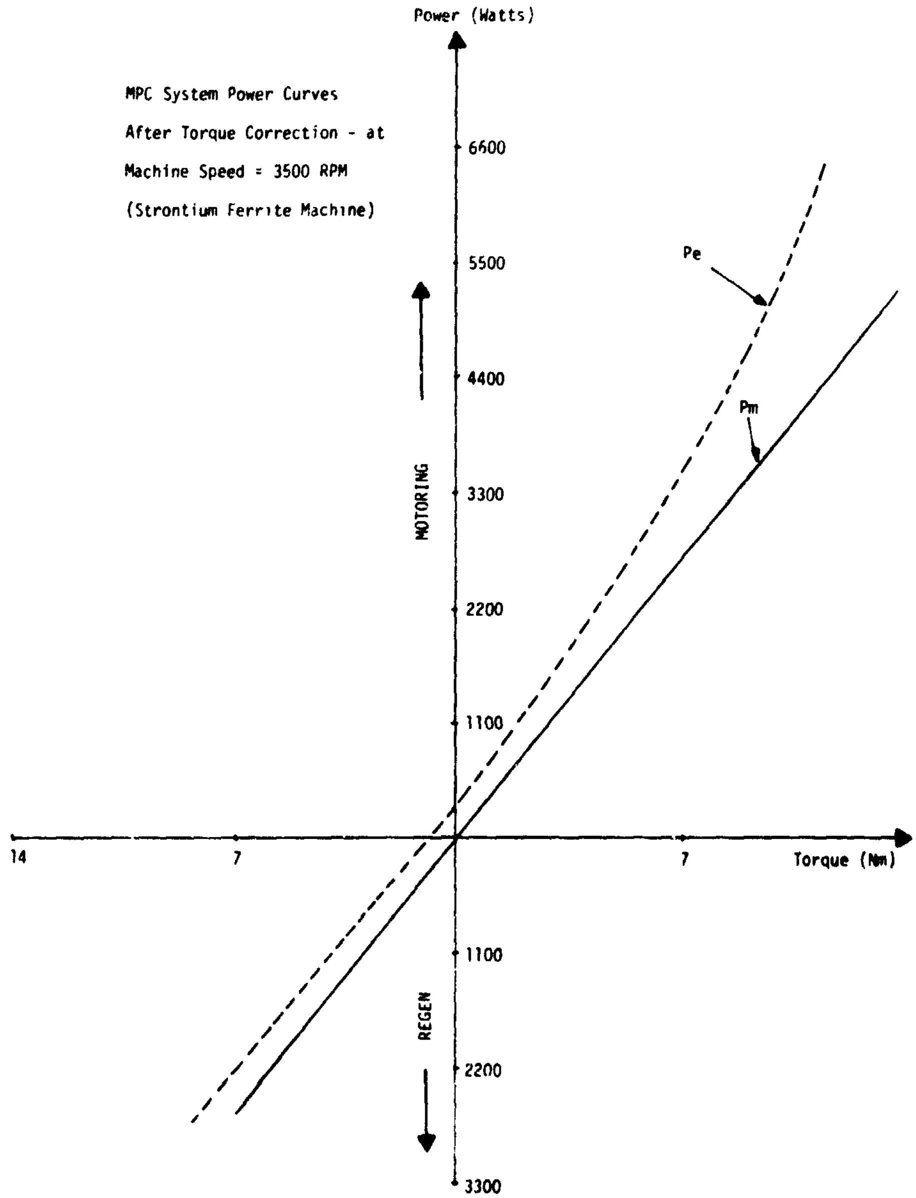

FIGURE (5.3-9) Plot of Electrical and Mechanical Powers Versus Torque at 3500 rpm for the Strontium Ferrite MPC System After Torque Shift

ORIGINAL PAGE IS
OF POOR QUALITY

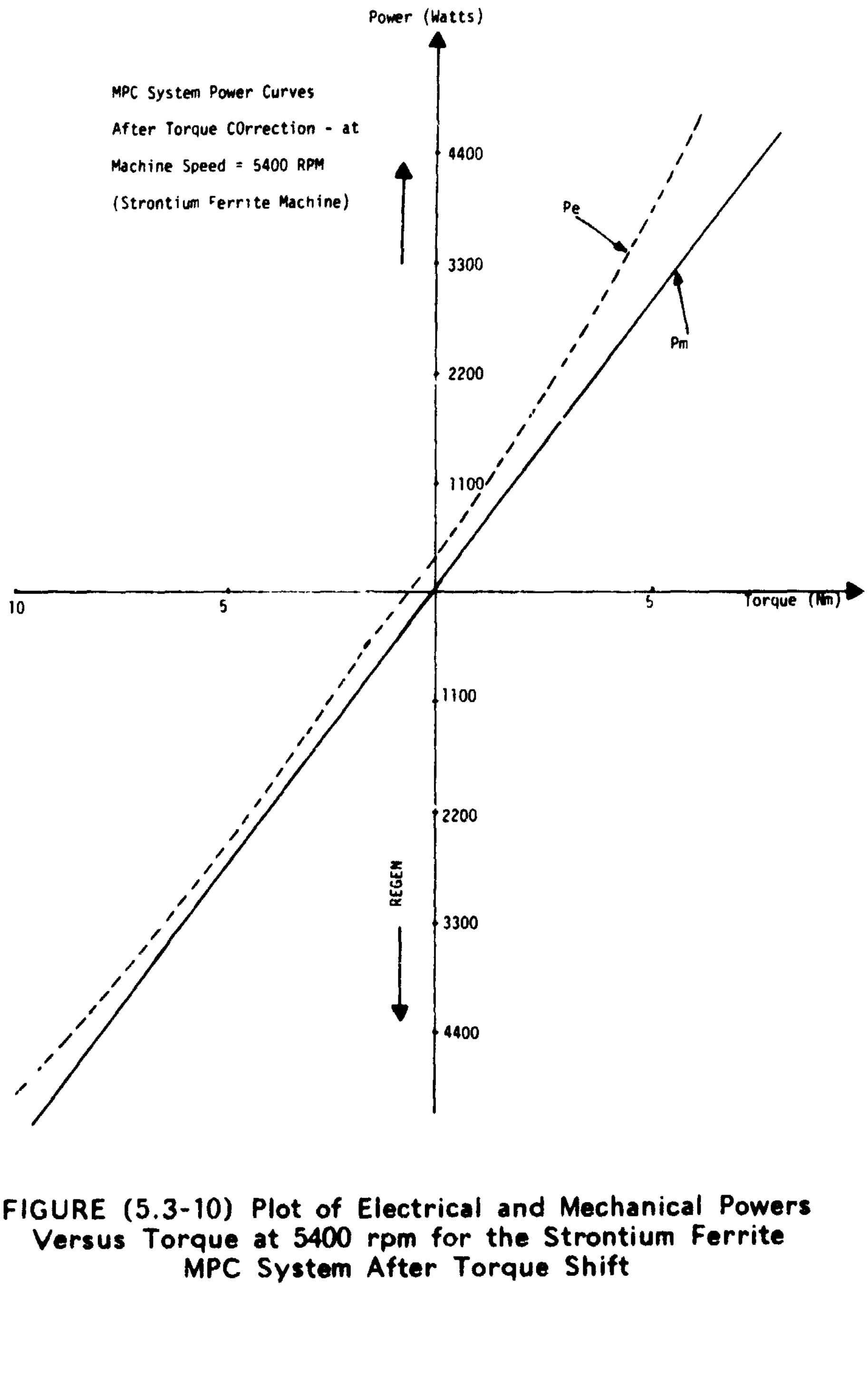

FIGURE (5.3-10) Plot of Electrical and Mechanical Powers Versus Torque at 5400 rpm for the Strontium Ferrite MPC System After Torque Shift

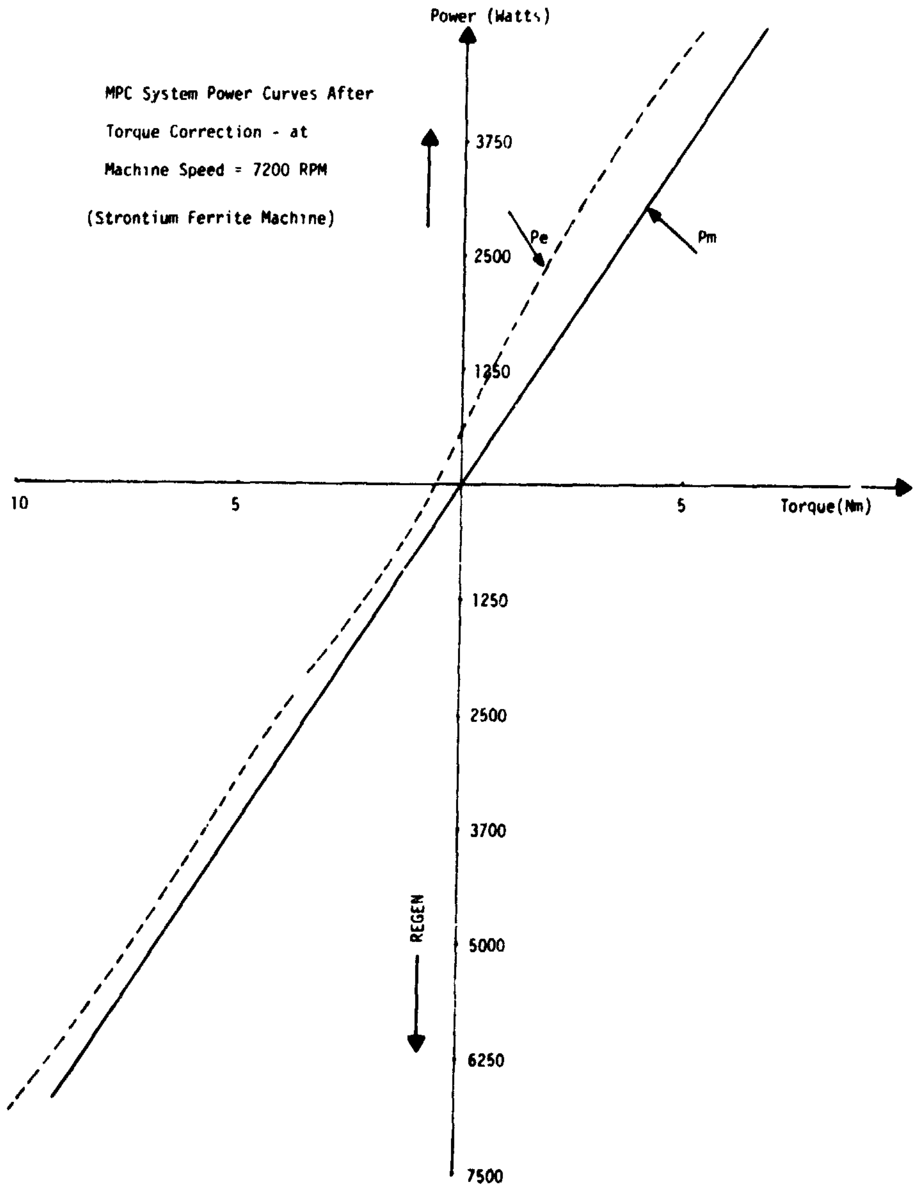

FIGURE (5.3-11) Plot of Electrical and Mechanical Powers Versus Torque at 7200 rpm for the Strontium Ferrite MPC System After Torque Shift

Given the above disadvantages of tabulating the data, one needs to present the data in a simple and more accessible form; that is in a mathematical form. This calls for curve fitting the given MPC system loss data using a suitable mathematical loss expression. Various interpolating techniques are given [1,2] in books on Numerical Methods. The technique used in numerical curve fitting of the system losses corresponding to the samarium cobalt and strontium ferrite MPC sytems in the motoring and regenerating mode is that which is based on the least-squares Approximation method. This method offers a means for all points in the test data collection, by minimizing the square of the error.

Consider either the motoring or the regenerating mode of operation of either the samarium cobalt or the strontium ferrite MPC system. The (rotational) losses in the machine portion of the system are dependent on the shaft speed and torque. This also applies to varying degrees to the stray losses in the machine, the switching losses in the power conditioner, and the ohmic losses in the MPC system. In other words, the system loss, SL, can be written as follows:

$$SL = f(\omega, T) \tag{5.3-8}$$

where ω is the shaft speed in radians/second, and T is the torque in Newton-meters. Let SL be a polynomial function as follows:

$$SL = c_1h_1(\omega,T) + c_2h_2(\omega,T) +\cdots+ c_nh_n(\omega,T)$$

$$= \Sigma_{i=1}^{n} c_ih_i(\omega,T) \tag{5.3-9}$$

where the $h_i(\omega,T)$ are various combinations of ω, ω^2, $\cdots$, T, T^2, $\cdots$, ωT, ωT^2, $\omega^2 T$, $\cdots$ and the coefficients c_i are chosen so that SL gives a best approximation to the system loss data. For each pair of ω and T, an equation can be written for the system loss as given by Equation (5.3-9). Thus for m pairs of ω and T (or m data points), m equations can be written. In matrix form, these equations are given by

$$\begin{bmatrix} SL_1 \\ SL_2 \\ \cdot \\ \cdot \\ \cdot \\ SL_m \end{bmatrix} = \begin{bmatrix} h_1(\omega_1,T_1)h_2(\omega_1,T_1)\cdots h_n(\omega_1,T_1) \\ h_1(\omega_2,T_2)h_2(\omega_2,T_2)\cdots h_n(\omega_2,T_2) \\ \cdot \quad \cdot \quad \cdot \\ \cdot \quad \cdot \quad \cdot \\ \cdot \quad \cdot \quad \cdot \\ h_1(\omega_m,T_m)h_2(\omega_m,T_m)\cdots h_n(\omega_m,T_m) \end{bmatrix} \begin{bmatrix} C_1 \\ C_2 \\ \cdot \\ \cdot \\ \cdot \\ C_n \end{bmatrix}$$

or

$$\underline{SL} = \underline{H} \cdot \underline{C} \tag{5.3-10}$$

Let the actual system loss be given by the vector $\underline{SL}^a$. The error introduced by approximating $\underline{SL}^a$ with $\underline{SL}$ is given by

$$\underline{E} = \underline{SL}^a - \underline{SL} = \underline{SL}^a - \underline{H} \cdot \underline{C} \tag{5.3-11}$$

Setting the error vector, to zero and solving for $\underline{C}$ in Equatin (5.3-11), one obtains the following:

$$\underline{C} = \underline{H}^{-1} \, \underline{SL}^{a} \tag{5.3-12}$$

Equation (5.3-12) can be easily programmed and solved by such methods as Gauss Elimination, Gauss-Seidel and so forth [1, 2]. By trying various combinations of the basic functions, $h_i(\omega, T)$, a vector $\underline{C}$ can be obtained which minimizes the square of the error, $\underline{E} \bullet \underline{E}^{T}$.

In our case a computer software package [3] was available to help solve Equation (5.3-12) subject to the smallest $\underline{E} \bullet \underline{E}^{T}$ possible. The results (system loss interpolation formulas) corresponding to the samarium cobalt MPC system in both the motoring and the regenerating modes and the strontium ferrite MPC system in both the motoring and the regenerating modes will be given in the next Section (5.4).

ORIGINAL PAGE IS
OF POOR QUALITY

5.4 CORRECTED TEST RESULTS AND INTERPOLATION FORMULAS FOR SYSTEM LOSS CALCULATION

The corrected values of torque and output or input power for the strontium ferrite based MPC system were arrived at as described in Section (5.3), and tabulated in the corrected torque and output or input power forms of Tables (5.2-5), (5.2-6) and (5.2-8). There was no apparent torque transducer error in the test data of the samarium cobalt based MPC system.

Application of the MPC system loss interpolation method described in Section (5.3.3) yielded the following general MPC system loss formula, which is valid for both machine systems at hand, in the motoring and regenerating modes of operation:

$$\text{MPC system losses} = c_1+c_2T+c_3T^2+c_4T^3+c_5T^4+c_6T^5 +c_7\omega+c_8\omega^2+c_9\omega^3+c_{10}\omega T+c_{11}\omega T^2 +c_{12}\omega^2T+c_{13}\omega^2T^2 \text{ Watts} \quad (5.4\text{-}1)$$

where T is the machine shaft torque in Newton Meters, and ω is the machine shaft speed in mechanical radians per second. The constants c_1 through c_{13} are given in Table (5.4-1) for parallel connected winding paths per phase, for the samarium cobalt based and strontium ferrite based systems, respectively. Notice also that equation (5.4-1) is not valid for loss calculation at a shaft speed $\omega = 0$. This loss formula includes the 200 Watts of losses in the low level control electronics associated with the MPC system for both machines.

Accordingly the relationship between the input power, output power and MPC system losses given by Equation (5.4-1) can best be understood for the motoring and regenerating modes by the power flow diagrams of Figures (5.4-1) and (5.4-2), respectively. On the basis of these figures, the MPC system efficiencies for motoring and regenerating modes can be expressed, respectively, as follows:

$$\eta_{Motoring} = P_{out}/P_{in} = [T.\omega/(T.\omega+\text{MPC System Losses})] \times 100\% \quad (5.4\text{-}2)$$

and

$$\eta_{Regenerating} = P_{out}/P_{in} = [(T.\omega-\text{MPC System Losses})/T.\omega \times 100\% \quad (5.4\text{-}3)$$

At this stage, examples of application of the loss and efficiency calculation formulas (5.4-1) through (5.4-3), to specific test runs in Tables (5.2-1) through (5.2-8) would be very useful.

TABLE (5.4-1) CONSTANTS OF MPC SYSTEM LOSS FORMULA, EQUATION (5.4-1)

Machine and Mode	Constants c_1	c_2	c_3	c_4	c_5
Samarium Cobalt Motoring	-2648.02442	1189.4347	-58.88318	1.55152	-0.03042
Samarium Cobalt Regeneration	-515.57409	995.91247	-328.54064	47.64375	-3.17101
Strontium Ferrite Motoring	-3432.20449	25.84914	127.05699	-12.[illegible]376	0.43403
Strontium Ferrite Regeneration	-1602.39470	1172.56686	-211.82710	20.27762	-1.00633

TABLE (5.4-1) Continued

Constants					
Machine and Mode	c_6	c_7	c_8	c_9	c_{10}
Samarium Cobalt Motoring	0.00026	3.85509	-0.00005	-5.01872	0.15377
Samarium Cobalt Regeneration	0.07896	0.49068	-0.00091	0.00000	-0.16417
Strontium Ferrite Motoring	-0.00499	18.75077	-0.02882	0.00002	-1.03153
Strontium Ferrite Regeneration	0.02091	-1.91232	0.01115	0.00000	-0.74595

TABLE (5.4-1) Continued

Constants

Machine and Mode	c_{11}	c_{12}	c_{13}
Samarium Cobalt Motoring	0.15377	0.00594	-0.00017
Samarium Cobalt Regeneration	0.03466	0.00012	0.00012
Strontium Ferrite Motoring	0.04923	0.00052	-0.00003
Strontium Ferrite Regeneration	0.05301	-0.00049	0.00002

POWER FLOW IN MPC SYSTEM (MOTORING)

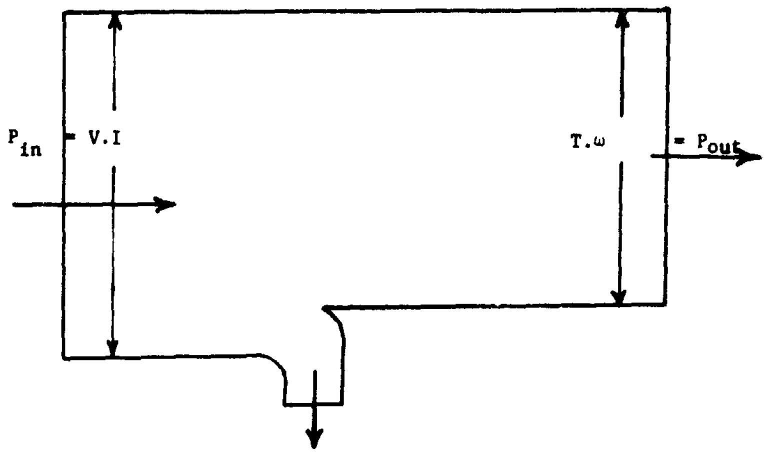

MPC System Losses

FIGURE (5.4-1) Power Flow - MPC System (Motoring)

POWER FLOW IN MPC SYSTEM (REGENERATION)

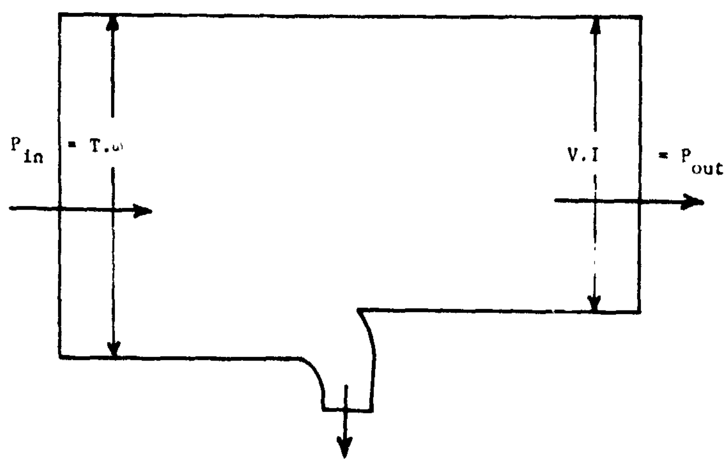

MPC System Losses

FIGURE (5.4-2) Power Flow - MPC System (Regenerating)

Example (1):
Consider motoring test run number 68 for the samarium cobalt based MPC system, Table (5.2-1). This run had a speed reading of 7200 RPM and a torque reading of 25.08 Newton Meters. Substituting

$$\omega = 7200 \times 2\pi/60 = 754.0 \text{ Radians/Sec.}$$

and T = 25.08 Newton Meters into Equation (5.4-1) yields an MPC system loss of 4211.7 Watts. Substituting this MPC system loss, and the above torque and speed into Equation (5.4-2) yields an MPC system efficiency, $\eta_{Motoring}$, of

$$\eta_{Motoring} = 81.8\%$$

The above should be compared with an MPC system loss value, based on test, of 4134.0 Watts and an MPC system efficiency of 82%. Notice that the MPC system loss and efficieny values obtained from test are very close to the corresponding values obtained from the "curve fitted" loss interpolation formula.

Example (2):
Consider regeneration test run number 79 for the samarium cobalt based MPC system, Table (5.2-4). This run had a speed reading of 8720 RPM and a torque reading of 8.81 Newton Meters. Substituting,

$\omega = 8720 \times 2\pi/60 = 913.2$ Radians/Sec.

and T = 8.81 Newton Meters

into Equation (5.4-1) yields an MPC system loss of 810.0 Watts. Substituting this MPC system loss, and the above torque and speed into Equation (5.4-3) yields an MPC system efficiency, $\eta_{Regenerating}$, of

$$\eta_{Regenerating} = 89.9\ \%$$

The above should be compared with an MPC system loss value based on test of 798.9 Watts and an MPC system efficiency of 90%. Notice that the MPC system loss and efficiency values obtained from test are very close to the corresponding values obtained from the "curve fitted" loss interpolation formula.

Example (3):
Consider motoring test run number 10 for the strontium ferrite based MPC system, Table (5.2-5). For this run, we have

$$\omega = 7160 \times 2\pi/60 = 749.8 \text{ Radians/Sec.}$$

and the corrected test reading of the torque, T, is

$$T = 13.17 \qquad \text{Newton Meters}$$

Hence, from Equation (5.4-1) we have

$$\text{MPC system loss} = 2353.0 \qquad \text{Watts}$$

and it follows from Equation (5.4-2) that

$$\eta_{\text{Motoring}} = 80.8 \quad \%$$

The above should be compared to the following obtained directly from corrected test data:

$$\text{MPC system loss} = 2215.1 \quad \text{Watts}$$

and

$$\eta_{\text{Motoring}} = 81.7 \quad \%.$$

Example (4):
Consider regeneration test run number 126 for the strontium ferrite based MPC system, Table (5.2-8). For this run, we have

$\omega = 7180 \times 2\pi/60 = 751.9$ Radians/Sec.
and the corrected test reading of the torque, T, is

$$T = 14.28 \qquad \text{Newton Meters.}$$

Hence, from Equation (5.4-1) we have

$$\text{MPC system loss} = 2567.9 \qquad \text{Watts}$$

and it follows from Equation (5.4-3) that

$$\eta_{\text{Regenerating}} = 76.1 \quad \%.$$

The above should be compared to the following obtained directly from corrected test data:

$$\text{MPC system loss} = 2526.0 \quad \text{Watts}$$

and

$$\eta_{\text{Regenerating}} = 76.5\%.$$

Furthermore, Tables (5.4-2) through (5.4-5) give a comparison between the MPC system losses obtained directly from test data, and the corresponding MPC system losses obtained from the loss iterpolation formula of Equation (5.4-1) at various torques and speeds, for both samarium cobalt and strontium ferrite based MPC systems in the motoring and regeneration modes. Furthermore, the equi-efficiency contours based on test for the samarium cobalt, and strontium ferrite based MPC systems are given in the Ampere-RPM plane in Figures (5.4-3) and (5.4-4), respectively.

The MPC system performance at rated (15hp) 11.2 kw and peak (35 hp) 26.1 kw motor output including MPCsystem test voltage, test current and corresponding losses and efficiences obtained from test are given in Tables (5.4-6) and (5.4-7), repectively, for both MPC systems developed and tested in this investigation. Observe that advanced commutation by 30°E was necessary to attain the 35 hp peak motor output for both machines. Detailed discussion of the effects of advanced commutation was given earlier in Chapters (2.0) and (3.0).

At this stage, the calculation of the cycle efficiency when such an MPC system is used to propel a 1364 kg (3000 Lbs.) vehicle over a standard 122 seconds SAE drive cycle is in order. This is given next.

TABLE (5.4-2) SAMARIUM COBALT (parallel) MACHINE - MOTORING

SPEED (RPM)	TORQUE (N-M)	LOSS(TEST) (watts)	LOSS(FORMULA) (watts)
8230	15.25	1849.1	1817.6
7200	25.08	4137.6	4211.7
8000	14.57	1806.0	1789.2
5400	1.35	296.7	305.0
5400	5.76	765.5	804.8
3600	6.10	553.2	520.9
6900	36.27	7916.5	7909.0
1865	6.42	584.8	534.5
1814	13.37	1085.4	1228.8
5499	15.26	1587.5	1480.1
7165	13.15	1690.6	1734.8
1812	23.90	2456.9	2307.6
3785	25.13	2776.3	2865.4
1935	31.10	3898.7	3944.4
5428	32.60	7886.1	7824.6
3720	38.05	11272.2	11284.6

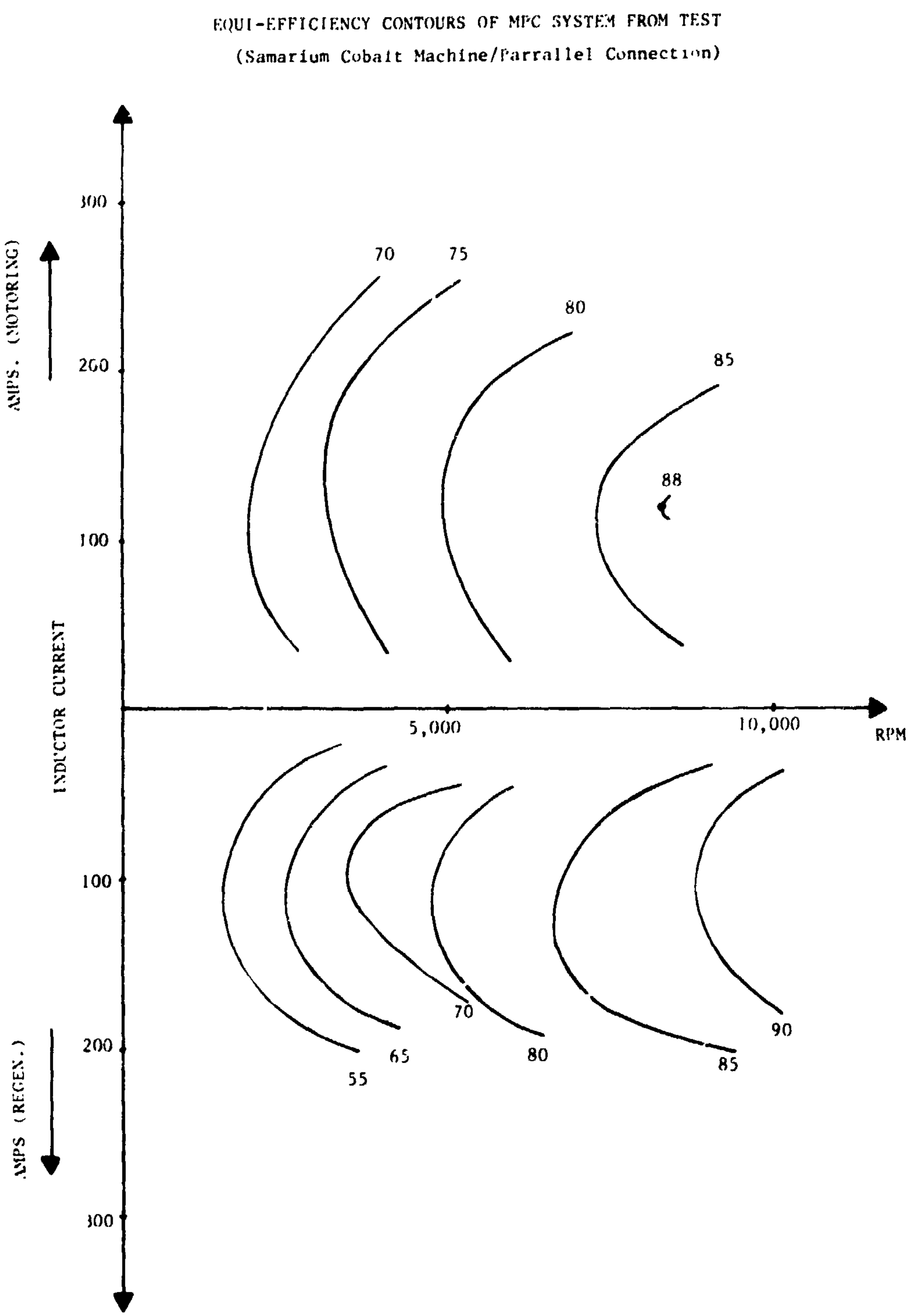

FIGURE (5.4-3) Equi-Efficiency Contours - Samarium Cobalt Case

EQUI-EFFICIENCY CONTOURS OF MPC SYSTEM FROM TEST
(Strontium Ferrite Machine/Parallel Connection)

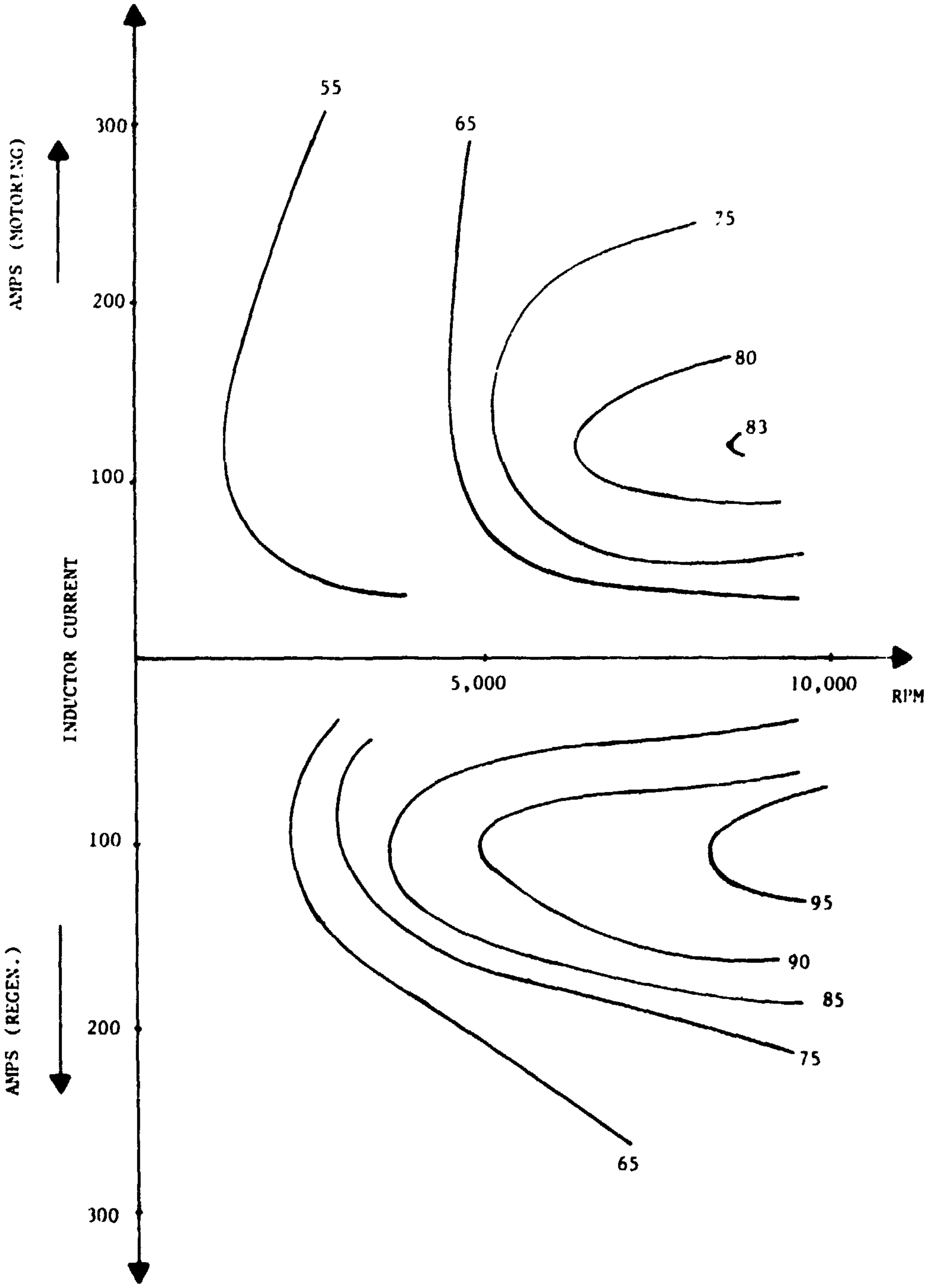

FIGURE (5.4-4) Equi Efficiency Contours - Strontium Ferrite Case

ORIGINAL PAGE IS
OF POOR QUALITY

TABLE (5.4-3) SAMARIUM COBALT (parallel)
MACHINE - REGENERATION

SPEED (RPM)	TORQUE (N-M)	LOSS(TEST) (watts)	LOSS(FORMULA) (watts)
8750	1.08	244.7	259.1
8750	5.15	534.8	53557
8720	8.81	797.3	810.0
8700	12.34	1274.8	1268.1
7140	5.15	596.4	542.6
7120	8.81	916.4	873.1
7100	12.07	1281.6	1373.0
5360	1.08	265.4	264.6
5350	5.15	566.8	558.0
5350	8.68	857.1	871.7
3590	5.15	505.2	562.6
3580	8.68	781.3	819.5
3560	11.79	1289.1	1200.8
1800	0.95	288.2	215.7
1790	8.68	689.5	676.6
5400	16.54	4301.6	4308.1
3600	14.78	2129.3	2085.8
3600	15.32	2456.0	2482.7
1800	14.91	1549.1	1593.8
1800	15.45	1986.9	1970.7
8600	14.64	2014.14	2015.5
8600	15.73	2922.6	2900.7

ORIGINAL PAGE IS
OF POOR QUALITY

TABLE (5.4-4) STRONTIUM FERRITE (parallel)
MACHINE - MOTORING

SPEED (RPM)	TORQUE (N-M)	LOSS(TEST) (watts)	LOSS(FORMULA) (watts)
9400	2.67	1335.6	1370.2
8900	5.72	1535.7	1528.8
8500	13.17	2341.0	2278.8
7110	5.04	1115.1	975.2
7160	13.17	2216.9	1353.0
5450	0.63	564.4	561.2
5450	5.72	1180.2	1292.4
5600	25.04	4300.5	4403.9
3760	11.14	3019.3	2974.7
3660	23.00	3932.8	3799.4
1850	5.72	841.9	843.8
6750	36.29	10536.3	10562.1
5400	30.46	8382.4	8204.0
3600	31.95	8595.6	8745.2
1800	29.38	4798.0	4956.5
1800	33.04	6610.7	6471.6
1800	22.60	2718.8	2703.8

TABLE (5.4-5) STRONTIUM FERRITE (parallel)
MACHINE - REGENERATING

SPEED LOSS(FORMULA) (watts)	(RPM)	TORQUE (N-M)	LOSS(TEST) (watts)
8820	5.13	559.9	563.6
8760	10.89	592.6	571.2
5400	1.40	461.2	462.4
5400	7.50	367.3	362.3
5360	10.89	793.6	794.0
1000	4.79	405.2	393.7
1803	7.84	547.0	576.5
1804	10.89	848.1	828.4
8430	14.96	3190.9	3322.7
8450	15.77	4273.1	4228.1
7180	14.28	2523.9	2567.9
7140	15.23	3604.3	3368.8
5400	14.96	2563.1	2649.8
5400	16.04	3380.7	3525.8
3600	15.23	2249.0	2255.3
3620	15.91	2837.6	2693.9
1810	14.96	1717.2	1714.2
1810	16.31	2301.9	2339.3

TABLE (5.4-6) PERFORMANCE OF THE SAMARIUM COBALT AND STRONTIUM FERRITE MACHINES AT RATED POWER CONDITION

Quantity Machine	Armature Connection	DC Line Voltage (Volts)	DC Line Current (Amps)	Speed (RPM)
Samarium Cobalt	Parallel	115.8	110.6	8640
Strontium Ferrite	Parallel	115.6	107.2	8760

Quantity Machine (%)	System Input (Watts/hp)	System Output (Watts/hp)	System Efficiency
Samarium Cobalt (15.2)	13013.2	11345.9 87.2	(17.4)
Strontium Ferritte (14.1)	12600.2	10531.1 83.6	(16.9)

TABLE (5.4-7) PERFORMANCE OF THE SAMARIUM COBALT AND STRONTIUM FERRITE MACHINES AT PEAK POWER CONDITION

Quantity / Machine	Armature Connection	DC Line Voltage (Volts)	DC Line Current (Amps)	Speed (RPM)
Samarium Cobalt	Parallel	116.9	290.1	6900
Strontium Ferrite	Parallel	120.9	297.6	6750

Quantity / Machine	System Input (Watts/hp)	System Output (Watts/hp)	System Efficiency (%)
Samarium Cobalt	34119.0	26207.5	(45.7)
(35.2)	76.8		
Strontium Ferrite	36183.4	25651.9	(48.5)
(34.4)	70.9		

EQUI-EFFICIENCY CONTOURS OF MPC SYSTEM FROM TEST

(Samarium Cobalt Machine/Parrallel Connection)

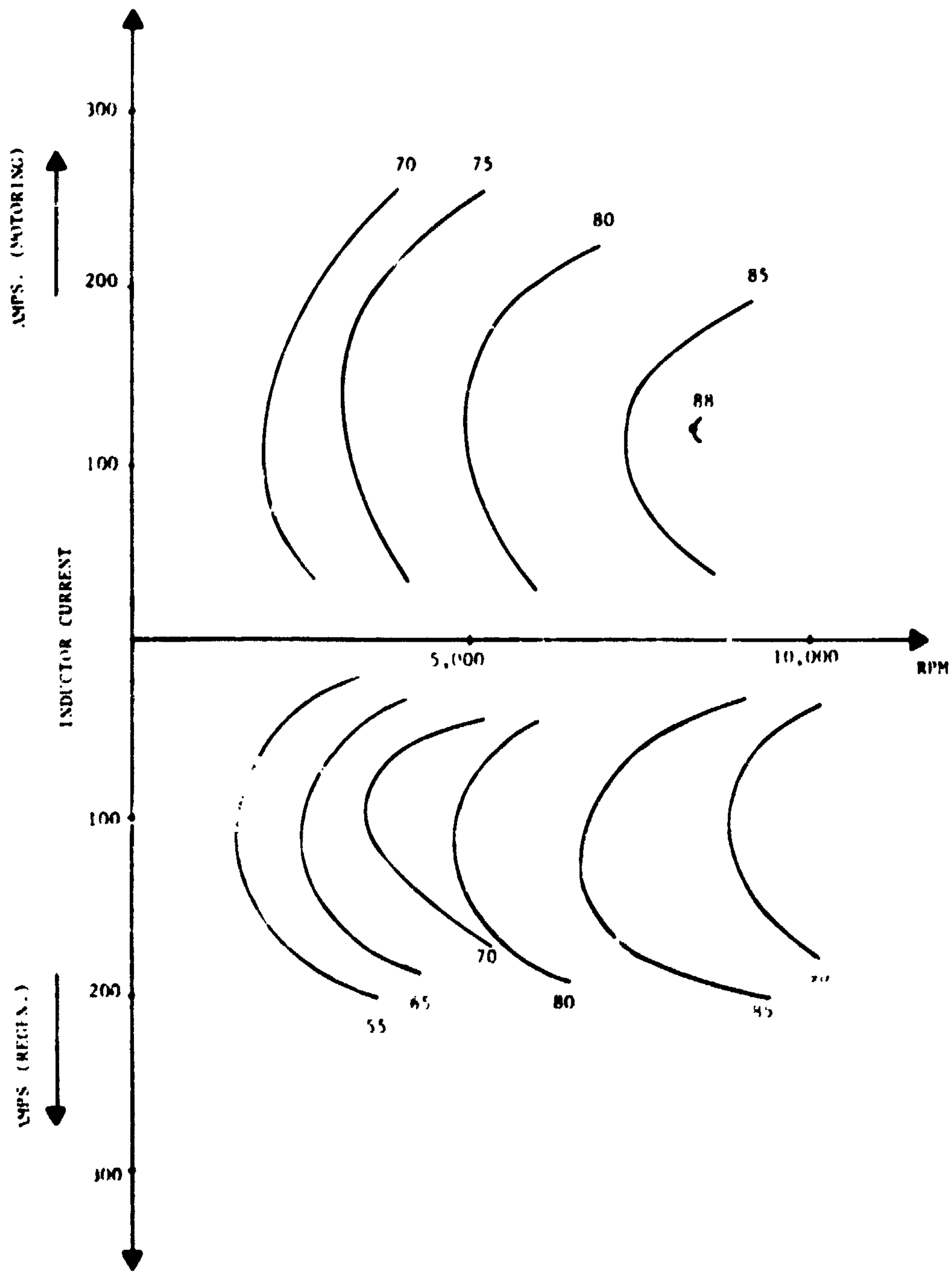

FIGURE (5.4-3) Equi-efficiency Contours
Samarium Cobalt Case

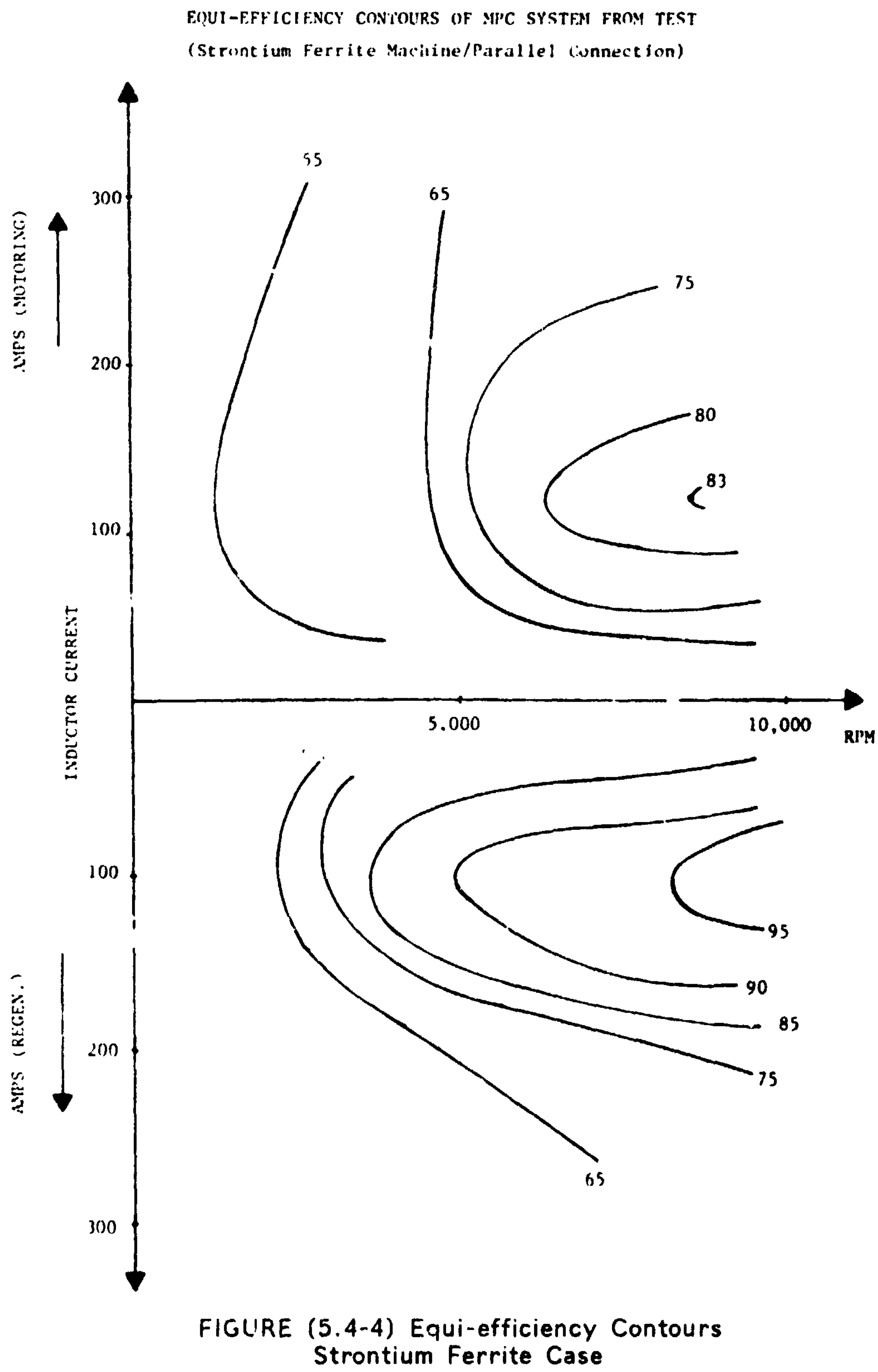

FIGURE (5.4-4) Equi-efficiency Contours
Strontium Ferrite Case

ORIGINAL PAGE IS
OF POOR QUALITY

5.5 VEHICULAR DRIVE CYCLE EFFICIENCY

In this section the samarium cobalt and stontium ferrite based MPC systems will be assumed to be utilized in the propulsion of a 1364 kg (3000 lbs.) vehicle, subject to the standard SAE drive cycle J227a-Schedule D shown in Figure (5.5-1), which depicts a typical urban pattern of driving. The performance of the two MPC systems developed during the course of this investigation is quantified here, subject to: (1) vehicular characteristics such as wind and tire resistances, as given in Reference [6], and (2) the above mentioned drive cycle.

Accordingly, the SAE J27a-Schedule D cycle efficiency of each of the two above mentioned MPC systems (when these systems are assumed to propel the above vehicle is calculated here. That is, the vehicle characteristics are always the governing factor in determining the MPC system torque and speed. This is accomplished by dividing the drive cycle into five regions, Regions (1) through (5), as shown in Figure (5.5-1). Furthermore, each region is divided into many time increments, Δt, during each of which the MPC system torque, T, and speed, ω, are calculated on the basis of the drive cycle and vehicle conditions, and are considered constant throughout the given Δt at their value at midpoint through Δt, see Figure (5.5-1). Once T and ω are calculated for each time increment, Equations (5.4-1) through (5.4-3) yield the MPC system losses, input and output powers, and efficiency, whether the system is in the motoring or regenerating mode of operation. The input energy into the MPC system and the output energy from the MPC system are thus calculated for each time increment $(\Delta t)_i$, i = 1, 2, •••, L, where L is the total number of time increments in a given region, j, under consideration, where j = 1, 2, •••, 5. Hence, for a region, j, one can write the following:

$$W(\text{losses})_j = \Sigma_{i=1}(\text{MPC Losses}_i)(\Delta t_i) \quad \text{Joules} \qquad (5.5\text{-}1)$$

$$W(\text{input})_j = \Sigma_{i=1}(P_{in_i})(\Delta t_i) \quad \text{Joules} \qquad (5.5\text{-}2)$$

$$W(\text{output})_j = \Sigma_{i=1}(P_{out_i})(\Delta t_i) \quad \text{Joules} \qquad (5.5\text{-}3)$$

where, $W(\text{losses})_j$ is the total lost energy in region, j, the MPC system using Equation (5.4-1) to obtain the system losses, (MPC Losses_i), and $W(\text{input})_j$ is the total input energy for the duration of region, j, into the MPC system. Notice that, if motoring

$$P_{in_i} = (T_i\omega_{m_i}) + (\text{MPC Losses}_i) \quad \text{Watts} \qquad (5.5\text{-}4)$$

and if regenerating,

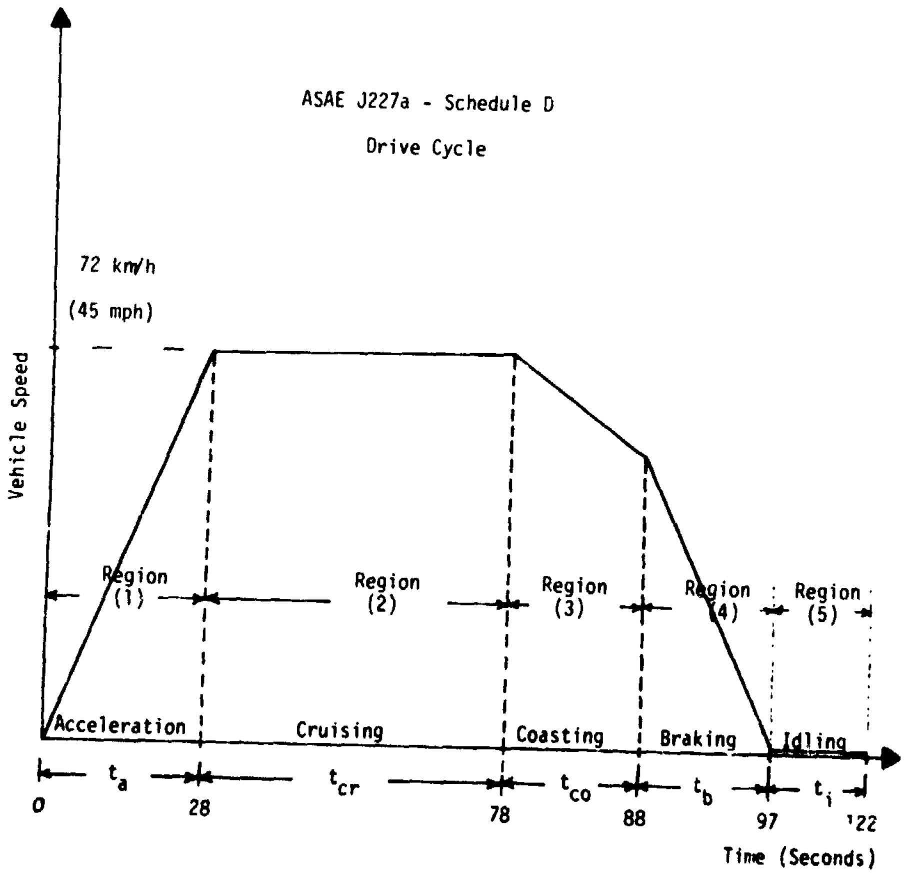

FIGURE (5.5-1) SCHEMATIC OF DRIVE CYCLE SAE J227a - SCHEDULE D

ORIGINAL PAGE IS OF POOR QUALITY

$$P_{in_i} = (T_i \omega_{m_i}) \quad \text{Watts.} \tag{5.5-5}$$

Here, ω_{m_i} is the machine speed for the i^{th} increment. Also, $W(output)_j$ is the toal output energy for the duration of region, j, from the MPC system. Notice that, if motoring,

$$P_{out_i} = (T_i \omega_{m_i}) \quad \text{Watts} \tag{5.5-6}$$

and if regenerating,

$$P_{out_i} = (T_i \omega_{m_i}) - (\text{MPC Losses}_i) \quad \text{Watts.} \tag{5.5-7}$$

The net input energy, W_{INTOT}, from the source into the MPC system is given by

$$W_{INTOT} = (\Sigma_{j=1} W(input)_j) - W(output)_4 \quad \text{Joules} \tag{5.5-8}$$

because regeneration takes place only during region (4). The net useful MPC system output energy to the drive shaft, W_{OUTTOT}, is

$$W_{OUTTOT} = \Sigma_{j=1} W(output)_j \quad \text{Joules} \tag{5.5-9}$$

because there is no useful output to the drive shaft in regions (3), (4), and (5).

Accordingly, the overall cycle effficiency is the ratio between the net useful output, W_{OUTTOT}, and the net input energy, W_{INTOT}, that is

$$\eta_{cycle} = W_{OUTTOT}/W_{INTOT} \times 100 \quad \% \tag{5.5-10}$$

Now the methods of calculation of all these powers and energies during each of the five regions are detailed next.

REGION (1):

In this region, Figure (5.5-1), the electric vehicle must be accelerated (propelled) from zero velocity to a cruising velocity of 72Km/h (45 mph) in 28 seconds subject to the forces shown in the schematic of Figure (5.5-2). Suppose that this region is divided into two subregions where the first subregion consists of accelerating the vehicle from

ORIGINAL PAGE IS
OF POOR QUALITY

VEHICLE DYNAMICS

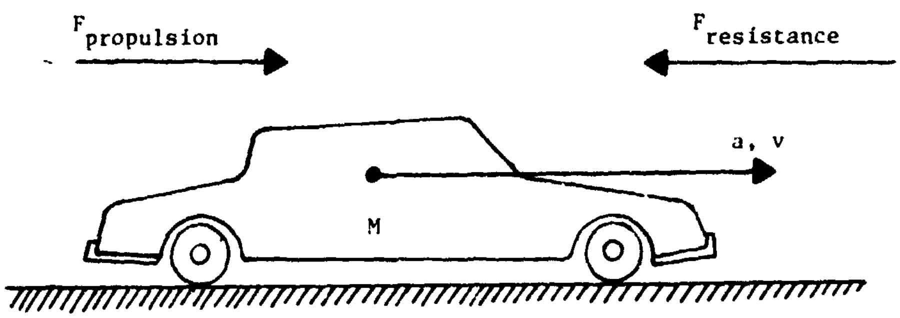

M	=	Mass of Vehicle, KG
$F_{propulsion}$	=	Propulsion Force, N
$F_{resistance}$	=	Tire (Road) and Wind (Drag) Resistance Force, N
a	=	Vehicle Acceleration, M/SEC^2
v	=	Vehicle Speed, M/SEC

FIGURE (5.5-2) VEHICLE MODELING FOR DRIVE CYCLE CALCULATIONS

ORIGINAL PAGE IS OF POOR QUALITY

zero velocity to a velocity, v_{GS}, at which the gear is shifted. In this application, V_{GS} is taken to be half of the cruising velocity, v_{CR}. The second subregion is the region from the velocity, v_{GS}, to the velocity, v_{CR}.

Let the time corresponding to the velocity v_{GS} be t_{GS}. Also let the constant acceleration of the vehicle within the first subregion be a_1 and the constant acceleration of the vehicle within the second subregion be a_2. Assume that the gear ratio at velocities below v_{GS} is GR_1 and the gear ratio at velocities above v_{GS} is GR_2. The gear ratio is defined here to be the ratio of the angular speed, ω_m, of the motor to the angular speed, ω_W, of the wheels of the vehicle. For rectilinear motion in the first subregion of region (1).

$$v_{GS} = a_1 \bullet t_{GS} \tag{5.5-11}$$

and for rectilinear motion in the second subregion,

$$v_{CR} = v_{GS} + a_2(t_a - t_{GS}) \tag{5.5-12}$$

where t_a is the time corresponding to the velocity v_{CR}. Substituting Equation (5.5-11) into Equation (5.5-12), where $v_{GS} = v_{CR}/2$ and assuming that $a_2 = a_1/2$, and solving for a_1, one obtains the following:

$$a_1 = (2v_{CR} - v_{GS})/t_a = 3\ v_{CR}/2t_a \tag{5.5-13}$$

from which

$$t_{GS} = v_{GS}/a_1 = t_a/3. \tag{5.5-14}$$

For the i^{th} instant of time, t_i, where

$$t_i = t_{i-1} + \Delta t \tag{5.5-15}$$

where Δt is a constant time increment used throughout the drive cycle in which $t_0 = 0$, one can write the following for the first subregion:

$$v_i = a_1 t_i. \tag{5.5-16}$$

The accelerating force (Newtonian) is given by

$$F_i = M \bullet a_1 \tag{5.5-17}$$

ORIGINAL PAGE IS
OF POOR QUALITY

where M is the mass of the vehicle under consideration. The rate of work done by this force is

$$P_i = F_i v_i. \tag{5.5-18}$$

Let the gear efficiency which is the ratio of the power supplied to the wheels to the power developed by the motor be k. In subsequent calculations for purposes of this work, k is taken to be unity (100% gear efficiency). Then, the power developed by the motor is given by

$$P_{m_i} = P_i/k. \tag{5.5-19}$$

If the radius of a wheel is R_W, then the angular speed of the wheel is given by

$$\omega_{W_i} = v_i/R_W \tag{5.5-20}$$

and the angular speed of the motor is given by

$$\omega_{m_i} = GR_1 \bullet \omega_{W_i}. \tag{5.5-21}$$

The motor shaft torque is therefore given by

$$T_{m_i} = P_{m_i}/\omega_{m_i}. \tag{5.5-22}$$

Now the system losses, MPC Losses$_i$, during motoring as a function of ω_{m_i} and T_{m_i} are then calculated using Equation (5.4-1) where the constants are given in the first and second rows of Table (5.4-1) for the two MPC systems developed in the course of this investigation. Hence, the total input power into the MPC system becomes

$$P_{in_i} = P_{m_i} + (\text{MPC Losses}_i). \tag{5.5-23}$$

Therefore, the change in input energy to the MPC system from time, t_{i-1} to time, t_i is given by

$$\Delta W_{in_i} = P_{in_i} \bullet \Delta t. \tag{5.5-24}$$

The change in output energy from the MPC system from t_{i-1} to t_i is given by

$$\Delta W_{out_i} = P_{m_i} \bullet \Delta t. \tag{5.5-25}$$

Thus, the total energy into the MPC system from time (= 0) to time (= t_{GS}) becomes

ORIGINAL PAGE IS
OF POOR QUALITY

$$W_{in_{11}} = \sum_{i=1}^{n_{11}} \Delta_{in_i} \qquad (5.5\text{-}26)$$

and the total energy output of the system in this time becomes

$$W_{out_{11}} = \sum_{i=1}^{n_{11}} \Delta W_{out_i} \qquad (5.5\text{-}27)$$

where $n_{11} = t_{GS}/\Delta t$.

Writing an equation similar to Equation (5.5-16) for the second subregion.

$$\begin{aligned} v_i &= v_{i-1} + a_2(t_i - t_{i-1}), \quad n_{12} \geq i > n_{11} \\ &= v_{i-1} + a_1 \Delta t/2, \quad n_{12} \geq i \leq n_{11} \end{aligned} \qquad (5.5\text{-}28)$$

where n_{11} and n_{12} designate the beginning and end of the second subregion in region (1), respectively. The accelerating force is given by

$$F_i = M \bullet a_1/2 \qquad (5.5\text{-}29)$$

and the rate of work done by this force is given by Equation (5.5-18). Also, the power developed by the motor and the angular speed of the wheels of the vehicle are given by Equation (5.5-19) and (5.5-20), respectively, for $n_{12} \geq i > n_{11}$. The angular speed of the motor is given by

$$\omega_{m_i} = GR_2 \bullet \omega_{W_i}. \qquad (5.5\text{-}30)$$

The corresponding motor shaft torque is given by Equation (5.5-22). As described earlier, the losses, MPC Losses$_i$, in the MPC system, the change in input energy to the MPC system, and the change in output energy for a duration of Δt seconds within this subregion are given by Equations (5.5-23) through (5.5-25), respectively. Therefore, the total energy into the MPC system from time (= t_{GS}) to time (= t_a) is given by

$$W_{in_{12}} = \sum_{i=n_{11}+1}^{n_{12}} \Delta W_{in_i} \qquad (5.5\text{-}31)$$

and the total energy out of the MPC system for this period becomes

$$W_{out_{12}} = \sum_{i=n_{11}+1}^{n_{12}} \Delta W_{out_i} \qquad (5.5\text{-}32)$$

where

$$n_{12} = t_a/\Delta t.$$

Hence, for Region (1), the total energy into the MPC system is given by Equations (5.5-26) and (5.5-31). That is,

$$W_{in_1} = \Sigma_{i=1}^{n_{11}} \Delta W_{in_i} + \Sigma_{i=n_{11}+1}^{n_{12}} \Delta W_{in_i}. \tag{5.5-33}$$

The total energy output of the MPC system for Region (1) is given by Equations (5.5-27) and (5.5-32). That is,

$$W_{out_1} = \Sigma_{i=1}^{n_{11}} \Delta W_{out_i} + \Sigma_{i=n_{11}+1}^{n_{12}} \Delta W_{out_i}. \tag{5.5-34}$$

REGION (2):

In this region, Figure (5.5-1), the electric vehicle must be maintained at the cruising velocity of 72 km/h (45 mph) for 50 seconds. This implies that the acceleration of the vehicle is zero and

$$v_i = v_{CR}, \quad n_2 \geq i > n_{12} \tag{5.5-35}$$

where n_{12} and n_2 designate the beginning and end of Region (2),, respectively. In addition, the power developed by the motor, P_{m_i}, the angular speed of the wheels, ω_{W_i}, the angular speed of the motor, ω_{m_i}, the developed motor torque, T_{m_i}, the input power to the MPC system, P_{in_i}, and the changes in input energy, ΔW_{in_i}, and output energy, ΔW_{out_i}, remain constant at their values at the end of Region (1), $i = n_{12}$.

Therefore, the total input energy into the MPC system in this region is given by

$$\begin{aligned} W_{in_2} &= \Sigma_{i=n_{12}+1}^{n_2} \Delta W_{in_i} \\ &= [(n_2 - n_{12}) \cdot \Delta W_{in_i}]_{i=n_{12}} \end{aligned} \tag{5.5-36}$$

and the corresponding total output energy from the MPC system is given by

$$W_{out_2} = \Sigma_{i=n_{12}+1} \Delta W_{out_i}$$
$$= [(n_2 - n_{12}) \cdot \Delta W_{out_i}]_{i=n_{12}} \qquad (5.5\text{-}37)$$

where $n_2 = (t_a + t_{CR})/\Delta{>}t$.

REGION (3):

In this region called the coasting region, Figure (5.5-1), the electric vehicle must be decelerated at a constant rate from the cruising velocity of 72 km/h for 10 seconds. This deceleration is accomplished by the resistance force acting on the vehicle due to the wind (or aerodynamics), tires to road friction, and chassis losses, see Figure (5.5-2). The above resistance was given in terms of power(in kw) as a function of velocity (in km/hr) in Reference [6]. This information is repeated here in mathematical form, as a polynomial function of velocity in Equation (5.5-38) below.

$$Res(v) = -33.3 + 201.5v - 0.11v^2 + 0.36v^3 \qquad (5.5\text{-}38)$$

where Res is the equivalent power of the resistance force in Watts and v is the velocity of the vehicle in meters per second.

At any instant, i, within this region ($n_3 \geq i > n_2$), where n_2 and n_3 designate the times at the beginning and end of region (3), respectively, the deceleration can be assumed to be equal to the deceleration at instant, (i-1), so long as the time interval, Δt between i and (i-1) is small enough. Let this deceleration (given below as negative acceleration) be a_3. Then applying Equations (5.5-17) and (5.5-18), a_3 is given as follows:

$$a_3 = -Res(v_{i-1})/v_{i-1} \cdot M. \qquad (5.5\text{-}39)$$

The velocity, v_i at instant i becomes

$$v_i = v_{i-1} + a_3\Delta t. \qquad (5.5\text{-}40)$$

The angular speed of the wheels is given by Equation (5.5-20) and the angular speed of the motor is given by Equation (5.5-21) or Equation (5.5-30) depending on whether the velocity, v_i is less than or greater than the velocity, v_{GS}, at which the gear is shifted.

By coasting, we mean that the accelerator is no longer applied, and the pwoer supplied from the battery to the MPC system, except the power (200 Watts) supplied to the low level control electroniccs, is immediately interrupted That is,

$$P_{in_i} = 200 \text{ Watts.} \tag{5.5-41}$$

Also, the vehicle attains its current velocity, v_i, by virtue of its stored kinetic energy or momentum less the energy spent to overcome the wind and tire resistance, as well as chassis losses mentioned earlier. This implies that the mechanical power out of the MPC system is zero. That is,

$$P_{out_i} = 0. \tag{5.5-42}$$

Therefore, the total energy supplied to the MPC system is given by

$$W_{in_3} = \Sigma_{i=n_2+1}^{n_3} P_{in_i} \bullet \Delta t = 200(n_3-n_2) \bullet \Delta t \tag{5.5-43}$$

and the total energy delivered by the motor is given by

$$W_{out_3} = \Sigma_{i=n_2+1}^{n_3} P_{out_i} \bullet \Delta t = 0 \tag{5.5-44}$$

where $n_3 = (t_a + t_{CR} + t_{CO})/\Delta t$.

REGION (4):

In this region, Figure (5.5-1), the electric vehicle is retarded until it attains zero velocity in 9 seconds. It is important to note that in this region the machine ceases to act as a motor but acts as a generator, returning its output power to the battery. To best understand what takes place within this region, consider that it is divided into two subregions: a regenerative braking subregion and a mechanical braking subregion. The reason for applying mechanical braking is the fact that at some point within the region, regeneration ceases to be possible because of low machine speed and generated emf. In order to stop the vehicle, mechanical braking is used to bring the vehicle to stand still (zero velocity).

Consider the regenerative braking subregion. Assume that the vehicle is retarded at a constant rate a_4 meters per second, until it attains zero velocity. Then for rectilinear motion of the vehicle from some velocity, v_{i-1}, at instant t_{i-1} to zero velocity at the instant $(t_a + t_{CR} + t_{CO} + t_b)$, the retardation (or negative acceleration) can be written as follows:

$$a_4 = -v_{i-1}/(TTB - t_{i-1}) \tag{5.5-45}$$

where $n_4 \geq i > n_3$. Therefore $(i-1) \geq n_3$ and $t_{i-1} \geq t_a + t_{CR} + t_{CO}$. Notice that in Equation (5.5-45), $TTB = t_a + t_{CR} + t_{CO} + t_b$, shown in Figure (5.5-1). Also, notice that n_3 and n_4 designate the instants in time at the beginning and end of Region (4), respectively.

The velocity, v_i, of the vehicle at instant, t_i becomes:

$$v_i = v_{i-1} + a_4 \bullet \Delta t. \qquad (5.5\text{-}45)$$

The angular speed of the wheels of the vehicle is given by Equation (5.5-20), from which the angular speed of the motor, ω_{m_i}, will be given by either Equation (5.5-21) or Equation (5.5-30), depending on whether the velocity of the vehicle, v_i, is less than or greater than its velocity, v_{GS}, when the gear is shifted.

From instant n_3 until such a time when regeneration is no longer practical, the brakes are applied essentially to instruct the control electronics of the MPC system to cause regeneration. In which case the machine is producing a torque opposite to the direction of the torque during motoring, that is, it produces a retarding torque. Notice that the machine torque in this case is opposite to the machine speed, ω_m.

From the plots of power versus torque shown in Figures (5.3-9) through (5.3-11) for the strontium ferrite MPC system and from similar plots for the samarium cobalt MPC system, optimum torque values of about 10 N-m and 14 N-m for the strontium ferrite and samarium cobalt machines, respectively, were found to regenerate the most power. Hence it will be assumed here that the brakes are applied such that a constant retarding torque of 10 (or 14) N-m is developed. That is,

$$T_{m_i} = TOR \quad \text{N-m} \qquad (5.5\text{-}47)$$

where TOR = 14 N-m or 10 N-m depending on whether the machine is the samarium cobalt or strontium ferrite type. The corresponding losses, $Loss_i$, in the MPC system are given as a function of the speed, w_{m_i}, and the torque T_{m_i} in Equation (5.4-1) with the constants of the second and fourth rows of Table (5.4-1).

The mechanical power from the machine is given by

$$P_{m_i} = T_{m_i} \cdot \omega_{m_i}. \tag{5.5-48}$$

Since the power returned from the MPC system to the battery is in a direction opposite to the input power from the b ttery to the MPC system, the former direction of flow of power will be assigned a negative direction to preserve the chosen convention. In other words, the input power from the battery to the MPC system during regenerative braking is given by

$$P_{in_i} = -P_{m_i} + (\text{MPC Losses}_i) \tag{5.5-49}$$

the change in input energy into the MPC system is given by Equation (5.5-24). Since none of the mechanical power developed by the machine is used to propel the vehicle, the "useful" output power and change in output energy are zero. Thus the total "useful" output energy during regenerative braking is given by

$$W_{out_{4rb}} = 0 \tag{5.5-50}$$

and the total input energy into the MPC system is given by

$$W_{in_{4rb}} = \Sigma_{i=1}^{n_{4r}} P_{in_i} \cdot \Delta t \tag{5.5-51}$$

where $n_3 < n_{4r} < n_4$, $n_4 = TTB/\Delta t$ and $n_{4r} = t_i/\Delta t$ corresponds to the instant at which regeneration ceases, when the motor speed is below a certain threshold beyond which regeneration is impractica.

Now consider the mechanical braking subregion. This subregion begins where regenerative braking stops. This point corresponds to the instant at which no net power is returned to the battery. Therefore, the input power into the MPC system is solely given by Equation (5.5-41), which is the 200 Watts supplied to the control electronics. The velocity of the vehicle and the instant at which regeneration ceases was determined by a simple iterative process. Let this instant be t_r, and let an instant, $t_{i-1} < t_r$ be when regeneration still holds. Instant, $t_i > t_r$, is when regeneration is no longer practicable. Notice that $(t_r - t_{i-1}) < (t_i - t_r)$. This iterative process to find t_r consists of successively halving the interval Δt between t_{i-1} and t_i until t_i approaches t_r. This is the point where the power, P_{in_i} at instant, t_i returned to the battery is zero (or is within some previously chosen tolerance value).

Beyond instant, t_r, mechanical braking takes place. Notice that when the mechanical brakes are aplied the control electronics are designed to deactivate the entire MPC system. In this case no power is consumed by the MPC system, except for the 200 Watts which must be delivered continuously to the control electronics. That is, the total energy supplied to the MPC system is given by

$$W_{in_{4mb}} = 200\ (n_4 - n_{4r}) \bullet \Delta t. \tag{5.5-52}$$

The "useful" output energy is zero

Therefore, for the braking region, the total input energy into the MPC system is given by

$$\begin{aligned} W_{in_4} &= W_{in_{4rb}} + W_{in_{4mb}} \\ &= \sum_{1}^{n_{4r}} P_{ini} \bullet \Delta t + 200(n_4 - n_{4r}) \bullet \Delta t. \end{aligned} \tag{5.5-53}$$

The "useful" output energy from the MPC system is given by

$$W_{out_4} = 0. \tag{5.5-54}$$

<u>REGION</u> (<u>5</u>):

By idling, Figure (5.5-1), we mean that the electric vehicle is at a standstill for 25 seonds. The only power consumed in the MPC system is the 200 Watts taken up by the low level control electronics. The total energy supplied by the battery to the MPC system is written as follows:

$$W_{in_5} = 200t_i \tag{5.5-55}$$

where t_i is the idling time, Figure (5.5-1), not to be confused with the general time instant, t_i, used throughout this development. The output energy from the MPC system used to propel the electric vehicle in Region (5) is therefore zero. That is,

$$W_{out_5} = 0. \tag{5.5-56}$$

Thus for the entire vehicular drive cycle, the total energy, W_{INTOT}, supplied from the batery to the MPC system can be written as follows:

$$W_{INTOT} = W_{in_1} + W_{in_2} + W_{in_3} + W_{in_4} + W_{in_5}. \qquad (5.5\text{-}57)$$

Also, for the entire vehicular drive cycle, the total output energy, W_{OUTTOT}, from the MPC system is given by

$$W_{OUTTOT} = W_{out_1} + W_{out_2} + W_{out_3} + W_{out_4} + W_{out_5}. \qquad (5.5\text{-}58)$$

Therefore from equations (5.5-57) and (5.5-58), the vehicular drive cycle efficiency, η_{cycle}, is given by Equation (5.5-10).

This method of drive cycle analysis described above was applied to the samarium cobalt based and strontium ferrite based MPC systems. In the case of the samarium cobalt based MPC system, a cycle efficiency, η_{cycle} = 83.6% was obtained. Meanwhile, in the case of the strontium ferrite based MPC system, a cycle efficiency, η_{cycle} = 75.0% was obtained.

The above cycle efficiencies were obtained subject to the following

v_{CR} = 20 meters/second = 72 km/h
v_{GS} = 10 meters/second = 36 km/h
M = 1364 kg
GR_1 = 20.1448
GR_2 = 10.0724
R_w = 0.279 meters

and

Δt = 1.0 seconds.

These cycle efficiency calculations complete the design, construction and testing of the two improved electronically commutated brushless dc machine systems developed in the course of this investigation. In the following chapter, conclusions, assessment of results and experience gained from this work, and prospective future effort is outlined.

C - 4

REFERENCES CITED IN CHAPTER (5)

1. Johnson, L. W. and Riess, R. D, Numerical Analysis, Addison-Wesley Co., 1977.

2. Beckett, R. and Hurt, J., Numerial Calculations and Algorithms, McGraw-Hill Co., 1967.

3. SAS User's Guide, SAS Institute, Inc. SAS Circle, Box 8000, Cary, NC, 27511-8000.

4. Demerdash, N. A., Miller, R. H., Nehl, T. W., Overton, B. P., and Ford, III, C. J., "Comparison Between Features and Performance of Fifteen HP Samarium Cobalt and Ferrite Brushless DC Motors Operated by Same Power Conditioner," IEEE Transactions on Power Apparatus and Systems, Vol. PAS-102, 1983, pp. 104-112. [See Appendix (10).]

5. Miller, R. H., Nehl, T. W., Demerdash, N. A., Overton, B. P., and Ford, C. J., "An Electronically Controlled Permanent Magnet Synchronous Machine-Conditioner System For Electric Passenger Vehicle Propulsion," Proceedings of the IEEE-IAS-1982 Meeting, San Francisco, October 4-7, 1982, pp. 506-511. [See Appendix (11).]

6. Ross, J. A., and Wooldridge, G. A., "Preliminary Power Train Design for a State of the Art Electric Vehicle," DOE/NASA/0592-78/1 Report, NASA CR-135340, Rohr Industries, Inc. RHR-78-035, April, 1978.

6.0 CONCLUSIONS AND PROPOSED IMPROVEMENTS

In this chapter, conclusions are drawn on the basis of the work reported on in Chapters (1.0) through (5.0) of this report. In addition, suggested options for future improvements on such brushless Machine-Power Conditioner system components are discussed in light of the findings of this investigation.

6.1 PROJECT ACCOMPLISHMENTS

The samarium cobalt and strontium ferrite based machine-power conditioner (MPC) systems developed in this investigation were dynamometer tested under rated 15 hp (11.2 kw) output conditions. These tests were run for each MPC system for a period of two hours. This was done to ascertain the thermal characteristics of each MPC system, and determine its ability to operate continuously under rated conditions. These tests were conducted successfully, and revealed overall MPC system efficiencies of about 88% and 84% for the samarium cobalt and strontium ferrite based systems, respectively, at rated 15 hp (11.2 kw) conditions.

The two MPC systems were also dynamometer tested successfully under peak load conditions of 35 hp (26.1 kw) for more than one minute each. These tests were made to ascertain the ability of both MPC systems to deliver high values of output power for short periods of time for purposes of acceleration, hill climbing, and other overload conditions. These tests revealed efficiencies of about 77% and 71% for the samarium cobalt and strontium ferrite based systems, respectively, at peak one minute output of 35 hp (26.1 kw).

Other loading conditions covering the entire range of output from zero to peak value were conducted successfully for purposes of obtaining the loss and efficiency characteristics for both systems. On the basis of thee tests, the SAE J227a Schedule D drive cycle efficiencies were calculated for both MPC systems developed here. These drive cycle efficiencies were found to be about 84% and 75% for the samarium cobalt and strontium ferrite based systems, respectively, when propelling a vehicle of 1364 kgs (3000 lbs). Accordingly, the goals of this project have been accomplished, and the experience gained here points to a number of possible future improvements which are discussed next.

6.2 PROPOSED MACHINE IMPROVEMENTS

An additional mechanical gear should be considered in lieu of the series-parallel switching arrangement which was designed into the motor. For both machines developed here, test results have demonstrated that the acceleration time of 28 seconds can be met using the parallel connection only. For faster acceleration or less battery drain, an additional mechanical gear would be more economical than the switching arrangement. In addition, an entirely mechanical gear shift would be less confusing to the operator than a hybrid mechanical-electrical system.

Sophisticated computer aided design tools have been perfected since the inception of this project. These tools are namely; 1) the ability to determine, with high degree of certainty, the magnetic loading conditions, and motor parameters using the method of magnetic field analysis by finite elements, 2) the ability to vary machine geometry in computer modeling, and study their impact on machine parameters, and 3) the ability to include parameters numerically obtained above in predicting MPC system dynamic performance. While the use of these tools would not be expected to achieve spectacular improvements in system performance, significant improvements would be anticipated. Perhaps the most significant benefit of this approach is the radical reduction of the risk of costly design mistakes, with their consequent prototype reconstruction.

Resorting to a higher voltage, lower current system would result in some advantages in the motor fabrication process and may lead to reduction in battery drain during starting and peak power conditions. Further discussion of the impact of higher voltages on the system performance is given in the next section.

The rotor position sensing could be accomplished with four detectors instead of the present six detectors. The magnet structure which excites these sensors could be simplified. Furthermore, the resort to sinusoidally shaped phase currents through power electronic control techniques can lead to some improvements in commutation, and associated motor performance, including possible reduction of losses.

6.3 PROPOSED POWER CONDITIONER IMPROVEMENTS

Since the beginning of this project, significant improvements in characteristics and capabilites of solid state power switching components have been introduced into the market. In any future effort of redesigning and building MPC systems similar to the two systems developed here, these new and improved solid state switching components (transistors and diodes) can have significant impact on design simplification, and improvement of efficiencies of such systems.

These improved transistors and diodes make it more feasible to eliminate the choke and chopper from the present power conditioner circuit, and merge their function of dc line current, torque and speed control into the inverter/converter bridge portion of the power conditioner. This would simplify significantly the physical layout and packaging of the power conditioner. It would also permit the additional operating mode of plugging, and would provide for continuous full regenerative braking torque through zero speed.

Built-in "flyback" diodes available with improved power transitors make it possible to choose smaller heat sinks, and further shorten leads, and other conections involved in the layout and packaging of such systems. This reduces system inductances and has beneficial effects on commutation characteristics, and accompanying losses. Liquid cooling schemes should also be considered for purposes of achieving packaging and layout improvements.

Improved power switching components, and reduced inductances of lead connections, resulting from improved packaging and layout, can lead to significant simplification of snubber and clamping circuitry, and achievement of higher MPC system ratings, if desired.

Resorting to higher values of rated supply voltage can lead to significant reduction in system current magnitudes, and hence can lead to improvements in system efficiencies. The newer improved transistors mentioned above are generally designed for higher voltage, lower current operation, and thus would be suited to the suggested higher operating voltages. This reduction in current magnitudes can also simplify the phase commutation process, and lead to alleviation of (L di/dt) problems associated with the commutation process. Namely, this would reduce voltage spikes associated with commutation. These are the voltage spikes which are a main cause of solid state switching component failure.

Much room is left for improvement of protective systems suited for use in these brushless dc electronically commutated machines. Such future improvements should be directed towards increasing user abuse resistance of such MPC systems. In additicn, faster "turn on"/"turn off" times of the low power level control electronic components would enable turning off most of the control electronics during idling and coasting periods. This would lead to further power conditioner performance improvements.

Finally. the acomplishments of this investigation, which were detailed above, should serve as a solid base from which future improvements can be launched.

ACKNOWLEDGEMENTS

The authors wish to acknowledge the efforts of Mr. B. P. Overton in the design, fabrication, and testing of the machines reported on here, and the efforts of Messers C. J. Ford and S. Coulon in the design, fabrication,and testing of the power conditioner used to operate these machines. Messers Overton, Ford, and Coulon are of the Industrial Drives Division of Kollmorgen Corporation, Radford, Virginia, formerly R and D Center of Inland Motor.

Our thanks also go to Dr. R. J. Churchill, former Vice President and Director of Inland Motor R and D in the early stages of this investigation, who provided the facilities for construction and testing of this hardware. Our thanks also go to Mr. W. Keeney, Vice President of Engineering, Industrial Drives Division of Kollmorgen Corporation, Radford, Virginia, who managed the Kollmorgen team in the final stages of this investigation.

The authors wish to acknowledge the efforts of numerous previous graduate students who obtained their MS or Ph.D. degrees on the basis of work related to this project. Prominent among those students is F. A. Fouad.

The authors wish to express their gratitude to Ms. Roxan J. Rickborn, Mrs. Lynne K. Sawyer and their associates for the patience and perseverance they exhibited in typing the manuscript of this report.

APPENDIX (1)

ON THE MAGNETIC FIELD ANALYSIS BY FINITE ELEMENTS

Fouad, F. A., Nehl, T. W., and Demerdash, N. A., "Magnetic Field Modeling of Permanent Magnet Type Electronically Operated Synchronous Machines Using Finite Elements," IEEE Transactions on Power Apparatus and Systems, PAS-Vol. 100, 1981, pp. 4125-5135.

MAGNETIC FIELD MODELING OF PERMANENT MAGNET TYPE ELECTRONICALLY OPERATED SYNCHRONOUS MACHINES USING FINITE ELEMENTS

F. A. Fouad, Student Member, T. W. Nehl, Member, N. A. Demerdash, Senior Member
Virginia Polytechnic Institute and State University
Blacksburg, VA 24061

Abstract-The finite element method is applied to the analysis of electronically operated permanent magnet type synchronous machines. In this class of machines, the armature MMF is a discretely forward stepping one of high harmonic content. The discretely stepping MMF is accounted for by a series of finite element field solutions as the rotor moves throughout one complete cycle of the ac armature current. Because of the discretely forward travelling MMF, a series of finite element grids depicting the rotor at various equally spaced locations, covering its movement during one cycle of the armature current, is required. This is accomplished by means of an automated algorithm for generation of the required finite element grids. This allows one to match any stator grid to any rotor grid for any given displacement between the two grids. This matching is done in the air gap region by fitting it with a suitable row of triangular elements. In addition, a permanent magnet model is developed based upon the magnet geometry and material properties. This method was applied to the analysis of a 15 hp samarium cobalt machine at both rated and no load conditions. The calculated results were in excellent agreement with search coil measurements at both of these operating conditions. These solutions were then used to determine the midgap EMF waveforms. The calculated midgap EMF was in excellent agreement with an oscillogram of the actual EMF in both waveshape and magnitude. The core losses at rated and no load conditions were also determined on the basis of this field analysis and found to be closer to test results than those calculated using standard design calculation procedures.

INTRODUCTION

Electronically operated permanent magnet type synchronous machines are finding increasing use in actuation, machine tool drives, vehicle propulsion, brushless excitation systems for large turbine generators, as well as other applications. In this class of machines, the armature MMF is a discretely forward stepping one of high harmonic content.

A review of the literature reveals that the bulk, if not the totality, of previous investigations of magnetic fields in synchronous machines, using various numerical techniques, was directed towards the study of large synchronous generators of the cylindrical and salient pole rotor type.[1-7] Also, Erdelyi et al[16] have investigated the ripple effect on the flux picture due to the movement of rotors versus stators in brush type dc machines. In these investigations, classical synchronously rotating, or stationary MMF concepts were used. That is, the MMFs due to the armature and field were considered stationary with respect to each other for a given load condition.

81 WM 179-1 A paper recommended and approved by the IEEE Rotating Machinery Committee of the IEEE Power Engineering Society for presentation at the IEEE PES Winter Meeting, Atlanta, Georgia, February 1-6, 1981. Manuscript submitted September 2, 1980; made available for printing December 1, 1980.

This, however, is not the case for electronically operated synchronous machines with nonsinusoidal armature currents. In this case, the field is no longer smoothly rotating, but rather a discretely forward stepping one. Hence, the classical approach mentioned above is not applicable. Therefore, a new approach, based on a series of finite element solutions, is introduced. In this approach, the stepping MMF is accounted for by a series of field solutions over one complete ac cycle of the armature current. This series of solutions corresponds to equally spaced rotor positions over the ac cycle. Based on the resulting series of solutions, a number of important performance characteristics are calculated. These calculated characteristics include core losses, eddy and hysteresis, in which minor loop effects due to distorted flux density profiles are included. These calculations include midgap flux density waveforms, induced midgap EMFs in the armature, magnetization and demagnetization patterns in the permanent magnets, as well as other parameters.[10]

Further use of this type of field analysis in the determination of key machine parameters for purposes of dynamic simulation of machine-power conditioner interaction is given in a companion paper.[14] It is shown in reference (14), how helpful such a magnetic field model is, in the prediciton of machine performance in the absence of actual hardware for physical testing.

SYSTEM DESCRIPTION

The method of analysis presented here is applied to a three phase, 15 hp, 7600 rpm,120 volt, 4 pole electronically operated samarium cobalt permanent magnet synchronous machine. This machine is fed by a transistorized power conditioner. The machine-power conditioner unit is shown in Figure (1).

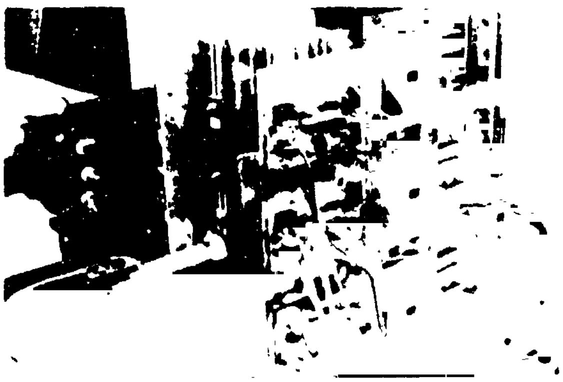

Figure 1. Machine-Power Conditioner Unit in its Final Form

A schematic diagram of the combined machine-power conditioner unit is depicted in Figure (2). The power conditioner consists of a two quadrant hysteresis type dc current chopper and a three phase transistorized inverter-converter bridge. The chopper controls the dc line current which feeds the inverter-converter bridge. This is equivalent to controlling machine torque. The bridge converts the dc current into three phase ac currents of approximately rectangular shape as idealized in Figure (2). Notice that during one complete cycle, there are six switching or current states. The switching from state to state is controlled by a rotor position sensor mounted on the motor shaft. The rectangular current blocks produce a discretely stepping stator (armature) MMF wave in the air gap as described next.

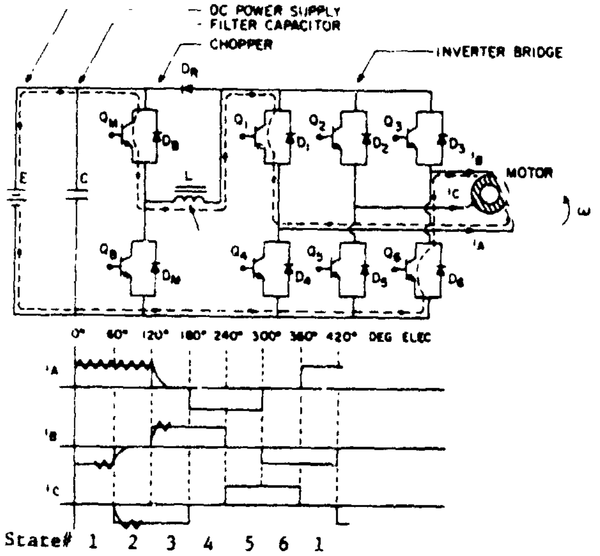

Figure 2. Machine-Power Conditioner Schematic and Idealized Phase Currents.

REPRESENTATION OF THE DISCRETELY STEPPING ARMATURE MMF

The behavior of permanent magnet synchronous machines with discretely stepping (or nonuniformly rotating) armature MMFs becomes clear upon examination of the electromagnetic interactions inside such a machine. Figure (3) gives a cross sectional view of the 15 hp machine described earlier. Included in this figure are the locations of the individual phase windings, A, B, and C in the fractional slot stator core.

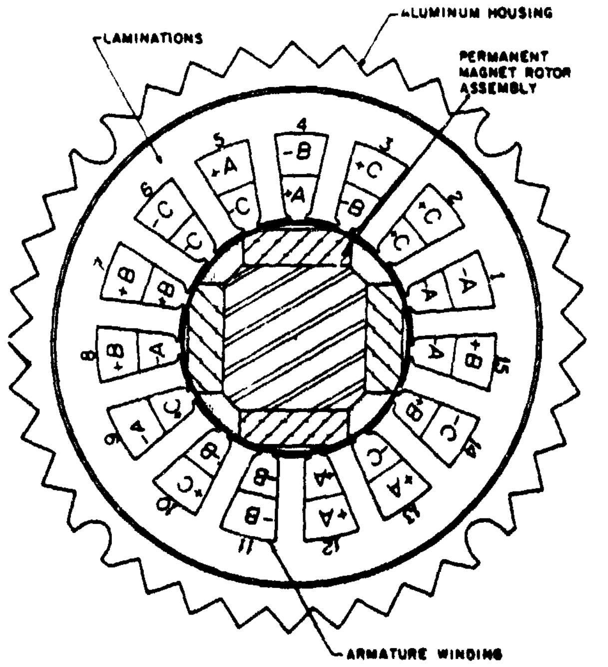

Figure 3. Machine Cross Section View with Location of Three Phase Windings.

Using this spatial distribution of the phase windings in conjunction with the idealized phase currents given in Figure (2), one obtains the spatial distribution of the armature MMF for selected points, over one complete ac current cycle. Each current cycle consists of six states as mentioned earlier. At the beginning of each state, during the motoring mode, the stator MMF leads the rotor MMF by 120 electrical degrees in the direction of rotation. This angle decreases at the end of the same state due to rotor motion and the fact that the armature MMF remains stationary during a state. At the end of such a state, the rotor position sensor signals the power conditioner to initiate the next current state. This produces a 60 electrical degree forward jump (or step) of the armature MMF in the direction of rotation. At this point, the two MMFs are again separated by 120 electrical degrees. This process is repeated six times over each ac current cycle. These repetitive, discrete armature MMF jumps lead to a machine operation which is analogous to a conventional synchronous machine operating with a variable torque angle that fluctuates between 120 and 60 electrical degrees six times in one ac cycle. Such operation would produce a pulsating torque profile.

To simulate the electromagnetic interactions during these current states, the location of the rotor with respect to the stator must be determined. Figure (5) depicts the currents inside the stator slots at the beginning of the first state. The resulting spatial distribution of the armature MMF is given immediately below the stator slots in the same figure. Notice that this waveform is unsymmetrical due to the fractional slot winding. The position of the rotor magnetic (MMF) axis lags by 120 electrical degrees at the beginning of this state as shown in Figure (4), while at the end of the same state, this angle reduces to 60 electrical degrees as shown in Figure (5). Figure (6) shows the beginning of the next state.

In order to adequately represent the stepping nature of the magnetic field picture inside this machine, thirty field solutions, spanning one ac cycle, were obtained using the method of finite elements. Consequently, each of the six current states is represented by five solutions. The implementation of these solutions requires the ability to rotate the rotor finite element grid with respect to the stator grid. Details of this process are given next.

GENERATION OF MACHINE FINITE ELEMENT GRIDS

The thirty field solutions mentioned above require thirty different finite element grids. Generation of these grids manually would be extremely tedious because of the complex topologies involved and the fact that all four pole pitches must be included due to the fractional slot winding in this case.

The stator grid is generated automatically by means of a generalized stator slot pitch module as shown in Figure (7). The rotor grid is generated in a similar manner using the generalized rotor pole module given in the same figure. These modules are totally flexible in the sense that all major geometrical dimensions can be specified at will. Furthermore, the number of stator and rotor modules in a given grid is completely controlled by the user. This allows one to model either a single pole pitch or the entire machine cross section if required.

The finite element grids for the thirty field solutions are generated by fixing the stator grid with respect to the coordinate axes and rotating the rotor grid with respect to the stator for the thirty positions.

At each position the rotor and stator grids are joined together in the air gap by means of a row of elements that is uniquely determined for each position by means of an air gap fitting algorithm, details of which are to be found in Appendix (A). It must be emphasized that the stator and rotor grids are generated only once during this sequence of solutions. The stepping of the rotor is accomplished by rotation of the nodal coordinates that form the rotor grid. However, the element equations that represent the rotor and stator portions are in-

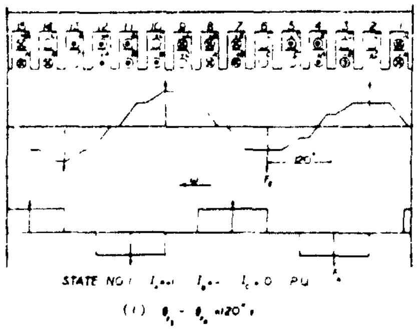

Fig. 4. Spatial Distribution of Stator and Rotor MMFs at Start of State (1)

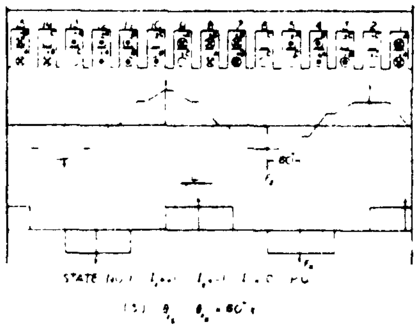

Fig. 5. Spatial Distribution of Stator and Rotor MMFs at End of State (1)

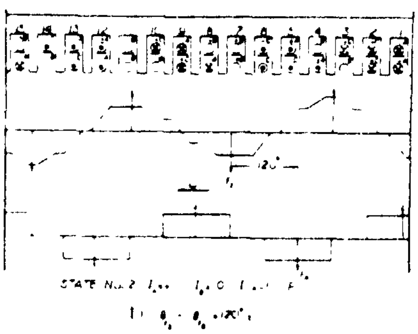

Fig. 6. Spatial Distribution of Stator and Rotor MMFs at Start of State (2)

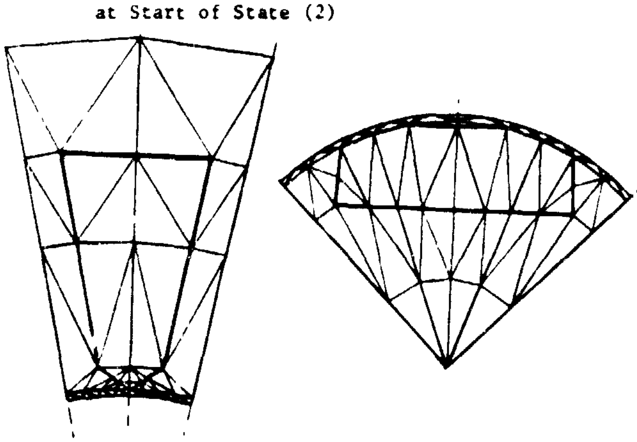

Fig. 7. Finite Element Grid of a Stator Slot and a Rotor Pole Pitch Modules

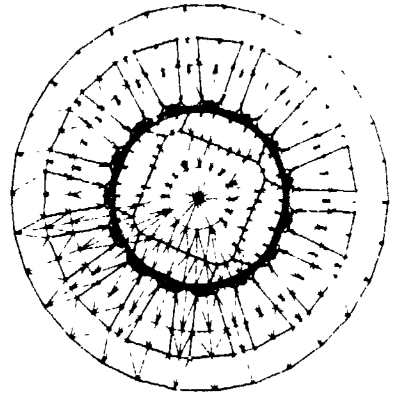

Fig. 8. Finite Element Grids at Start of State (1)

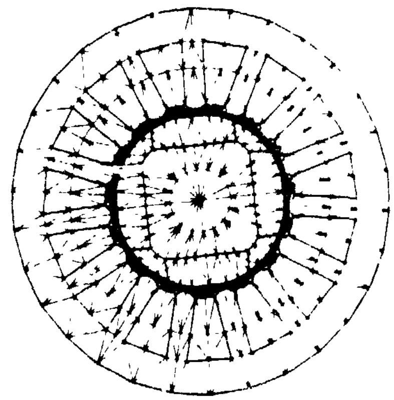

Fig. 9. Finite Element Grids at End of State (1)

variant to this angular displacement (or stepping) and hence are calculated only once. This counterclockwise rotation of the rotor grid versus the stator is clearly shown in Figures (8) and (9) which depict the rotor positions at the beginning and end of state number one, respectively. In the next section, a magnet model applicable to the finite element method is derived. This model is based upon the magnet geometry and material properties.

PERMANENT MAGNET MODEL

A permanent magnet model suitable for use with the finite element method is derived in this section in terms of the magnet geometry and material properties. Consider the simple magnetic circuit consisting of a permanent magnet in series with an iron core and air gap, as shown on the left side of Figure (10). If one neglects the MMF drop in the iron core, the operating point of the magnet is obtained from the intersection of the magnet's normal demagnetization characteristic and the air gap line. This intersection is marked by point #1 on the right side of Figure (10). Inclusion of the magnetic saturation in the iron core (that is, the MMF drop in the iron), shifts the operating point to point #2 as shown in the figure.

This magnetic circuit can be replaced by an equivalent circuit consisting of a coil in series with the same iron core and air gap. This coil has the same dimensions and magnetization profile as the magnet. However, the intersection of this profile with the H (field intensity) axis is shifted from the point, $-H_C$

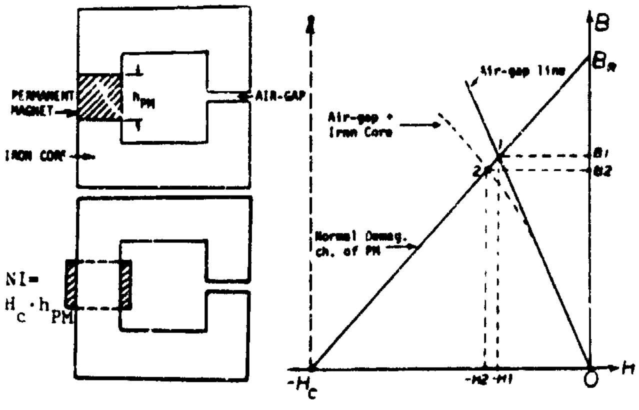

Fig. 10. Operating Point of a Magnetic Circuit Containing a Permanent Magnet

(coercivity), to the origin, Figure (10). The ampere turns, NI, of this equivalent coil are obtained by multiplying the height of the magnet in the direction of magnetization, h_{PM}, by the coercivity, H_C, in the case of rectangular shaped magnets.

For nonrectangular magnets, such as the one shown in Figure (11), modifications to the above mentioned approach are required. The curved portions of such magnets are represented by a series of infinitely thin rectangular layers which approximate this curve in a staircase fashion. This yields the continuous current sheets shown also in Figure (11). This technique has been successfully applied to the 15 hp machine introduced earlier. The accuracy of this approach is verified later in this paper by means of search coil flux and flux density measurements, under both rated and open circuit conditions. Calculated and oscillogram waveformes of the midgap EMFs were also in agreement both in shape and magnitude as will be shown later in this paper.

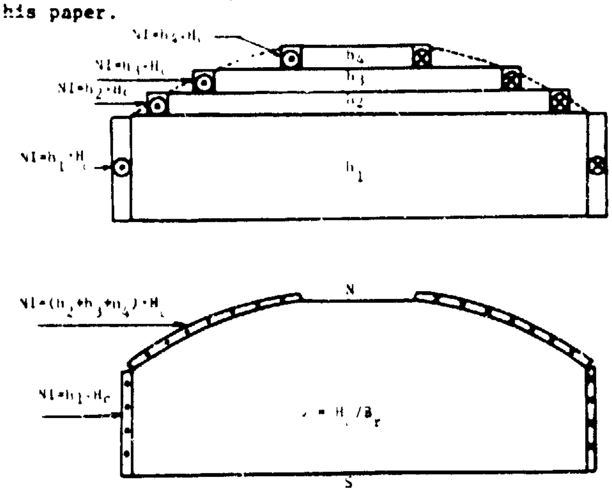

Fig. 11. Equivalent Representation of Samarium Cobalt Magnet of the 15 HP Machine

FINITE ELEMENT SOLUTIONS OF THE 15 HP MACHINE

The automatic grid generation process and the magnet model were applied to the analysis of the electronically operated 15 hp samarium cobalt permanent magnet synchronous machine. The no load and rated load field distributions were obtained by means of the finite element method for two dimensional nonlinear magnetostatic field problems. The nonlinear algebraic equations were solved by the Newton Raphson algorithm[8,9,10] Furthermore, these results are used to calculate core losses and back EMF waveform during both no load and rated load operation.

Rated Load Case

Under rated load condition a number of field solutions is required for each of the six states in an ac cycle. Five solutions per state were found adequate. That is the rated load condition was simulated by thirty field solutions, which cover one complete ac cycle, in order to include the effects of the stepping armature MMF. These solutions are later used to determine the core losses in the stator laminations. Three of these thirty field solutions are depicted in Figures (12) through (14), by means of magnetic vector potential contours, corresponding to the beginning, middle and end of state number one respectively. It is assumed all along in these solutions that magnetostatic field formulation holds in spite of any minor eddy current disturbance caused by the sudden stator MMF jumps.

The radial air gap flux density waveforms for the beginning and end of state number one are shown in Figures (15) and (16), respectively. The effect of the slot openings and the rotor movement are clearly visible in these figures. The radial air gap flux densities are used later in this paper to generate the phase midgap EMF profiles.

No Load Case

The field distribution and radial air gap flux density waveforms at no load were obtained for eight equally spaced rotor positions spanning one stator slot pitch of 24 mechanical degrees. Covering only one slot pitch during no load operation is sufficient to accurately account for the effects of flux pulsations due to slotting.

The field distribution inside the machine, at the first of these eight rotor positions, is given in Figure (17). The corresponding radial air gap flux density profile is given in Figure (18). This profile is used to determine the no load (or open circuit) back EMF waveform later in this paper.

SEARCH COIL VERIFICATION OF RESULTS

The machine, analyzed in the previous section, was constructed with two search coils for flux measurements. One of these coils was wrapped around a stator tooth near the air gap to measure the average tooth flux density. The other coil was wrapped around three teeth in order to give an approximate value of the total flux per pole. The exact flux per pole can not be measured by such means in this machine due to the fractional slot winding.

The induced search coil voltages under rated and no load conditions were recorded by an oscilloscope. These voltages were then Fourier analyzed and integrated to yield flux profiles.[10] The flux profile, of the coil around one tooth, was subsequently divided by the cross-sectional area of the tooth stem yielding the average tooth flux density waveform.

The average tooth flux density profiles, based on search coil measurements at rated and no load, are given by the solid line curves in Figures (19) and (20) respectively. The corresponding finite element calculated flux densities in each of the fifteen teeth are indicated by the circled points. These flux densities were calculated by averaging the elemental radial flux densities in the lower tooth stems. Examination of these figures reveals excellent agreement between measured and calculated results.

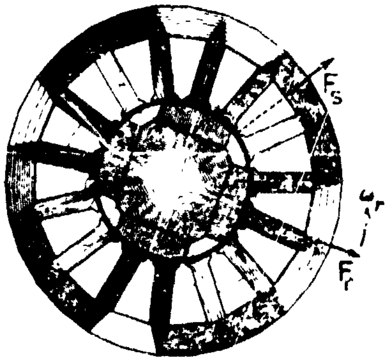

Fig. 12. Flux Distribution at Rated Load, Start of State (1)

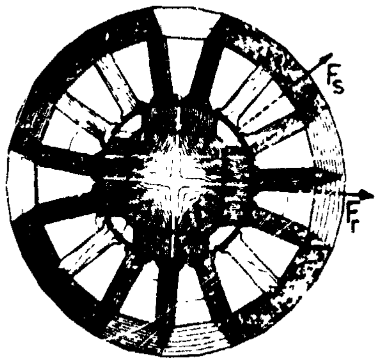

Fig. 13. Flux Distribution at Rated Load, Middle of State (1)

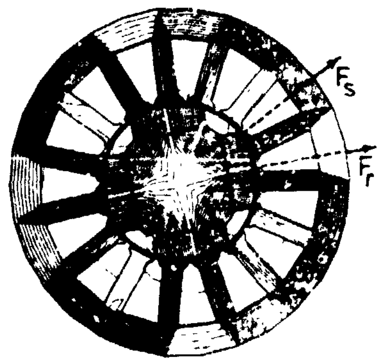

Fig. 14. Flux Distribution at Rated Load, End of State (1)

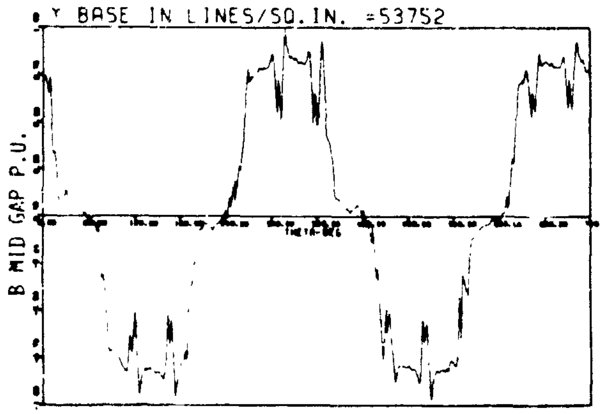

Fig. 15. Mid-Gap Radial Flux Density Waveform at Rated Load, Start of State (1)

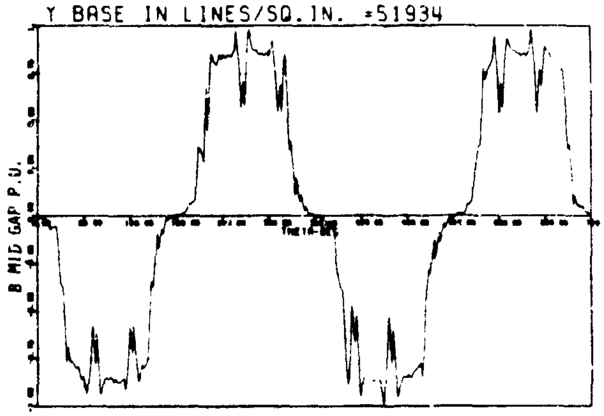

Fig. 18. Mid-Gap Radial Flux Density Waveform at No Load

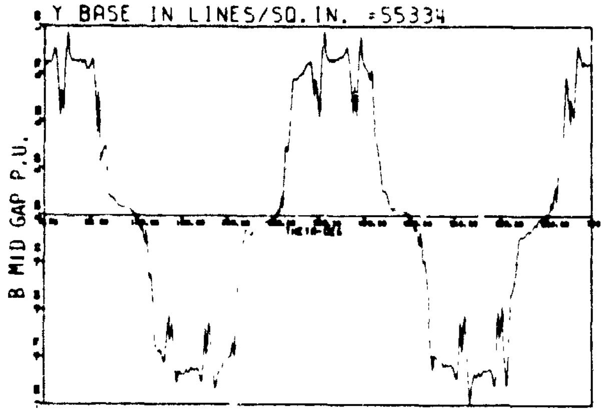

Fig. 16. Mid-Gap Radial Flux Density Waveform at Rated Load, End of State (1)

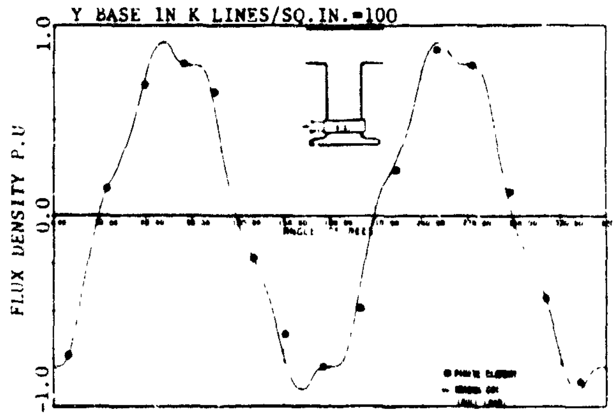

Fig. 19. Average Tooth Flux Density at Rated Load

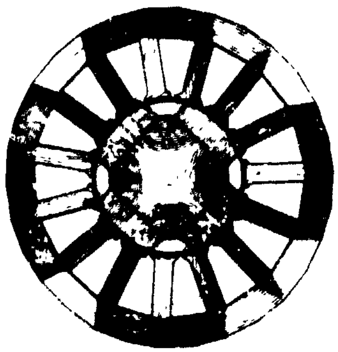

Fig. 17. Flux Distribution at No Load

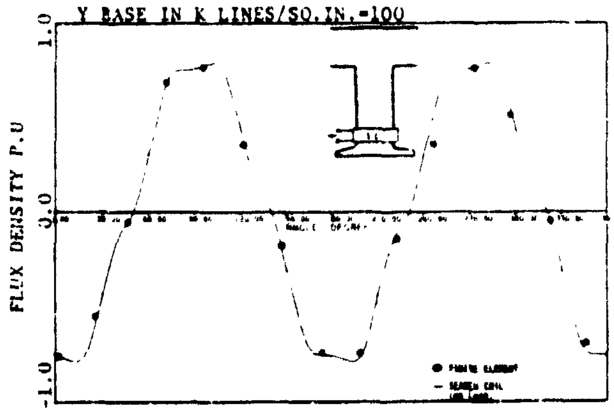

Fig. 20. Average Tooth Flux Density at No Load

The measured profiles of the total flux passing through the search coil that spans three teeth are given by the solid line curves in Figures (21) and (22) for rated and no load operation respectively. The corresponding finite element flux values are indicated by the circled dots in the figures. These points were obtained by calculating the total flux passing through fifteen consecutive sets of three teeth. That is, flux in teeth (1,2,3), flux in teeth (2,3,4), ..., and flux in teeth (15,1,2). Examination of these figures reveals excellent agreement between measured and calculated results.

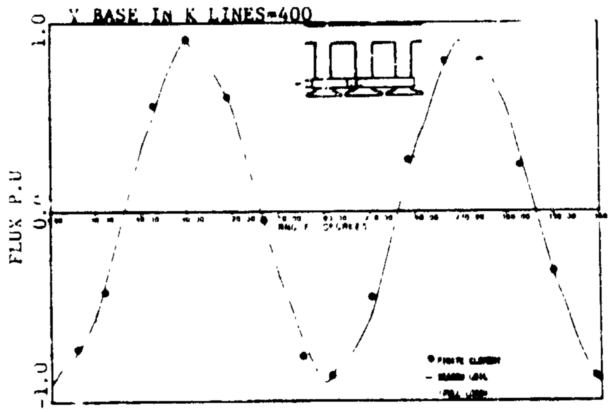

Fig. 21. Flux Through Three Consecutive Stator Teeth at Rated Load

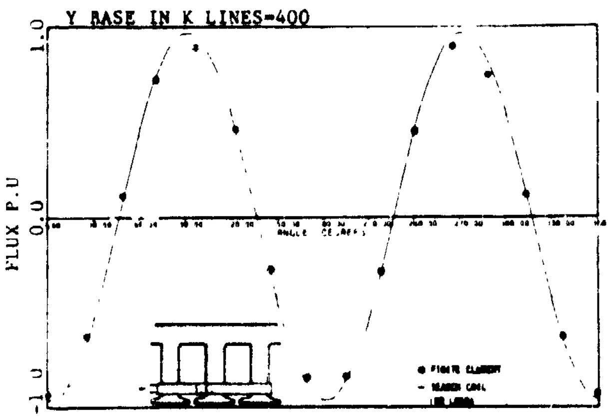

Fig. 22. Flux Through Three Consecutive Stator Teeth at No Load

This agreement between search coil measurements and the finite element results confirms the validity of the magnet model for this class of machines. Such accurate values of local flux densities and total flux are necessary for the precise determination of core losses and midgap EMF waveforms, respectively. The calculation of these parameters is discussed next.

CALCULATION OF THE MIDGAP EMF WAVEFORM

The midgap EMF waveforms during rated and no load operation were obtained from the finite element solutions given earlier. The starting point for this calculation is the radial air gap flux density distribution. This distribution is represented by a Fourier series as follows:

$$B_g(\theta) = \sum_{h=1}^{N_h} [a_h \sin(h\theta) + b_h \cos(h\theta)] \tag{1}$$

where: $B_g(\theta)$ is the radial air gap flux density
θ is the space angle (electrical degrees)
h is the harmonic order
N_h is the total number of harmonics
a_h, b_h are average values of the Fourier coefficients corresponding to the set of rotor positions per state.

The harmonic components of the flux per pole, ϕ_h, are then calculated from the machine geometry and the air gap flux density, equation (1), as follows:

$$\phi_h = \frac{2}{\pi} \ell_m \tau_p [a_h \sin(h\theta) + b_h \cos(h\theta)]/h \tag{2}$$

where: ℓ_m is the effective machine length (stator axial length times stacking factor)
τ_p is the pole pitch at mid air gap

Once the harmonic flux per pole is known, the midgap EMF waveform, e_{ph}, is obtained from the time rate of change of this flux in conjunction with the harmonic winding factors, k_{w_h}, and the number of series turns per phase, T_{ph}, as follows:

$$e_{ph} = -T_{ph} \sum_{h=1}^{N_h} k_{w_h} \frac{d\phi_h}{dt} \tag{3}$$

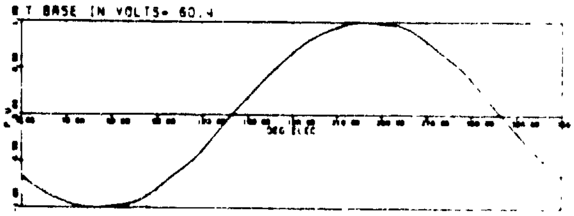

Fig. 23. Midgap EMF Per Phase at Rated Load

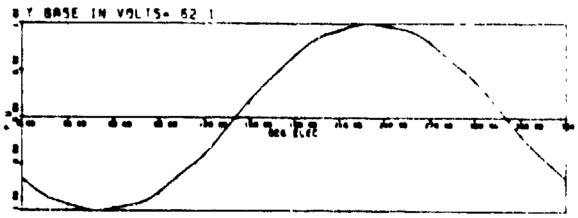

Fig. 24. Midgap EMF Per Phase at No Load

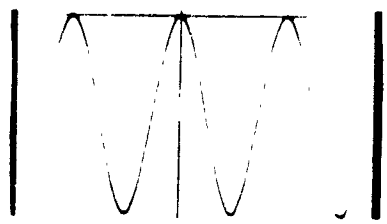

Fig. 25. Measured EMF Per Phase at No Load (Open Circuit Peak Voltage = 63.5 V)

The midgap EMF profiles for the 15 hp machine at rated and no load were calculated using this procedure at a speed of 7750 rpm. The rated and no load midgap EMF profiles for these conditions are given in Figures (23) and (24), respectively. These waveforms include all 15 harmonics used to analyze the radial air gap flux density waveforms. The measured EMF waveform per phase (open circuit voltage) at no load at a speed of 7750 rpm is given in the oscillogram of Figure (25). Comparison of the no load EMFs, Figure (24) and (25), reveals excellent agreement in both waveshape and magnitudes (within 2.2%). The EMF profiles are nearly sinusoidal due to the fractional slot winding. As expected, the midgap EMF under load drops from its no load value due to the demagnetization effect of the armature reaction. However, this drop in the EMF is very slight because of the properties of samarium cobalt magnets which have a permeability close to that of air. That is, armature demagnetization is almost negligible.

These midgap EMF waveforms are used in a network model of this machine-power conditioner unit as described in a companion paper.[14] This model is used to simulate the dynamic interactions between the machine and its associated solid state power conditioner. A further application of these field solutions for the determination of core losses is given next.

CALCULATION OF HYSTERESIS AND EDDY CURRENT CORE LOSSES

Due to the nature of the magnetic fields in this class of machines, flux density variations with time in many regions of the stator laminated core are not sinusoidal, but rather highly distorted waveforms with considerable harmonic content. This is particularly the case near the tooth tips. Under such conditions, an actual flux density waveform (radial and tangential components) in the various parts of the stator laminations must be used to obtain a better estimate of the core losses.

One of the salient advantages of using the finite element method in this analysis is that one can obtain the flux density profile in each part of the stator core over a complete cycle of the armature current, including the influence of the switching pattern of the given power conditioner to which the machine is connected. Using the 30 finite element solutions described earlier, the radial and tangential flux density profiles over one complete ac cycle of the rated armature current is obtained for each of the twenty four iron elements in one slot pitch module, Figure (7). Three of these flux density profiles are given in Figures (26), (27) and (28) for elements located in the tooth tip, in the tooth stem, and in the core, respectively. Notice that all of these profiles are nonsinusoidal. Also, notice the flux density in the tooth stem is essentially radial, as expected, while in the core it is mainly tangential.

A similar procedure was followed to obtain the flux density profiles in these elements at no load. For a given no load solution the tangential and radial flux density values are determined in each element of a given slot module and its corresponding sister elements in all other modules of the core. These fifteen flux density values are distributed with a shift of one slot pitch from one another. This process is repeated for

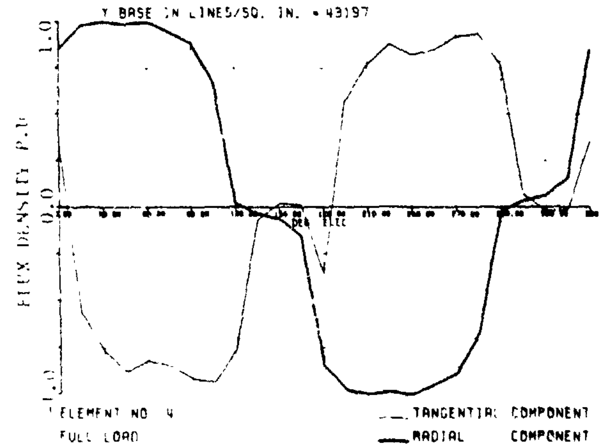

Fig. 26. Flux Density Profile in the Stator Tooth Tip at Rated Load

each of the eight no load solutions in which the rotor was shifted in equal steps over a stator slot pitch as described earlier. This is in order to assure accurate flux density profiles.

The hysteresis and eddy current core losses at rated and no load are calculated using these flux density profiles and the measured Epstien loss curves.

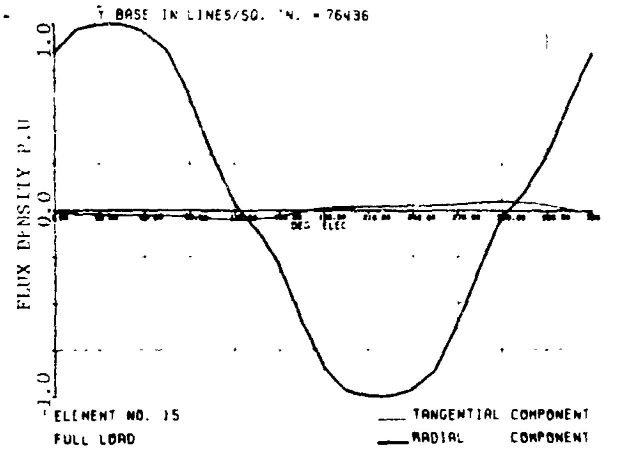

Fig. 27. Flux Density Profile in the Stator Tooth Stem at Rated Load

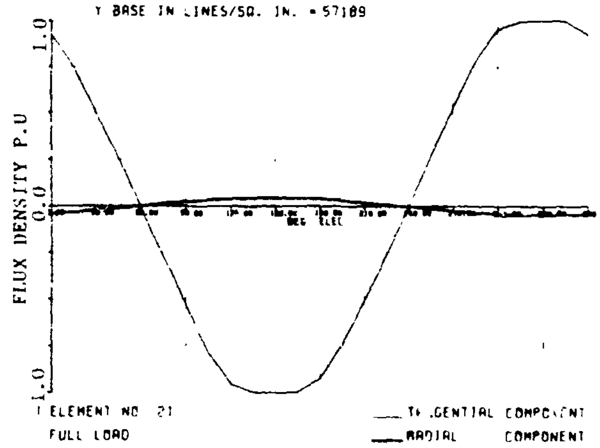

Fig. 28. Flux Density Profile in the Stator Core at Rated Load

The combined eddy and hysteresis losses per unit weight, w_t, can be expressed as follows:

$$w_t = w_e + w_h \qquad (4)$$

where w_e is the eddy current loss component given by

$$w_e = k_e c_1 f^2 B_p^2 \qquad (5)$$

and w_h is the hysteresis loss component defined by

$$w_h = k_h c_2 f B_p^{\alpha} \qquad (6)$$

The value of the peak flux density, B_p, in a given element in the core is obtained from the flux density profile of that element such as shown in Figures (26)-(28). The frequency, f, is the fundamental frequency of this waveform (or profile). The constants c_1, c_2 and α are determined from the Epstein loss characteristic for the given lamination, which is based on sinusoidally time varying flux densities. This loss characteristic can be expressed mathematically as a sum of the eddy and hysteresis components as follows:[15]

$$w = c_1 f^2 B^2 + c_2 f B^{\alpha} \qquad (7)$$

The correction factors k_e and k_h in equations (5) and (6), which account for the effect of distortion of the flux density waveform are determined on the basis of harmonic flux density magnitudes and flux density reversals, respectively, as outlined in a method successfully introduced by Lavers, et al.[11,12,13]

The method outlined above was applied to the 15 hp machine given earlier. The resulting core losses under rated and no load conditions are given in Table (1) for a speed of 7750 rpm. Also given here is the core loss

Table (1) Core Losses Results

	Finite Element Calculation		Design Calculation	Test Total Core Losses
	Rated Load	No Load		
Eddy current loss (watts)	121.5	124.5	--	--
Hysteresis loss (watts)	70.3	70.5	--	--
Total core loss (watts)	191.8	195.0	136.5	330

calculated by standard design techniques that account only for the fundamental component of flux density. It must be noted that the core losses obtained from testing actual machines are generally 1.5 to 2.0 times higher than those calculated values. This is due to interlaminations short circuits resulting from the high pressure applied to stator cores to improve the stacking factor, etc. Reference (15) contains detailed explanations of this phenomenon. One must notice from Table (1) that the finite element based core loss values are much closer to test than those given by standard design calculations.

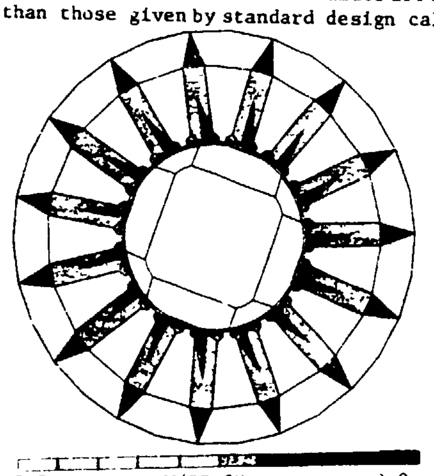

Fig. 29. Core Loss Density Distribution at Rated Load

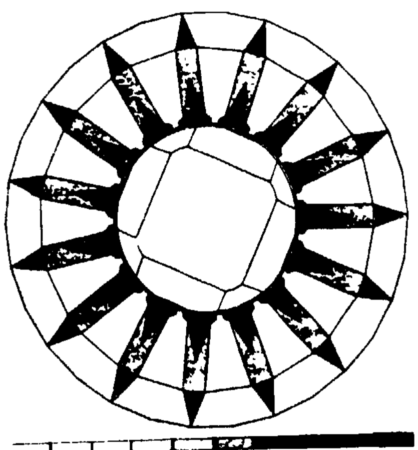

Fig. 30. Core Loss Density Distribution at No Load

Figures (29) and (30) show the total core loss density distributions under both rated and no load conditions. The regions of high loss densities are easily visible in these plots and are, as expected, in the tooth tips and in the tooth stems near the stator core. Notice also the shift in the position of these regions under rated load conditions due to armature reaction. This type of distribution may be used as input data to a thermal analysis program for design calculations and optimization.

CONCLUSIONS

The essential components of a finite element model for the simulation of the electromagnetic performance of electronically operated permanent magnet synchronous machines were introduced. These included a model for simulating permanent magnets, based upon geometrical and material properties, and a generalized automatic finite element grid generator which allows rotation of any rotor versus any stator grids. The stepping nature of the armature MMF was accounted for by taking a series of field solutions corresponding to the movement of a rotor during one cycle of the armature current.

This approach was applied to a 15 hp samarium cobalt machine. The rated and no load field solutions for this machine were verified by means of flux and flux density measurements obtained from search coils. Excellent agreement was obtained in all cases between measured and calculated results. The midgap EMF waveforms were calculated with excellent agreement between numerical and corresponding test results in magnitude and profile. The core losses in the stator core were also calculated and were closer to test values in comparison to those calculated by standard design procedures. The approach given here is presently being extended to include the calculation of winding inductances for various rotor positions and levels of saturation. Machine parameters which were calculated on the basis of these field solutions were key elements in a machine-power conditioner network model which was used to simulate the dynamic interactions between the electromagnetic and electronic parts of such systems as outlined in reference (14).

ACKNOWLEDGEMENTS

These authors wish to acknowledge the financial support of the following contracts: 1) DOE/NASA LeRC contract Number DEN3-65 and 2) Air Force SCEEE contract number SIP/78-17. In particular we wish to acknowledge the interest and the many stimulating discussions of Mr. E. Maslowski of NASA LeRC and Dr. F. Brockhust of the APL at WPAFB. We also wish to acknowledge the efforts of Mr. B. P. Overton of Inland Motor R&D, Radford, VA, in the design, fabrication and testing of the machine studied here. Our thanks also go to Dr. R. Churchill, Director of Inland Motor R&D who provided the facilities for construction and testing of this hardware.

REFERENCES

1. Ahamed, S. V. and Erdelyi, E. A., "Nonlinear Vector Potential Equations for Highly Saturated Heteropolar Electrical Machines," IEEE Transactions on Aero-Space, Vol. 2, pp. 896-903, 1964.
2. Erdelyi, E. A., Ahamed, S. V., and Hopkins, R. E., "Nonlinear Theory of Synchronous Machines On-Load," Transactions IEEE, Power Apparatus and Systems, Vol. PAS-85, pp. 792-801, 1966.
3. Chari, M. V. K. and Silvester, P., "Analysis of Turbo Alternator Magnetic Field by Finite Elements," IEEE Transactions on Power Apparatus and Systems, Vol. PAS-90, pp. 454-464, 1971.
4. Demerdash, N. A., Hamilton, H. B., and Brown, G. W., "Simulation for Design Purposes of Magnetic Fields in Turbogenerators with Symmetrical and Asymmetrical Rotors - Part I - Model Development and Solution Technique," IEEE Transactions on Power Apparatus and Systems, PAS, Vol. 91, pp. 1985-1992, 1972.
5. Demerdash, N. A. and Hamilton, H. B., "Simulation for Design Purposes of Magnetic Fields in Turbogenerators with Symmetrical and Asymmetrical Rotors - Part II - Model Calibration and Applica-

ORIGINAL PAGE IS OF POOR QUALITY

tions," IEEE Transactions on Power Apparatus and Systems, PAS, Vol. 91, pp. 1992-1999, 1972.

6. Fuchs, E. F. and Erdelyi, E. A., "Nonlinear Theory of Turboalternators Part II: Load Dependent Synchronous Reactances," IEEE Trans. on Power Apparatus and Systems, PAS, Vol. 92, pp. 592-599, 1973.

7. Chari, M. V. K., Minnich, S. H., Tandon, S. C., Csendes, Z. J. and Berkery, J. "Load Characteristics of Synchronous Generators by the Finite-Element Method," Paper presented at IEEE PES Winter Power Meeting, New York, NY, February 1980.

8. Chari, M. V. K., "Finite-Element Analysis of Nonlinear Magnetic Fields," Ph.D. Dissertation, McGill University, Montreal, Quebec, 1970.

9. Silvester, P. and Chari, M. V. K., "Finite Element Solution of Saturable Magnetic Field Problems," IEEE Transactions on Power Apparatus and Systems, Vol. PAS-89, pp. 1642-1652, 1970.

10. Fouad, F. A., "Finite Element Analysis for Design and Optimization Purposes for Electronically Operated Electric Machines in Propulsion and Actuation Applications," Ph.D. Dissertation, Electrical Engineering Dept., Virginia Polytechnic Institute and State University, Expected 1980/81.

11. Lavers, J. D. and Biringer, P. P., "Prediction of Core Losses for High Flux Densities and Distorted Flux Waveforms," IEEE Transactions on Magnetics, Vol. MAG-12, No. 6, November 1976.

12. Lavers, J. D., Biringer, P. P. and Hollitscher, H., "A Simple Method of Estimating the Minor Loop Hysteresis Loss in Thin Laminations," IEEE Transactions on Magnetics, Vol. MAG-14, No. 5, September 1978.

13. Lavers, J. D., Biringer, P. P. and Hollitscher, H., "Estimation of Core Losses when the Flux Waveform Contains the Fundamental plus a Single Odd Harmonic Component," IEEE Transactions on Magnetics, Vol. MAG-13, No. 5, September 1977.

14. Demerdash, N. A., Nehl, T. W. and Maslowski, E., "Dynamic Modeling of Brushless DC Motors in Electronic Propulsion and Electromechanical Activation by Digital Techniques," 1980 IAS Annual Meeting Conference Record, pp. 570-579, Oct. 1980.

15. "Magnetic Circuits and Transformers," By Members of the Staff of the Elec. Eng. Dept., the MIT Press.

16. Erdelyi, E. A. and Fuchs, E. F., "Nonlinear Magnetic Field Analysis of DC Machines, Part I and II," Trans. IEEE on Power Apparatus and Systems, Vol. PAS-89, 1970, pp. 1546-1564.

APPENDIX (A)

The grid fitting (matching) which must take place in the air gap to combine the stator and rotor grids, at each of these rotor positions, was accomplished by means of an algorithm designed for that purpose. This algorithm ties the two grids by the generation of a row of elements in the air gap region. The unique feature of this algorithm is that it is independent of the number of rotor poles or stator slots, and can be used to match any two FE grids with a common boundary. The two node lines shown in Figure (31-A) represent the innermost and outermost layers of nodes of the stator and rotor grids, respectively.

The following steps summarize the salient features of this algorithm:

1. The number of nodes along the inner and outermost layers of the stator and rotor grids, respectively, are counted. The one with the fewer number of nodes is designated side (I) and the other is designated side (II) as shown in Figure (31-A). If both sides have the same number of nodes, then one side is arbitrarily designated side (I) and the other, side (II).

2. Side (II) is then divided into regions, R_1, R_2,..., R_k, which are defined by the nodes of side (I) as shown in Figure (31-B).

3. Determine the midpoints of each region.

4. Next, those nodes on side (II) that are closest to these midpoints are identified as "pivot," nodes, p_1, p_2, ..., p_k.

5. Starting with the right-hand most node on side (I), one connects this node with the first pivot node on side (II), and then to the next node on side (I) and so on, in a zigzag fashion. This process is repeated until the last node on side (I) is reached as shown in Figure (31-C).

6. The nodes between each pair of pivots on side (II) (if any) are joined with the node on side (I) to which these pivots have been connected, as shown in Figure (31-D).

7. If only one pole pitch is simulated, then the two nodes at each end of the two sides are connected together as shown in Figure (31-D). This completes the connection of the two grids.

8. If the entire machine is represented, as was the case here, the two ends meet on the same line. Further details on the implementation of this scheme as well as the automatic machine finite element grid generation are to be found in reference (10).

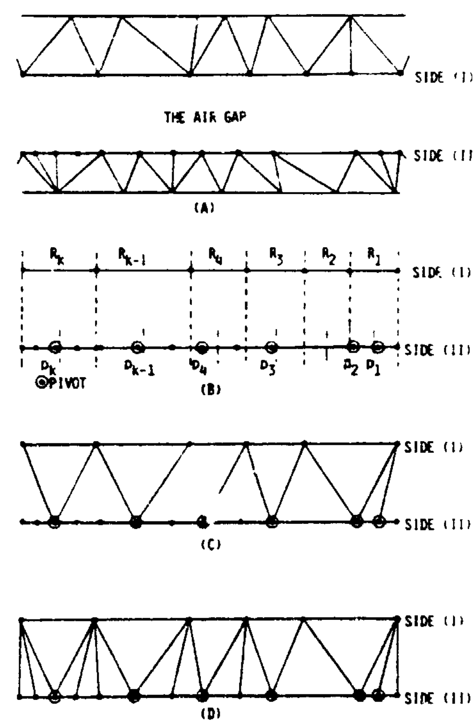

Fig. 31. Automation of Rotor and Stator Finite Element Grid Matching in the Air Gap

For biographical scketches of the authors please refere to other papers in the IEEE PAS Transactions.

Discussions

Stephen H. Minnich (General Electric Corporate Research and Development, Schenectady, NY): This paper provides a valuable illustration of the application of the finite element method to the analysis of an electrical machine of complicated geometry. Of particular value is the demonstration of a method for automatically stepping the rotor portion of the finite element grid in angular position to simulate the rotation of the rotor. While the paper seems basically well done, the following comments are offered.

In equation (2), it appears that the sines and cosines should be interchanged in the two terms inside the brackets. If (2) was derived from (1) by integrating the flux density to obtain the flux, the sine would integrate into the cosine, the vice versa. The authors then proceed to derive a quantity called the "midgap EMF" which is compared with the "measured EMF waveform". Was the "measured EMF waveform" the terminal voltage, or was it actually derived from a measurement in the airgap? The authors say that comparison of Figures (24) and (25) "reveals" excellent agreement in both waveshape and magnitudes. Clearly this comparison cannot be made by the reader, since (24) has no voltage scale, and to the eye both (24) and (25) look sinusoidal. If a numerical figure of merit was used on the waveshape to get the numerical figure quoted (2.2%), that figure of merit should be described. The authors further state that the "midgap EMF" drops only slightly under load. A numerical comparison of the calculated value versus the measured value at load could have been given, and the term, "slightly", could have been quantified.

In any event, the "midgap EMF" bears only a quanitative relationship to the terminal voltage. It is a classical approximation used when no further information is available, and is not appropriate to use in processing finite element results.

Rigorously, the phase terminal voltage is the time derivative of the armature phase flux linkages. The flux linkages for any single armature turn can be found from the difference between the vector potentials of the two conductors forming the turn. The vector potential for each (transposed) conductor is the average of the vector potentials over the area of the conductor (and clearly must be evaluated in the slot and not in the airgap). The total phase flux linkages, for a given rotor position, are found by summing the individual turn flux linkages. If the flux linkages are thus determined for each rotor position, the time waveform of the armature flux linkages is determined, and differentiation of this time waveform gives the terminal voltage. The authors had this information available from their stepped finite element solutions, and the paper would have been more meaningful, had it been used.

Further, the finite element solution is two dimensional. While the length of the machine is not mentioned, it can be assumed that the machine is short enough that end effects are important. Apparently, no correction for end effects was attempted. If so, and in view of the inexact estimate of the terminal voltage discussed above, isn't the degree of agreement of the calculated and measured terminal voltages somewhat less meaningful than implied in the paper?

A similar comment applies to the core loss comparison. The fact that the present calculated value was higher than a conventional one and that the measured losses were even higher is a rather vague justification. The coarseness of the core loss profiles indicated in Figures (29) and (30) belies much exactitude in calculation described.

The paper remains a valuable illustration of a useful and necessary technique in the application of finite elements. This discussor wished only to point out a conceptual error in the terminal voltage calculation and to mention other objective factors bearing on the comparison of the results with test.

Manuscript received March 2, 1981.

S. T. Lakhavani (Westinghouse Electric Corp., Pittsburgh, PA): The authors are to be commended on their contribution to finite element modeling of losses in electric machines. Accurate prediction of core loss is important to the electric machine designer particularly for the design of high efficiency machines.

The existence of rotational flux is clear from Figures 12, 13 and 14 in the region where the tooth stem joins the stator core. Perhaps the authors would like to incorporate estimation of rotational losses in regions where these occur. These losses are also known as iron losses due to elliptically polarized mangetic fields and can be estimated by taking the sum of the individual alternating power loss due to the magnitude of the major and minor axis flux densities.[1,2] Taking rotational loss into account could lead to further improvement in the prediction of core loss.

Some questions for the authors that come to my mind are:

1. Did you establish bounds on the aspect ratio of the triangular elements generated by the air gap fitting algorithm?
2. Did you use the solution obtained at a particular time as initial condition to obtain solution at the subsequent time step?
3. What harmonics are present in stator tooth tip at rated load (Fig. 26)? Did your loss calculation take into consideration all harmonics?

REFERENCES

[1] F. J. Young and H. L. Schenk, "Iron Losses Due to Elliptically Polarized Magnetic Fields" Journal of Applied Physics, Vol. 37, No. 3, pp. 1210-1212, March 1966.

[2] T. Yamaguchi and K. Narita, "Rotational Power Loss in Commercial Silicon-Iron Laminations" Electrical Engineering in Japan, Vol. 96, No. 4, 1976.

Manuscript received March 2, 1981.

F. A. Fouad, T. W. Nehl, and N. A. Demerdash: We wish to thank the discussors Mr. Lakhavani and Mr. Minnich for their interest in the paper and for their stimulating questions which help complete the record on this work. We will first respond to the points raised by Dr. Lakhavani, then to those raised by Mr. Minnich as follows:

1) Dr. Lakhavani is correct in pointing out that the nature of the magnetic field in many regions in the core, particularly those where the teeth and yoke join, is indeed elliptic. This consideration has been taken into account in a manner very similar to the procedure described in references (1) and (2) in the discussion.
2) Dr. Lakhavani raises the point of whether criteria were established to avoid creation of elements with large aspect ratios by the airgap fitting algorithm. The design of the logic of this algorithm included provisions which would circumvent the problem in practical cases. However, in extreme cases where large discrepency exists between the number of nodes on the two sides (boundaries) of two adjacent grids, one can not rule out ill conditioned (large aspect ratio) type elements. This was never encountered in all the cases we have solved using this algorithm.
3) We answer the second questions (2) raised by Dr. Lakhavani in the affirmative. The solution obtained at a particular rotor position (time) was used as the initial condition in obtaining the solution at the next rotor position (next instant in time).
4) Harmonics up to the fifteenth order were of significance in the flux density waveform of Figure (26). The loss calculation included the effect of all harmonic components which could be calculated with reasonable accuracy based on the number of flux density data points used in forming the elemental flux density waveforms.
5) Mr. Minnich is correct in noticing the typographical error in equation (1). This equation should read as follows:

$$B_g(\theta) = \sum_{h=1}^{N_h} [a_h \, \mathrm{Cos}(h\theta) - b_h \, \mathrm{Sin}\,(h\theta)]/h \qquad (1)$$

6) In response to one of Mr. Minnich's questions concerning the comparison between the calculated and measured emf waveforms, we wish to state that the test waveform was obtained under no load condition, and represents the no-load phase to neutral voltage waveform. For this condition, the flux is almost entirely radial through the teeth, see Figure (17), and hence, the induced emf can be calculated from the midgap flux with reasonable accuracy in that class of machines. This, however, is not the case in problems involving large synchronous machines with significantly higher degrees of saturation in the teeth. In such cases with high saturation one should calculate flux linkages and induced emfs from the mean magnetic vector potentials in the conductors, as was done earlier in the work of Demerdash, et. al., see references (4) and (5) in the paper, as well as reference (17) given below.

   It is worth pointing out that the peak values of the calculated and measured emfs are 62.1 volts and 63.5 volts, respectively. The calculated value of the emf under load is 60.4 volts. Incidentally, all this information is in the paper, see Figures (23) through (25).
7) Mr. Minnich points to the fact that "Rigorously, the phase terminal voltage is the time derivative of the armature phase flux

linkage". We are well aware of that and as pointed out above have used this approach since 1971. However, these emfs generated here were intended for further use as forcing functions in a simplified machine-power conditioner model (18), in which individual machine winding inductances must be represented. That meant that the emfs behind these inductances must be used. It must be pointed out that this approach gave numerical results of machine-power conditioner current and voltage waveforms that were in excellent agreement with corresponding test data as evidenced in reference (18). Obviously, this approach would not be valid in machines with considerable saturation such as turbogenerators.

8) With regard to end region effects on the induced emf at no load in such machines, our experience confirms that these effects can be neglected. Under load, the flux linkage through three teeth (approximately a phase belt span) was measured by a search coil, Figures (21). Plotted also in that figure are the calculated values of flux without end effects, where one can see clearly the agreement between calculated and measured data. This would not be true if end effects were significant as suggested by Mr. Minnich.
9) The core loss calculations inherently contain many uncertainties due to factors such as interlamination shorts, etc. It is generally recognized that calculated loss values are usually 50% to 60% of measured values, see reference (15). Accordingly, the method introduced here represents some improvement over previous efforts. Also, the resulting loss density distribution, Figures (35) and (36), are of value to designers in predicting possible locations of hot spots.

Finally, we hope we have responded adequately to all the interesting and pertinent questions raised by the discussors.

REFERENCES

[17] N. A. Demerdash and H. B. Hamilton, "A Simplified Approach of Determination of Saturated Synchronous Reactances of Large Turbogenerators Under Load," *IEEE Transactions on Power Apparatus and System,* PAS, Vol. 95, 1976, pp. 650-569.
[18] N. A. Demerdash, T. W. Nehl, and E. Maslowski, "Dynamic Modeling of Brushless Motors in Electric Propulsion and Electromechanical Actuation by Digital Techniques," *Proceedings of the 1980 IEEE Industry Applications Society Annual Meeting,* 80 CH 1575, Cincinnati, Ohio, Sept. 28-Oct. 3, 1980, pp. 570-579.

Manuscript received May 11, 1981

APPENDIX (2)

ON MAGNETIC FIELD ANALYSIS BY FINITE ELEMENTS

Fouad, F. A., Nehl, T. W., Demerdash, N. A., "Permanent Magnet Modeling for Use in Vector Potential Finite Element Analysis in Electrical Machinery," IEEE Transactions on Magnetics, Vol. MAG-17, 1981, pp. 3002-3004.

PERMANENT MAGNET MODELING FOR USE IN VECTOR POTENTIAL FINITE ELEMENT ANALYSIS IN ELECTRICAL MACHINERY

F. A. Fouad T. W. Nehl N. A. Demerdash

Abstract - A method for simulation of permanent magnet effects on the magnetic field in electrical machines is given. The method is suited for use with magnetic vector potential numerical models for the analysis of magnetic fields in electrical machines containing permanent magnets. The method was applied to the solution of magnetic fields under no load and load in two 15HP, 120 volt ferrite and samarium cobalt permanent magnet type brushless dc machines using finite elements. Search coil measurements of both flux and flux densities in the two machines were used to verify the present permanent magnet model. The numerical analysis and measurement results of the flux densities were in excellent agreement.

INTRODUCTION

Previous investigators introduced a number of permanent magnet models for field calculations, some examples of these can be found in references (1) and (2). Many of these methods contained assumptions which restricted their use. In this paper, a simplified and practical way of modeling permanent magnets for numerical field solutions is introduced. The method is applicable to magnet structures of various geometries and materials.

Experimental verification of the validity of this magnet modeling approach was carried out by applying this model combined with the finite element method, to the analysis of the magnetic fields in two 15HP electronically commutated brushless dc machines. These machines were designed and built for use in propulsion of commuter type electric passenger vehicles. One of these machines contains a 6-pole strontium ferrite No. 8 rotor structure, while the other contains a 4-pole 18 MGO, samarium cobalt rotor structure.

PERMANENT MAGNET MODEL

Consider a simple magnetic circuit which consists of a permanent in series with an iron core and airgap as shown in Figure (1). If the MMF drop in the iron core is neglected, one obtains the operating point of the magnet from the intersection of the magnet's normal demagnetization characteristic and the airgap line, point #1 in Figure (1). Inclusion of magnetic saturation in the iron core shifts the operating point to point #2 as depicted in the figure.

This magnetic circuit can be replaced by an equivalent one which consists of a coil in series with the same iron core and airgap as shown in Figure (2). This coil and its core have the same dimensions and magnetization profile as the magnet. However, the intersection of this profile with the H axis is shifted from the point, $-H_C$ (coercivity), to the origin as shown in the figure. The flux densities at the operating points #1 and #2 of this circuit would be identical to those of the previous magnetic circuit, Figure (1), if the following relation is satisfied:

$$NI = H_C \cdot h_{pm} \tag{1}$$

where NI is the coil's ampere-turns (MMF) and h_{pm} is the height of the magnet in the direction of magnetization.

Manuscript received March 23, 1981.

These authors acknowledge the financial support of the following contracts: 1) DOE/NASA LeRC contract NO. DEN3-65 and USAF/SCEEE Contract NO. SIP/78-17. We also wish to acknowledge Inland Motor R&D, Radford, Virginia in the design, fabrication and testing of the machines studies here.

T. W. Nehl, F. A. Fouad, and N. A. Demerdash are with the Department of Electrical Engineering, Virginia Polytechnic Institute and State University, Blacksburg, Virginia 24061, U.S.A.

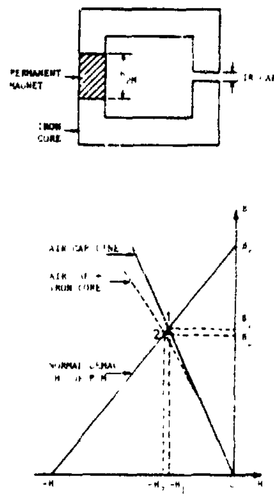

Fig. (1) Operating Point of a Magnetic Circuit Containing a Permanent Magnet.

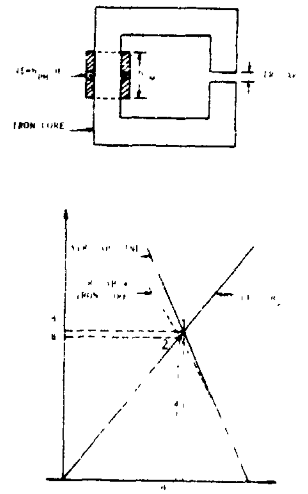

Fig. (2) Operating Point of an Equivalent Magnetic Circuit.

This means that a permanent magnet whose cross-section along the direction of magnetization is rectangular, is magnetically equivalent to a piece of magnetic material, with the same dimensions and B-H profile, shifted to the origin, that is excited by an equivalent current sheet as shown in Figure (2). This current sheet must be oriented such that it magnetizes the material in the same direction as the magnetization of the original magnet. The value of the MMF of this current sheet is given by equation (1).

Application of this approach must be modified for cases where the magnet geometry is nonrectangular such as in the examples given next.

Example (1):

Consider a nonrectangular magnet, such as the one shown in Figure (3-A). To apply the above method to such a magnet, the curved portion is approximated by a finite number of thin rectangular layers in a staircase fashion, as shown also in Figure (3-B). The values of the MMFs on each side of these rectangular layers can be obtained as described above. If one increases the number of these layers to infinity, the magnet model will consist of two pairs of current sheets as shown in Figure (3-C).

Example (2):

In this example, the permanent magnet is tangentially oriented with a trapezoidal cross-section as shown in Figure (4-A). The equivalent system of current sheets for this type of magnet can be approximated by dividing the trapezoidal shape into a series of thin rectangular layers as shown in Figure (4-B). The overall effect of the simultaneous presence of all these current sheets leads to a cancellation process at the interfaces from layer to layer with only a residual current sheet left to represent the difference between the current sheets of two adjacent layers, Figure (4-C). The final configurations of the equivalent current sheets, when the number of these layers reaches infinity, is shown in Figure (4-D).

One must notice that in this modeling approach, the current sheet equivalents are independent of the number of layers used to explain the modeling process.

306

ORIGINAL PAGE IS

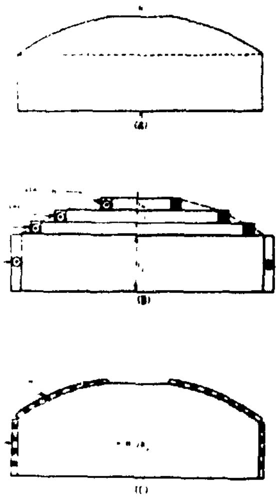

Fig. (3) Equivalent Representation of a Composite Shape Radially Oriented Magnet.

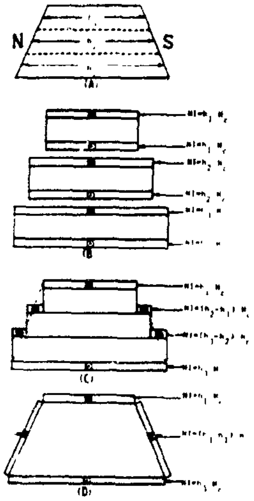

Fig. (4) Equivalent Representation of a Trapezoidal. Tangentially Oriented Magnet.

APPLICATION OF THE MAGNET MODEL TO PRACTICAL PROBLEMS

The model detailed above yields current sheet equivalents of permanent magnets. These current sheet equivalents can be converted to nodal currents on the outer boundaries of these magnets in any finite element (4) or finite difference (5) magnetic field simulation. Accordingly, this model coupled with the finite element method was used in the calculation of the field distributions inside the two permanent magnet brushless dc machines mentioned earlier, under no load and load conditions. The nonlinear partial differential equation governing the fields in these machines is (3, 4):

$$\frac{\partial}{\partial x}\left(\nu\frac{\partial A}{\partial x}\right) + \frac{\partial}{\partial y}\left(\nu\frac{\partial A}{\partial y}\right) = -J \qquad (2)$$

where A and J are the z components of the magnetic vector potential (MVP), and current density, respectively, while ν is the nonlinear material reluctivity.

No Load Case

The brushless dc machine with strontium ferrite No. 8 magnets: A suitable finite element (FE) discretization of the cross-section of this machine is shown in Figure (5). The no load magnetic field distribution was determined and is depicted by the equal MVP contours of Figure (6).

Radial flux densities in stator tooth stems closest to the airgap were measured by search coils, and the corresponding waveform is given in Figure (7). Also, plotted in the same figure are the corresponding radial flux densities calculated using the present magnet model. It is clear from this figure that the measured and numerically obtained flux densities are in close agreement.

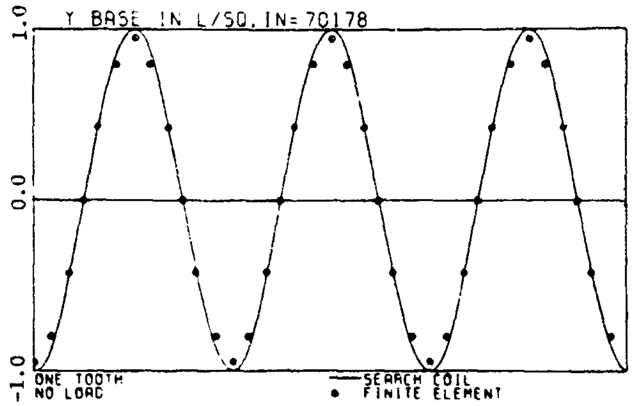

Fig. (7) Experimental and Digital Results of the Average Tooth Flux Density at No Load of the Ferrite Magnet Machine.

The Load Case

Under load, one must inject armature phase currents in these finite element grids at stator slot locations according to the actual phase belt distribution, as detailed in a previous paper by these authors (5). The stator currents are directly related to, and electronically controlled by the rotor position as explained in references (5), (6) and (7). It must be pointed out that proper design of these machines requires that the armature MMF (reaction) be weak in comparison with the equivalent magent MMF to avoid permanent magnet demagnetization (8).

Accordingly, the magnetic field distributions under rated load conditions in the ferrite and samarium cobalt machines mentioned above were calculated and are depicted by the equal MVP contours of Figures (8) and (9). Comparison between the calculated and search coil measured radial tooth flux densities in both machines under rated load are given in Figures (10) and (11) for the ferrite and samarium cobalt cases, respectively. Close agreement between measured and calculated densities are evident. This confirms the validity of this magnet modeling approach under load for the two magnet types.

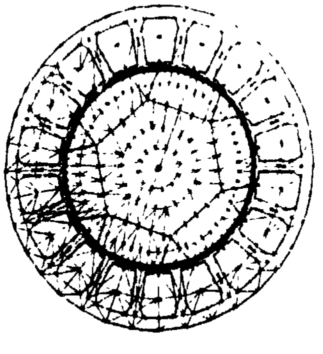

Fig. (5) Finite Element Grid of the Ferrite Magnet Machine.

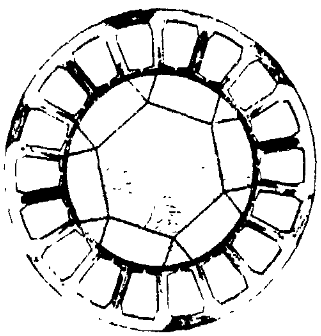

Fig. (6) Flux Distribution at No Load of the Ferrite Magnet Machine

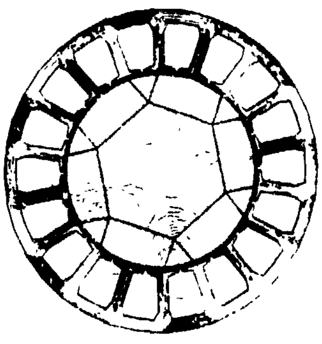

Fig. (8) Flux Distribution at Load of the Ferrite Machine.

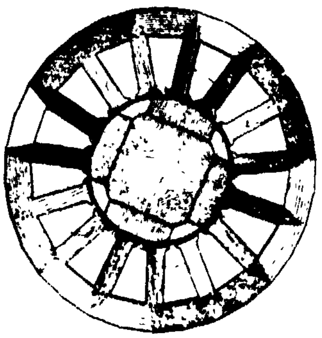

Fig. (9) Flux Distribution at Load of the Samarium Cobalt Machine.

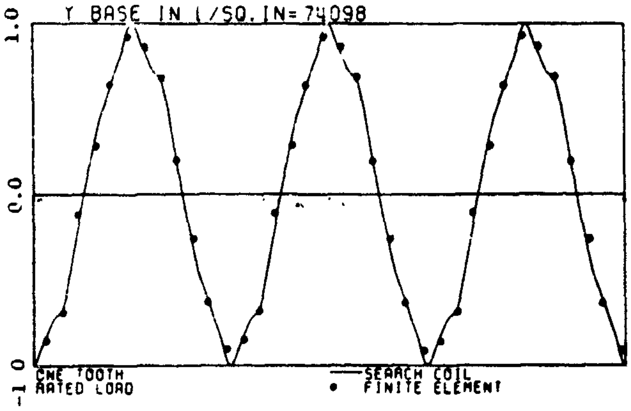

Fig. (10) Average Tooth flux Density at Load of the Ferrite Machine.

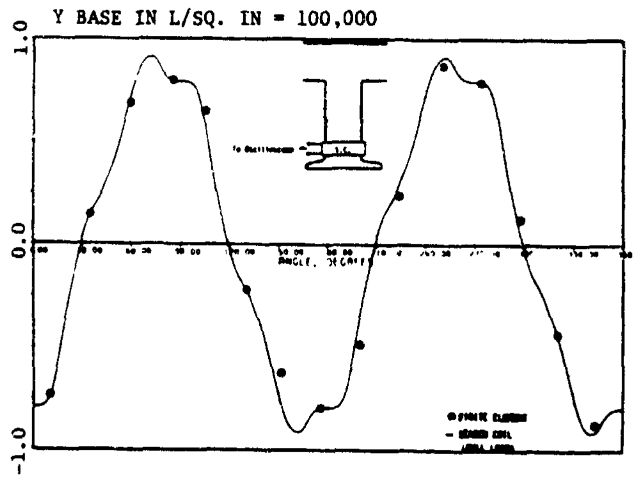

Fig. (11) Average Tooth flux Density at Load of the Samarium Cobalt Machine.

CONCLUSIONS

A permanent magnet model suited for use with the two dimensional magnetic vector potential finite element method was presented in this paper. This model is simple to implement in practical problems in the form of equivalent current sheets. These current sheets are functions of magnet geometries and material characteristics. This magnet model has been used in the numerical solution of the magnetic fields in two machines with ferrite and samarium cobalt magnets. The comparison between the search coil test and numerically obtained flux densities reveals the validity of this magnet model in the calculation of the magnetic field in such machines under no load as well as load conditions.

REFERENCES

[1] K. Reichert, "The Calculation of Magnetic Circuits with Permanent Magnets by Digital Computers", IEEE Transactions on Magnetics, Vol. MAG-6, 1970, pp. 283-288.

[2] W. J. Harrold, "Calculation of Equipotentials and Flux Lines in Axially Symmetrical Permanent Magnet Assemblies by Computer", IEEE Transactions of Magnetics, Vol. MAG-8, 1972, pp. 23-29.

[3] P. Silvester, and M. V. K. Chari, "Finite Element Solution of Saturable Magnetic Field Problems", IEEE Transactions on Power Apparatus and Systems, Vol. PAS-89, pp. 1642-1652, 1970.

[4] N. A. Demerdash, and H. B. Hamilton, "Simulation for Design Purposes of Magnetic Fields in Turbogenerators with Symmetrical and Asymmetrical Rotors - Parts I and II", IEEE Transactions on Power Apparatus and Systems, PAS, Vol. 91, pp. 1985-1999, 1972.

[5] F. A. Fouad, T. W. Nehl, and N. A. Demerdash, "Magnetic Field Modeling of Permanent Magnet Type Electronically Operated Synchrounous Machines Using Finite Elements," Paper No. 81WM179-1, Accepted for Publication in Full in the IEEE Transactions on Power Apparatus and Systems.

[6] T. W. Nehl, "A Discrete Time Model of a Power Conditioner Fed Permanent Magnet Brushless DC Motor Systems for Aerospace and Electric Vehicle Applications for Design Purposes Using Finite Elements for Machine Parameter Determination", Ph.D. Dissertation, Department of Electrical Engineering, Virginia Polytechnic Institute and State University, May 1980.

[7] F. A. Fouad, "Finite Element Analysis for Design of Classical and Electronically Operated Electric Machines", Ph.D. Dissertation, Electrical Engineering Dept., Virginia Polytechnic Institute and State University, May 1981.

[8] M. McCaig, "Permanent Magnets in Theory and Practice", John Wiley & Sons, 1977.

APPENDIX (3)

ON CALCULATION OF MACHINE WINDING INDUCTANCES BY ENERGY PERTURBATION AND FINITE ELEMENT METHODS

Nehl, T. W., Fouad, F. A., and Demerdash, N. A., "Determination of Saturateu Values of Rotating Machinery Incremental and Apparent Inducatances by an Energy Perturbation Method," IEEE Transactions on Power Apparatus and Systems, PAS-Vol. 101, 1982, pp. 4441-4451.

DETERMINATION OF SATURATED VALUES OF ROTATING MACHINERY INCREMENTAL AND APPARENT INDUCTANCES BY AN ENERGY PERTURBATION METHOD

T. W. Nehl, Member F. A. Fouad, Member N. A. Demerdash, Senior Member
Virginia Polytechnic Institute and State University
Blacksburg, VA 24061

Abstract - Energy and winding current perturbations form the basis of a method for calculation of the saturated apparent and incremental inductances of rotating machinery as functions of rotor position and machine winding excitation currents. The method is totally general and utilizes numerical field calculation techniques in obtaining stored energy in the magnetic circuits of such machines. Thus, it can be applied to a wide class of machinery with practically any cross-sectional contours and number of windings. It can be used at any given set of excitations (any loads). This method was applied to the calculation of the apparent and incremental inductances of a 15 hp samarium cobalt permanent magnet synchronous machine. The necessary numerical field solutions were obtained by finite elements at both rated and no load conditions. The calculated inductances, at various rotor positions, were compared with those obtained during laboratory measurements and the agreement between calculated and measured values was consistently very good. The advantage of this method over the more traditional calculations of only the direct and quadrature axes inductances (or reactances, including transient and subtransient components) is that the entire n × n matrix of incremental inductances that truely govern the dynamic performance of an n winding machine can be determined regardless of the validity of a rotating d-q-o frame of reference.

INTRODUCTION

The accurate calculation of machine winding apparent and incremental inductances and their variation with saturation and rotor angle is crucial to the dynamic analysis of such devices. This is especially true in the case of electronically operated machines [1-3], which are often characterized by nonsinusoidal current waveforms, and consequently nonsinusoidal MMF waveforms. These MMF waveforms often move in discrete jumps rather than the familiar uniform rotation when sinusoidal currents are involved [4]. Such machines are finding increasing acceptance in many applications.

Previous investigations have centered almost exclusively on the calculation of saturated values of the steady state and transient reactances such as the direct and quadrature synchronous reactances, etc., see references [5] through [9], [18]. Such reactances are useful when both the machine currents and MMF are sinusoidal, in which case one can resort to a uniformly rotating d-q-o frame of reference for machine modeling [10,11]. However, with the rapid increase in the use of electronically operated machines, the currents and MMFs are no longer sinusoidal in many cases, and the armature MMF no longer rotates uniformly but rather jumps in discrete steps. Therefore, the concept of a uniformly rotating d-q-o frame of reference, and its associated direct and quadrature reactances is ill suited. This is due to the fact that the relative angular position of stator MMF with respect to the rotor d-axis is cyclically alternating between upper and lower bounds (equivalent to a pulsating load (torque) angle). These bounds are set by the phase current commutation timings. Also, in such electronically operated machines the time rates of change of currents (di/dt) are much higher than those encountered in conventional ones, because of the fast (high frequency) electronic switching involved. Accordingly, in order to predict accurately the dynamic behavior and performance of such machine systems one must have accurate knowledge of values of the self and mutual incremental ($d\lambda/di$) machine winding inductances, rather than the apparent values (λ/i). This is because inductive voltage terms ($d\lambda/dt$) encountered in such machine models can be readily expressed as $[(d\lambda/di)(di/dt)]$ when saturation is an important factor.

The crucial role played by such machine inductances is demonstrated in references [8,14,15] in which the performance of a 15 hp ferrite permanent magnet machine was analyzed for two different winding configurations (inductances) corresponding to 12 and 9 series turns per phase. For the winding with 12 series turns, the maximum power attainable at the rated speed and voltage was only 4 hp. Reducing the number of series turns by three to a total of 9 turns and modification of slot configuration reduced the machine inductances drastically. This permitted an increase in the peak horsepower output capability of that machine to over 34 hp for the same supply voltage. This example clearly illustrates the need for accurate knowledge of such inductance values during the design stage.

In this paper, an approach for accurate calculation of the apparent and incremental self and mutual inductances of rotating machinery in terms of saturation level and rotor angle is given. This approach is based on the perturbation of the magnetic field distribution inside the machine for a given set of winding currents (saturation level) by means of small current increments (perturbations). The magnetic field distributions and the energy perturbations due to such current increments are determined by means of the finite element method. For a machine with n windings, this method is used to determine the complete (n × n) inductance matrix for each set of specified winding currents and rotor angle (position). By obtaining these inductances for a series of current sets spanning one complete ac cycle of operation, one can calculate the variation of these inductances during both normal and abnormal modes of operation.

To experimentally verify the validity of this approach, the inductances of a prototype 15 hp samarium cobalt permanent magnet synchronous machine are calculated for both no load and rated load operating conditions as functions of the rotor angle. The calculated and experimentally measured values of inductance were found to be in good agreement.

ENERGY STORED IN MULTI-WINDING ROTATING MACHINES

Any multi-winding rotating machine consisting of n coupled windings (coils) can be electrically modeled in terms of the terminal voltage, v_j, the winding cur-

82 WM 237-6 A paper recommended and approved by the IEEE Rotating Machinery Committee of the IEEE Power Engineering Society for presentation at the IEEE PES 1982 Winter Meeting, New York, New York, January 31-February 5, 1982. Manuscript submitted September 14, 1981; made available for printing December 2, 1981.

0018-9510/82/1200-4441$00.75 1982 IEEE

rent, i_j, and the total flux linkage, λ_j, of the jth coil as follows:

$$v_j = R_j\, i_j + \frac{d\lambda_j}{dt} \tag{1}$$

where j = 1, 2, 3,..., n.
A special case of such a machine with 3 coils on the stator and two coils on the direct and quadrature axes of the rotor is shown schematically in Figure (1).

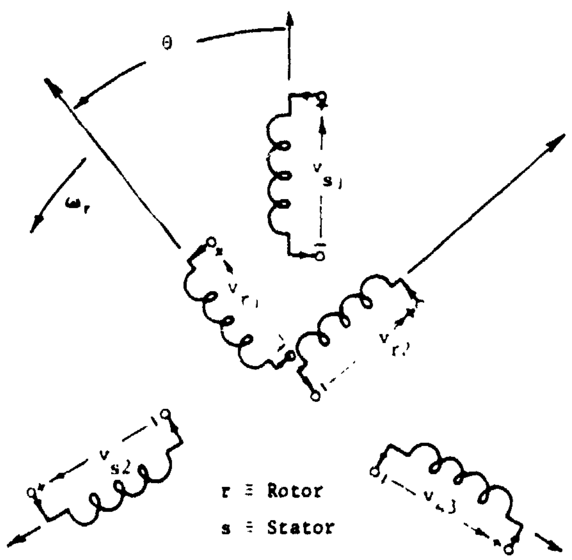

Figure (1) A Schematic of Representation of a Rotating Machine with a Three Coil Armature and a Two Coil Field Windings.

Due to magnetic saturation, the total flux linkage of the jth coil becomes a nonlinear function of the n-winding currents at a given rotor angle, θ. Therefore, one can write

$$\lambda_j = \lambda_j\,(i_1, i_2, \ldots, i_j, \ldots, i_n, \theta) \tag{2}$$

Accordingly, for the jth coil, equation (1) can be expanded using the chain rule as follows:

$$v_j = R_j\, i_j + \frac{\partial\lambda_j}{\partial i_1}\frac{di_1}{dt} + \frac{\partial\lambda_j}{\partial i_2}\frac{di_2}{dt} + \cdots + \frac{\partial\lambda_j}{\partial i_j}\frac{di_j}{dt} + \cdots\cdots + \frac{\partial\lambda_j}{\partial i_n}\frac{di_n}{dt} + \frac{\partial\lambda_j}{\partial\theta}\frac{d\theta}{dt} \tag{3}$$

However, for a fixed rotor position the last term in equation (3) equals zero because (dθ/dt) which equals the rotor angular speed would be equal to zero. Here in equation (3) the partial derivative of the flux linkage, λ_j with respect to a winding current i_k, (k = 1, 2,...,j, ...,n) is the incremental inductance, L_{jk}^{inc}, that is

$$L_{jk}^{inc} = \frac{\partial\lambda_j}{\partial i_k} \tag{4}$$

where j = 1, 2,..., n and k = 1, 2,...,n. Accordingly, for a given fixed rotor position, upon substituting equation (4) into equation (3), one obtains the terminal voltage of the jth coil in terms of the incremental inductance coefficients as follows:

$$v_j = R_j\, i_j + L_{j1}^{inc}\frac{di_1}{dt} + L_{j2}^{inc}\frac{di_2}{dt} + \cdots + L_{jj}^{inc}\frac{di_j}{dt} + \cdots + L_{jn}^{inc}\frac{di_n}{dt} \tag{5}$$

The instantaneous terminal power of the jth coil, P_j, can be obtained by multiplying equation (5) by the coil current, i_j, that is

$$P_j = v_j\, i_j = R_j\, i_j^2 + i_j\, L_{j1}^{inc}\frac{di_1}{dt} + i_j\, L_{j2}^{inc}\frac{di_2}{dt} + \cdots + i_j\, L_{jj}^{inc}\frac{di_j}{dt} + \cdots + i_j\, L_{jn}^{inc}\frac{di_n}{dt} \tag{6}$$

The first term in this equation, which contains R_j, represents the instantaneous power dissipated in the jth coil, while the remaining terms represent the instantaneous magnetic energy storage of the jth coil. Accordingly the stored magnetic energy, w_j, due to the flux linkage, λ_j, can be expressed as follows:

$$w_j = \sum_{k=1}^{n} \int_{i_k(0)}^{i_k(t)} (L_{jk}^{inc}\, i_j)\, di_k \tag{7}$$

Therefore, the total stored global energy, w, associated with the entire system of n coupled coils can be written as follows:

$$w = \sum_{j=1}^{n} w_j = \sum_{j=1}^{n}\left\{\sum_{k=1}^{n}\int_{i_k(0)}^{i_k(t)} (L_{jk}^{inc}\, i_j)\, di_k\right\} \tag{8}$$

If one disturbs the n currents by increments of current, Δi_j, j = 1,2,...n, which are so small that the incremental inductances, L_{jk}^{inc}, can be assumed to remain constant, one can express the corresponding incremental change, Δw, in the total energy, w, as follows:

$$\Delta w = \sum_{j=1}^{n}\left\{\sum_{k=1}^{n} L_{jk}^{inc}\int_{i_k}^{i_k+\Delta i_k} (i_j)\, di_k\right\} \tag{9}$$

Splitting the summation in equation (9) into the self (diagonal, j = k) term and mutual (off diagonal, j ≠ k) terms yields the following:

$$\Delta w = \sum_{j=1}^{n} L_{jj}^{inc}\int_{i_j}^{i_j+\Delta i_j} (i_j)\, di_j + \sum_{j=1}^{n}\left\{\sum_{\substack{k=1\\(k\neq j)}}^{n} L_{jk}^{inc}\int_{i_k}^{i_k+\Delta i_k} (i_j)\, di_k\right\} \tag{10}$$

In order to numerically perform the integration in equation (10), the mean value concept (trapezoidal rule) is assumed to prevail regarding the current functions. Accordingly, equation (10) can be rewritten in summation form as follows

ORIGINAL PAGE IS
OF POOR QUALITY

$$\Delta w = \sum_{j=1}^{n} (i_j \Delta i_j + \Delta i_j^2/2)\, L_{jj}^{inc} \; +$$

$$\sum_{j=1}^{n} \left\{ \sum_{\substack{k=1 \\ (k \neq j)}}^{n} (i_j + \Delta i_j/2)\, \Delta i_k\, L_{jk}^{inc} \right\} \qquad (11)$$

Hence, the total energy stored in the magnetic field, including the effects of current perturbation, that is the new (perturbed) global energy, $\hat{w}$, associated with the new set of currents $((i_j + \Delta i_j),\ j = 1,2,\ldots,n)$ can be expressed as the sum of w and Δw of equations (8) and (11) respectively, that is

$$\hat{w} = w + \Delta w \qquad (12)$$

CALCULATION OF INDUCTANCE FROM ENERGY PERTURBATION

Since the incremental inductances, L_{jk}^{inc}, are assumed to remain constant around the quiescent point $i_j (j = 1, 2, \ldots n)$ these inductances are considered independent of the small variations in the winding currents, $\Delta i_j (j = 1, 2, \ldots, n)$ that is:

$$\frac{\partial L_{jk}^{inc}}{\partial(\Delta i_j)} = 0 \qquad (13)$$

Furthermore, the global energy, w, associated with the quiescent point is independent of the incremental current perturbations, $\Delta i_j, (j = 1,2,\ldots,n)$.
Hence, we have

$$\frac{\partial w}{\partial(\Delta i_j)} = 0 \qquad (14)$$

Therefore,

$$\frac{\partial \hat{w}}{\partial(\Delta i_j)} = \frac{\partial w}{\partial(\Delta i_j)} + \frac{\partial(\Delta w)}{\partial(\Delta i_j)} = \frac{\partial(\Delta w)}{\partial(\Delta i_j)} \qquad (15)$$

substituting for Δw from equation (11) into equation (15) yields the following:

$$\frac{\partial \hat{w}}{\partial(\Delta i_j)} = (i_j + \Delta i_j)\, L_{jj}^{inc} + \sum_{\substack{k=1 \\ (k \neq j)}}^{n} \Delta i_k (L_{jk}^{inc} + L_{kj}^{inc})/2 \qquad (16)$$

Taking the partial derivative of equation (16) with respect to (Δi_j) gives

$$L_{jj}^{inc} = \frac{\partial^2 \hat{w}}{\partial(\Delta i_j)^2} \qquad (17)$$

Furthermore, taking the partial derivative of equation (16) with respect to (Δi_k) yields

$$(L_{jk}^{inc} + L_{kj}^{inc})/2 = \frac{\partial^2 \hat{w}}{\partial(\Delta i_j)\partial(\Delta i_k)} \qquad (18)$$

However, for this type of machine, the mutual inductances are between windings of equal number of turns. Hence, even under saturation, these mutuals are equal, that is:

$$L_{jk}^{inc} = L_{kj}^{inc} \qquad (19)$$

The relationship prevailing in this case does not restrict the applicability of this method in cases where the mutual inductances are not equal.

Hence one can write the following:

$$L_{jk}^{inc} = \frac{\partial^2 \hat{w}}{\partial(\Delta i_j)\partial(\Delta i_k)} \qquad (20)$$

Let the global energy, w, calculated at an operating point with perturbed excitation currents, $(i_1, i_2, \ldots, (i_j \pm \Delta i_j), \ldots, i_n)$, be referred to as $w(i_j \pm \Delta i_j)$. Also let the global energy, w, calculated at an operating point with perturbed excitation currents, $(i_1, i_2, \ldots, (i_j \pm \Delta i_j), \ldots, (i_k \pm \Delta i_k), \ldots, i_n)$, be referred to as $w(i_j \pm \Delta i_j,\ i_k \pm \Delta i_k)$. Here, $j = 1, 2, \ldots, n$ and $k = 1, 2, \ldots, n$.

From standard partial difference equations, see reference [13], the partial derivatives in equations (17) and (20) that define the incremental inductances, L_{jj}^{inc} and L_{jk}^{inc}, can be written in terms of the perturbed global energies defined above as follows:

$$L_{jj}^{inc} = \frac{\partial^2 \hat{w}}{\partial(\Delta i_j)^2} = [w(i_j - \Delta i_j) - 2w + w(i_j + \Delta i_j)]/(\Delta i_j)^2 \qquad (21)$$

and

$$\begin{aligned} L_{jk}^{inc} = \frac{\partial^2 \hat{w}}{\partial(\Delta i_j)\partial(\Delta i_k)} = [&w(i_j + \Delta i_j,\ i_k + \Delta i_k) \\ &- w(i_j - \Delta i_j,\ i_k + \Delta i_k) \\ &- w(i_j + \Delta i_j,\ i_k - \Delta i_k) \\ &+ w(i_j - \Delta i_j,\ i_k - \Delta i_k)]/(4 \cdot \Delta i_j \cdot \Delta i_k) \end{aligned} \qquad (22)$$

IMPLEMENTATION OF THE ENERGY PERTURBATION METHOD FOR INDUCTANCE CALCULATIONS

The global stored magnetic energy w for a given set of winding currents $(i_1, i_2, \ldots, i_n)$ and a given (fixed) rotor position, θ, is calculated by means of the nonlinear, two dimensional finite element method as described in reference (14) The nonlinear algebraic equations that result from the finite element discretization are solved using the quadratically convergent Newton Raphson method.

The nonlinear finite element solution yields the flux density in each triangular element of the chosen grid. Given these flux densities, one can define the operating point along the B-H curve of each element as shown in Figure (2). Based on this operating point one can define two values of reluctivity; incremental, ν_e^{inc}, and apparent, ν_e^{app}, for each element, e, as follows:

$$\nu_e^{inc} = \frac{\partial H}{\partial B}\bigg|_{quiescent} \qquad (23)$$

$$\nu_e^{app} = \frac{H}{B}\bigg|_{quiescent} \qquad (24)$$

where the symbol $\Big|_{quiescent}$ indicates that the expres-

[redacted]

sion is to be evaluated at the quiescent operating point of the given element as determined from the nonlinear field solution. In general, one can write the following

$$\nu_e^{inc} \leq \nu_e^{app} \tag{25}$$

However, in the case of linear media (linear B-H characteristic), the two reluctivities are equal:

$$\nu_e^{inc} = \nu_e^{app} \tag{26}$$

In order to calculate the L_{jj} and L_{jk}, incremental or apparent inductance values, equations (21) and (22) are valid. However, this requires the calculation of the perturbed energies $w(i_j \pm \Delta i_j)$ and $w(i_j \pm \Delta i_j,\ i_k \pm \Delta i_k)$ associated with the current increments $\pm\Delta i_j$ and $\pm \Delta i_k$ about the operating point $(i_1, i_2, \ldots, i_j, \ldots, i_k,$

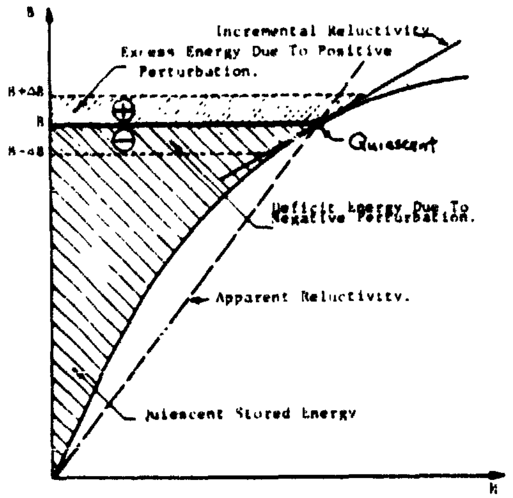

Figure (2) Graphical Representation of Apparent and Incremental Reluctivities in Nonlinear Materials Including Energy Perturbation.

$\ldots, i_n)$. Since the current disturbances are small, the reluctivity of each element can be assumed constant for these current increments and equal to one of the two values defined by equations (23) and (24) for the given operating point. Consequently the algebraic equations produced by the finite element discretization are linearized about (around) the quiescent operating point, Figure (2). Hence no iterations are required to obtain $w(i_j \pm \Delta i_j)$ and $w(i_j \pm \Delta i_j,\ i_k \pm \Delta i_k)$ once the operating point of each element has been determined for a given set of currents. If the incremental reluctivities, as defined by equation (23), Figure (2), are used to determine the perturbations in energies, Δw, (excess or deficit as shown in Figure (2)) due to the current perturbations, equations (21) and (22) will yield the incremental values of L_{jj} and L_{jk}, namely L_{jj}^{inc} and L_{jk}^{inc}. Similarily the use of the apparent values of elemental reluctivities, equation (24), leads to the apparent values of inductances.

It must be emphasized that the incremental values rather than the apparent values of inductances are the ones of primary importance in the dynamic analysis of electronically operated machines. This is again due to the highly nonsinusoidal nature of the current and MMF waveforms involved, and the nonlinearities in the various magnetic circuits of such systems.

APPLICATION OF THE ENERGY PERTURBATION TECHNIQUE TO A 15 HP PERMANENT MAGNET MACHINE

The 15 hp samarium-cobalt permanent magnet synchronous machine under investigation as a practical example was built as a component of an advanced electronically commutated electric vehicle propulsion unit. The machine has an 18 slot stator which houses the three phase Y-connected armature winding. Each phase winding is split into two halves which can be connected either in series or parallel (for a total of 24 series turns or 12 series turns in parallel with another 12 series turns). The purpose of this series/parallel arrangement is to provide a different torque sensitivity for each of the low and high speed operation.

The rotor consists of a six pole samarium cobalt permanent magnet structure. The magnets are retained by a nonmagnetic stainless steel sleeve to allow high speed (9000 rpm) operation.

Machine Inductance Measurement

The line to line and phase to neutral inductances for the series and parallel connections, were measured at no load, using an a. RLC Digibridge, at different rotor positions (angles). These inductances are given in Table (1), for rotor angles covering an entire 360° electrical cycle.

It must be pointed out that such a machine can be represented by three armature (stator) coils, while the samarium-cobalt magnet structure is equivalent to a field winding coil which carries constant current [14]. Hence, in the inductance calculation which follows one must obtain the three self and three mutual inductances of the armature winding. The self inductances were directly measured in the test described above, and are given in Table (1) by the phase to neutral inductance readings. However, the mutual inductances were only indirectly measured, and are incorporated in the values of the line to line inductance readings given in Table (1). For example, the measured line to line inductance $L(\theta)_{line(a)-line(b)}$ (from terminal (a) to terminal (b)) can be expressed in terms of the self inductances, $L_{aa}(\theta)$ and $L_{bb}(\theta)$, as well as the mutual inductance, $L_{ab}(\theta)$, as follows:

$$L(\theta)_{line(a)-line(b)} = L(\theta)_{aa} + L(\theta)_{bb} + 2L(\theta)_{ab} \tag{27}$$

where θ is the rotor angular position defined in Figure (1). Thus, measurement of that inductance is an indirect means of verifying the mutual term $L_{ab}(\theta)$. It must also be pointed out that all these measured values are apparent inductances, obtained at the no load condition (zero armature current).

Calculation of the Apparent and Incremental Machine Inductances

The present energy perturbation method for calculation of saturated values of apparent and incremental inductances, was used here in the calculation of the apparent and incremental winding inductances of the 15 hp permanent magnet synchronous machine described above. For this type of machine the armature is represented by three coils, a_1, a_2 and a_3, as shown schematically in Figure (1). In this case, these are the a, b and c phase windings. The rotor contains one equivalent winding on the direct axis. This winding is carrying a fixed value of field current, i_f, (that is $(di_f/dt) = 0$) as an equivalent representation to the magnetic effects of a permanent magnet, see reference [16]. Furthermore, past experience has shown that rotor damping effects are negligible for this type of machine construction as shown in the work of Nagarketti [19], hence no damper windings are considered. Accordingly, the inductance matrix representing the armature windings, for a given (fixed) rotor position, θ, can be written as follows:

$$\underline{L}(\theta)_{abc} = \begin{bmatrix} L(\theta)_{aa} & L(\theta)_{ab} & L(\theta)_{ac} \\ L(\theta)_{ba} & L(\theta)_{bb} & L(\theta)_{bc} \\ L(\theta)_{ca} & L(\theta)_{cb} & L(\theta)_{cc} \end{bmatrix} \qquad (28)$$

where $L^{(\theta)}_{ab} = L^{(\theta)}_{ba}$, $L^{(\theta)}_{ac} = L^{(\theta)}_{ca}$ and $L^{(\theta)}_{bc} = L^{(\theta)}_{cb}$ because the number of turns per phase for the a, b and c windings is the same. These inductance coefficients can represent either the apparent or incremental values depending on the type of analysis and application under consideration. These coefficients were determined using the method presented above as described next.

Inductances at No Load - The Self Inductances

At no load, the only flux sustaining excitation is that associated with the permanent magnets on the rotor. Accordingly, a quiescent field solution point is that in which the armature (stator) windings carry no current. The magnetic vector potential (m.v.p.) contour lines for a quiescent point at a given rotor position, θ, are given in Figure (3). An entire cross-section is covered in order to render the algorithm readily applicable to cases with fractional slot windings.

In order to obtain the apparent self inductance of phase (a) of the armature winding, equation (21) in conjunction with the apparent reluctivities of equation (24) are used. Equation (21) requires two current perturbations in the phase (a) winding. These current perturbations, $(+\Delta i_a)$ and $(-\Delta i_a)$, where Δi_a is about 10% of the rated load current produce two m.v.p. contours for $(+\Delta i_a)$ and $(-\Delta i_a)$ at the given rotor position as shown in Figures (4) and (5), respectively, for the series armature winding connection. The magnetic field energies at the quiescent point and the two perturbation points were thus determined and substituted in equation (21) to yield the apparent self inductance of phase (a) for the series connection.

Repeating this process at different rotor position angles yields the inductances term $L^{app}_{aa}(\theta)$. This apparent phase (a) inductance is plotted in Figure (6) over a complete cycle of 360° electrical range of the rotor angle, θ, for the series winding connection. The test measurement values of $L^{app}_{aa}(\theta)$ are also plotted in the same figure. One can see that the range of calculated values of $L^{app}_{aa}(\theta)$ varies slightly with the rotor position between about 156.5 and 158.2 micro Henries (μH). This should be viewed in comparison with a range between 169.8 and 168.1 μH for the measured values of the same inductance for the series connection given in Table (1). The difference between the test and calculated values is due to the inductance component associated with the end turns, which is included in the measured values. This end turn inductance is not included in the calculated values. This is because the calculations are based on two dimensional field solutions which do not include the three dimensional armature winding end effects. The phase (a) winding apparent inductances when connected parallel, were obtained from calculations and from test measurements and are given in Figure (7).

Repeating the steps described above for calculation of the magnetic energies using current perturbation $(+\Delta i_a)$ and $(-\Delta i_a)$, while using the incremental reluctivities of equation (23) in place of the apparent reluctivities for the finite elements in the field solution, one obtains the incremental self inductance of phase (a) at a given rotor position. Varying the rotor position over 360° electrical and repeating the perturbation process one obtains the incremental inductance, $L^{inc}_{aa}(\theta)$, as a function of the rotor position, θ, as given in Figure (6) and (7) for the series and parallel phase winding connections, respectively. As one expects, whenever some degree of saturation is present in a given magnetic circuit, the values of the incremental inductances are less than the corresponding apparent inductances, see reference [17]. This is exactly what the results presented here reveal. One would expect that the incremental inductance values would be reduced further from the corresponding apparent ones as the degree of saturation in the magnetic circuit, at the quiescent point, is increased. It must be pointed out that in permanent magnet machines such as the one at hand only moderate levels of magnetic saturation are encountered.

The self inductance terms $L^{app}_{bb}(\theta)$, $L^{inc}_{bb}(\theta)$, $L^{app}_{cc}(\theta)$ and $L^{inc}_{cc}(\theta)$, can be directly obtained from $L^{app}_{aa}(\theta)$ and $L^{inc}_{aa}(\theta)$ by phase shifts in the curves of Figures (6) and (7) of 120° and 240° electrical, respectively. This is because of the inherent symmetry in the three phase armature winding at hand.

Inductances at No Load - The Mutual Inductances

In order to determine the mutual inductance terms $L_{ab}(\theta)$, $L_{bc}(\theta)$ and $L_{ca}(\theta)$ of equation (28) at no-load, using equation (22) above, one starts with a no-load quiescent field solution for a given rotor position such as the quiescent field solution of Figure (3). In addition, when one wishes to determine the apparent and incremental values of say $L_{ab}(\theta)$, one must obtain four perturbed field solutions corresponding to four set of current perturbations $(+\Delta i_a, +\Delta i_b)$, $(+\Delta i_a, -\Delta i_b)$, $(-\Delta i_a, +\Delta i_b)$ and $(-\Delta i_a, -\Delta i_b)$. In one calculation, one must use the apparent values of elemental reluctivities at the quiescent point, to obtain four solutions and energies for calculation of the apparent inductance, $L^{app}_{ab}(\theta)$. In another calculation, one must repeat the process using the incremental values of elemental re-

Table (1) Measured Inductances of the Y-Connected 15 HP Samarium-Cobalt Permanent Magnet Synchronous Machine

Test	Phase Winding Connection	Inductance [μH] versus Rotor Angle								
		Rotor Angle - Electrical Degrees								
		0°	45°	90°	135°	180°	225°	270°	315°	360°
Phase to Neutral	Series	168.1	169.3	169.5	168.9	168.5	168.1	169.8	169.0	168.3
Phase to Neutral	Parallel	42.1	42.5	42.4	42.4	42.0	42.2	42.4	42.4	42.2
Line to Line	Series	376.7	375	363.6	361.5	364.7	376.2	375	364.3	365.7
Line to Line	Parallel	93.8	93.3	90.9	89.9	90.8	93.9	93.5	91.0	91.0

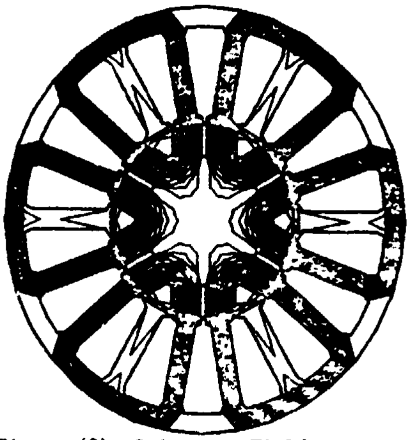

Figure (3) Quiescent Field Solution at No Load

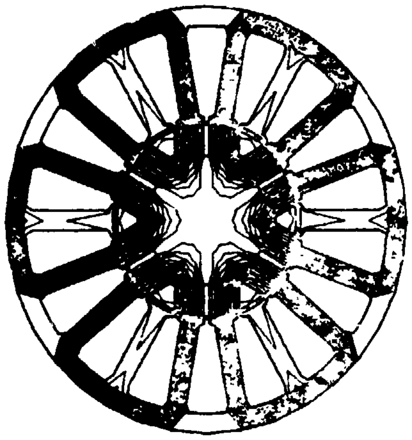

Figure (4) Perturbed Field Due to a Perturbation Current $(+\Delta i_a)$

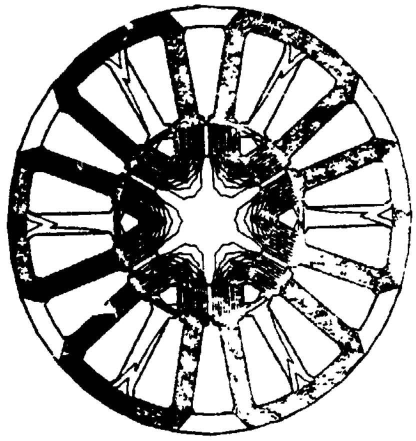

Figure (5) Perturbed Field Due to a Perturbation Current $(-\Delta i_a)$

luctivities at the quiescent point to obtain four additional field solutions and energies for the calculation of the incremental inductance, $L_{ab}^{inc}(\theta)$. Thus, one obtains a total of eight perturbed field solutions at a given rotor position in order to obtain the in-

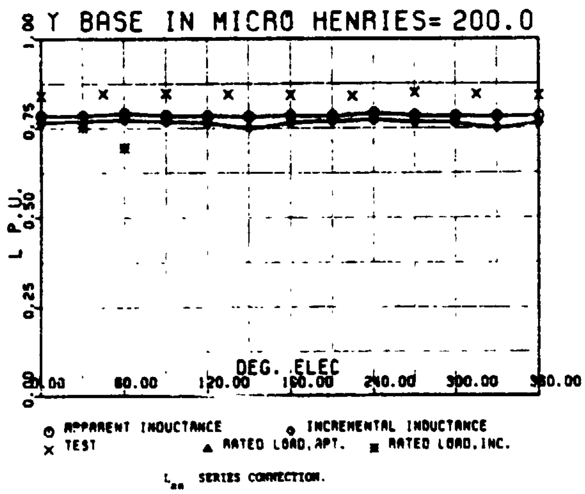

Figure (6) Inductance, $L_{aa}(\theta)$, for Series Phase Winding

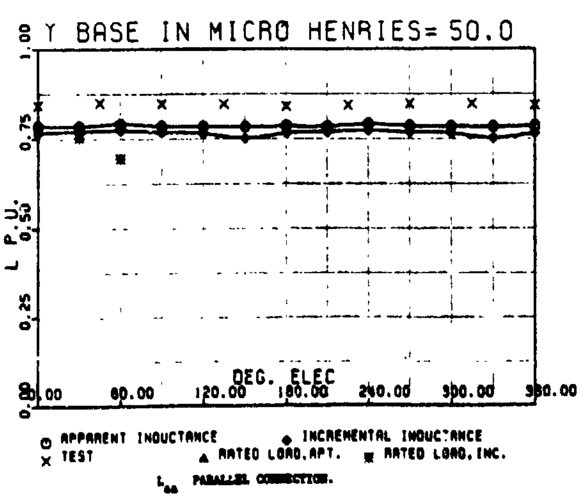

Figure (7) Inductance $L_{aa}(\theta)$, for Parallel Phase Winding

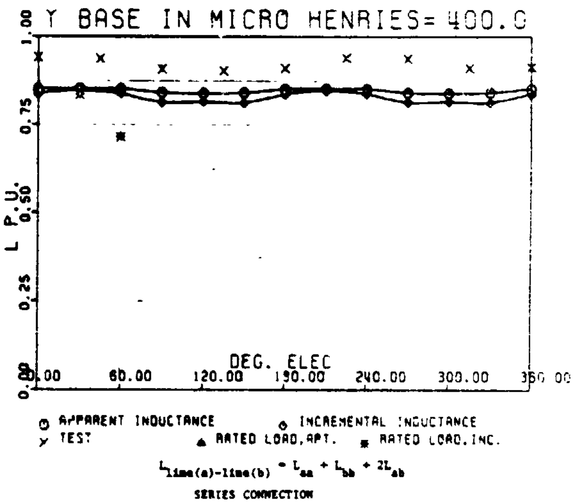

Figure (8) Inductance, $L_{line\ (a)-line\ (b)}$, for the Series Phase Winding

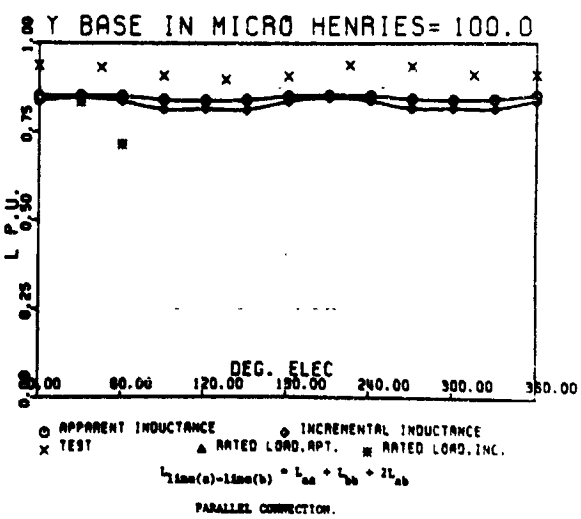

Figure (9) Inductance, $L_{line\ (a)-line\ (b)}$, for the Parallel Phase Winding

ductance values $L_{ab}^{app}(\theta)$ and $L_{ab}^{inc}(\theta)$. While this may seem excessive from a computational standpoint, in reality it is not. This is because none of the perturbed solutions requires any iterations on the elemental reluctivities, where such elemental reluctivity values are frozen at the quiescent point as explained earlier, see Figure (2). The process is repeated for as many rotor positions, θ, as one desires. Again, in this case the current perturbations Δi_a and Δi_b were about 10% of the rated load current.

Upon calculating the values of $L_{ab}^{app}(\theta)$ and $L_{ab}^{inc}(\theta)$ over a range of rotor positions covering a complete cycle of 360° electrical, for the series and parallel phase winding connections, the apparent and incremental values of the line (a) to line (b) inductances, $L^{app}_{line(a)-line(b)}(\theta)$ and $L^{inc}_{line(a)-line(b)}(\theta)$, were calculated by means of equation (27). The results of these calculations are given in Figures (8) and (9) for the series and parallel phase winding connections, respectively. Also, given in the same figures are the measured values of apparent line (a) to line (b) inductances. It should be noted that the calculated apparent values of this inductance ranged from 335 to 341 μH for the series connection, while the corresponding measured test values ranged from 362 to 377 μH. This represents very good agreement between test and calculations when one takes notice of the fact (mentioned earlier) that the calculations do not include the three dimensional armature winding end effects. This is because all the numerical field analysis given here are only two dimensional.

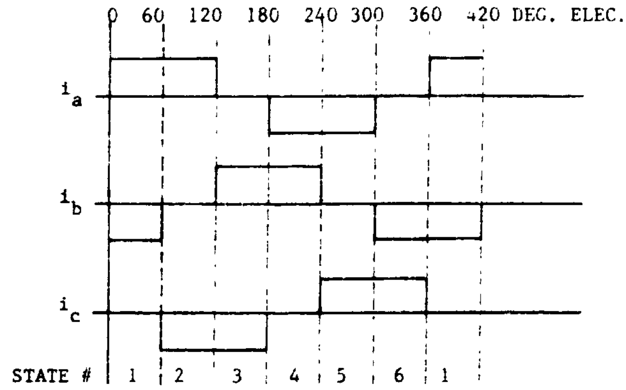

Figure (10) Idealized Phase Current of the Analysed Electronically Operated Synchronous Machine.

__Inductances at Load - The Self and Mutual Inductances__

In this type of machine only two phases of the armature winding carry current of equal magnitude and opposite polarity under load, except during very short periods of time when phase current commutation takes place. That is, throughout the 360° electrical of armature current cycle one can represent the armature current by six current states, #1 through #6, as shown schematically in Figure (10), where the very short commutation periods are neglected.

Accordingly, during state #1, the armature winding carries current in phase (a) and phase (b) only. Hence, with magnitudes of armature current at their rated load value (115 Amperes), the phase (a) and (b) windings, each in the parallel connection mode, were excited accordingly. Thus, a quiescent field solution representing state #1 was obtained in this machine at a rotor position corresponding to its location, with respect to the armature windings, at the beginning of the state. This solution is shown in m.v.p. contour form in Figure (11). Two more quiescent field solutions were obtained for the appropriate rotor positions at the middle and end of state #1, as shown in Figures (12) and (13), respectively.

Current perturbations ($i_a + \Delta i_a$, i_b) and ($i_a - \Delta i_a$, i_b) were performed using the apparent reluctivities. The corresponding perturbed field solutions are shown in m.v.p. contour form in Figures (14) and (15) respectively, for the initial rotor position in state #1, which is shown in Figure (11). The process was repeated for the two other rotor positions covering the state, and the apparent self inductances of phase (a) were calculated. The resulting three values of apparent self inductances under load were calculated from the resulting values of perturbed energies according to equation (21). The process was repeated using incremental reluctivities in the elements, from which the incremental self inductances under load were also obtained at the three rotor positions covering state #1. Results of both apparent and incremental self inductances of phase (a) under load are plotted in Figure (7) for the parallel phase winding connection. Inspection of this figure shows the effect of load on the values of the self inductances. This load effect is not as pronounced in this type of machine, in which the magnetic circuit is not heavily saturated. However, such an effect would be much more pronounced in other machines in which considerable saturation is encountered in their magnetic circuits. Such an effect would tend to decrease or increase such inductance values depending on whether the armature load current tends to magnetize or demagnetize the magnetic circuit of a given machine, respectively.

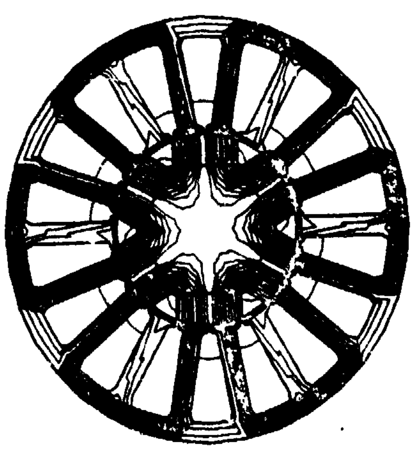

Fig. (11) Quiescent Field Solution at Rated Load, Rotor Position at Beginning of State #1.

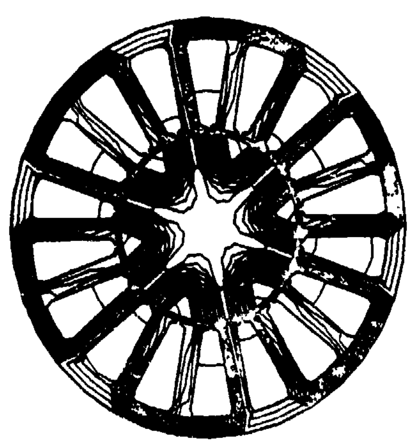

Fig. (12) Quiescent Field Solution at Rated Load, Rotor Position at Middle of State #1.

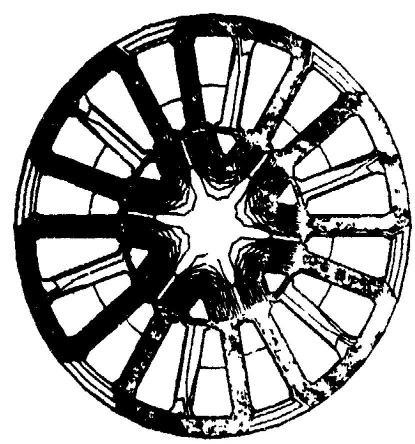

Fig. (13) Quiescent Field Solution at Rated Load, Rotor Position at End of State #1.

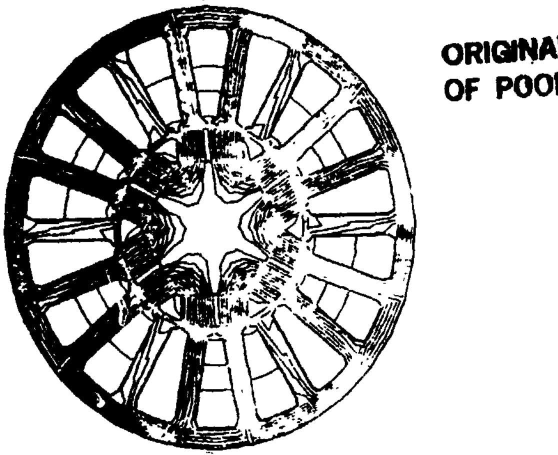

Figure (14) Perturbed Field Solution Due to a Perturbed Current $(i_a + \Delta i_a,\ i_b)$.

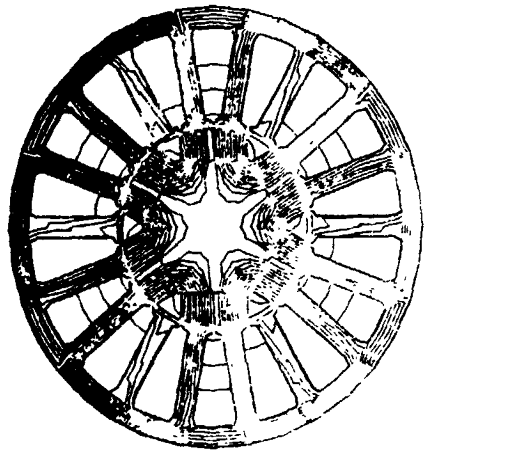

Figure (15) Perturbed Field Solution Due to a Perturbed Current $(i_a - \Delta i_a,\ i_b)$.

A process of current perturbation and corresponding perturbed field solutions was carried out using apparent then incremental finite element reluctivities, starting from the aforementioned three quiescent load points (with three rotor positions) covering state #1. The perturbation currents were $(i_a + \Delta i_a,\ i_b + \Delta i_b)$, $(i_a + \Delta i_a,\ i_b - \Delta i_b)$, $(i_a - \Delta i_a,\ i_b + \Delta i_b)$ and $(i_a - \Delta i_a,\ i_b - \Delta i_b)$. Hence, the corresponding magnetic energies were obtained for use in equation (22) to determine the apparent and incremental mutual inductances, $L_{ab}^{app}(\theta)$ and $L_{ab}^{inc}(\theta)$, at load.

Using the load values of the self and mutual, apparent and incremental inductances determined as described above, the corresponding line (a) to line (b) apparent and incremental inductances were calculated using equation (27). These results are plotted for the parallel phase winding connection in Figure (9).

CONCLUSIONS AND RECOMMENDATIONS

A method for determination of saturated values of apparent and incremental inductances of windings in rotating machinery was introduced. The method is based on current and energy perturbation concepts, as well as numerical solution of the nonlinear field problems in such rotating machinery. The method takes full account of the two dimensional intricacies of magnetic circuit geometry and nonlinearity in such machines, as well as machine winding interactions. The method was applied successfully to a 15 hp, six pole, samarium-cobalt permanent magnet electronically operated synchronous machine. Results of calculation of winding self and mutual inductances were in very good agreement with corresponding measured values, bearing in mind that armature winding end effects were not included in the numerical procedure of inductance calculation.

Prediction during the design and development stage of machine winding inductances, particularly in electronically commutated machines, where the high rates of current switching (high frequencies) are encountered is extremely important. This is because of the crucial role played by the inductive voltage drop terms $(d\lambda/dt)$ in determining the overall performance of such machines. Such important role is also played in conventional machinery applications where accurate knowledge of values of winding inductances (or reactances) is key in successful and accurate performance and design calculations. This method is most suited for such a role. Application of this powerful method to determination of inductances in heavily saturated machines will be reported in the future by these authors. Furthermore, if three dimensional field effects in end regions of machine windings are included in the future, as a result of further advanced in computer technologies and field analysis, one could envisage applying this present energy and current perturbation in the determination of more accurate values of such machine inductances at any desired normal or abnormal loading conditions.

ACKNOWLEDGEMENTS

These authors wish to acknowledge the financial support given by NASA Lewis Research Center/Department of Energy Contract NO: DEN3-65, and wish to acknowledge in particular the keen interest of the contract monitor Mr. E. Maslowski of NASA, LeRC in the various investigations conducted under this contract, of which this is one. The authors wish to thank Dr. R. Churchill, Vice-President, and Mr. B. P. Overton, Senior Design Engineer, of the Research and Development Center, Industrial Drives Division, Kollmorgen Corporation, for availing and providing access to the manufacturing and test facilities of the R and D Center and the Industrial Drives Division.

REFERENCES

[1] Delco Electronics, "Final Report on the Electromechanical Flight Control Actuator," Final Report NASA-JSC Contract NO. NAS9-14952, General Motors Corporation, Delco Electronics Div., Santa Barbara Operations, Goleta, CA, 1978.

[2] Sawyer, B., and Edge, J. T., "Design of a Samarium Cobalt Brushless DC Motor for Electromechanical Actuator Applications", Proceedings, of the IEEE-National Aerospace and Electronics Conference, Dayton, Ohio, 1977.

[3] Edge, J. T., "An Electromechanical Actuator Technology Development Program", Paper NO. 780581, Society of Automotive Engineers, Proceedings of the Aerospace Fluid Power and Control Technologies Symposium, 1978.

[4] Demerdash, N. A., and Nehl, T. W., "Dynamic Modeling of Brushless DC Motors for Aerospace Acutation", IEEE Transactions on Aerospace and Electronic Systems, Vol. 16, No. 6, 1980, pp. 811-821.

[5] Chari, M. V. K. and Silvester, P. "Analysis of Turbo Alternator Magnetic Field by Finite Elements". IEEE Transactions on Power Apparatus and Systems, Vol. PAS-90, pp. 454-464, 1971.

[6] Demerdash, N. A. and Hamilton, H. B., "Simulation for Design Purposes of Magnetic Fields in Turbogenerators with Symmetrical and Asymmetrical Rotors - Part I Model Development and Solution Technique, and Part II - Model Calibration and Applications", IEEE Transactions on Power Apparatus and Systems, PAS, Vol. 91, 1972, pp. 1985-1999.

[7] Fuchs, E. F. and Erdelyi, E. A., "Nonlinear Theory of Turboalternators Part II: Load Dependent Synchronous Reactances", IEEE Trans. on Power Apparatus and Systems, PAS, Vol. 92, pp. 592-599, 1973.

[8] Demerdash, N. A. and Hamilton, H. B., "A Simplified Approach to Determination of Saturated Synchronous Reactances of Large Turbogenerators Under Load", IEEE Trans. on Power Apparatus and Systems, PAS, Vol. 95, pp. 560-569, 1976.

[9] Chari, M. V. K., Csendes, Z. J., Minnich, S. H., Tandon, S. C. and Berkery, J., "Load Characteristics of Synchronous Generators by the Finite Element Method", IEEE Transactions on Power Apparatus and Systems, Vol. PAS-100, 1981, pp. 1-13.

[10] Concordia, C., "Synchronous Machines Theory and Performance," John Wiley & Sons, Inc., New York, 1951.

[11] Say, M. F., Alternating Current Machines, John Wiley and Sons, New York, 1976.

[12] Nehl, T. W., Fouad, F. A., Demerdash, N. A., and Maslowski, E., "Dynamic Simulation of Radially Oriented Permanent Magnet Type Electronically Operated Synchronous Machines with Parameters Obtained from Finite Element Field Solutions", Paper Accepted for Publication in the IEEE Transactions on Industry Applications, Presented at the 1980 IAS Meeting, Cincinnati, Ohio.

[13] Brice, Carnahan, Luther, H. A. and Wilkes, J. O., "Applied Numerical Methods", John Wiley & Sons, Inc., 1969.

[14] Fouad, F.A., "Finite Element Analysis For Design of Classical and Electronically Operated Machines", Ph.D. Dissertation, Electrical Engineering Department, Virginia Polytechnic Institute and State University, Blacksburg, VA, May 1981.

[15] Nehl, T. W., "A Discrete Time Model of a Power Conditioner Fed Permanent Magnet Brushless DC Motor Systems for Aerospace and Electric Vehicle Applications for Design Purposes Using Finite Elements for Machine Parameter Determination", Ph.D. Dissertation, Department of Electrical Engineering, Virginia Polytechnic Institute and State University, Blacksburg, VA, May 1980.

[16] Fouad, F. A., Nehl, T. W., and Demerdash, N. A., "Magnetic Field Modeling of Permanent Magnet Type Electronically Operated Synchronous Machines Using Finite Elements", IEEE Transactions on Power Apparatus and Systems, PAS-Vol. 100, 1981, pp. 4125-4135.

[17] Fano, R. M., Chu, L. J. and Adler, R. B., "Electromagnetic Fields, Energy and Forces", The MIT Press, 1968.

[18] Hannalla, A. Y., "Analysis of Transient Field Problems in Electrical Machines Allowing for End Leakage and External Reactances", IEEE Transactions on Magnetics, Vol. MAG-17, pp. 1240-1243, 1981.

[19] Nagarkatti, A. K., "Study of Performance and Certain Special Aspects of Electronically Commutated Brushless D.C. Motor for Electric Vehicles", M.S. Thesis, Department of Electrical Engineering, Virginia Polytechnic Institute and State University, Blacksburg, VA, May 1980.

THOMAS W. NEHL (M' 79) was born in Tubingen, West Germany, on December 22, 1952. He received the B.S., M.S., and Ph.D. degrees in electrical engineering from Virginia Polytechnic Institute and State University in 1974, 1976, and 1980 respectively.

During the summer of 1976 Dr. Nehl was employed by the National Bureau of Standards where he developed a finite element package for the solution of their nondestructive testing program. During the summer of 1977 he was employed at the NASA Johnson Space Flight center where he was engaged in the modeling of brushless dc machine type electromechanical actuator systems. From 1978 to 1980, he was employed as a research associate in the Department of Electrical Engineering at VPI&SU.

Dr. Nehl is presently an assistant professor of electrical engineering at VPI&SU. His current research activities include; finite element field analysis of machines, digital simulation of electronically operated machines, simulation of machine and electronic failure modes in electronically operated machine systems, nondestructive testing and evaluation, and power electronics.

Dr. Nehl is currently serving on the Synchronous and the Machine Theory Subcommittees of the IEEE/PES. He is a member of ASEE, Sigma Xi, Phi Kappa Phi, and Eta Kappa Nu. Dr. Nehl is the author and co-author of more than 20 transactions and technical papers in the power and magnetic field areas.

FAKHRY A. FOUAD was born in Cairo, Egypt, on January 18, 1948. He received the B.Sc.E.E. with honors and M.Sc. degrees from Cairo University, Egypt in 1971 and 1975, respectively. In June 1981, he received the Ph.D. degree in Electrical Engineering from Virginia Polytechnic Institute and State University.

From 1971 to 1977 he was with the Faculty of Engineering, Zagazig University, Egypt as a Demonstrator. He was with the Department of Electrical Engineering at VPI&SU as a Graduate Research Assistant and Research Associate from 1977 to 1979 and from 1979 to 1981, respectively. Presently Dr. Fouad is a Visiting Assistant Professor in the Department of Electrical Engineering, VPI&SU.

Dr. Fouad is a member of the Honor Society of Phi Kappa Phi, Sigma Xi, AAAS and IEEE. Dr. Fouad's current interests include numerical analysis of electromagnetic field in electric machinery for design and optimization purposes, as well as the dynamic modeling of machines including interaction with any associated power electronics and control subsystems.

NABEEL A. DEMERDASH (M'65 - SM'7[illegible]) was born in Cairo, Egypt, on April 26, 1943. He received the B.Sc. E.E. degree with distinction and first class honors from Cairo University, Egypt, in 1964 and the M.S. and Ph.D. degrees in Electrical Engineering from the University of Pittsburgh, Pittsburgh, Pennsylvania, in 1967 and 1971, respectively.

From 1964 to 1966 he was with the Faculty of Engineering, Cairo University as a Demonstrator. From 1966 to 1968 he was with the Department of Electrical Engineering, University of Pittsburgh, as a Graduate Teaching Assistant. In 1968 he joined the Large Rotating Apparatus Division of Westinghouse Electric Corporation, East Pittsburgh, Pennsylvania as a Development Engineer, where he worked on Electromagnetic Field Modeling in Rotating Machinery and the development of the asymmetrical rotor for large steam turbine-driven generators. Since 1972 Dr. Demerdash has been with the Virginia Polytechnic Institute and State University, Blacksburg, VA, where he is presently a Professor in the Department of Electrical Engineering.

Dr. Demerdash is a Senior Member of IEEE and is currently serving as a member of the Rotating Machinery Committee of PES, IEEE, as well as the Synchronous Machinery and the Machine Theory Subcommittees of PES, IEEE. He previously served as secretary and subsequently vice chairman of the Synchronous Machines Subcommittee of PES, IEEE. Dr. Demerdash is a past Chairman of the Virginia Mountain Section of IEEE. He is a member of ASEE, Sigma Xi and Eta Kappa Nu. Dr. Demerdash is the author and co-author of numerous papers in various IEEE Transactions. Dr. Demerdash's current interests and research activities include Electromechanical Propulsion and Acutation, Dynamic Modeling of Solid State Controlled and Operated Electrical Machines, Numerical Analysis of Electromagnetic Fields in Electric Machinery, as well as Machine-Power System Dynamics.

Discussion

S. H. Minnich (General Electric Co., Schenectady, NY): The authors have made a distinction between two kinds of reluctivity (permeability) which can be defined at a given operating point on the B-H characteristic. Their use of the term "incremental" reluctivity, in the sense they have defined it is a natural one, in terms of the common meaning of that word. Unfortunately, in magnetics, the term "incremental" has a special, and different, meaning.[1,2,3] Figure 1 shows the "incremental" loops which are obtained when small perturbations in H are applied around a fixed operating point. The slope of these small loops is the incremental permeability

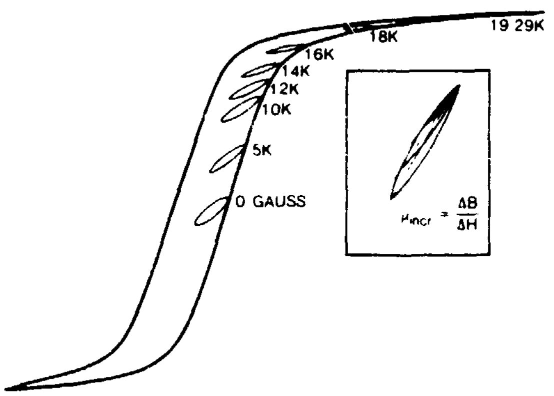

Figure 1. Schematic Representation of Incremental Minor Loops

The technically accepted terminology for the concept to which the authors refer is "differential" permeability.[1] It is the slope, dB/dH, of the B-H characteristic at the point in question. I believe that the above distinction is widely recognized. The authors should consider changing their terminology to minimize future confusion. A possible terminology for the inductance corresponding to the differential permeability would be the differential inductance. Although it is not so crucial, I would point out that what the authors call the "apparent" permeability is called the "normal" permeability in [1].

It appears that the no-load inductance measurements the authors refer to were made with a locked rotor, in which case it should have been (for small signals) the incremental permeability that described the B-H path in the stator iron. In that case, the measured value might have been expected to be smaller than a value corresponding to the "apparent" permeability or to the "differential" permeability; the latter are the calculated values which the authors use for comparison, and the measured value was actually larger than either. The authors correctly point out that the end winding inductances would have to be subtracted from the measured value for a true comparison. It is not possible to comment further without understanding the kind of iron used in the stator, and the open-circuit operating point on its B-H characteristic. Since permanent magnet machines have magnetic circuits which are (effectively) mostly air, the inductances may be insensitive to *any* assumption made about the stator permeability. It does not appear that the comparisons made are significant in sorting out the different kinds of inductance.

The authors have couched all their calculations in terms of the energy method of evaluating inductances. It appears that the same concepts would apply if the inductances were calculated in terms of flux linkages. Only one calculation would be necessary per inductance in that case. Would the authors comment on this point.

In the middle of the second column of page 1, the authors describe an increase in machine capability obtained from a decrease in the number of turns in the phase windings. This argument seems somewhat irrelevant. Decreasing the number of turns from 12 to 9 will decrease the inductances by $(3/4)^2$ or nearly a factor of one-half. This has nothing to do with any magnetic calculation procedure. It is mentioned that this increase in capability was obtained at the "same" supply voltage. This is a rather artificial result. The selection of the number of turns in the winding and the selection of the rated supply voltage are interrelated in a well known way in order to assure that the machine draws rated current (a number usually set by thermal limits). If the turns are changed without changing the terminal voltage, one or the other of the configurations was not a consistent design. Perhaps the authors would like to clarify this point.

REFERENCES

1. Bozorth, *Ferromagnetism*, Van Nostrand, New York, 1951, pp 6, 539ff, 845ff.
2. *Magnetic Circuits and Transformers*, Staff, Electrical Engineering Department- MIT, MIT Press, 1965, p. 198.
3. S. H. Minnich, "Incremental Permeabilities for Transient Analysis of Large Generators by the Finite—Element Method," J. Appl. Phys. *52* (3), March 1981, p. 2428.

Manuscript received February 26, 1982.

T. W. Nehl, F. A. Fouad and N. A. Demerdash: These authors wish to thank Mr. S. H. Minnich for his interest in the paper, and offer the following in response to the various points and queries put forward by Mr. Minnich:

1) The use of the term "incremental permeability" as utilized in our paper is an accepted way of refering to the physical process and method of calculation explained in the paper. Identical utilization of the same term can be found in many textbooks, an example of which is a book by Fano, Chu and Adler, which is Reference (17) in our paper. In this particular type of application (samarium cobalt permanent magnet machines, with M15-29 Gauge Stator Laminations), subject of this paper the hysteresis effect is almost nonexistant. That is, the B-H characteristic of the stator core lamination material is a single valued curve for all practical purposes. Hence, the slope of the minor hysteresis loops, refered to by Mr. Minnich as the "incremental permeability" is equal to the slope of the tangent to the single valued B-H characteristic used in the paper. Again, minor hysteresis loops are almost nonexistant in this class of applications.

2) The authors wish to point out that the use of the term "apparent permeability" in place of what Mr. Minnich refers to as the "normal permeability" is an acceptable usage in many textbooks on magnetic fields, an example of which is again Reference (17) in our paper.

3) Because of the almost nonexistant hysteresis effect in the type of application subject of our paper, the distinction suggested by Mr. Minnich between 'differential permeability or inductance" and "incremental permeability or inductance" is negligible. Hence, for all practical purposes, the two terms are one and the same in this class of applications. The above line of reasoning is further enhanced by the low level of saturation which inherently exists in magnetic circuits of permanent magnet machines of the type at hand. This is in addition to their large effective airgap reluctance in proportion to the ferrous portion of the magnetic circuit reluctance.

4) We wish to confirm that the no load inductance measurements were made with a locked rotor. Also, the incremental and apparent permeabilities as defined in the paper were used in the corresponding calculations. The inductance measurement was carried out using a commercially available inductance bridge.

However, we wish to point out to Mr. Minnich that the main reason both the calculated incremental and apparent inductances are lower than the measured inductance values is due to the fact mentioned in our paper, namely that the contribution of the end connections (with its three dimensional magnetic field nature) to the values of inductances could not be included in the two dimensional field calcultion, while it naturally is included in the measured values. Thus, the fact that the measured inductance values were greater than those calculated from the two dimensional field model is consistent with what one would have expected as a result of the inability to account for the end turn connections in a two dimensional field model. It must be pointed out that the proportion of the end connections to the effective length of the armature conductors burried in the armature slots is not insignificant. Therefore, without including the three dimensional end connection effect, one could not possibly have expected to have measured values of inductances that would be less than those calculated ones. This is particularly the case in view of the lightly saturated state of the magnetic circuit. Accordingly, we could not agree with Mr. Minnich in suggesting that the measured values should have been less than the calculated ones. In fact, based on "educated intuition" one would expect the opposite of what Mr. Minnich suggested.

5) Mr. Minnich raises the question as to why we chose to calculate the various machine winding inductances through energy calculations, rather than directly by flux linkages with the various windings. The choice of the energy calculation concept was made because it is independent of the degree of complexity of the contours of the ferrous (iron) and current carrying parts of any magnetic circuit under consideration.

Thus, the same algorithm of inductance calculation can be utilized, in conjunction with any two-dimensional magnetic field calculation algorithm, to determine the inductances associated with any given electric device. On the other hand, had we chosen the flux linkages approach, the resulting algorithm would have been limited to the contours of the case at hand, or at most to that class of contours for the particular type of machine being analyzed.

6) The decrease of the values of the machine inductances by a factor $(3/4)^2$ due to reduction in the number of turn from 12 to 9 per coil is a key factor in the design of the type of machine at hand, where high rates of current switching is encountered (as high as 400 Hz for the inverter switching). This leads to the imposition of a limitation on the rate of phase current build-up from the instant of "switching on" of a given phase, which is inversely proportional to the value of line to line machine inductance. This is because the rate of current build up, (di/dt), per phase is equal to (neglecting resistance):

$$(di/dt) \simeq 1/L\ (E - e(t)) \qquad [1]$$

where E is the dc voltage source, while e(t) is the instantaneous value of the back emf induced in the phases by magnet rotation. Thus based on equation (1) above, the higher the inductance, the lower the (di/dt). This is while the available switching time per phase in an ac cycle is determined by the inverter frequency, and hence no flexibility is possible in its duration. Therefore, unless the current build up rate, (di/dt), is higher than a minimum value (function of the inverter frequency), one may not be able to reach the desired value of armature current per phase within the period of time during which this particular phase is "switched on", see the "on" and "off" periods in the phase current cycle diagram Figure (10) in the paper.

The fact that the peak current values, and hence peak power (and in some instances rated power) capabilities of this class of machines are indeed heavily dependant on the motor inductances, are well documented in a number of earlier papers and publications by these authors, see Reference (15) of the paper, as well as References (18) and (19) listed below.

In all such investigations, one must have access to reliable values of machine winding inductances during the design stage in order to predict the current build-up rate given in the above equation. Designers, in so far as we know, are usually unable to provide such data with certainty, and hence the use of a method such as the one given in this paper for obtaining these inductances is almost indespensible for accurate prediction of performance of machine systems of this type.

The line of reasoning offered by Mr. Minnich in the relationship between the number of turns, the supply voltage, and rated current is valid for constant speed machines. However, it is rather simplistic and totally inconsistent with the basic design facts of this class of machines in which operating speeds vary widely. Mr. Minnich states in his discussion that, "the selection of the number of turns in the winding and the selection of the rated supply voltage are interrelated in a well known way in order to assure that the machine draws rated current." We wish to point to Mr. Minnich that this relationship becomes very direct and simple only if one is dealing with sinusoidal current and voltage waveforms, and when the machine speed is function of a given supply frequency in addition to the number of poles (synchronons speed). This is not the case at hand, where the phase currents are from pure sinusoidals, and the rated speed of a given machine is only limited by the upper bounds of mechanical stresses on the rotating members.

Accordingly in the case of the machine at hand, one can keep the same supply voltage, while reducing the number of turns and increasing the rated machine speed for the same magnetic circuit flux per pole (permanent magnet) while maintaining that level of supply voltage. Thus, reduction of the number of turns per phase was how lower machine winding inductances were achieved, in order to allow the necessary current buildup rate, equation (1). This is in order to reach the required current levels during the fast switching periods to which the machine winding is subjected. Based on the above, we could not disagree more with the statement made by Mr. Minnich that, "If the turns are changed without changing the terminal voltage, one or the other of the configurations was not a consistant design." Thus, one can see the key role of the inductance values in setting machine current build up rates, and hence machine current leveles during the available "on" time per phase. Notice, the machine power capability is directly proportional to the machine current level.

We hope we have responded adequately to all pertinent points in Mr. Minnich's discussion. We finally wish to express our appreciation to Mr. Minnich for his interest in the paper, and for his various queries, which we are sure were very helpful in enabling us to clarify ambiguities in this investigation.

REFERENCES

18. T. W. Nehl, F. A. Fouad, N. A. Demerdash, "Digital Simulation of Power Conditioner-Machine Interaction for Electronically Commutated DC Permanent Magnet Machines." *IEEE Transactions on Magnetics*, Vol. MAG-17, No. 5, 1981, pp. 3284-3286.
19. T. W. Nehl, F. A. Fouad, N. A. Demerdash and E. Maslowski, "Dynamic Simulation of Radially Oriented Permanent Magnet Type Electronically Operated Synchronous Machines with Parameters Obtained from Finite Element Field Solutions." *IEEE Transactions on Industry Applications*, Vol. IA-18, Number 2, 1982, pp. 172-182.

Manuscript received June 22, 1982

APPENDIX (4)

ON CALCULATION OF MACHINE WINDING INDUCTANCES BY ENERGY PERTURBATION AND FINITE ELEMENT METHODS

Demerdash, N. A., Fouad, F. A., and Nehl, T W., "Determination of Winding Inductances in Ferrite Type Permanent Magnet Electric Machinery by Finite Elements," IEEE Transactions on Magnetics, VOL. MAG-18, 1982, pp. 1052-1054.

DETERMINATION OF WINDING INDUCTANCES IN FERRITE TYPE PERMANENT MAGNET ELECTRIC MACHINERY BY FINITE ELEMENTS

N. A. Demerdash, F. A. Fouad, and T. W. Nehl *

Abstract

A key design factor in ferrite type permanent magnet machines is the accurate knowledge of the values of machine winding inductances during the design stage. In the present paper, a method which is based on perturbation of the energy stored in the magnetic field, and on numerical models of simulation of such permanent magnets is used in calculating machine inductances. The effect of change in the values of these winding inductances with magnet position throughout the cycle of operation of such machines is given. These inductances also include the apparent and incremental values, whose definition is directly related to the choice of apparent or incremental reluctivities in the energy perturbation process. Results of application of this method to the calculation of inductances in a 15 hp 6-pole ferrite type electronically operated permanent magnet machine are given. These calculated values of inductances are in good agreement with the measured values.

INTRODUCTION

Permanent magnet machines are finding increasing acceptance and use in many applications. These applications include machine tool drives, electro-mechanical propulsion in electric vehicles, and recently in robotics. In most of these applications, solid-state control and operation of these machines is used. In applications where machine weight and volume must be kept to a minimum, samarium-cobalt (rare earth) materials are most preferred for use in manufacturing the needed permanent magnets. However, because of the relatively high price, availability, and problems of security of supply of cobalt, ferrite type magnets are proving to be just as effective in the manufacturing of machines with performance equivalent to those manufactured with samarium cobalt magnets[1]. This is done at an acceptable sacrifice in increase in machine weight and volume, and represents no difficulties in many of those applications where weight and volume limitations are not stringent.

An example of such a machine is a 15 hp, 120 volt, 6-pole, 8840 rpm electronically commutated brushless dc machine (operated from a dc source through a 3 phase solid-state inverter/converter) which was built and tested for possible use as a propulsion unit for electric vehicles, a cross-section of which is given in Figure (1). The armature (stator) winding of such a machine is of the 3 phase type. A successful design of such machines is predicated upon reasonably accurate knowledge of the armature winding self and mutual phase inductances. The crucial role played by these inductances is due to the fast electronic switching of the phase currents during commutation. Hence, the L(di/dt) terms play a major role in determining the ability of the machine and its corresponding electronic controller to achieve the necessary current buildup rate and level to meet the rated power and peak power requirements. The phase current buildup during commutation (di/dt), can be approximated by:

$$(di/dt) \approx [E - e(t)]/L \tag{1}$$

where E is the dc source voltage, while e(t) is the instantaneous value of the back emf induced in the given phase undergoing commutation. Thus, on the basis of equation (1) above, the higher the inductance, L, the lower the current buildup rate (di/dt), the longer it takes to reach the necessary rated current. This is while the available switching time during which current buildup can take place is limited in an ac cycle of armature current by the aforementioned 3 phase inverter/converter frequency. Further details on these aspects are to be found in reference [2]. Accordingly, the accurate calculation during the design stage of winding inductances in such permanent magnet electronically commutated machines is of paramount importance.

BACKGROUND OF METHOD OF INDUCTANCE CALCULATION

In a previous paper[3], these authors presented a method, which is based on perturbations of winding currents, and the associated incremental change in the energy stored in the magnetic field, to calculate such machine inductances. This approach enables one to circumvent the difficulties associated with calculating such parameters using the flux-linkage approach, particularly in the presence of complex, and continuously changing contours (due to rotor position change) in rotating machinery. This perturbation method will only be briefly described here for the sake of continuity. The perturbation method at hand is applied in the calculation of the 3 phase armature winding inductances of the above mentioned 15 ferrite type permanent magnet brushless dc machine, a schematic representation of which is given in Figure (2).

The method of finite elements[5] is used to determine the field distribution under no load, as well as some load cases. Representation of the ferrite permanent magnet pieces mounted on the rotor was carried out in the finite element magnetic field modeling according to a method described by these authors in a previous paper[4]. In this approach a permanent magnet is replaced by an electromagnet whose excitation is supplied from a constant current source, Figure (2), and whose total ampere turns are functions of the permanent magnet geometry and coercivity.

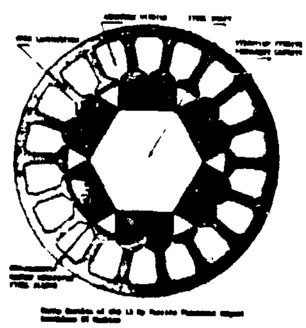

Fig. 1.

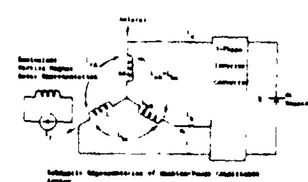

Fig. 2.

The current/energy perturbation method of calculation of inductances[3] is based upon consideration of the total energy stored in the magnetic field of a given device comprising n windings. Consider the voltage at the terminals of the jth winding, one can write

$$v_j = R_j\, i_j + \frac{\partial \lambda_j}{\partial i_1}\frac{di_1}{dt} + \frac{\partial \lambda_j}{\partial i_2}\frac{di_2}{dt} + \cdots + \frac{\partial \lambda_j}{\partial i_j}\frac{di_j}{dt} + \cdots\cdots + \frac{\partial \lambda_j}{\partial i_n}\frac{di_n}{dt} + \frac{\partial \lambda_j}{\partial \theta}\frac{d\theta}{dt} \tag{2}$$

However, for a fixed rotor position the last term in equation (2) equals zero because (dθ/dt)

*Manuscript received June 20, 1982.
The authors are with Virginia Polytechnic Institute and State University, Blacksburg, VA 24061.

0018-9464/82/1100-1052$00.75©1982 IEEE

which equals the rotor angular speed would be equal to zero. Here in equation (2) the partial derivative of the flux linkage, λ_j with respect to a winding current i_k, $(k = 1, 2,.,j,..,n)$ is the incremental inductance, L^{inc}_{jk}. Therefore the total stored global energy, w, associated with the system of n-coupled windings can be written as:

$$w = \sum_{j=1}^{n} w_j = \sum_{j=1}^{n} \left| \sum_{k=1}^{n} \int_{i_k(0)}^{i_k(t)} (L^{inc}_{jk}\ i_j)\ di_k \right| \quad (3)$$

In reference [3], it was shown that the self and mutual inductance terms of the various n windings can be expressed as the partial derivatives of the global stored energy, w, with respect to various winding current perturbations, Δi_j. These derivatives can, in turn, be expanded around a "quiescent" magnetic field solution obtained for a given set of winding currents, in terms of various current perturbations $\pm\Delta i_j$ and $\pm\Delta i_k$ in the j<u>th</u> and k<u>th</u> wind-windings, and the resulting change in the global energy. For the type of machine at hand where $L_{jk} = L_{kj}$, this process yields for the self and mutual inductance terms the following:

$$L_{jj} = \frac{\partial^2 w}{\partial(\Delta i_j)^2} = [w(i_j - \Delta i_j) - 2w + w(i_j + \Delta i_j)]/(\Delta i_j)^2 \quad (4)$$

and

$$L_{jk} = \frac{\partial^2 w}{\partial(\Delta i_j)\partial(\Delta i_k)} = [w(i_j + \Delta i_j,\ i_k + \Delta i_k) - w(i_j - \Delta i_j,\ i_k + \Delta i_k) - w(i_j + \Delta i_j,\ i_k - \Delta i_k) + w(i_j - \Delta i_j,\ i_k - \Delta i_k)]/(4 \cdot \Delta i_j \cdot \Delta i_k) \quad (5)$$

Here, the global energy w at the quiescent point is calculated from a magnetic field solution whose excitation current set in the n windings is $(i_1, i_2, \ldots, i_j, \ldots, i_k, \ldots i_n)$. Also, the global energy $w(i_j \pm \Delta i_j)$ is the energy calculated from a magnetic field solution whose excitation current set in the n windings is $(i_1, i_2, \ldots, \ldots, (i_j \pm \Delta i_j), \ldots, i_n)$, and the global energy $w(i_j \pm \Delta i_j,\ i_k \pm \Delta i_k)$ is the energy calculated from a magnetic field solution whose excitation current in the n windings is $(i_1, i_2, \ldots, (i_j \pm \Delta i_j), \ldots, (i_k \pm \Delta i_k), \ldots, i_n)$.

The perturbed field solutions can either be obtained using the incremental or apparent reluctivities of the various finite elements, thus, yielding the incremental or apparent winding self and mutual inductances as will be shown in the next section.

MODELING OF THE PERTURBED EXCITATION CURRENTS

Upon obtaining a solution to the nonlinear magnetic field problem in the cross-section of a given machine, for a given set of winding excitation currents (which will be referred to as the quiescent solution point for that set of excitation currents), one obtains a given value of reluctivity for each element within the cross-section, including those elements in iron. Samples of such quiescent solutions are displayed graphically in Figures (3) and (4) for a no-load case, as well as rated load case, respectively, for a given rotor position.

At any such given quiescent solution the status of each iron element can be represented in the B-H

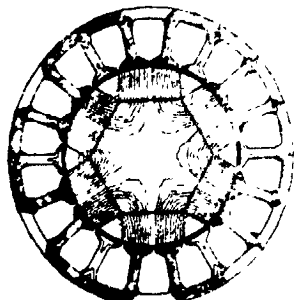

Fig. 3.

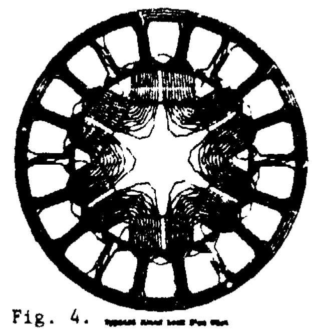

Fig. 4.

saturation characteristic by the quiescent value of reluctivity (permeability) shown graphically in Figure (5). Also, the magnetic energy stored in the field within each element is equal to the product of the shaded area of Figure (5) times elemental area times the effective axial length of a given machine.

Once a nonlinear field solution is determined throughout the continuum (the quiescent solution), the incremental and apparent reluctivities for each element are known, and are graphically displayed for a given iron element by the tangent and cord passing through the quiescent point as shown in Figures (6) and (7) respectively. A perturbation of the excitation of any winding in a given machine yields a change in the field intensity in an element which is shown by $(\pm\Delta H)$ in Figures (6) and (7).

Should one desire to obtain the incremental inductances, one must carry out the perturbation process to the field solution along the incremental reluctivity line as shown in Figure (6). In this process the incremental reluctivities are "frozen" at their quiescent point values. This is done while solving for the effect of excitation perturbation throughout the field region, using a linearized finite element solution (along the incremental reluctivity line) around the quiescent point. This process yields for every element an excess or deficite energy per element due to the positive and negative current perturbations, respectively. These energies are represented schematically by the shaded areas in Figure (6). Thus, the new global energies, $w(i_j \pm \Delta i_j)$ are determined as the algebraic sum of the quiescent and excess or deficit energies for all the elements.

Substituting $w(i_j \pm \Delta i_j)$ in equation (4) yields the incremental self inductance, L^{inc}_{jj}, of the j<u>th</u> winding. Perturbing two currents i_j and i_k in the j^{jj} and k windings, one can similarily obtain the four global energies, $w(i_j \pm \Delta i_j,\ i_k \pm \Delta i_k)$. Upon substituting these four energies in equation (5), one obtains the incremental mutual inductance, L^{inc}_{jk}.

A similar process, with the perturbed field solutions having been determined, using the values of the apparent reluctivities at the quiescent point of Figure (7), yields the apparent self and mutual inductances L^{app}_{jj} and L^{app}_{jk}, respectively. Results of such calculations are compared with measured inductance values for the above mentioned 15 hp ferrite permanent magnet machine, and are given next.

RESULTS

The method described above was used to calculate the inductances associated with the three phase armature winding of the 15 hp ferrite type permanent magnet electronically commutated brushless dc machine mentioned above. These 15 hp machine winding inductances were also measured in the laboratory,

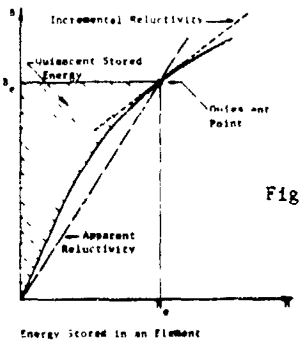

Fig. 5.

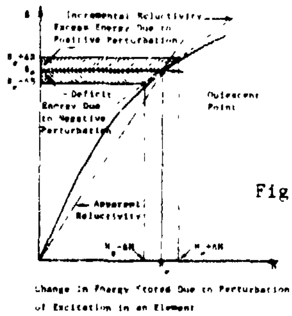

Fig. 6.

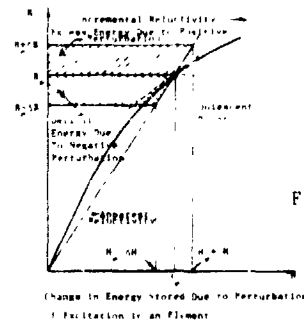

Fig. 7.

using a commercially available digital inductance bridge.

The results of calculation and measurement of phase to neutral self inductances, L_{aa}, at various rotor positions, θ, which cover the entire 360° electrical cycle are given in Figure (8). These are the values of the familiar term of the self inductance per phase. The calculated and measured values were obtained at no load, and are compared in the same Figure (8).

It must be pointed out that the measured values of self inductances naturally include the contribution of the end connections of the coils of the windings. However, the end connection contribution to these inductance values is not included in the calculated values, because the calculation algorithm is based on a two dimensional field solution, while such end effects would require three dimensional field modeling for their inclusion in the calculated values. Because of the small contribution of the end connections, this was not done in the calculated values. This also explains the slight difference in values between the calculated and measured inductances which are plotted in Figure (8).

The results of calculation and measurement of the line to line inductance, $L_{line(a)-line(b)}$, which is calculated from the values of the phase self inductances, L_{aa} and L_{bb}, and mutual inductance, L_{ab}, as

$$L^{(\theta)}_{line(a)-line(b)} = L^{(\theta)}_{aa} + L^{(\theta)}_{bb} + 2L^{(\theta)}_{ab} \qquad (7)$$

is plotted in Figure (9) as a function of the rotor position angle, θ, over the complete 360° electrical cycle. This line to line inductance calculation is shown rather than the mutual inductance term, since a direct measurement of that value was far easier to obtain in the laboratory. The closeness of the results of the calculation and measurement is indicative of the validity of the mutual inductance term, $L^{(\theta)}_{ab}$, obtained by calculation using the energy and excitation current perturbation method outlined above. The slight discrepancy between the calculated and measured values is due to the fact, mentioned above, that the present calculation method does not include the effect of the end connections of the coils, while the measured values, naturally include the end connection contribution to the winding inductances.

The values of the phase self inductance, and line to line inductance were calculated under rated load conditions, and plotted in Figures (8) and (9) respectively. The effect of the load (armature) currents on the winding inductances is negligible as can be clearly seen in both figures.

CONCLUSIONS

The present energy and excitation current perturbation method has been shown here to be effective in the calculation of self and mutual inductances of windings of machines containing ferrite type permanent magnets. These calculated inductances were checked versus measured values of inductances in a 15 hp ferrite-type permanent magnet brushless dc machine, and good correlation between the calculation and measurement values was obtained. The method can therefore be most effectively used during design stages of such machines, to determine the suitability of machine inductance values from the standpoint of high speed switching (electronic commutation) applications. This is to allow the determination of necessary design modifications in the magnetic circuits of such machines before final choices are made in the manufacturing process of such equipment, which would help avoid costly design changes at later stages.

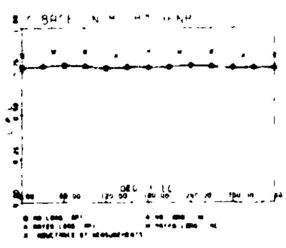

Fig. 8.

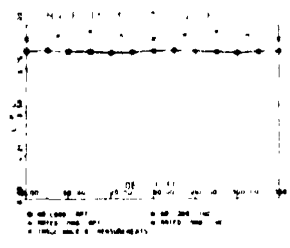

Fig. 9.

REFERENCES

[1] Demerdash, N. A., Miller, R. H., Nehl, T. W., Overton, B. P., and Ford, C. J., "Comparison Between Features and Performance Characteristics of Fifteen HP Samarium Cobalt and Ferrite Based Brushless DC Motors Operated by the Same Power Conditioner," paper accepted for publication in full in the IEEE Transactions on Power Apparatus and Systems and has been presented at the 1982 PES Winter Meeting, New York.

[2] Nehl, T. W., Fouad, F. A., Demerdash, N. A., and Maslowski, E., "Dynamic Simulation of Radially Oriented Permanent Magnet Type Electronically Operated Synchronous Machines With Parameters Obtained From Finite Element Field Solutions," IEEE Transactions on Industry Applications, Vol. IA-18, No. 2, pp. 172-182, 1982.

[3] Nehl, T. W., Fouad, F. A., and Demerdash, N. A., "Determination of Saturated Values of Rotating Machinery Incremental and Apparent Inductances by a Perturbation Method." Paper accepted for publication in full in the IEEE Transactions on Power Apparatus and Systems and has been presented at the 1982 PES Winter Power Meeting, New York.

[4] Nehl, T. W., Fouad, F. A., Demerdash, N. A., "Digital Simulation of Power Conditioner-Machine Interaction for Electronically Commutated DC Permanent Magnet Machines." IEEE Transactions on Magnetics, Vol. MAG-17, No. 5, 1981, pp. 3284-3286.

[5] Silvester, P., and Chari, M. V. K., "Finite Element Solution of Saturable Magnetic Field Problems." IEEE Transactions on Power Apparatus and Systems, Vol. PAS-89, pp. 1642-1652, 1970.

APPENDIX (5)

ON SIMULATION OF MACHINE-POWER CONDITIONER DYNAMIC INTERACTION OF BRUSHLESS DC MOTOR SYSTEMS

Nehl, T. W., Fouad, F. A., Demerdash, N. A., and Maslowski, E., "Dynamic Simulation of Radially Oriented Permanent Magnet Type Electronically Operated Synchronous Machines With Parameters Obtained From Finite Element Field Solutions," IEEE Transactions on Industry Applications, Vol. IA-18, 1982, pp. 172-182.

Dynamic Simulation of Radially Oriented Permanent Magnet-Type Electronically Operated Synchronous Machines with Parameters Obtained from Finite Element Field Solutions

THOMAS W. NEHL, MEMBER, IEEE, FAKHRY A. FOUAD, NABEEL A. DEMERDASH, SENIOR MEMBER, IEEE, AND EDWARD A. MASLOWSKI

Abstract—**A dynamic model for simulation of the transient interaction between radially oriented permanent magnet-type synchronous machines and their corresponding transistorized current source power conditioners is presented. Some key machine parameters used in this dynamic model were obtained from finite element field solutions. This dynamic model was used to obtain the transient interaction between a 15-hp samarium cobalt radially oriented permanent magnet electronically operated synchronous machine and its corresponding power conditioner. The machine was constructed for electric vehicle propulsion. Excellent correlation between various digitally simulated and actual test current and voltage waveforms, in various branches of the machine–conditioner network, has been achieved. These results are given. This modeling approach is applied to machines during the design stage, where the finite element modeling is the only way to obtain the necessary machine parameters for dynamic simulation. It is shown how such a combination of the computer-aided design tools can help in prevention of design misjudgements that can prove costly to remedy once the hardware is in place. This is done through an actual design example of an additional machine being manufactured for electric propulsion applications.**

INTRODUCTION

ELECTRONICALLY operated permanent magnet-type synchronous machines are finding increasing application as prime movers in actuation, machine tool drives, and vehicle propulsion [2], [3], [5]. These machines, when operated from square-wave current-source-type power conditioners, experience discretely stepping armature magnetomotive forces (MMF's), rather than the smoothly rotating MMF's of classical systems with sinusoidally time-varying armature currents. For this reason, classical frequency domain-type approaches are invalid and can lead to substantial errors when used to predict the performance of such devices [2].

In this paper, a totally digital approach to the simulation of the instantaneous interactions between such machine-power conditioner systems is described and verified against measured results. This modeling approach combines use of the two-dimensional finite element method for solving nonlinear magnetostatic field problems and associated machine parameter determination [1], [2], [3], with a discrete time nonlinear network model based on generalized network graph theory concepts [2], [6]. The advantages of the approach presented here over those used in similar problems by other investigators [7]-[13] can be summarized in the following points.

1) The machine parameters are determined by the finite element method. Therefore, the impact of machine winding and geometry changes on the overall system can be assessed without the construction of costly prototypes.

2) The voltage drops across all power switching elements (transistors, thyristors, diodes, etc.) are included.

3) The entire machine-power conditioner network (excluding the snubbers) are included in the analysis using only one network graph. No reduced order network models corresponding to the individual switching states of the network are used because the voltage drops across the switching elements are not neglected. This greatly simplifies the modeling of systems with a large number of different switching states, since only one network graph and its corresponding state equations need be used. Furthermore, the use of one network graph to cover all states and modes of operation results in a model that is more general.

4) No rotating reference frames, which tend to obscure the physical interpretation of parameters and results, are used. Consequently, all model parameters can be obtained directly from test measurements, if available, or by means of the finite element method and/or from design calculations.

5) The instantaneous branch voltages, currents, and powers throughout the system, as well as the instantaneous electromagnetic machine torque and power, are calculated and automatically plotted versus time.

Paper IPCSD 81-22, approved by the Industrial Drives Committee of the IEEE Industry Applications Society for presentation at the 1980 Industry Applications Society Annual Meeting, Cincinnati, OH, September 28–October 3. This paper was supported by U.S. Department of Energy/National Aeronautics and Space Administration LeRC Contract No. DEN3-65 and U.S. Air Force SCEEE Contract No. SIP/78-17. Manuscript released for publication June 1, 1981.

T. W. Nehl, F. A. Fouad, and N. A. Demerdash are with the Department of Electrical Engineering, Virginia Polytechnic Institute and State University, Blacksburg, VA 24061.

E. A. Maslowski is with the NASA Lewis Research Center, Cleveland, OH.

0093-9994/82/0300-0172$00.75 © 1982 IEEE

6) Furthermore, the status of all power switches (transistors, thyristors, diodes, etc.) is determined and automatically plotted versus time.

7) Constant, as well as variable-speed, operation can be accommodated, including the dynamics of the rotating masses [2], [5].

8) Digital, rather than analog or hybrid, techniques are used to integrate the differential equations, which result in higher accuracy, lower cost, and greater flexibility.

The combined finite element field analysis and the discrete time machine-power conditioner modeling approach introduced in this paper are applied to two prototype systems. The first is a 15-hp 120-V samarium cobalt permanent magnet (radially oriented) synchronous machine for a electric vehicle propulsion, which is operated from a current-source-type power conditioner. The no-load back electromotive force (EMF) waveforms for this machine were obtained by means of the finite element method. These waveforms are in excellent agreement with the measured waveforms [1], [2], [3]. The finite element calculated EMF's are subsequently used, as will be shown in a later section of this paper, as forcing functions for the discrete time machine-power conditioner network model. Excellent agreement between simulation and measured voltage and current waveforms is achieved.

This method is then applied to the design of a similar system in which a ferrite-type magnet machine is the prime mover. The effects of winding inductances, stator slot skewing, and commutation advance on the overall system performance are given prior to actual construction. Significant design "pitfalls" were avoided as a result of using this approach, as will be seen in later sections.

NETWORK MODEL FOR RADIALLY ORIENTED PERMANENT MAGNET SYNCHRONOUS MACHINES

A lumped parameter network model for radially oriented permanent magnet synchronous machines based upon a four-winding machine representation is derived. Three of the four windings represent the three armature phases, a, b, and c. The fourth one, f, is a fictitious winding, which is an equivalent field winding that represents the permanent magnet system on the rotor as was shown in the companion paper [1]. It will be shown that the effect of the fictitious field winding together with its corresponding dc field current is equivalent to a set of three-phase back EMF waveforms that can be readily obtained from testing the actual hardware, if available, or by means of the finite element method using design data if such hardware is not available [1], [2], [3].

Because of the poor electrical conductivities associated with samarium cobalt and ferrite-type magnets, and the relatively low level of induced eddy currents in the thin high resistivity stainless steel sleeve used in retaining the magnets [4], rotor damping effects can be neglected for the machines studied here without affecting the accuracy of the simulation results. Hence, no damper windings are included in this model. The voltages and currents of the various machine windings are therefore governed by the coupled circuit equation (1), expressed in matrix form as follows [2]:

$$\begin{bmatrix} v_a \\ v_b \\ v_c \\ v_f \end{bmatrix} = \begin{bmatrix} R_a & 0 & 0 & 0 \\ 0 & R_b & 0 & 0 \\ 0 & 0 & R_c & 0 \\ 0 & 0 & 0 & R_f \end{bmatrix} \cdot \begin{bmatrix} i_a \\ i_b \\ i_c \\ i_f \end{bmatrix} + \frac{d}{dt}\left\{ \begin{bmatrix} L_{aa} & L_{ab} & L_{ac} & L_{af} \\ L_{ba} & L_{bb} & L_{bc} & L_{bf} \\ L_{ca} & L_{cb} & L_{cc} & L_{cf} \\ L_{fa} & L_{fb} & L_{fc} & L_{ff} \end{bmatrix} \cdot \begin{bmatrix} i_a \\ i_b \\ i_c \\ i_f \end{bmatrix} \right\} \tag{1}$$

where R_a, R_b, R_c are the phase-to-neutral winding resistances $[\Omega]$; R_f is the field winding resistance $[\Omega]$; L_{aa}, L_{bb}, L_{cc} are the phase-to-neutral self-inductances $[H]$; L_{ff} is the field winding self-inductance $[H]$; and $L_{ab}, \cdots, L_{fc}$ are the mutual inductances $[H]$.

In reality, the permanent magnet (field excitation) system is equivalent to a constant current field winding, whose ampere turns are proportional to the coercivity of the permanent magnet material and the magnet geometries [1]; therefore the field current i_f is constant. Also, it was found from magnetic field search coil measurements [1], for this class of machines, that the armature currents have little (or negligible) effects on the magnet flux distributions under normal load operating conditions. That is, no significant demagnetizations are experienced as long as the armature current remains within the same order of magnitude as the rated design values; see [1]. Therefore, the mutual inductance terms L_{fa}, L_{fb}, and L_{fc}, which represent the armature reaction, can be dropped from (1) without significantly affecting the accuracy of the modeling approach. Therefore, for this class of machines, (1) can be rewritten as follows:

$$\begin{bmatrix} v_a \\ v_b \\ v_c \end{bmatrix} = \begin{bmatrix} R_a & 0 & 0 \\ 0 & R_b & 0 \\ 0 & 0 & R_c \end{bmatrix} \begin{bmatrix} i_a \\ i_b \\ i_c \end{bmatrix} + \frac{d}{dt}\left\{ \begin{bmatrix} L_{aa} & L_{ab} & L_{ac} \\ L_{ba} & L_{bb} & L_{bc} \\ L_{ca} & L_{cb} & L_{cc} \end{bmatrix} \begin{bmatrix} i_a \\ i_b \\ i_c \end{bmatrix} \right\} + \frac{d}{dt} \begin{bmatrix} L_{af} \cdot i_f \\ L_{bf} \cdot i_f \\ L_{cf} \cdot i_f \end{bmatrix}. \tag{2}$$

The samarium cobalt or ferrite-type permanent magnets used in the radially oriented rotor structures examined here have permeabilities close to that of free space. Therefore, saliency effects normally associated with such structures can be neglected. This was borne out by measurements of the line-to-line winding inductance of the 15-hp samarium cobalt machines, which is analyzed later in this paper and used in comparisons between simulation results obtained from this model and corresponding test results. In this machine, the maximum variation of the line-to-line inductance with respect to the rotor position was only ±4.8 percent from a nominal value of 105 μH; see [2]. Consequently, the self inductances L_{aa}, L_{bb}, and L_{cc}, as well as the phase mutuals L_{ab}, L_{ba}, L_{ac}, L_{ca}, L_{bc}, and L_{cb}, are assumed constant and independent of rotor position. Accordingly, in a balanced three-phase case, such as the cases for which this model is intended, one can write

$$L_{aa} = L_{bb} = L_{cc} = L \tag{3}$$

$$L_{ab} = L_{ba} = L_{ac} = L_{ca} = L_{bc} = L_{cb} = M \tag{4}$$

$$R_a = R_b = R_c = R. \tag{5}$$

Substituting from (3), (4), and (5) into (2) yields the following:

$$\begin{bmatrix} v_a \\ v_b \\ v_c \end{bmatrix} = \left\{ \begin{bmatrix} R & 0 & 0 \\ 0 & R & 0 \\ 0 & 0 & R \end{bmatrix} \begin{bmatrix} i_a \\ i_b \\ i_c \end{bmatrix} \right\} + \left\{ \begin{bmatrix} L & M & M \\ M & L & M \\ M & M & L \end{bmatrix} \cdot \frac{d}{dt} \begin{bmatrix} i_a \\ i_b \\ i_c \end{bmatrix} \right\} + \left\{ i_f \frac{d}{dt} \begin{bmatrix} L_{af} \\ L_{bf} \\ L_{cf} \end{bmatrix} \right\}. \tag{6}$$

The mutual inductances between the field and the phase windings L_{af}, L_{bf}, and L_{cf}, on the other hand, are functions of the rotor position $\theta(t)$. Therefore, the last vector term of (6) can be rewritten as follows:

$$i_f \cdot \frac{d}{dt} \begin{bmatrix} L_{af}(\theta) \\ L_{bf}(\theta) \\ L_{cf}(\theta) \end{bmatrix} = i_f \cdot \begin{bmatrix} \dfrac{\partial L_{af}(\theta)}{\partial \theta} \\ \dfrac{\partial L_{bf}(\theta)}{\partial \theta} \\ \dfrac{\partial L_{cf}(\theta)}{\partial \theta} \end{bmatrix} \cdot \frac{d\theta}{dt}. \tag{7}$$

The derivative of the rotor angle $\theta(t)$, with respect to time, is the angular velocity ω of the rotor. Inspection of (7) reveals that the induced voltage in the phase windings due to the permanent magnet rotor is proportional to 1) the strength of the magnets i_f, 2) the speed of the rotor ω; and 3) the rate of change of the magnetic coupling between the stator and rotor at a given rotor position θ. Consequently, this vector term is the no-load phase-to-neutral back EMF vector with components, e_a, e_b, and e_c. Therefore, (7) can be written as follows:

$$\omega i_f \begin{bmatrix} \dfrac{\partial L_{af}}{\partial \theta} \\ \dfrac{\partial L_{bf}}{\partial \theta} \\ \dfrac{\partial L_{cf}}{\partial \theta} \end{bmatrix} = \begin{bmatrix} e_a \\ e_b \\ e_c \end{bmatrix}. \tag{8}$$

Also, because of the nature of the floating neutral Y-connection to the attached power conditioner units, the phase currents must satisfy the following.

$$i_a + i_b + i_c = 0, \tag{9}$$

that is,

$$\frac{di_a}{dt} + \frac{di_b}{dt} + \frac{di_c}{dt} = 0. \tag{10}$$

Substituting from (8) and (10) into (6) gives, after simplification, the following system of first-order differential equations which govern machine dynamics in this case:

$$\begin{bmatrix} v_a \\ v_b \\ v_c \end{bmatrix} = \left\{ \begin{bmatrix} R & 0 & 0 \\ 0 & R & 0 \\ 0 & 0 & R \end{bmatrix} \begin{bmatrix} i_a \\ i_b \\ i_c \end{bmatrix} \right\} + \left\{ \begin{bmatrix} (L-M) & 0 & 0 \\ 0 & (L-M) & 0 \\ 0 & 0 & (L-M) \end{bmatrix} \cdot \frac{d}{dt} \begin{bmatrix} i_a \\ i_b \\ i_c \end{bmatrix} \right\} + \begin{bmatrix} e_1 \\ e_2 \\ e_3 \end{bmatrix}. \tag{11}$$

This is a simple decoupled system of equations in which the inductance term $(L-M)$ is equal to half the open-circuit line-to-line inductance $(2L-2M)$. This can easily be calculated [3] or measured if the hardware is available. The accuracy of this model in predicting instantaneous machine voltage and current waveforms during various modes of operation is demonstrated later in this paper by comparison with oscillograms obtained during dynomomenter load testing of a 15-hp samarium cobalt machine of this type. In the next section, the machine model is combined with a network model of the electronic power conditioner unit which is used to drive this machine.

COMBINED MACHINE-POWER CONDITIONER NETWORK MODEL

The radially oriented permanent magnet synchronous machines can be driven in a variety of ways. These include sinusoidal voltage and current sources as well as nonsinusoidal voltage or current-source power conditioners. In particular, the simulation of the instantaneous interactions between such machines and a nonsinusoidal current source inverter-converter (or power conditioner) is examined here.

The schematic diagram of a transistorized current-source power conditioner and its attached machine is given in Fig. 1. The power conditioner consists of 1) a two-quadrant hysteresis-type current chopper for current magnitude control; and 2) a three-phase inverter–converter bridge which inverts dc into ac during motoring and vice versa during regenerative braking. The switching of the inverter transistors during the motoring mode is controlled by a Hall effect rotor position sensor mounted on the rotor shaft. The power conditioner produces

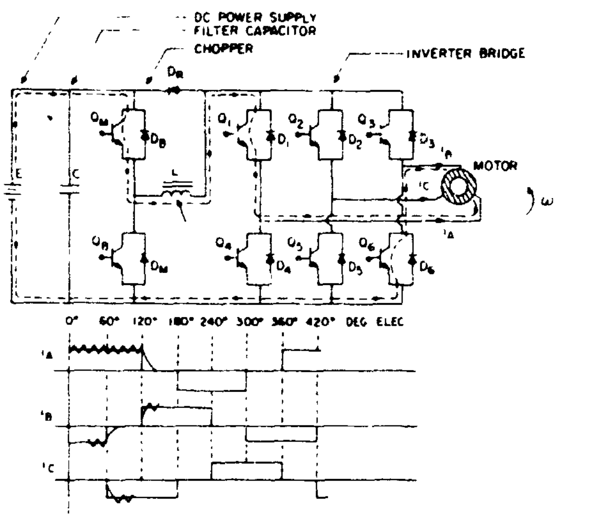

Fig. 1. Machine-power conditioner schematic and idealized motor currents.

a three-phase armature current which is rectangular in nature, as shown in the idealized current waveforms in Fig. 1.

The machine is modeled by (11). This equation is equivalent, on a per phase basis, to the phase-to-neutral winding resistance, one half of the line-to-line winding inductance $(L\text{-}M)$, and the phase-to-neutral back EMF voltage, all connected in series. The three phases are wye-connected with a floating neutral. The attached power conditioner is also represented by a lumped parameter network model [2]. The switching action of the antiparallel transistor diode pairs is represented by nonlinear resistances. These resistances assume low values corresponding to the forward conduction resistance while in the "on" state, and assume large resistances to simulate the "off" state [2], [5]. The status of the nonlinear resistors representing the power transistors is controlled by Boolean representations of the chopper and inverter switching logic. The status of each of the diode resistors is determined on the basis of the diode voltages themselves, forward or reversed biased. The other components of the power conditioner are modeled by standard lumped parameter circuit elements. The state equations for this nonlinear, nonplanar network are obtained using network graph theorems [2], [5], [6] in the standard form.

$$x = A \cdot x + B \cdot u \tag{12}$$

where x is the state vector which consists of the capacitor voltage, the current through the chopper inductor, and the currents through two of the machine inductances, and u is the forcing function vector consisting of the battery voltage and the three back EMF's, e_a, e_b, and e_c, and A and B are the nonlinear coefficient matrices of the network [2].

The branch voltages v_B and currents i_B throughout the network are completely defined in terms of the state vector x and the forcing function vector u as follows [2]:

$$v_B = G \cdot x + H \cdot u \tag{13}$$

and

$$i_B = L \cdot x + M \cdot u \tag{14}$$

where G, H, L, and M are functions of the network topology [2].

The nonlinear state model, (12), is integrated forward in time over equally spaced time intervals τ. These time intervals are taken small enough so that the nonlinear coefficient matrices A and B can be assumed constant over the integration interval (nonlinearity of A and B is caused only by the status of the diodes and transistors and not by machine inductances which are assumed constant throughout for this type of system). The integration was performed by a modified exponential series in which the state variables at the t_{k+1} instant of time, $x(t_{k+1})$, are related to the state variables and inputs at time t_k, $x(t_k)$ and $u(t_k)$ by

$$x(t_{k+1}) = \Phi(k) \cdot x(t_k) + \theta(k) \cdot u(t_k) \tag{15}$$

where $\Phi(k)$ and $\theta(k)$ are the state transition matrices [6] calculated at time $t = t_k$.

The back EMF's which constitute part of the input forcing function vector u in the machine-power conditioner network model are obtained either from test measurements if the hardware is available, or from finite element solutions of the magnetic field over the cross section of the machine under investigation [1], [2], [3], [5]. In either case, the EMF profile is represented by a Fourier series of the following form:

$$e(\theta_R, \phi) = \sum_{h=1}^{N_h} \left[a_h \sin\left(\frac{ph\,\theta_R}{2} + \phi_h\right) + b_h \cos\left(\frac{ph\,\theta_R}{2} + \phi_h\right)\right] \tag{16}$$

where

e	EMF constant [V/mech. rad/s],
N_h	number of harmonics,
a_h, b_h	Fourier coefficients [V/mech. rad/s],
θ_R	rotor position [mech. rad],
ϕ_h	phase shift [elec. rad],
p	number of poles.

The back EMF's, e_a, e_b, and e_c, can therefore be written in terms of $e(\theta_R, \phi)$ as follows.

$$e_a = \omega e(\theta_R, 0), \quad e_b = \omega e(\theta_R, (-2\pi/3)),$$
$$e_c = \omega e(\theta_R, (-4\pi/3)). \tag{17}$$

These EMF waveforms were obtained from finite element field analysis and from test. Excellent agreement between calculated and measured EMF's was achieved as demonstrated in [1], for the 15-hp machine analyzed in the next section.

The modeling approach outlined here, and given in detail in [2], is applied to the analysis of a 15-hp samarium cobalt synchronous machine designed, fabricated, and tested for use in electric vehicle propulsion. It will be demonstrated that combining the finite element method for EMF determination with the machine-power conditioner network model gives excellent results when compared with actual hardware test data.

EXPERIMENTAL VERIFICATION OF THE COMBINED FINITE ELEMENT FIELD ANALYSIS AND MACHINE-POWER CONDITIONER NETWORK MODEL

The discrete time machine-power conditioner model in conjunction with the finite element field analysis method were applied to the simulation of the 15-hp 120-V radially oriented samarium cobalt permanent magnet synchronous machine mentioned earlier. This machine was designed, built, and tested for use in electric vehicle propulsion. The machine is operated by means of a current-source power conditioner similar to the one shown in Fig. 1.

The back EMF waveforms for this machine were determined by means of the finite element method, as described in detail in [1]. For the sake of completeness, the back EMF voltage waveforms, obtained from the field analysis under rated and no-load conditions at a machine speed of 7750 r/min, are given in Figs. 2 and 3, respectively. The peak of the no-load back EMF agrees to within 2.2 percent of the measured peak [1]. Inspection of these figures reveals that the armature reaction at rated load has a negligible effect on both the shape and peak magnitude of the EMF's, as expected. The finite element determined no-load EMF waveform of Fig. 3 is represented by (17) in the discrete time machine-power conditioner model.

This machine-power conditioner system was tested under a variety of operating conditions using the dynamometer test setup shown in Fig. 4. Table I summarizes the modes of operation (motoring or regenerative braking), the commanded currents (or torque), and the machine speeds for the three representative test cases against which the model is verified here.

The oscillogram and computer-simulated waveforms (CSWF) of the machine phase current for case 1 are given in Fig. 5. Excellent agreement between the two is evident in both overall waveshapes and magnitudes and in the frequency of the sawtooth component caused by the current chopper. The central commutation spikes, which are clearly visible in the CSWF, can be seen in the original oscillogram but were too faint for reproduction.

The oscillogram and CSWF of the phase current for case 2 is given in Fig. 6. The agreement between the measured and simulated results is excellent. Notice also that in this case the phase current failed to reach the commanded current of 300 A. This is due to the current-limiting effect of the winding inductance at higher speeds. This can have a significant impact on the overall system performance, as will be demonstrated in the next section. The oscillogram and CSWF of the line-to-line machine voltage, for this case, is given in Fig. 7. Again the agreement between measured and calculated results is excellent.

The first two cases verified the accuracy and validity of the model for simulating the machine power-conditioner operation in the motoring mode.

The oscillogram of the machine phase current during regenerative braking, case 3 of Table I, is in excellent agreement with the corresponding CSWF, as shown in Fig. 8. Additional verifications of this model are given in [2], including other machines of this type.

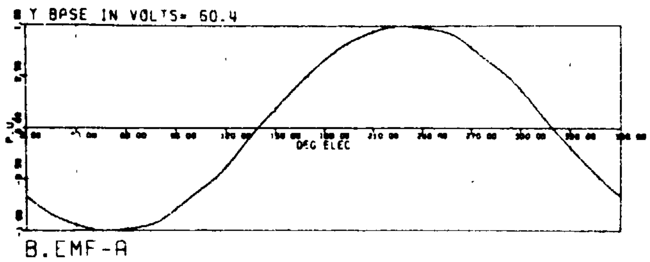

Fig. 2. Finite element-determined back EMF's at rated load of the samarium cobalt machine

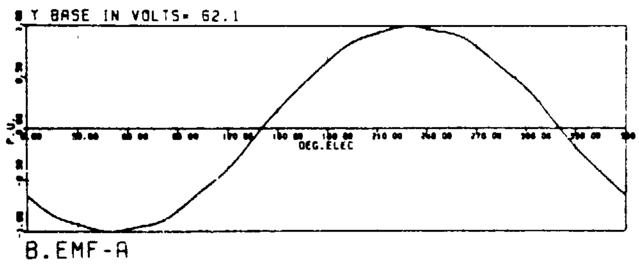

Fig. 3. Finite element-determined back EMF's at no-load of the samarium cobalt machine.

Fig. 4. Dynamometer testing of the samarium cobalt machine.

TABLE I
SUMMARY OF TEST RUNS SIMULATED

Case Number	Mode of Operation	Current Command [A]	Rotor Speed [rpm]
1	Motoring	68.5	3100
2	Motoring	Maximum (300)	7750
3	Regeneration	91.0	7440

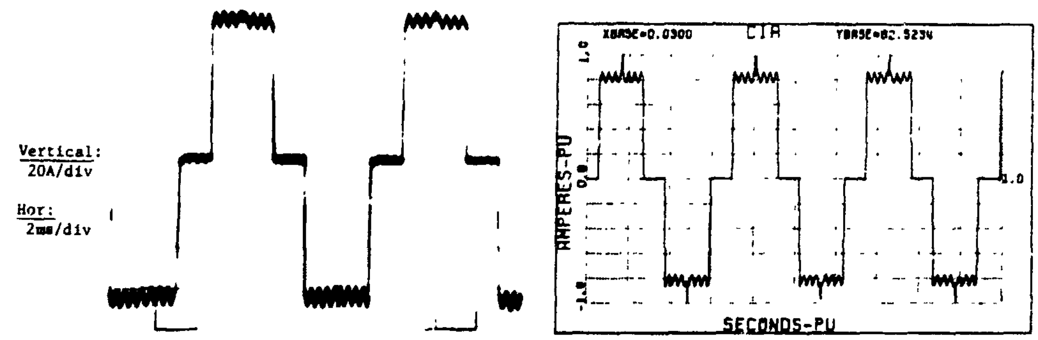

OSCILLOGRAM CSWF

Fig. 5. Oscillogram and CSWF phase current, motoring at 3100 r/min, current command of 68.5 A.

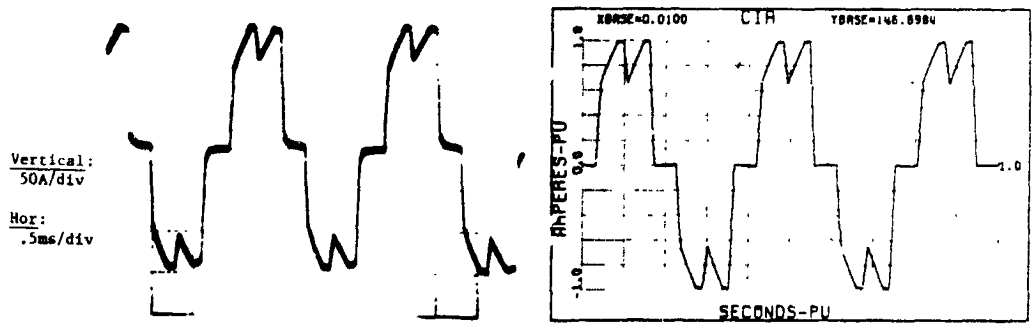

OSCILLOGRAM CSWF

Fig. 6. Oscillogram and CSWF of phase current, motoring at 7750 r/min, Q_M fully "on."

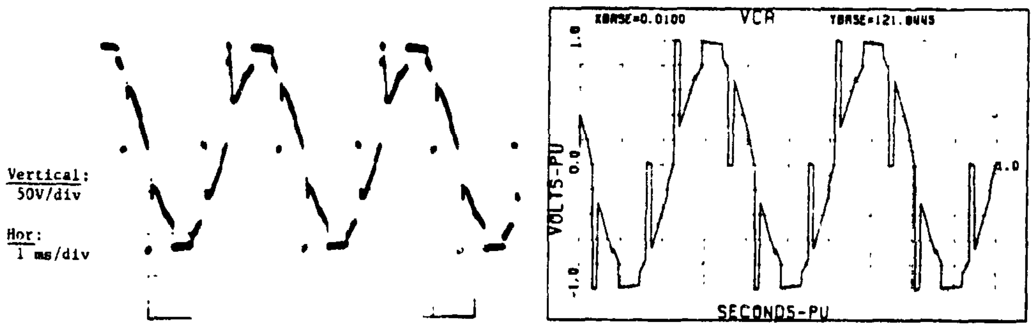

OSCILLOGRAM CSWF

Fig. 7. Oscillogram and CSWF of line-to-line voltage, motoring at 7750 r/min, Q_M fully "on."

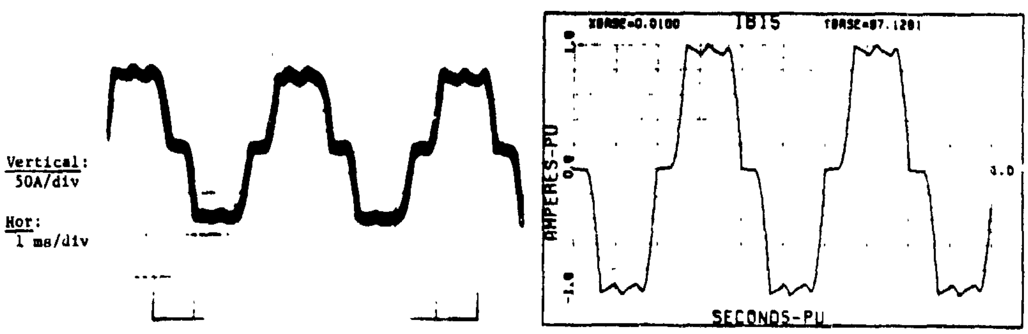

OSCILLOGRAM CSWF

Fig. 8. Oscillogram and CSWF of phase current, regenerative braking at 7740 r/min, current command of 91 A.

APPLICATION OF THE COMBINED FINITE ELEMENT FIELD ANALYSIS AND NETWORK MODEL TO THE PREDICTION OF THE DYNAMIC PERFORMANCE OF A PROPULSION UNIT PRIOR TO CONSTRUCTION

The primary application for this simulation model is as a design tool to save on prototype development costs and to speed up the design process. The design optimization procedure, using the modeling techniques described in this work, can be summarized as follows.

1) First, the ratings of the machine and the power conditioner unit are determined from the basic system requirements and constraints.

2) The machine horsepower and torque requirements are then used to obtain a specific machine volume and geometry depending upon the required performance of the machine.

3) The selected machine geometry is then inputted into a nonlinear finite element magnetic field analysis program, which was given in [1], from which the motor open-circuit EMF waveforms, inductances, flux distributions, and core losses are calculated [1], [3].

4) The calculated machine parameters are then fed into the system network model along with the preliminary power conditioner parameters.

5) The simulated performance is then used to reiterate the machine and power conditioner designs.

6) Steps 1-5 are repeated until the optimum machine-power conditioner design for the given specifications and constraints is found.

This design procedure eliminates much of the guesswork out of the design process, and at the same time provides better accuracy than less sophisticated methods commonly used at present.

The usefulness of this modeling technique in the design process can best be illustrated by an actual design example. Specifically, this approach was applied to the analysis of a new design for a radially oriented permanent magnet synchronous machine for electric vehicle applications. In this proposed machine, use is made of cheaper ferrite permanent magnets for the magnet structure as an alternative to the more expensive samarium cobalt permanent magnets used in the aforementioned 15-hp prototype motor.

This proposed ferrite machine must conform to similar performance specifications required of the samarium cobalt unit described earlier. That is, the machine must have a 15-hp continuous 2-h rating and a peak 1-min rating of 35 hp. The machine is connected to a current-source power conditioner which has an absolute maximum current rating of 400 A due to the transistor switches. This conditioner is energized from a 120-V dc battery supply. The desired speed at rated conditions is 9000 r/min; however, this rated speed does not represent one of the design constraints and can be adjusted to higher or lower values if required.

A first cut design of this machine consisted of an 18-slot stator and a 6-pole rotor structure. The pole pieces were designed using M8 ferrite magnets with a residual induction of 3.85 KG and 3.25 KG at 20°C and 100°C, respectively. The initial three-phase winding consists of 12 series turns per phase. The fractional slot winding of the samarium cobalt machine was abandoned due to the higher fabrication costs involved with such windings. The calculated line-to-line inductance of this configuration was 173.2 μH.

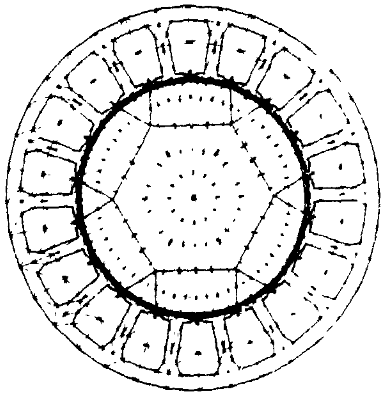

Fig. 9. Finite element discretization of the ferrite machine.

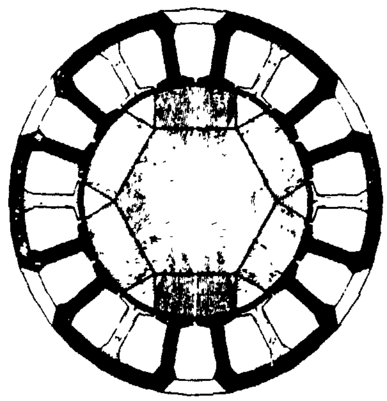

Fig. 10. Finite element-determined no-load flux distribution in the ferrite machine.

In order to predict the performance of this preliminary machine design, it was necessary to obtain accurate back EMF's for the machine-power conditioner network model. This was accomplished by means of a finite element solution for the magnetic field distribution inside the machine at no-load, as described in [1]. The finite element grid used to discretize the cross section of the ferrite machine is given in Fig. 9. The corresponding no-load flux distribution, assuming a worst-case magnet temperature of 100°C, is given in Fig. 10. The radial air-gap flux density profile was then obtained using the procedure outlined in [1]. This profile is given in Fig. 11 over one electrical cycle. Notice that the peak air-gap flux density for the ferrite machine is only 16 000 lines/in^2 compared with 50 000 lines/in^2 for the samarium cobalt machine [1], [2], [3].

Once the air-gap flux density profile is known, the back EMF's are obtained in terms of a Fourier series using a procedure given in [1], [2], and [3]. Since a fractional slot winding is not used in this case, it was decided to examine the effects of stator slot skewing on the back EMF's in order to eliminate harmonics as well as to reduce the tendency for cogging. The impact of skewing was accounted for by means of a skewing factor [14]. The finite element calculated back EMF waveforms corresponding to a skewing factor of zero, one half, and one slot pitch are given in Figs. 12, 13, and 14, respec-

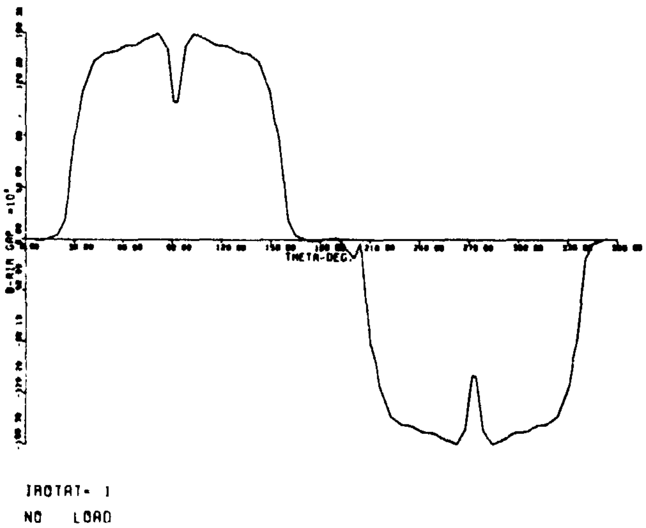

Fig. 11. Finite element-determined no-load radial air-gap flux density profile of the ferrite machine.

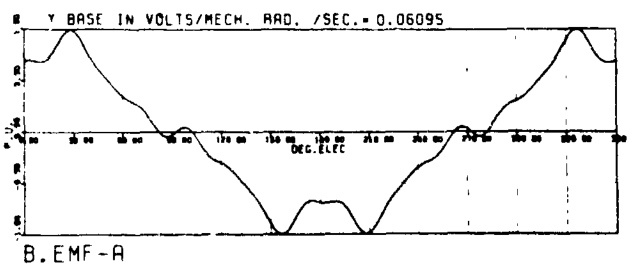

Fig. 12. Finite element-determined no-load back EMF profile of the ferrite machine with no skewing.

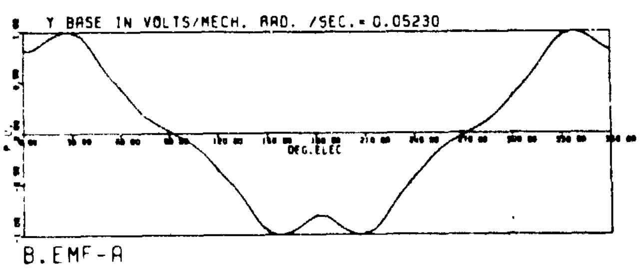

Fig. 13. Finite element-determined no-load back EMF profile of the ferrite machine with half-slot pitch skewing.

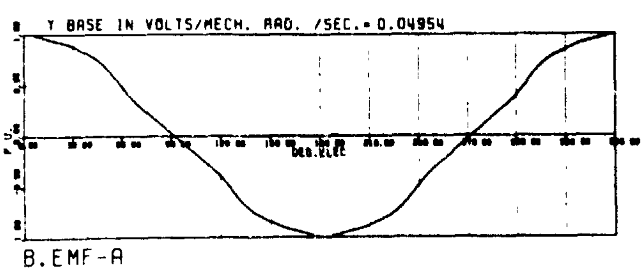

Fig. 14. Finite element-determined no-load back EMF profile of the ferrite machine with one-slot pitch skewing.

TABLE II
FINITE ELEMENT-DETERMINED PEAK PHASE-TO-NEUTRAL BACK EMF VOLTAGE SENSITIVITIES (V/mech. rad/s) OF THE FERRITE MACHINE

	Amount of Slot-Skewing		
	None	Half Slot Pitch	Full Slot Pitch
9 Turns per Phase	0.06095	0.05230	0.04954
12 Turns per Phase	0.08127	0.06973	0.06605

TABLE III
FERRITE MACHINE SIMULATION RESULTS

	Simulation Run Identification				
	Run #1	Run #2	Run #3	Run #4	Run #5
Speed [rpm]	8000	9000	9000	9500	10000
Series Turns Per Phase	12	9	9	9	9
Line to Line Inductance [μH]	173.2	92.8	92.8	92.8	92.8
Commutation Advance [elec. deg.]	0	0	30	30	30
Peak Phase Voltage [V]	63.3	43.4	43.4	45.8	48.2
Peak Phase Current [A]	30.0	287.4	346.1	307.6	272.2
Peak Electro-magnetic Power [hp]	4.0	25.9	38.7	36.3	33.8
Skewing	None	1 slot	1 slot	1 slot	1 slot
Current Command [A]	400	400	400	400	400

tively. Inspection of these figures clearly demonstrates the harmonic filtering effects produced by skewing. The peak voltages per mechanical radian per second for these three cases are given in Table II for windings with 9 and 12 series turns, respectively.

These back EMF profiles were used as input forcing functions to the combined machine-power conditioner system model in order to predict the system response to changes in the following system parameters: 1) winding inductances (9 and 12 series turns per phase); 2) stator slot skewing; 3) commutation advance angle; and 4) machine speed.

The commutation advance angle is the relative displacement between the peak of the fundamental of the phase current and the peak of the fundamental of the phase back EMF. Zero commutation advance means that the two peaks have zero displacement between them. An advance of 30 electrical degrees means that the phase current leads the phase EMF by 30 electrical degrees.

Five different simulation runs were made using the system model. These runs are designated run 1, ⋯, run 5, and are given in Table III. The results of these runs; the phase current and the developed electromagnetic machine power are also given in this table.

The first simulation, run 1, was made with the high inductance winding (12 turns per phase), zero commutation advance, and no skewing. Under these conditions, a peak developed electromagnetic power of only 4 hp was well below the required 35-hp peak rating. This is due to the fact that the phase-current steady-state value dropped from an initial value of 150 A to a final value of only 30-A peak at a constant machine speed of 8000 r/min, as shown in Fig. 15. This rapid decay of the machine current is due to the fact that the rectangular phase currents, produced by the current-source inverter, see Fig. 1, produces discretely forward stepping arma-

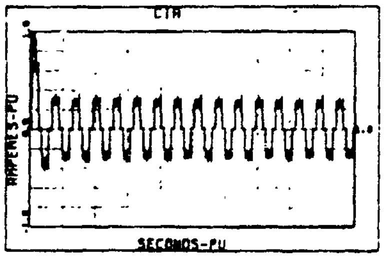

0 DEGREE ADVANCE

Fig. 15. Simulated current decay in the ferrite machine for simulation run 1.

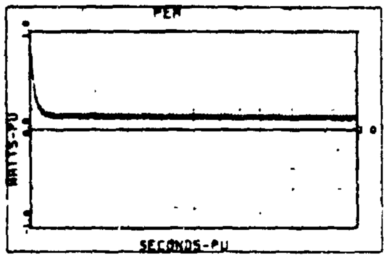

0 DEGREE ADVANCE

Fig. 16. Simulated developed electromagnetic power of the ferrite machine for simulation run 1.

ture MMF's [1], [2], [3]. This means that the field picture inside the machine must change almost instantaneously to follow the nearly instantaneous change in the armature currents at the six switching points during an ac cycle (Fig. 1). Obviously, the rate at which these currents can change is limited by the inductance of the winding. Therefore, as the machine speed (and hence inverter frequency and magnitudes of back EMF's) increases, the amount of current buildup during the decreasing period of an ac cycle drops dramatically, as displayed vividly in Fig. 15. This drop in the phase current produces a corresponding drop in the developed electromagnetic machine power, as shown in Fig. 16. This inductance limiting effect is much more severe in systems of this type than in machines with sinusoidally time-varying currents. Consequently, applying classical frequency domain-type analysis to such devices can only lead to gross errors in the prediction of the performance.

To alleviate this current limiting, a second winding design consisting of nine series turns per phase, which reduces the inductance almost in half, was analyzed. Four additional simulation runs (runs 2, 3, and 4) were made (Table III). Inspection of the results of these four simulations reveals that reducing the inductance nearly in half (and hence dropping the EMF's by 25 percent) produces nearly an order of magnitude difference in the maximum machine output. This is clearly illustrated in Figs. 17 and 18, which show the current and power buildup, respectively, corresponding to an initial phase current of 150 A and a machine speed of 9000 r/min. The current, and hence machine power, at this speed can be increased even further by initiating the phase-current buildup when the opposing EMF is zero (commutation advance of 30 electrical degrees), as shown in Figs. 19 and 20. The penalty for this is increased torque or power ripple, which can be clearly seen by comparing Figs. 18 and 20.

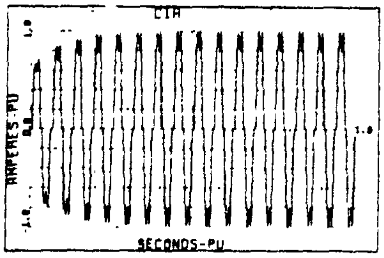

0 DEGREE ADVANCE

Fig. 17. Simulated current buildup in the ferrite machine for simulation run 2.

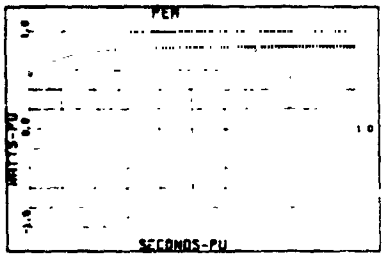

0 DEGREE ADVANCE

Fig. 18. Simulated developed electromagnetic power of the ferrite machine for simulation run 2.

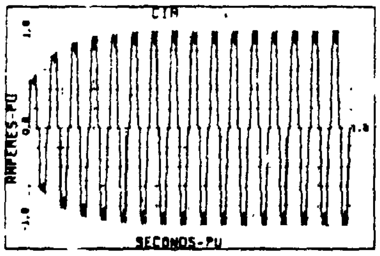

30 DEGREE ADVANCE

Fig. 19. Simulated current buildup in the ferrite machine for simulation run 3.

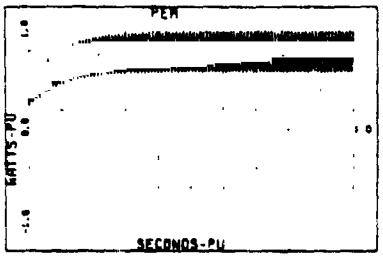

30 DEGREE ADVANCE

Fig. 20. Simulated developed electromagnetic power of the ferrite machine for simulation run 3.

The fourth and fifth simulation runs demonstrate the trade-offs between machine speed (or EMF) and maximum current and power. These trade-offs are very critical in transistorized power conditioners, where the peak currents must be held below a certain threshold value to prevent device failure.

This design example demonstrates the usefulness of this modeling approach in the design evaluation process in pointing out windings with suitable inductance values which permit fulfilling the specified machine output. The cost of a typical simulation (constant speed) run is $7.87 and requires 74 s of central processing unit (CPU) time on an IBM 3032 digital computer. For this modest expenditure of computer resources, the engineer obtains plots of all 23 branch voltages, currents, and powers versus time, a plot of all logic signals versus time, as well as plots of many other variables as specified by the user.

CONCLUSION

A modeling approach, which combines the finite element method for machine parameter determination with a discrete time machine-power network model, was successfully applied to the simulation of solid-state operated, radially oriented permanent magnet synchronous machines. The approach was applied to the simulation of a 15-hp samarium cobalt synchronous machine connected to a current-source power conditioner, which was designed, built, and tested for use in electric vehicle propulsion. Excellent agreement was obtained between computer and measured voltage and current waveforms throughout this system.

The model was then applied to the design of a similar system using less expensive ferrite permanent magnets. The effects of winding inductance, stator slot skewing, and advancing the firing or commutation angle were thoroughly analyzed. The results of this analysis clearly demonstrated the inadequacy of classical frequency domain-type approaches to such problems. Furthermore, it was shown that this totally digital approach produces results rapidly and is inexpensive to use, thereby freeing the designer from many tedious hand calculations and guesswork, and at the same time providing valuable insight into the behavior of such devices during the design process.

ACKNOWLEDGMENT

These authors wish to acknowledge the efforts of Mr. B. P. Overton of Inland Motor R&D in the design, fabrication, and testing of the machine studied here. Our thanks also go to Dr. R Churchill, Vice President and Director of Inland Motor R&D, who provided the facilities for construction and testing of this hardware.

REFERENCES

[1] F. A. Fouad, T W. Nehl, and N. A. Demerdash, "Magnetic field modeling of permanent magnet-type electronically operated synchronous machines using finite elements," *IEEE Trans Power App Syst.*, vol. PAS-100, no. 9, pp. 4125–4135, 1981

[2] T W. Nehl, "A discrete time model of a power conditioner-fed permanent magnet brushless dc motor system for aerospace and electric vehicle applications for design purposes using finite elements for machine parameter determination," Ph.D. dissertation, Dep. Elec. Eng., Virginia Polytechnic Inst and State Univ., Blacksburg, May 1980.

[3] F A Fouad, "Finite element analysis for design of classical and electronically operated electric machines," Ph.D. dissertaion, Dep. Elec. Eng. Virginia Polytechnic Inst. and State Univ., Blacksburg, May 1981.

[4] A K Nagarkatti, "Study of performance of certain special aspects of electronically commutated dc motor for electric vehicles," M.S. thesis, Dep. Elec. Eng. Virginia Polytechic Inst. and State Univ., Blacksburg, May 1980.

[5] N. A. Demerdash and T. W. Nehl, "Dynamic modeling of brushless dc motor-power conditioner unit for electromechanical actuator application," Power Electronics Specialists' Conf., 1979.

[6] N. Balabanian and T. A. Bickart, *Electrical Network Theory*. New York: Wiley, 1969.

[7] D. W Novotny and F. A Fath, "The analysis of induction machines controlled by series connected semiconductor switches," *IEEE Trans. Power App. Syst.*, vol PAS-87, no 2, pp 597–605, 1968.

[8] P. C. Krause and T A. Lipo, "Analysis and simplified representations of a rectifier-inverter induction motor drive," *IEEE Trans. Power App. Syst.*, vol. PAS-88, no. 5, pp 588–596, 1969

[9] T A. Lipo, "The analysis of induction motors with voltage control by symmetrically triggered thyristors," *IEEE Trans Power App Syst.*, vol. PAS-90, no 2, pp. 515–525, 1971

[10] T. A Lipo and F G Turnbull, "Analysis and comparison of two types of square wave inverter drives," *IEEE Trans Ind Appl*, vol IA-11, no. 2, pp 137–147, 1975.

[11] G. Singh and B C. Kuo, "Modeling and simulation of variable-reluctance step motors with application to a high-performance printer system," *IEEE Trans Ind Appl*, vol IA-11, no 4, pp 373–383, 1975.

[12] T A Lipo and E. P Cornell, "State-variable steady-state analysis of a controlled current induction motor drive," *IEEE Trans Ind Appl.*, vol. IA-11, no. 6, pp. 704–712, 1975

[13] R. L. Steigerwald and T. A. Lipo, "Analysis of a novel force-commutation starting scheme for a load-commutated synchronous motor drive," *IEEE Trans Ind. Appl.*, vol IA-15, no 1, pp 14–24, 1979

[14] M. G. Say, *The Performance and Design of Alternating Current Machines*. London: Pitman and Sons, 1963

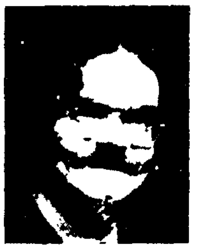

Thomas W. Nehl (M'79) was born in Tubingen, West Germany, on December 22, 1952 He received the B.S., M.S, and Ph D degrees in electrical engineering from Virginia Polytechnic Institute and State University, Blacksburg, in 1974, 1976, and 1980, respectively

He consulted for the Fairfax, VA, County Department of Public Works in the summer of 1974 on explosion-proofing the existing electrical switchgear and motors utilized in their pumping stations During the summer of 1976 he was employed by the National Bureau of Standards as an engineering intern, where he developed a finite element package for the solution of sinusoidal eddy current problems in support of their nondestructive testing program. During the summer of 1977 he was employed as an engineering intern at the NASA Johnson Space Flight Center, Houston, TX, where he was engaged in the modeling of brushless dc machine type electromechanical actuator systems. From 1978 to 1980, he was employed as a Research Associate in the Department of Electrical Engineering at Virginia Polytechnic Institute and State University where he was involved in the design, fabrication, and analysis of brushless dc motors for actuation and propulsion applications as well as finite element field analysis in support of the computer simulations and analysis of these systems. He joined the faculty of Virginia Polytechnic Institute and State University as an Assistant Professor of Electrical Engineering during the summer of 1980, where he is presently employed His current research activities include finite element field analysis of machines, digital simulation of electronically operated machines, simulation of machine and electronic failure modes in electronically operated machine systems, nondestructive testing and evaluation and power electronics

Dr. Nehl is currently serving on the Synchronous and the Machine Theory Subcommittees of the IEEE Power Engineering Society He is a member of the American Society of Engineering Education, Sigma Xi, Phi Kappa Phi, and Eta Kappa Nu.

Fakhry A. Fouad was born in Cairo, Egypt, on January 18, 1948. He received the B.Sc E.E with honors and M.Sc degrees from Cairo University, Cairo, in 1971 and 1975, respectively; and the Ph D degree in electrical engineering from Virginia Polytechnic Institute and State University, Blackburg, in 1981

From 1971 to 1977 he was with the Faculty of Engineering, Zagazig University, Egypt, as a Demonstrator. He was with the Department of Electrical Engineering at Virginia Polytechnic Institute and State University as a Graduate Research Assistant and

Research Associate from 1977 to 1979 and from 1979 to 1981 respectively He is presently a Visting Assistant Professor in the Department of Electrical Engineering at that institution. His current interests include numerical analysis of electromagnetic fields in electric machinery for design and optimization purposes, as well as the dynamic modeling of machines, including interaction with any associated power electronics and control subsystems

Dr Fouad is a member of the Honor Society of Phi Kappa Phi, the Scientific Research Society of Sigma Xi, and the American Association for Advancement of Science.

Nabeel A. Demerdash (M'65–SM'74) was born in Cairo, Egypt, on April 26, 1943. He received the B.Sc.E.E. degree with distinction and first class honors from Cario University, Cairo, in 1964, and the M.S. and Ph.D. degrees in electrical engineering from the University of Pittsburgh, Pittsburgh, PA, in 1967 and 1971, respectively.

From 1964 to 1966 he was with the Faculty of Engineering, Cairo University, as a Demonstrator. From 1966 to 1968 he was with the Department of Electrical Engineering, University of Pittsburgh, as a Graduate Teaching Assistant. In 1968 he joined the Large Rotating Apparatus Division of Westinghouse Electric Corporation, East Pittsburgh, PA, as a Development Engineer, where he worked on electromagnetic field modeling in rotating machinery and the development of the asymmetrical rotor for large steam turbine-driven generators. Since 1972 he has been with the Virginia Polytechnic Institute and State University, Blacksburg, VA, where he is presently a Professor in the Department of Electrical Engineering. He consulted for NASA Johnson Space Center, Houston, TX, during the summers of 1975 and 1976 on modeling of electronically controlled motors for aerospace applications. His current interests and research activities include electromechanical propulsion and acutation, dynamic modeling of solid-state controlled and operated electrical machines, numerical analysis of electromagnetic fields in electric machinery, as well as machine-power system dynamics.

Dr. Demerdash currently serves as a member of the Rotating Machinery Committee to IEEE Power Engineering Society (PES) as well as the Synchronous Machinery and the Machine Theory Subcommittees of PES He previously served as Secretary and subsequently Vice Chairman of the Synchronous Machines Subcommittee of PES He is a past Chairman of the Virginia Mountain Section of IEEE. He is a member of the American Society for Engineering Education, Sigma Xi, and Eta Kappa Nu

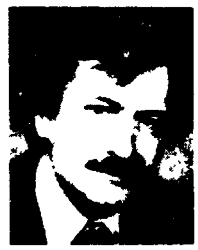

Edward A. Maslowski was born in Foster Township, PA, on August 17, 1934. He received the B.S. degree in physics from John Carroll University, Cleveland, OH, in 1958, and the M.S. degree in electrical engineering from the University of Toledo, Toledo, OH, in 1976

From 1959 to 1961, he was employed by the Frankford Arsenal, Philadelphia, PA, where he was engaged in research on metal embrittlement caused by the absorption of gases From 1961 to the present he has been employed by the NASA Lewis Research Center, Cleveland, OH, and has been involved in the design of a space environmental facility for the scale testing of space power systems, research on radiation effects on power semiconductors, design of the radioisotope Brayton power system, development of energy conversion devices for laser power transmission, development of applications of satellite data for land use applications, and development of electric vehicle traction motors for a joint NASA and Department of Energy (DOE) program. He has authored and co-authored a number of NASA publications in the areas of vacuum technology, instrumentation, and electric vehicle testing.

APPENDIX (6)

ON SIMULATION OF MACHINE-POWER CONDITIONER DYNAMIC INTERACTION OF BRUSHLESS DC MOTOR SYSTEMS

Nehl, T. W., Fouad, F. A., and Demerdash, N. A., "Digital Simulation of Power Conditioner - Machine Interaction for Electronically Commutated DC Permanent Magnet Machines," IEEE Transactions on Magnetics, Vol. MAG-17, 1981, pp. 3284-3286.

DIGITAL SIMULATION OF POWER CONDITIONER-MACHINE INTERACTION FOR ELECTRONICALLY COMMUTATED DC PERMANENT MAGNET MACHINES

T. W. Nehl, Member F. A. Fouad, Member N. A. Demerdash, Senior Member

Abstract - The electromagnetic interactions between a transistorized chopper-inverter power conditioner and its associated permanent magnet machine is analyzed digitally by an experimentally verified time domain state model. The model is applied to the design of a system based on a ferrite type machine. The impact on the overall system performance of skewing the stator core to reduce the harmonics in the induced machine EMF is determined using this model. The EMF waveforms for zero, half, and one slot pitch skewing are determined by finite element analysis of the fields inside the machine. Furthermore, the impact on the system performance of varying the commutation angle to overcome inductance caused performance limitations is examined for each of the three cases of stator skewing.

INTRODUCTION

Electronically commutated permanent magnet dc machines are finding increasing use as primemovers in actuation, industrial drives, and vehicle propulsion. When operated from square wave current source power conditioners, such machines exhibit armature MMFs which rotate in discrete steps or jumps of 60 electrical degrees each. For this reason, frequency domain type models based on smoothly rotating MMFs are inadequate. In this paper, a discrete time model of such a machine power conditioner system, Figure (1), which includes the voltage drops across the power switches, references (1) through (3), is used, in conjunction with machine parameters determined by finite elements (FE), references (4) and (5), to simulate the dynamic interactions between the machine and its associated power conditioner, during the design process of a 15 HP, 120 V ferrite permanent magnet brushless dc machine. This system was designed as a prime mover for the propulsion of electric passenger vehicles. In this paper three aspects of this design process will be analyzed in detail, namely:

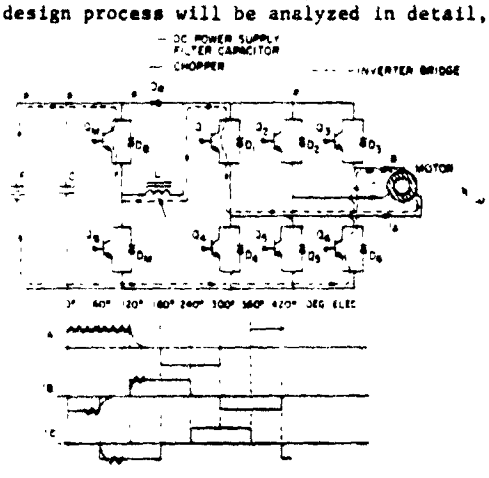

Figure (1) Schematic of the Machine-Power Conditioner Unit.

Manuscript received March 23, 1981

These authors acknowledge the financial support of the following contracts: 1) DOE/NASA LeRC contract NO. DEN3-65, and USAF/SCEEE Contract NO. SIP/78-17. We also wish to acknowledge Inland Motor R&D, Radford, Virginia in the design, fabrication and testing of the machines studied here.

T. W. Nehl, F. A. Fouad and N. A. Demerdash are with the Department of Electrical Engineering, Virginia Polytechnic Institute and State University, Blacksburg, Virginia 24061, U.S.A.

1) The impact on the induced machine EMF of skewing the stator core by zero, one half, and one slot pitch. This is determined by means of the finite element method as detailed in references (4) and (5). It will be shown that, for non-fractional slot windings, skewing greatly reduces the harmonic content of the EMF and thus reduces losses, noise, and the tendency for cogging.

2) The combined effects of the machine inductances and EMF waveshapes, for the above three cases of skewing, on the overall system performance is determined using the system state model.

3) The effect of varying the commutation angle on machine performance for the three cases of skewing is studied.

MODEL DESCRIPTION

The ferrite based machine-power conditioner system analyzed here consists of a current chopper in series with a three phase inverter-converter bridge. This power conditioner is in turn connected to the three phase permanent magnet machine as shown schematically in Figure (1). This entire system is represented by a nonlinear state model, reference (3), as follows:

$$\underline{\dot{X}} = \underline{A}\ \underline{x} + \underline{B}\ \underline{u} \quad (1)$$

and

$$\underline{Y} = \underline{C}\ \underline{z} + \underline{D}\ \underline{u} \quad (2)$$

where $\underline{x}$ is the vector of state variables,
$\underline{u}$ is the vector of forcing functions,
$\underline{A},\underline{B}$ are nonlinear coefficient matrices,
$\underline{Y}$ is the vector of output variables (branch currents, voltages, etc.), and
$\underline{C},\underline{D}$ are nonlinear coefficient matrices.

The nonlinearity is due to the fact that the status of the diodes and transistors is simulated by low resistances during conduction and high resistances during the off state. The status of the transistors is determined by boolean logic which simulates the actual control logic of the system. The status of the diodes is determined after each time integration by an iterative procedure which sets the diode resistances according to the voltages across these devices.

This model has been successfully applied to both an electromechanical actuator for flight control applications and to an electromechanical propulsion unit for electric vehicles with excellent agreement between oscillograms and computer simulated waveforms, references (1) through (4). For the sake of completeness a sample of these results is included here in Figures (2) and for a similar electric vehicles propulsion unit that has the same performance specifications but uses a samarium cobalt based machine. Examination of these figures reveals excellent agreement between the simulations and test. Further comparisons are given in the references mentioned above.

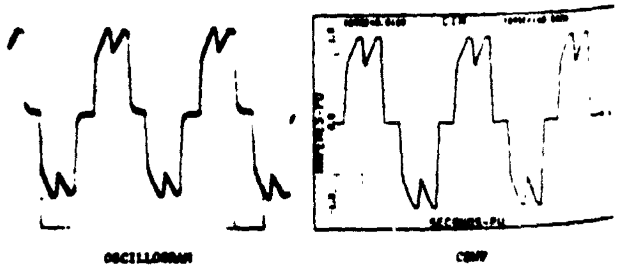

Figure (2) Oscillogram and Computer Simulated Waveforms of the Phase Current at 16 HP of the Samarium Cobalt Machine.

0018-9464/81/1100-3284$00.75 © 1981 IEEE

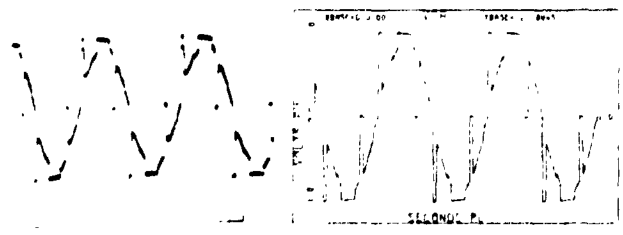

Figure (3) Oscillogram and Computer Simulated Line to Neutral Phase Voltages at 16 HP of the Samarium Cobalt Machine.

This model will now be used to assess the impact stator slot skewing and commutation angle on the overall system performance of a new ferrite based de...

APPLICATION OF MODEL TO THE FERRITE MACHINE

...ect of Skewing the Stator Core on the EMF

The ferrite machine consists of an 18 slot, three ... armature winding and a 6 pole, ferrite permanent ... rotor structure. Since there is only one slot ... pole per phase one expects a large harmonic content ... the induced phase voltages. These harmonics increase ... magnitude of the torque pulsations and they tend to ... the buildup of phase currents at heavy loads. Furthermore, the even number of slots increases the ten... of the machine to cog due to the variable reluct... between the stator and rotor.

In order to reduce the EMF harmonics and the ten... for cogging, it was decided to explore the possi...ity of skewing the stator core over one half and one... slot pitch. The induced phase to neutral EMF was ...termined by a two dimensional nonlinear finite element ... solution over the cross-section of the machine as ...cribed in references (4) and (5). The effects of ...wing were accounted for by means of harmonic skewing ...tors applied to the flux linkage per phase, see ...rences (5) and (6).

Figures (4-A) through (4-C) display the predicted ...se to neutral EMF for the ferrite machine for zero, ... half slot pitch, and one full slot pitch skew, re...spectively. Notice the large third harmonic component ... the unskewed stator core. Increasing the skew of ... stator core to one slot pitch results in an almost sinusoidal EMF waveform, Figure (4-C). The effects of these different stator cores on the overall system performances will be determined next.

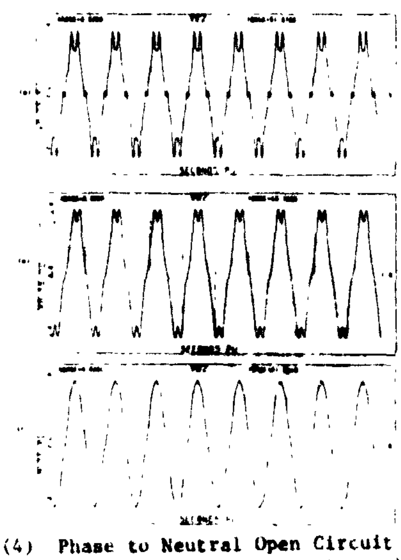

Figure (4) Phase to Neutral Open Circuit Voltage Waveform for a) No Skewing, b) Half Slot Pitch Skewing, c) Full Slot Pitch Skewing.

Effect of Stator Skew and Commutation Advance on the Overall Machine-Power Conditioner Performance

The three EMF waveforms given in Figure (4) were used as forcing functions for the system state model described earlier. The system performance was then obtained for the three cases of skewing with comutation advances of 0° and 30° electrical, respectively, at a machine speed of 8000 rpm and a battery voltage of 100. A commutation advance of 0° means that the phase current is injected 30° electrical after the zero crossing of the no load phase EMF. A commutation advance of 30° electrical refers to the injection of the phase current at the instant of zero crossing of the EMF. Advancing the commutation allows a larger buildup of current during heavy loading since the motor voltage opposing the current buildup is reduced. Commutation advance is of particular importance in square wave, current source type inverters since the stator MMF jumps in discrete steps at the six commutation points in an ac cycle.

Plots of the instantaneous machine phase currents and electromagnetic torques for skewing of zero, one half, and one slot pitch, all with zero commutation advance are given in Figures (5) through (7). Inspection of these Figures reveals that the torque ripple is reduced by 50 percent as the skewing of the stator increases from 0 to one slot pitch. The reduced EMF harmonics, as skewing is increased, also allows the current to buildup to larger values, as demonstrated by the current waveforms, from 201 to 227 Amperes (peak).

The effects of the commutation advance on the three cases is clearly evident by comparison between Figures (5), (6), and (7) and the corresponding three cases with commutation advance of 30° electrical given in Figures (8), (9) and (10), respectively. In all three cases, significant increases in the phase current were realized by advancing the commutation by 30° electrical. An increase in the current buildup of up to 287 Amperes (peak) is demonstrated. The one negative aspect of advancing commutation is the increase in torque ripple which is clearly evident in these figures.

CONCLUSIONS

The impact of skewing the stator core of a ferrite permanent magnet machine on the overall performance of an electronically commutated brushless propulsion system for electric passenger vehicles was determined. It was found that skewing the core by one slot pitch reduced the torque ripple by 50 percent. Furthermore, it was found that the machine phase currents reached values higher by more than 13 percent for the skewed stators.

The impact of advancing the commutation to aid current buildup under heavy loads was also determined. It was found in all cases that advancing the commutation significantly increased the maximum level of the phase current by as high as 44 percent. Based on these results a new prototype ferrite permanent magnet brushless dc machine was constructed and is currently undergoing testing.

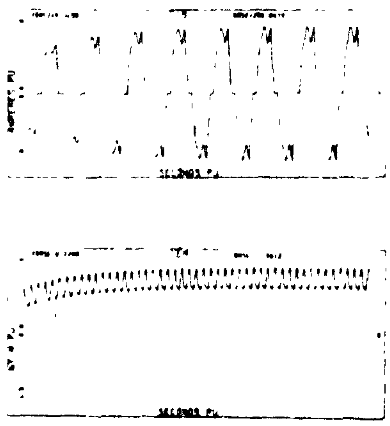

Figure (5) Machine Phase Current and Electromagnetic Torque, Unskewed Stator, Zero Commutation Advance.

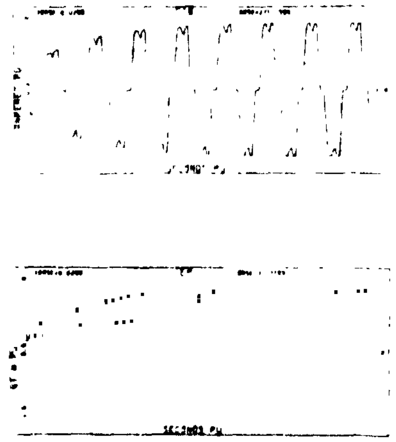

Figure (6) Machine Phase Current and Electromagnetic Torque, Stator Skewed One Half Slot Pitch, Zero Commutation Advance.

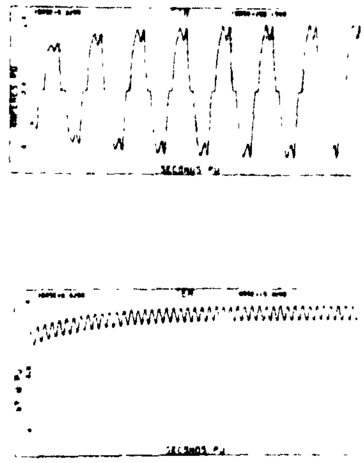

Figure (7) Machine Phase Current and Electromagnetic Torque, Stator Skewed One Slot Pitch, Zero Commutation Advance.

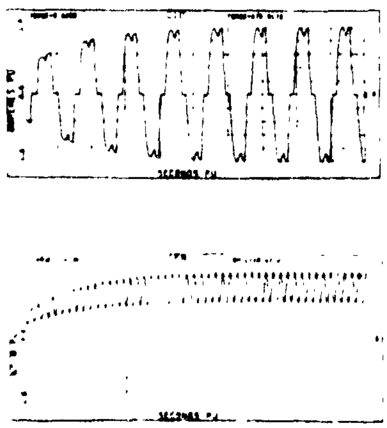

Figure (8) Machine Phase Current and Electromagnetic Torque, Unskewed Stator, 30^{o} Commutation Advance.

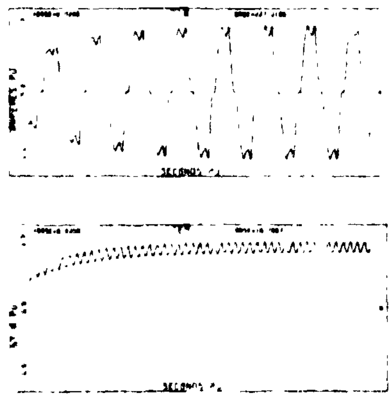

Figure (9) Machine Phase Current and Electromagnetic Torque, Stator Skewed One Half Slot Pitch, 30^{o} Commutation Advance.

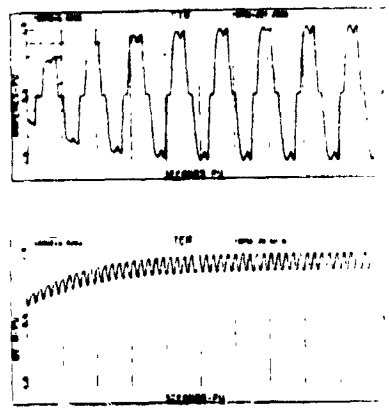

Figure (10) Machine Phase Current and Electromagnetic Torque, Stator Skewed One Slot Pitch, 30^{o} Commutation Advance.

REFERENCES

[1] T. W. Nehl, "A Discrete Time Model of a Power Conditioner Fed Permanent Magnet Brushless DC Motor Systems for Aerospace and Electric Vehicle Applications for Design Purposes Using Finite Ph.D. Dissertation, Department of Electrical Engineering, Virginia Polytechnic Institute and State University, May 1980.

[2] N. A. Demerdash, T. W. Nehl and E. Maslowski, "Dynamic Modeling of Brushless Motors in Electric Propulsion and Electromechanical Acutation by Digital Techniques," Proceedings of the 1980 IEEE Industry Applications Society Annual Meeting, 80 CH 1575, Cincinnati, Ohio, Sept. 28-Oct. 3, 1980, pp. 570-579.

[3] N. A. Demerdash and T. W. Nehl, "Dynamic Modeling of Brushless DC Motors for Aerospace Acutuation," IEEE Transactions on Aerospace and Electronic Systems, Vol. AES-16, No. 6, 1980, pp. 811-8[illegible].

[4] F. A. Fouad, T. W. Nehl, and N. A. Demerdash, "Magnetic Field Modeling of Permanent Magnet Type Electronically Operated Synchronous Machines Using Finite, Elements," Paper Accepted for Publication in Full in the IEEE Transactions on Power Apparatus and Syrtems, presented at the IEEE/PES Winter Meeting, Atlanta, Georgia, Feb. 1-6, 1981.

[5] F. A. Fouad, "Finite Element Analysis for Design of Classical and Electronically Operated Electric Machines," Ph.D. Dissertation, Electrical Engineering Dept., Virginia Polytechnic Institute and State University, May 1981.

[6] M. G. Say, Alternating Current Machines, John Wiley and Sons, New York, 1976.

APPENDIX (7)

ON SIMULATION OF MACHINE-POWER CONDITIONER DYNAMIC INTERACTION OF BRUSHLESS DC MOTOR SYSTEMS

Demerdash, N. A., and Nehl, T. W., Dynamic Modeling of Bushless DC Motors IEEE Transactions on Aerospace and Electronic Systems, Vol. AES-16, 1980, pp. 811-821.

Dynamic Modeling of Brushless dc Motors for Aerospace Actuation

N.A DEMERDASH, Senior Member, IEEE
T.W NEHL, Member, IEEE
Virginia Polytechnic Institute and State University

Dynamic Modeling of Brushless dc Motors for Aerospace Actuation

N.A DEMERDASH, Senior Member, IEEE
T.W NEHL, Member, IEEE
Virginia Polytechnic Institute and State University

Abstract

A discrete time model for simulation of the dynamics of samarium cobalt-type permanent magnet brushless dc machines is presented. The similation model includes modeling of the interaction between these machines and their attached power conditioners. These are transistorized conditioner units. This model is part of an overall discrete-time analysis of the dynamic performance of electromechanical actuators, which was conducted as part of prototype development of such actuators studied and built for NASA-Johnson Space Center as a prospective alternative to hydraulic actuators presently used in shuttle orbiter applications. The resulting numerical simulations of the various machine and power conditioner current and voltage waveforms gave excellent correlation to the actual waveforms collected from actual hardware experimental testing. These results, numerical and experimental, are presented here for machine motoring, regeneration and dynamic braking modes. Application of the resulting model to the determination of machine current and torque profiles during closed-loop actuator operation were also analyzed and the results are given here. These results are given in light of an overall view of the actuator system components. The applicability of this method of analysis to design optimization and trouble-shooting in such prototype development is also discussed in light of the results at hand.

Manuscript received December 14, 1979; revised April 12, 1980.

This work was supported by the National Aeronautics and Space Administration Johnson Space Center Contract NAS9-15091.

Authors' address: Department of Electrical Engineering, Virginia Polytechnic Institute and State University, Blacksburg, VA 24061.

0018-9251/80/1100-0811 $00.75

Introduction

The bulk of the simulation models and studies of solid-state power conditioner-fed electrical machines were based on either steady-state phasor-equivalent circuit concepts or hybrid-analogue simulation of power conditioner-machine dynamics. Details of these studies can be found in the literature in references such as [1] through [10]. These methods were proven useful in many cases. However, there are other applications in which a totally digital approach with an abandonment of the bulk of classical steady-state machine theory concepts may prove more advantageous. The work reported on in this paper lies within such a category where these authors believe a digital approach is most suitable.

In this paper the ingredients of an instantaneous machine-power conditioner dynamic modeling approach are given. This approach is part of an overall electromechanical actuator (EMA) model which is to be reported on in forthcoming papers. The power conditioner-machine (PCM) modeling approach is used in the development of an instantaneous simulation model to predict the transient performance of a power conditioner (PC) fed samarium-cobalt permanent magnet brushless dc machine. Features of this PCM prototype and the accompanying EMA system are given in the following sections.

Numerical results of this simulation model reveal, when compared with experimental test data collected from the EMA-PCM prototype, a high degree of correlation in both amplitudes as well as profiles of various instantaneous currents and voltages.

Results of this analysis presented here include also the determination of motor torque and dc line current profiles during normal closed-loop actuator applications.

Overall System Description

The 17-hp, 270-V, 8-pole, 9000 rpm brushless dc motor, subject of this paper, was built as a prime mover in an EMA system. This system was manufactured for the NASA-Johnson Space Center for the purpose of studying possible replacements of present hydraulic actuator systems in aerospace control applications. The main incentives for such an actuator replacement are weight and volume reductions, increased reliability, facility of maintenance, reduction of fire and toxicity hazards, controllability as well as possible economic benefits.

The EMA for which this motor was built consists of four independent servo loop channels, a functional block diagram of which is shown in Fig. 1. Each channel consists of a low-level control electronics (LLCE) package, an electronic power conditioner (PC) which consists of a chopper inverter arrangement, a PC-fed 17-hp permanent magnet-three phase stator wound brushless dc machine and a gear box

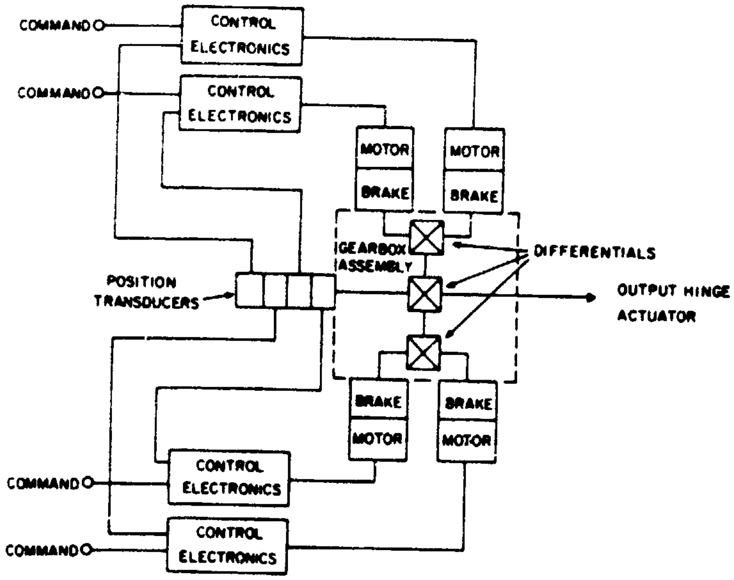

Fig. 1. Functional block diagram of EMA.

Fig. 2. Cross section of EMA motor.

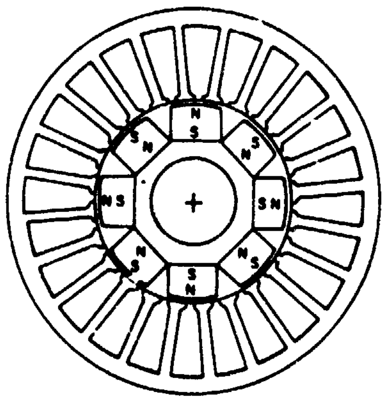

assembly which couples the active (rotating) motor outputs to a common hinge output actuator shaft.

Description of Machine and Power Conditioner

Of particular interest in this paper are the *instantaneous* dynamic performance of the machine-power conditioner portion of each channel and the means of digitally simulating such performance. A salient feature of this 17-hp motor is the 24-slot 7-mil vanadium-permendur laminated stator structure housing the three-phase PC-fed stator winding. This is a sealed stator assembly which can allow the circulation of a coolant fluid through the partially filled stator slots [11, 12]. Another salient feature of this motor is the 8-pole samarium-cobalt permanent magnet rotor structure. This rotor assembly consists of 48 blocks (6 blocks per pole) of 18 MGO samarium-cobalt material mounted on an octagonal rotor shaft. The magnet retaining scheme consists of fiber glass banding cured in epoxy compounds. A cross-sectional view of the rotor and stator is given in Fig. 2, while a photograph of the actual rotor is given in Fig. 3. Under rated 17 hp, 9000 rpm conditions this motor produces an output

Fig. 3. Assembled rotor.

Fig. 4. Power conditioner machine schematic.

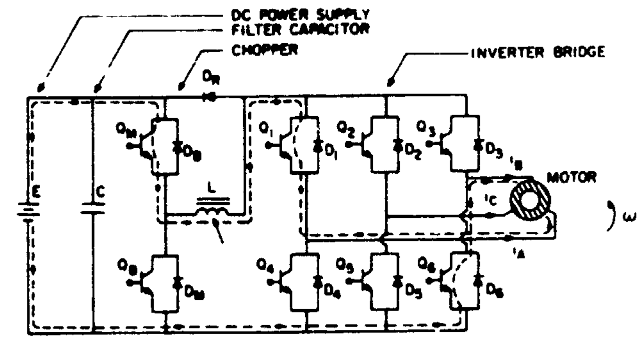

torque of 13.558 N-m (120 lb-in) at a rated line voltage of 270 V and a dc line current of 60 A.

The power conditioner shown schematically in Fig. 4 consists of an input filter (capacitor), a combination series/shunt type chopper for dc line current magnitude limiting and control, a chopper inductor, and a configuration of six transistor-diode switches which form the three-phase inverter/converter bridge. This bridge has a capability of allowing the machine to function in three modes of operation, namely, motoring, plugging (dynamic braking), and regenerative braking, in both the forward and reverse rotational direction for each. Also shown in Fig. 4 is the current path through which the conditioner and machine during one of the six switching states which take place during motoring.

Shown in Fig. 5 in idealized form are the A, B, and C machine phase currents during a forward motoring mode. These phase currents, with their block (rectangular pulse) nature, produce a stepping (hopping) armature (stator) at each inverter switching instant. This magnetomotive force (MMF) stepping occurs every 60 electrical degrees, as demonstrated schematically in Fig. 5 for this 17-hp machine corresponding to points (1) and (2) before and after a switching instant, as marked in the idealized currents. Torque is produced as a result of this angular displacement between the position of the peak of the armature MMF and the corresponding position of the

344

peak of the rotor MMF (the rotor MMF is produced by the permanent magnets). This torque is proportional in magnitude to the product of the two MMF amplitudes and the trigonometric sine of the angular displacement between the two MMF peaks (18). The torque angles between the stator and rotor MMFs are depicted at the beginning and end of a switching state in Fig. 6. The expected motor torque profile is also shown in the figure. This predicted profile will be confirmed in the results of this dynamic simulation given in this paper. Accordingly, the rotor is forced into a rotational motion in a direction which tends to decrease the angular displacement between the two peaks (rotor MMF tries to follow armature MMF). This continues until the next switching instant, at which time the armature MMF moves forward in a discrete stepping fashion as explained earlier. This in turn maximizes the angular displacement between the two MMFs, and increases the torque, and the process of rotor motion is repeated to diminish this angular displacement. This results in a pulsating torque profile versus angular rotor position (or time) such as demonstrated schematically in Fig. 6.

The initiation of switching of the inverter transistors is accomplished by means of low-level logic signals generated by a rotor position sensor (RPS). The RPS-generated signals insure a switching sequence which guarantees that the armature MMF would remain leading the rotor MMF (magnets) in the direction of motion during the motoring mode, while the opposite is the case during the plugging mode. The RPS sensors are part of the LLCE depicted schematically in Fig. 1. Another key element in the LLCE package is a dc line current sensor which is used to control the duty cycle of the chopper transistors (on/off periods) in accordance with the torque (or current) commands. It is important to note that for this class of machines the *average* electromagnetic torque is linearly proportional to the magnitude of the average dc line current. Hence in this case, current commands and torque commands are synonymous.

Machine-Power Conditioner Modeling Approach

This model is used to predict instantaneous machine currents, voltages, torques, speeds, as well as instantaneous voltages, currents and power dissipation throughout the various components of the PC. It also gives the instantaneous values of the various control signals throughout the EMA system. Therefore, this model is not to be confused with any frequency domain type approaches for prediction of EMA dynamics. The state-space discrete time approach [15] is utilized throughout. This includes the machine model, the PC, the control system, and the rotating masses.

The model, in its present form offers the capability of simulating the entire closed-loop operation of the EMA. This is accomplished by means of a

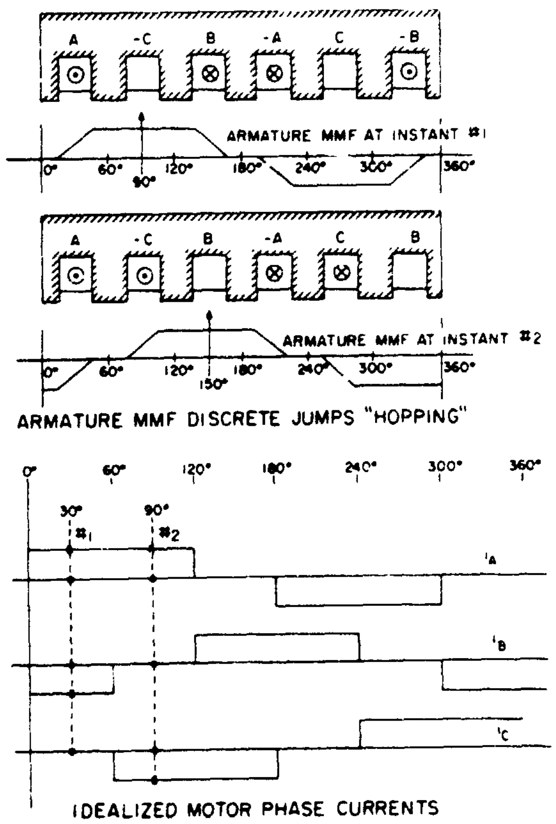

Fig. 5 Armature (stator) MMF immediately before and after a switching instant.

Fig. 6 Torque angles and torque profile due to conditioner switching.

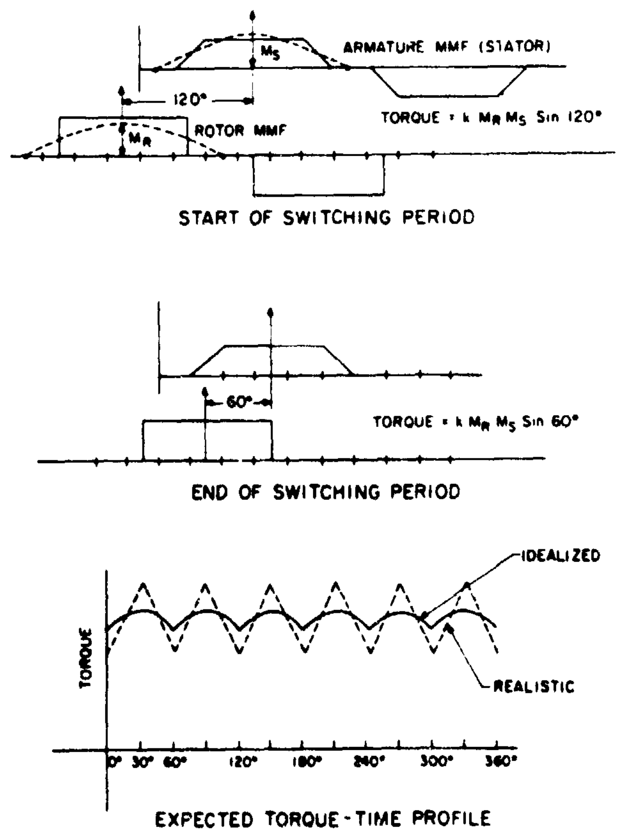

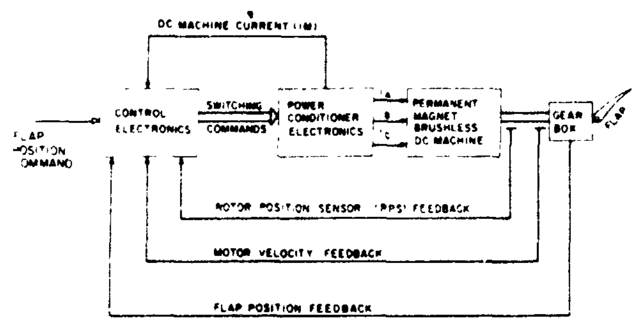

Fig. 7 Functional block diagram of overall EMA in single-channel format.

Fig. 8 Power conditioner machine network graph.

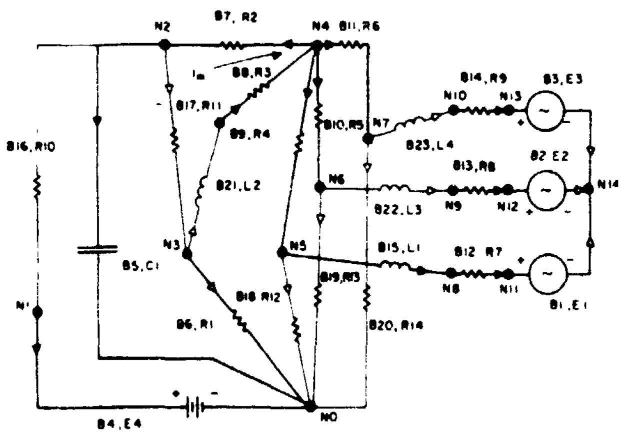

fourteenth-order state variable model. The model was used in obtaining instantaneous values of the system state variables in response to a given input position command (step, ramp, etc.). In this simulation the dynamics of all the major components of the EMA are included. An overall block diagram representation of the components of this model and their interactions is depicted in Fig. 7. Further details on the complete EMA model will be given in forthcoming papers. Also, [11] contains details of this portion of the study.

Representation of Components of the Power Conditioner

An essential element of the composition and development of this model is the representation of individual components in the PCM network. All transistors are represented by nonlinear resistances. These resistances assume extremely low values to simulate the "on" states for such devices. The value of this resistance is based upon the collector-to-emitter voltage drop at rated transistor current. Likewise, extremely high values of resistances are used to simulate the "off" state of such transistors.

Diodes are represented by similar nonlinear resistances which assume extremely low values during forward bias (based on the voltge drop across a diode at rated current), and extremely high values during reverse bias.

Other discrete components of the PC are the input filter capacitor which is represented as a time invariant capacitance, the battery which is modeled as an ideal emf source in series with a resistance which represents the internal ohmic dissipation in the battery, and the chopper inductor which is represented as a nonlinear time variant inductance whose value is dependent upon the saturation status in the inductor core. This time-variant inductance is therefore dependent upon current through the choke winding.

Machine Representation

In this model, each phase is represented with its leakage inductance in series with the active self and mutual components of the phase inductance, where the active self and mutual inductance voltage drop is nothing other than the induced back emf due to the resultant flux distribution linking the stator windings. Further, in series with this emf-leakage inductance is a resistance representing the ohmic dissipation and voltage drop in each phase.

Power Conditioner-Machine Network State Equations (PCMNSE)

Substitution of the component models described above in the PCM schematic of Fig. 4 yields the nonplanar network graph shown in Fig. 8. This network is nonlinear because of the inherent nonlinearities in the component characteristics as detailed above.

The heavy-lined branches in this figure represent the twigs of the chosen tree. The thin-lined branches belong to the cotree, see [14]. The assumed direction of the current in each of these branches is indicated by a solid arrow for the twigs, and by the outline of an arrow for the links. The sense of the branch voltages with respect to the assumed current orientations is determined by employing the consumer (load) system of notation.

For purposes of identification, each branch is characterized by two different labels; a branch label and a branch component label. The branch label identifies the branch number and is denoted by the prefix B and the branch number. For example, B1 denotes branch one. The component labels are identified by the prefixes C, E, L, and R (capacitor, emf, inductor, and resistor) and the component number. In addition to the branch labels, each node is identified by the prefix N and the chosen node number. Node NO is taken to be at ground or zero volts potential and is therefore used as the reference for the other node voltages.

Branch currents are denoted by the prefix IB followed by the appropriate branch number. For ex-

Similarly, the branch voltage is symbolized by VB16. The state variables for this network are the branch voltages of the twig capacitors and the currents through the link inductors. This corresponds to VB5, IB21, IB22, and IB23.

Standard graph theory techniques [14] were applied to this network, from which one obtains a system of first-order differential equations whose coefficients are nonliner (chopper inductor, back of equations can be written in abbreviated matrix notation as follows:

$$F_n \cdot x_n = G_n \cdot x_n + H_n \cdot u_n . \tag{1}$$

In expanded form, following the branch current and voltage notations explained above with reference to Fig. 9, (1) can be rewritten as follows:

$$\begin{bmatrix} C1 & 0 & 0 & 0 \\ 0 & L2 & 0 & 0 \\ 0 & 0 & L1+L3 & L1 \\ 0 & 0 & L1 & L1+L4 \end{bmatrix} \cdot \frac{d}{dt} \begin{bmatrix} VB5 \\ IB21 \\ IB22 \\ IB23 \end{bmatrix}$$

$$= \begin{bmatrix} -1/R10 - 1/(R1+R10) - (C11+C21+C31) & 1 - R1/(R1+R11) - (C12+C22+C32) & -(C13+C23+C33) & -(C14+C24+C34) \\ -1 + R1/(R1+R11) + R2(C11+C21+C31) & R1\,R1/(R1+R11) - (R1+R2+R3) + R2(C12+C22+C32) & R2(C13+C23+C33) & R2(C14+C24+C34) \\ C11\,R4 - C21\,R5 & C12\,R4 - C22\,R5 & C13\,R4 - C23\,R5 - (R4+R5+R7+R8) & -(R4+R7) + C14\,R4 - C24\,R5 \\ C11\,R4 - C31\,R6 & C12\,R4 - C32\,R5 & -(R4+R7) + C13\,R4 - C33\,R6 & C14\,R4 - C34\,R6 - (R4+R6+R7+R9) \end{bmatrix} \cdot \begin{bmatrix} VB5 \\ IB21 \\ IB22 \\ IB23 \end{bmatrix}$$

$$\begin{bmatrix} 0 & 0 & 0 & \frac{1}{R10} \\ 0 & 0 & 0 & 0 \\ 1 & -1 & 0 & 0 \\ 1 & 0 & -1 & 0 \end{bmatrix} \cdot \begin{bmatrix} E1 \\ E2 \\ E3 \\ E4 \end{bmatrix} \tag{2}$$

Equation (1) was transformed to the standard state-space format by premultiplying equation (1) by the inverse of F_n which gives:

$$x_n = (F_n^{-1} \cdot G_n) \cdot x_n + (F_n^{-1} \cdot H_n) \cdot u_n \tag{3}$$

where F_n^{-1} is given as follows:

$$F_n^{-1} = \begin{bmatrix} \frac{1}{C1} & 0 & 0 & 0 \\ 0 & \frac{1}{L2} & 0 & 0 \\ 0 & 0 & \frac{(L1+L4)}{L1L4 + L3L1 + L3L4} & \frac{-L1}{L1L4 + L3L1 + L3L4} \\ 0 & 0 & \frac{-L1}{L1L4 + L3L1 + L3L4} & \frac{(L1+L3)}{L1L4 + L3L1 + L3L4} \end{bmatrix} \tag{4}$$

TABLE I
Summary of Experimental Test Cases

mode of operation	motor speed in rpm	ICMDs amperes
Motoring (forward)	4500, 5000, 5025	41.5, 31.5, 32.5
Regenerating (forward)	5101	-38.0
Plugging (forward)	240	32.0

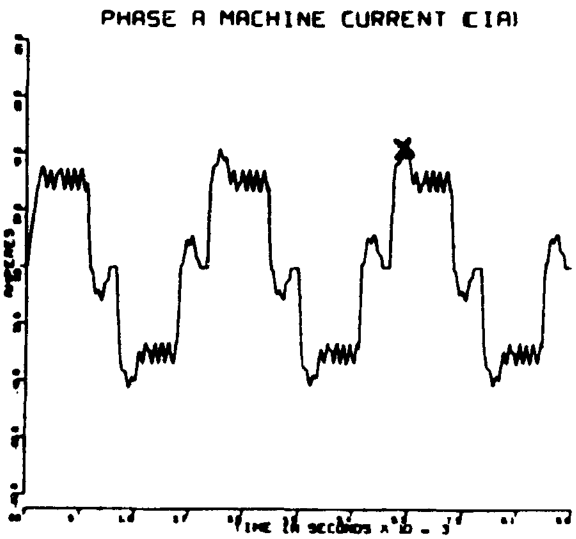

(A)

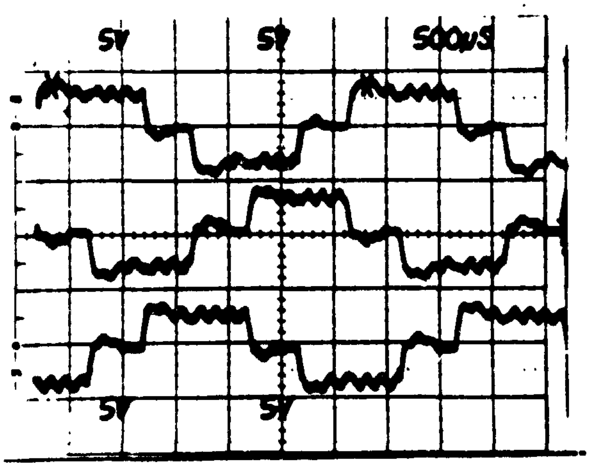

(B)

Fig. 9. (A) CSWF of machine phase A current during forward motoring. Speed 5000 rpm, ICMD 31.5 A, and 30° commutation advance. (B) Oscillogram of machine phase currents during forward motoring. Speed 5000 rpm, ICMD 31.5 A, and 30° commutation advance.

In this final formulation of the PCM model, all matrix manipulations were carried out in explicit parametric symbolic form in order to minimize computational effort and time. This is the case since a number of these coefficient matrices have to be updated at every increment for which the network parameters' values change.

The discrete-time solution approach was based entirely on a modified exponential series (state-space) method [19]. Thus the PCM model was put in the form $\dot{x} = A \cdot x + B \cdot u$, where the values of the state variables at the $(K+1)$th time instant are related to the values of the state variables at the (k)th time step by the state transition matrices $\Phi_k(\tau)$ and $\Theta_k(\tau)$ as follows:

$$x(t_{k+1}) = \Phi_k(\tau) \cdot x(t_k) + \Theta_k(\tau) \cdot u(t_k) \tag{5}$$

where τ is the chosen time increment. Here, one must reemphasize that the matrices Φ_k and Θ_k may be reevaluated at every instant k in the time solution, depending on the status of changes in the network parameters. These parameters are in turn functions of the state variables and switching commands as outlined earlier.

This approach was used in conjunction with a solution algorithm which is detailed in [11] and [12] as well as [19]. In this algorithm successive incrementation of time takes place over the transient period under consideration accompanied by nonlinear network iterative techniques to ascertain the status of all the diodes in the network. In the following section, results of practical application of this algorithm are compared with corresponding experimental test data obtained from the actual EMA hardware.

Comparison Between Numerically and Experimentally Obtained Performance Data

A number of conventions must be established to facilitate the comparison between experimental and numerical data included here. It will be agreed upon, in this paper, that the time origin in all the waveforms included here is at the farthest left-hand side of the figures. The edge of a positive half waveform closer to the time origin will be referred to as the "leading edge." On the other hand, the edge of a positive half waveform farthest from the time origin will be referred to as the "trailing edge." The computer simulated waveforms for various currents and voltages which were obtained using the model presented in this paper, will be referred to by the abbreviation CSWF. It should be pointed out that various CSWFs and their corresponding oscillogram counterparts have been obtained under slightly different operating conditions (speed, current, command, etc.). This is because of the fact that these investigators had no direct control over the experimental test procedures and conditions, since they were performed at a different facility.

The PCM model is verified by comparisons of CSWFs with actual oscillograms obtained from tests performed on the EMA. These comparisons are made for modes of operation, speeds and dc line current commands, ICMDs which are summarized in Table I for the actual test conditions.

Fig. 9(B) shows experimentally obtained oscillograms of the machine phase currents at a speed of 5000 rpm and with a commutation advance of 30 elec-

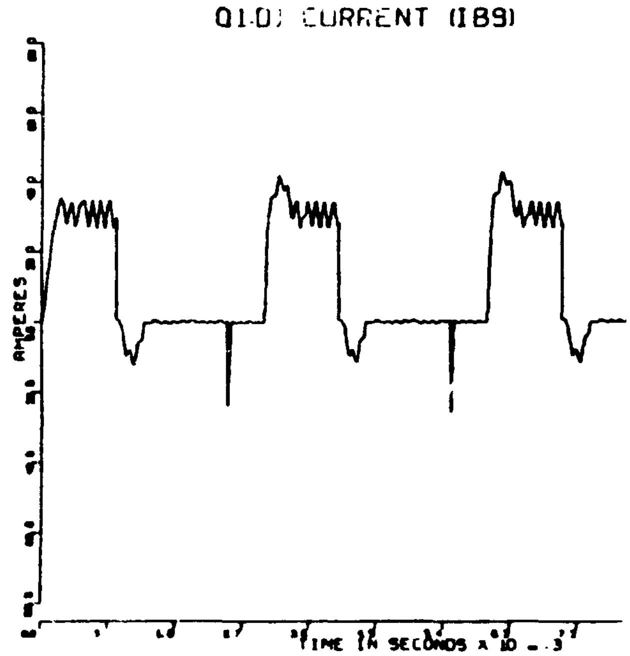

(A)

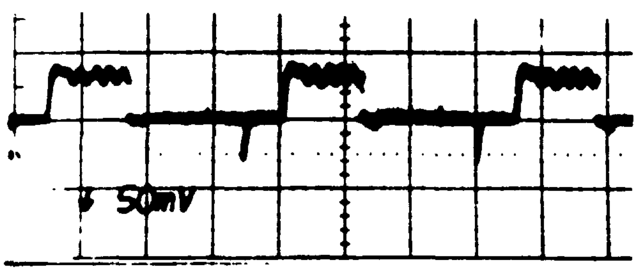

(B)

Fig. 10. (A) CSWF of current through Q1-D1 inverter switch during forward motoring. Speed 500 rpm, ICMD 31.5 A, and 30° commutation advance. (B) Oscillogram of current through Q2-D2 inverter switch during forward motoring. Speed 5025 rpm, ICMD 32.5 A, and 30° commutation advance.

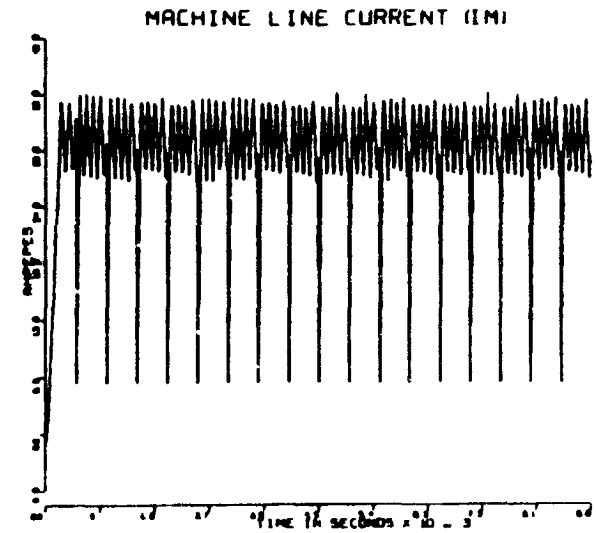

(A)

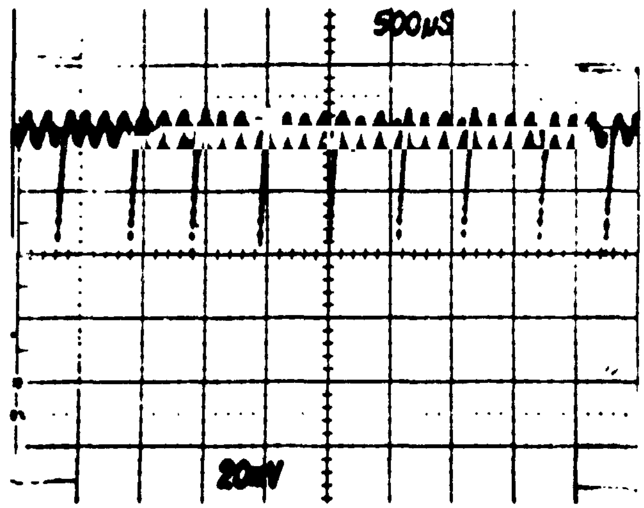

(B)

Fig. 11. (A) CSWF of IM during forward motoring. Speed 5000 rpm, ICMD 32.5 A, and 30° commutation advance. (B) Oscillogram of IM during forward motoring. Speed 4500 rpm, ICMD 41.5 A, and 30° commutation advance.

trical degrees. Examination of the current waveforms reveals the same characteristic overshoot and undershoot at the leading and trailing edges of the oscillogram and the CSWF given in Fig. 9(A). The positive peaks of the current oscillograms shown in Fig. 9 are indicated by an X on the corresponding CSWF. Both the oscillogram and the CSWF display the same chopper frequency of 9 peaks per half cycle. Notice also the two slope current transient present in both cases in the middle of the positive and negative current cycle. This can be attributed to the switching "on" of diode DR shown in Fig. 4 during commutation.

Figure 10(B) depicts the oscillogram of the current through one of the transistor-diode switches in the six-legged inverter-converter bridge leading to the machine phases. A corresponding CSWF is given in Fig. 10(A). Excellent correlation between the various ripples and pulses in the oscillogram and the CSWF are self-evident upon examining these figures. Time congruence between the occurrence of the various ripples and pulses is also evident in these figures.

Fig. 11(B) depicts the oscillogram of the main dc line current for a motoring mode. Notice the current dips which are occurring at regular intervals. The almost identical ripple and dip pattern is also evident in the CSWF given here in Fig. 11(A). Again the agreement between the numerical and test results is excellent.

Fig. 12(B) gives the oscillogram of phase current for the generating (or regenerative braking) mode at a rotor speed of 5101 rpm, while Fig. 12(A) depicts the corresponding CSWF of one of the three phase currents at the same speed. Again agreement between the oscillogram and the CSWF is excellent.

Fig. 13(B) depicts the oscillogram of the phase current obtained while the PCM was operating in the braking mode at a speed of 240 rpm. The corresponding CSWF for the same phase current is given in Fig. 13(A). Again, excellent correlation can be seen between the two waveforms.

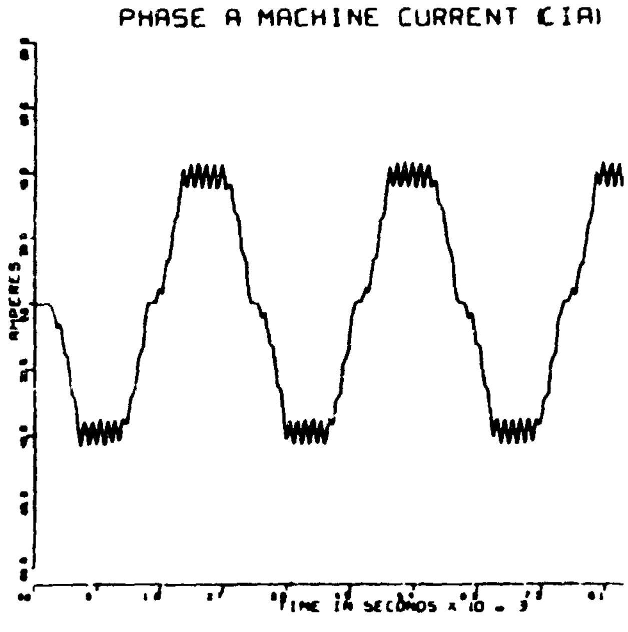

(A)

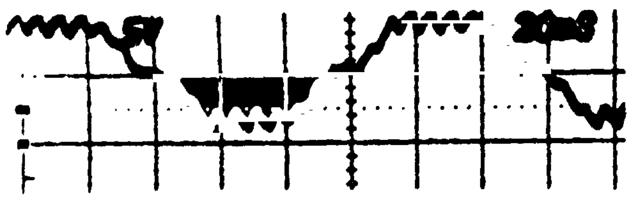

(B)

Fig. 12. CSWF of machine phase A current during forward regeneration. Speed 5101 rpm and ICMD -38.0 A. (B) Oscillogram of machine phase current during forward regeneration. Speed 5101 rpm and ICMD -38.0 A.

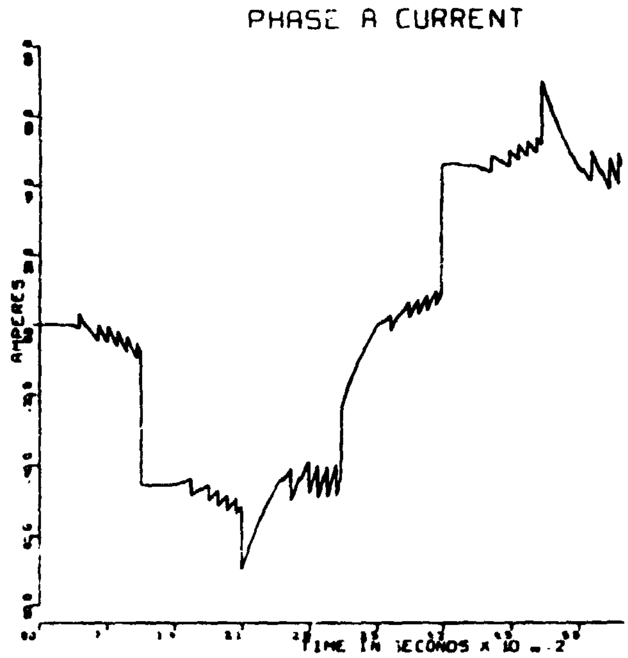

(A)

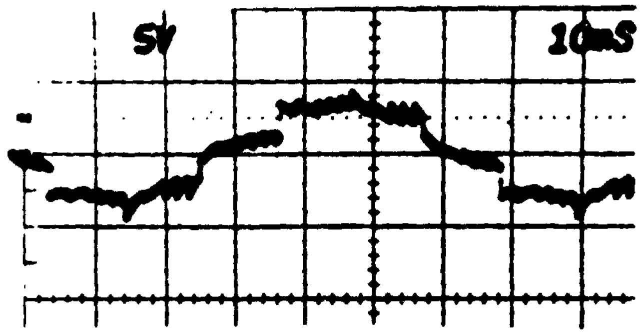

(B)

Fig. 13. (A) CSWF of machine phase A current during forward plugging. Speed 240 rpm, ICMD 40 A, and 30° commutation advance. (B) Oscillogram of current through phase B (top curve) and current through Q2-D2 inverter switch during forward plugging. Speed 240 rpm, ICMD 32 A, and 30° commutation advance.

A major performance characteristic which is a key in determining the dynamic performance of the motor is the developed electromagnetic (electromechanical) machine torque. This was calculated as the sum of the products of the phase back emf times the phase current for the A, B, and C windings, divided by the machine speed. The resulting transient electromagnetic torque profile is given in Fig. 14. As expected, the resulting profile gives a pulsating type torque with a nonzero average superimposed on which is a torque ripple of substantial magnitude. This confirms the earlier prediction associated with the variable torque angle between the armature and rotor MMFs, due to the "hopping" nature of the stator MMF. This is equivalent to a classical synchronous machine in which the torque angle varies in a cyclical fashion.

This torque is a key component in the determination of the overall EMA servo-loop performance to various input position commands. Results of this additional work have been reported on by these authors in [12] and will be expanded on and reported on in forthcoming papers. For instance, this present model can be used to predict the torque and dc machine line current throughout the duration following a step input flap position command. This is demonstrated in the profiles given in Figs. 15 and 16 for the machine current and torque including the effect of all components in the servo loop. Here, positive current and torque represent motoring mode, and negative values indicate regenerative or dynamic breaking, depending on machine speed. The profiles in Figs. 15 and 16 correspond to a step command of 2.75° mechanical in flap position.

Based on the set of results presented above, and the excellent correlation between the digitally simulated and experimentally obtained data, one can see clearly the validity of the modeling approach presented here for the PCM package. This is a major incentive towards further application and use of this model in the simulation of design modifications and new designs of this class of motors and power conditioners. This can save significant prototype production costs during optimization (design improvement). Also,

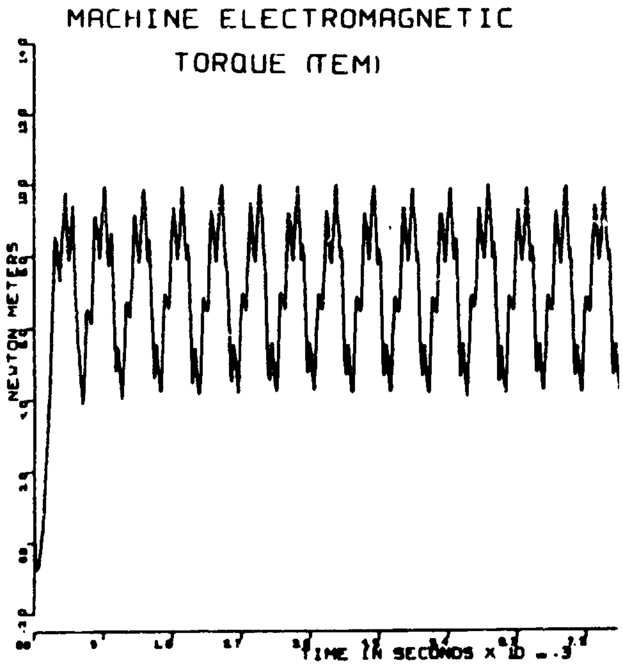

Fig. 14. Transient torque of motor during forward motoring. Speed 5000 rpm, ICMD 32.5 A, and 30° commutation advance.

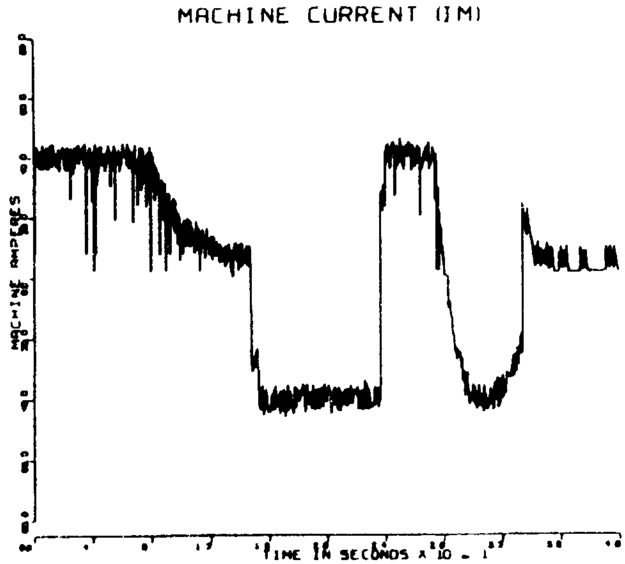

Fig. 15. Machine current following 2.75° flap command

Fig. 16. Machine torque following 2.75° flap command

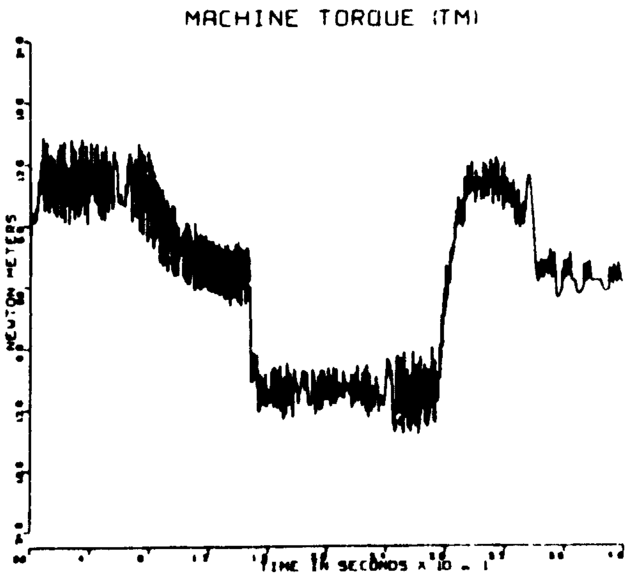

this model can be used as a trouble-shooting tool as will be outlined in the next section, namely in trouble-shooting related to electrical transients in such a system.

Use of Switching Logic Diagram in Diagnosis of Design Problems and Trouble-Shooting of Transients

In studying the electrical transients which are produced during the operation of such a PCM package, one is confronted with the extreme difficulties associated with the fast changing state (topology) of the network. This is due to the many electronic switching operations involved

Upon examining the voltage and current waveforms throughout the machine-network combination, one can easily spot spikes and pulses in such waveforms, where at first glance it is extremely difficult to attribute such transients to their proper cause (source). To alleviate this difficulty of identification of the cause (source) of a specific transient, a logic diagram was computer plotted with the help of the present EMA-PCM model, Fig. 17, in which the status of the various on-off periods of all the switches and diodes in the network are given over the simulation of duration of operation. The notation in Fig. 17 corresponds to that in Fig. 4. If the time (x axis) scale is chosen properly to correspond to the obtained current and voltage waveforms, one can superimpose this graph of Fig. 17 for the forward motoring mode, or others similar to it in other modes, on top of any current waveforms such as given in Figs. 9-13. This is to help identify the specific switching operation which is the cause of a particular spike or pulse contained in these waveforms.

For example, one can trace the relationship, on a one-to-one basis, between the on-off periods of the chopper transistor QM and diode DM during the motoring mode, the on-off status of which are shown in Fig. 17, and the corresponding sawtooth-like component of the phase current evident in Fig. 9.

Another example of identification of the cause of a transient, using the logic diagram of Fig. 17, is the congruence, in the time frame, of the undershoots (negative) and overshoots (positive) in the phase current waveforms preceding each of the negative and positive half cycle with the "on" periods of the

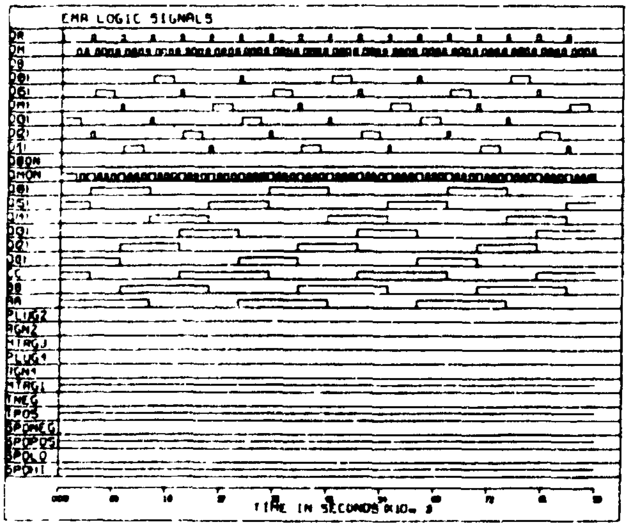

Fig 17 EMA logic signals during forward motoring. Speed 5000 rpm, ICMD 32.5 A, and 30° commutation advance.

diodes D4 and D1, respectively. Reference should be made here to the PCM schematic, Fig. 4.

It is now evident that such a diagram, Fig. 17, is an extremely valuable educational tool in helping one understand the complex interactions which take place in the operation of such a PCM system. Furthermore, this simulation model, if used in conjunction with a magnetic field finite element [16, 17] analysis tool for prediction of motor parameters (emf waveforms, inductances, etc.) can be applied to extensive ends in the magnetic design tailoring to a particular motor improvement as well as power conditioner design and vice versa to achieve goals specified by constraints in a given case. Aspects of the application and use of the present model along these lines will be covered in forthcoming papers.

Conclusions

The development of a detailed transient model for simulation of the instantaneous performance of a power conditioner fed samarium-cobalt permanent magnet brushless dc machine has been presented. The model emphasized in this paper was part of a more comprehensive development of an overall fourteenth-order electromechanical actuator dynamic model for the simulation of the transient performance of an EMA prototype manufactured for NASA-JSC. The fourteenth-order model will be reported on in forthcoming papers.

The numerical results of the instantaneous machine and power conditioner currents and voltages had a high degree of correlation to actual experimental test data performed on the prototype. This was the case under all possible operating modes (motoring, regenerative braking, and plugging). The accuracy of the model and its suitability for parametric design studies enabled these authors to use it in investigations of improvement of machine-power conditioner commutation characteristics, to reduce electrical transients and improvement of instantaneous torque profiles.

This model will be further improved by the addition of a motor magnetic field analysis capability using the method of finite elements. This will enable one to use the present model as a comprehensive design optimization and analysis tool in lieu of costly prototype fabrication and testing. Also, it will bring the performance of prototypes of such devices, whenever they are fabricated, closer than ever to the ultimate goals and constraints set for them. It will help identify unreasonable or impractical goals. This in itself results in substantial savings in development costs in laboratory and shop work. Further, this technique can be extended to encompass other power conditioner configurations.

Acknowledgment

We wish to acknowledge in particular the encouragement and enthusiasm offered by Mr. J.T. Edge of the Johnson Space Center. We wish to thank Mr. Edge for his many stimulating and useful suggestions which he offered freely throughout the duration of the contract, and without which this work would have been incomplete.

References

[1] R.L. Steigerwald and T.A. Lipo, "Analysis of a novel forced-commutation starting scheme for a load-commutated synchronous motor drive," *IEEE Trans. Ind. Gen. Appl.*, Jan./Feb. 1979.

[2] F. Harashima, H. Naitoh, and T. Haneyoshi, "Dynamic performance of self-controlled synchronous motors fed by current-source inverters," *IEEE Trans. Ind. Gen. Appl.*, Jan./Feb. 1979.

[3] W. McMurray, "Thyristor commutation in dc choppers—A comparative study," *IEEE Trans. Ind. Gen. Appl.*, Nov./Dec. 1978.

[4] S. Martinez and F. Aldana, "Current-source double dc-side forced commutated inverter," *IEEE Trans. Ind. Gen. Appl.*, Nov./Dec. 1978.

[5] E.P. Cornell and T.A. Lipo, "Modeling and design of controlled current induction motor drive systems," *IEEE Trans. Ind. Gen. Appl.*, July/Aug. 1977.

[6] E.P. Cornell and T.A. Lipo, "State-variable steady-state analysis of a controlled current induction motor drive," *IEEE Trans. Ind. Gen. Appl.*, Nov./Dec. 1975.

[7] T.A. Lipo, and F.G. Turnbull, "Analysis and comparison of two types of square-wave inverter drives," *IEEE Trans. Ind. Gen. Appl.*, Mar./Apr., 1975.

[8] G.R. Slemon, S.B. Dewan, and J.W.A. Wilson, "Synchronous motor drive with current-source inverter," *IEEE Trans. Ind. Gen. Appl.*, Vol. IA-10, May/June 1974, pp. 412-416.

[9] R.A. Turton and G.R. Slemon, "Stability of synchronous motors supplied from current source inverters," *IEEE Power Engineering Soc.*, 1978 Summer Meeting, Los Angeles, Paper No. F78-741-1.

[10] R.A. Turton and G.R. Slemon, "Stability of a synchronous motor drive using a current source inverter with power factor control," *IEEE Power Engineering Soc.*, New York, 1979 Winter Power Meeting, Paper No. F79-217-1.

[11] T.W. Nehl, Ph.D. Dissertation, Dep. of Electrical Engineering, Virginia Polytechnic Institute and State Univ., Blacksburg, Va., May 1980.

[12] N.A. Demerdash and T.W. Nehl, "Numerical simulation of dynamics of brushless dc motors for aerospace and other applications," Final Rep. Virginia Polytechnic Institute and State Univ.-NASA (JSC) Contract No. NAS9-1509, submitted to NASA-Johnson Space Center, Houston, TX, 1978.

[13] Delco Electronics, "Final report on the electromechanical flight control actuator," Final Rep. Contract No. NAS9-14952, General Motors Corporation, Delco Electronics Div., Santa Barbara Operations, Goleta, CA, 1978.

[14] N. Balbanian and T.A. Bickart, *Electrical Network Theory*. New York: Wiley, 1969.

[15] J.A. Cadzow and H.R. Martens, *Discrete-Time and Computer Controlled Systems*. Englewood Cliffs, NJ: Prentice-Hall, 1970.

[16] N.A. Demerdash and T.W. Nehl, "An evaluation of the methods of finite elements and finite differences in the solution of nonlinear electromagnetic fields in electrical machines," *IEEE Trans. Power App. Syst.*, Vol. PAS-98, pp. 74-87, 1979.

[17] P. Silvester and M.V.K. Chari, "Finite element solution of saturable magnetic field problems," *IEEE Trans. Power App. Syst.*, Vol. PAS-89, pp. 1642-1652, 1970.

[18] A.E. Fitzgerald and C. Kingsley, Jr., *Electric Machinery*, Second Ed. New York: McGraw-Hill, 1961.

[19] N.A. Demerdash and T.W. Nehl, "Dynamic modeling of brushless dc motor-power conditioner unit for electromechanical actuator application," *Proc. Power Electronics Specialists Conf.*, San Diego, 1979, pp. 333-343.

Nabeel A. Demerdash (M'65—SM'74) was born in Cairo, Egypt, on April 26, 1943. He received the B.Sc.E.E. degree with distinction and first class honors from Cairo University, Egypt, in 1964, and the M.S. and Ph.D. degrees in Electrical Engineering from the University of Pittsburgh in 1967 and 1971, respectively.

From 1964 to 1966 he was with the Faculty of Engineering, Cairo University as a Demonstrator. From 1966 to 1968 he was with the Department of Electrical Engineering, University of Pittsburgh, as a Graduate Teaching Assistant. In 1968 he joined the Large Rotating Apparatus Division of Westinghouse Electric Corporation, East Pittsburgh, Pennsylvania, as a Development Engineer, where he worked on Electromagnetic Field Modeling in Rotating Machinery and the development of the asymmetrical rotor for large steam turbine-driven generators. Since 1972 he has been with the Virginia Polytechnic Institute and State University, Blacksburg, where he is presently an Associate Professor in the Department of Electrical Engineering. He consulted for the Power Distribution and Control Branch of the Control Systems Development Division as a visiting scientist at the NASA-Johnson Space Center, Houston, during the summers of 1975 and 1976, on modeling of electrical motors for aerospace applications.

Dr. Demerdash is currently serving as a member of the Rotating Machinery Committee of IEEE, as well as Chairman of the Synchronous Machinery Subcommittee and a member of the Machine Theory Subcommittee of the IEEE. Dr. Demerdash is the Vice-Chairman of the Virginia Mountain Section of IEEE. He is also a past Chairman of the Industrial Applications Chapter of the Virginia Mountain Section of IEEE. He is a member of the American Society of Engineering Education, Sigma Xi, and Eta Kappa Nu. Dr. Demerdash is the author and coauthor of more than 30 transactions and technical papers in the power and magnetic fields areas. Dr. Demerdash's current interests include electromechanical propulsion and actuation, dynamic modeling of solid-state controlled and operated electrical machines, numerical analysis of electromagnetic fields in electric machinery, as well as machine-power system dynamics.

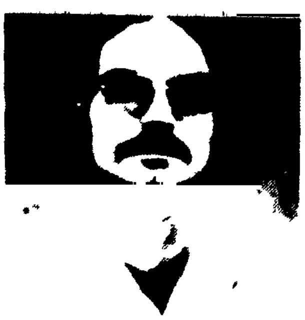

Thomas W. Nehl (M'78) was born in Tuebingen, West Germany, on December 22, 1952. He received the B.S.E.E., M.S.E.E., and Ph.D. degrees from Virginia Polytechnic Institute and State University in 1974, 1976, and 1980, respectively. Presently he is an Assistant Professor of Electrical Engineering at VPI&SU.

He consulted for the Fairfax County Department of Public Works in the summer of 1974 on explosion proofing of the electrical switchgear and motors utilized in pumping stations. During the summer of 1976 he was employed by the National Bureau of Standards as an engineering intern, where he developed a finite element package for the solution of sinusoidal eddy current problems in support of their nondestructive testing program. During the summer of 1977 he was employed as an engineering intern at the NASA Johnson Space Flight center where he was engaged in the modeling of electromechanical actuator systems, using permanent magnet brushless dc motors.

Dr. Nehl is a member of the machine theory and synchronous machines subcommittee of IEEE, PES. He is also a member of Sigma Xi, Eta Kappa Nu, and Phi Kappa Phi. Dr. Nehl's current interests include numerical analysis of electromagnetic fields in electrical machines and the dynamic modeling of machines and their associated power electronics.

APPENDIX (8)

ON IMPACT OF INDUCTANCES OF MACHINE WINDINGS ON BRUSHLESS DC SYSTEM PERFORMANCE

Nehl, T. W., Demerdash, N. A., and Fouad, F. A., "Impact of Winding Inductances and Other Parameters on the Design and Performance of Brushless DC Motors," Paper Accepted by IEEE-PAS, for publication in the IEEE Transactions on Power Apparatus and Systems.

IMPACT OF WINDING INDUCTANCES AND OTHER PARAMETERS ON THE DESIGN AND PERFORMANCE OF BRUSHLESS DC MOTORS

T. W. Nehl, Member

N. A. Demerdash, Senior Member

F. A. Fouad, Member

Virginia Polytechnic Institute and State University

SUMMARY

The computer aided design process applied to two electronically operated brushless dc motors intended for use in electric vehicle propulsion is described. The components of this process are a time domain dynamic simulation model of the brushless dc motor system in which the machine parameters, inductances and emfs, are obtained entirely from finite element field analysis of the magnetic circuit arrived at by the designer. This computer aided design process is used to determine the correct winding configurations for two machines. One of these machines utilizes a samarium cobalt permanent magnet rotor, while the other utilizes a strontium ferrite permanent magnet rotor. Both machines are required to achieve, as a minimum, 15 hp continuous and 35 hp peak motor ratings subject to the constraints of a maximum dc supply voltage of 120V, a speed range of 6000 to 9000 rpm, and a maximum current of 400A. This 400A limit is due to limitations on the available power switching components. A schematic diagram of the main components of these two systems, is given in Figure (1).

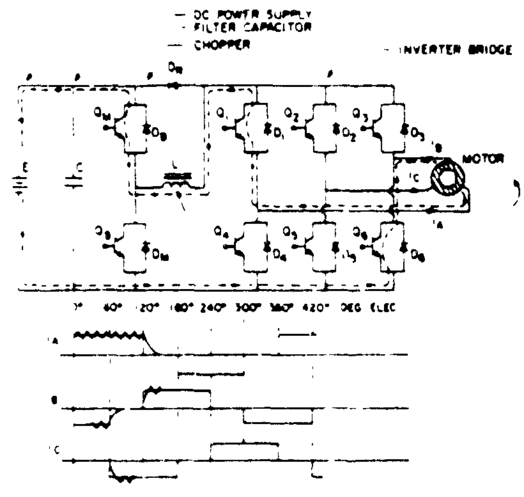

Figure (1) Schematic of Brushless DC Motor System.

The computer aided design process is used to analyze two preliminary winding designs per machine that appeared feasible based on standard design procedures. The difference between the various preliminary designs was the total number of series turns per phase.

The winding inductances and the induced back emf waveforms (fundamental and harmonics) are obtained by finite element field analysis of these preliminary designs. These key machine parameters, which critically impact the performance of the system, are then used in the dynamic simulation model of the entire machine-power conditioner unit that forms the brushless dc machine.

This model was used to predict the maximum power developed over the desired speed range for the four cases considered here. The effect of the zero and thirty degree commutation advance (detailed in the paper) on the performance of the system was also determined. A sample of these results is displayed in Figure (2) for the samarium cobalt machine.

Figure (2) Maximum Power Curves for the Samarium Cobalt Machine.

Based on this computer aided prediction, the two designs with the lower number of series turns were implemented, see Figure (3) and subsequently tested. In these tests, both machines met the desired performance goals for rated and peak power conditions without any design modifications. This demonstrates the usefulness of such a computer aided design approach in the design of electronically operated machine systems.

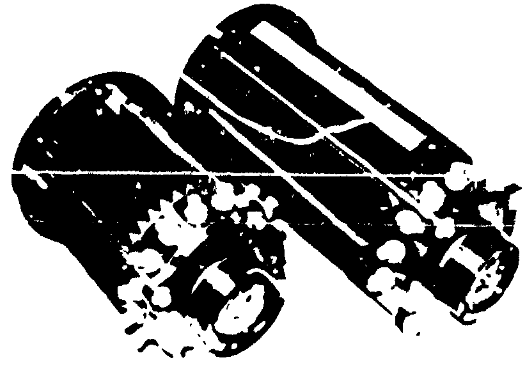

Figure (3) The Assembled Motors (Samarium Cobalt - Short Machine).

ORIGINAL PAGE IS OF POOR QUALITY

IMPACT OF WINDING INDUCTANCES AND OTHER PARAMETERS ON THE DESIGN AND PERFORMANCE OF BRUSHLESS DC MOTORS

T.W. Nehl, Member

N.A. Demerdash, Senior Member

F.A. Fouad*, Member

Virginia Polytechnic Institute and State University

ABSTRACT The computer aided design process of two electronically operated brushless dc motors intended for use in electric vehicle propulsion is described. The components of this process are a time domain dynamic simulation model of the brushless dc motor system in which the machine paramenters, inductances and emfs, are obtained entirely from finite element field analysis of the magnetic circuit arrived at by the designer. This computer aided design process is used to determine the correct winding configurations for two machines, the permanent magnet rotor one of which is of samarium cobalt, and of ferrite for the other. Both machines are required to achieve 15 hp continuous and 35 hp peak ratings as motors, subject to the constraints of a maximum dc supply voltage of 120 V and a maximum current of 400 A due to limitations on the available power switching components. In addition, the effects of changes in the firing angle of the inverter transistors, with respect to the induced winding emf's, are examined. The results of this work demonstrate that the performance of such systems is inductance limited especially in high speed (frequency) applications. The two machine designs selected as a result of this analysis were fabricated and subsequently tested in the laboratory. Both machines met the desired performance goals as predicted by the computer aided design process. These results, as well as those from previous investigations, demonstrate the usefulness of this approach in analyzing electronically operated machine systems with nonsinusoidal phase currents and emf's which cannot adequately be handled by classical frequency domain analysis.

INTRODUCTION

Electronically operated brushless dc motors are presently being investigated for possible use in a number of applications such as electric vehicle propulsion [1] and flight control actuation [2], [3]. This is due to the potential performance advantages of these motors such as reduced weight and volume, reduced maintenance, and increased reliability. The machine phase voltages and currents are highly nonsinusoidal due to the switching action of the power conditioner switches; therefore, classical frequency domain techniques are not well suited to the analysis of such systems [4], [5]. For this reason, a time domain dynamic simulation model suitable for implementation on the digital computer is desirable. Such a model is available and has been used successfully to predict the dynamic behavior of both an electromechanical flight control actuator [4] and an electric vehicle propulsion unit [5].

The major difficulty in the implementation of this design process at its early stages is the uncertainity of the values of machine inductance and emf parameters obtained by established design techniques. For this reason a numerical method for the calculation of these parameters was chosen to bridge this gap in the design process. The finite element method [6] is well suited to this task. In this work the winding inductances are calculated by means of an energy perturbational approach using the finite element method which was detailed in earlier references [7], [8]. Due to the low level of saturation in the cores of the machines considered here, [9], the induced emf waveforms resulting from the armature flux linkage are calculated from the midgap flux density waveforms which are obtained from finite element field solutions [9]. The use of numerically determined parameters as inputs to the dynamic simulation model represents a powerful computer aided design step for such systems.

In this work, the above mentioned computer aided design tools are applied to the design of two brushless dc motors, for electric vehicle propulsion, subject to the same set of performance and system constraints. One of these motors is based on a samarium cobalt permanent magnet rotor, while the other is based on a strontium ferrite magnet rotor. The analysis presented here is restricted to the selection of one of two possible winding configurations, obtained from a preliminary design for each machine. The selection of the correct windings takes into account the effects of changing the firing angle of the inverter power switching transistors. The selected machine designs were implemented and both met all of the required performance and system constraints, thereby validating this design approach.

SYSTEM DESCRIPTION

The basic configuration of the two brushless dc machine systems under consideration is shown in Figure (1). Each of these systems consists of a 120V supply battery which is a constraint on the rated voltage of the system, a transistorized power conditioner, and a three phase permanent magnet machine. The intended application for these systems is electric vehicle propulsion. For this application the required performance specifications are:

1. A continuous two hour rating of 15 hp corresponding to a vehicle cruising speed of 55 mph
2. A peak rating of 35 hp for one minute for hill climbing.

Notice that these performance specifications must be met with a maximum supply voltage of only 120 V (battery constraint). Under this constraint, the machine winding inductances become a very important factor in whether or not these performance specifications can be met. This low supply voltage also imposes large currents of several hundred amperes which must be switched by the power transistors. Consequently, the transistor ratings must also be considered in the design process.

Power Conditioner Description

One power conditioner is used to drive either one of the two machines. This power conditioner consists of a transistorized current chopper for current magnitude control and a three phase transistorized inverter/converter bridge for inverting dc to three phase ac and vice versa, [1]. The chopper and inverter both make use of Toshiba 2SD648 monolitic darlington power transistors rated at 300 V $V_{CE(SUS)}$ and a 400 A maximum collector current. These limits must be satisfied at both the continuous and peak rated operating points.

Voltage transients seen by these transistors are affected largely by the transistor switching speed, circuit layout and by the snubber networks. It will be assumed in this work that the snubber networks are capable of keeping the voltage transients below 300 V. Therefore the snubber networks will not be considered here. The current rating, however, was imposed as one of the constraints on the system during the design process.

The basic function of the power conditioner is illustrated by the idealized current waveforms during the motoring mode of operation shown below the circuit diagram in Figure (1). During this mode of operation,

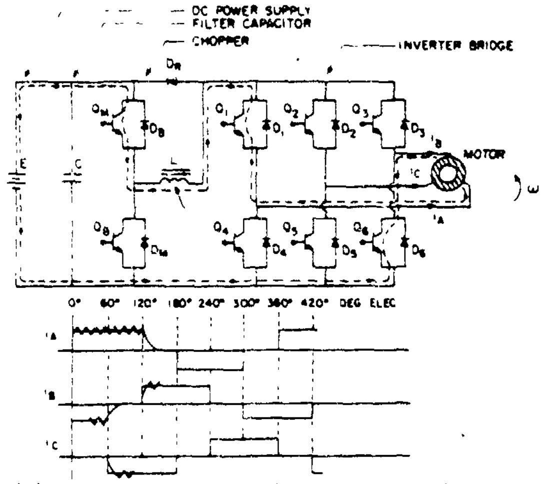

Figure (1) Machine-Power Conditioner Schematic and Idealized Phase Currents

the power conditioner control logic receives information on the position of the rotor via two sets of three equally spaced Hall devices, [1]. One set of Hall devices is used for normal firing while the other set is used to advance the firing by thirty degrees at high load conditions, [1]. The rotor position is translated into one of six discrete current states as shown in Figure (1). Each current state produces an armature mmf which remains fixed in space for sixty electrical degrees until the next current state. After the rotor completes sixty electrical degrees of rotation the phase currents are, ideally, switched instantaneously into the succeeding current state. This would result in a step or hop (of the armature mmf) of sixty electrical degrees in the direction of rotation. This process is repeated six times per electrical revolution resulting in a discretely jumping or hopping mmf, [4], [5]. In an actual physical system, however, the magnetic fields inside such a machine cannot change instantaneously due to stored magnetic energy associated with the currents flowing in the windings. Therefore, these winding inductances play an important role in determining the overall system performance especially at high frequency and high load conditions, [5].

The power conditioner can also function in the regenerative braking mode in order to recover some of the kinetic energy associated with a moving vehicle during braking. During this mode the six inverter transistors are turned off resulting in a three phase full wave rectifier bridge. This paper will deal only with the motoring mode of operation, consequently regeneration will not be considered here.

Machine Descriptions

The above mentioned power conditioner was designed to operate either one of two machines. One machine uses high energy product samarium cobalt permanent magnets while the other one makes use of cheaper and more readily available strontium ferrite permanent magnets. From previous experience with a four pole, fifteen slot samarium cobalt motor of the same rating; it was decided to increase the number of poles to six and the number of slots to eighteen. This was done to decrease the machine volume and weight as well as reduce the complexity of the machine winding. Since the fractional slot winding was abandoned, it was decided that both armatures would be skewed one full slot pitch to reduce harmonics in the backemf, [10]. Based upon these assumptions, the stator laminations and rotor structure were designed using standard magnetic, thermal, and mechanical design procedures. The resulting preliminary designs of the samarium cobalt and ferrite machines are shown in the cross-sectional views of Figures (2) and (3), respectively.

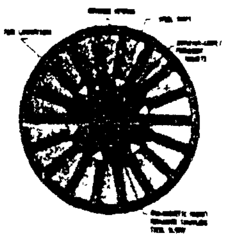

Figure (2) Cross-Section of the Samarium Cobalt Machine

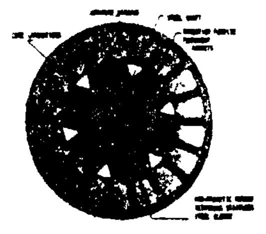

Figure (3) Cross-section Strontium Ferrite Machine

The desired speed range for the rated 15 hp point was chosen between 6,000 and 9,000 rpm due to core loss, mechanical, and other design considerations.

For the samarium cobalt machine, the preliminary design process indicated that windings with twelve and fifteen turns per phase were feasible. For the strontium ferrite machine the choice was found to be between two designs, one with nine and the other with twelve turns per phase.

Therefore the design problem at this stage is reduced to picking the correct number of turns for the armature windings of the two machines. The various factors influencing the final choice of the winding configuration are discussed next.

FACTORS AFFECTING MACHINE PERFORMANCE

The correct choice of the number of turns for the two machine designs given above depends on a number of factors such as the backemf constant of the machine, the winding inductances, and the angle between the phase currents and emfs (commutation angle).

Impact of Emfs and Inductances

The machine winding inductances must be low enough so that the current can buildup to the required values at continuous and peak operating points, under the above mentioned supply voltage constraint of 120 V. Also, the maximum allowable value of this inductance is strongly dependent upon the number of poles since this determines the frequency of the phase currents. If the inductances are too large, the required power must be obtained at a lower speed (frequency) and hence reduced backemf. Therefore, the magnitude of the current must increase correspondingly to keep the machine output power constant. This situation can be tolerated so long as the maximum current handling capability of the transistors is not exceeded.

The winding inductance varies with the square of the number of turns while the induced backemf varies linearly with speed. Therefore small changes in the total number of turns reduces the no load speed only linearily while dramatically reducing the inductances. Such small changes in the winding can produce dramatic changes in the maximum machine power output at a given speed and supply voltage, as will be shown later. Ideally, the inductance of a machine should be kept as low as possible for a given emf constant. This can be accomplished in a number of ways such as operating the core at higher flux densities, improved permanent magnet materials, reducing the slot and end leakage inductances, and so on.

Impact of the Commutation Angle

Another factor affecting the machine output is the angle between the injected phase currents and the induced phase voltages, [1], [10]. Normally, current is injected into a phase winding thirty electrical degrees after the backemf passes through zero (zero commutation advance or normal firing). Since the period of conduction is 120 electrical degrees, the phase current and emf waveforms are centered with respect to each other. This maximizes the volt-ampere product for a given current and machine speed. Under heavy loads this firing angle limits the maximum value of current buildup since the current is injected only after the backemf reaches sin(30°) of its peak value (for sinusoidal backemfs). Since this emf opposes the current buildup,it may be necessary, under peak load conditions, to advance the firing of the inverter transistors by thirty degrees to the point where the induced backemf is zero (thirty degree commutation advance or advanced firing). This reduces the volt-ampere product, however this is more than compensated for by the substantial increase in current magnitude, as will be seen later.

The following two sections will describe the machine-power conditioner model used in the computer aided design process and how the machine parameters are determined. These computer aided design models are then applied to the preliminary designs of the two machines mentioned above to determine the effects of the emfs, inductances and commutation advance on the overall system performance.

MACHINE MODEL AND PARAMETER DETERMINATION

The electrical behavior of the two wye connected (floating neutral) brushless dc machines is modeled by a wye connected three phase network consisting of a series connected resistance, inductance, and voltage source per phase, see Figure (4).

The justification for this rather simple model was given earlier in reference [5]. Also, this model has been used very successfully in the analysis of similar machines in previous investigations, [4], [10].

The voltage sources in the three legs of this model represent the induced backemfs per phase produced by the rotating permanent magnet rotors. The backemf waveforms are calculated from the midgap flux density waveforms which are obtained from two dimensional nonlinear finite element field analysis, [9].

Figure (4) Machine Model

The emfs can be calculated in this manner because the stator core and teeth are only lightly saturated, hence almost all the airgap flux links equally all the armature conductors. The effects of the one slot pitch skewing of the stator are included in the emf calculations, [10]. It has been shown in earlier work, [9], that the backemfs are relatively independent of the armature reaction due to the small magnitude of armature mmf in relation to the equivalent magnet mmf in the normal operating range for these machines. For this reason there is practically no difference between the no load and load backemfs.

The finite element calculated no load backemf waveforms for the samarium cobalt and strontium ferrite machines are given in Figures (5) and (6) respectively. These were calculated by finite elements using the permanent magnet demagnetization curves at 25°C. Notice that both emfs are nearly sinusoidal. This is due to the one slot pitch skew in both stator cores.

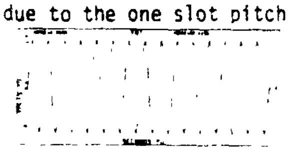

Figure (5) No Load Backemf Waveform of the Samarium Cobalt Machine

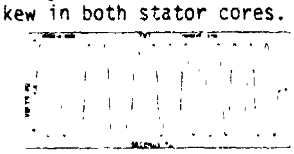

Figure (6) No Load Backemf Waveform of the Strontium Ferrite Machine

Comparision of the calculated emf constants, in Volts/mechanical radians/second, with the measured values, see Table (1), reveals excellent agreement between the two sets of numbers. The emf waveforms are represented by a fourier series and the magnitudes are assumed to vary linearly with speed.

Table (1) FE Determined and Measured Phase to Neutral EMF Constants Volts/Mech. Radian/Sec.

	SAMARIUM COBALT 12 Turns/Phase	FERRITE 9 Turns/Phase
FE	0.0693	0.0594
Measured	0.0658	0.0573

The inductances in the machine model of Figure (4) are equal to one half of the line to line incremental inductance, see reference [5]. These inductances were calculated using an energy perturbation apprach coupled with the finite element method, [7], [8]. In that, work it was found that the variation of these inductances is virtually independent of rotor angle because of the large effective airgap in such machines due to the low permeability of the magnets. This fact was also verified by test measurements, [8]. The calculated and measured values of one half of the line to line inductances are given in Table (2). Notice that the measured values are consistently higher than the calculated ones. This is because end effects were neglected in the two dimensional finite element field calculations.

Table (2) FE Determined and Measured (Line to Line/2) Inductances

	SAMARIUM COBALT	
	12 Turns/Phase	15 Turns/Phase
FE	41.85 μH	65.35 μH
MEASURED	44.95 μH	Not available
	FERRITE	
	9 Turns/Phase	12 Turns/Phase
FE	42.5 μH	75.5 μH
MEASURED	46.0 μH	Not available

In summary there are three basic simplifications which lead to this rather simple machine model and which are justified on the basis of the physical nature of these brushless machines at hand. These simplifications are as follows:

1. The series inductance per phase in the equivalent circuit model is for all practical purposes independent of the rotor position, as determined by both finite element field analysis and inductance measurement from the actual hardware, see reference [8]. This is largely due to the large effective airgap that is inherent to such machines. This large effective airgap is caused by the fact that the magnetic permeability of magnet materials, samarium cobalt or ferrite is practically equal to air.

2. The permanent magnets are electrically and electromagnetically equivalent to a field winding with a constant excitation current. Hence, the transient inductance phenomenon and corresponding time constants associated with ac armature - dc field interaction during dynamic conditions is not present here.

3. The eddy current damping effects in the rotors of such machines have been shown to be rather insignificant in comparison to machine ratings, see the work of reference [12]. Accordingly, the subtransient inductance phenomenon, and corresponding time constants associated with ac armature - rotor damping interaction during dynamic conditions is absent here for all practical purposes.

The above three factors lead to the rather simple model of an induced armature emf in series with an inductance equal to the phase to neutral self inductance minus the mutual phase to phase inductance per each leg of the three phases in the machine. Further details were included in this aspect in references [5] and [8].

This machine model is incorporated into the dynamic simulation model of the entire machine-power conditioner system which is described next.

MACHINE-POWER CONDITIONER DYNAMIC SIMULATION MODEL

The dynamic simulation model used here to analyze the above mentioned machine designs was developed originally to analyze a similar system intended for use as an electromechanical actuator for flight control applications, [4]. Later, the same model was successfully applied to the analysis of an electronically commutated brushless dc motor for electric vehicle propulsion, [5]. In this previous work, some or all of the machine inductances and emfs were obtained from test measurements. However, in this work at hand, both the machine inductances and backemfs were calculated using the finite element method applied to the given preliminary magnetic circuit and winding designs.

In this model, the machine-power conditioner shown schematically in Figure (1) is replaced by a lumped parameter nonlinear network model shown in Figure (7). Inspection of this figure reveals that the machine is replaced by the simplified machine model of Figure (4). The power switches are modeled by nonlinear resistances which take on low values during conduction and high values when switched off.

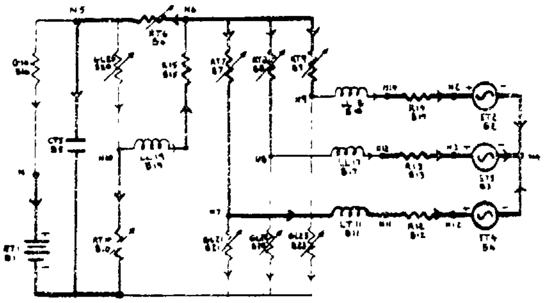

Figure (7) Machine-Power Conditioner Network Model

The dynamic simulation model is written in standard state space form as

$$\dot{\underline{x}} = \underline{A}\underline{x} + \underline{B}\underline{u} \qquad (1)$$

where $\underline{x}$ is the vector of state variables which consists of the cotree inductor currents and the tree capacitor voltages, $\dot{\underline{x}}$ is the derivative of $\underline{x}$ with respect to time, $\underline{A}$, $\underline{B}$ are coefficient matrices, which must be recalculated whenever a diode or transistor changes state, and $\underline{u}$ is the vector of forcing functions, which are the battery voltage and the backemfs. The branch voltages, currents, powers, etc. are refered to as the output variables and are symbolized by the vector $\underline{y}$. These can be defined in terms of the state variables, $\underline{x}$, and the forcing functions, $\underline{u}$ as follows:

$$\underline{y} = \underline{C}\underline{x} + \underline{D}\underline{u} \qquad (2)$$

where $\underline{C}$,$\underline{D}$ are coefficient matrices which must be updated whenever a transistor or diode changes state (switches on or off). Since the state model is a function of the status of the diodes and transistors, the four coefficient matriccs must be recalculated whenever the network changes state. A simplified flow chart of the algorithm used to implement this model is given in Figure (8). Further details on this model can be found in references [4] and [11]. Sample comparisions between phase current, transistor switch voltage, phase to neutral and line to line voltages obtained by this model and from test are quoted from reference [11] in Appendix A for convenience. The application of this model to the two machines described earlier is given next.

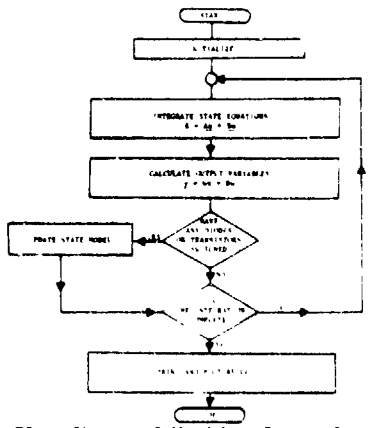

Figure (8) Flow Chart of Machine-Power Conditioner Dynamic Model

RESULTS

The two machines described earlier are required to produce at least 15 hp continuous and 35 hp peak ratings using up to the full thirty degree commutation advance if necessary. These power ratings have to be developed under the following constraints:

1. Maximum supply voltage of 120 V,
2. Maximum transistor currents of 400 A, and
3. Machine speeds should fall in the speed range of 6000 to 9000 rpm if possible.

In order to determine whether or not the two machine designs are capable of delivering these ratings the following simulation studies using the data of Tables (1) and (2), were performed:

Study (1)

The performance of the two samarium cbalt and the two ferrite machines was calculated for speeds of 6000, 7500, and 9000 rpm with a fixed battery voltage of 120 V, with the chopper transistor Q_M fully on, and with zero commutation advance.

Study (2)

The runs described above were repeated except that the commutation advance was increased to the full thrity degrees.

Portions of these results are displayed in Figures (9) throught (12). The maximum powers and peak currents developed by the two proposed winding designs of the samarium cobalt machine between 6000 and 9000 rpm are plotted in Figures (9) and (10), respectively. Inspection of Figure (9) reveals that the fifteen turn version of the samarium cobalt machine is unable to achieve the 35 hp peak power within the desired speed range even with the full thirty degree commutation advance. The twelve turn version, on the other hand, meets all of the performance specifications with phase currents less than 400 A, see Figure (10). Notice that the 400 A points are indicated in Figures (9) and (11) by the 'x's.

Inspection of Figures (11) and (12) revealed a similar picture for the two designs of the strontium ferrite machine. The version with the twelve turns was unable to meet the performance specifications while the nine turn version did. Notice that the ferrite machine produced more than 15 hp throughout the specified speed range. This is no problem since the 15 hp rating is a minimum rather than an absolute rating. Also the copper transistor Q_M can be switched to produce any output less than the maximum.

Sample current and power waveforms obtained from the various simulation runs are given in Figures (13) through (16) for the twelve turn version of samarium cobalt machine at 9000 rpm and the two firing angles. The phase currents at zero and thirty degree commutation advances are displayed in Figures (13) and (14) respectively. Notice that with zero advance the phase current decays from its initial value of 150 A to a final peak value of 87 A. Advancing the firing by thirty degrees produces a dramatic increase in the magnitude of the steady state phase currents over the previous case.

The impact of the commutation advance on the electromagnetic power, is also clearly shown in Figures (15) and (16). Notice that both the magnitude of the power as well as the percentage of the power ripple increase with increasing commutation advance, see Figure (16).

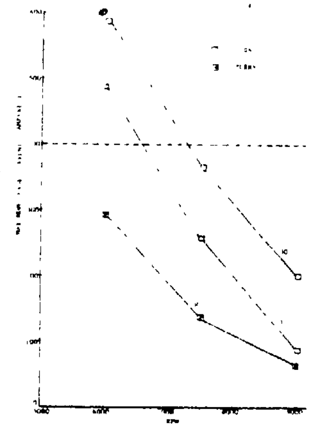

Figure (9) Maximum Power Curves for the Samarium Cobalt Machine

Figure (10) Peak Current Curves for the Samarium Cobalt Machine

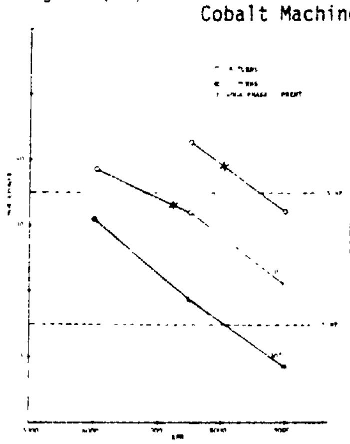

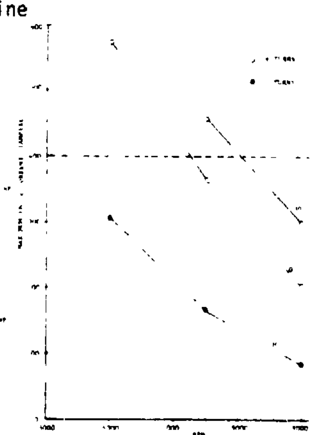

Figure (11) Maximum Power Curves for the Strontium Ferrite Machine

Figure (12) Peak Current Curves for the Stontium Ferrite Machine

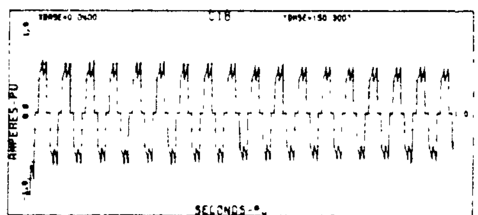

Figure (13) Phase Current of the Samarium Cobalt Machine with the 12 Turn Winding at 9000 rpm and 0° Commutation Advance

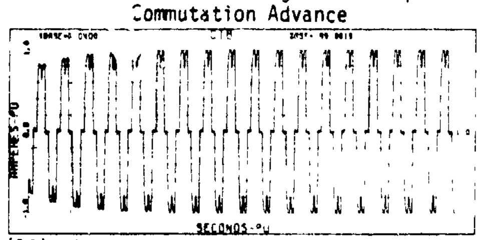

Figure (14) Phase Current of the Samarium Cobalt Machine with the 12 Turn Winding at 9000 rpm and 30° Commutation Advance

Based upon these results, the samarium cobalt machine was constructed with twelve series turns per phase and the strontium ferrite machine was constructed with nine series turns per phase, see Figure (17). These machines were tested in the lab and both met the required performance goals as documented previously in reference [1].

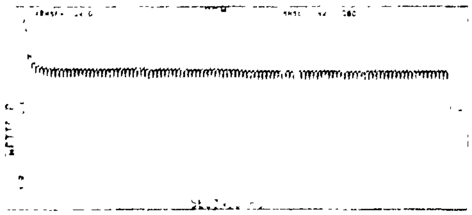

Figure (15) Electromagnetic Power of the Samarium Cobalt Machine with the 12 Turn Winding at 9000 rpm and 0° Commutation Advance

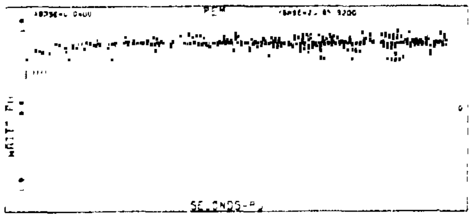

Figure (16) Electromagnetic Power of the Samarium Cobalt Machine with the 12 Turn Winding at 9000 rpm and 30° Commutation Advance

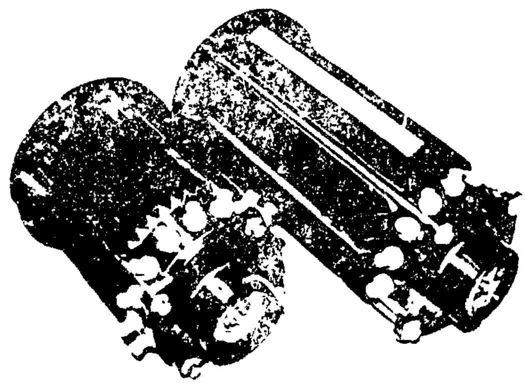

Figure (17) The Assembled Brushless DC Motors. (Samarium Cobalt-Short Machine, Strontium Ferrite-Long Machine)

CONCLUSIONS

The impact of winding inductances and the commutation angle between the phase currents and induced backemfs per phase on the performance of two brushless dc motor designs was determined using the given computer aided designed approach. The performance of two brushless motors, one based on samarium cobalt magnets and the other one on strontium ferrite magnets was obtained from a time domain dynamic simulation model of such systems. A time domain model is necessary since the majority of the voltages and currents are nonsinusoidal. The motor emf and inductance paramters used in this simulation were obtained directly from finite element field analysis of the preliminary machine designs.

The analysis demonstrated the importance of the machine inductances on the performance of such systems over a given speed (frequency) range. Furthermore, varying the commutation advance was shown to produce dramatic changes in the machine output over the entire speed range. Based on these results, the designs of the two machines were finalized and implemented. Subsequent testing of the two machines confirmed their ability to meet all of the design goals as predicted. Accordingly, this computer aided design approach presented here is well suited for the design of such systems.

Future efforts in this area should be directed towards more detailed machine models suited for more complex systems in which the inductance variations due to rotor position and saturation level cannot be ignored in their dynamic simulations. Results from this design example demonstrated very strongly the usefulness of such computer aided design tools in the analysis and design discussions taken in the course of this project of brushless dc motor systems with their nonsinusoidal voltages and currents.

ACKNOWLEDGEMENTS

These authors wish to acknowledge the Electric and Hybrid Vehicle Office of the NASA-Lewis Research Center and the Electric and Hybrid Vehicle Division of DOE for their financial support of this project under NASA/DOE Contract DEN3-65.

REFERENCES

[1] * Demerdash, N. A., Miller, R. H., Nehl, T. W., Overton, B. P., and Ford, C. J., "Comparison between Features and Peformance Characteristics of Fifteen HP Samarium Cobalt and Ferrite Based Brushless DC Motors Operated by Same Power Conditioner," Paper accepted for publication in the *IEEE Transactions on Power Apparatus and Systems*, presented at the PES Winter meeting, New York, January 31 - February 5, 1982.

[2] Edge, J. T., "An Electromechanical Actuator Technology Development Program," Paper No. 780581, *Society of Automotive Engineers, Proceedings of the Control Technologies Symposium*, 1978.

[3] Sawyer, B. and Edge, J. T., "Design of a Samarium Cobalt Brushless DC Motor for Electromechanical Actuator Applications," *Proceedings of the IEEE-National Aerospace and Electronics Conference*, Dayton, Ohio, 1977.

[4] * Demerdash, N. A. and Nehl, T. W., "Dynamic Modeling of Brushless DC Motors for Aerospace Actuation," *IEEE Transactions on Aerospace and Electronic Systems*, Vol. AES-16, No. 6, 1980, pp. 811-821.

[5] * Nehl, T. W., Fouad, F. A., Demerdash, N. A. and Maslowski, E., "Dynamic Simulation of Radially Oriented Permanent Magnet Type Electronically Operated Synchronous Machines with Parameters Obtained from Finite Element Field Solutions," *IEEE Transactions on Industry Applications*, Vol. IA-18, Number 2, 1982, pp. 172-182.

[6] Chari, M. V. K. and Silvester, P. "Analysis of Turbo Alternator Magnetic Field by Finite Elements." *IEEE Transactions on Power Apparatus and Systems*, Vol. PAS-90, 1971, pp. 454-464.

[7] * Fouad, F. A. "Finite Element Analysis For Design of Classical and Electronically Operated Machines," *Ph.D. Dissertation*, Virginia Polytechnic Institute and State University, Blacksburg, VA, May 1981.

[8] * Nehl, T. W., Fouad, F. A., and Demerdash, N. A., "Determination of Saturated Values of Rotating Machinery Incremental and Apparent Inductances by and Energy Perturbation Method," Paper accepted for publication in the *IEEE Transactions on Power Apparatus and Systems*, presented at the PES Winter meeting, New York, January 31 - February 5, 1982.

[9] * Fouad, F. A., Nehl, T. W., Demerdash, N. A., "Magnetic Field Modeling of Permanent Magnet Type

Electronically Operated Synchronous Machines Using Finite, Elements," *IEEE Transactions on Power Apparatus and Systems*, Vol. PAS-100, No. 4, Sept. 1981, pp. 4125-2135.

[10] Nehl, T. W., Fouad, F. A., and Demerdash, N. A., * "Digital Simulation of Power Conditioner - Machine Interaction for Electronically Commutated DC Permanet Magnet Machines," *IEEE Transactions on Magnetics*, Vol. MAG-17, No. 6, 1981, pp. 3284-3286.

[11] Nehl, T. W., "A Discrete Time Model for a Power * Conditioner Fed Permanent Magnet Brushless DC Motor System for Aerospace and Electric Vehicle Applications for Design Purposes Using Finite Elements for Machine Paramater Determination," *Ph.D. Dissertation*, Virginia Polytechnic Institute and State University, Blacksburg, VA, May 1980.

[12] Nagarkatti, A. K., Mohammed, O. A., and Demerdash, * N. A., "Special Losses in Rotors of Electronically Commutated Brushless dc Motors Induced by Non-Uniformly Rotating Armature MMFs," Papaer presented at the *1982 PES Winter Power Meeting*, New York, NY, and will be published in full in the *IEEE Transactions on Power Apparatus and Systems*.

* Names and Affiliations are Blanked Out During the Review Process in Accordance with the IEEE-PES Author-Reviewer Anonymity Rules.

APPENDIX

The dynamic simulation model used in this work was verified using oscillograms obtained during laboratory testing of similar brushless dc motors from previous investigations, see references [4], [5], and [11]. For the sake of completeness, portions of these results will be repeated here.

Prior to the design and construction of the two motors described in this paper, the model was verified using test results obtained from a four pole, fifteen slot samarium cobalt brushless dc motor for electric vehicle propulsion, [5], [11]. The continuous and peak ratings of this macine were identical to those of the two machines subject of this paper.

Various oscillograms and their corresponding computer simulated waveforms (CSWF) during the motoring mode of operation, at a speed of 7750, are given in Figures (A-1) through (A-4). Inspection of these figures reveals excellent agreement between the two sets of results. Further verification of this model can be found in references [4], [5], and [11].

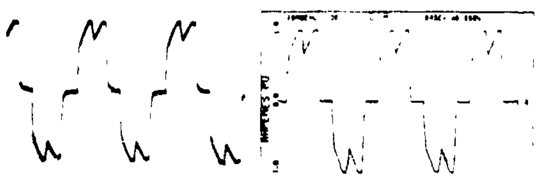

Figure (A-1) Oscillogram and CSWF of the Phase Current. [Horizontal: 1 ms/div, Vertical: 50V/div]

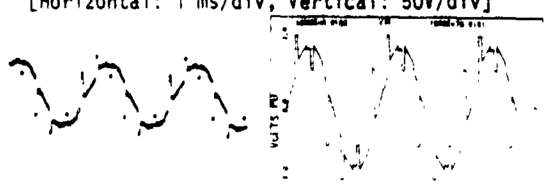

Figure (A-2) Oscillogram and CSWF of the Phase Voltage. [Horizontal: 1 ms/div, Vertical: 50V/div]

Figure (A-3) Oscillogram and CSWF of the Line to Line Voltage. [Horizontal: 1 ms/div, Vertical: 50V/div]

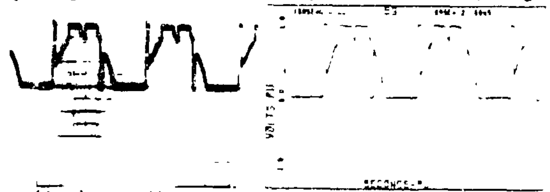

Figure (A-4) Oscillogram and CSWF of an Inverter Transistor Voltage. [Horizontal: 1 ms/div, Vertical: 50V/div] permanent magnets (p.m.) which are of rare earth cobalt, give a partly flat internal surface which one could instead safely assume to be circular. However, in order to further simplify the analysis, and since the radial thickness of the p.m. is substantial, we have assumed the p.m. to extend to the axis, except in the intermagnet regions where epoxy fills the space below the sleeve. This greatly simplifies the calculations but makes the analysis somewhat approximate. We justify this in the light of a more drastic assumption usually made in such problems, namely that the currents are purely axial as though the conductor is isolated. The so called end effects that exist in finite length conductors are ignored.

For a sinusoidal time variation of the current one may represent the rotor current density vector as $\bar{J}(r,\psi,z,t) = \sqrt{2}\,\bar{J}_{rms}(r,\psi,z)\cos(\omega t-\theta)$, where $\omega = 2\pi f$. The space components of the r.m.s. vector $\bar{J}_{rms}$ are J_r, J_ψ and J_z, which are themselves r.m.s. quantities. The current being assumed axial, hence, $J_r = 0$, $J_\psi = 0$ and $\partial J_z/\partial z = 0$ everywhere. Consider a whole composite cylinder, with a solid inner core of the p.m. enveloped by a stainless steel sleeve of radii b and c, where $b > c$. By symmetry consideration, $\partial J_z/\partial\psi = 0$. Then from Maxwell's equations it follows that J_z satisfies the Helmholtz equation, that is [2,3]

$$\frac{d^2J_z}{dr^2} + \frac{1}{r}\frac{dJ_z}{dr} - \tau^2 J_z = 0, \text{ where } \tau^2 = j\mu\sigma\omega,\ j = \sqrt{-1},\ \mu \text{ and}$$

σ are the relative permeability and conductivity of the material. This is a modified Bessel equation of order zero. Its general solution may be expressed as:

$$J_z(r) = A\ I_o(\tau r) + B\ K_o(\tau r), \tag{1}$$

where I_o and K_o are the modified Bessel functions of the first and second kinds, both of order zero, and A and B are constants (see references [3] and [5]).

The r.m.s. electric and magnetic fields satisfy the relations: curl $\bar{E}_{rms} = -j\mu\omega\bar{H}_{rms}$ and $\bar{E}_{rms} = \bar{J}_{rms}/\sigma$. The current being axial, the only non-zero components of $\bar{E}_{rms}$ and $\bar{H}_{rms}$ are E_z and H_ψ. These relations then yield the following:

$$-j\mu\omega H_\psi = -\frac{\partial E_z}{\partial r} = \frac{-1}{\sigma}\frac{\partial J_z}{\partial r} = \frac{-\tau}{\sigma}\left(A\ I_o'(\tau r) + B\ K_o'(\tau r)\right)$$

hence, one can write

$$H_\psi(r) = \frac{1}{\tau}\left(A\ I_1(\tau r) - B\ K_1(\tau r)\right), \tag{2}$$

since $I_o' = I_1$ and $K_o' = -K_1$, where I_1 and K_1 are the modified Bessel functions of the first and second kind, both of order one [3]. Except for these functions, the subscript 1 will denote quantities for the sleeve while subscript 2 will denote those for the p.m. It is assumed that the rotor surface r.m.s. current density J_s is known.

Applying eq. (1) to the p.m., and letting B = o, since $K_o(\tau r)\to\infty$ as $r\to o$, at r = c let J_{s1} and J_{s2} be the r.m.s. current densities in the sleeve and the p.m., respectively. Then $J_{z2}(r) = A(I_o(\tau_2 r))$ where $A = J_{s2}/I_o(\tau_2 c)$ and $\tau_2 = (j\mu 2\sigma 2\omega)^{\frac{1}{2}}$. Accordingly, from equation (2) we obtain the field on the surface of the p.m. as

$$H_{\psi 2}(c) = J_{s2}\ C_2, \tag{3}$$

where $$C_2 = I_1(\tau_2 c)/(\tau_2 I_o(\tau_2 c)) \tag{4}$$

The power loss for length ℓ of the p.m. is given by:

$$P_2 = \int_o^c \left|J_{z2}\right|^2 \frac{2\pi\ell r}{\sigma_2}\,dr.$$

One obtains the following result [3]:

$$P_2 = \left|J_{s2}\right|^2 \frac{1}{\sigma_2} \text{ Real } (C_2)\ 2\pi c\ell. \tag{5}$$

At the common boundary the continuity of the electric and magnetic fields yields the relations: $E_{z1}(c) = E_{z2}(c)$ and $H_{\psi 1}(c) = H_{\psi 2}(c)$. By Ohm's law the former becomes $J_{s1}/\sigma_1 = J_{s2}/\sigma_2$, while by use of equation (3) the latter condition yields $H_{\psi 1}(c) = J_{s2}C_2$. Using these values for the sleeve in equations (1) and (2), one obtains:

$$A = J_{s_1}\left(K_1(\tau_1 c) + \tau_1\frac{\sigma_2}{\sigma_1}C_2K_o(\tau_1 c)\right)/F(c,c),$$

$$B = J_{s_1}\left(I_1(\tau_1 c) - \tau_1\frac{\sigma_2}{\sigma_1}C_2I_o(\tau_1 c)\right)/F(c,c),$$

where the denominator is defined by the function: $F(x,y) = I_1(\tau_1 x)K_o(\tau_1 y) + K_1(\tau_1 x)I_o(\tau_1 y)$.

From equation (1), one obtains for r = b,

$$J_s = J_{z_1}(b) = J_{s_1}C_1 = J_{s_2}\frac{\sigma_1}{\sigma_2}C_1, \tag{6}$$

$$\text{where } C_1 = \left(F(c,b) + \frac{\sigma_2}{\sigma_1}C_2G_o\right)/F(c,c), \tag{7}$$

$$\text{with } G_0 = \tau_1\left(K_o(\tau_1 c)I_o(\tau_1 b) - I_o(\tau_1 c)K_o(\tau_1 b)\right). \tag{8}$$

From equations (2) and (6) one obtains:

$$H_{\psi 1}(b) = J_sC_c, \tag{9}$$

$$\text{where } C_c = \left(G_1 + \frac{\sigma_2}{\sigma_1}C_2F(b,c)\right)/\left(C_1F(c,c)\right), \tag{10}$$

$$\text{with } G_1 = \frac{1}{\tau_1}\left(I_1(\tau_1 b)K_1(\tau_1 c) - K_1(\tau_1 b)I_1(\tau_1 c)\right) \tag{11}$$

The power loss in the sleeve may be found in the same manner as in the p.m. However, to avoid solving many integrals in this case, we use the fact that the total dissipative loss per unit length in the composite system is the real part of the product of the conjugate of the total r.m.s. current I in the composite conductor. and the r.m.s. voltage drop per unit length [3]. The latter being the same throughout the conductor as the surface value which is J_s/σ_1. Now by Ampere's law

$$I = H_{\psi 1}(b)\ 2\pi b = J_sC_c2\pi b. \tag{12}$$

Hence the total loss in length ℓ of the composite conductor is

$$P = \left|J_s\right|^2 \frac{1}{\sigma_1} \text{ Real } (C_c)2\pi b\ell. \tag{13}$$

The loss formula for the p.m., equation (5), can be written in terms of J_s as

$$P_2 = \left|J_s\right|^2\left(\frac{\sigma_2}{|C_1|^2\sigma_1^2}\right)\left(\text{Real } (C_2)\right)2\pi c\ell. \tag{14}$$

Therefore, the power loss for length ℓ of the sleeve is

$$P_1 = P - P_2,$$

$$\text{or } P_1 = \left|J_s\right|^2\frac{1}{\sigma_1}\text{ Real }\left(C_c - \frac{C_2}{|C_1|^2}\frac{\sigma_2}{\sigma_1}\frac{c}{b}\right)2\pi b\ell. \tag{15}$$

If the system consists of the sleeve only, the loss is still given by equation (15) or equation (13) after substituting $\sigma_2 = 0$. This makes $P_2 = 0$, and

$$C_c = G_1/F(c,b). \tag{16}$$

PRECEDING PAGE BLANK NOT FILMED 363 → 364

Omitting the factor $2\pi b\ell$ or $2\pi c\ell$ in the loss formulas one can evaluate the loss per unit surface area of the sleeve and the p.m. Integrating these losses over the total area of these members we obtain an estimate for the loss in these members for the given system configuration.

When evaluating C_c and the other constants of Bessel functions with complex arguments involving τ are encountered. These functions are then themselves complex, and are expressible as shown in equations (17) below in terms of Kelvin's functions which are well tabulated [3,5].

$$I_n(j^{1/2}x) = j^{-n}(\mathrm{ber}_n x + j\ \mathrm{bei}_n x), \tag{17a}$$

$$K_n(j^{1/2}x) = j^{n}(\mathrm{ker}_n x + j\ \mathrm{kei}_n x). \tag{17b}$$

The loss formulas stated above require a knowledge of the rotor surface r.m.s. current density J_s, which we now proceed to determine. Further details are in Ref. [6].

TANGENTIAL FIELD ON ROTOR SURFACE DUE TO STATOR CURRENT

Figure (3) shows a portion of the stator current sheet idealized as a thin layer of conductors, and also the m.m.f. and current sheet space relationship. Consider the loop 1-2-3-4-1 of tangential width, W, and negligible radial height, with the side 3-4 lying very close to the rotor surface (r=b). From Ampere's law we have the approximate relationship:

$H_{\psi 1}(b)\ .\ 2W$ = r.m.s. current enclosed by the loop.

Let A and A_m represent the r.m.s. value and the amplitude of the stator current sheet in amperes per unit circumferential length. Then the right hand side of the previous equation has the value AW. Hence $H_{\psi 1}(b) = A/2$. Combining this with equation (9) and noting that $A = A_m/\sqrt{2}$ we obtain

$$\left|J_s\right| = A_m/(2\sqrt{2}\left|C_c\right|). \tag{18}$$

If F_m is the amplitude of the stator fundamental m.m.f. wave, a quantity that is known from the motor design details, then from basic theory and with reference to Figure (3), one has the relationship:

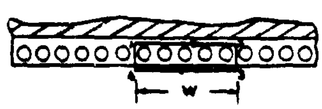

Idealized stator current sheet

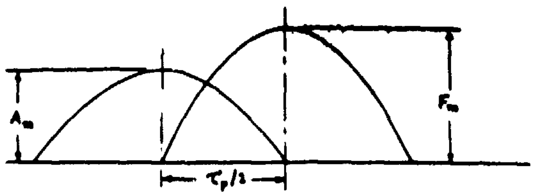

Figure (3). Stator Current Sheet and M.M.F. Waveform Relationship.

$$F_m = \frac{2}{\pi} A_m \times \frac{\text{pole pitch}}{2}$$

If the stator bore is of radius a, then the pole pitch = $\pi a/p$, where p is the number of pole-pairs.

$$A_m = F_m\, p/a . \tag{19}$$

This value of A_m cannot be used directly in equation (18). This is because as seen by a rotor point, the excitation function will be in general a discontinuous periodic sinusoid, as will be explained below. However, this function can be resolved into harmonic components using the above value of A_m. Each harmonic amplitude can then be substituted for A_m in equation (18) to obtain J_s corresponding to that harmonic. The losses are then found by applying the loss formulas to each harmonic.

HARMONICS OF STATOR EXCITATION FUNCTION

We shall consider only the fundamental component of the stator m.m.f. and ignore the effect of the space harmonics of the latter. To simplify the analysis we will regard the fundamental to be centered on the polar (direct) axis even though it is displaced for the latter, when on load, by the load angle. Now, different points on the rotor surface will be swept by different 60 degree bands of the stator m.m.f. wave during a switching operation. This is because the portion of the stator m.m.f. wave seen by a rotor point is a function of its position, which we designate by its angular distance γ from the interpolar (quadrature) axis. As seen by a rotor point the excitation function, which is the stator current sheet, will therefore have waveforms such as depicted in Figure (4) depending on its position angle γ. Clearly these waveforms possess substantial harmonic content, besides a non-zero average when $\gamma \neq 0$. These waveforms may be represented by the general formula[6].

$$A(\theta) = A_m \cos(\theta - \frac{2\pi}{3} + \gamma), \tag{20}$$

where $0 \leq \gamma \leq \pi/2$, and A_m is given by equation (19). The general waveform, which has the period $T = 2\pi/6$ can be represented by the following Fourier series:

$$A(\theta) = \frac{a_o}{2} + \sum_{n=1}^{\infty} (a_n \cos n\theta + b_n \sin n\theta), \tag{21}$$

$$\text{where } a_n = \frac{2}{T}\int_0^T A(\theta)\cos\left(\frac{2\pi n\theta}{T}\right)d\theta,\ n = 0,1,2,\ldots,\infty.$$

$$\text{Also, } b_n = \frac{2}{T}\int_0^T A(\theta)\sin\left(\frac{2\pi n\theta}{T}\right)d\theta,\ n = 1,2,\ldots,\infty.$$

Substituting for $A(\theta)$ from equation (20) and solving these integrals, one obtains for the harmonic amplitudes the following results, in which $K1_n = (6n-1)\pi/3$, $K2_n = (6n+1)\pi/3$, and $\phi = 2\pi/3 - \gamma$:

$$a_n = A_m(\alpha 1_n + \alpha 2_n), \tag{22}$$

$$\text{and}\quad b_n = A_m(\beta 1_n + \beta 2_n), \tag{23}$$

$$\text{where } \alpha 1_n = \left[\sin(K1_n + \phi) - \sin\phi\right]/K1_n$$

$$\alpha 2_n = \left[\sin(K2_n - \phi) + \sin\phi\right]/K2_n,$$

$$\beta 1_n = \left[\cos\phi - \cos(K1_n + \phi)\right]/K1_n,$$

$$\beta 2_n = \left[\cos\phi - \cos(K2_n - \phi)\right]/K2_n,$$

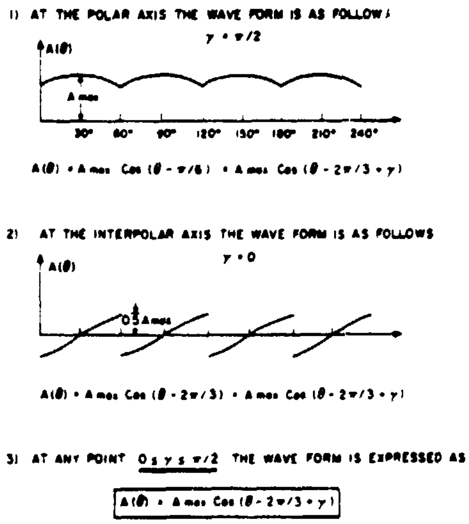

Figure (4). Waveforms of Stator Excitation Currents.

PROCEDURE FOR CALCULATING POWER LOSS

The loss at a rotor point is clearly a function of its position angle γ. A closed form solution that aims at integrating the power loss per unit area over the range of γ is not practicable, partly because of the varying geometry of the rotor. As such one has to resort to numerical integration. For this, the range of γ is divided into a number of small intervals, and the loss for each interval is calculated based upon the value of γ for its mid-point. The procedure is outlined below [6].

Step: 1 Obtain value of F_m and other motor particulars from motor design sheet.

Step: 2 Calculate value of A_m from equation (19).

Step: 3 Calculate the fundamental frequency in hertz from $f = 6p \times$ R.P.M./60, where p is the number of pole-pairs and R.P.M. is the rotor speed in revolutions per minute. The factor 6 is for the number of switching operations per cycle.

Step: 4 Divide the region between the quadrature and direct axes into a number of small intervals. Assign position angle values γ_1, γ_2, γ_3, ... to the mid-points of these intervals. Convert mechanical degrees into electrical radians by multiplying the former by $p\pi/180$.

Step: 5 Starting with $\gamma = \gamma_1$, determine the excitation function harmonic amplitudes using equations (22) and (23).

Step: 6 Set n = 1 to begin with the fundamental.

Step: 7 Find value of C_c from equation (10) corresponding to the harmonic frequency nf. Where only the sleeve exists set $\sigma_2 = 0$, or obtain C_c from equation (16).

Step: 8 Assign value of harmonic amplitude to A_m in equation (18), and calculate $|J_s|$ corresponding to this harmonic.

Step: 9 Evaluate losses for this harmonic in the composite system, the p.m., and the sleeve using equations (13), (14) and (15). The factor 2π in these equations must now be replaced by the angular width $\Delta\gamma$ of the interval. Multiply the losses obtained by 4p; this is because γ varies over a range of $\pi/2$ rather than 2π radians, and as there are p pole-pairs.

Step:10 Increment n by unity, and repeat steps 7 through 10 until all harmonics found significant have been considered.

Step:11 Repeat steps 6 through 10 for all other interval angles, namely γ_2, γ_3, ..., and add up the harmonic loss components.

SUMMARY OF RESULTS

The foregoing procedure was applied in the case of a 15 hp, 120 volt brushless d.c. motor, the relevant details of which are stated in Appendix (A).

A computer program was written to evaluate the losses. Tables of the Kelvin functions in equation (17) were stored in arrays, and interpolation was done by cubic splines. The results obtained are summarized below for two speeds and three different currents, while the variation of the losses with the position angle γ, at one particular speed and current, is depicted in Figure (5). Further results can be found in Reference [6].

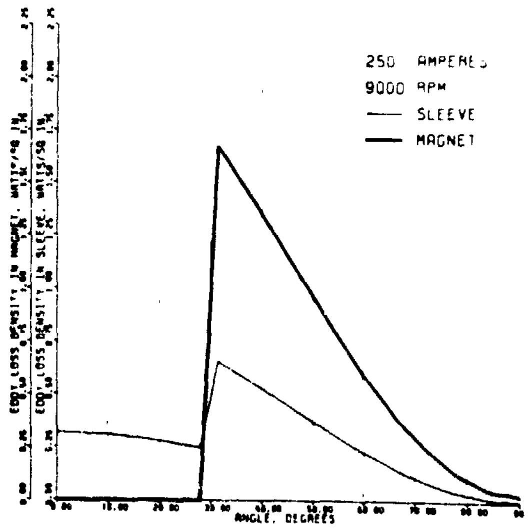

Figure (5). Eddy Current Loss Densities at Different Position Angles for 9000 r.p.m., 250A.

Speed, r.p.m.	Current A	Loss in sleeve, W	Loss in p.m., W	Total loss, W
9000	250*	15.6	25.9	41.5
9000	180	8.1	13.4	21.5
9000	110	3.0	5.0	8.0
4500	250*	9.2	18.6	27.8
4500	180	4.8	9.7	14.5
4500	110	1.8	3.6	5.4

*This corresponds to about a 35 hp peak rating (for one minute operation)

CONCLUSIONS

The main conclusions can be summarized in the following points:

1. The rotor losses are significantly affected by the motor speed, that is, by the frequency of switching operations, and vary as the square of the current, as is to be expected.
2. The loss in the permanent magnets is about two

thirds of the total losses in the rotor of this machine.

3. As several simplifying assumptions were made in the theory, such as treating J_2 as a function of the depth (r) only, ignoring the end effects, etc., the loss values obtained must be regarded as the least rotor losses to be expected.
4. The rotor losses considered here are those due to the tangential field excitation. Those due to the radial field are excluded here because their calculation is part of the design routine and because their magnitude is relatively very small in machines with semi-closed slots and large air gaps, as was confirmed by actual calculation in this case.

REFERENCES

[1] N. A. Demerdash, F. C. Lee, T. W. Nehl, and B. P. Overton, "A brushless d.c. motor-power conditioner unit designed and built for propulsion of electric passenger vehicles - Phase 1" in Proc. Int. 1980 Elec. Veh. Expo. & Conf., St. Louis, MO, May 20-22, 1980.

[2] P. Moon and D. E. Spencer, Foundations of Electrodynamics, Boston Tech. Publ., 1965, pp. 138-144.

[3] N. W. McLachlan, Bessel Functions for Engineers, Oxford Univ. Press, 1941, pp. 134-141.

[4] R. L. Stoll, The Analysis of Eddy Currents, Clarendon Press, 1974, p. 10.

[5] Abramowitz, M. and Stegun, I.A., Editors "Handbook of Mathematical Functions with Formulas, Graphs, and Mathematical Tables," U. S. Department of Commerce, National Bureau of Standards Applied Mathematics Series. 55, November 1970.

[6] A. K. Nagarkatti, "Study of Performance and Certain Special Aspects of Electronically Commutated Brushless D.C. Motor for Electric Vehicles", M.S. Thesis, Department of Electrical Engineering, Virginia Polytechnic Institute and State University, May, 1980.

Acknowledgements

This investigation was part of a larger project[1] funded by NASA(Lewis)/DOE under NASA Contract DEN3-65 in DOE's program of research on electric vehicle technology. The authors are grateful to all their colleagues in this project for their contributions, in particular to Dr. R. J. Churchill, Vice-President, and Mr. B. P. Overton, both of The R and D Center, Industrial Drives Division, Kollmorgen Corporation, for participating in fruitful discussions and supplying the necessary data.

APPENDIX (A)

Number of pole-pairs, p = 2
Length of rotor core, ℓ = 6 in. (15.24cm)
Stator bore radius, a = 1.531 in. (3.89cm)
For stainless steel sleeve:
- Outer radius, b = 1.505 in. (3.82cm)
- Inner radius, c = 1.470 in. (3.73cm)
- Resistivity, $1/\sigma_1 = 28.35 \times 10^{-6}$ Ohm-in. (7.2×10^{-7} Ohm-meter)
- Permeability, μ_1 = 3.10 lines/Amp.in (12.2×10^{-7} $\frac{\text{henery}}{\text{meter}}$)

For permanent magnets:
- Width of pole, w = 1.44 in. (3.657cm)
- Resistivity, $1/\sigma_2 = 19.60 \times 10^{-6}$ Ohm-in. (4.978×10^{-7} Ohm-meter)
- Permeability, μ_2 = 3.19 lines/Amp.in (12.566×10^{-7} $\frac{\text{henery}}{\text{meter}}$)

Ampere-turns per pole, F_m = 3.92 per Ampere.

Further details on this motor can be found in reference [1].

ASHOK A. NAGARKATTI was born June 30, 1934 in Bangalore, India. Graduated with degrees in mathematics and physics in 1953 from Nagpur University, and in electrical power engineering in 1957 from Birla Inst. of Technology and Science both in India and an M.S.E.E. from Virginia Polytechnic Institute and State University in May, 1980. Worked 5 years with GEC (England) as apprentice/junior engineer, 5 years with Heavy Electricals (India) as motor designer, and 10 years with Kirloskar Electric in Bangalore responsible for design and development of large high voltage motors.

OSAMA A. MOHAMMED was born on November 29, 1953 in Cairo, Egypt. He received a B.Sc. in Electrical Engineering from the Faculty of Engineering, Zagazig University at Shaubra, Cairo with first class distinction and honors in June 1977. Since that time he served as a demonstrator of electrical engineering in his faculty until December 1978. In January 1979, he joined the graduate program at the Electrical Engineering Department, Virginia Polytechnic Institute and State University, Blacksburg, Virginia, as a graduate research assistant. He received the M.S. degree in electrical engineering in September 1980 and is working towards his Ph.D. degree. His current interests involve numerical techniques of analysis of electromagnetic fields in electrical devices.

Mr. Mohammed is a student member of the Institute of Electrical and Electronics Engineers.

NABEEL A. DEMERDASH (M'65 - SM'74) was born in Cairo, Egypt, on April 26, 1943. He received the B.Sc. E.E. degree with distinction and first class honors from Cairo University, Egypt, in 1964 and the M.S. and Ph.D. degrees in Electrical Engineering from the University of Pittsburgh, Pittsburgh, Pennsylvania, in 1967 and 1971, respectively.

From 1964 to 1966 he was with the Faculty of Engineering, Cairo University as a Demonstrator. From 1966 to 1968 he was with the Department of Electrical Engineering, University of Pittsburgh, as a Graduate Teaching Assistant. In 1968 he joined the Large Rotating Apparatus Division of Westinghouse Electric Corporation, East Pittsburgh, Pennsylvania, as a Development Engineer, where he worked on Electromagnetic Field Modeling in Rotating Machinery and the development of the asymmetrical rotor for large steam turbine-driven generators. Since 1972 Dr. Demerdash has been with the Virginia Polytechnic Institute and State University, Blacksburg, VA, where he is presently a Professor in the Department of Electrical Engineering.

Dr. Demerdash is a Senior Member of IEEE and is currently serving as a member of the Rotating Machinery Committee of PES, IEEE, as well as the Synchronous Machinery and the Machine Theory Subcommittees of PES, IEEE. He previously served as secretary and subsequently vice chairman of the Synchronous Machines Subcommittee of PES, IEEE. Dr. Demerdash is a past Chairman of the Virginia Mountain Section of IEEE. He is a member of ASEE, Sigma Xi and Eta Kappa Nu. Dr. Demerdash is the author and co-author of numerous papers in various IEEE Transactions. Dr. Demerdash's current interests and research activities include Electromechanical Propulsion and Acutation, Dynamic Modeling of Solid State Controlled and Operated Electrical Machines, Numerical Analysis of Electromagnetic Fields in Electric Machinery, as well as Machine-Power System Dynamics.

Discussions

John A. Mallick (General Electric Company, Schenectady, NY): The authors of this paper have attempted to calculate the eddy current losses in the permanent magnet and support pieces of an electronically commutated motor, but this discusser is not convinced of the validity of their modelling and calculation procedure.

First of all, the authors mention that the losses calculated here are due only to the tangential component of the magnetic field of the stator winding; this is not true, since the radial and tangential field components are connected via Gauss' law for magnetic fields. Given their model of a machine with an infinitesimal air gap between the outer shell and the stator current sheet, their use of the tangential magnetic field as an outer boundary condition is proper; however, this model will then account for *all* of the losses due to that current sheet excitation, not just those due to the tangential field.

The authors have chosen a model in which the field quantities are independent to the angle ψ; a much more realistic model could have included the angular variation at very little increase in complexity, since only the space fundamental is used. Why have the authors chosen such a model as they did?

The determination of $h_{\psi l}$ (b) in the paragraph preceding equation 18 is in error. The authors' model uses a current sheet backed by stator iron which presumably has a permeability much greater than that of free space; therefore, H_ψ will exist only on the air gap side of the current sheet, being near zero parallel to the iron surface. Thus equation 18 should be multiplied by a factor of 2 to account for the change in the line integral of H_ψ. The calculated losses will increase by a factor of 4.

The authors do not indicate how many harmonics were used in evaluation of the loss formula presented. Using the data given in Appendix A, one can calculate a classical skin depth for the fundamental at 9000 RPM to be on the order of 0.5 inches, with higher order skin depths varying . . $^{-1/2}$. This skin depth is large compared to the sleeve thickness, so it seems to this discusser that using Bessel functions to calculate the current there to be somewhat of an overkill; a simpler approach would give comparable accuracy.

Manuscript received February 26, 1982.

A. K. Nagarkatti, O. A. Mohammed and N. A. Demerdash: These authors wish to thank Dr. J. A. Mallick for his interest in the paper, and offer the following clarifications and comments in response to the various points raised in Dr. Mallick's discussion:

1) The authors wish to reemphasize what was already stated in the paper, namely that the calculation method given in this paper is presented only as an approximation to the eddy current losses in the metalic sleeves of such machines. There is experimental evidence based on measured rotational losses at no-load and load conditions in the motor at hand, which demonstrates the validity of the results obtained by this approximate calculation method. This evidence is given in the Table below, in which the rotational losses are given for the 15hp motor at hand under no load as well as at rated load operating conditions:

Measured Rotational Losses at 7800 R.P.M.

Rotational Losses at No-Load	Rotational Losses at Rated Load, at a Current = 134 Amps dc line
490 Watts	520 Watts

This table reveals that an increase in the value of rotational loss of only 30 Watts took place at a load of 134 Amps of line current (slightly above rated), in comparison with the no-load rotational loss. This increase is attributed to the additional sleeve and magnet losses at load as well as changes in the core losses resulting from the existence of an armature mmf under load. Our calculation as shown in the paper predicts a sleeve and magnet loss greater than 8 Watts and less than 21.5 Watts according to the loss table given in the paper. This range lies within the total increase in rotational losses of 30 Watts mentioned above, which includes the aforementioned increase in the core losses as well as the sleeve and magnet eddy current losses subject of this paper. Therefore, it seems that despite the assumptions made in the analysis, the resulting calculated loss values are within the bounds obtained from the experimental data, and hence the method represents a reasonable approach.

2) We wish to emphasize that our statement that "only losses due to the tangential component of the stator magnetic field are considered here" meant that we are not including the flux density pulsations (ripples) due to the tooth-slot effect as the sleeve and magnet rotate continuously past the slotted stator. This pulsation which results from the variation in, the radial magnetic reluctance from tooth to slot experienced by every portion of the sleeve and magnet is not accounted for here. Also, the one dimensional nature of our formulation, which is acceptable in many similar applications, tends to ignore the largely two dimensional nature (tangential and radial) of the stator field effects on the axially induced eddy currents. We do not believe that any magnetic field laws were violated, subject to the stated assumptions.

3) We disagree with Dr. Mallick's statement that "the authors have chosen a model in which the field quantities are independent to the angle, ψ". Indeed the excitation function along the outer sleeve boundary with the airgap is a complicated function of the angular position along the sleeve as shown in Figure (4) of the paper and explained in the section on "HARMONICS OF STATOR EXCITATION FUNCTION".

Dr. Mallick states that "a much more realistic model could have included the angular variation at very little increase in complexity, since only the space fundamental is used". We wish to emphasize that this analysis indeed allows for the angular variation in the tangential excitation function, and not only considers the fundamental component of excitation at every discretized point on the sleeve, but also its harmonic components, again as given in equations (21) through (23), and as subsequently explained in the algorithm.

4) We do not agree with Dr. Mallick's suggestion that the excitation function in equation (18) should be multiplied by a factor of two. This is because of the fact that closer examination of the magnetic field lines linking the stator conductors (which are the source of excitation) reveals that these lines have to cross teeth and slots, in much the same manner as the leakage flux path.

Because of the large slot to tooth width in the conductor region, it is not an unreasonable assumption to take the return field path shown in Figure (3) by line (1-2) in the loop to be effectively air. Hence, the justification arises for the statement "$H_{\psi l}$ (b)·2ω = r.m.s current enclosed by loop".

5) The authors do not agree with the suggestion made by Dr. Mallick that skin depth does not warrant the use of Bessel functions. This is because of the existance of a conducting medium below the sleeve, namely the permanent magnet, which adds a considerable conducting thickness below the sleeve. Also, it must be noticed that the frequency of the excitation function is six times that of the inverter frequency (motor speed). This is because of the nature of the excitation wave form, see Figure (4) of the paper. Thus, we believe that the 0.5 inches depth of penetration mentioned by Dr. Mallick is incorrect.

We conclude by again thanking Dr. Mallick for the opportunity given to us by his questions to illucidate the various points of potential ambiguity which he raised in his discussion.

Manuscript received June 7, 1982.

APPENDIX (10)

ON THE PERFORMANCE OF THE SAMARIUM-COBALT AND STRONTIUM-FERRITE BASED BRUSHLESS DC MACHINE-POWER CONDITIONER SYSTEMS

Demerdash, N. A., Miller, R. H., Nehl, T. W., Overton, B. P., and Ford, C. J., "Comparison Between Features and Performance of Fifteen HP Samarium Cobalt and Ferrite Brushless DC Motors Operated by Same Power Conditioner," IEEE Transactions on Power Apparatus and Systems, Vol. PAS-102.

COMPARISON BETWEEN FEATURES AND PERFORMANCE CHARACTERISTICS OF FIFTEEN HP SAMARIUM COBALT AND FERRITE BASED BRUSHLESS DC MOTORS OPERATED BY SAME POWER CONDITIONER

N. A. Demerdash, Senior Member R. H. Miller, Member T. W. Nehl, Member
Virginia Polytechnic Institute and State University
Blacksburg, Virginia

B. P. Overton, Senior Member C. J. Ford, III, Member
R and D Center, Industrial Drives Division
Kollmorgen Corporation
Radford, Virginia

Abstract - The impact of samarium-cobalt and ferrite magnet materials on the design and performance characteristics of electronically commutated brushless dc motors of equal horsepower output is presented. This is accomplished through the design, construction and testing of two 15 hp, 120 volt brushless dc motors built for propulsion of electric vehicles, and similar applications. In one of these motors, samarium-cobalt ($Sm\ Co_5$) is used as permanent magnet material, while in the other the magnets were made of strontium ferrite number 8. The two machines were built to operate from the same power conditioner, which consisted of a transistor chopper in series with a three phase full wave inverter/converter bridge, which consists of six transistor-diode switches. Both of the two motors achieved a continuous 2 hour rating of more than 15 hp with a peak one minute rating of 35 hp. System efficiency (combined motor and conditioner) under rated conditions of 90% was achieved for both machines. Details of these and other performance characteristics and design parameters are presented and analyzed to assess the impact of the choice of magnet material on design and performance for this, as well as other applications.

INTRODUCTION

Electronically commutated brushless dc motors are increasingly becoming practical for numerous industrial applications. These applications include electromechanical propulsion as well as many actuation systems. Examples of such developments can be found in the literature such as [1] through [4].

The elimination of the classical brush type commutator allows one to design such machines for operation at much higher speeds than standard brush type dc machines. Such high rated speeds lead to considerable reduction in weight and volume of these electronically commutated machines in comparison with a brush type machine of the same rated horsepower.

The use of permanent magnets as sources of excitation on the rotors of these machines leads to the elimination of rotating armatures. Accordingly, with the resulting stationary armatures in these brushless machines, considerable improvement in the thermal characteristics of such motors can be achieved for a given horsepower rating. Also, the elimination of a rotating armature leads to a number of additional winding design simplifications.

The advent of magnetically powerful samarium-cobalt type permanent magnets made it possible to design and construct such motors with increasing horsepower ratings so as to make them suitable for possible use in propulsion of electric passenger vehicles and similar applications[1-4]. Only samarium-cobalt was used in the development of brushless dc motors in these previous efforts[1-4]. However, the cost and the uncertain availability of cobalt as a strategic material have become of increasing concern to many potential users of such brushless dc motors. This was a major factor in propelling the authors to develop, build and test two brushless dc motors of the same characteristics. One was built with 18 MGO samarium-cobalt rotor magnets, while the other was built using strontium-ferrite number 8 magnets, for purposes of comparison and assessment of ferrites as substitutes for samarium-cobalt.

The two motors are rated 15 hp, at 120 volts dc line voltage, and can be operated by the same electronic power conditioner. Both motors were tested, and can safely develop a peak horsepower of 35 hp for one minute. Overall motor-conditioner efficiencies of about 90% were encountered when operating both machines. Comparison between the various design features and aspects involved in both motors, as well as the resulting performance is believed to contain several contributions to the present state of the art.

ELECTRONIC POWER CONDITIONER-MOTOR INTERACTION

It is only recently that electronically commutated brushless dc motor systems have been developed using samarium-cobalt permanent magnets and power transistors as switching elements for electronic commutation (power conditioning), see references [1] through [6]. In such a system, the machine consists of a three phase type ac armature mounted on the stator, and a rotor whose excitation is supplied by a system of permanent magnet poles. As shown in the machine-power conditioner schematic of Figure (1), the three phase armature is connected to a three phase inverter/converter (motoring/regenerative braking) bridge which contains six power transistor-diode switches, Q_1-D_1 through Q_6-D_6. The three phase inverter/converter bridge is connected to a series/shunt type two quadrant chopper for dc line current magnitude limiting and control. Since the dc line current is proportional to the motor torque, the chopper functions also as a torque controller. In this chopper, the transistor Q_M conducts during the "on" state while the diode D_M conducts during the "off" state of the chopper in the motoring mode. The transistor Q_s conducts during the "on" state while the diode D_3 conducts during the "off" state of the chopper in the regenerative braking mode. This permits motoring and regeneration when the line to line value of the motor back emf is considerably lower than the supply voltage. Both motors were designed so that at rated power and speed the chopper was continuously on to minimize switching losses. The chopper is connected to the dc supply through an input capacitor filter for ripple reduction. This conditioner permits the machine to function in a motoring state and in a regenerative braking state, which is desirable for better efficiency in electromechanical propulsion and similar applications.

The inverter transistors Q_1 through Q_6 are switched "on" and "off" by control signals generated by a Hall-effect rotor position sensor (rps). In this work, the rps effectively consisted of two sets of three Hall devices displaced from each other by 30° electrical.

82 WM 241-8 A paper recommended and approved by the IEEE Rotating Machinery Committee of the IEEE Power Engineering Society for presentation at the IEEE PES 1982 Winter Meeting, New York, New York, January 31-February 5, 1982. Manuscript submitted September 14, 1981; made available for printing November 18, 1981.

0018-9510/83/0001-0104$01.00 © 1983 IEEE

This is to enable one to use a normal inverter transistor firing mode under rated 15 hp conditions and an advanced inverter transistor firing mode for peak power of 35 hp. Technical aspects of the need for advanced firing are discussed later on in this paper.

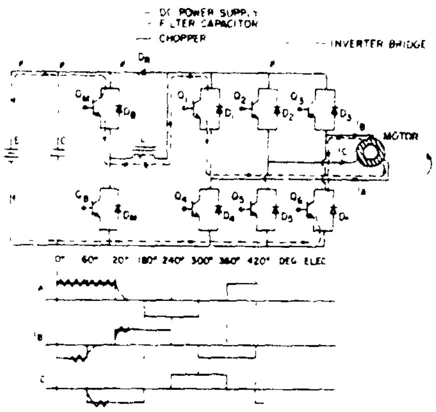

Figure (1) Machine-Power Conditioner Schematic and Idialized Motoring Currents

Proper sequential switching of Q_1 through Q_6 leads to a, b and c phase current wave forms such as idealized in block form in Figure (1). In this figure one can see the existance of six distinct armature current states. This establishes in the motor a stator (armature) mmf which travels in discrete jumps of 60° electrical each time switching takes place from one current state to the next. The rotor mmf (magnets) is continuously forced to follow that motion. The result is equivalent to that of a synchronous machine in which the torque angle (angle between armature and field mmfs) varies cyclically from beginning to end of each of the six armature current states between 120° and 60° electrical during normal inverter transistors' firing, and between 150° and 90° electrical for a 30° electrically advanced firing of Q_1 through Q_6, as shown in Figure (2). Shown in dotted line form for convenience in Figure (1) is the path of the current through the conditioner and machine during the first 60° electrical of the armature current cycle given in the figure

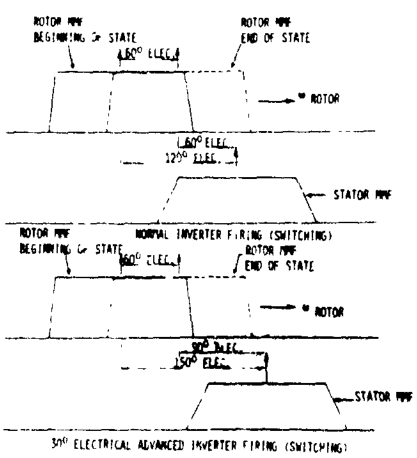

Figure (2) Internal Torque Angles for Normal and 30° Electrical of Advanced Inverter Transistor Firing, at Beginning and End of an Armature Current State

The diodes, D_1 through D_6, provide current paths during phase current commutation. They also function as a three phase full wave rectifier bridge during machine operation in the regenerative braking mode. The diodes, D_M and D_B, provide the necessary dc line current paths during the "off' periods of the transistors Q_M and Q_B in the motoring and regenerative braking modes, respectively. The function of the diode, D_R, is to provide a return path for the current through the chopper inductor during the switching instances when the path through the inverter may be blocked momentarily. Thus it eliminates the danger of any severe (Ldi/dt) type voltage transients. Figure (3) shows the overall machine-power conditioner system and supporting instrumentation during dynamometer testing of the ferrite permanent magnet based motor.

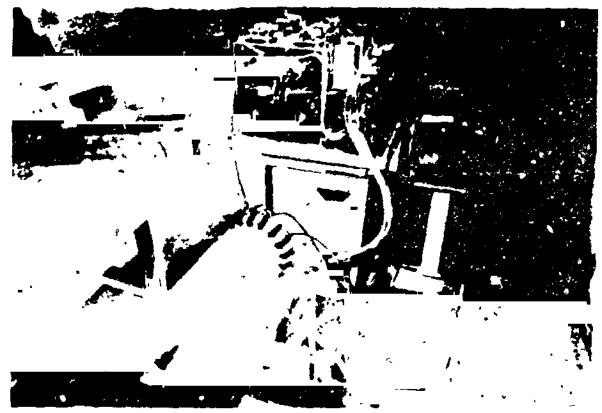

Figure (3) Motor-Power Conditioner During Dynameter Testing of the Ferrite Based Machine

IMPACT OF SYSTEM PERFORMANCE REQUIREMENTS ON ROTOR POSITION SENSOR (RPS) DESIGN

Both the ferrite based and samarium cobalt based motors developed in this work were intended for propulsionof a 1363 kg (3000 lb.) passenger vehicle. A number of stringent performance requirements had to be met. These included continuous operation for 2 hours under rated torque and speed, performance under schedule D of the SAE J227 a standard drive cycle (see reference [7] for details), as well as requirements of hill climbing of up to 10% grade, etc. Accordingly, both of these motors were required to have a 15 hp continuous (2 hours) rating and a peak 35 hp one minute rating, both at a nominal voltage of about 115 volts. The peak power requirement meant that the system must have the capability of withstanding and building up to a peak dc line current of about 300 Amperes, and sustaining this current for one minute, with the motor winding at its normal operating temperature.

However, it has been shown in two previous investigations by Nehl, et.al. [5, 6] that the system capability of build up of dc line current, for purposes of achieving peak horsepower output at rated voltage, is heavily dependent on a number of factors. These factors are: 1) winding inductance values, 2) the waveform profiles of induced back emfs in the armature phases, and 3) the time of firing of an inverter transistor switch of a given phase with respect to the back emf wave form of that phase. The third factor mentioned above is a key element in the design of a suitable rps for these motors.

It will be agreed here that when an inverter transistor is fired at the instant of zero crossing in the phase emf wave form, with a positive rate of increase of that emf with respect to time, such firing will be refered to as a 30° electrical advanced firing. Meanwhile, when such firing takes place with a delay of 30° electrical after the above mentioned zero crossing in the emf wave form, such firing will be refered to as normal (or zero° electrical advanced) firing, Figure (2).

It was found by Nehl, et. al. [5, 6] that skewing of the armature slots by one slot pitch, in addition to 30° electrical advanced inverter transistor firing is necessary to achieve the required peak horsepower rating of 35 hp at 115 volts dc line voltage. Advanced inverter transistor firing facilitates the process of dc line current buildup, because it permits the buildup process to start at a time when the phase back emf of the motor, opposing the supply voltage and flow of the dc line current, is at its lowest value. That emf is zero at the instant of start of the transistor firing. For details references [5, 6] should be consulted.

This advanced firing state has a slight adverse effect on the motor efficiency. Accordingly, it was decided to use such advanced firing only for peak power operating conditions, and use normal firing during rated operating conditions. Therefore, the rps for each of the motors at hand was designed with the equivalent of two sets of three Hall effect devices, as can be seen in Figure (4). One set of three Hall devices (normal firing) is activated during normal rated operating conditions, while the other set (30° elec. advanced firing) is activated for peak output power operation.

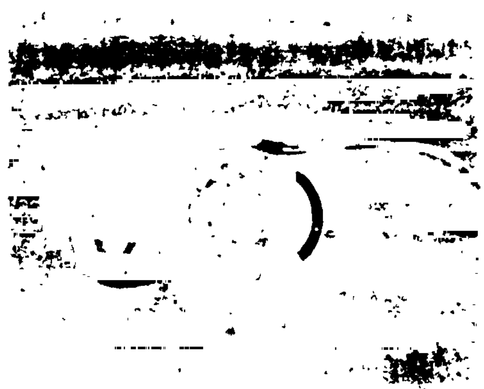

Figure (4) Rotor Position Sensor

DESIGN OF THE SAMARIUM-COBALT BASED AND FERRITE BASED MOTORS

The samarium cobalt and ferrite based motors developed in this investigation are shown in cross-section in Figures (5) and (6) respectively. Again, these motors were both designed for a continuous rating of 15 hp at 115 volts dc line voltage, with a capability for a peak one minute rating of 35 hp at the same rated voltage (the supply voltage specified could range from 90 to 120 volts). The stator core lamination stack of the samarium-cobalt based motor can be seen in Figure (7). Meanwhile, the rotor and assembled armature in its housing are given in Figure (8). The stator core lamination stack of the ferrite based motor is shown in Figure (9). The rotor and assembled armature in its housing are given in Figure (10).

Details on the various design characteristics of these two motors are given in Table (1). It should be observed that the outside core (stator laminations) diameter was 6.518 inches (16.56 cm) in both designs. Meanwhile, the stack length of the samarium-cobalt motor was 4 inches ([illegible] cm), and [illegible] the ferrite motor was 8.5 inches (21.59 cm). It is interesting to point out that the weight of the samarium-cobalt motor, about 60 lbs. (27 kg), is less than half of the weight of the ferrite motor, about 127 lbs. (57.796 kg). It is also interesting for one to compare the weight ratio of the two motors, which is about 1.0 to 2.0, to the ratio of the energy product of the particular samarium-cobalt and ferrite materials used, which is about 5.0 to 1.0.

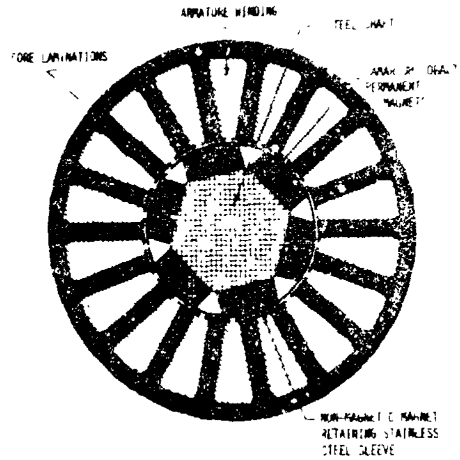

Figure (5) Cross-Section of the Samarium-Cobalt Motor-Outer Lamination Diameter = 6.518 Inches (16.556 cm)

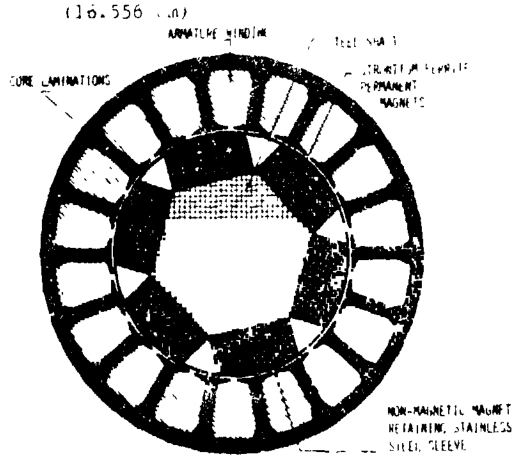

Figure (6) Cross-Section of the Ferrite Motor-Outer Lamination Diameter = 6.518 Inches (16.556 cm)

Figure (7) Stator Core of the Samarium-Cobalt Motor

Figure (8) Assembled Armature, Housing and Rotor of the Samarium-Cobalt Motor

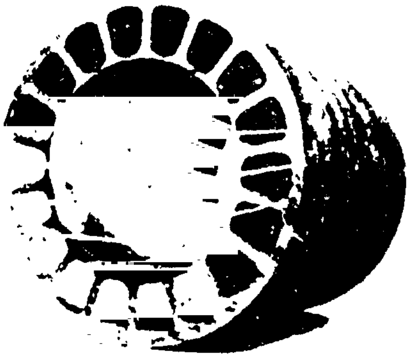

Figure (9) Stator Core of the Ferrite Motor

Figure (10) Assembled Armature, Housing and Rotor of the Ferrite Motor

Another important feature of the armature windings of both motors is the existance of two groups of coils per phase. This is to enable one to operate both machines as shown in Figure (11) with a series mode (one path per phase) or a parallel mode (two parallel paths per phase), for low speed and high (rated) speed, respectively.

These motors were designed for operation in conjunction with a two speed vehicle transmission. Accordingly, the series winding connection is intended for vehicle speeds below 15 m.p.h. (24 km.p.h.). The parallel winding connection is intended for vehicle speeds above 15 m.p.h. Above a vehicle speed of 30 m.p.h. (48 km.p.h.) the high speed transmission gear ratio is used in conjunction with the parallel winding connection.

Both machines were designed in such a manner that natural air cooling would be sufficient for normal operating conditions, in both motors T.E.N.V. enclosures were used. As will be shown later, the temperture rise of the ferrite motor was not large enough to affect the magnet strength in such a way as to adversely affect the performance.

Tabel (1) Parameters and Characteristics of the Samarium-Cobalt Based and Ferrite Based Motors From Design Calculations and Test

Parameter and Units	Samarium-Cobalt Sm Co_5 Design	Strontium Ferrite #8 Design
motor outside diameter, in. (cm)	7.88(20.02)	7.88 (20.02)
motor length, in. (cm)	13.35(33.91)	18.85 (47.88)
weight, lbs. (kg)	60.0 (27.2)	127.0 (57.6)
stator lamination outside diameter, in. (cm)	6.518(16.56)	6.518 (15.56)
stator lamination stack length, in. (cm)	4.00 (10.16)	8.50 (21.59)
stator lamination inside diameter, in. (cm)	3.062(7.78)	4.07[illegible] (10.34)
number of stator slots	18	18
number of poles	6	6
rotor (magnet str.) outside diameter, excluding sleeve, in. (cm)	2.930(7.44)	3.930 (9.98)
rotor outside diameter, including sleeve, in. (cm)	3.000(7.62)	4.000 (10.16
rotor (magnet structure) axial length, in. (cm)	3.60 (9.14)	8.75 (22.23)
magnet (radial) length (in direction of magnetization), in. (cm)	0.490(1.24)	0.740 (1.88)
magnet cross-sectional area per pole (perpendicular to flux), in.^{2}(cm^2)	3.766(24.30)	12.163(78.47)
total magnet volume (all poles), in.^{3} (cm^3)	11.072(181.4)	54.004(885.0)
total magnet weight (all poles), lbs. (kg)	3.23(1.47)	9.56(4.34)
rotor inertia constant, lb. ft. sec^2 (kg. m^2)	0.00234(0.00317)	0.01200(0.0163)

Table (1) Continued

Parameter and Units	Samarium-Cobalt Sm Co_5 Design	Strontium Ferrite #8 Design
Y-connected armature winding	yes	yes
armature winding configuration (connection)	series/parallel	series/parallel
method of harmonic reduction	skewing by one stator slot	skewing by one stator slot
maximum allowable winding temp., °c	170.0	170.0
rated input voltage (on dc side), volts	120.0	120.0
rated armature current (on dc side), amperes	125.0	125.0
rated horsepower, hp	15.0	15.0
*speed at rated horsepower, r.p.m.	*8680	*8840
*torque sensitivity at high speed armature winding connection, lb. ft./ampere (Newton Meter/ Ampere)	*0.0885(0.11999)	*(0.0992)
back emf sensitivity (constant) at peak of sine wave for high speed armature winding connection, volts/ mech. radian/sec.	0.1200	0.0993
armature winding resistance (line to line) for high speed armature connection 25°C, ohms	0.0047	0.0049
*torque sensitivity at low speed armature connection, lb. ft./ampere (Newton Meter/ ampere)	*0.1770(0.23998)	*0.1464(0.19849)
back emf sensitivity at peak of sine wave for low speed armature connection, volts/mech. radian/ sec.	0.2400	0.1986
armature winding resistance (line to line) for low speed armature connection 25°C, ohms	0.0188	0.0196
maximum r.p.m. for low speed armature connection, r.p.m.	4300	4500
maximum horsepower hp	35.0	35.0
*motor speed at maximum horsepower r.p.m.	*6900	*6750
armature current at maximum horsepower, amperes	291.6	291.6
Thermal Time Constant (minutes)	35 min.	45 min.
Steady State Top Rise Above Amb. 25°C	128°C	113°C
*Obtained from Test Measurements		

PERFORMANCE CHARACTERISTICS OF THE SAMARIUM-COBALT AND FERRITE MOTORS

The two motors were dynamometer tested under rated and peak power conditions. The corresponding performance data are given below.

Rated Power Performance Test Results

The two motors were dynamometer tested under rated conditions, using the same power conditioner described above. This test was run continuously for two hours to obtain the thermal characteristics of both motors as well as the conditioner. This is in order to ensure the ability of both units to operate continuously under rated conditions.

Typical readings of input dc line voltage, dc line current, motor speed, motor input power, motor output power, and motor as well as overall system (combined motor-conditioner) efficiences, obtained during this test, are given in Table (2) for both motors. It should be noted that these test readings are subject to normal instrumentation errors of about 2%.

Examination of the data of Table (2) reveals that both motors performed equally well, and that motor efficiencies of 97% are possible, with an attainable combined system (motor-conditioner) efficiency of about 90%. (Design calculations indicated motor efficiency of 96% for both units).

Oscillograms of machine phase current, line to neutral voltage, and line to line voltage at rated load for the samarium-cobalt motor are given in Figures (12), (13) and (14), respectively. Also, oscillograms of machine phase current, line to neutral voltage and line to line voltage at rated load are given in Figures (15), (16) and (17), respectively for the ferrite motor.

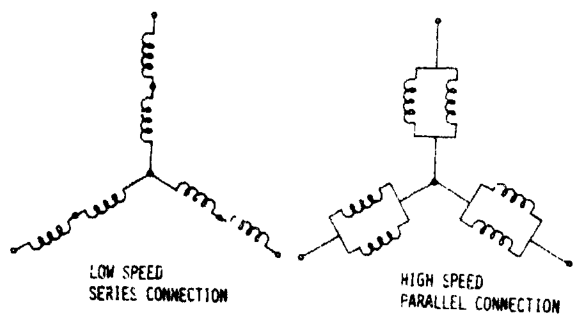

Figure (11) Schematics of Armature Winding for Low Speed and High Speed Connections

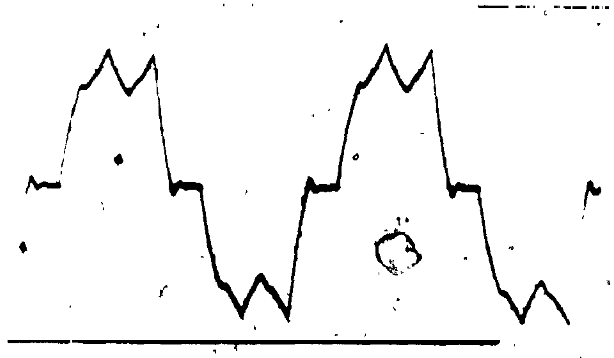

Figure (12) Phase Current Oscillogram of the Samarium-Cobalt Motor Under Rated Load (Ordinate = 80.4 Amperes/div., Abscissa = 0.5 m sec/div.)

Table (2) Performance of the Samarium-Cobalt and Ferrite Motors at Rated Conditions

Performance Quantity / Motor	Armature Connection	DC Line Voltage (Volts	DC Line Current (Amps	Motor Speed (RPM)	Motor Input (Watts	Motor Output (Watts (hp)	Motor Efficiency (%)	Overall System Efficiency (%)
Samarium-Cobalt Motor	Parallel	116.0	110.2	8680	11672.7	11341.7/15.2	97.16	88.72
Ferrite Motor	Parallel	115.6	107.3	8840	11648.0	11299.7/15.1	97.00	91.18

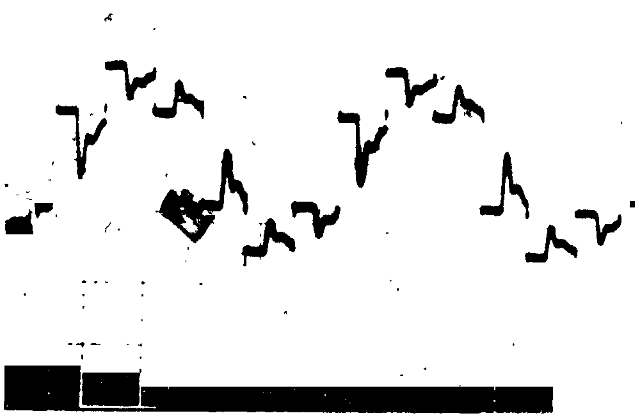

Figure (13) Line to Neutral Voltage Oscillogram of the Samarium-Cobalt Motor Under Rated Load (Ordinate = 50 Volts/div., Abscissa = 0.5 m sec./div.)

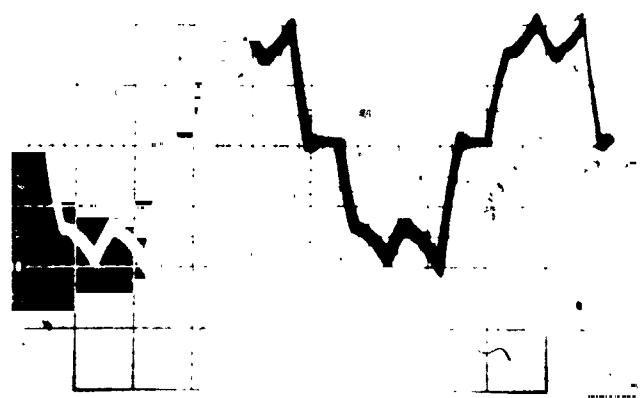

Figure (15) Phase Current Oscillogram of Ferrite Motor Under Rated Load (Ordinate = 80.5 Amperes/div., Abscissa = 0.5 m sec./div.)

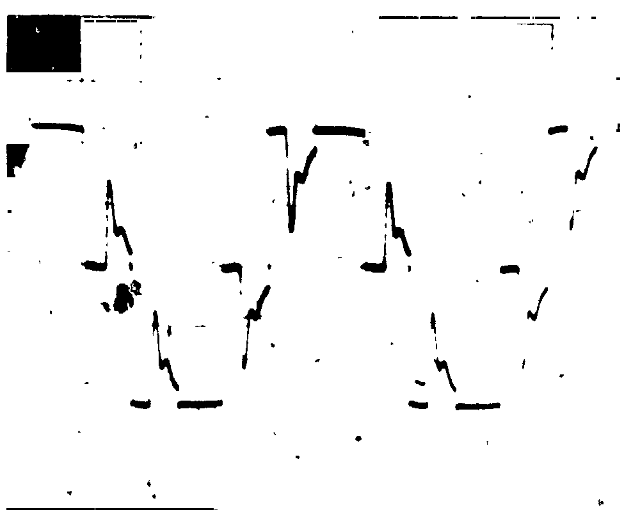

Figure (14) Line to Line Voltage Oscillogram of the Samarium-Cobalt Motor Under Rated Load (Ordinate = 50 Volts/div., Abscissa = 0.5 m sec./div.)

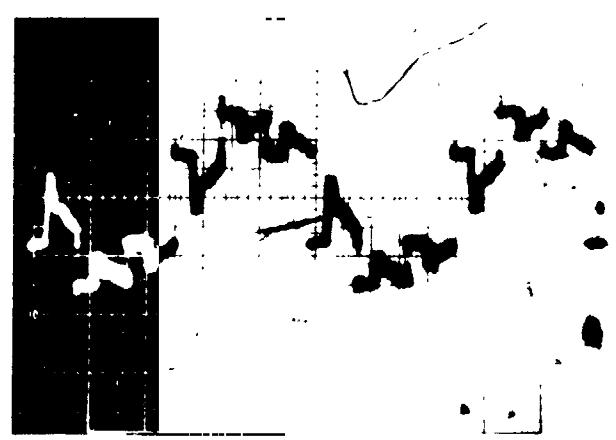

Figure (16) Line to Neutral Voltage Oscillogram of the Ferrite Motor Under Rated Load (Ordinate = 50 Volts/div., Abscissa = 0.5 m sec./div.)

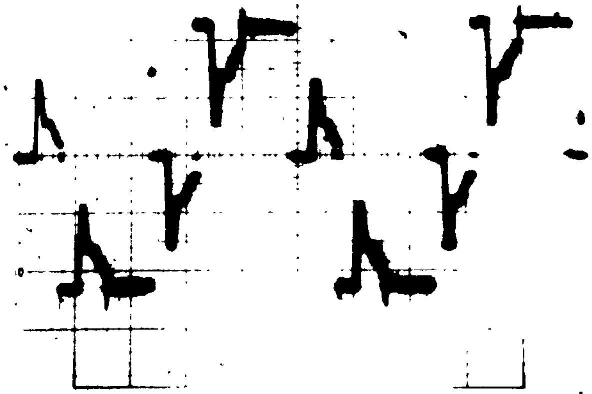

Figure (17) Line to Line Voltage Oscillogram of the Ferrite Motor Under Rated Load (Ordinate = 50 Volts/div., Abscissa = 0.5 m sec./div.)

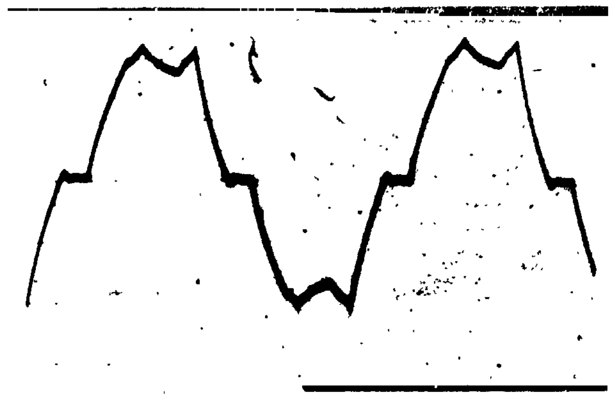

Figure (18) Phase Current Oscillogram of the Samarium-Cobalt Motor Under Peak Load (Ordinate = 201 Amperes/div., Abscissa = 0.5 m sec./div.)

Peak Power Performance Test Results

The two motors were dynamometer tested under peak load contitions of more than 35.0 hp for more than one minute each. This test is supposed to ascertain the ability of the motor and conditioner to deliver high values of output power for short periods of time, for purposes of acceleration and other overload conditions.

Readings of input dc line voltage, dc line current, motor speed, motor output power, and overall system (motor-conditioner) efficiencies, obtained during peak power dynamometer testing, are given in Table (3) for both motors. Noise problems were encountered in the digital instrument reading the motor input power. Therefore, this power and the isolated motor efficiency are not available in this data.

It should be pointed out that it was necessary to advance fire the inverter transistors by 30° electrical in order to achieve the dc line current build up necessary to attain a peak motor output power of 35 hp, for both motors with a terminal dc voltage of about 120 volts or less.

Examination of the test data in Table (3) reveals that both motors performed well, with a somewhat higher overall system efficiency for the samarium-cobalt motor under peak power conditions. It is worth mentioning that peak powers of more than 42 hp have been reached by these motors at a dc line voltage of 150 volts.

Oscillograms of machine phase current, line to neutral voltage, and line to line voltage at peak load conditions are given in Figures (18) through (23), for the samarium-cobalt and ferrite motors, respectively.

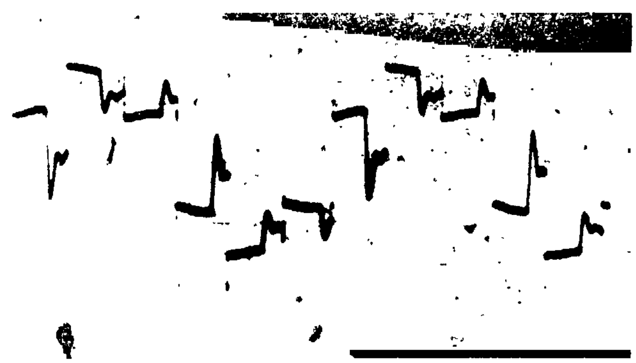

Figure (19) Line to Neutral Voltage Oscillogram of the Samarium-Cobalt Motor Under Peak Load (Ordinate = 50 Volts/div., Abscissa = 0.5 m sec./div.)

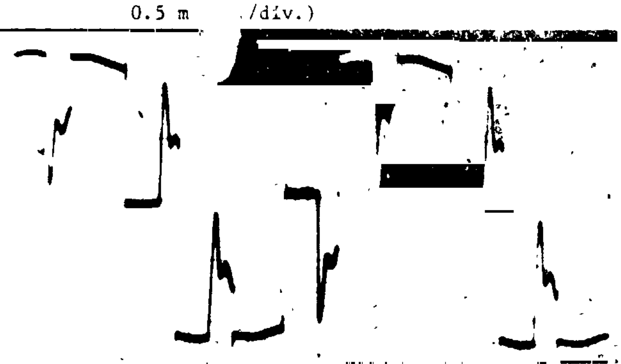

Figure (20) Line to Line Voltage Oscillogram of the Samarium-Cobalt Motor Under Peak Load (Ordinate = 50 Volts/div., Abscissa = 0.5 m sec./div.)

Table (3) Performance of the Samarium-Cobalt and Ferrite Motors at Peak Power of 35 HP

Performance Quantity / Motor	Armature Connection	DC Line Voltage (Volts)	DC Line Current (Amps)	Motor Speed (RPM)	Motor Input (Watts)	Motor Output (Watts)/(hp)	Motor Efficiency (%)	Overall System (%)
Samarium-Cobalt Motor	Parallel	115.0	287.5	6900	*	26184.6/35.1	**	79.2
Ferrite Motor	Parallel	120.9	297.6	6750	*	26632.2/35.7	**	74.0

* Motor Input Power Reading Was Not Obtained

** Could Not Be Calculated Because Motor Input Power Is Not Known.

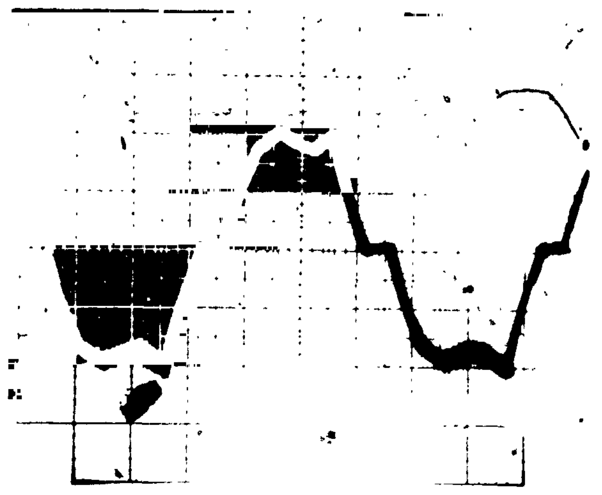

Figure (21) Phase Current Oscillogram of the Ferrite Motor Under Peak Load (Ordinate = 201 Amperes/div., Abscissa = o.5 m sec./div.)

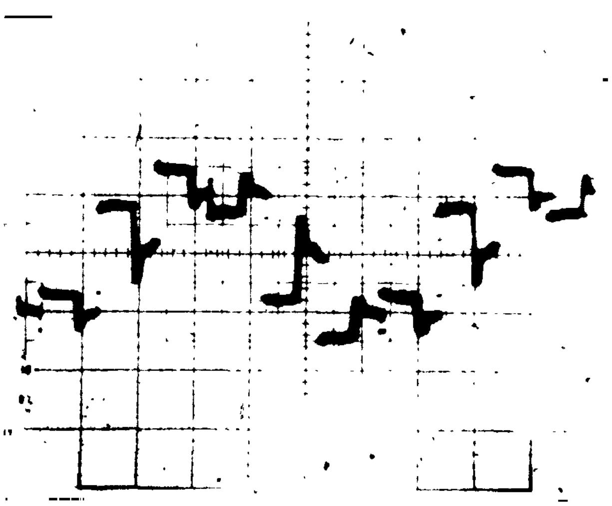

Figure (22) Line to Neutral Voltage Oscillogram of the Ferrite Motor Under Peak Load (Ordinate = 50 Volts/div., Abscissa = 0.5 m sec./div.)

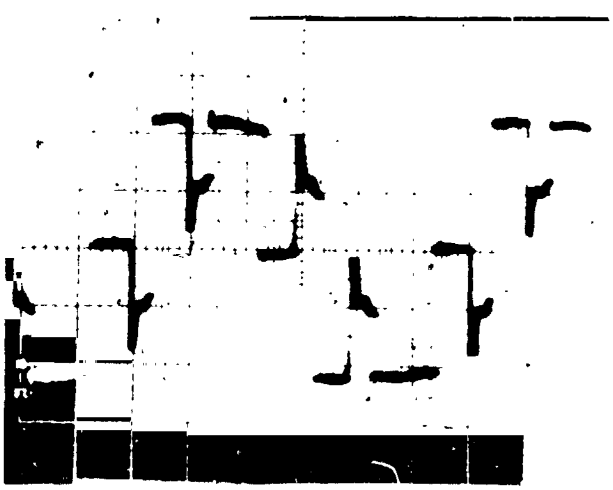

Figure (23) Line to Line Voltage Oscillogram of the Ferrite Motor Under Peak Load (Ordinate = 50 Volts/div., Abscissa = 0.5 m sec./div.)

DISCUSSION OF RESULTS

The test results given above indicate that the differences in the rated power, efficency, peak power capability as well as motor-conditioner interaction characteristics of the two machines were insignificant. However, there are significant differences in some of the design parameters.

The most obvious difference is in the volume and weight ratios of the two motors. Both ratios were about 2.0 to 1.0 in favor of the samarium-cobalt motor. This indicates that, in applications where weight or volume is of primary importance, samarium-cobalt designs would be favored.

A comparison between the rotor inertias of the two machines shows a ratio of about 5.0 to 1.0 in favor of the samarium-cobalt. This may be significant in servo type applications where fast response is an important consideration.

The cost of the permanent magnet material for the samarium-cobalt motor was about five times that of the ferrite motor. However, this was slightly offset by the longer stack and additional copper as well as labor for the ferrite motor. Whenever magnet material availability and security of supply is of primary consideration, the ferrite motor may be favored. The above considerations indicate that for general purpose propulsion and similar applications, the ferrite design is preferable.

CONCLUSIONS

Results of this investigation show that electronically commutated brushless dc motors of equal horsepower and equal performance can be constructed using samarium-cobalt or ferrites for magnet materials. The choice of the magnet material impacts weight, volume and motor inertia the most, with samarium-cobalt leading to significant reductions in all three. From the standpoint of magnet material cost and security of supply, ferrites appear to be preferable. It has been shown that motor-power conditioner efficiencies of 90% or better are practical and achievable It has also been shown that peak horsepower outputs of more than double the rated value are achievable, especially by use of the concept of advanced phase current firing to maximize dc line current build-up during commutation. Power conditioners built entirely by use of power transistors for the present ratings were shown to be practical.

ACKNOWLEDGEMENTS

These authors wish to acknowledge the financial support given by NASA Lewis Research Center/Department Energy Contract No: DEN3-65, and wish to acknowledge the keen interest and useful guidance of the contract monitor Mr. E. Maslowski of the Lewis Research Center. The authors wish to thank Dr. R. Churchill, Vice-President, Research and Development Center, Industrial Drives Division, Kollmorgen Corporation, Radford, Va., for availing the manufacturing and test facilities of both the R and D Center and the Industrial Drives Division.

REFERENCES

[1] Delco Electronics, "Final Report on the Electromechanical Flight Control Actuator", Final Report NASA-JSC Contract NO. NAS9-14952, General Motors Corporation, Delco Electronics Div., Santa Barbara Operations, Goleta, CA, 1978.

[2] Sawyer, B. and Edge, J. T., "Design of a Samarium-Cobalt Brushless DC Motor for Electromechanical Actuator Applications", Proceedings of the IEEE-National Aerospace and Electronics Conference, Dayton, Ohio, 1977.

ORIGINAL PAGE IS OF POOR QUALITY

[3] Edge, J. T., "An Electromechanical Actuator Technology Development Program", Paper NO. 780581, Society of Automotive Engineers, Proceedings of the Aerospace Fluid Power and Control Technologies Symposium, 1978.

[4] Demerdash, N. A., Lee, F. C., Nehl, T. W. and Overton, B. P., "A Brushless DC Motor-Power Conditioner Unit Designed and Built for Propulsion of Electric Passenger Vehicles Phase (I)", Paper NO. EVC 8013, Proceedings of the International Electric Vehicle Conference and Exposition, St. Louis, NO, 1980.

[5] Nehl, T. W., Fouad, F. A. and Demerdash, N. A., "Digital Simulation of Power Conditioner-Machine Interaction For Electronically Commutated DC Permanent Magnet Machines", Paper Presented at the IEEE-Intermag 81, Grenable, France, Accepted for Publication in the November, 1981 IEEE Transaction on Magnetics.

[6] Nehl, T. W., Fouad, F. A., Demerdash, N. A., and Maslowski, E., "Dynamic Simulation of Radially Oriented Permanent Magnet Type Electronically Operated Synchronous Machines with Paramenters Obtained from Finite Element Field Solutions", Paper Accepted for Publication in the IEEE Transactions on Industry Applications.

[7] "Electric Vehicle Test Procedure-SAE J227a", Society of Automotive Engineers, Inc., 1976.

NABEEL A. DEMERDASH (M'65 - SM'74) was born in Cairo, Egypt, on April 26, 1943. He received the B.Sc. E.E. degree with distinction and first class honors from Cairo University, Egypt, in 1964 and the M.S. and Ph.D. degrees in Electrical Engineering from the University of Pittsburgh, Pittsburgh, Pennsylvania, in 1967 and 1971, respectively.

From 1964 to 1966 he was with the Faculty of Engineering, Cairo University as a Demonstrator. From 1966 to 1968 he was with the Department of Electrical Engineering, University of Pittsburgh, as a Graduate Teaching Assistant. In 1968 he joined the Large Rotating Apparatus Division of Westinghouse Electric Corporation, East Pittsburgh, Pennsylvania, as a Development Engineer, where he worked on Electromagnetic Field Modeling in Rotating Machinery and the development of the asymmetrical rotor for large steam turbine-driven generators. Since 1972 Dr. Demerdash has been with the Virginia Polytechnic Institute and State University, Blacksburg, VA, where he is presently a Professor in the Department of Electrical Engineering.

Dr. Demerdash is a Senior Member of IEEE and is currently serving as a member of the Rotating Machinery Committee of PES, IEEE, as well as the Synchronous Machinery and the Machine Theory Subcommittees of PES, IEEE. He previously served as secretary and subsequently vice chairman of the Synchronous Machines Subcommittee of PES, IEEE. Dr. Demerdash is a past Chairman of the Virginia Mountain Section of IEEE. He is a member of ASEE, Sigma Xi and Eta Kappa Nu. Dr. Demerdash is the author and co-author of numerous papers in various IEEE Transactions. Dr. Demerdash's current interests and research activities include Electromechanical Propulsion and Acutation, Dynamic Modeling of Solid State Controlled and Operated Electrical Machines, Numerical Analysis of Electromagnetic Fields in Electric Machinery, as well as Machine-Power System Dynamics.

ROBERT H. MILLER (S'47 - M'48) was born on Nov. 28 1925 in Glenside, Pennsylvania. He received the B.S. degree in electrical engineering from Virginia Polytechnic Institute in 1948 and the Ph.D. degree from M.I.T. in instrumentation in 1964.

From 1948 to 1949 he worked on carrier communications systems for Western Union Research Laboratories in New York, N.Y. From 1949 to 1950 he worked on magnetic amplifiers and resolvers for Kearfott Company in New York. From 1950 to 1953 he was involved with aircraft equipment specifications for Grumman Aircraft in Bethpage, N.Y. From 1954 to 1963 he was on the staff of Poly-Scientific Corporation, Blacksburg, VA, first as chief electrical engineer, and later as chief engineer, vice president for engineering, and then vice president for research and development. Since 1964 he has been a member of the faculty of Virginia Polytechnic Institute and State University, where he is currently an associate professor of Electrical Engineering. His research interests are in the area of electromechanical devices.

THOMAS W. NEHL (M' 79) was born in Tubingen, West Germany, on December 22, 1952. He received the B.S., M.S., and Ph.D. degrees in electrical engineering from Virginia Polytechnic Institute and State University in 1974, 1976, and 1980 respectively.

During the summer of 1976 Dr. Nehl was employed by the National Bureau of Standards where he developed a finite element package for the solution of their nondestructive testing program. During the summer of 1977 he was employed at the NASA Johnson Space Flight center where he was engaged in the modeling of brushless dc machine type electromechanical actuator systems. From 1978 to 1980, he was employed as a research associate in the Department of Electrical Engineering at VPI&SU.

Dr. Nehl is presently an assistant professor of electrical engineering at VPI&SU. His current research activities include; finite element field analysis of machines, digital simulation of electronically operated machines, simulation of machine and electronic failure modes in electronically operated machine systems, nondestructive testing and evaluation, and power electronics.

Dr. Nehl is currently serving on the Synchronous and the Machine Theory Subcommittees of the IEEE/PES. He is a member of ASEE, Sigma Xi, Phi Kappa Phi, and Eta Kappa Nu. Dr. Nehl is the author and co-author of more than 20 transactions and technical papers in the power and magnetic field areas.

BERNARD P. OVERTON was born in Prince Edward County, Virginia on November 14, 1923. He received a B.S. degree in Electrical Engineering from Virginia Polytechnic Institute in 1956.

From 1956 to 1967 he was with the Wright Machinery Company Division, Sperry Rand Corporation, Durham, North Carolina as an Associate Engineer, Senior Engineer and Acting Section Head, motor Development Group. Responsibilities included the design and development of special and unusual motor components such as AC servo motors, AC tachometers, DC motors and stepper motors, both permanent magnet and variable reluctance. Since 1967 he has been with Inland Motor Divisions, Kollmorgen Corporation, Radford, Virginia as a Senior Engineer, and Senior Staff Engineer - Research and Development Center. Responsibilities include the design of special DC motors, alternators, steper motors, motor-generator sets and power DC servo motors.

Mr. Overton is a member of Tau Beta Pi and a senior member IEEE. He is currently the chairman of the IAS chapter, Virginia Mountain Section, IEEE.

CHARLES J. FORD, III was born in Richmond, Virginia on November 2, 1954. He received a B.Sc. degree in Electrical Engineering Technology from Virginia Polytechnic Institute and State University in 1977. He is currently doing graduate work toward a M.Sc. in Electrical Engineering at VPI&SU as a part-time student.

During his undergraduate studies, Mr. Ford worked at the Reynolds Metal Can Development Center as part of the cooperative work-study program. In 1977 he joined the Research and Development Group of Inland Motor Division of Kollmorgen Corporation, in Radford, Virginia. His responsibilities have included the development of brushless d.c. motor controllers for electric vehicle applications and for underwater drives.

APPENDIX (11)

ON THE PERFORMANCE OF THE SAMARIUM-COBALT AND STRONTIUM-FERRITE BASED BRUSHLESS DC MACHINE-POWER CONDITIONER SYSTEMS

Miller, R. H., Nehl, T. W., Demerdash, N. A., Overton, B. P., and Ford, C. J., "An Electronically Controlled Permanent Magnet Synchronous Machine - Conditioner System for Electric Passenger Vehicle Propulsion," Proceedings of the 1982 IEEE-IAS Annual Meeting 82CH1817-6, San Francisco, October 4-7, 1982, pp. 506-511.

AN ELECTRONICALLY CONTROLLED PERMANENT MAGNET SYNCHRONOUS MACHINE-CONDITIONER SYSTEM FOR ELECTRIC PASSENGER VEHICLE PROPULSION

R. H. Miller, Member T. W. Nehl, Member N. A. Demerdash, Senior Member
Virginia Polytechnic Institute and State University
Blacksburg, Virginia

B. P. Overton, Senior Member C. J. Ford, III, Member
R and D Center, Industrial Drives Division
Kollmorgen Corporation
Radford, Virginia

Abstract - An electronically commutated brushless dc motor system was designed and built for the propulsion of a 3000 lb (1362 kg) passenger vehicle. For this system, an electronic power conditioner and two motors were built. One of the motors used samarium-cobalt magnets and the other used strontium ferrite magnets for the field excitation. Some of the major details of the design of the motors and of the power conditioner are presented. Dynamometer tests were run on the machines. The results of this testing are described. The machines were demonstrated to be capable of developing 15 hp continuously and 35 hp intermittantly. Under rated operating conditions, the efficiency of either machine was about 90%.

INTRODUCTION

The development of large power transistors has made possible the electronic commutation of integral horsepower brushless dc motors. Such motors are increasingly becoming practical for various industrial applications, such as machine tool drives or actuators for robots or aircraft. Examples of such applications are listed in references [1] through [3].

The elimination of the brushes and commutator, which is made possible by the electronic commutation, provides several important advantages:

(1) Much higher rotor speeds are possible. This leads to a pronounced reduction in weight and size for a given horsepower rating.

(2) The armature windings can be placed on the stator, where the cooling of the coils can more readily be accomplished.

(3) The placing of the armature windings on the stator simplifies the winding configuration.

As the external energy product of permanent magnets has increased, it has become practical to design brushless dc motors of larger horsepower ratings. By using rotor magnets of 18 MGO samarium-cobalt and of strontium-ferrite number 8, the authors were able to design, build and test two motors of sufficient power rating as to make them suitable for the propulsion of electric passenger vehicles.

The goal of the work was to develop an electronic power conditioner-motor system capable of propelling a 3000 lb (1362 kg) vehicle under schedule D of the SAE J227a standard drive cycle[4]. This required that the system be capable of sustained (2 hour) operation at an output of 15 hp and short-term (1 minute) operation at an output of 35 hp. As the test results show, each of these goals has been met.

Description of the Motors

In this work, two motors were designed and built. For the purpose of minimizing the size and weight, one of the motors was constructed using samarium-cobalt magnets for the field excitation. Because of the expense and possible scarcity of this magnet material, a second motor was designed and built using strontium-ferrite magnets. The performance of the two motors was nearly the same, while the ferrite excited motor was about twice the weight and one and one-half times the volume of the samarium-cobalt excited motor.

In both motors, balanced three-phase Y-connected windings were used. These windings were arranged in two groups so that they could be connected in series or in parallel. This arrangement was made so that higher starting torque could be obtained without excessive current in the electronic power conditioner. However, the test results confirmed that sufficient torque was available in the parallel connection to meet the drive cycle specification. Accordingly, no provision was made in the final system hardware to switch to series operation at low speed.

Both machines used natural air cooling of the T.E.N.V. enclosures. Photographs of the major components of the two machines are shown in Figures (1) and (2). The major design parameters are listed in Table (1).

Figure (1) Components of the Samarium-cobalt Motor

Figure (2) Components of the Ferrite Motor

Table (1) Major Design Parameters		
Parameter, Units	Samarium-Cobalt $SmCo_5$ Design	Strontium Ferrite #8 Design
motor outside diameter, in. (cm)	7.88 (20.02)	7.88 (20.02)
motor length, in. (cm)	13.35 (33.91)	18.85 (47.88)
motor weight, Lb. (kg)	60.0 (27.2)	127.0 (57.6)
total magnet weight, Lb. (kg)	3.23 (1.47)	9.56 (4.34)
rotor inertia constant, Lb. ft. sec^2 ($kg.m^2$)	0.00234 (0.00317)	0.0120 (0.0163)
rated horsepower, hp (continuous 2 hour rating)	15.0	15.0
peak horsepower, hp (one minute rating)	35.0	35.0
speed at rated horsepower	8680	8840
number of poles	6	6
torque sensitivity (parallel connection) Lb.ft/ampere (Newton meter/ampere	0.0885 (0 11999)	0.0732 (0.0993)
emf sensitivity (line to line), volts/mech. rad./sec.	0.1200	0.0993
thermal time constant, minutes	35	45
supply voltage, volts	120	120

Mounted on the shaft of the machines was a set of six small magnets which were used to control three Hall effect sensors to determine the rotor position in order to synchronize the switching of the electronic drive circuit. This rotor position sensor divided a rotation of 360 electrical degrees into six arcs of 60 electrical degrees. This provided the timing for the switching sequence described in the next section. A second set of Hall-effect sensors was mounted in a position 30 electrical degrees removed from the first set. By using this alternate set of sensors, advanced firing of the commutating transistors could be accomplished. The need for this provision is discussed below.

Description of the Power Conditioner

The function of the electronic power conditioner was two-fold: to convert the dc supply voltage to three-phase ac voltage of the proper phase to drive the motor, and to control the current supplied to the motor in order to regulate the developed torque. The development of this type of power conditioner is described in references [1]-[3] and [5]-[7].

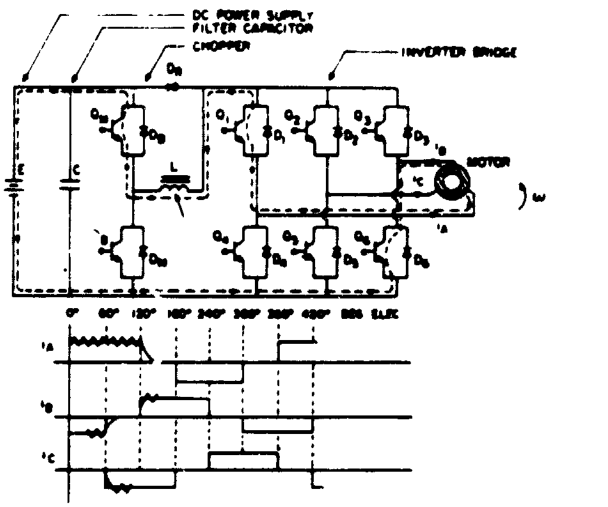

Figure (3) Motor-Power Conditioner Network Schematic

A schematic diagram of the circuit including the major power switching elements is shown in Figure (3). In this diagram, the commutation is accomplished by the three phase inverter/converter (motoring/regenerative braking) bridge comprising the six transistors, Q_1 through Q_6, and the six diodes, D_1 through D_6. The current control is accomplished by the two quadrant chopper comprising transistors Q_M and Q_B and diodes D_M and D_B.

In the motoring mode, the chopper regulates the current to the motor by turning on Q_M if the inductor current is too low. When the inductor current has increased by a predetermined increment beyond the set value, Q_M turns off, and the inductor current flows through diode D_M. During regenerative braking, the transistor Q_B is turned on until the inductor current has risen by an increment above the set value. Q_B is then turned off, and the inductor current flows through D_B and onto the battery.

In the motoring mode, proper switching of Q_1 through Q_6 leads to phase a, b and c current waveforms such as are idealized in Figure (3). In this figure, one can see the existence of six distinct armature states. This establishes in the motor a stator (armature) mmf which travels in discrete jumps of 60 electrical degrees. The rotor mmf (magnets) is continusouly forced to follow that motion. The result is equivalent to that of a synchronous machine in which the torque angle (between the two mmfs) varies during each switching cycle between an initial 120° and a final 60° electrical angle. For advanced firing of the commutating transistors, this angle varies between 150° and 90° electrical as shown in Figure (4).

The diodes, D_1 through D_6, provide current paths during the switching operation when the inverter transistors are momentarily off. They also function as a three-phase full wave rectifier bridge in the regenerative braking mode. Diode D_B provides a path for the inductor current during the switching instances when the path through the inverter is momentarily blocked.

In order to eliminate one transistor which reduces cost, and to prevent any accidental firing of Q_M and Q_B simultaneously, one transistor was used for both functions. This transistor was switched between the two positions by means of a DPDT relay.

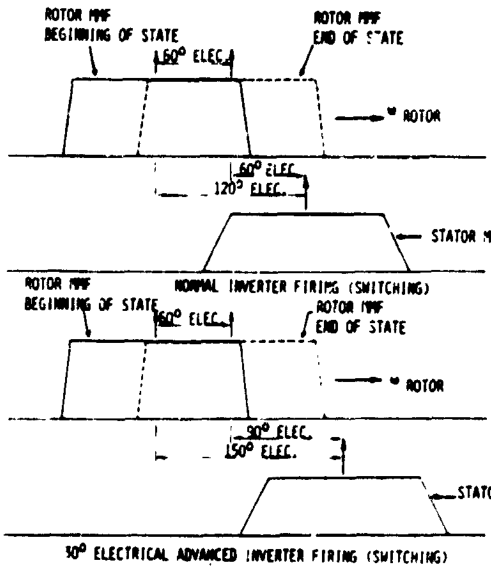

Figure (4) Advanced Firing Concept

IMPACT OF COMPUTER AIDED ANALYSIS ON THE MOTOR-CONDITIONER SYSTEM DESIGN

It is worth emphasizing that the various voltage and current waveforms throughout such motor-conditioner systems are heavily nonsinusoidal in nature, see references [1]-[3] and [5]-[7]. Hence, many classical frequency domain (phasor type) methods are not applicable to the analysis and prediction of performance of such systems. In fact, use of such methods without regard to their limitations when analyzing such systems can lead to misleading results. This led to the development of a dynamic time-domain simulation model, see reference [7], suited for the analysis of such systems. This model requires: 1) knowledge of the waveforms of phase emfs induced in the armature windings of such machines, 2) the values of the self and mutual inductances of the phase windings of such motors, and 3) other motor-conditioner circuit parameters. The determination of the emf waveforms, and inductances, associated with such machines is accomplished by use of the method of finite elements to analyze the magnetic field in these machines, as described in detail in references [8] and [9], respectively.

The above mentioned computer-aided analysis tools were used to examine the validity of the preliminary designs of the motor-conditioner systems at hand before such designs were finalized and implemented. This was carried out in the following order:

1) Upon obtaining preliminary designs of the samarium-cobalt and ferrite motors, the emf waveforms and winding inductances were determined for both machines by finite elements, using methods described in references [8] and [9], respectively.
2) These parameters were used in the dynamic simulation model of the motor-conditioner system, see reference [7] and [6] for further details. The results of the simulation revealed that under the constraint (imposed by customer) of a supply voltage of 120 volts dc, only 4 hp peak output could be obtained at the rated speed [6]. This rather limited output capability can be attributed directly to the machine inductances. In order to rectify this situation, the number of winding turns per phase was reduced, see references [9] and [6].

   This design change was also simulated, and it led to a new peak output of 26 hp. This was much closer to the goal of 35 hp. However, additional design changes were necessary to achieve the 35 hp goal.
3) The idea of advancing the firing time of the inverter transistors by 30 electrical degrees was also simulated. This reduces the value of the emf opposing the current buildup at the instant of switching.

   The combined reduction in the number of turns and advanced firing led to a predicted motor-conditioner peak output of about 38.7 hp. With this result in mind, these design changes were introduced to the final design, and implemented in the construction of the hardware. Results of the actual testing of the hardware given later in this paper reveal that the developed system is capable of producing the required 35 hp one minute output rating in both the samarium-cobalt and ferrite motor cases.

Power Conditioner Design Features

The power transistors used for both the chopper and inverter transistors were Toshiba 2SD548, with a rated collector current of 400 A and a rated voltage V_{CEO} of 300 V. The 300 V rating required that careful attention be given to the snubber design to prevent excessive voltage spikes during the switching instants. The snubber circuit is shown in Figure (5). Even with these snubbers, it was necessary to place a 9000 μF capacitor bank across the inverter buss to prevent excessive voltage spikes.

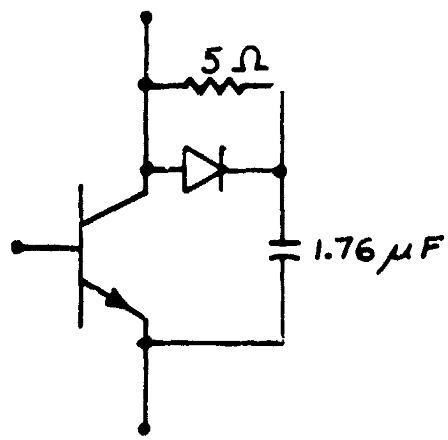

Figure (5) Snubber Network

The power transistors and power diodes were mounted on heat sinks which were arranged in the form of a tunnel through which cooling air was forced (see Figure (6)). However, since the only practical way of mounting these diodes was on heat sinks that were much larger than necessary, the system remained very cool. Case temperatures for the inverter and chopper transistors, at the end of the two hour 15 hp run, were 35° and 44.2°C, respectively. If the electronic package were arranged so that the tunnel was vertical, natural convective cooling would probably have been sufficient. However, project constraints precluded that option.

The inductor was built on an Allegheny-Ludlum L-10 core, using a stack height of 3.75 in. (9.53 cm.). Each air gap was .125 in. (.318 cm.). On this core, two coils were placed, each coil consisting of ten parallel strands of #8 A.W.G. wire. These two coils were connected in parallel. This arrangement provided an inductance of 425 μH at 200 A. The loss in this inductor at the rated current of 120 A was only 31 W.

Figure (6) System Hardware During Testing

In order to measure the current in the inductor for the purpose of controlling the chopper, a pair of Hall effect sensors was used. Each sensor consisted of a toroidal ferrite core with a slot cut in it to provide an air gap of .093 in. (.236 cm.). In this air gap a Sprague #UGN-3501 T Hall effect sensor was mounted. The assembly was then placed around the wire leading to the inductor. This provided a reasonably linear current measurement with a sensitivity of 3.3 mV/A. One of these sensors controlled the chopper in the motoring mode, while the other sensor controlled the chopper in the regenerative braking mode. The output of the two sensors was compared and the difference fed to an alarm circuit, so that failure of a sensor would generate an alarm and shut down the system before the chopper transistor could be destroyed.

A schematic diagram of the low-level electronic logic and control circuit is shown in Figure (7). At the heart of the control network is a pair of N82S126N programmable read-only memories. Each of these memories has eight inputs and four outputs (256 × 4). Six of the inputs are used by the two rotor position sensors (normal and advanced firing), and six of the outputs are used for the control of the inverter transistors. The remaining two inputs are used for a forward/reverse control (to control the order of firing of the inverter transistors) and for a normal/advanced firing control (to select which rotor position sensor will control the inverter transistors). The remaining two outputs, one on each PROM, are connected to an alarm circuit to shut down the system in the event of an abnormal set of signals from the rotor position sensors.

One of the PROM inhibit inputs is used to shut down the inverter in the event of a malfunction alarm in response to an excessive inductor current, loss of a current sensor, or malfunction of a rotor position sensor. The other PROM inhibit input is used to shut down the inverter for a period of 0.5 second during switching operations between motoring and regenerative braking modes (or during a series/parallel switching if this were used).

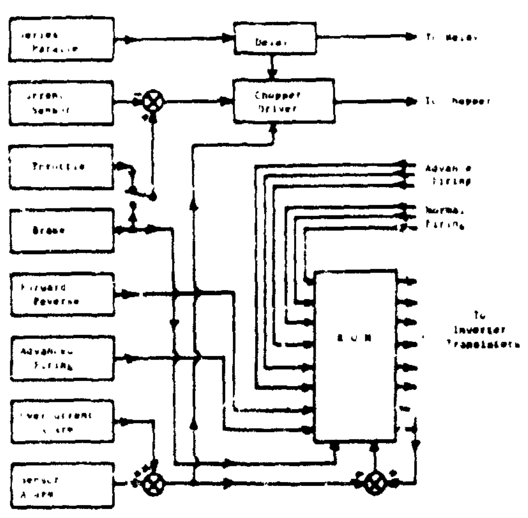

Figure (7) Low Level Control Logic

PERFORMANCE OF MOTOR-CONDITIONER SYSTEM

In order to evaluate the performance of the two machines described above, both were operated using the same power conditioner detailed above. This included the testing of both motors using a standard dynamometer test setup. The testing program consisted of the following:

1) Testing of the motor-power conditioner systems was carried out at an output equal to the rated value of 15 hp. This test was carried out for a continuous period of two hours to simulate cruising by a 3000 Lb vehicle at a speed of 55 mph (88 kph) on level road. The highlights of the data obtained from this test are given in Table (2). As can be seen, the overall system efficiencies under rated conditions were 88.72% and 91.18% for the samarium-cobalt and ferrite motor cases, respectively.

Table (2) Performance of the Samarium-Cobalt and Ferrite Motors at Rated Conditions

Performance Quantity Motor	DC Line Voltage (Volts)	DC Line Current (Amps)	Motor Speed (RPM)	Motor Output (Watts) (hp)	Overall System efficiency (%)
Samarium-Cobalt Motor	116.0	110.2	8680	11341.7/ 15.2	88.72
Ferrite Motor	115.6	107.3	8840	11299.7/ 15.1	91.18

2) Testing of the motor-power conditioner systems was carried out at an output equal to 35 hp. This test was performed for a period of one minute to simulate a 10% grade hill climbing by a 3000 Lb vehicle at a speed of about 30 mph (48 kph). The highlights of the data obtained from this test are given in Table (3). As can be seen the goal of 35 hp was reached by both motors. However, this power was developed at speeds lower than the rated ones for both machines. Advanced firing (commutation) of the inverter transistors by 30 electrical degrees was required to achieve the 35 hp output in both cases.

3) Testing of the motor-power conditioner systems was carried out at various other horsepower outputs and speeds. This data was obtained in order to establish the system characteristic performance over the entire motoring range of operation. This data is plotted in the form of equi-efficiency contours in the torque-

Table (3) Performance of the Samarium-Cobalt and Ferrite Motors at Peak Power of 35 HP					
Performance Quantity Motor	DC Line Voltage (volts)	DC Line Current (Amps)	Motor Speed (RPM)	Motor Output (Watts) (hp)	Overall System (%)
Samarium-Cobalt Motor	115.0	287.5	6900	26184.6/ 35.1	79.2
Ferrite Motor	120.9	297.6	6750	26632.2/ 35.7	74.0

speed plane as given in Figures (8) and (9) for the samarium-cobalt and ferrite motors, respectively.

Numerous oscillograms of voltage and current waveforms in the conditioner and motor at various load conditions were taken and are given in references [5] and [10].

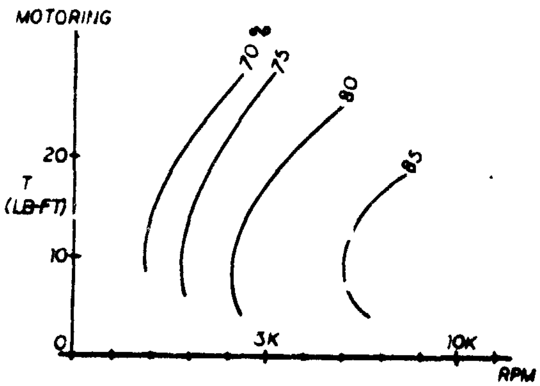

Figure (8) Equi-Efficiency Contours in the Torque-Speed Plane (First Quadrant), Samarium-Cobalt Case.

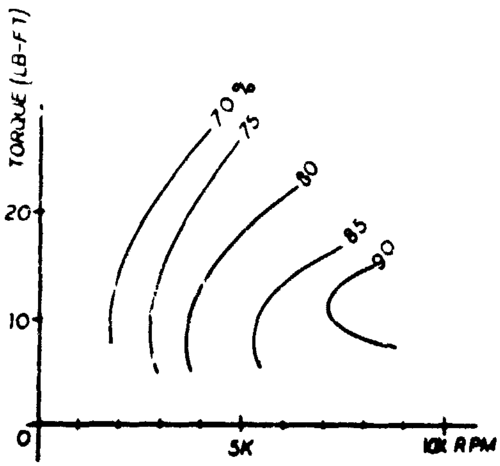

Figure (9) Equi-Efficiency Contours in the Torque-Speed Plane (First Quadrant), Ferrite Case.

CONCLUSIONS

This work revealed that ferrite type permanent magnets can be used in motor designs to produce machine performance characteristics equivalent to those produced by machines designed with samarium-cobalt magnets. However, this is done at the expense of increased motor weight and volume as given in the paper. The ferrites are certainly preferable in applications where weight and volume are not critical. The secure availability of ferrites in comparison to samarium-cobalt render these ferrites an attractive alternative to rare earth materials.

Furthermore, this work demonstrates that power transistors are well suited for integral horsepower motor control applications of this kind. Both goals of a continuous 2 hours 15 hp output at efficiences of about 90%, and one minute 35 hp output were accomplished. Furthermore, with a higher supply voltage of 150 volts, an output of more than 42 hp was achieved. These results reveal that such systems are well suited for propulsion of electric vehicles and similar applications.

ACKNOWLEDGEMENTS

These authors wish to acknowledge the financial support given by NASA Lewis Research Center/Department Energy Contract No: DEN3-65, and wish to acknowledge the keen interest and useful guidance of the contract monitor Mr. E. Maslowski of the Lewis Research Center. The authors wish to thank Dr. R. Churchill, Vice-President, Research and Development Center, Industrial Drives Division, Kollmorgen Corporation, Radford, Va., for availing the manufacturing and test facilities of both the R and D Center and the Industrial Drives Division.

REFERENCES

[1] Delco Electronics, "Final Report on the Electro-mechanical Flight Control Actuator", Final Report NASA-JSC Contract NO. NAS9-14952, General Motors Corporation, Delco Electronics Div., Santa Barbara Operations, Goleta, CA, 1978.

[2] Sawyer, B. and Edge, J. T., "Design of a Samarium-Cobalt Brushless DC Motor for Electromechanical Actuator Applications", Proceedings of the IEEE-National Aerospace and Electronics Conference, Dayton, Ohio, 1977.

[3] Edge, J. T., "An Electromechanical Actuator Technology Development Program", Paper NO. 780581, Society of Automotive Engineers, Proceedings of the Aerospace Fluid Power and Control Technologies Symposium, 1978.

[4] "Electric Vehicle Test Procedure-SAE J227a", Society of Automotive Engineers, Inc., 1976.

[5] Demerdash, N. A., Miller, R. H., Nehl, T. W., Overton, B. P., Ford, C. J., "Comparison Between Features and Performance Characteristics of Fifteen HP Samarium Cobalt and Ferrite Based Brushless DC Motors Operated by Same Power Conditioner", Paper presented at the 1982-IEEE PES Winter Meeting, New York, N.Y. Jan. 31-Feb. 5, 1982, Accepted for Publication in the IEEE Transactions on Power Apparatus and Systems.

[6] Nehl, T. W., Fouad, F. A., Demerdash, N. A., and Maslowski, E., "Dynamic Simulation of Radially Oriented Permanent Magnet Type Electronically Operated Synchronous Machines with Parameters Obtained from Finite Element Field Solutions", IEEE Transactions on Industry Applications, Vol. IA-18, pp. 172-182, 1982.

[7] Demerdash, N. A. and Nehl, T. W., 'Dynamic Modeling of Brushless dc Motor for Aerospace Actuation", IEEE Transactions on Aerospace and Electronic

Systems, Vol. 16, Number 6, pp. 811-821, 1980.

[8] Fouad, F. A., Nehl, T. W., and Demerdash, N. A., "Magnetic field modeling of permanent magnet-type electronically operated synchronous machines using finite elements," IEEE Trans. Power App. Syst., Vol. PAS-100, no. 9, pp. 4125-4135, 1981.

[9] Nehl, T. W., Fouad, F. A., and Demerdash, N. A., "Determination of Saturated Values of Rotating Machinery Incremental and Apparent Inductances by a Perturbation Method", Paper presented at the IEEE-PES Winter Meeting, New York, Jan. 31-Feb. 5, 1982, Accepted for publication in full in the IEEE Transactions on Power Apparatus and Systems.

[10] Final Report on NASA/DOE Contract DEN3-65, "Improved Electronically Commutated Brushless DC Motors for Electric Vehicle Propulsion," to be published in December, 1982.

C-5

APPENDIX (12)

ON THE PERFORMANCE OF A FUNCTINAL PROOTYPE OF A SAMARIUM-COBALT BASED BRUSHLESS DC MACHINE-POWER CONDITIONER SYSTEM - PHASE (I)

Demerdash, N. A., Lee, F. C., Nehl, T. W., and Overton, B. P., "Practical Application of Power Conditioning to Electric Propulsion for Passenger Vehicles," Proceedings of the 1980 IEEE Power Electronics Specialists Conference 80CH1529-7, Atlanta, June 16-20, 1980, pp. 211-219.

Reprinted From:

pesc '80 RECORD

IEEE Power Electronics SPECIALISTS CONFERENCE—1980

Formerly POWER CONDITIONING SPECIALISTS CONFERENCE (1970-71)
POWER PROCESSING AND ELECTRONICS SPECIALISTS CONFERENCE (1972)
POWER ELECTRONICS SPECIALISTS CONFERENCE (1973-80)

Dunfey Hotel

Atlanta, Georgia

June 16-20, 1980

The 1980 Power Electronics Specialists Conference was sponsored by the Aerospace and Electronic Systems Society, the Electron Devices Society, the Industrial Control and Instrumentation Society, the Magnetics Society, the Power Engineering Society, the Circuits and Systems Society and the Region 6 San Diego Section.

80CH1529-7

PRACTICAL APPLICATION OF POWER CONDITIONING
TO ELECTRIC PROPULSION FOR PASSENGER VEHICLES

N. A. Demerdash, F. C. Lee, T. W. Nehl
Department of Electrical Engineering
Virginia Polytechnic Institute
and State University
Blacksburg, VA 24061

B. P. Overton
Research and Development
Inland Motor Division
Kollmorgen Corporation
Radford, VA 24141

ABSTRACT

A functional model (prototype) 15 HP (continous rating), 120 volt, 4-pole, 7600 r.p.m. samarium-cobalt permanent magnet type brushless dc motor-transistorized power conditioner unit was designed, fabricated and tested for specific use in propulsion of electric passenger vehicles. (This work was funded by NASA-Lewis/DOE under phase (I) of NASA contract No. DEN3-65 as part of DOE's program on research and development of electric vehicle technology.) This new brushless motor system including its power conditioner package has a number of important advantages over existing systems such as reduced weight and volume, higher reliability, potential for improvements in efficiencies, etc. These advantages are discussed in this paper in light of the substantial test data collected during experimentation with the newly developed conditioner motor propulsion system. Details of the power conditioner design philosophy and particulars are given in the paper. Also, described here are the low level (signal) electronic design and operation in relation to the remainder of the system.

INTRODUCTION

By and large almost all primemovers in various electrical propulsion systems are brush-type traction d.c. series or compound connected motors. These motors, if properly designed, perform their intended function quite adequately. However, there are various advantages that are attributed to brushless type propulsion systems which are lacking in ordinary brush d.c. motor type systems. Some of the major advantages of the present brushless system, built around an electronically commutated samarium-cobalt type permanent magnet motor as a primemover, can be summarized as follows: 1) the elimination of brushes leads to reduction in maintenance requirements and hence a potentially more reliable system, 2) the elimination of brushes leads directly to higher upper bounds on possible motor rated speeds and consequently reduced weight and volume of electric machinery for a given horsepower, 3) in a brushless motor a permanent magnet type rotor is utilized, hence the so familiar rotating armature winding of the classical d.c. machine is eliminated, which means simpler and potentially cheaper construction, and 4) the elimination of a rotating armature, with consequent mounting of an armature winding on the stator leads to improved thermal characteristics for such machines with potential for improved motor overall performance and efficiencies. This is in addition to a number of other indirect but tangible advantages which are inherent in a brushless motor and are lacking in classical brush type machines.

Accordingly, an electronically commutated brushless d.c. motor propulsion system for use in electric passenger vehicles, with specific vehicle weight and performance characteristics was developed, fabricated and tested. This was done with a main goal of meeting specific vehicle performance requirements as given in SAE electric vehicle drive cycle J227a Scheduled-D standards. The main design, fabrication, testing steps and procedures as well as performance characteristics of this system are summarized with emphasis given here to the transitorized power conditioner built for this motor. The main components of the system are described next.

MOTOR-POWER CONDITIONER

A permanent magnet type brushless d.c. machine, designed to withstand a peak load of 35 HP for one minute duration was constructed. A schematic diagram showing the cross sectional configuration of the machine is given in Figure (1). As can be seen the motor consists of a 15 slot wound stator using a standard laminated structure for the magnetic circuit of the stator. A fractional slot stator winding design was chosen to reduce armature e.m.f. and m.m.f. harmonics and hence reduce any tendencies for cogging. The stator core was installed in a corrigated aluminum housing for improved loss dissipation and hence better machine thermal characteristics.

CH1529-7/80/0000-0211$00.75

The rotor consists of a 4-pole permanent magnet arrangement glued to a suitable steel shaft. A nonmagnetic stainless steel magnet retaining sleeve in conjunction with suitable "Epoxy" type glue were used surrounding the magnets for bonding and retainment purposes.

The stator winding was built with an interesting feature of 3-taps per phase, which allows one to vary the operative (effective) number of turns per phase in the stator winding. This feature provides the operator the flexibility of controlling the torque speed characteristics of the motor. This torque-speed controlability feature is demonstrated clearly in the torque speed characteristics given in Figure (2), which were obtained on the basis of measured motor torque sensitivities (Lb.Ft/Ampere) for each of the three stator winding taps per phase. This feature can be used if desired to supply the partial function of a transmission, hence it provides the option of overall design simplification of the drive train by virtue of this torque-speed characteristic controllability. This feature, if exploited to its full extent, can either lead to extreme simplification or elimination of a mechanical transmission, thus leading to savings in weight, volume, reliability and cost of an overall drive train. The taps can be seen clearly in Figure (3) in the partially assembled view of the stator and its housing, and in the multi-terminal appearance of the motor (9 terminals, 3 terminals per phase) in Figure (4).

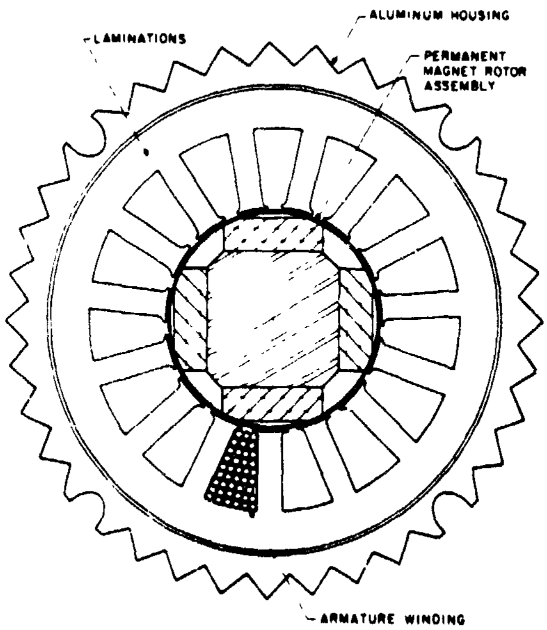

MOTOR CROSS SECTION

Figure (1)
Motor Cross-Section

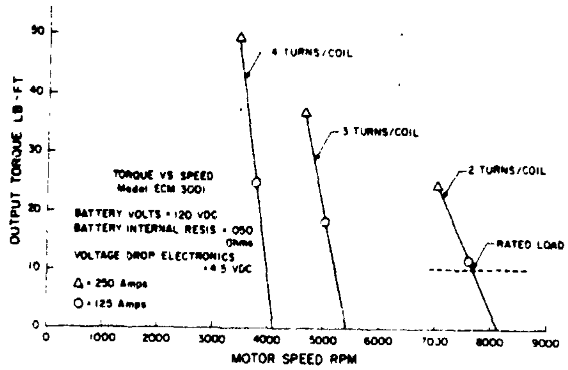

MOTOR TORQUE SPEED CHARACTERISTICS BASED ON MEASURED TORQUE CONSTANTS AND MEASURED ROTATIONAL LOSSES

Figure (2)
Torque Speed Characteristics

Figure (3)
Partially Assembled Armature

Figure (4)
Assembled Motor

ORIGINAL PAGE
BLACK AND WHITE PHOTOGRAPH

The motor is energized by a solid state transistorized power conditioner (P.C.) shown schematically in Figure (5). Shown also in Figure (5) are the idealized motor phase currents, i_A, i_B, and i_C. The main functions of the P.C. in relation to motor operations are mainly two. The first of these is proper sequencing and switching of the phase currents of the motor, which is demonstrated by the idealized current wave forms of Figure (5). This properly sequenced switching leads to a continuously forward stepping stator m.m.f. which is kept 120 electrical degrees ahead of the rotor m.m.f. at the instant of occurance of every switching opertion. The proper angular displacement between the stator and rotor m.m.f.s is controlled and guaranteed by a Hall-effect rotor position sensor, which is elaborated on in following sections of this paper. The second of these functions is the controlability of the magnitude of the d.c. line current. In this type of machines torque is linearly proportional to the magnitude of the d.c. line current, hence controlability of the line current or motor torque are synonimous. Description of the P.C. and functions of its various components and control scheme is given next.

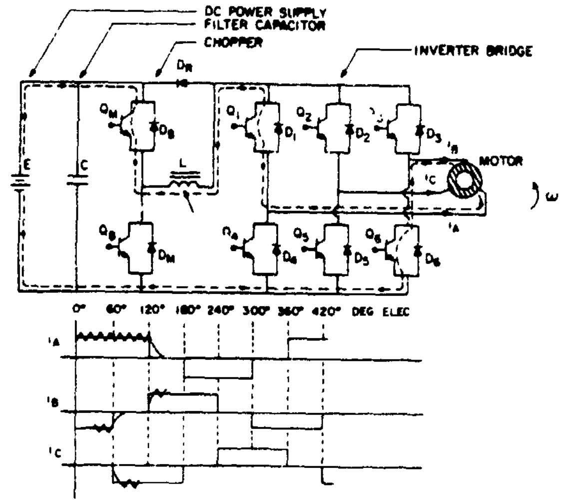

MOTOR POWER CONDITIONER SCHEMATIC AND IDEALIZED MOTOR CURRENTS

Figure (5)
Motor-Conditioner Schematic

POWER CONDITIONER FEATURES

The main features of the power conditioner shown schematically in Figure (5) are: 1) a d.c. line input capacitor filter for ripple elimination and/or reduction, 2) a combination series/shunt type (two quadrant) chopper for d.c. line current (motor torque) magnitude limiting and control, and 3) a configuration of six transistor-diode switches which constitute the three phase inverter/converter bridge.

The inverter/converter bridge has a capability of allowing the machine to function in three separate modes of operation. Namely, these modes are: motoring, plugging (dynamic braking) and regenerative braking. Shown also in Figure (5) in idealized form are the A, B and C machine phase currents during a forward motoring mode. Shown in dotted line form is the path of current through conditioner and machine during the first 60° electrical of the current cycle given in Figure (5), with the chopper in the "on" position for motoring. The "on/off" signals which activate the six transistors in the inverter bridge are generated by a Hall-effect rotor position sensor (R.P.S.) which is shown schematically in Figure (6), with the actual hardware shown in Figure (7).

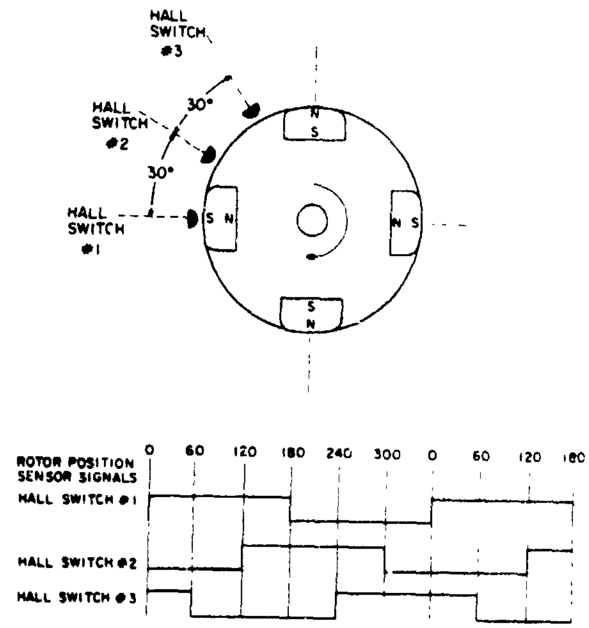

POSITION SENSOR

Figure (6)
Position Sensor Schematic and Output Signals

THE ROTOR POSITION SENSOR AND LOW LEVEL SIGNAL ELECTRONICS

The rotor position sensor divides each 360 degrees electrical into six segments or current states of 60 degree widths. The three RPS output signals for nine consecutive current states are shown in the bottom part of the Figure (6). The RPS consists of a separate rotor and stator core which contains three Hall devices mounted in slots displaced from each other by 30 mechanical or 60 electrical degrees. The adjustable RPS stator core makes it possible to vary the commutation angle if needed.

The output signals generated by the RPS are used as an address to "look up" the status of the six inverter transistors from a 32x8 bit programmable read only memory or PROM which is shown schematically in Figure (8). The PROM contains the inverter switch configurations, in table form, for all six states during both forward and reverse motoring, while during regenerative braking, all inverter switches are kept off regardless of the current state. The PROM is also used in the over current protection scheme to turn off all eight transistors by means of the chip disable line. Use of the PROM to perform these decoding tasks greatly simplifies the circuitry when compared with discrete logic gate type implementation.

Figure (7)
Hall Effect Rotor Position Sensor R.P.S.

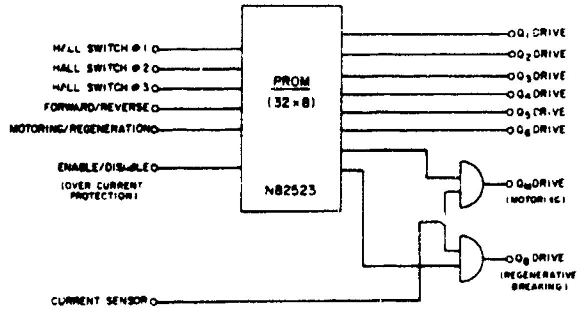

Figure (8)
Digital Processor

Controlling the chopper is a d.c. line current sensor coupled with a hysteresis type control approach which is depicted schematicaly in Figure (9). This current sensor-hysteresis controller controls the duty cycle (on/off times) of the transistor switch, Q_M in the motoring mode, and controls the duty cycle of the transistor switch, Q_B, in the braking mode. The output signal of the current sensing and control device which is also depicted in Figure (9) is fed into the digital processor of Figure (8). The output signals of the processor control the two chopper transistors, Q_M and Q_B, as well as the inverter/converter bridge transistors, Q_1 through Q_6.

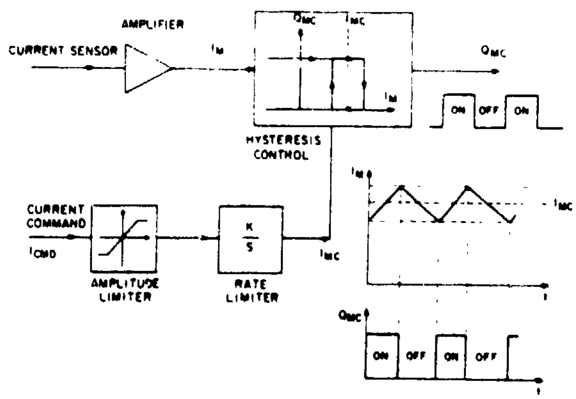

Figure (9)
D.C. Line Current Sensor and Chopper Control

THE D.C. LINE CURRENT SENSOR-CONTROLLER SCHEME

The regulation of the average machine torque (or current) can be accomplished by means of an open loop technique such as pulse width modulation (PWM) or by means of a closed loop system utilizing a hysteresis type controller, Figure (9). The closed loop approach was chosen for this application because of the following advantages: inherent stability, controllabe dc ripple, and simplfication of the protection schemes. The current sensor consists of a coaxial type current shunt, which is located in the dc link between the chopper and inverter network, and an amplifier which is used to boost the output of the current shunt. The input current command, ICMD, is amplitude limited at around 300A for protection purposes. The amplitude limited current command is then passed through a rate limiter to filter out rapid variations or noise in the ICMD. The rate and magnitude limited current command signal, IMC, is then compared with the output of the current sensor, IM, using a hysteresis type comparator. The comparator produces a logical valued output, QMC, which controls the switching of Q_M and Q_B at a rate required to keep IM within the specified tolerance during motoring and regeneration respectively. One additional feature of this controller is that the maximum chopping frequency can be controlled by varying the specified current tolerance. The frequency decreases for increases in the current tolerance and vice versa.

The diodes, D_1 through D_6, provide current paths during phase current commutation. They also constitute the converter bridge in the braking mode. The diodes, D_M and D_B, provide the necessary d.c. line current paths during the "off" periods of Q_M and Q_B respectively. The main function of the diode, D_R, is to provide a return path to the current through the chopper inductor back into the source at the switching instances when such a path through the inverter may be blocked momentarily, thus it eliminates the danger of any severe voltage transients which may accompany the transistor switching of Q_1 through Q_6.

The chopper transistors Q_M and Q_B employ a high frequency, triple-diffused four-terminal power Darlington, and the inverter transistors employ a single- diffused power Darlington for ruggedness. The high frequency Darlington block MT-1144 consists of one driver PT-4500 which feeds three paralleled PT-4500 transistors that forms the power stage to provide 300 amperes of current. The law frequency power Darlington block MT-1146 is made up of one driver PT-7511 which feeds six-paralleled PT-7511 transistors that provide 300 Amperes rating. A view of the motor-power conditioner hardware during the final assembly stages is given in Figures (10) and (11).

Figure (10)
Power Conditioning During Assembly

Figure (11)
Final Assembly of Motor and Conditioner

BASE DRIVE SCHEME FOR POWER TRANSISTORS

The particular Darlington power block employed in the electric vehicle propulsion system has an intriguing feature; that is, the availability of a second base terminal. The extra base terminal of the four-terminal power Darlington provides the opportunity to drive reverse current through the emitter and base junction of both the power stage and the driver stage.

A noteworthy base drive scheme was developed for the four terminal Darlington device (2). This base drive has the ability to provide two reverse currents independent of each other allowing the driver stage and power stage of the Darlington to be turned off at their own charge seep-out rates. This two loop control of the reverse current enhances the possibility of a quicker turn-off, Figure (12), when $d_1(t)$ is clocked off $d_2(t)$ is clocked on for a predescribed length of time. The pulse width of $d_2(t)$ is proportional to the amount of time needed to fully turn off the switching device. With $d_2(t)$ clocked high, a high influx of current enters the dot on the primary side. By transformer action a current is induced on the tapped secondary which supplies two independent currents for reverse biasing the device. The magnitude of current needed for the driver stage loop and the power stage loop is dictated by the amount of minority carriers stored in the base-emitter junction of both, respectively. The diodes on the secondary of the current transformer are to provide a high impedance path during the "on" state of the power Darlington to prevent any drive current being shunted to ground. For detailed description and performance testing of the two-loop base drive scheme reference (2) should be consulted.

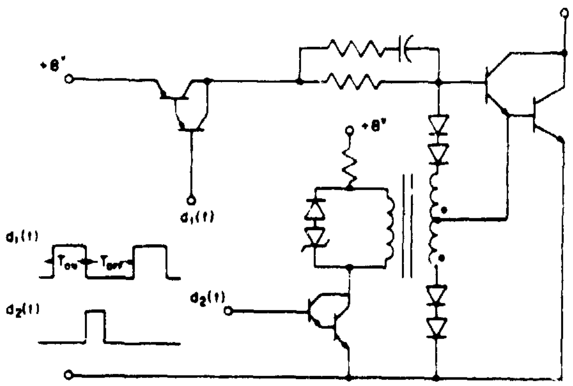

BASE DRIVE CIRCUIT

Figure (12)
Schematic of Base Drive Circuitry

MOTOR-POWER CONDITIONER (M.P.C.) TEST RESULTS

The motor-power conditioner (M.P.C.) are shown during dynamoter load testing in Figure (13). A typical wave form of the phase current during motoring, with d.c. line current chopper fully operative is shown in the oscillogram of Figure (14) at partial load conditions (72.6 Amperes), with corresponding line to line voltage oscillogram given in Figure (15).

Figure (13)
Motor-Conditioner Unit During Dynamometer Load Testing

Also, shown in Figure (16) is an oscillogram of the collector to emitter voltage across the chopper transistor Q_M, while in Figure (17) the corresponding oscillogram of current through Q_M is given. Furthermore, the oscillogram of the current through the chopper inductor under the same operating load conditions is shown in Figure (18).

The motor-power conditioner system was further tested while the chopper was completely in the "on" operating mode at all times. The line current was 146.6 Ameres at a motor speed of 7755 r.p.m. This corresponds to a motor net output power of 16 HP. The corresponding oscillogram of the phase current for this case is given in Figure (19) with corresponding line to line voltage waveform shown in the oscillogram of Figure (20). The corresponding collector to emitter voltage across one of the inverter transistor switches is shown in the oscillogram of Figure (21).

A typical wave form of the phase current during regenerative braking, with chopper control in operation is depicted in the oscillogram of Figure (22) at a current of 95 Amperes peak, with the corresponding line to line voltage oscillogram depicted in Figure (23). Also, depicted in Figure (24) is an oscillogram of the current through the chopper transistor, Q_B, during this regeneration condition. Many other voltage and current oscillograms under various loading conditions and machine tap positions were obtained but limitations on publication space will not permit including them here. For further details reference (1) should be consulted.

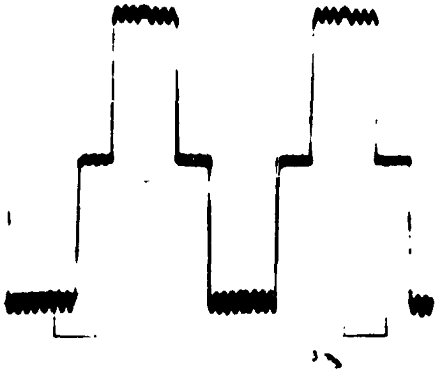

Figure (14)
Phase Current at 72.6 Amperes D.C. Line Current With Chopper Operating

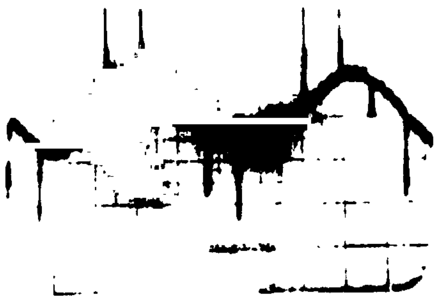

Figure (15)
Line to Line Voltage at 72.6 Amperes D.C.

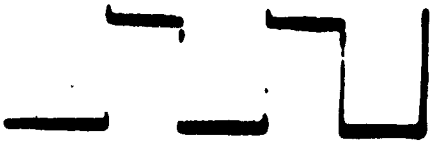

Figure (16)
Voltage Across Q_M at 72.6 Amperes D.C.

Figure (17)
Current Through Q_M at 72.6 Amperes D.C. Line

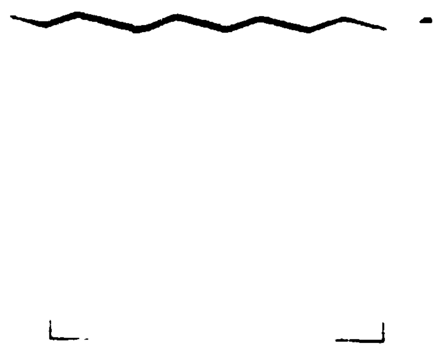

Figure (18)
D.C. Line Current With Chopper Operating-Average Value 72.6 Amperes

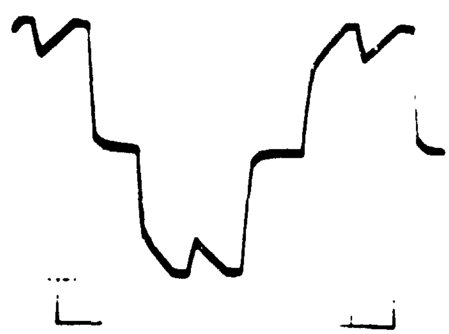

Figure (19)
Phase Curr--t at 146.6 Amperes D.C.

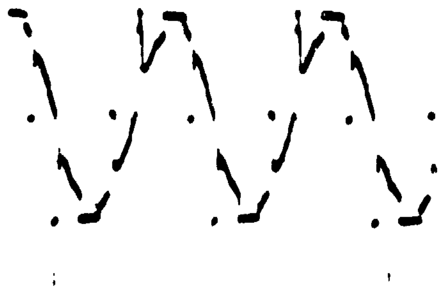

Figure (20)
Line to Line Voltage at 146.6 Amperes D.C.

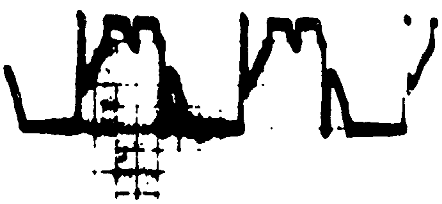

Figure (21)
Voltage Across an Inverter Switch at 146.6 Amperes D.C.

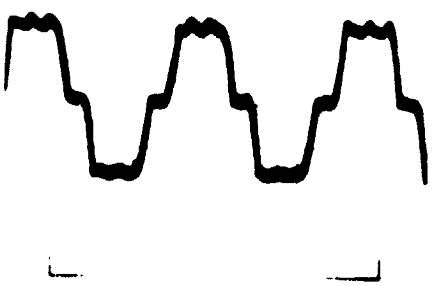

Figure (22)
Phase Current at Regenerative Braking at 95 Amperes D.C.

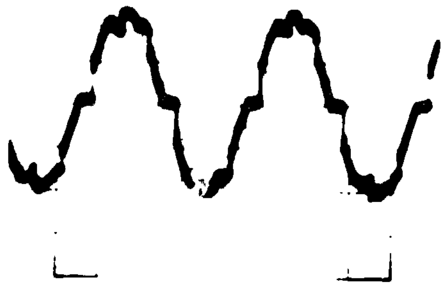

Figure (23)
Line to Line Voltage at Regenerative Braking at 95 Amperes D.C.

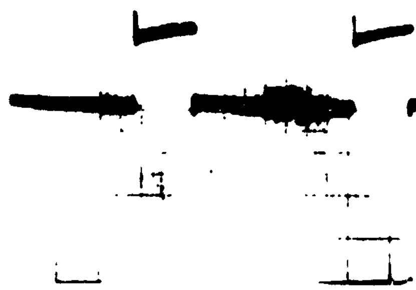

Figure (24)
Current Through Q_8 at Regenerative Braking at 95 Amperes D.C.

Numerous load tests were conducted on the M.P.C. unit given here ranging from fractional to rated as well as over rated load conditions. Complete documentation of these test results are to be found in reference (1). However, a typical and representative sample of these results is given here. Foremost among the tests conducted on this M.P.C. unit was a two-hour 16 HP load run to evaluated the thermal, loss and efficiency characteristics of the unit during practical continuous use. During this two hour (slightly above rated) test it was found out that the breakdown of the input, output, loss powers and other data are as given in Table (1).

Table (1)

Two Hour 16 HP Test Run

Quantity	Test Value
D.C. Line Voltage	120.0 volts
D.C. Line Current	133.7 Amperes
Motor Speed	7813 R.P.M.
Tap Position	Two Turns/Coil
M.P.C. Unit Input Power	15341 Watts
P.C. Losses	2432 Watts
Motor Armature Ohmic Losses	341 Watts
Motor Rotational Losses	517 Watts
M.P.C. Unit Output Power	12051 Watts
Motor Efficiency, η_M	93.4%
P.C Efficiency, $\eta_{P.C.}$	84.1%
M.P.C. Combined Efficiency, $\eta_{M.P.C.}$	78.6%

Other runs with various motor speeds, currents and winding tap positions were made and loss as well as efficiency data of these runs are to be found in reference (1). Based on this set of data numerically simulated M.P.C. overall drive cycle efficiencies for the SAE drive cycle J227a-schedule-D were found to be as follows:

$\eta_{M.P.C.}$ = 76%, η_M = 90.46%

and $\eta_{P.C.}$ = 84.47%

A peak horsepower of more than 22 HP for one minute was reached by the motor-power conditioner unit, where transistor voltage transients due to high current switching precluded higher loads unless some P.C. design changes were made. However, thermal motor characterictics indicated capability of reaching the goal 35 HP for one minute without any difficulty.

FUTURE DEVELOPMENTS AND CONCLUSIONS

A prototype of an electronically commutated brushless d.c. motor for electric passanger vehicle propulsion has been built. Motor efficiencies and other operating characteristis exceeded the preset (required) goals with motor rated efficiency better than 93.4%. An overall motor weight of less than 85 Lbs was reached. The scheme at hand offered the use of control of motor torque-speed characteristics through winding tap changing as an option in lieu of part, or all, of a transmission function in the drive train. The majority of the preset goals for the power conditioner were met. However, some design changes may be necessary to improve the efficiency and to be able to meet the 35 HP for one minute as a peak rating. These necessary improvements in the power conditioner in addition to further motor design improvements will be reported on in conclusion to phase (II) of this project.

ACKNOWLEDGEMENTS

These authors wish to acknowledge the Electric and Hybrid Vehicle Office of the NASA-Lewis Research Center and the Electric and Hybrid Vehicle Division of DOE for their financial support of this project under Phase (I) of NASA Lewis Contract No. DEN3-65. In particular we wish to acknolwledge Mr. Edward Maslowski of NASA-Lewis for his many comments and useful as well as stimulating suggestions without which this work would have been left incomplete. We wish to acknowledge Messers. D. J. Shortt, R. Carter, P. S. Coulon and C. Ford for their work on the design, fabrication and testing of many of the subsystems of this M.P.C. Unit, all of VPI and SU, Blacksburg, VA and Inland Motor R and D, Radford, VA, respectively.

REFERENCES

[1] Demerdash, N. A., Lee, F. C. and Nehl, T. W., "An Improved Electronically Commutated Brushless D.C. Motor for Electric Passenger Vehicle Propulsion Phase (I)", A Final Report to Phase (I) of NASA-Lewis/ Contract No. DEN3-65, to be submitted to NASA Lewis Research Center, Cleveland, OH.

[2] Carter, R. A., and Lee, F. C., "A New Base Drive for Transistorized Electric Vehicle Propulsion", Power Con 7, Proceedings, 1980.

1. Report No. NASA CR 168053	2. Government Accession No.	3. Recipient's Catalog No.

4. Title and Subtitle

Improved Transistor-Controlled and Commutated Brushless DC Motors for Electric Vehicle Propulsion

5. Report Date

January 1, 1983

6. Performing Organization Code

7. Author(s)

N. A. Demerdash, R. H. Miller, T. W. Nehl, and T. A. Nyamusa

8. Performing Organization Report No.

10. Work Unit No.

9. Performing Organization Name and Address

Virginia Polytechnic Institute and State University
Blacksburg, Virginia 24061

11. Contract or Grant No.

DEN 3-65

13. Type of Report and Period Covered

Contractor Report

12. Sponsoring Agency Name and Address

U. S. Department of Energy
Office of Vehicle and Engine R&D
Washington, D.C. 20545

14. Sponsoring Agency Code

DOE/NASA/0065-83-1

15. Supplementary Notes

Final report. Report prepared under Interagency Agreement DE-AI01-77CS51044. Project Manager, Edward Maslowski, Transportation Propulsion Division, NASA Lewis Research Center, Cleveland, Ohio 44135.

16. Abstract

The development, design, construction, and testing processes of two electronically (transistor) controlled and commutated permanent magnet brushless dc machine systems, for propulsion of electric vehicles are detailed in this report. One machine system was designed and constructed using samarium cobalt for permanent magnets, which supply the rotor (field) excitation. Meanwhile, the other machine system was designed and constructed with strontium ferrite permanent magnets as the source of rotor (field) excitation.

These machine systems were designed for continuous rated power output of 15 hp (11.2 kw), and a peak one minute rated power output of 35 hp (26.1 kw). Both power ratings are for a rated voltage of 115 volts dc, assuming a voltage drop in the source (battery) of about 5 volts. That is, an internal source voltage of 120 volts dc.

Machine-power conditioner system computer-aided simulations were used extensively in the design process. These simulations relied heavily on the magnetic field analysis in these machines using the method of finite elements, as well as methods of modeling of the machine-power conditioner system dynamic interaction. These simulation processes are detailed in this report.

Testing revealed that typical machine system efficiencies at 15 hp (11.2 kw) were about 88% and 84% for the samarium cobalt and strontium ferrite based machine systems, respectively. Both systems met the peak one minute rating of 35 hp. Under a standard SAE drive cycle J227a Schedule D, the cycle efficiencies were found to be 84% and 75%, for the samarium cobalt and strontium ferrite based systems, respectively.

17. Key Words (Suggested by Author(s))

Electric vehicle
Electric propulsion
Electronic commutation
Permanent magnet motor
Computer simulation

18. Distribution Statement

Unclassified - unlimited
STAR Category 33
DOE Category UC-96

19. Security Classif. (of this report) Unclassified	20. Security Classif. (of this page) Unclassified	21. No. of Pages	22. Price*

* For sale by the National Technical Information Service, Springfield, Virginia 22161

NASA-C-168 (Rev. 10-75)